Investigation of Charged Aerosol Transport and Deposition in Human Airway Models

A thesis submitted for the degree of Doctor of Philosophy

by

Diew Koolpiruck

Electronic and Computer Engineering

School of Engineering and Design, Brunel University

March 2005

Abstract

Several theoretical and experimental studies of charged aerosol deposition in human airways have been reported. These studies suggest that higher charge values on particles lead to improve deposition efficiency in the human lung, especially in the alveolar region. Most of the previous numerical studies in realistic 3D geometrical models have been investigated only for uncharged particles. Hence, this research was aimed at numerically investigating aerosol transport and deposition by including the effect of electrostatic forces (both space and image charge forces). The numerical models that have been developed and presented in this thesis, treat the aerodynamics and electrodynamics as a coupled problem and successfully integrate both mechanisms.

The physical model of the human lung used for this research consists of three sub-models: a 3D bifurcation airway model, a 3D reconstructed airway model representing the tracheobronchial region, and a 2D alveolar airway model representing the alveolar region. The airflow dynamics in these geometrical models were carried out using a Computational Fluid Dynamic software (CFD) with given boundary conditions related to corresponding breathing conditions. The space charge force was calculated using the Particle Mesh (PM) method, and the image charge force was computed using the mesh configuration. Both airflow dynamics and electrodynamics are integrated in the newly developed software, and the particle trajectories are then calculated.

The numerical study of electrostatic forces is primarily focused on the submicron particle. The numerical study in the 3D tubular airway model gives a better understanding of parameters affecting the predicted deposition efficiency. The numerical study in the 3D tubular airway model focuses on the transport and deposition of particles near the branching regions between the parent and daughter tubes, where airflow profile is significantly altered, and secondary airflow also arises. Many charged particles are deposited near the

carinae by the strong skewed axial velocity and image charge force. The space charge will influence the deposition efficiency if the number concentration of particles is high. Similarly, the charged particles in the 3D reconstructed airway model tends to have the deposition pattern near the branching regions, depending on the local airflow and charge value. In the 2D alveolar model, the image charge force can improve deposition efficiency.

The outcome of this research clearly shows how the electrostatic forces play an important role in aerosol transport and deposition in human airways. The integrated numerical model provides a valuable tool for respiratory clinicians and the pharmaceutical industry to study the complex mechanism of drug aerosol deposition in human airways. Although this model is adequate for the intended purpose, it can be further improved by extending this work to develop a complete 3D model of entire human airways incorporating the full breathing cycle. Such a model would require extensive computing facilities, nevertheless it would be an enormous benefit to develop a better treatment for respiratory diseases.

Acknowledgements

I would like to express my gratitude to Professor Wamadeva Balachandran, who is my first supervisor and head of research group, not only for his guidance and support throughout my research, but also for allowing me to join his research group. I also would like to thank Dr. Simant Prakoonwit, my second supervisor, for his suggestions, his valuable comments and encouragement.

I would like to thank Dr. Rommanee Jirawimut and Dr. Pakorn Keawprakoonpong for their suggestions and support with warm friendship and kindness. I also would like to thank Dr. Jeremy Ahern and Mr. Mark OLeary for their corrections through my thesis.

Members of Systems Engineering department, especially Linda Hedges, Karen Thomson and Margaret Hudson are thanked for their kind support. I wish to thank all my friends in Electronic Systems and Information Technology Research Group for their friendship.

I am grateful to the Overseas Research Students Awards Scheme (ORS) and System Engineering department for their financial support for my study. I also would like thank King Mongkut's University of Technology Thonburi for granting me study leave.

Finally, special thanks go to my family for their unconditional love and inspiration encouragement throughout these years.

List of Nomenclature

1D	One Dimension
2D	Two Dimension
3D	Three Dimension
CAD	Computer Aided Design
CIC	Cloud In Cell
CFD	Computational Fluid Dynamics
CMD	Count Median Diameter
CMAD	Count Median Aerodynamic Diameter
CT	Computed Tomography
DPI	Dry Powder Inhaler
FEA	Finite Element Analysis
FFT	Fast Fourier Transform
ICRP	International Commission on Radiation Protection
IFFT	Inverse Fast Fourier Transform
MDI	Metered Dose Inhaler
MMD	Mass Median Diameter
MMAD	Mass Median Aerodynamic Diameter
MRI	Magnetic Resonance Imaging
NCRP	National Council on Radiation Protection and Measurement
NGP	Nearest Grid Point
PDE	Partial Differential Equation
PIC	Particle-In-Cell
PM	Particle-Mesh
PP	Particle-Particle
pMDI	pressurised Metered Dose Inhaler
PET	Positron Emission Tomography
SPECT	Single Photon Emission Computed Tomography
TSC	Triangular Shaped Cloud

Contents

List of Figures

List of Tables

List of Symbols

α	ratio of P_{spc} to P_{img}
α_w	Womersley number
β	fraction of dispersed phase volume to the total mixed volume
γ	mass loading
ε	relative permittivity
ε_0	permittivity of free space
ε_r	dielectric constant
ε_s	steady boundary layer
θ_g	gravity angle
μ	fluid viscosity
ν	kinematic viscosity
ρ_p	particle density
ρ_f	fluid density
ρ_q	charge density
σ	Boltzmann constant
τ_c	average time between particle-particle collision
τ_d	time constant of charge decay function
τ_e	dimensionless residence time
τ_v	relaxation time
χ	dynamic shape factor
ω	angular frequency
Γ	diffusion efficiency
Δt	sampling time
Φ	field variable
Φ_e	electrical potential
Ψ	ratio of particle density to fluid density

d_p	particle diameter
e	electronic charges ($e = 1.6 \times 10^{-19} C$)
f	breathing frequency
f_{Re}	drag factor
g	gravitational acceleration
$\mathbf{g}$	gravitational acceleration vector
i	internal energy
m_p	particle mass
p	pressure
n_L	charge limit
q	charge value
r_c	critical radius
t	time
$\mathbf{u}$	velocity vector of fluid (air)
$\mathbf{u_p}$	velocity vector of particle
u	vector of velocity component in x - direction
v	vector of velocity component in y - direction
w	vector of velocity component in z - direction
$\mathbf{x}$	position vector
$\mathbf{x_p}$	position vector of particle
x	vector of position component in x - direction
y	vector of position component in y - direction
z	vector of position component in z - direction
B	particle mobility
C_c	Cunningham correction factor
C_D	drag coefficient
C_M	added mass coefficient
D	tubular diamter
De	Dean number

E	electrical field
E_b	breakdown Electrical field
$\mathbf{E}$	vector of electrical field
$\mathbf{F}$	vector of force
$\mathbf{F}_{Bn}$	vector of Brownian force
$\mathbf{F}_D$	vector of drag force
$\mathbf{F}_H$	vector of Basset history force
$\mathbf{F}_L$	vector of lift force
$\mathbf{F}_S$	vector of fluid stress gradient force
$\mathbf{F}_S$	vector of wall interaction force
$\mathbf{F}_g$	vector of gravity force
$\mathbf{F}_{img}$	vector of image charge force at position $\mathbf{x}$
$\mathbf{F}_{spc}$	vector of space charge force at position $\mathbf{x}$
H	cell width
N	particle per unit volume
N_g	numbers of grids
N_i	concentration of ions
N_p	numbers of particles
P_d	deposition efficiency by diffusion
P_i	deposition efficiency by impaction
P_{img}	deposition efficiency by image charge
P_s	deposition efficiency by gravity
P_{s+img}	deposition efficiency by the combined mechanism of gravity and image charge
P_{spc}	deposition efficiency by space charge
P_E	deposition efficiency in extrathoracic region
P_T	total deposition efficiency
Q	inhalation flow rate
Re	Reynolds number
S	cloud shape function

St	Strouhal number
Stk	Stoke number
T	temperature
U	average velocity
V_p	particle volume
W	assignment function

Chapter 1

Introduction

The field of inhaled pharmaceutical aerosol plays a key role in drug delivery to human airways. Many indicators suggest that this field will grow rapdily as new drugs are developed for inhalation therapy. The topic of inhaled drug deposition in the human lung has been continuously studied for many decades. Due to the complexity of lung anatomy, the investigation of airflow and aerosol transport has been carried out based on the assumptions of simple airflow dynamics and simple tubular structures of the airways. Nowadays, owing to the advent of high-performance computer systems, it is possible to develop more realistic computer models to accommodate the complex airflow and aerosol transport in the human respiratory system.

Investigations of charged aerosol transport and deposition in human airways are studied mainly by numerical techniques. These researches require a fundamental understanding of the anatomy and morphology of the respiratory tract, physiology of breathing, and the basic mechanisms of aerosols, which are overviewed in section 1.1. In addition, the devices for aerosol inhalation and medical method for assessment of aerosol deposition are detailed in section 1.1. The existing aerosol deposition models are reviewed in section 1.2. The motivation, aim and objectives, and contribution to knowledge are then given in section 1.3, 1.4 and 1.5, respectively. Finally, the outline of this thesis is provided in section 1.6.

1.1 Background

1.1.1 Anatomy and morphology of respiratory tract

Anatomical parts of human respiratory system shown in Figure 1.1 can be classified into 3 main regions: extrathoracic, tracheobronchial, and alveolar. The summary of the subdivisions of the respiratory tract based on Weibel's lung model is given in Table 1.1.

1.1.1.1 Extrathoracic region

This region comprises the anterior nasal passage (ET1) and posterior nasal passage, larynx, pharynx, and mouth (ET2). The function of this region is to condition and clean the inhaled air and conduct air into the lungs. Cleaning begins by impaction or diffusion in the anterior nares, and continues with filtration by hairs behind the nasal entrance. The larynx is a part of the upper respiratory tract between the pharynx and trachea, and contains the vocal cords to reduce the air passage to a variable-size slit. It is a major resistive part to airflow and increases airflow velocity, leading to particle impaction on the wall of trachea.

1.1.1.2 Tracheobronchial region

The tracheobronchial region (TB) consists of bronchial (BB) sub-region, (also known as upper bronchial including the trachea, bronchi), and bronchiolar (bb) sub-region (also called lower bronchial including bronchioles and terminal bronchioles). Figure 1.2 shows a cast of the human airways that mainly represents the tracheobronchial region. The bronchial sub-region (BB) is a part of the air conducting system within the thorax and accounts for Weibel's generations 0 to 8. The airway tree starts with a single tube representing the trachea, which is kept open by rings of cartilage. The trachea divides into two main bronchi, which further divide into the lobar bronchi; three enter into the right lung and two enter into the left lung. The volume of trachea and bronchi

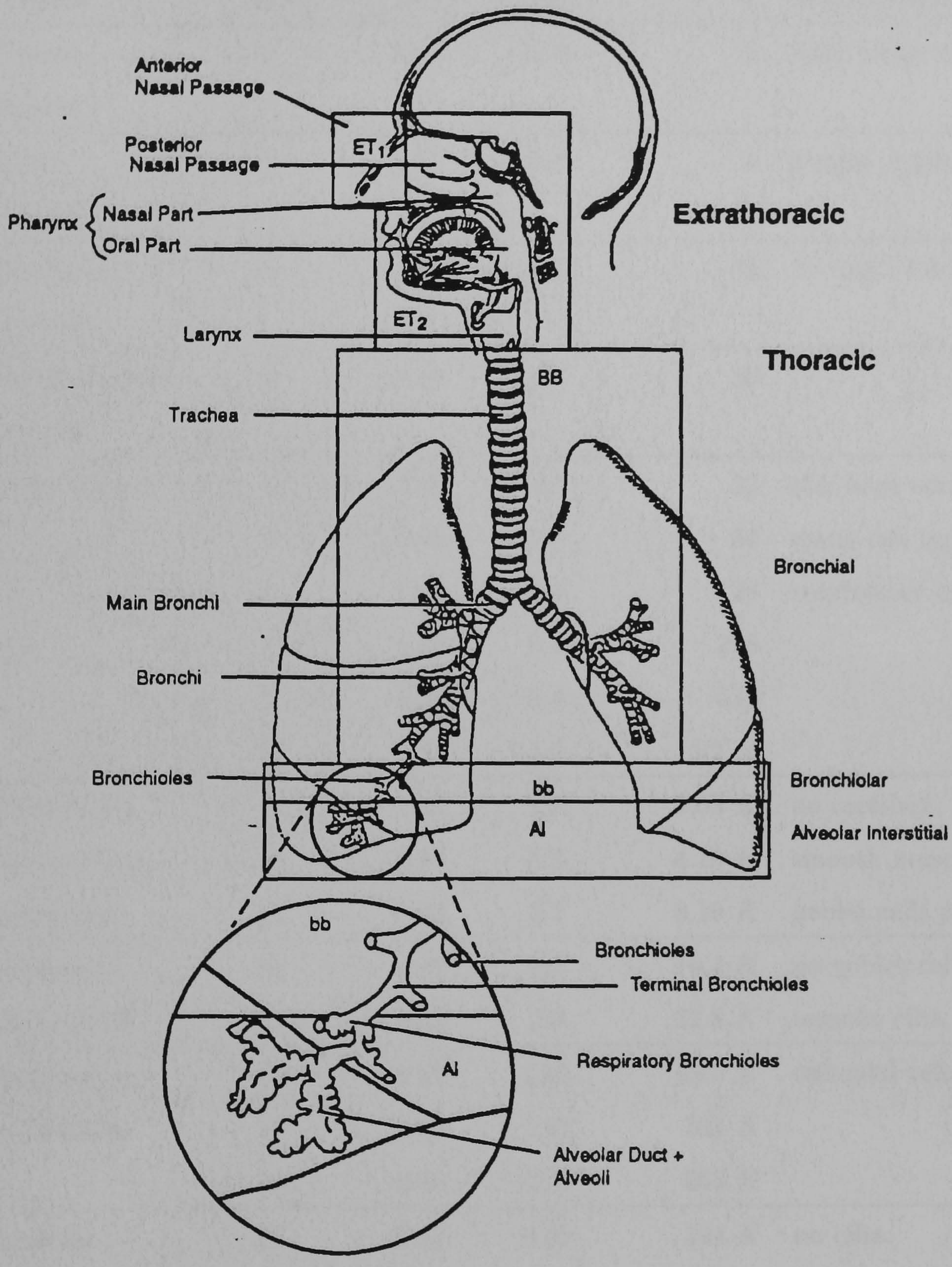

Figure 1.1: Anatomical regions of human respiratory tract [140]

Table 1.1: A summary subdivision of human respiratory tract (adapted from [193])

Airways name	generation number	diameter (mm)	length (mm)	number per generation	histological note
Trachea	0	18.0	120	1	wealth of goblet cells
Primary bronchi	1	12.2	47.6	2	right larger than left
Lobar bronchi	2	8.30	9.0	5	3 right, 2 left
Segmental bronchi	3	5.60	7.6	19	10 right, 9 left
Sub-segmental bronchi	4	4.50	12.7	20	
Small bronchi	5	3.50	10.7	32	still have cartilage;
	6	2.80	9.0	64	many cell types and
	7	2.30	7.6	128	respiratory epithelium
	8	1.86	6.4	256	
	9	1.54	5.4	512	
	10	1.30	4.6	1.02 K	
Bronchioles primary and secondary	11	1.09	3.9	2.05 K	no cartilage;
	12	0.95	3.3	4.10 K	smooth muscle, cilia,
	13	0.82	2.7	8.19 K	goblet cells present
Terminal bronchioles	14	0.74	2.3	16.4 K	no goblet cell; smooth
	15	0.66	2.0	32.8 K	muscle, cilia, and
Respiratory bronchioles	16	0.60	1.65	65.5 K	cuboidal cells
	17	0.54	1.41	131 K	
	18	0.50	1.17	262 K	
Alveolar duct	19	0.47	0.99	524 K	no cilia;
	20	0.45	0.83	1.05 M	cuboidal cells
	21	0.43	0.70	2.10 M	
	22	0.41	0.59	4.19 M	
	23	0.41	0.50	8.39 M	
Alveoli	24	0.244	0.238	300 M	

is approximately $5 \times 10^{-5}\ m^3$, and the surface area of bronchi (Weibel's generation 1-8) is about $2.9 \times 10^{-2}\ m^2$. The bronchiolar sub-region (bb) is the second part of conducting airways represented by generation number 9 to 15. The bronchioles branch dichotomously and are randomly oriented with respect to gravity. The volume of nonrespiratory bronchioles is nearly $5.0 \times 10^{-5}\ m^3$ and the surface area of that is approximately $2.4 \times 10^{-1}\ m^2$.

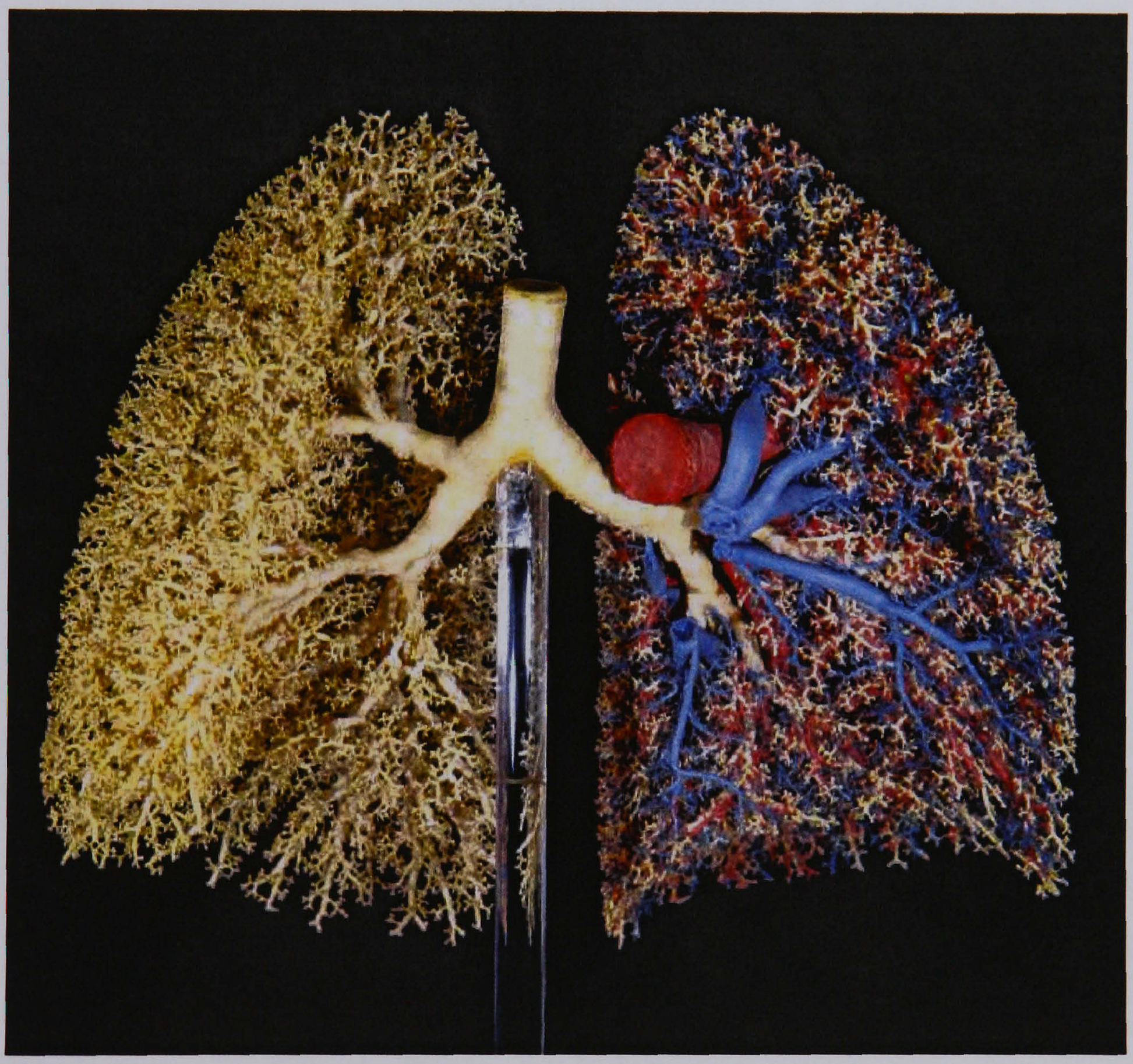

Figure 1.2: Detailed cast of the human respiratory airways (Anterior view). Image courtesy of Weibel [193]

1.1.1.3 Alveolar region

The alveolar region includes respiratory bronchioles, alveolar ducts, alveolar sacs, and alveoli. The structures of the alveolar region are shown in Figure

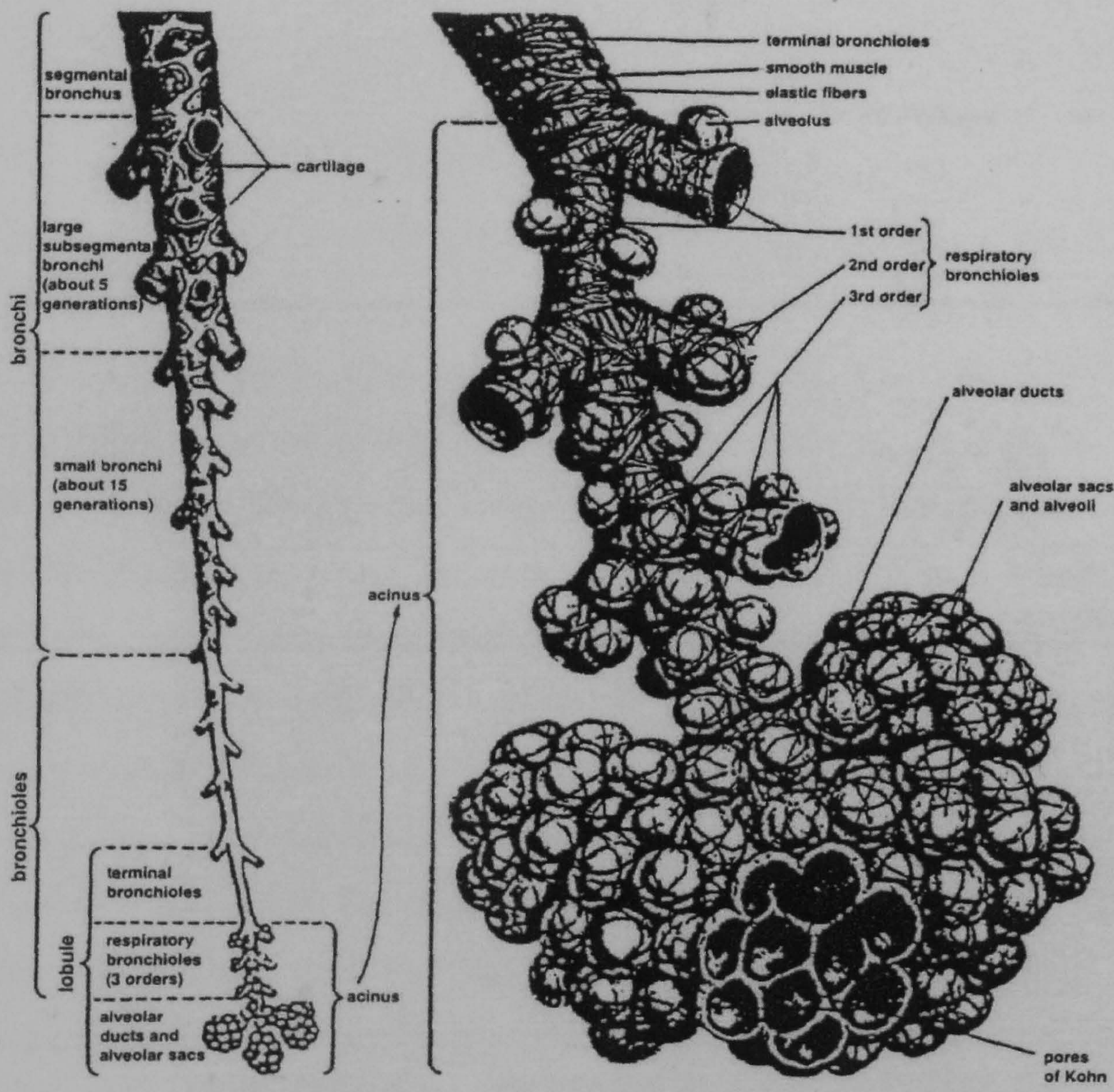

Figure 1.3: Structure of Bronchiolar and Alveolar parts [72]

1.3. Their main function is to exchange oxygen and carbon dioxide with blood, and are represented by Weibel's generation number 16-24. Most of the inhaled particles reaching this region are deposited by sedimentation and/or diffusion. The terminal bronchioles branch into respiratory bronchioles, which consist of alveolar ducts and alveolar sacs. The total volume of the respiratory bronchioles is approximately 2.0×10^{-4} m^3, and the total surface area is about 7.5 m^2.

1.1.1.4 Morphological lung model

A significant number of morphological lung models have been presented in the literature. The morphological models were obtained by measuring various dimensions of the parts of the respiratory tract. These structures of airways are 3 dimensional in nature and depend on many factors, i.e., age, gender and health conditions. However, many of the airways can be approximated by a cylindrical shape with a small number of parameters: the number of tubes in generation, tube lengths, tube diameters, branching angles, etc,. Morphological models can be grouped into 2 basic types: a deterministic model described by average parameters and a stochastic model provided by the average value, the probability distribution and the correlation of parameters.

Deterministic models are often used to represent numerous morphological models. Weibel [193] published the most influential deterministic model. By measuring dimensions of the major conducting airway branches from the plastic cast of human lungs, he obtained this model. Measurements of branch length and diameter were performed down to generation 4, then were less complete down to generation 10. The small bronchiole measurements were obtained by assuming regular dichotomy and hence predicting the missing measurements. The Weibel-A model assumed that the generation of lung branches symmetrically into two identical daughter branches: generations 0-16 are the tracheo-bronchial region, while generations 17-23 defined the alveolar region. The values of diameters and lengths of the alveolated airways in Weibel-A

model compared to the average anatomical airways are known to be too small and start at high generation numbers. Haefeli-Bleuer and Weibel [74] published a revised model, which addjusts the values of diameters and lengths of the alveolated airways. Additionally, the original Weibel A model corresponds to a lung volume of 4,800 cm^2, while an average adult male has a lung volume approximately 3,000 cm^2. Yu and Diu [200] changed the dimensions to adjust Weibel's lung to a new total volume of 3000 cm^3. The 3D Weibel's model based on the morphological lung data of airway generation 0-12 is given in Figure 1.4. It shows that the Weibel's model is the symmetrical structure of lung model and results in the difference of the lung's shape from the anatomical lungs.

Horsefield and Cumming [90] performed measurements on a resin cast of human lungs, starting from the trachea down to airways 0.7mm in diameter. They estimated that there are 27,992 terminal bronchioles in the lungs. Later, Horsefield et al. [91] presented another irregular structure that defines the number of sequence tubes leading from airways closed to air-sacs and counting upward to the trachea. The assigned generation number increases from generation number 0 at the end of which branches are equal or greater than 0.7 mm. in diameter toward to the trachea. Yeh and Schum [198] developed different dimension of a morphological lung model based on the five lobes of lungs including left upper, left lower, right upper,right medium and right lower.

For the stochastic morphological model, Koblinger and Hofman [107] derived parameters of distributions of the lengths, diameters and branching angles, and the correlation between them. Note that all of the above morphological models are measured based on normal adult lungs. Subjects with lung diseases affecting part of the lungs such as asthma, cystic fibrosis etc., have a geometry different to normal (Finley [57]), thus geometrical models for specific lung diseases are required for more accurate studies in physiological and aerosol transport studies.

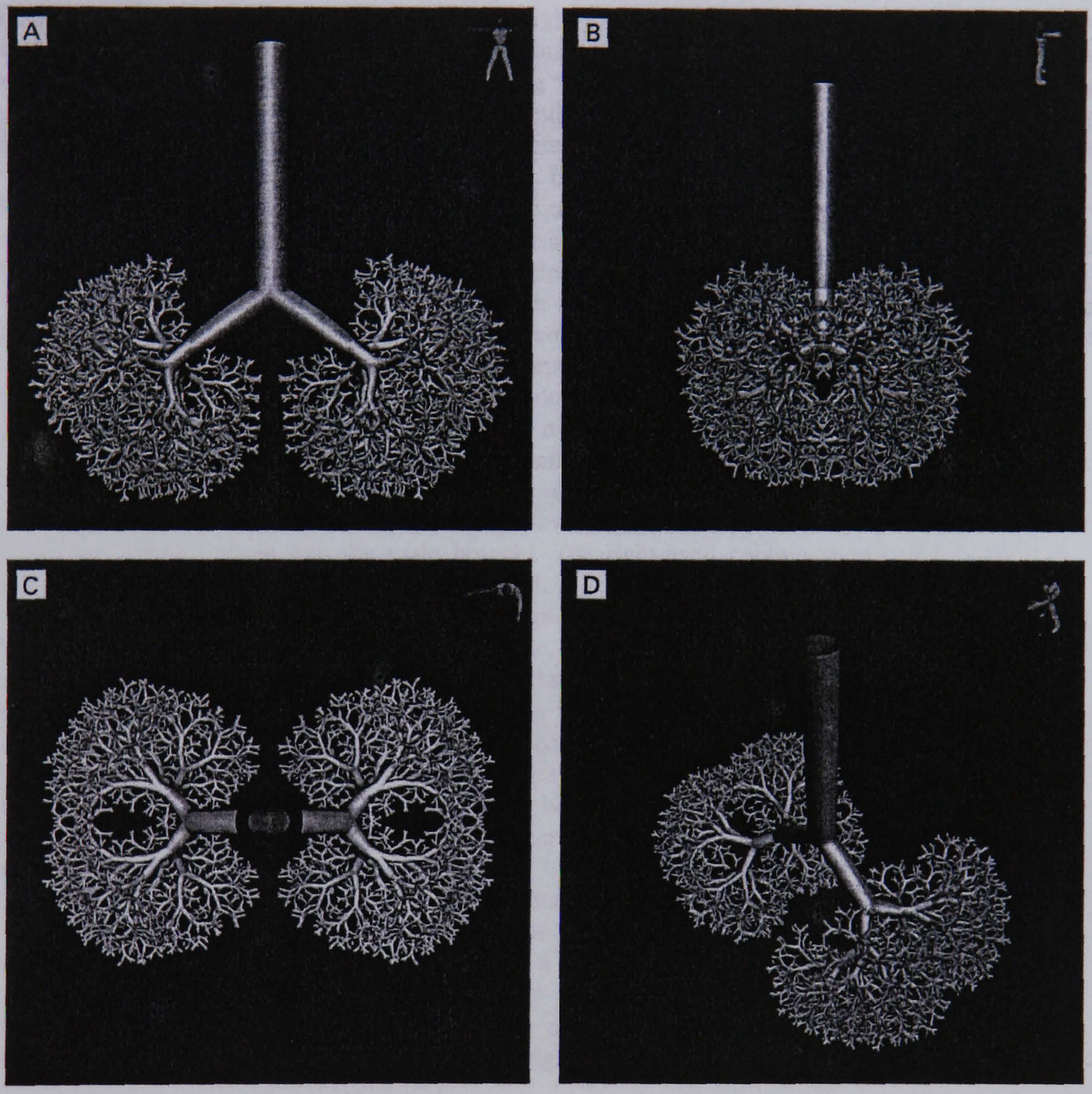

Figure 1.4: Three-dimensional branching airway structure of 0-12 generations based on Weibel's morphometrical model (A-Front view, B-Side view, C-Top view, D-Oblique view) [173]

1.1.2 Physiology of respiratory tract

Physiology is an important variable for analysing the fluid dynamic and aerosol transport in the human airway. The physiological parameters (e.g. breathing rate, lung volume) vary slightly among different populations in the world, and also vary between individuals as well. The basic physiological parameters consist of lung volume and ventilation. The diagram of lung volumes with various breathing patterns is shown in Figure 1.5. Lung volume is classified into 2 groups as basic volumes and capacities (combined volumes), which are defined as follow:

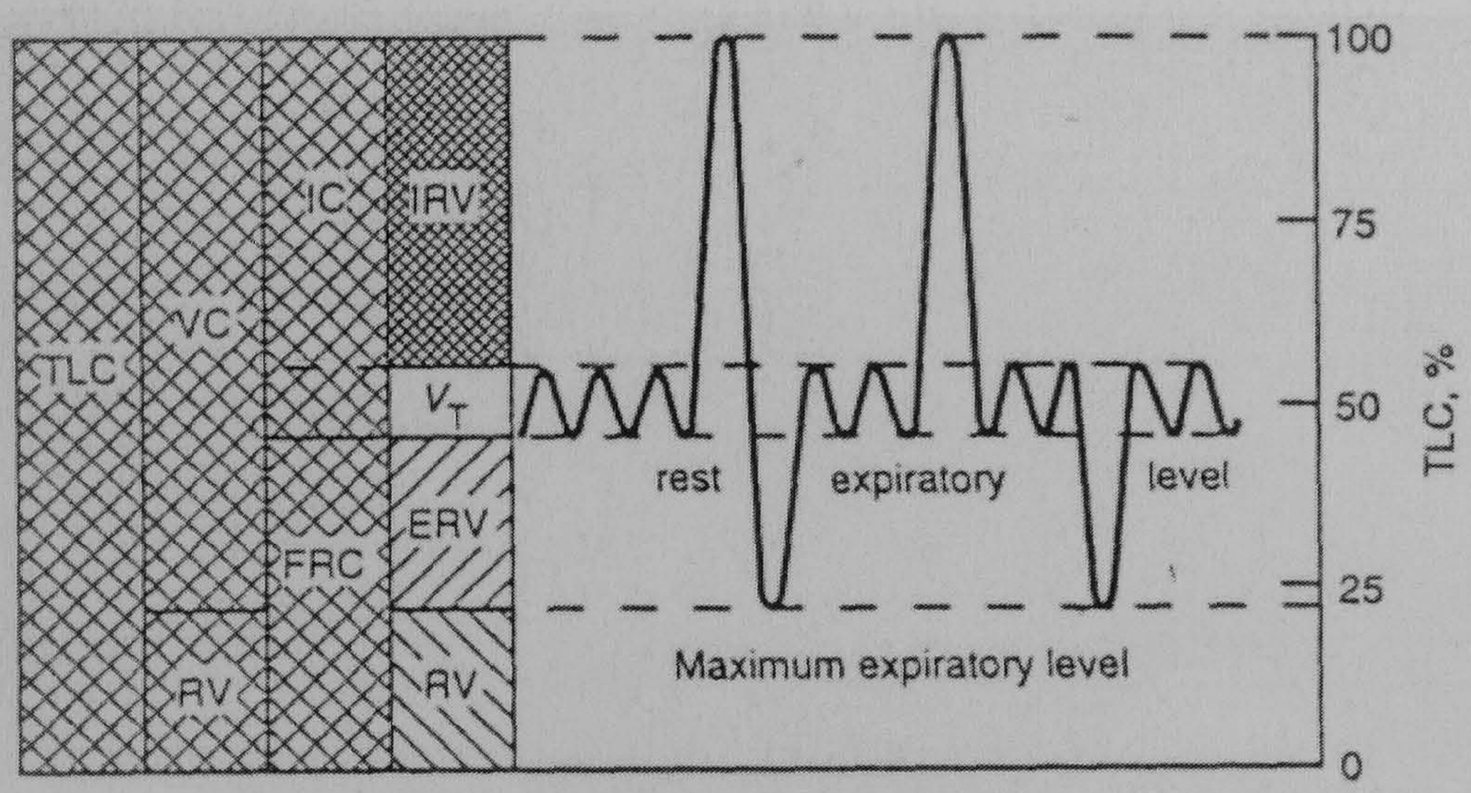

Figure 1.5: Resipiratory volumes ([140])

1. Basic volumes

- *Tidal volume* (V_T): volume of gas exchanged each breath. It can change as ventilation pattern changes.

- *Inspiratory Reserve volume* (IRV): maximum volume that can be inspired, starting from the end of inspiratory position of V_T.

- *Expiratory Reserve volume* (ERV): maximum volume that can be expired, starting from the end of expiratory position of V_T.

- *Residual volume* (RV): volume remaining in the lungs and airways following a maximum expiratory effort.

2. Capacities.

- *Vital Capacity* (VC): maximum volume of gas that can be exchanged in a single breath.

  $VC = V_T + IRV + ERV$

- *Total Lung Capacity* (TLC): maximum volume of gas that the lung can contain.

  $TLC = VC + RV$

- *Functional Residual Capacity* (FRC): volume of gas remaining in the lungs and airways at the end of expiratory position of V_T.

  $FRC = RV + ERV$

- *Inspiratory capacity* (IC): maximum volume of gas that can be inspired from the end of expiratory position of V_T.

  $IC = V_T + IRV$

Ventilation can be defined in terms of respiration rate, ventilation rate, and maximum ventilation, which are defined as follow:

- *Respiratory rate*: the number of breaths per unit time.

- *Ventilation rate* (V_E): total volume inspired or expired per unit time; sometimes known as Minute volume when measured per minute.

  $V_E = f \times V_T$

- *Maximum ventilation*: maximum volume of gas that can be inspired and expired per unit time.

More details of respiratory physiology can be found in [195]. The reference of basic respiratory parameters for workers (both men and women) proposed by ICRP [140] is outlined in Table 1.2. The other recommended reference values of physiology parameters for human respiration with various age, sex and ethnic groups of interest are also given in [140].

Table 1.2: Reference values for human respiration (Adapted from [140])

Physiology parameters	**Average values for workers**
Volume and capacity variables	(L)
Tidal volume (V_T)	0.60
Inspiratory reserved volume (IRV)	3.08
Expiratory reserved volume (ERV)	1.34
Residual volume (RV)	1.96
Vital capacity (VC)	5.02
Total lung capacity (TLC)	6.98
Functional residual capacity (FRC)	3.30
Anatomical dead space (V_D)	0.146
Ventilation rates	$(L \cdot min^{-1})$
Sleep	7.5
Rest, sitting	9.0
Light exercise	25.0
Heavy exercise	50.0

1.1.3 Basic mechanisms of aerosol transport and deposition

Primary aerosol mechanisms in the transport and deposition of aerosols consist of inertial impaction, sedimentation, diffusion and electrostatic forces. Brief details of these mechanisms are summarised below:

- *Inertial impaction*

  Particles with sufficient momentum will be affected by the centrifugal forces generated where the airway network changes direction rapidly. This mechanism is a function of Stokes number, which is directly proportional to particle size and particle velocity. This mechanism is primarily concerned in large airways (Extrathoracic and Upper bronchial regions) because of the high flow rates. Most of the large particles are deposited in these regions due to inertial impaction. However, it is not a significant mechanism for small particles ($d_p \leqslant 1\ \mu m$).

- *Sedimentation*

  Particles of sufficient mass can be deposited by gravity in regions where the particle has a long residence time. In smaller airways and alveolar regions, sedimentation is a dominant mechanism with its maximum removal effect in horizontal airways.

- *Diffusion*

  Particles of sub-micron size have a random Brownian motion due to molecular collisions with gas molecules. The consequence of random Brownian motion may lead to trapping particles on lung walls. The movement of particles by Brownian motion can be regarded as a Markov random process. The probability distribution of random distances is a function of the diffusion coefficient of the particles. Diffusion is an important mechanism for small particle sizes and plays an important role in the alveolar region, where distances are short and residence times

comparatively long.

- *Electrostatic forces*

  The particles invariably carry net electrical charge and this mechanism concerns the effects of electrostatic forces due to these charges. The study of particle deposition in the respiratory tract generally accounts for only the space and image charge forces. The space charge is due to the mutual repulsion of particles, which is a function of concentration of particles and charge values on the particles. The image charge force is the interaction of charged particles with the lung wall.

1.1.4 Medical devices for drug delivery

Medical devices for drug delivery to the lung are important in delivering high concentrations of drug with potential therapeutic effects directly into lung airways . Based on techniques to generate inhaled aerosols, these inhaler devices can be categorised into three types: Metered-Dose Inhalers (MDIs), Dry-Powder Inhalers (DPIs) and nebulizers. Both MDIs and DPIs are the most common forms of drug aerosol delivery, because they are pocket-sized, hand-held devices. Nebulizers are typically used for intensive therapy that require hospitalisation. Table 1.3 shows the percentage of Asthma drug inhaler systems on the pharmaceutical market in the United States and Britain. It indicates that MDI devices are still the most popular inhaler devices on the market.

Currently many new inhaler devices are being developed. Optimal drug delivery to the lung is determined by the complex interaction among inhaler devices, the drug formulation and the patient who uses these devices. This section aims to explore these major categories of inhaler devices.

Table 1.3: Percentage of asthma drug inhaler systems on the pharmaceutical market in United States and Great Britain [28]

Drug Inhaler system	United States	Britain
Metered dose inhalers	81%	64%
Dry Powder Inhalers	3%	30%
Nebulizers	16%	6%

1.1.4.1 Metered-Dose Inhalers (MDIs)

The Metered-Dosed Inhaler is the most popular inhaler drug delivery device, commonly known as pMDI (pressurised Metered-Dosed Inhaler). It is a pocket-sized, hand-held, pressurized multiple-dose inhalation delivery system. It also delivers small, precisely measured therapeutic doses, greatly minimizing the risk of side effects. The essential parts of pMDI consist of :

1. A reservoir (or canister), which contains drug suspended or dissolved in liquefied gas propellant.

2. A metering valve for delivering a known volume when depressed.

3. Spray actuator, which is combined with the stem of metering valve. It comprises a twin orifice expansion chamber and spray nozzle to generate spray.

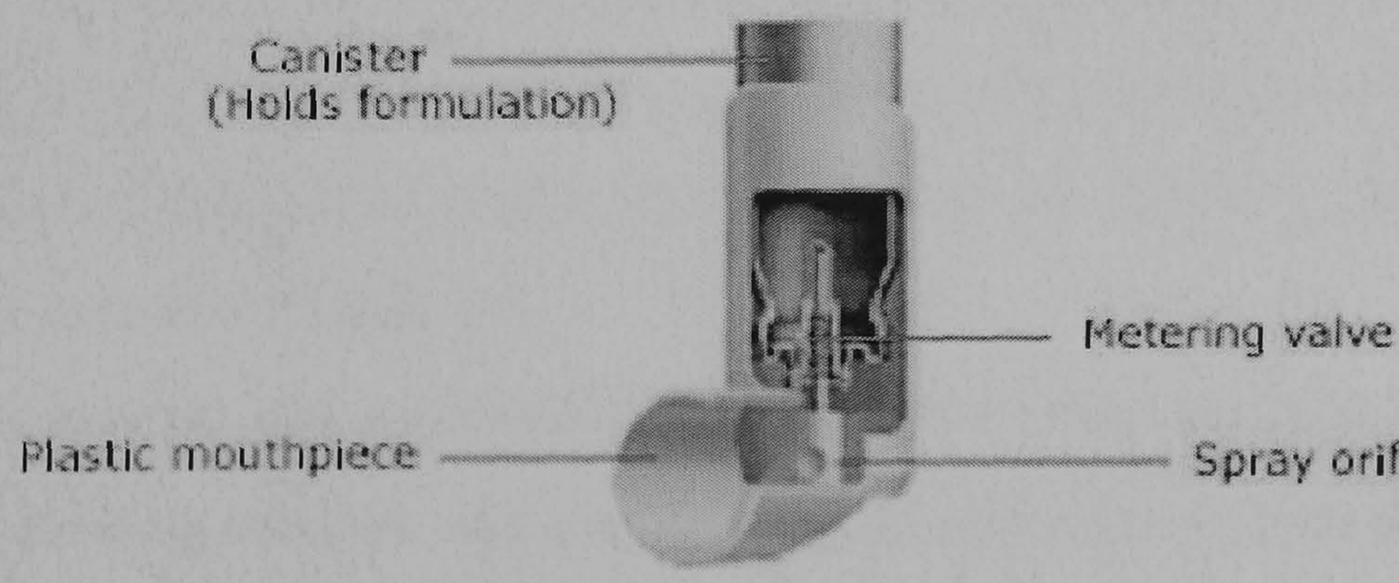

Figure 1.6: Metered-Dosed Inhaler compartment([1])

The mechanism of particle formulation starts after the storage canister is placed down into the actuator. Then the propellant (at high vapour-pressure)

contained under pressure in the canister is released, sending liquid propellant at high speed from the canister which rapidly evaporates. The result is a very fine mist of drug.

Before 1996, all pMDIs were formulated with a mixture of two or three CFC propellants, in which initial droplet diameter is rather high ($\geq$ 10 μm). The amount of drug deposited in the lungs from a CFC-based pMDI averages 10-15 percents of most products ([137]). In addition, the efficiency of drug delivery from pMDI also relied on the patient's use. Optimal inhalation for pMDIs has been suggested by three key elements ([135])as follow.

1. Firing the inhaler during inhalation

2. Inhaling slowly and steadily (about 30 litres/min), so that a complete inhalation takes typically about 5-10 secs.

3. Holding the breath for about 10 secs.

At present pMDIs are reformulated for new propellants with one of the hydrofluoroalkanes (HFAs 134a and HFAs 227) that do not contain ozone-depleting chlorine. The HFA-based formulation yields a higher fine-particle dose, and deposits a greater percentage of dose in the lungs than those of CFC based formulations [113]. Significant novel developments are performed to overcome the problems with the use of pMDIs. The breath-actuated MDI is an example of a design to reduce the problem of time of actuation. Examples of commercial designs of breath-actuated MDIs are shown in Figure 1.7, and also summarised in Table 1.4.

A spacer is an add-on device for MDI to allow droplets more time to evaporate before being inhaled, and produce the smaller particle size and less deposition on the mouth and throat. It requires less co-ordination between actuation and inhalation for decreasing oropharyngeal deposition. However, a electrostatic problem in the spacer can lead to adherence of drug particles to its wall.

(a) General MDI [1]

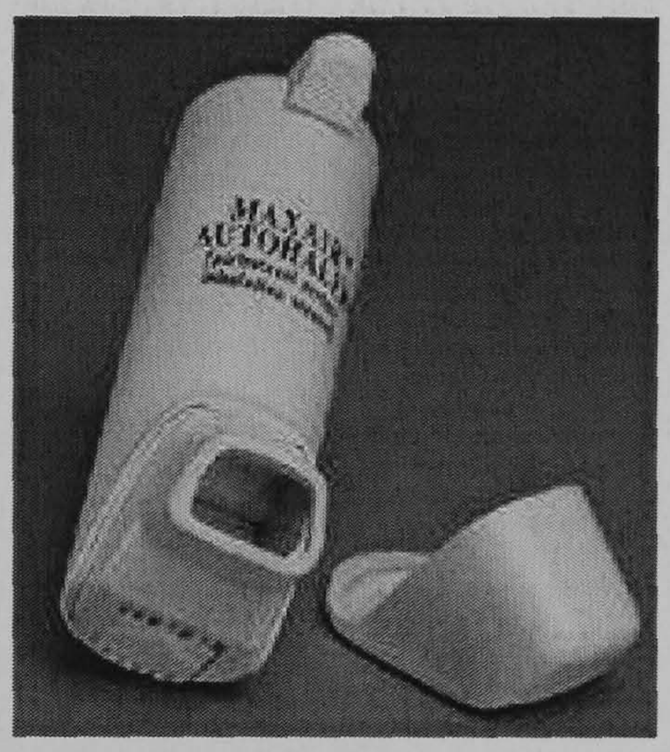

(b) Autohaler [2]

(c) Easi-breathe [148]

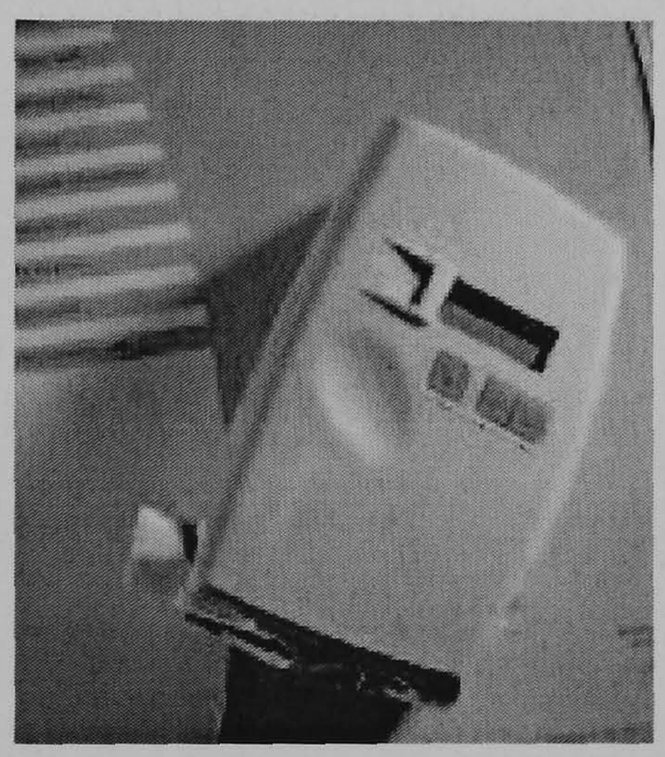

(d) SmartMist [120]

Figure 1.7: Examples of commercial Metered-Dosed Inhaler products

Table 1.4: Examples of commercial Metered-Dosed Inhaler products

Breath-actuated MDI	Manufacturer	Description
Autohaler	3M healthcare, USA	A device distinguished from a standard pMDI; the canister is completely enclosed with in the body of device. The device is primed by lifting a latching lever at the top. The act of inhalation actuates the metering value when the patient breaths in. It eliminates the needs for coordination.
Easi-Breathe inhaler	Norton health-care Ltd.,UK	A device is primed when the mouthpiece is opened and is automatically actuated when patient breaths in. It works on a pneumatic principle. It can be actuated at a very low flow of approximately 20 litres/min
SmartMist	Aradigm Corpo-ration, USA	It is a hand-held breath-actuated micropro-cessor controlled accessory. A microproces sor analyses an inspiratory flow profile which automatically actuates the pMDI.
Spacehaler	Evans medical, USA	This device is a relatively new actuator/ mouthpiece designed to be used in conjunct-ion with a pressurised metered-dose canister. It can reduce the emitted velocity compared to a standard MDI.

MDIs will continue to be one of the most popular drug delivery devices for inhaled drug. Future research for MDI improvement will rely on these main areas; to reduce the marked variability in deposition of drug in the lower bronchial, to reduce the extrathoracic deposition, and to include compliance monitors in delivery devices [137].

1.1.4.2 Dry-Powder Inhalers

A Dry-Powder Inhaler (DPI) is a small, pocket-sized, portable inhaler device, designed to disperse small powder particle into the lungs during a single breath. The Spinhaler was the first successful commercial DPI for the delivery of disodium cromoglycate. Various different dosing principles of DPIs usually involve the small micronized drug particles mixed with larger carriers, such as lactose particles. The size of micronized drug particles should have an aerodynamic diameter of about 2-4 μm or smaller to have a good chance to reach the lower airways. The structure of all DPIs typically comprises of 4 basis features: dose-metering, aerosolisation, deaggregation, and adaptor parts. The general concepts of aerosol generation from DPIs are given in Figure 1.8.

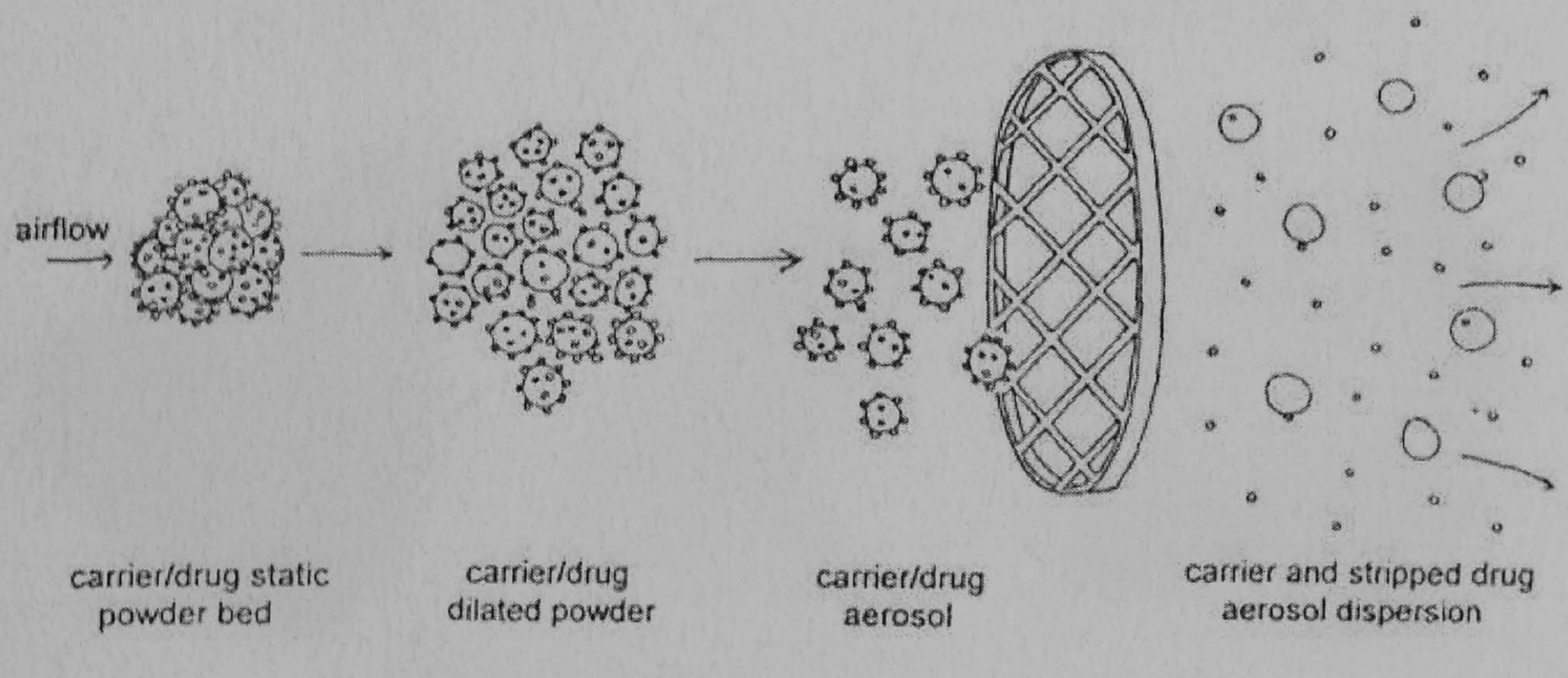

Figure 1.8: Concept of aerosol generation in Dry-Powder Inhaler ([19])

When the inhalation starts, it initiates the dispersion of particles. The pressure difference between the air contained in the powder and the motion of air passing over the powder is developed and then the powder is fluidised.

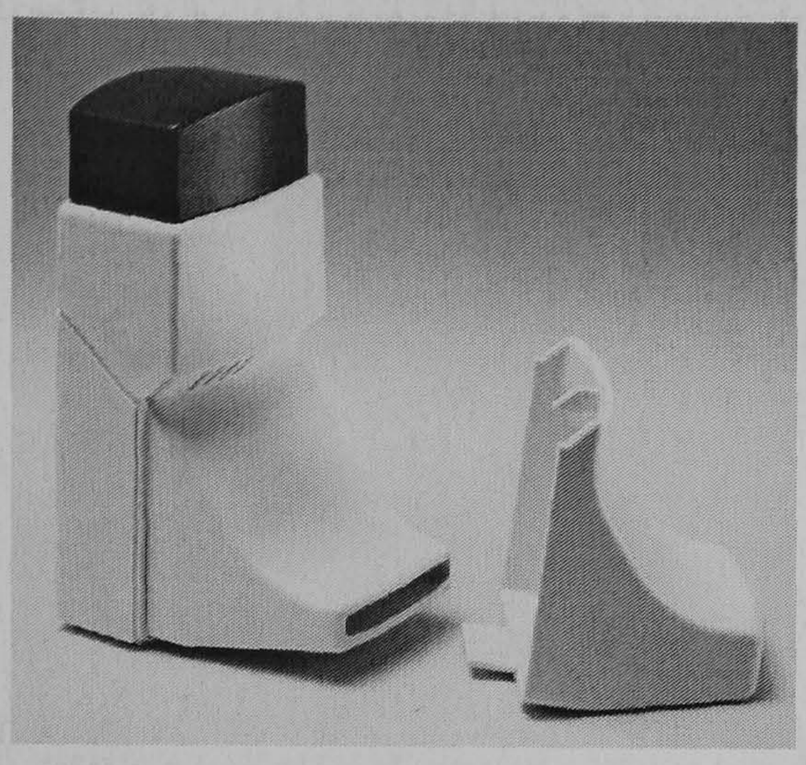

(a) Clickhaler [93]

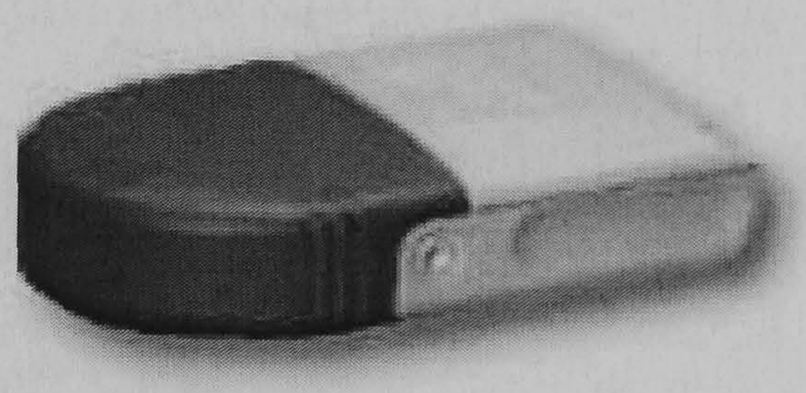

(b) Diskhaler [68]

(c) Aerolizer [136]

(d) Accuhaler [4]

(e) Easyhaler [132]

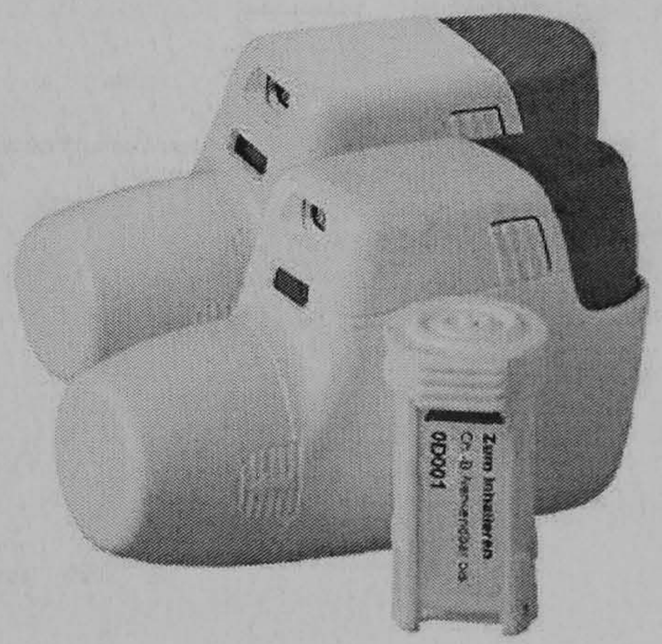

(f) Novolizer [190]

Figure 1.9: Examples of commercial Dry-Powder Inhaler products

Table 1.5: Examples of commercial Dry-Powder Inhaler products (Adapted from [19])

Device name	Manufacturer	Description
Aerolizer	Novartis, Switzerland	A single-capsule inhaler marketed for the inhalation of formoterol and budesonide
Clickhaler	ML Laboratory PLC, UK	A multidose inhaler containing up to 200 doses mainly for the inhalation of salbutamol and beclomethasone dispropionate
Diskhaler	Glaxo-SmithKline, UK	A 4- or 8-dose inhaler based on a disk with aluminum foil blister
Accuhaler	Glaxo-SmithKline,UK	A multidose inhaler with 60 doses contained in blisters on a foil strip and blended with lactose as carrier
Easyhaler	Orion Farmos Finland	An inhaler with 200 doses in a drug/lactose mixture
Inhalator Ingelheim	Boehringer ingelheim, Germany	A single-capsule device with the formulation containing glucose and carrier.
Inhale Inhaler	Inhale Therapeutic System, USA	An inhaler device that aerosolises the dry powder by the assistance of compressed gas and used for deliver insulin mixed with lactose.
Novolizer	Asta Medica Germany	A reusable device containing 200 doses of drug lactose mixture
Pulvinal	Chiesi Italy	A multidose reservoir containing 100 doses of powder mixture
Rotahaler	Glaxo - SmithKline, UK	A single dose device using powder drug such beclomethasone dipropionate and salbutamol combined with a lactose carrier
Spinhaler	Aventis, UK	One of the first mass-produced dry powder inhaler and used for the delivery of DSCG.
Spiros	Dura pharmaceutical	A reusable device containing either a disposable, prefilled plastic cassette with 30 doses or an aluminum blister disk with 16 doses

Then, aggregates of carriers and drug particles are dispersed into primary particles. This process requires forces to overcome adhesive and cohesive forces among small particles. Finally drug particles move into the mouth via the adaptor part.

At the present, many commercial DPIs are designed with good efficiency. Examples of commercial DPIs in the pharmaceutical market are shown in Figure 1.9, and also summarised in Table 1.5.

1.1.4.3 Nebulizers

Nebulizers have been employed for inhaled therapies since the 19th century. Only two groups of nebulizers, which are jet and ultrasonic nebulizers, are used in clinical practice. The basic operating principle of the jet nebulizer is that a pressurised source supplies high pressure air flowing through a nozzle. The droplets are then produced by disintegration of the liquid jet, commonly known as atomisation. The emitted droplet sizes depend on jet design, gas density, gas flowrate, surface tension, and viscosity of drug solution. The ultrasonic nebulizer applies an ultrasonic wave to make surface vibrations and cavitation to produce droplets. The size of droplet generated by ultrasonic nebulizer depends on device design and drug solution (i.e., surface tension and density). More designed details of these traditional nebulizers can be found in [77], [41].

Nowadays, many new nebulizer technologies have been introduced to improve efficiency, they can be grouped into 4 classes [42]:

1. *New adaptations of existing jet nebulizer technology to produce dosemetric system, i.e., HaloLite (Profile Therapeutics, UK) and Carculaire (WestMed Inc., USA).*

HaloLite (Figure 1.10a) is a hand-held delivery system incorporating a jet nebulizer operated from a dedicated compressor. It uses a software-driven monitoring and control system marketed as adaptive aerosol delivery (AAD) that performs the appropriate aerosol pulse time dependent on patient's breathing pattern. Results from clinical trails based on

(a) Halolite [148]

(b) Circulaire [194]

(c) AeroNeb [3]

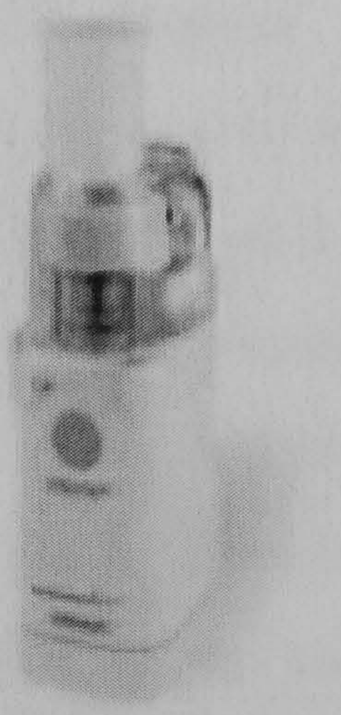

(d) Omron nebulizer (NE-U22V) [139]

(e) Respimat [18]

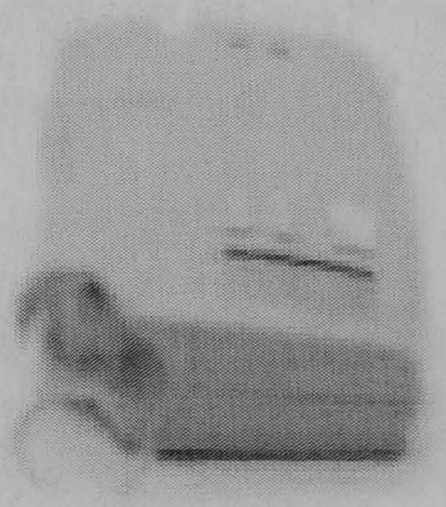

(f) AERx Ultra [6]

Figure 1.10: Examples of commercial nebulizers

HaloLite can be found in [157] [168]. The Circulaire nebulizer system (Figure 1.10b)is developed from a jet nebulizer by adding an exhalation valve and plastic reservoir bags intended to minimize waste aerosol. While the subject inhales, aerosol is drawn from the system by inspiration. During the subject's breath hold and exhalation, the exhaled air containing aerosols flow into an inflatable plastic bag for subsequent inhalation. Comparisons of Circulaire to conventional nebulizers have been reported in [130], [85].

2. *New adaptations of existing ultrasonic nebulizer technology to produce a dosemetric system, i.e., AeroNeb (Aerogen Inc., USA company) and Omron Ultrasonic Nebulizer (Omron Healthcare Inc., Japan).*

   AeroNeb (Figure 1.10c) is a silent, portable nebulizer system which has its operating principle as an ultrasonic nebulizer. It comprises a reservoir cup for storing the liquid drug, and a capillary system supplying the liquid drug to a shell containing an array of conical holes. A piezo electric cystal generates vibratory energy to oscillate the shell. Then it induces instability of the liquid jets emitted from the holes in the shell. The characteristics of AeroNeb have been reported by Fink [56]. With a similar concept, the Omron nebulizer (Figure 1.10d) employs a ceramic mesh and double horn oscilator that combine to release a fairly fine liquid aerosol with relative low power consumption. Some details of these ceramic mesh type ultrasonic atomization are given by Takano [178].

3. *New nebulizer delivery devices designed to delivery specific drug formulation, e.g., Respimat (Boehringer Ingelheim, Germany), and AERx (Aradigm Corporation, USA).*

   Respimat (Figure 1.10e) has a unique delivery mechanism, which is propellant free and delivers a metered dosage of medication as a fine mist. The device is prepared by compressing the spring by turning the lower half of the device through 180 degrees, simultaneously measuring the

amount of drug solution into the dosing system. After pressing the dose button release spring, it raises the pressure and forces the solution into the nozzle structure to generate the fine aersol. The reviews of Respimat have been given by Freund [64]. The fine droplet aerosols generated from Respimat are reported to be a better value of fine particle fraction than that of a CFC-MDI with very slow emitted velocity. The scintigraphic deposition study of Respimat confirmed that Respimat has a better lung deposition than pMDI [133]. AERx system (Figure 1.10f) is a nebulizing system similar to Respimat. It is designed to remind the patient to comply with the instruction for use. This systems help to encourage optimal breathing pattern through flow sensing technology linked to electronic feedback. The aerosol is not emitted unless the patient is breathing at the correct flow. The aerosol generation of AERx system is operated by a piston to force drug into a reservoir by flow through a micromachined array of holes into the inhalation path. More details of design and mechanism have been given by Schuster [167], [166].

4. *New nebulizer designs that are only just emerging whose nebulized aerosol application have not yet been fully defined, e.g., Touch-spray (Technology Partnership (TTP), UK).*

   Touchspray is a novel nebulizer technology that utilizes a perforated membrane vibrating at high frequencies against the body of fluid. The vibration source is generated by a piezoelectric element. During vibration motion, sound pressure is built up in the vicinity of membrane, then fluid is ejected through the holes in the membrane as droplets. The technology is very similar to AeroNeb. The jet-stream has a low velocity, and the atomization head can generate an aerosol in any orientation of the device. The details of this principle are given by Dhand [44]. These devices are under development for commercial purposes.

1.1.5 Clinical methods for assessment of aerosol deposition

Two basic approaches to the direct assessment of lung dose are pharmacokinetic and imaging techniques. The pharmacokinetic technique normally determines the pulmonary dose indirectly by measuring drug concentrations in the circulation, or more indirectly still, the urine. The number of pharmacokinetic studies is less than the imaging techniques due to difficulties involving measuring the small quantities of drug delivered to the patient. Nevertheless, pharmacokinetic techniques can provide some information that cannot be obtained through conventional imaging such as pulmonary clearance. Further advantages include the ability to avoid using radiation and repetition of the studies several times in the same subject [49].

The *in vivo* assessment of inhaled drug deposition using imaging techniques has been quantified and visualised by adding a radiolabelled substance to the aerosol and acquiring quantities of drug delivered to the patient by imaging techniques. The most common technique is Gamma scintigraphy, also known as Planar Imaging, which is regarded as the best practice for assessment of two-dimensional drug deposition. In three-dimensional imaging systems, Single Photon Emission Computed Tomography (SPECT) and Positron Emission Tomography (PET) may also have applications for assessment of regional lung deposition from aerosol inhalers. This regional information can help to answer questions regarding the optimal site of deposition and help to improve the clinical efficiency.

1.1.5.1 Planar Imaging

Planar imaging is a method which directly assesses both the total and regional deposition of inhaled aerosol. This technique is the most popular imaging technique for assessment of lung deposition because it is cheaper and easier to implement than other techniques. Planar Imaging gives a two-dimensional

image of radioactive-aerosol using a static gamma camera. The image can be acquired in both anterior and posterior views to compensate for any effects of attenuation by the body tissues. Many such studies have been published involving a range of subjects, including preterm ventilated and nonventilated infants [62], young children [43], adults and elderly [95] and have also included a variety of disease states.

The regional deposition within the lungs can be evaluated by regions of interest on the image which represent the central and peripheral region of lungs. However, regional lung deposition is imprecise in relation to the anatomy.

1.1.5.2 Single Photon Emission Computed Tomography (SPECT)

SPECT is a technique giving three-dimensional image data representing the distribution of a gamma-ray emitting nuclides. The process uses a gamma camera rotating through 360° around the patient. The imaging data can be viewed in coronal, sagittal, and transverse views. With its 3D resolution, SPECT imaging gives a statistically significant improvement in accuracy of assessing central and periperal deposition [151]. However, the accessing time of SPECT normally is much longer than that of Planar imaging to perform a complete thoracic scan with higher radioactivity needed.

Over recent years SPECT has provided much more sophisticated information regarding the pattern of radionuclide deposition using the information obtained by computed tomography (CT) and magnetic resonance imaging (MRI) to improve anatomical lung borders [59]. Nevertheless, it requires image registration techniques to align these data, and it may introduce further errors in analysis. Due to the higher cost and complex implementation, this technique is typically only used for fundamental research studies.

1.1.5.3 Position Emission Tomography (PET)

Positron emission tomography scanning uses specific cyclotron-produced positron-emitting radionuclides that chemically bind to drug molecules rather than a

physical attachment to drug particles. A PET scanner consists of a ring-shape array of detectors surrounding the patient to detect positron emission. This technique gives a three dimensional imaging data similar to SPECT with faster scanning speed to provide accurate and highly specific information about the dose and distribution of an inhaled or injected PET tracker in the lung ([165], [156]). The advantages of PET are that geometry is constant and that the corrections are applied to each pixel in each slide. When the lungs are imaged over time, the kinetics of the drug can be described for the whole lung as well as for specific regions. However the cost of implementation is greater than both planar and SPECT imaging techniques.

A comparison of planar, SPECT and PET techniques can be summarized by techniques, cost, and applications as shown in Table 1.6. The reviews of these imaging techniques for drug delivery can be found in [134].

1.2 Existing models for aerosol transport and deposition

An investigation of aerosol transport and deposition in the human lung requires knowledge of the anatomical lung model, breathing pattern, description of the aerosol and models of aerosol mechanism. An overview of the anatomical lung model and physiological variables of breathing are described in the previous sections. Primary aerosol mechanisms applied for aerosol transport and deposition consist of inertial impaction, sedimentation and diffusion already briefly discussed in section 1.1.3. Recent deposition models can be classified into three common types to represent the fluid and particle motions in the lung: Empirical model, Lagrangian dynamical model and Eulerian dynamical model.

Empirical models are the simplest model described by algebraic equations, which fit *in vivo* experimental data. These models do not consider the mechanics of fluid and particles. The National Council on Radiation Protection

Table 1.6: Comparison of Planar, SPECT, and PET techniques for accesing the aerosol deposition in human lungs(Adapted from [134])

	Planar	**SPECT**	**PET**
Imaging	2D	3D	3D
Regional lung deposition data	Imprecise relation to anatomy	More precise relation to anatomy	More precise realation to anatomy
Radionuclides Radiolabelling	Gamma-emitters Physical attachment to drug particle	Gamma-emitters Physical attachment to drug particle	Positron-emitter Chemical binding to drug molecule
Radioactivity needed	Low	High	High
Scan times	Short	Long	Short
Cost	$	$$	$$$
Applicability to multidose inhaler	Easy	Difficult	Difficult
Function	Product development/Regulatory studies	Fundamental research	Fundamental research

and Measurements (NCRP) [150] developed a lung deposition and clearance model for radiation protection proposes. The model was incorporated into a computer program that could be employed on a personal computer. The NCRP model consisted of the description of the respiratory tract region, a morphometrical model, and a regional deposition curve based on equations for sedimentation, impaction, and diffusion of particles onto airway surfaces. The NCRP model was not confined to use in healthy adult workers exposed to radioactive aerosols in an occupational setting, but it recognised the need to provide a flexible tool for a variety of conditions and ages. Similarly the ICRP (International Commission on Radiation Protection) model had drawn on experimental data. The ICRP model [140] was intended to take advantage of new developments in lung macro- and micro-morphology, new information in respiratory physiology, and made use of a complex computation possible on personal computers with the corrections for age, mode of breathing (nasal and oronasal), ethnicity, and gender.

The Lagrangian dynamical model treats the entire respiratory tract and particles in one dimension through an ideal lung geometry. The particles are convected through the lung at average local flow velocity. The first mathematical model for respiratory tract deposition by Findeisen (1935) assumed simple expressions for the particles in each generation under three mechanisms; Brownian motion, sedimentation and impaction. The calculation in Findeisen's model was limited to a single breathing pattern. Later the modified Findeisen's model by Landahl [110] added two upper airways compartments and an additional alveolar duct generation. Many derivative secondary models were still based on the Findeisen's mathematical model (see details in [80]). Beeckmans [15] developed the model based on Weibel's symmetric morphometric model including an extrathoracic region for oral breathing. With the asymmetrical morphometric model, Yeh and Schum [198] modified Findeisen-Landahl deposition model based on a morphometric model of Yeh and Schum including an extrathoracic region for nasal breathing. Using a Monte-Carlo

technique (a statistical technique), Koblinger and Hofmann [108] performed the stochastic transport and deposition model for a wide variety of particle size and flow rates. The principal limitations of these Lagragian models stem from their use of only one spatial dimension and the simplified assumption of fluid dynamics.

The Eulerian dynamic model is represented by a convection-diffusion equation for the aerosol in the simple lung morphometry model. Many theoretical predictions have been reported for specifically predicting the deposition site of drug aerosol based on the Eulerian dynamical model. Similar to the Lagrangian model, all presented versions of Eulerian deposition models treat the entire respiratory tract as one dimension. One dimensional models can be derived by considering the equation for mass conservation of the aerosol particles. Deposition in any respiratory region can be obtained from the integration of particle loss over the entire airway length and breathing-cycle period and divided by the number of particles inspired. Taulbee-Yu [181] proposed thoracic particle losses of spherical particles based on morphometric data of Weibel's symmetric model and incorporated with Scherer's trumpet model. Yu and Diu ([201]) extended the Taulbee-Yu model for oral and nasal breathing as a function of particle characteristics, breathing patterns, and intersubject differences in airways dimensions. Egan and Nixon [48] also modified Taulbee-Yu model with the treatment of effective axial diffusion. The results of inhaled aerosol depositions were improved and reflected in a better comparison with the experimental data. Futhermore, Edwards [46],[47] successfully applied macro transport theory to the same experimental data of Heyder et al. [78]. Based on the symmetrical Weibel Model A, he provided a complete theoretical expression for determining each of the first three moments of an exhaled aerosol bolus, thereby relating aerosol deposition to the mean velocity and dispersivity of exhaled aerosol bolus for varying depths of bolus penetration into lung. Generalising Eulerian models to more than one spatial dimension is difficult because impaction is more naturally dealt with by tracking individual parti-

cles. However, generalising a purely Lagrangian approach to multiple spatial dimension is also difficult due to the dispersion of aerosol bolus. Hence, deposition models with more than one spatial dimension tend to mix models, in which the fluid phase is treated in a Eulerian domain and particles are tracked in a Lagragian reference frame.

Recently, a significant number of numerical studies of aerosol transport and deposition within two- or three-dimensional geometrical lung models have been investgated. The airflow is usually calculated using the Computational Fluid Dynamic (CFD) software to give more realistic local flow fields in the models. These studies provide more understanding of aerosol transport and local deposition. Due to the limitation of computational resources and the complexity of lung structures, they are restricted to study only certain parts i.e., Extrathoracic and series of bifurcations, also known as the Partial Lung Simulation. In the extrathoracic region, Martonen et al. [123], and Zhang et al. [206] developed a three-dimensional simulation model of aerosol particle transport and deposition in a realistic oral-pharyngeal model reconstructed from a cast model. In the tracheobronchial region, numerous studies have been undertaken in the single and double bifurcation models based on the morphometrical lung model. Comer et al. [32] used a symmetric double-bifurcation airway. The resulting deposition patterns, particle distribution, trajectories and time evolution were analyzed and compared with experimental data. Zhang et al. [205] extended the study for a triple bifurcation model with a cyclic inhalation pattern. In the alveolar region, Darquenne [38], [39] simulated the particle deposition within the two-dimensional six generation structure representative of human acinus. The results showed that large heterogeneities of deposition patterns occur in the alveolar region. Nevertheless, all of these numerical studies often neglect the effect of moving boundaries and histology of airway wall due to their complexity of the structure and the lack of theoretical and experimental studies.

1.3 Motivation

In the drug delivery application, the generation of therapeutic aerosols from medical devices such as nebulizer, MDI and DPI always results in generation of charged aerosols. Lewis [114] studied the effect of modification of particle charge on an air-blast and ultrasonic nebulizer and showed that there are differences between the two types of device. Many experiments in animal lung (Fraser [63], Vincent [191], and Ferin [51]) and *in vivo*experiments in human lung (Melandri et al. [128], Tarronni et al. [180], and Melandri et al. [129]) have all shown that charged particles significantly increase deposition in lungs.

The theoretical study of charged particle deposition in the respiratory tract has been studied by Yu [203] using his previous analysis of precipitation of unipolarly charged particles in cylindrical and spherical geometries [202]. Balachandran et al. [10] developed a computer model which accounted for gravitational, Brownian diffusion, inertial impaction and electrostatic force. The simulation results highlighted the importance of particle charge-to-mass ratio in determining specific site of deposition. Furthermore, for particles less than 2 μm., the electrostatic forces were dominant in the deposition in the deeper airways. Bailey et al. [8] demonstrated how electrical charge on inhaled particles may increase particle retention in lung with complete inhalation and exhalation cycles.

The trends of computational models of aerosol transport and deposition in the lungs are towards calculation based on a more realistic geometrical lung models with the accurate analysis of airflow and aerosol transport. Recently, a European Union funded project, COPHIT (Computer Optimised Pulmonary Delivery in Human of Inhaled Therapies) was conducted, which focused on the development of a comprehensive simulation system tool for the study of inhaled therapies [127]. The simulation was proposed to track the progress of the drug delivered from an inhaler device through the entire respiratory system. In particular an accurate prediction of the distribution of the drug within the

lung could enable targeted drug delivery depending on the desired purpose of the drug, i.e. whether the action of the drug was to take place at a local or systemic level. The project commenced in April 2000 and was carried out over 30 months, bringing together a multidisciplinary consortium of simulation experts, fluid dynamicists, clinical scientists, clinicians and end users. Project partners included the University of Sheffield, Air Refreshing Control, INO Therapeutics GmbH, Aventis Pharma and the University of Mainz. After the end of the COPHIT project, the developed software within the project was further enhanced as a commercial software package, named COPHIT. The framework of this software consists of three main parts as follows:

1. Input parameter: This requires the specific inhaler device characteristics, drug characteristics, bronchial airways characteristics, peripheral airway characteristics and configuration of fluid solver.

2. A computational fluid solver: This part is used to compute gas flow and drug deposition.

3. Output data: It is designed to enable quantitative evaluation of airflow, deposition pattern and systematic drug uptake.

The model of airways in the COPHIT project is the combination of 3D reconstructed and peripheral airway models. A range of peripheral models are fully-coupled dynamic to systems and accounting for elastic properties of airway walls. A simpler system of periperal airways permits the rapid calculation of more approximate results. However, there have been a few studies involving the aerosol transport and deposition in the periperal airways. In addition, it is not clear how the interface between reconstructed and pheripheral models is implemented. The COPHIT software package is still under development to complete its designed framework.

Nevertheless, most of previous numerical studies have been developed mainly for uncharged aerosol particles. Thus, this research is primarily directed to-

wards the development of an integrated numerical model of aerosol transportation and deposition in the human airways to include the effect of electrostatic forces. The study extends the existing numerical studies of uncharged particles by adding both space and image charge forces. This study provides a better understanding of charged aerosol transport and deposition with the realistic flow conditions in a physical model of human lungs.

With respect to the geometrical model of human lung, many researchers have studied subjects with normal lung geometry based on the average adult data. However, the respiratory airways are significantly altered by gender, age, and health condition (i.e., pulmonary disease). The reconstructed model created directly from patient image data enables development of a more realistic lung model for the specified subject. Although the reconstructed model is more realistic than the morphometrical model, it requires multi-disciplinary expertise to create a model using extensive computation resources. The work reported in this thesis is validated by comparing the simulation results with published experimental data. However, clinical experiments are needed to validate the numerical model.

1.4 Aim and Objectives

The aim of this research is to numerically study the transport and deposition of charged inhaled aerosols in the geometrical human airway models. The objectives are listed as follows:

- To develop a code for computing the space and image charge forces of charged aerosol particles.
- To develop a code to calulate particle trajectories incorporating both electrostatic forces and fluid forces provided by computational fluid dynamic (CFD) software in the Lagrangian reference frame.
- To study the transport and deposition of charged aerosols in the recon-

structed human airway model.

- To study the transport and deposition of charged aerosols in the bifucation airway model based on morphological data.

- To study the transport and deposition of charged aerosol in the two-dimensional alveolar model.

1.5 Contribution to knowledge

According to the numerical studies of charged aerosol transport and deposition in the geometrical airway models, the principal contribution to the scientific area of inhaled drug delivery are listed as follows:

1. **Reconstruction of a realistic 3-D model of human airways from CT data based on existing techniques.**
   The geometrical model of reconstructed airways is generated by extracting the airway surface directly from the voxel data of scanned image (obtained by CT scanner) based on existing techniques.

2. **The techniques for computing the electrostatic forces of aerosol particles (both space and image charge forces) for drug delivery application.**
   Using the Lagrangian reference frame, the computation of space charge forces requires calculation of the interacting forces among all particles with a complexity of $O(n^2)$. This thesis presents the Particle Mesh method to reduce the complexity of computation. The computation of the image charge force also has been newly developed for the complex surface model

3. **A guideline to develop a numerical model to incorporate electrostatic forces and fluid forces obtained by CFD for charged particle transport and deposition.**

Due to lack of commercial CFD software that can include both space and image charge forces with a significant number of particles, the newly developed program codes are implemented to integrate the aerodynamics and electrodynamics encountered in the human airways as a coupling problem for the transport and deposition of charged particles.

4. **Greater understanding of the role of electrostatic forces in the transport and deposition of charged aerosols in the airway models, i.e., local deposition patterns.**

   This thesis focuses on the study of charged particle transport and deposition in both tracheobronchial and alveolar region using realistic airflow conditions and geometrical models,including the 3D tubular, 3D bifurcation, 2D alveolar and 3D reconstructed airway models. The numerical results provide a better understanding of the electrostatic effects on aerosol transport and deposition.

1.6 Thesis outline

The overall structure of work presented in this thesis can be described using the diagram shown in Figure 1.11. The numerical models developed and reported in this thesis can be divided into three main stages: preprocessing, processing and postprocessing.

The preprocessing stage is mainly proposed to create the geometrical model of airways consisting of 3D bifucation, 2D alveolar, and 3D reconstructed airway models. The bifurcation model and two dimensional alveolar model are created based on morphometrical lung data using the Pro/Engineer and GAMBIT softwares, but the reconstructed human airway model is directly reconstructed from the scanned image data of a male cadaver using imaging techniques. Additionally, the initialisation conditions of particles are also generated in this step to model the particle cloud in terms of particle size, position distribution, initial velocity, etc.

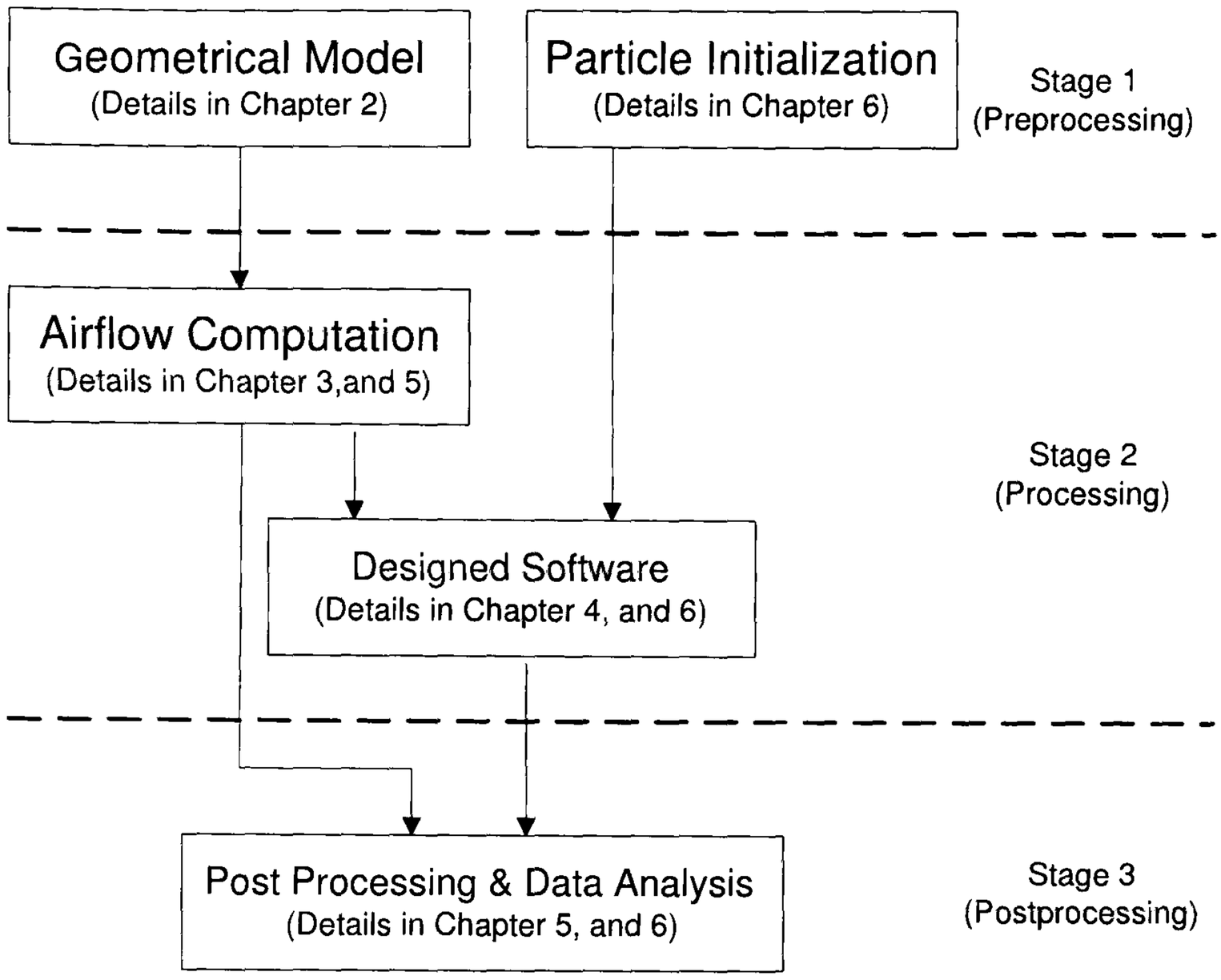

Figure 1.11: Diagram of general processing scheme employed in the thesis

The second stage involves the development of the computer code to calculate particle trajectories including the effects of electrostatic forces. Since the particle cloud is assumed to be a dilute particle cloud, the airflow can be calculated independently from the calculations of particle motion. The airflow velocity components are solved by using FLUENT, a CFD software package. Then these velocity values are imported into the designed software to calculate particle trajectories.

The postprocessing and data analysis of airflow and particle transport are employed using the files generated by the CFD package and designed software. These numerical results are then compared with the experimental data provided in previous publications. The details of implemented software used in all steps are summarised in Table 1.7.

The rest of the contents of the thesis are organized as follows. In Chapter 2 the details for the creation of three geometrical airway models are given. The mesh generation for these geometrical models is then provided. These meshes are used for the numerical computation of airflow.

Table 1.7: List of implemented softwares in the thesis

Process	**Implementation softwares**
Geometrical Model	GAMBIT/TGRID (Fluent Inc.)
	MIMICS (Materialise NV)
	3D STUDIO (Autodesk Inc.)
	Pro/Engineer (Parametric Technology Corp.))
Particle Initialization	MATLAB (the MathWorks Inc.)
Airflow computation	FLUENT 6.0 (Fluent Inc.)
Designed software	Microsoft Visual C++ (Microsoft Corp.)
Post processing &	MATLAB (The MathWorks Inc.)
Data analysis	FIELDVIEWS (Intelligent Light Inc.)

Chapter 3 provides the theory of the dispersed phase flow for the inhaled drug delivery application, e.g., the governing equations of airflow and particles in the first section. The overview of numerical techniques to solve these governing equations is also discussed. Then the airflow analysis in human airways based on the morphometrical model is introduced. The last section gives a description of the particle deposition in human airways based on basic mechanisms, i.e., impaction, sedimentation and diffusion, using one-dimensional analysis.

In Chapter 4 electrostatic force computations are introduced, both space charge and image charge forces. The details of Particle Mesh (PM) techniques proposed for space charge force computation are given step by step consisting of charge density assignment, potential solver and force interpolation, respectively. Finally, the image charge force computation is discussed.

Implementation and numerical results of airflow in the geometrical models are presented in Chapter 5. The details of numerical techniques, and simulation parameters are also given. Later the numerical results of airflow transport are discussed.

In Chapter 6, the details of software implementation including mesh and

CFD data files, tracking cell position, trajectory computation and post-processing analysis are given. Then the model validation and numerical results of charged aerosol transport in geometrical airway models are discussed.

The conclusion and some suggested topics for further research are given in Chapter 7. Finally, the list of publications, dimensions of geometrical models, tables of numerical results, and special functions are provided in Appendix A, B, C, and D, respectively.

Chapter 2

Geometrical Airway Models

As mentioned in the previous chapter, a preprocessing step is required to create a geometrical model of airways. This chapter provides the details of geometrical airway models used for the numerical investigation of charged aerosol transport and deposition.

The current and future researches of numerical studies of airflow and aerosol transport within the human lung are based on a 3D geometrical lung models, which can be grouped into 3D morphology based and 3D reconstructed geometrical models. The morphology based technique is to develop a model based on morphology and the statistical characteristics of airways. This approach usually contains an algorithm to generate branches without overlapping structure. Kitaoka et al. [106] developed a 3D branching tube system of airways inside a boundary shape of the lung. The rules of the algorithm for generating branches are defined based on two principles: 1) the amount of fluid delivery through a branch is proportional to the volume of the region it supplies; and 2) the terminal branches are arranged homogenously within the organ. The resulting model was achieved using iterative steps from the central airways to small airways with an approximate total of 55,000 branches. Spencer et al. [173] presented a method of generating 3D human lung airway networks using data-driving. This method is concerned more with the development of surface features that can be used in aerosol transport studies. Using MRI scanned

data, Tawhai [182] performed the 3D host-filling algorithm. The algorithm was developed based on a Monte Carlo method for growth of bifurcation systems suggested by Wang et al. [192]. The algorithm started to fill a fine uniform grid of points in the host volume, then an iterative algorithm was performed to create a new branch lying inside the host volume until all pathways were terminated by the terminal airways.

In an alternative method to create a geometrical model, the reconstruction technique generates a 3D model directly from scanned image data using advanced imaging techniques. The reconstructed models may be highly realistic. In addition, this technique may allow for the effects of respiratory diseases in the airways. It makes it possible to study the airflow and aerosol transport specified for an individual case for disease. Few studies which have involved the use of reconstructed airways have been published. For an example, Fetita and Pretuex [54] presented the 3D reconstruction of the human bronchial tree from volumetric data acquired by using a High Resolution Computerised Tomography (HCRT) system. The study performed a fully-automated 2D segmentation of bronchi based on mathematical morphology theory. The 3D propagation was controlled by a 3D oriented and multi-valued structure describing the topology of the segmented sequence. The comparison between morphology based and reconstruction techniques are summarised in Table 2.1.

The numerical investigations of airflow and aerosol deposition in geometrical respiratory models that have been studied recently are restricted to some regions of the bronchial airway network (i.e., extrathoracic, tracheobronchial or alveolar region) because of the complexity associated with a large number of branches, and the limitation of computational resources. In addition, the Computational Fluid Dynamics (CFD) package also requires a significant number of meshes for a complex structure, which is limited by computation resources. This thesis is mainly studied for tracheobronchial and alveolar regions. The bifurcation and reconstructed airway models are implemented to represent the tracheobronchial region, while the two-dimensional alveolar air-

Table 2.1: Comparison between morphology based and reconstruction techniques for creating the geometrical airway model

Geometrical model	Comments
Morphology based technique	*Advantages* - A model is created based on average morphological data. There are many previous studies of lung in term of morphological model. - Anatomical synthesis of the model is easier than the reconstruction techniques. Thus the investigation of fluid flow and particle transport with airway generation is easy. *Disadvantages* - The implementation of a 3-D model of many generations is complex because it requires an automatic algorithm for branching tubes without intersection of model. In addition, it requires an algorithm to smooth the surfaces in transition regions between parent tube and daughter tubes. - With a more realistic model, the asymmetrical morphology is required with a random technique to fill branches of airways into the host volume of the lung. - In case of lung variation due to lung disease, age, and sex, it requires additional information on morphology to modify the model. In lung disease, the abnormal airways have different patterns corresponding to individual patient.
Reconstruction technique	*Advantages* - A model is more realistic than the morphology based technique and can be fitted to individual patients. It enables us to study lungs with the effect of age, sex and diseases. - The image tools tend to have much better intelligence, and faster features

Geometry model	Comments
	Disadvantages - Automatic segmentation is too complex to identify airways from the image data. - It is difficult to reconstruct an airway model with small airways due to the limitation of image resolution - An anatomical synthesis is required to identify an airway generation in the model for the investigation of fluid flow and particle transport

way model is implemented for the alveolar region. Since the nature of these airway models is a complex structure, the models are usually represented by their surfaces. Various types of surface representations can be applied to the model, i.e., triangular surface mesh, subdivision surface, parametric surface, and NURBS surface. A brief summary of representations is given below:

- Triangular mesh: A surface is described by a set of flat triangular surfaces. The density of triangles in different areas can be varied to achieve a good approximation. This surface representation is popular for complex structures.

- Subdivision surface: It represents a surface that starts with initial polygonal mesh, then is repeatedly refined to generate finer mesh with some rules. After the recursive process, the final surface ends up with a higher degree of smoothness than the initial mesh.

- Parametric surface: It defines the surface using the function of parameters for giving the collections of co-ordinate points. By choosing suitable parameters, the more complex surface can be represented.

- B-Spline surface: Similar to parametric surface, B-Spline surface defines the function using a piecewise polynomial and the change of function

occurs at knot points. The main difficulty is to find suitable parameters, and the number of knots and their positions.

- NURBS (Non Uniform Rational B-Splines) surface: The NURBS surface improves the technique from B-Spline. The detailed algorithms are given by Piegl [154]. This type is industry standard for the representation and design of complex geometry. It is often used in modern CAD/CAM systems, because it offers one common mathematical form for both standard analytical shapes (e.g. conics) and free form shapes, and provides the flexibility to design a large variety of shapes;

Three geometrical airway models were used in this thesis to represent the tracheobronchial and alveolar regions including 3D bifurcation, 2D alveolar, and 3D reconstructed airway models, which are discussed in section 2.1, 2.2, and 2.3, respectively. The mesh generation must be performed in these geometrical models to create the volumetric mesh for the CFD computation. The details of mesh generation are then given in section 2.4.

2.1 Geometrical Bifurcation airway model

Bifurcation airway models are the most popular geometrical lung structure for the studies of airflow, aerosol transport and deposition in human lung. Since the lung structure can be modelled as a sequence of bifurcation airway models, studies using these bifurcation models can gain a better understanding of aerosol transport and deposition within the complex airway structures.

The earliest contribution to flow measurement in the single bifurcation model proposed by Schroter and Sudlow [164] provided flow velocity profile patterns using hot-wire probes and smoke tracers under steady airflow condition. Using different experimental techniques, Zhao and Liber [207] presented experimental studies of airflow in a single bifurcation using a laser doppler anemometer. The bifurcation model was defined by a set of equations, which

were quite general and could be changed by modifying the flow divider length, the radius of curvature of daughter branches, the parent/daughter tube diameter or the bifurcation angle. Many experimental studies of particle deposition have been performed such as that of Bell and Friedlander [16], Johnston et al. [97], Kim and Iglesias [105] for different flow rates, particle sizes, and branching angles. Recently, Kim and Fisher [104] presented the experimental results of aerosol deposition pattern based on the glass tube model of the double bifurcation model.

Focusing on the 3D numerical studies of aerosol transport and deposition, Gradon and Orlicki [70] reported particle deposition in a bifurcation model without the effect of inertial impaction. Balachazy and Hofmann [11] [12] performed the analysis of deposition patterns in a single bifurcation using the Monte-Carlo method under the simultaneous action of different deposition mechanisms. However, these studies were concerned only with laminar flows. Li and Ahmadi [116] developed a computational model for predicting the particle dispersion for laminar flow. The instantaneous fluctuating velocity was modelled by a continuously varying Gaussian vector random process. Recently Comer et al. [33][32] performed numerical studies in the double bifurcation model, based on the studies of Kim and Fisher [104]. They provided the airflow patterns (both axial and secondary velocities), and particle deposition patterns at different Reynolds numbers based on various breathing conditions. Similarly, the airflow and particle deposition patterns in the triple bifurcation airway model were studied by Zhang et al. [205].

The bifurcation geometrical model proposed for this study is a double planar bifurcation model based on the studies of Comer et al. [33][32]. The dimensional details of the model are given in Appendix B. The geometrical model created by CAD Pro/Engineer package is shown in Figure 2.1. The model represents a symmetrical branching of generation numbers 3-5 in the Weibel's morphological model with sharp carinal ridges.

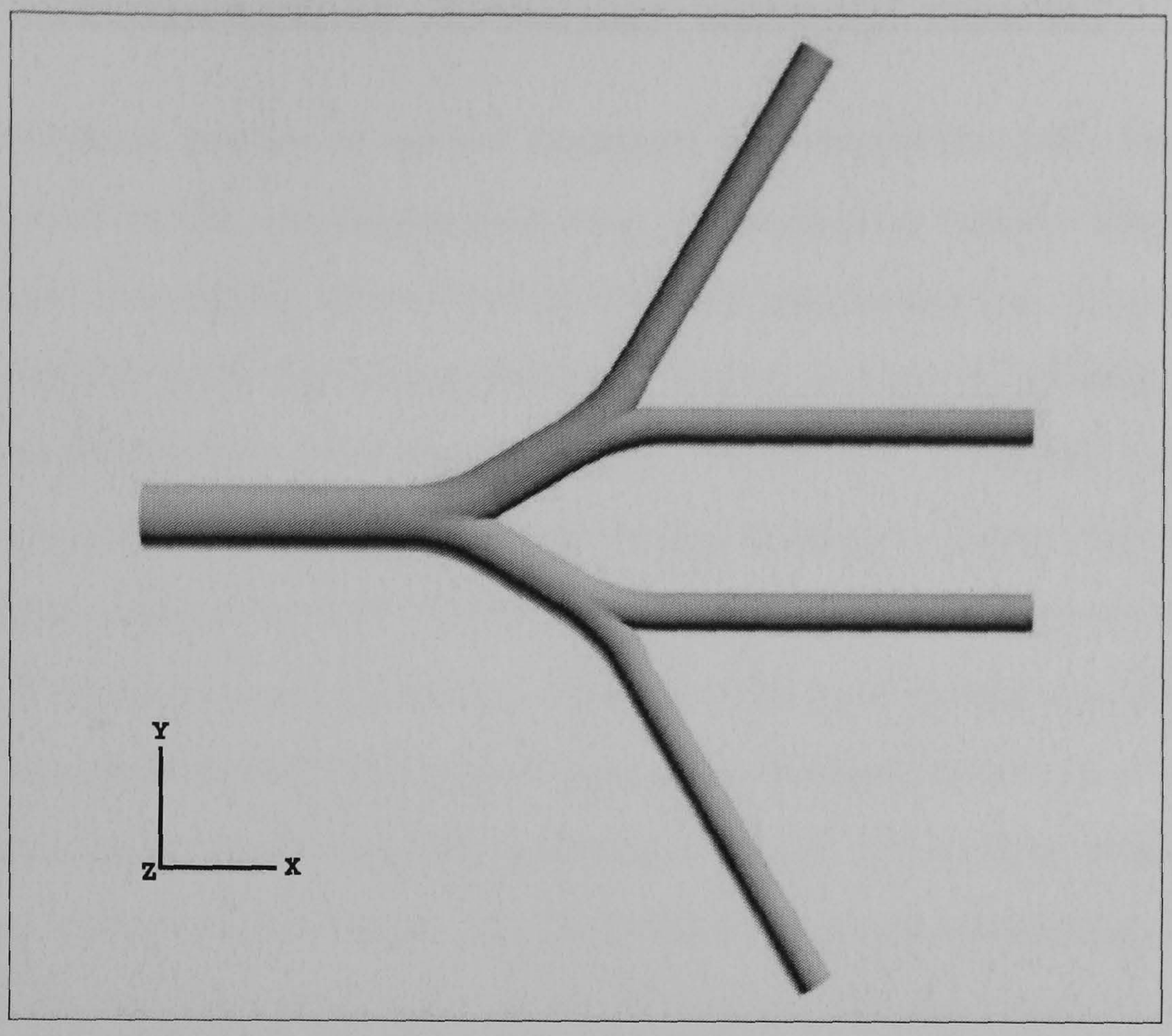

(a) top view

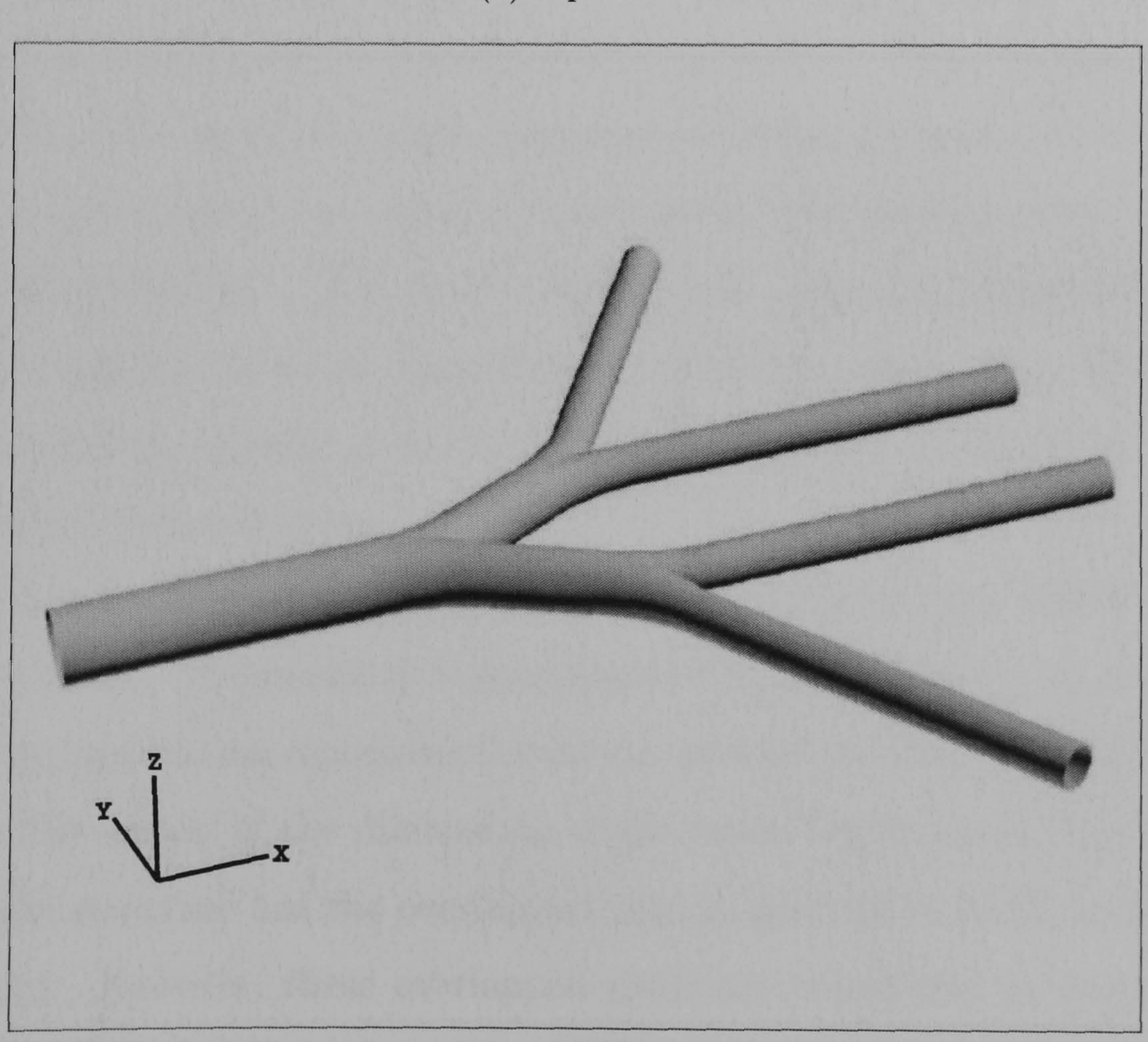

(b) oblique view

Figure 2.1: Geometrical model of 3D double bifurcation airway

2.2 Geometrical Alveolar airway model

Many analytical studies of aerosol transport and deposition have been performed based on the one-dimensional lung of the alveolar region. These models provided reasonable estimations of the total deposition, but they did not provide realistic local deposition patterns. Several studies specifically investigated local deposition in the alveolar region. Tsuda et al. [186][187] published the first numerical study of intra-acinar aerosol transport. They combined the Monte-Carlo simulation and conditional probability analysis to provide mechanisms of acinar aerosol deposition. These studies were based on a 2D model representing an infinitely long central channel surrounded by alveoli of circular shape. Darquenne and Paiva [37] proposed a similar 2D simulation of aerosol transport and deposition in a four generation structure of alveolar zone as well as a 3D model simulation of aerosol transport and deposition in a single alveolar duct. Their simulation results showed that the streamline pattern of the flow was very sensitive to alveolar duct geometry. Then, Darquenne [38] developed a new model of a multi-genertion structure of alveolar ducts. Their model included bifurcation areas that connected the alveolar ducts to form a branching structure. The results showed that large heterogeneities in the deposition pattern occur at alveolar level. With the same model, Darquenne [39] extended the studies to focus on the heterogeneity of deposition due to gravitational sedimentation.

The alveolar geometrical model in this thesis was developed based on Darquenne's model. It consists of 6 generations of alveolated ducts in which the first airway generation represents the airway generation number 18 of Weibel's model. The details of the dimensions of the model are given in Appendix B. The whole structure has the overlapped part in generation 21-23 as shown in Figure 2.2. However, these overlapped parts are considered as independent parts for airflow calculation. Each of eight outlets of the central unit has a similar structure defined as section A-H shown in Figure 2.3. This model is

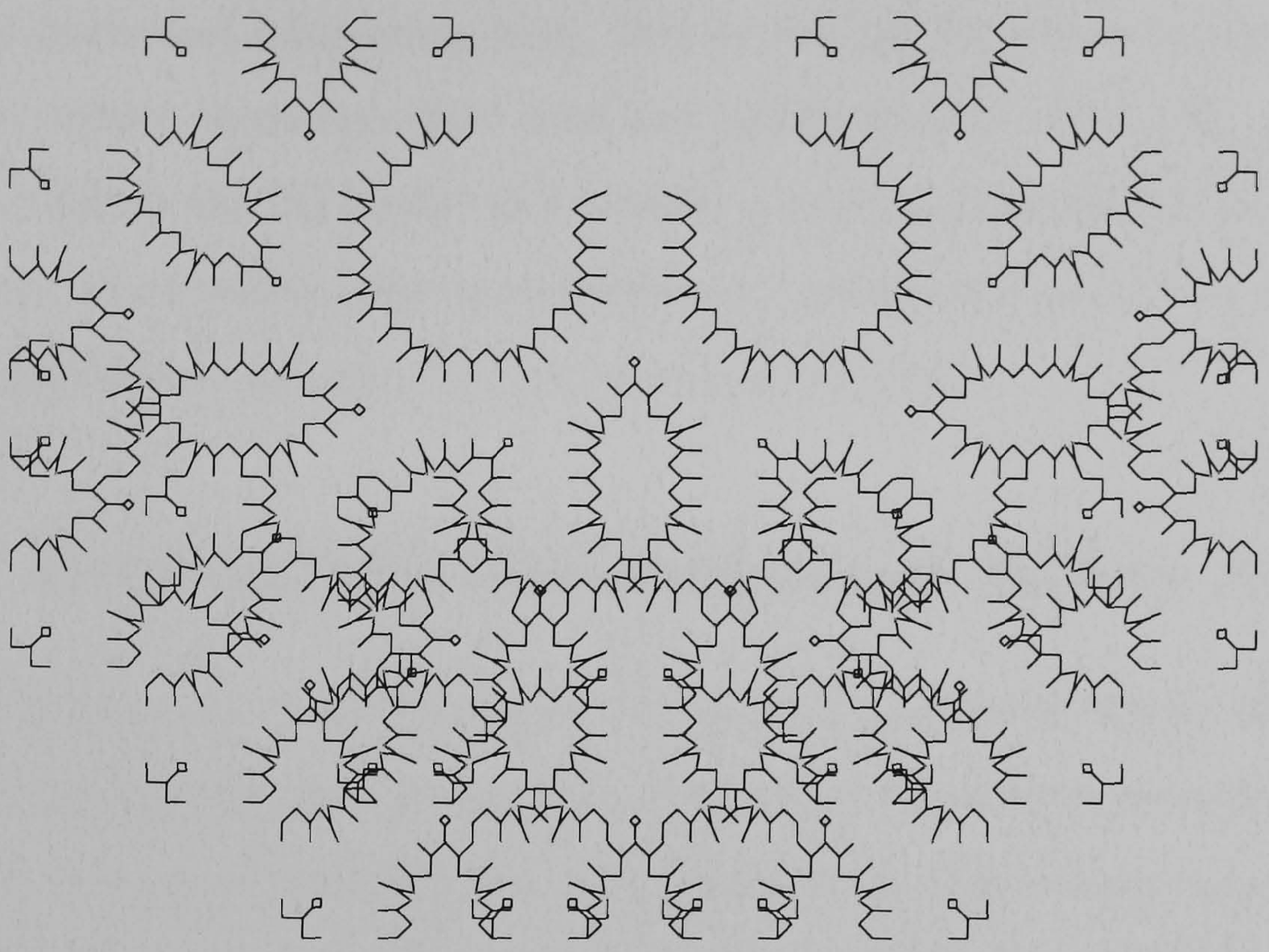

Figure 2.2: Geometrical model of 2D alveolar airways

Figure 2.3: Defined sections of the 2D alveolar airway model (displayed sections: main, A, C, F, and H)

more realistic than previous alveolar models, therefore, it includes both the alveolar ducts and bifurcation area. Due to the low Reynolds number in the alveolar region, secondary flow does not predominantly affect the particle's motion. Hence the 2D model can provide a good approximation to the real structure. Nevertheless, this model does not consider the volumetric deformation of alveoli but assumes the wall as a rigid structure.

2.3 Geometrical Reconstructed airway model

Several numerical studies of airflow and aerosol transports within 3D reconstructed geometrical model have been developed. These models (such as Li et al. [117], Katz and martonen [98], and Cheng et al. [24]) mainly focus on the extrathoracic region. These studies investigated and compared results with *in vitro* experiment in the cast of a human oral-pharyngeal model.

An innovative technique of *in vivo* experiment using dynamic hyperpolarised helium-3 Magnetic Resonance Imaging (MRI) enables us to visualise ventilation for validating airflow and particle transport. By contrast, in conventional (proton-based) MRI techniques a gas is used as a contrast agent which can be directly visualised, thus revealing the airways in a more direct manner rather than by relying on indirect effects. The details of this technique are given by Gast et al. [67], Kauczor et al. [100] and Tooker et al.[185].

The 3D reconstructed airway model in this thesis is focused on the tracheobronchial region starting from trachea and followed by a few generations of branches (about 5-6 generations). The model is created based on present imaging technologies, which is available in commercial medical visualisation software. Recent efforts of airway reconstruction are being directed toward the development of a fully automatic algorithms to generate the models. An overview of the reconstruction process is presented in section 2.3.1. The implementations for creating the reconstructed airway model are then given in section 2.3.2

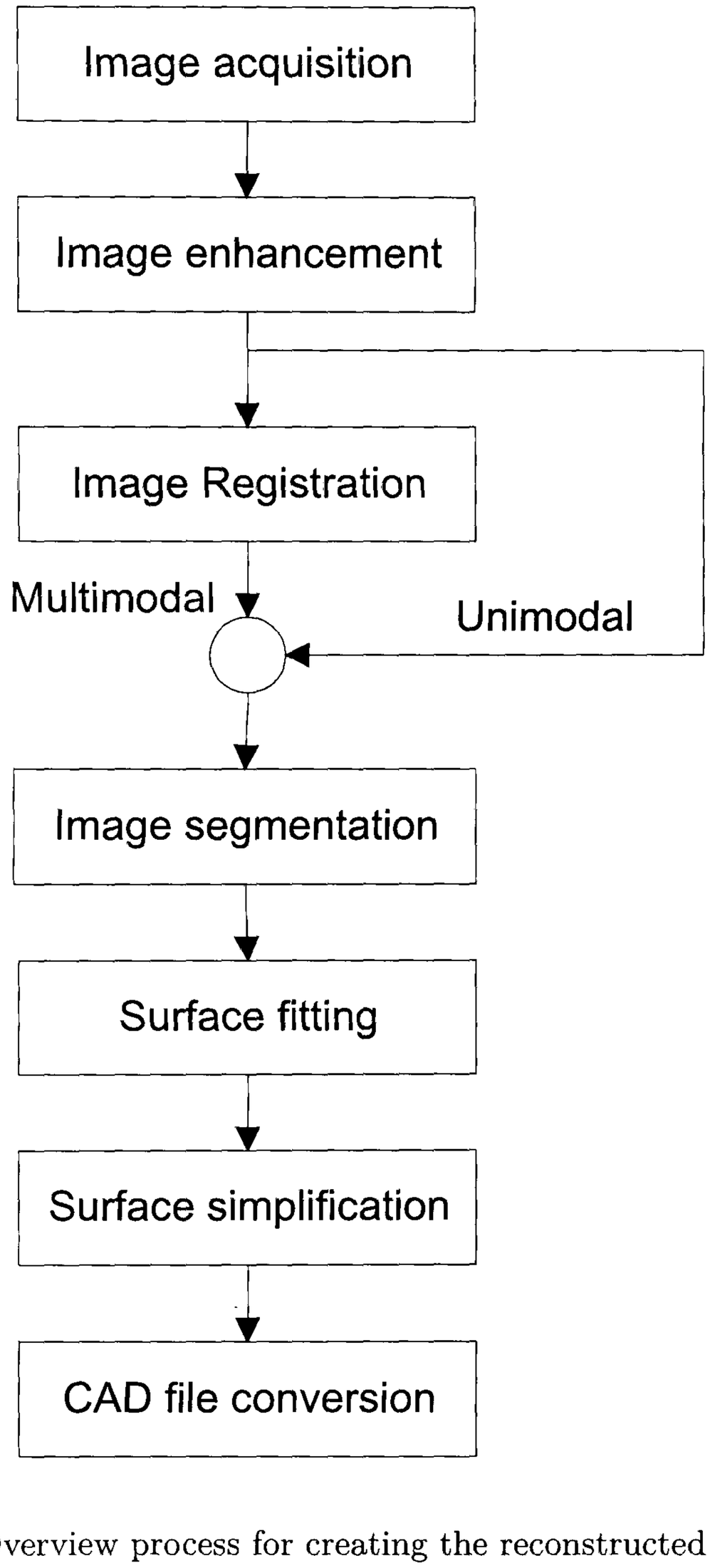

Figure 2.4: Overview process for creating the reconstructed airway model

2.3.1 Overviews of the reconstruction process

The overview process for creating the reconstructed airway model is summarised in the diagram shown in Figure 2.4. Firstly the image data is acquired from the scanning system (i.e., CT and MRI scanning systems), also known as the image acquisition. Then image enhancement on the raw image data are implemented to improve the image quality and contrast. In the case of the integration of image data of different modalities from the same body, image registration is required to bring the modalities involved into spatial alignment. The next step is image segmentation, which is the most important but complicated process. This step aims to extract the airways from the image data. After that, these segmented airways are used to create a surface model by the surface fitting process. Therefore the results of the surface model may consist of a large amount of data to represent the surface. The surface model can be simplified to reduce the number of data points with an optimum accuracy. Finally, the simplified surface model is converted into the standard CAD file for the mesh generation and airflow computation.

2.3.1.1 Airway scanning data

The image datasets are obtained by using an image acquisition system that captures and records localised information about the physical/or functional properties of organ and tissue. Various types of image acquisition system can be implemented using different concepts of operation, i.e., CT (Computed Tomography), MRI (Magnetic Resonance Imaging), Ultrasound and bio-magnetic scanner systems. Typically, the reconstructed airways model is most often created by using the data from CT and MRI scanner systems. Therefore CT and MRI scanning systems are discussed in detail.

The CT scanner systems use the same concept of operation as X-ray, which uses the principle that the amount of absorbtion of radiation depends on the physical density, the atomic composition of the organ structures, and the energy of X-ray. The conventional CT scanner uses a single X-ray tube rotating

a full 360 rotation for each slice. To acquire multiple images for adjacent slices, the table moves to increase step (called slice thickness) until the scan is complete over all required regions. Scan time for a single slice usually takes 1-2 seconds [158], so multiple slices take more time depending on the length of scanned region. Some systems that have been developed based on the conventional CT scans, include spiral CT, multi-detector CT, and Electron Beam CT scan systems. In Spiral CT scanning, the projection of acquisition tracks a spiral rather than a sequence of parallel slices. This scanner allows a large volume to be scanned in a few seconds (such as the whole chest or abdominal volume). The multi-detector CT improves the speed of scanning by extending multi-detector arrays. The operation of multi-detector CT is similar to spiral CT scanning, except that multiple parallel detector arrays record the data. With multiple slice profile detection, a scanning speed is achieved that compares to spiral CT. The Electron Beam CT, a novel development of CT scan system, is primary used for cardiac imaging and functional assessment. The Electron Beam CT uses a different concept from conventional CT, in that it uses a focused electron beam sweep across the target to produce multiple angles of view. Therefore, there is no mechanical rotation in this system, and images can be acquired approximately every 50 to 100 milliseconds. At this speed it is possible to capture the physiological motion in the body such as flowing blood or the beating heart.

The CT image data are often represented by a scale of CT number, which gives the attenuation coefficients of human body tissues and organs. The value of CT number may employ a discrete value ranging between -1000 to 1000, also known as the Hounsfield scale. The standard CT number given in Table 2.2 can represent the various human body tissues and organs. In the CT data file, the image data are stored in two-dimensional arrays such as a 512x512 matrix and the values are often represented in a positive integer range such as a 12-bit value (0 to 4096).

The MRI scanning system has been developed using the concept of perturb-

Table 2.2: Standard (Hounsfield) scale for X-ray CT number [13]

Tissue	CT number (HU)
Bone	1000
Liver	40 - 60
White matter (brain)	46
Grey matter (brain)	43
Blood	40
Muscle	10 - 40
Kidney	30
Cerebrospinal fluid	15
Water	0
Fat	(-50) - (-100)
Lungs	(-750) - (-900)
Air	(-1000)

ing magnetic fields with radiowaves [158]. There are many ways to produce selected contrast among different anatomy structures. The MRI scanning system has a good efficiency for acquiring soft tissue images such as the brain parts, and thus provides highly detailed structural images.

2.3.1.2 Image enhancement

In medical scanning processes, many interference sources can affect the quality of images. The nature of physiological systems also diminish the contrast and visibility of details. Therefore image enhancement is required to reduce image noise and improve the contrast of the structures of interest. Enhancement techniques can be divided into 3 common groups : histogram operation, spatial filtering and frequency filtering. The histogram techniques adjust the histogram of the image (also called grey-level probability distribution function) using analytical transformation. For example, histogram equalisation aims to adjust the histogram to be a uniform distribution. However, these techniques have limited success in many practical cases because various details in the

wide size ranges and small grey-level differences among tissue types effect the histogram operations. The local adaptive histogram is the other method used for locally adjusting the histogram.

Spatial filtering involves the replacement of image values of each pixel with some functions of a considered pixel and neighbouring pixels. A simple example of spatial filtering is mean filtering, which computes a new image value by averaging with the neighbouring pixels. The number of neighbouring pixels considered also known as the kernel of convolution can vary. Many functions can be applied for different purposes such as median, low-pass, and high-pass filtering.

Frequency filtering uses a different concept in which the spatial domain is transformed into a frequency domain (also called Fourier domain). The image data after transformation are represented as the sum of the sinusoidal basis function at various frequencies, amplitudes, and relative phases. The computation of the frequency domain (such as low-pass, high-pass and band-pass filters) is often faster than spatial convolution. For example, the image noise can be represented as high frequency in the images and that can be reduced using the low-pass frequency filtering. The details of histogram operation, spatial filtering and frequency filtering are given in many books on image processing (e.g., [22],[69], [96]).

2.3.1.3 Image registration

Image registration is a process to bring the various modalities of image data involved into spatial alignment for integrating information acquired from the same object. An application of registering can be found in the preparation of surgery where the patients may undergo various CT, MRI and other modalities. A significant number of registration techniques have been proposed for different applications. However this study is mainly based on unimodal data, and the details of image registration are not discussed in this section. The medical image registration has been reviewed by Maintz and Viergever [121].

2.3.1.4 Image Segmentation

Segmentation may be defined as spatial portioning of an image into its constituent parts or isolating specific objects in an image. Segmentation techniques can be grouped into three general types, based on computational concepts: manual, automatic and semi-automatic segmentations. The manual techniques are probably the most accurate, but they require a good knowledge of the extracted object by the user. They are often time consuming. On the other hand, automatic segmentation uses various rules and knowledge to perform the entire segmentation without the human intervention. Many researches focus on automatic segmentation using various concepts such as fuzzy logic, neural networks, and wavelet transform. However there still may be some errors from the various image types, image characteristics, and selective parameters. Semi-automatic segmentation combines both manual and automatic segmentation, in which human intervention is used to initiate some parameters and information for automatic segmentation. In general, most techniques discussed above rely on basic image segmentation methods consisting of threshold, region growth, water-shed algorithm, edge-based algorithm and multi-spectral algorithms. These techniques are reviewed in [158], and [13].

2.3.1.5 Surface fitting

Surface fitting (sometimes known as feature extraction or iso-surfacing) aims to fit surface primitives such as polygons or patches to the constant-value contour of volume datasets using thresholds defined by the user. The surface-fitting method typically tries to minimise the function, which captures a trade off between accuracy and conciseness. Various surface fitting techniques have been proposed, i.e., contour-connecting, opaque cube, marching cubes, marching tetrahedra, etc,.

1. Contouring-connecting

This method is the oldest method performed to find the corresponding contour region in each slice and connect the oriented contour lines between adjacent slices. This method was first suggested by Keppel [101]. The algorithm starts by operating on individual slices by finding the closed curve contour using specific threshold. Then the second step is to find the tesselation connecting the curves in each pair of adjacent slices. This step often has a problem in finding an optimal tesselation connection. Many techniques have been suggested to reduce this problem, such as that of Fuch [65] and Barequet [14].

2. Opaque cube

   The Opaque cube (also called Cuberille algorithm) was the first widely used method and was proposed by Herman and Liu [76]. The method involves finding a particular volume, which is a part of a surface. This is a two stage process. Firstly the algorithm undertakes to make cubic voxels from volume data set. If the distance between slices is larger than the size of pixel, then data must be resampled to represent the gap between slices with the same size as the pixels. Secondly the algorithm decides the voxel belonging to the object using binary segmentation with a user selected threshold. It produces a continuous surface of voxels. These voxels are merged together to make up the surface representing individual voxels. However, the number of voxels affects the quality of surfaces. If the number of voxels is not large enough, the surface will be like square bricks. The cuberille algorithm suffers from the greatest deficiencies of surface-fitting algorithms, but it is simple to implement and fast at finding surfaces.

3. Marching cubes

   The marching cube algorithm proposed by Lorensen [118] has been implemented as a variation on the cuberille algorithm. The Marching cube algorithm undertakes to look at each element of volume datasets, and

decide whether their vertices are inside or outside the isosurface. This decision is made by comparing the values at the vertices of elements using a threshold value. If the surface passes through the element, the approximate position on the element is calculated. At the vertices of these cells, the values are set to one if the vertices are inside the surface and set to zero if the vertices are outside the surface. Since there are eight vertices in each cube and logical values of vertices (0 or 1), there are 256 combinations of surface intersection in the cube. These combination can be reduced from 256 cases into 15 patterns as shown in Figure 2.5 by excluding cases which are rotationally symmetric. However, the marching cube algorithm has several ambiguous cases, which can lead to holes in the final image. These ambiguities occur due to a wrong decision in defining inside or outside values, or the wrong chosen triangles.

4. Dividing cubes

   Dividing cubes described by Cline et al.[30] was developed to eliminate the scan conversion step of the polygonal display algorithms. When a voxel is encountered with corner values that cross the threshold, the algorithm subdivides the voxel into small cubes, and projects the intensity of each cube onto the viewing plane, forming a gradient shaded representation. This subdivision process increases the accuracy of the interpolation. The voxel scale is selected to make the smaller cubes equal to the pixel size on the raster display. Each subcell is rendered as a surface point that contains the information of value, location in object and calculated gradient for shading.

5. Marching Tetrahedral

   Based on the Marching cube algorithm, this technique proposed by Shirley [170] can reduce ambiguous point connecting by subdiving a cell into five, six or 24 tetrahedra and text edge intersections using the table-based method. For example, five tetrahedra are fitted exactly within a

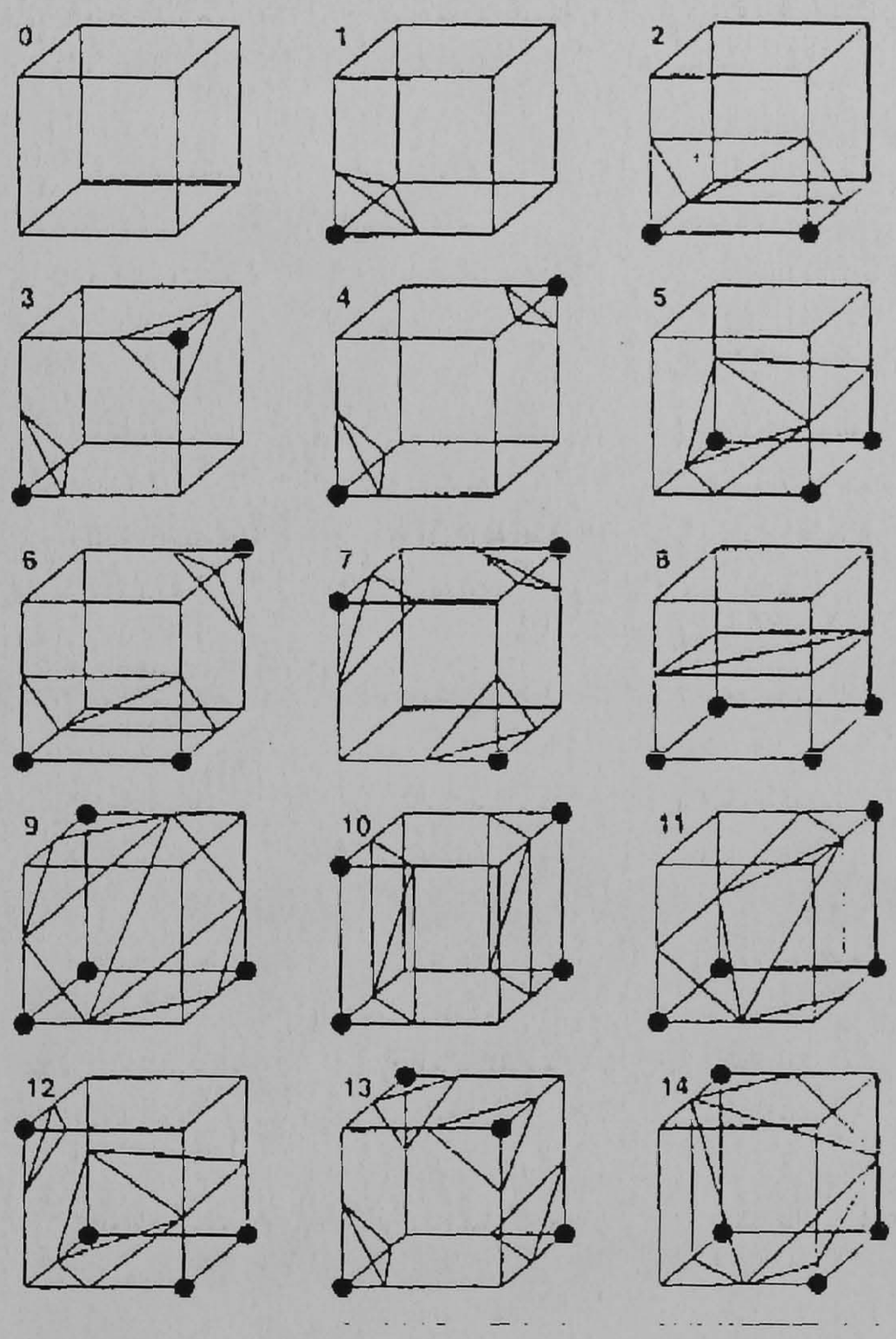

Figure 2.5: Combination of surface intersect in Marching Cube algorithm (Solid nodes representing the vertices inside the surface). Adapted from [118]

cube shown in Figure 2.6. This topology gives a finer detailed surface. However ambiguities are still present because the isosurface is created by considering only neighbouring data points. Therefore, since a tetrahedron has only six edges, two triangles are enough to show the isosurfaces inside the tetrahedral cell as shown in Figure 2.7. The algorithm generates a greater number of triangles than that of the marching cube algorithm with correspondingly more computational time.

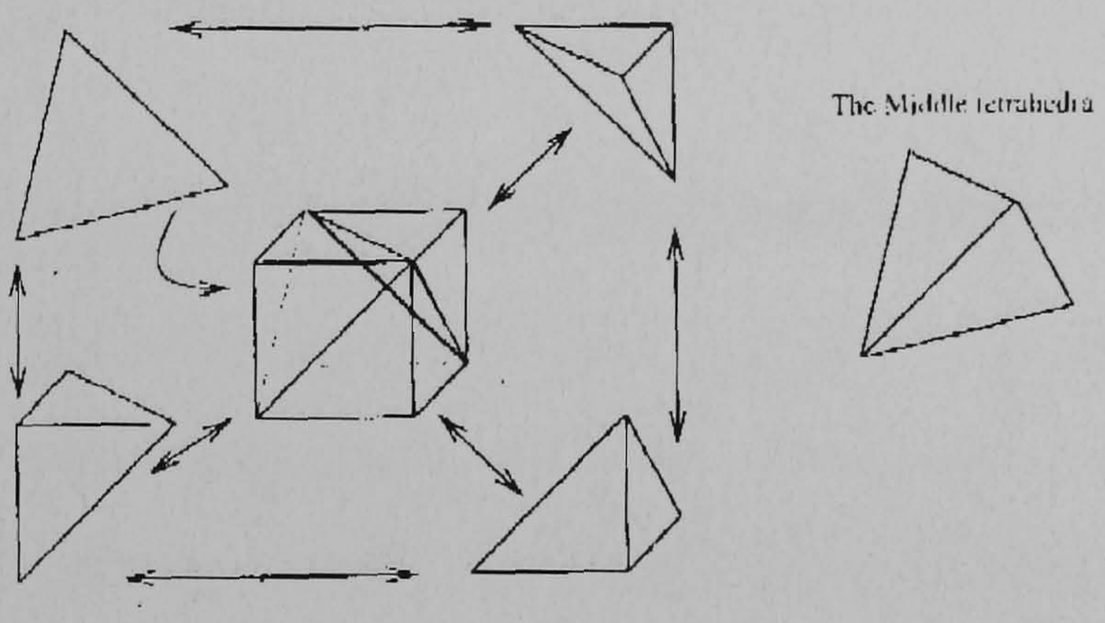

Figure 2.6: Configuration of five tetrahedra fitted in the cubic voxel [170]

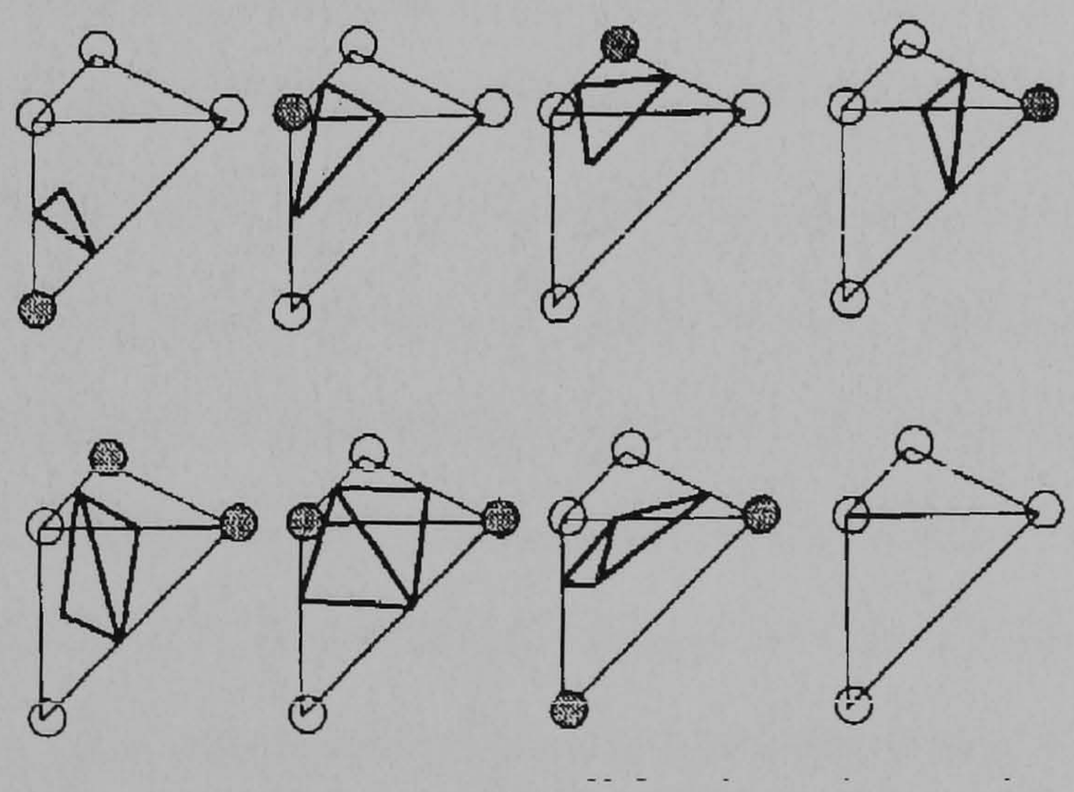

Figure 2.7: Combination of surface intersect in Marching Tetrahedral algorithm [170]

2.3.1.6 Surface simplification and smoothing

After extracting the surface from the volumetric data using a surface fitting algorithm (i.e., marching cubes or marching tetrahedral), the surface is usually composed of a large number of polygons. Surface simplification is an important

process in the generation of a compact approximation of shape, because it has the benefit of storage, transmission, computation, and efficient display. The classification of surface simplification can be divided into 3 main groups consisting of height field, manifold and non-manifold surface approximations. However, only the manifold surface approximation is relevant to this study. Many simplification techniques can be proposed for manifold surface such as Re-tiling [189], Decimation [163], [31], Energy optimisation [89], and Wavelet [45].

2.3.2 Geometrical model of reconstructed airways

The image data applied in this study were obtained from CT data of a male cadaver of the Visible Human Project [138] which aims to create a digital image dataset of complete human male and female cadavers in MRI, CT and anatomical modes. In the Visible Human Project, the MR images of head and longitudinal sections of the rest of the body are taken at 4 mm intervals. The MR images have a 256x256 pixel resolution with 12 bits of grey level. The CT data is composed of axial CT scans of the entire body taken at 1 mm intervals at a resolution of 512×512 pixels where each pixel has 12 bits of grey level. There are 1871 cross-sections for the CT axial images obtained from the male cadaver. The anatomical cross-sections are also at 1 mm intervals with an image resolution of 2048×1216 pixels and 24 bits of colour. Examples of raw scanning image data of CT, and MRI obtained by the Visible Human Project are shown in Figure 2.8. In this thesis, the reconstructed airway model uses only CT data, because the interval and resolution of scanning images are more accurate than the MRI data.

The reconstructing model of the airways is mainly performed by the Mimics software developed by the Materialise company [124]. Mimics software is an interactive tool for visualisation and segmentation of CT images as well as MRI images and other scanned images. It consists of five modules: Mimic-Base, CT-convert, CTM, CSup, and MedCad modules. The links between Mimic

(a) CT image

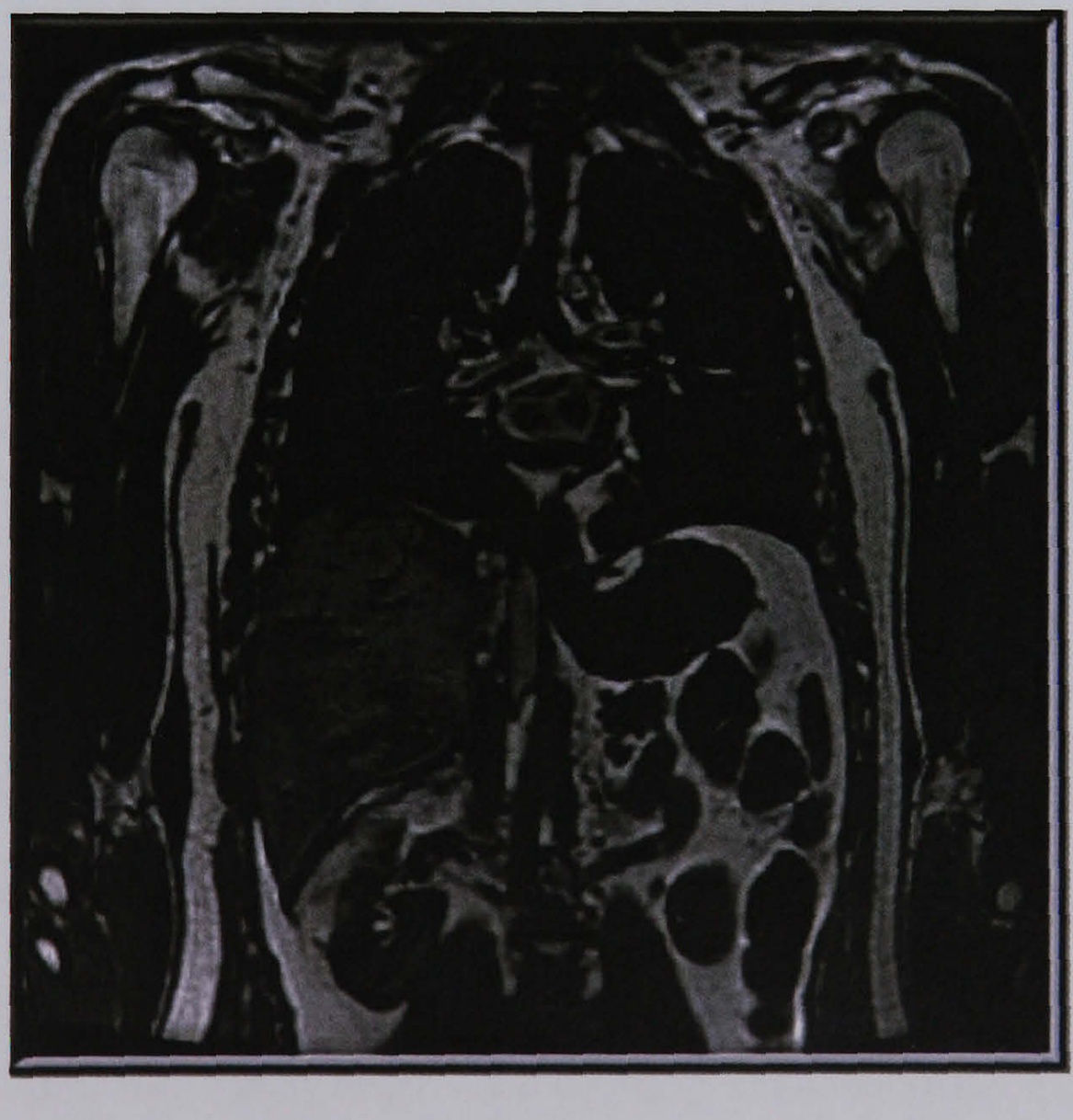

(b) MRI image

Figure 2.8: Examples of raw scanning image data of the Visible Human Project

Base and other modules are shown in Figure 2.9. These modules perform the processes of image segmentation, surface fitting, surface simplification, and CAD file conversion.

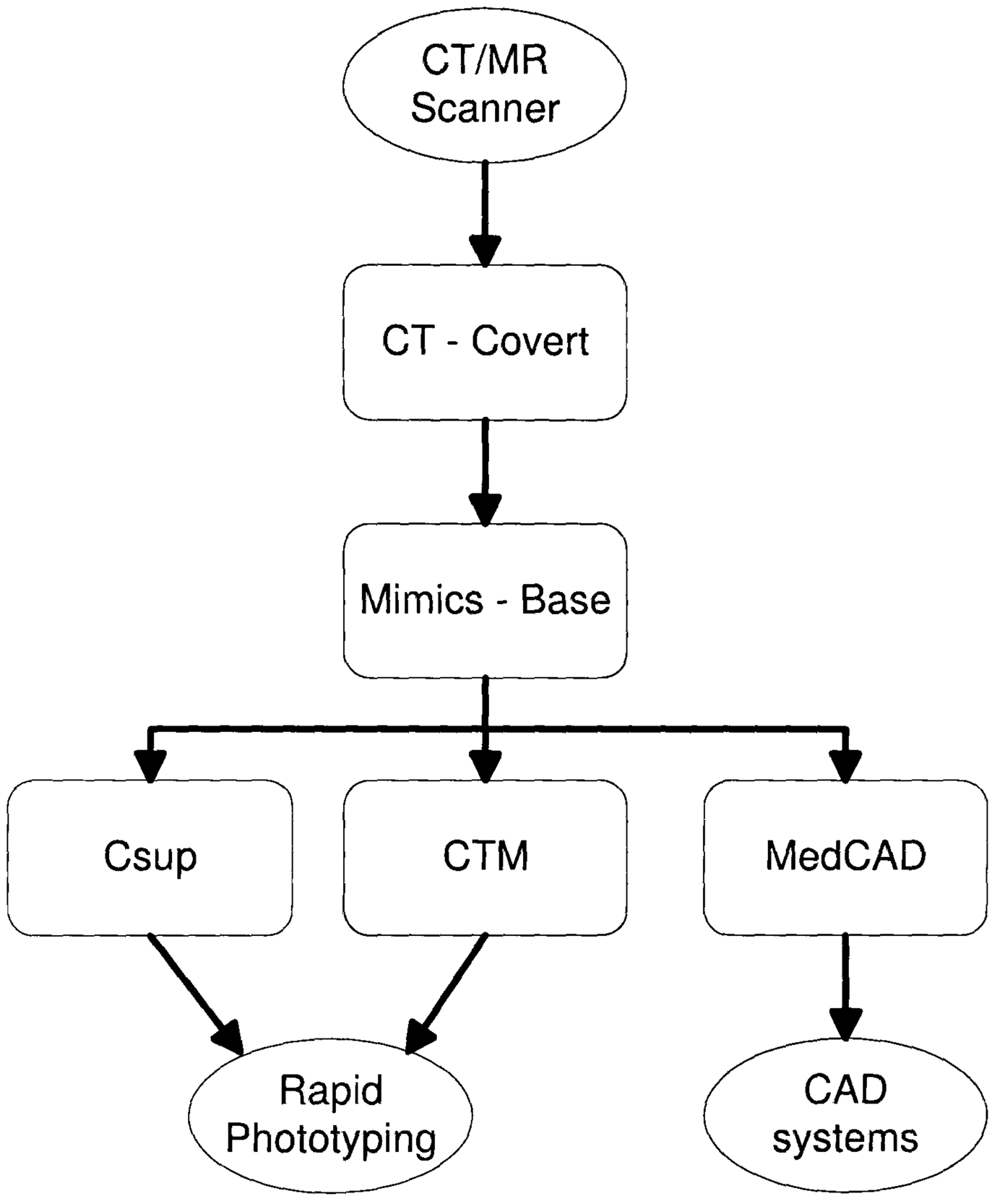

Figure 2.9: Interface of Mimic-Based and other supported modules

The Mimics-Base is the medical front end in which the segmentation of structure can be done with sophisticated three dimensional editing and visualisation tools. The basic segmentation tools include thresholding, region growing, editing, dynamic region growing and morphology operations. The CT-convert modules are tools that can import images from a variety of scanners and convert them to an open 12 bit format. The CTM and Csup modules support a structure for interfacing directly with Rapid Phototyping systems. Finally, the MedCAD modules are tools for interfacing the surface data to CAD or FEA (Finite Element Analysis) by exporting files in the appropriate

file format. The method for creating the airway surface model in this thesis uses only three modules consisting of Mimics-Base, CT-convert and MedCAD modules.

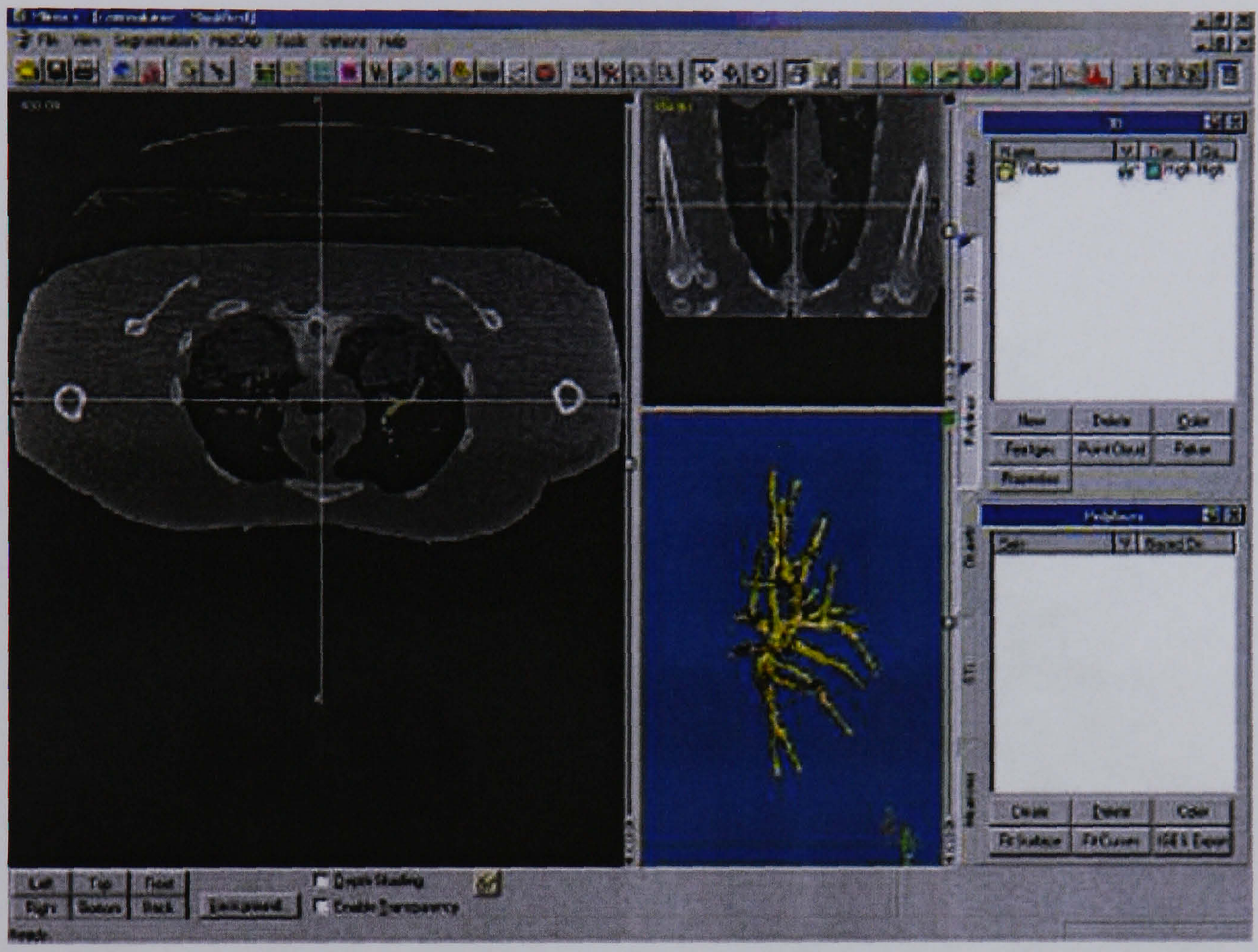

Figure 2.10: Graphical user interface of Mimics program

The reconstruction process starts by importing image data from the CT-convert module into the Mimic-Base. After that the segmentation process for the airway model is mainly performed by thresholding and editing tools. When the segmentation operates, the results of segmentation can be previewed using the visualisation display. The surface model can be generated from the segmented objects and exported to CAD files by the MedCAD modules. The output of the CAD file is represented in STL (Stereolithography) format, which is the standard industrial data format. In this step, the MedCAD module can also perform the surface simplification and smoothing process. The final results of the airway surface modelling by Mimics are displayed in Figure 2.11. The airway models fitted into the reconstructed whole lung of the front, back,

side and top views are shown in Figure 2.12(a), 2.12(b), 2.12(c), and 2.12(d), respectively.

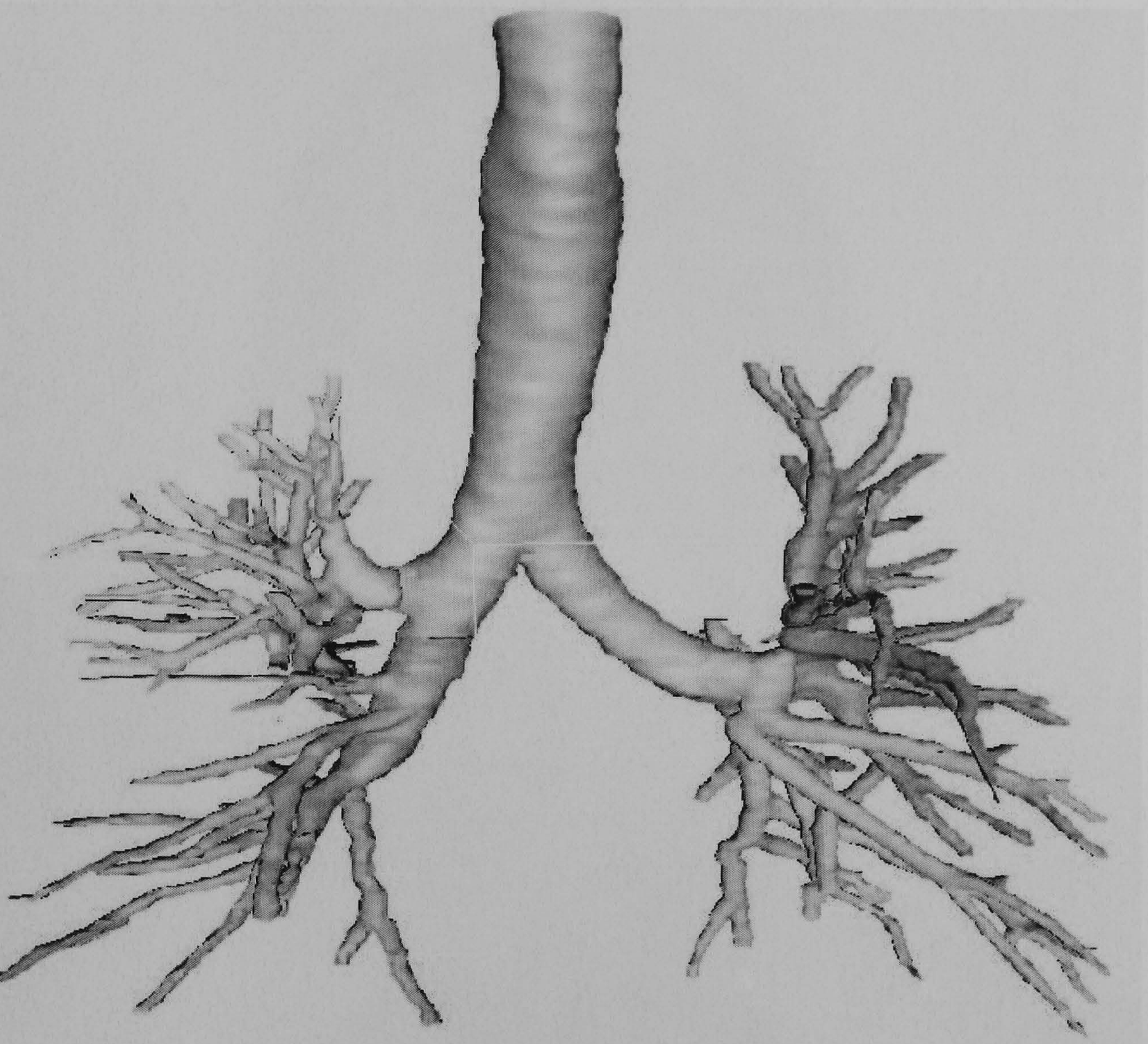

Figure 2.11: Geometrical model of the reconstructed airways

The airway surface model obtained from the Mimics software cannot be imported directly into the CFD software because there are ambiguous and unwanted surfaces in the STL file format. The airway surfaces can be improved by removing ambiguous surfaces and deleting unwanted surfaces from the original surface model using the 3-D studio software, and then modifying surfaces for a better quality using TGRID software. Finally, the definition of boundary types and the creation of a volumetric model of the airway surface was produced by GAMBIT/TGRID software.

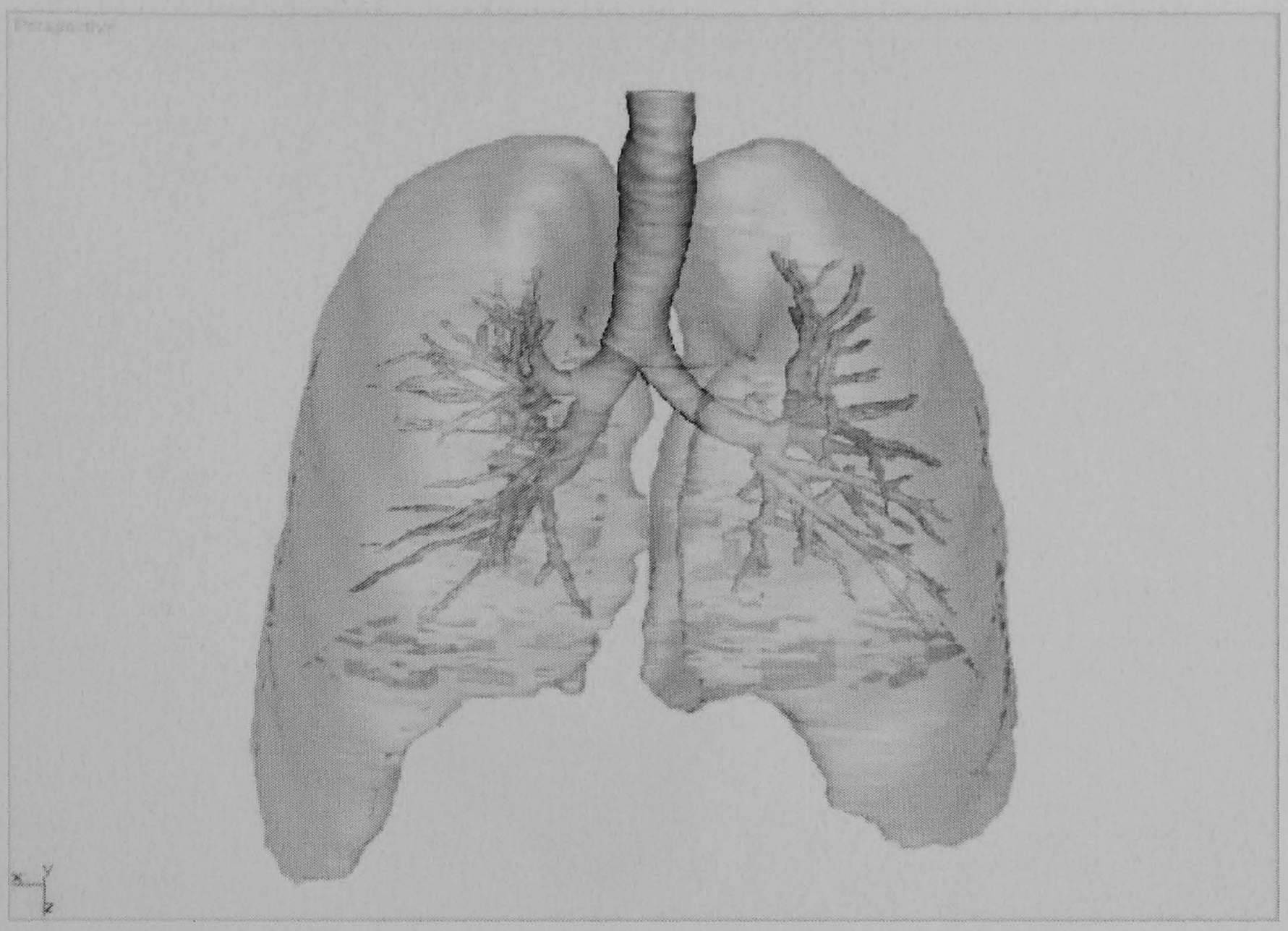

(a) front view

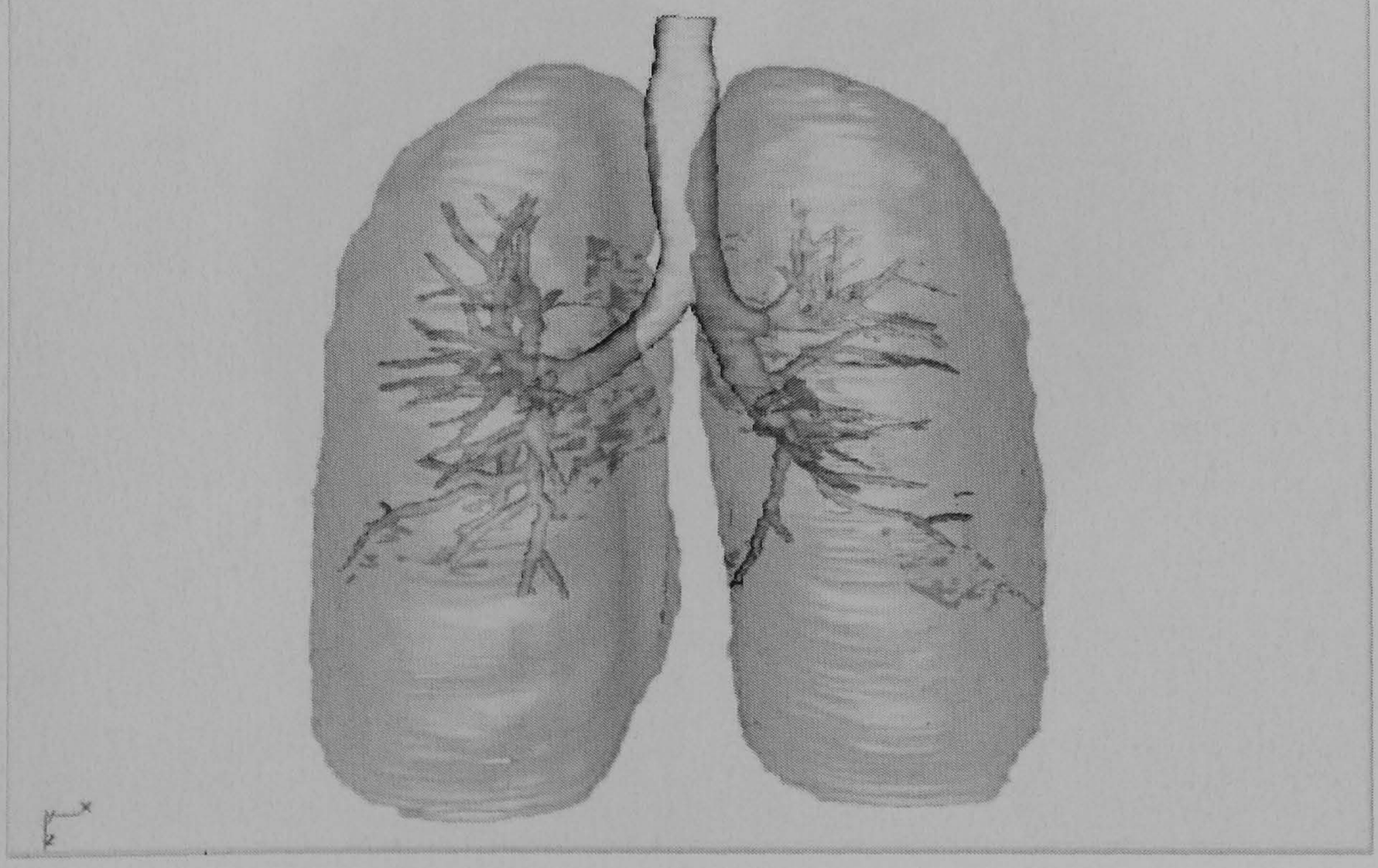

(b) back view

Figure 2.12: Geometrical model of the 3D reconstructed airways and lung shapes

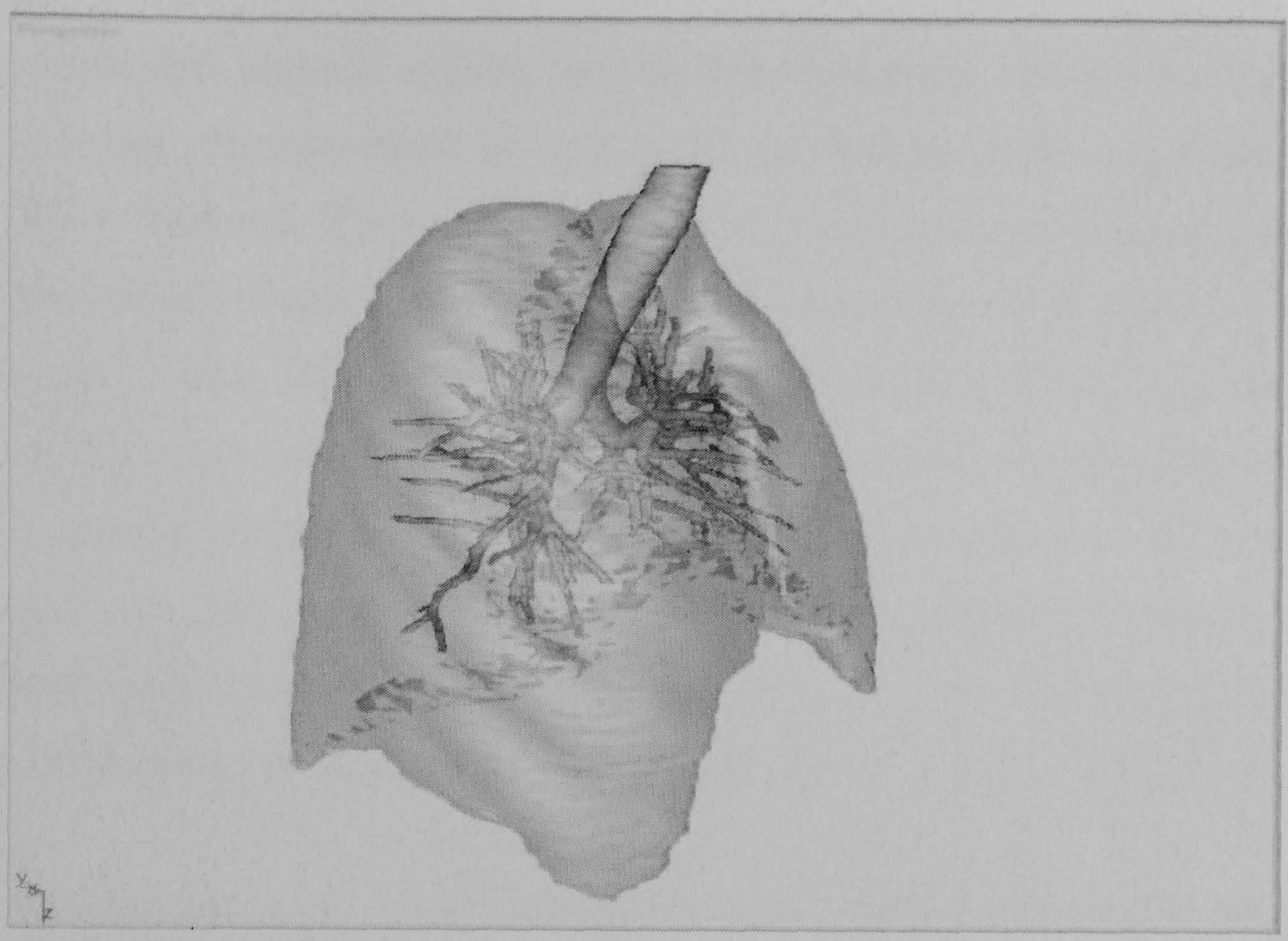

(c) side view

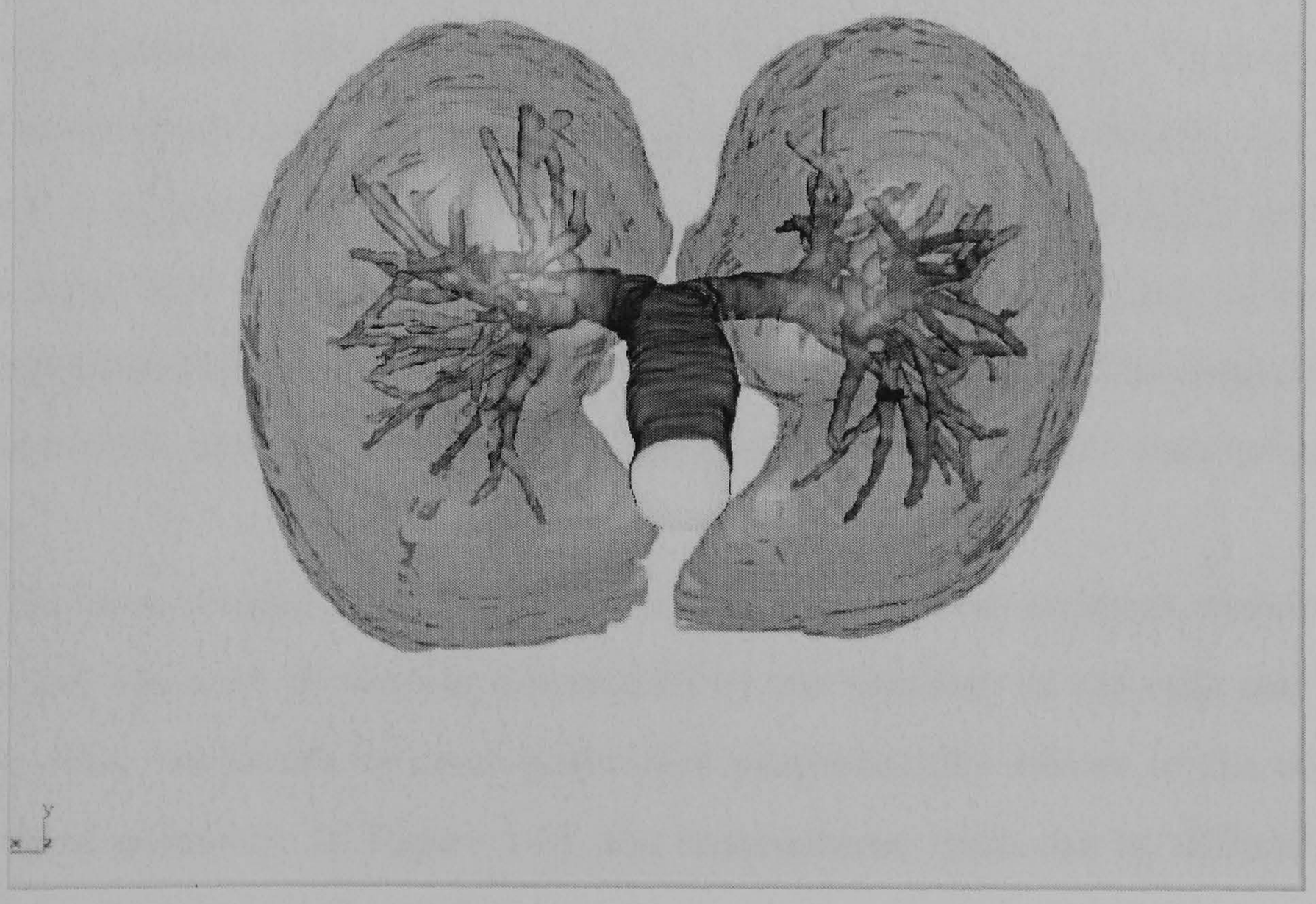

(d) top view

Figure 2.12: Geometrical model of the 3D reconstructed airways and lung shapes (Cont.)

2.4 Mesh generation

In a continuum physical system such as fluid dynamics, electromagnetic or heat transfer, the numerical techniques for solving the governing equations (i.e., Finite Different, Finite Volume, and Finite Element methods) often need the discretised volume in the computation domain, known as mesh or grid structures. These volumetric meshes consist of nodes or mesh elements to represent the continuum variables such as velocity, pressure, temperature, etc. The number of meshes influence the resolution and convergence of the numerical solutions. The elements of the mesh may be represented by tetrahedron, hexahedron, pyramid or wedge meshes. Each element can be composed of different node patterns depending on mesh interpolation schemes shown in figure 2.13.

The mesh structures can be classified by their configuration into 2 common types including structured and unstructured meshes. The structured mesh has a regular arrangement formed by specifying the parameters. Each cell is not defined separately. For example, the mesh shown in Figure 2.14 is represented by the structure mesh in which the parameters can be specified by setting $numX = 5, numY = 4, numZ = 2$. Nodes of geometry can be defined by the data array with a size of $numX \times NumY \times numZ$. The regularity of mesh arrangement allows the fast solver to be used. Vectorizaion and Parallelization are also much easier to implement in the structured mesh than the unstructured mesh.

The unstructured mesh has irregular connectivity with adjacent elements. Each cell has a set of vertices determined by the topology of the cells and its order. The complexity of mesh generation proportionally relates to the complexity of geometry. In Figure 2.15, the unstructured mesh can be defined by the data structure as shown below:

$num\ of\ Element = 3$, $num\ of\ Nodes = 8$,

$element\ Type = \{hexahedral, tetrahedral, tetrahedral\}$

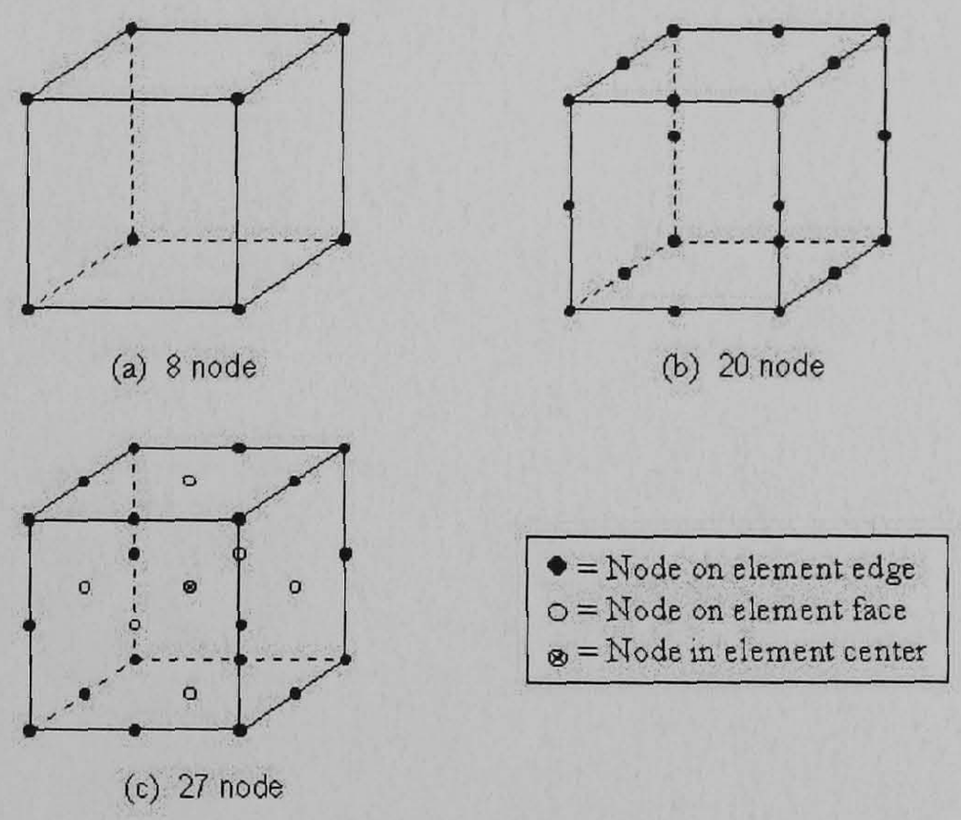

(a) Hexahedral Element

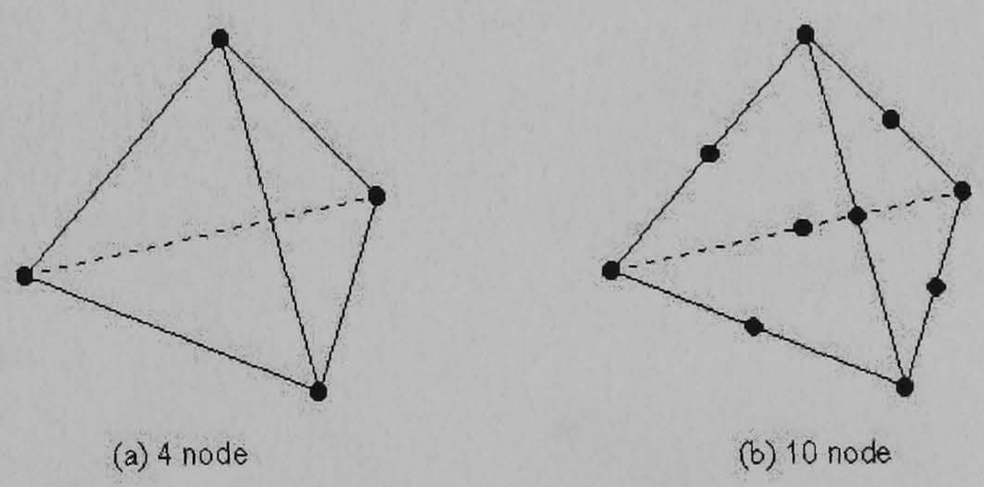

(b) Tetrahedral Element

Figure 2.13: The node configuration in the element [61]

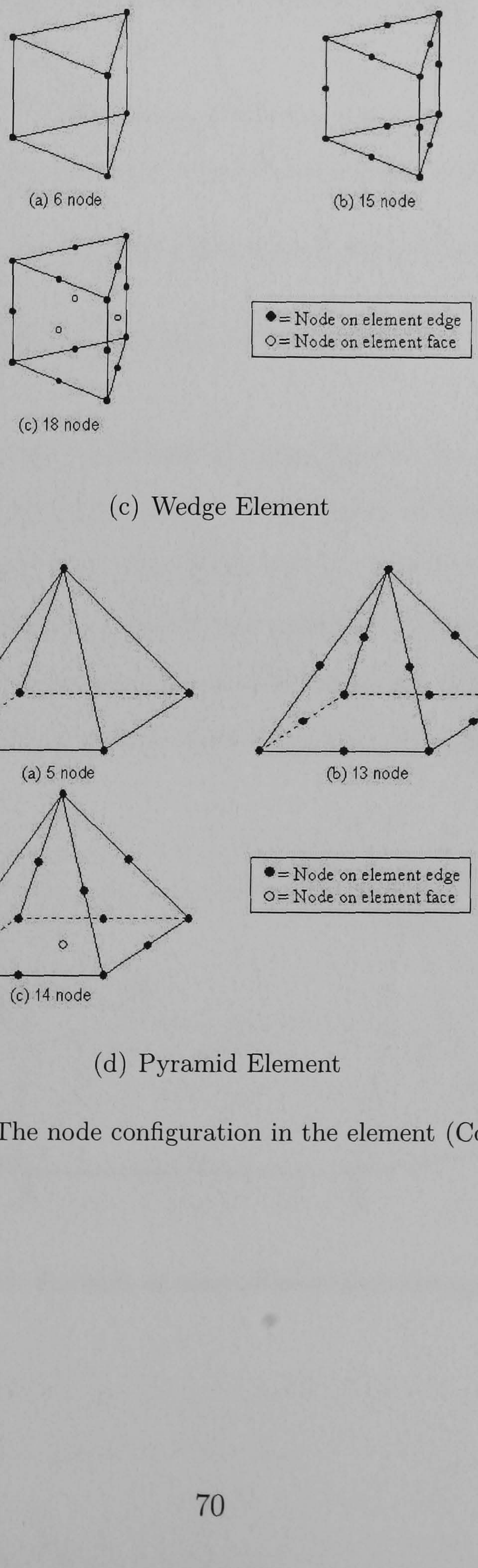

(c) Wedge Element

(d) Pyramid Element

Figure 2.13: The node configuration in the element (Cont.) [61]

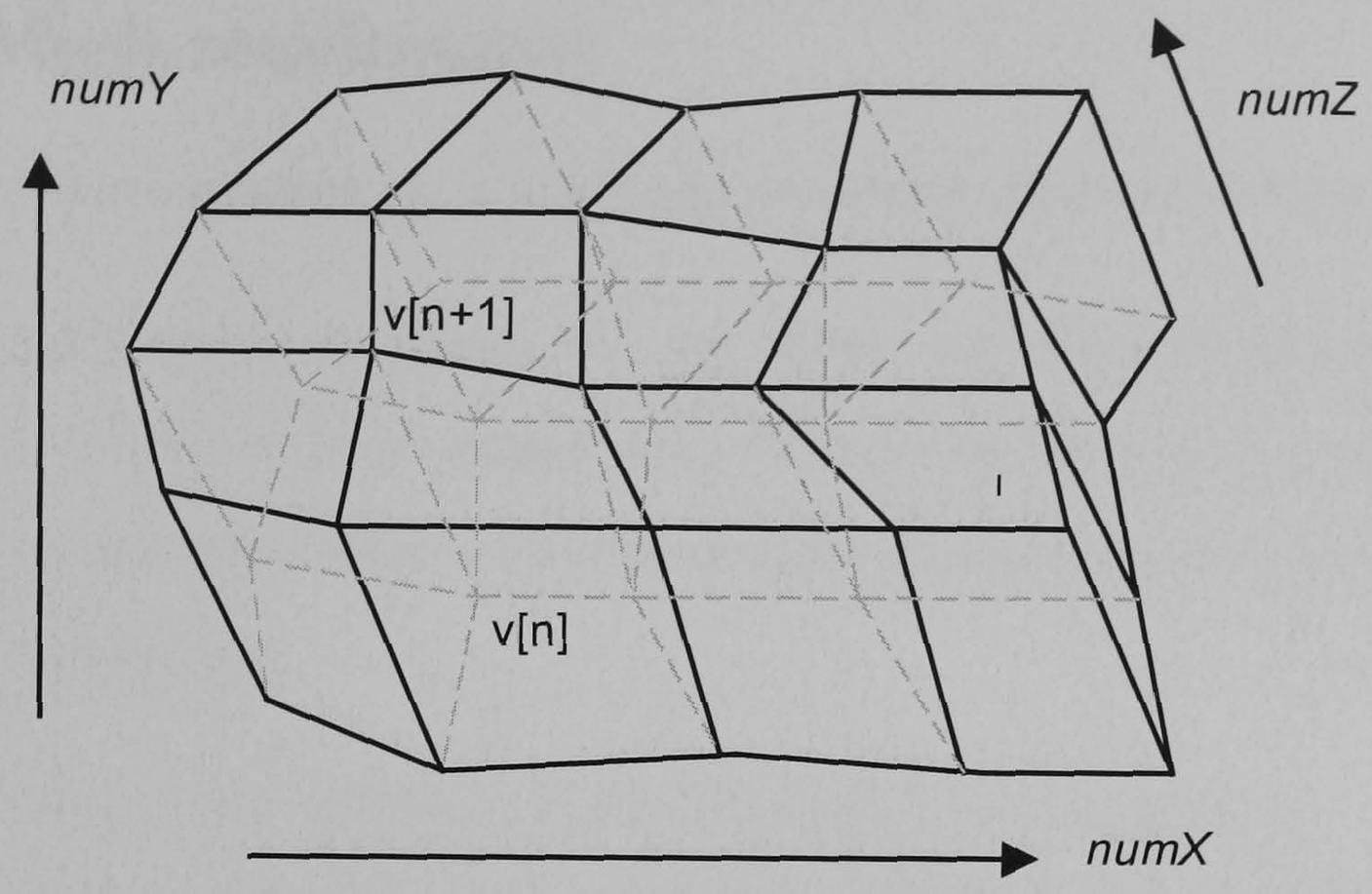

Figure 2.14: Example of structured mesh arrangement

$element\ Node = \{1, 7, 0, 2, 5, 3, 0, 6, 7, 1, 2, 5, 3, 4\}$.

Vertices of geometry can be defined by an array of x, y, z coordinations such as $xNode[i], yNode[i], zNode[i]$, where i is the index of vertices. The topology of unstructured mesh can be divided into Tri/Tetrahedral, Quad/Hexahedral, Pyramid and Wedge meshes. A significant number of algorithms are proposed for the automatic mesh generation for specific topology. However the complex-irregular shape of the airway model often relies on triangular/tetrahedral mesh generation.

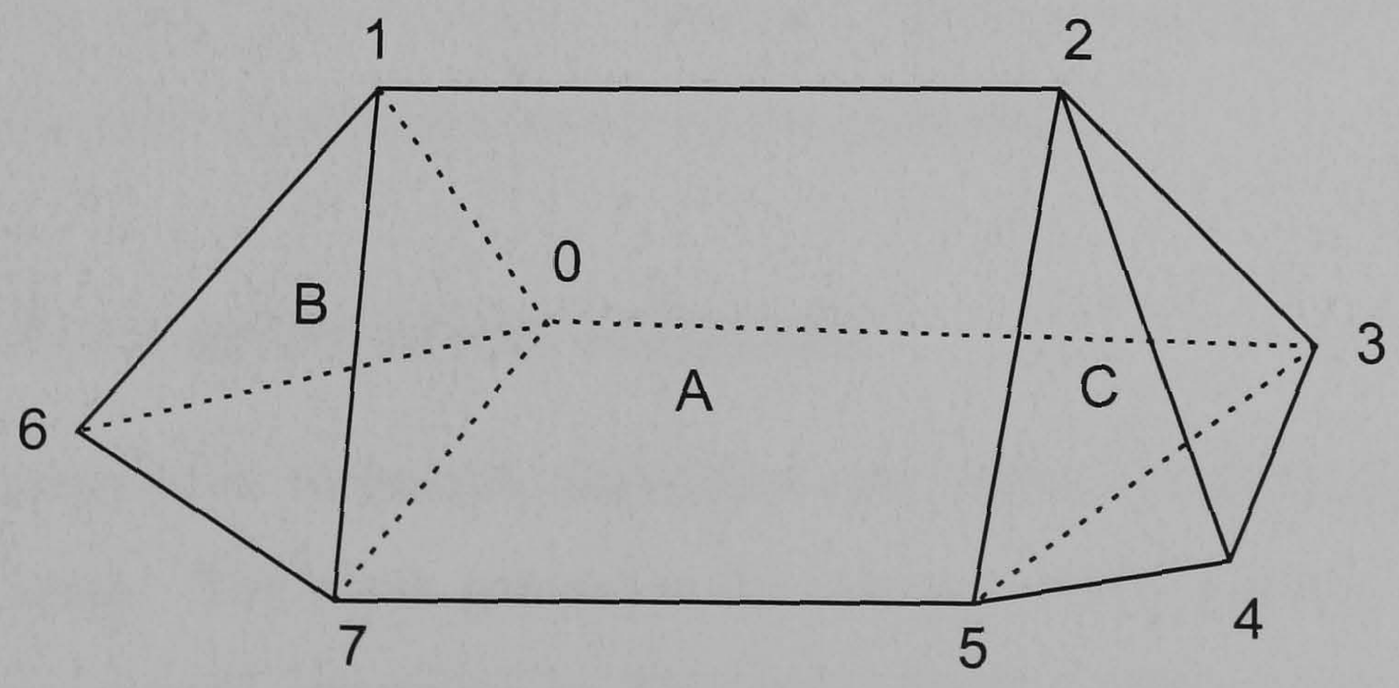

Figure 2.15: Example of unstructured mesh arrangement

2.4.1 Mesh requirement

The certain requirements on a mesh can be summarised as follows [55]:

- The mesh must be valid, i.e. no holes, no self-intersection, no faces joined at two or more edges, etc. This is an obvious requirement, but many mesh generation schemes require a large amount of checking for these conditions.

- The mesh must confirm to the boundary of the domain. Again this is an obvious requirement, but some schemes (e.g., a straightforward Delaunay triangulation) do not satisfy this, and the generation scheme needs to check and correct any edges/faces that intersect the boundary.

- The density of the mesh must be controllable, to balance the trade-off between accuracy and solution time.

- The grid density can vary depending on local accuracy requirements, but this variation must be smooth to reduce or eliminate numerical diffusion/refraction effects.

- The shape of elements should have a good skewness value, e.g. equilateral triangles, regular tetrahedra. A poor quality mesh (high skewness values, e.g. long, thin triangles, squashed tetrahedra) can affect numerical stability and cause convergence speed problems.

2.4.2 Mesh generation software

The mesh generation technique associates with either a structured or an unstructured mesh. The mesh generator for the structured mesh is also known as "a grid generator" (reviewed by Thompson [184] and Farrashkhalvat et al. [50]). The results of meshes generated by a structured grid generator are often represented by all quad/hexahedral meshes. The mesh is also involved with the complex iterative smoothing techniques that attempt to align elements with

boundary and physical domains. On the other hand, the unstructured mesh generator relaxes the node requirement. Triangular and tetrahedral elements are most commonly used for unstructured meshing, although quad/hexahedral, wedge or pyramid mesh can also used. Numerous unstructured mesh generators can be implemented (Owen [144] and Teng [183]). After the mesh is obtained from the mesh generator, it is rare to satisfy the optimal point without mesh post-processing to improve the overall quality of elements. Three operations are involved in the mesh post-processing; smoothing, clean-up and refinement. Smoothing methods aim to adjust node locations while maintaining the element configuration. Clean-up methods are similar to the smoothing process, but these methods are employed to change the element connectivity. Finally, refinement methods are defined as any operation performed on a mesh that effectively reduce the local element size. Several refinement methods in themselves can be considered as mesh generation algorithms starting with a coarse mesh, then performing refinement until the nodal density has been achieved. A good review of these mesh post-processing operations can be found in [144].

To use the GAMBIT/TGRID softwares (FLUENT preprocessing packages), the volumetric mesh requires various parameters such as meshing scheme, mesh node spacing, and the meshing option. The mesh element options in the GAMBIT/TGRID software are listed in Table 2.3. The selection of mesh schemes associated with the mesh elements is summarised in Table 2.4.

Table 2.3: Mesh element options in GAMBIT [61]

Option	Description
Hex	Specifies that mesh includes only hexahedral mesh elements
Hex/Wedge	Specifies that mesh primarily consists of hexahedral mesh elements, but may includes wedges where appropriate
Tet/Hybrid	Specifies that mesh primarily consists of tetrahedral mesh elements, but may include hexahedral, pyramidal and wedge elements where appropriate

Table 2.4: Mesh scheme options in GAMBIT [61]

Option	Description	Hex	Hex/ Wedge	Tet/ Hybrid
Map	Creates a regular structure grid of hexahedral mesh	X		
Submap	Divides an unmappable volume into mappable regions and then performs Map scheme	X		
Tet-Primitive	Divides a four-sided volume into four hexahedral regions and creates a mapped mesh in each region	X	X	
Cooper	Sweeps the mesh node patterns of specified source faces through the volume	X	X	
TGrid	Creates an unstructured grid of tetrahedral mesh			X
Stairstep	Creates a regular hexahedral mesh and faceted volume that approximates the shape of the original volume	X		

The volumetric mesh of the geometrical airway models in this thesis is mainly obtained by both manual and automatic Tri/Tetrahedral mesh generation process with the TGrid scheme. The TGrid scheme uses a robust, fast, and highly automated Delaunay scheme ([131], [125], and [88]) that produces a 3D volume mesh from independently defined surface triangulation.

The mesh generation process in the GAMBIT/TGRID software is separated into 2 phases: initialisation and refinement processes. The initialisation phase aims to create a mesh containing all the boundary nodes and boundary faces. The automatic initialisation procedure can be listed as follows:

1. Merge free node.

2. Delete unused nodes.

3. Improve surface mesh.

4. Initialise mesh.

The automatic refinement process inserts interior nodes into the mesh to produce a reasonable mesh with a good quality. The grid quality can be assessed in the presence of the numerical field solution. However, the GAMBIT/TGRID software measures the quality of meshes independent of the solver by using skewness to provide a simple rule of thumb for deciding whether a mesh will be sufficient before an actual solution is generated. The skewness value can be calculated by using the following equation.

$$skewness = \frac{optimal\_cell\_size - cell\_size}{optimal\_cell\_size} \tag{2.1}$$

where *optimal_cell_size* is the size of an equilateral cell with the same radius.

The refinement process modifies the mesh to achieve low cell skewness. The number of refinement levels can be controlled by setting the number of the level parameter. The automatic refinement procedure can be summarised as follows:

1. Sort boundary faces by size.

2. Refine cells on boundary.

3. Reverse sort cells by skewness.

4. Refined active cell zone(s).

5. Swap faces on cells

6. Reverse sort cells by skewness.

7. Smooth mesh.

8. Remove boundary slivers.

The mesh can also be altered after getting the numerical results (also known as grid adaptation) by refining and/or coarsening the mesh based on the numerical solution data. By using a solution adaptation refinement (i.e, gradient and iso-value adaptations), cells can be added when they are needed in the mesh, thus enabling the feature of the flow field to be better resolved. When adaption is used properly, the resulting mesh is optimal for the flow solution because the solution is used to determine where cells should be added. The features of grid adaptation in FLUENT software can be found in [60].

2.5 Summary

Numerical studies of airflow and aerosol transport within the geometrical airway models have a trend to be based on both the 3D morphological based and 3D reconstructed airway models. The morphology based airway model is created by an algorithm based on the morphology and statistical characteristics of airways without overlapping parts. The reconstructed airway model is generated directly from the scanned image data using imaging techniques. However, these geometrical airway models (also known as partial lung simulation (PLS)) are limited in some parts of the respiratory airways, since the whole respiratory tract is too demanding of computational resources. In this

thesis, the geometrical human airway model proposed consists of 3 models: 3D bifurcation, 2D alveolar, and 3D reconstructed airway models. Deposition in these models can be predicted more accurately with this approach than with the simplified 1D deposition model (i.e., Lagrangian and Eulerian dynamic models). At the present time, the PLSs are not yet ready to supplant the 1D deposition model, but they can be used to allow research aimed at improving the 1D deposition model.

Firstly, the 3D bifurcation airway model is a double bifurcation model representing the airway generation numbers 3-5. The bifurcation model is a symmetrical branching structure with sharp carinal ridges. Secondly, the 2D alveolar model consists of 6 generations of alveolar ducts in which the first generation represents the airway generation 18 of Weibel's model. The alveolar model is more realistic than previous alveolar model in that it integrates both the alveolar duct and bifurcation areas. The alveolar ducts of the model are fully surrounded by alveoli. Finally, the reconstructed airway model was created directly from CT image data provided by The Visible Human project. The process of reconstruction includes image enhancement, image segmentation, surface fitting, surface simplification and CAD file conversion. These processes have been mainly implemented using the Mimics software.

The mesh generation of these geometrical airway models is required for the numerical techniques to solve the governing equations of the airflow. The physical models are represented by unstructured meshes containing triangle/tetrahedral elements obtained using the GAMBIT/TGRID software. The process of mesh generation in the GAMBIT/TGRID software can be separated into 2 phases: the mesh initialisation and the mesh refinement process. The initialisation aims to create a mesh, and then the refinement process improves the mesh quality.

These geometrical models are static models that neglect the effects of model deformation between parts of the breathing cycle. The realistic anatomical wall surfaces (histology) within the models depend on the respiratory regions

given in detail by ICRP publication 66 [140]. For example, the wall surface of the bronchial region has cilia covered with a gel layer (mucus). Therefore the airflow over these realistic walls is complex, and both theoretical and experimental studies of such complex flows are lacking. In this study the walls of airways are simplified as smooth rigid walls. Additionally, all airway models and data used in this thesis are based on healthy adult lungs.

Chapter 3

Transport and Deposition of Pharmaceutical Aerosols

This chapter describes the theory of aerosol transport and deposition in human airways that are used in the processing step of the diagram in Figure 1.11. The theory discussed in this chapter focuses on the uncharged particle case with mechanisms of impaction, gravitational sedimentation, and diffusion.

The transport of pharmaceutical aerosols can be considered as a dispersed phase flow problem in which the dispersed phase does not not materially connect with the continuous phase. The introduction to the dispersed phase is reviewed in section 3.1. The description of the dispersed phase is explained in terms of dilute and dense flow with phase coupling. The classification of both the continuous and dispersed phases are also discussed in this section. The governing equations of the continuous phase and dispersed phase flows can be modelled using the transport equations of mass, momentum, and energy given in section 3.2 and 3.3, respectively. The non-dimensional analysis of airflow in human airways is then described in section 3.4. Finally, section 3.5 explains the non-dimensional analysis of aerosol transport and deposition based on aerosol mechanisms within the morphological human lung model.

3.1 Introduction

The dispersed phase flow is a flow in which the dispersed phase is not materially connected with the continuous phase, e.g., gas-droplet, gas-particle and liquid-particle flows. The classification of a dispersed phase can be divided into dilute and dense dispersed phase flows. The dilute dispersed phase flow is defined when the effects of particle-particle interaction are not significant. The particle motion is mainly dominated by the fluid forces. On the other hand, the dense flow can be described as the situation where particle motion is primary controlled by particle collision. The simple criteria for classifying dilute or dense nature of flow can be considered using the ratio of the momentum response time of particles to the collision time [36]. The flow can be considered as dilute if

$$\frac{\tau_v}{\tau_c} < 1 \tag{3.1}$$

where τ_v is the relaxation time (momentum response time) and τ_c is the average time between particle-particle collision. It means that the particles have sufficient time to respond to the local fluid force before the next collision. If this ratio is more than one, it can be considered as a dense flow. More details of the criteria can be found in [119].

Based on the study by Sommerfield [172], the maximum particle size for dilute flow at the mass loading of unity with a standard deviation of the particle fluctuation velocity of 1.0 m/s would be about 20 μm, where the mass loading is defined as the particle mass per unit volume of mixture divided by the continuous-fluid mass per unit volume of mixture

$$\gamma = \frac{\beta \rho_p}{\rho_c} \tag{3.2}$$

where β is the fraction of dispersed phase volume to the total mixed volume. Due to the small particle size of pharmaceutical aerosols, the aerosol transport in the human respiratory system can be modelled as dilute dispersed phase flow, similar to many of the previous studies, e.g. [205], [32], and [123]. Thus the details of dispersed phase flow discussed in this chapter relates only to the

dilute dispersed phase system. The details of dense dispersed phase flow can be found in [36],[5],[188].

3.1.1 Phase coupling

The coupling between the continuous phase and the dispersed phase is an important concept in flow analysis. The coupling can be divided into one-way coupling and two-way coupling. The continuous phase in many applications will effect the dispersed phase, but not *vice versa*. In one-way coupling, it is assumed that the dispersed phase has no reverse effect on the continuous phase flow. On the other hand, two-way coupling has effects between both phases. The coupling upon both phases can be modelled through the interphase transfer of mass, momentum, and energy. Mass coupling may involve the addition of mass to the continuous phase by evaporation or removal of mass by condensation. Momentum coupling is the result of drag forces between both phases. Energy coupling occurs through heat transfer between phases. One of the criteria for defining coupling as one or two-way can also be the mass loading. The dispersed phase flow can be considered as one-way coupling if the mass loading is much smaller than unity ($\gamma \ll 1$) [36].

3.1.2 Classification of continuous phase flow description

Continuous phase simulation is commonly carried out in an Eulerian reference frame. The fluid characteristics (e.g., velocity, temperature, pressure) are represented by the different spatial discretization, e.g. constant, linear, and quadratic. The solution of these equations may be solved by finite-difference, finite-volume or finite-element methods, which will be briefly described in section 3.2.4. However, although the continuous fluid can be represented in a Lagrangain manner [75],[21], this is rarely used in the general problems.

The continuous domain can be treated as either an inviscid or a viscous formulation. The inviscid formulation does not account for the effect of vis-

cosity to fluid motion. This formulation is not suitable for the application of potential flow, rotational flow and compressible rotational flow. The viscous formulation includes the effect of viscosity. There are two viscous flow categories consisting of laminar and turbulent flow. The criteria for defining either laminar or turbulent flow often uses the Reynolds number, which gives a measure of the relative importance of inertia and viscous forces. In experiments a flow with Reynolds number below the critical Reynolds number is smooth and adjacent layers of flow slide pass each other; this is called "laminar flow". At values above the critical Reynolds number, the flow velocity and all other flow properties vary in random and chaotic ways, known as "turbulent flow". The turbulent flow can be classified by flow description in terms of unresolved-eddy (also known as time-average flow) and resolved-eddy (which predicts the individual spatio-temporal features of the turbulence eddy structure).

The unresolved eddy formation for turbulent flow is primarily based on Reynolds Average Navier-Stokes (RANS) equation, where all spatial velocity components are the combination of average and fluctuating components. The main aim of RANS model is to represent the Reynolds-stress term which appears in the flow transport equation. There are many models for estimating the Reynolds-stress term namely: zero equation model (mixing length), two-equation model (k-ϵ, k-ω, q-ω model), Reynolds stress equation, and Algebraic stress model. The details of these sub RANS models are explained in many fluid dynamics books, e.g., [174],[20], and [146].

The unresolved eddy formulation predicts the individual spatio-temperal feature of the turbulence eddy structure, i.e, vertex dynamical model, proper orthogonal decomposition model, large eddy simulation model and direct numerical simulation. More details of these formulations can be found in [146], and [119]. However, most of these formulations require huge computational resources.

3.1.3 Classification of dispersed phase flow description

The description of dispersed phase flow can be classified into 2 types including the Eulerian and Lagrangian representations.

3.1.3.1 Eulerian representation

The Eulerian representation describes the dispersed phase as another fluid phase using the same reference as the continuous phase. It can be subdivided into mixed-fluid and separated-fluid approaches.

The mixed-fluid approach is based on the assumption that the dispersed and continuous phases can be analysed as a single-phase fluid flow. Both phases are assumed to be in dynamic and thermodynamic equilibrium and the rate of transport between two phases is small in comparison to that of the whole fluid flow. This approximation is also known as Locally Homogenous Flow (LHF). The advantage of mixed-fluid approach is the minimum requirement of dispersed phase characteristics such as size, shape, and velocity distribution. However, this technique cannot resolve phases moving at different rates.

The separated-fluid approach in the Eulerian representation makes the assumption that both phases are comprised of separate continua. The interaction between both phases is accommodated via extra source terms introduced into the continuous phase transport equation. There are three complications in using the Eulerian techniques: (1) particle reflection from the surface, (2) significant polydispersion of size, and (3) turbulence diffusion. The details of a mathematical model of the Eulerian approach can be found in [119].

3.1.3.2 Lagrangian representation

The description of the dispersed phase in a Lagrangian reference frame can be divided into point-volume particles and resolved-volume particles, as shown in Figure 3.1a. The point-volume representation assumes that integrated mass and heat transfer and surface stress around the particle surface are average quantities. It may neglect the effect of particle volume in the continuous phase.

This technique requires models of drag, lift and other forces acting on particles. The resolved-volume approach describes the particle volume and interface as a part of the computation domain displayed in Figure 3.1b. This simulation technique usually limits the number of particles because of the need for describing the spatial and temporal scales associated with the particle's local external and internal flowfield. As the results, it requires a high performance CPU and computational resources.

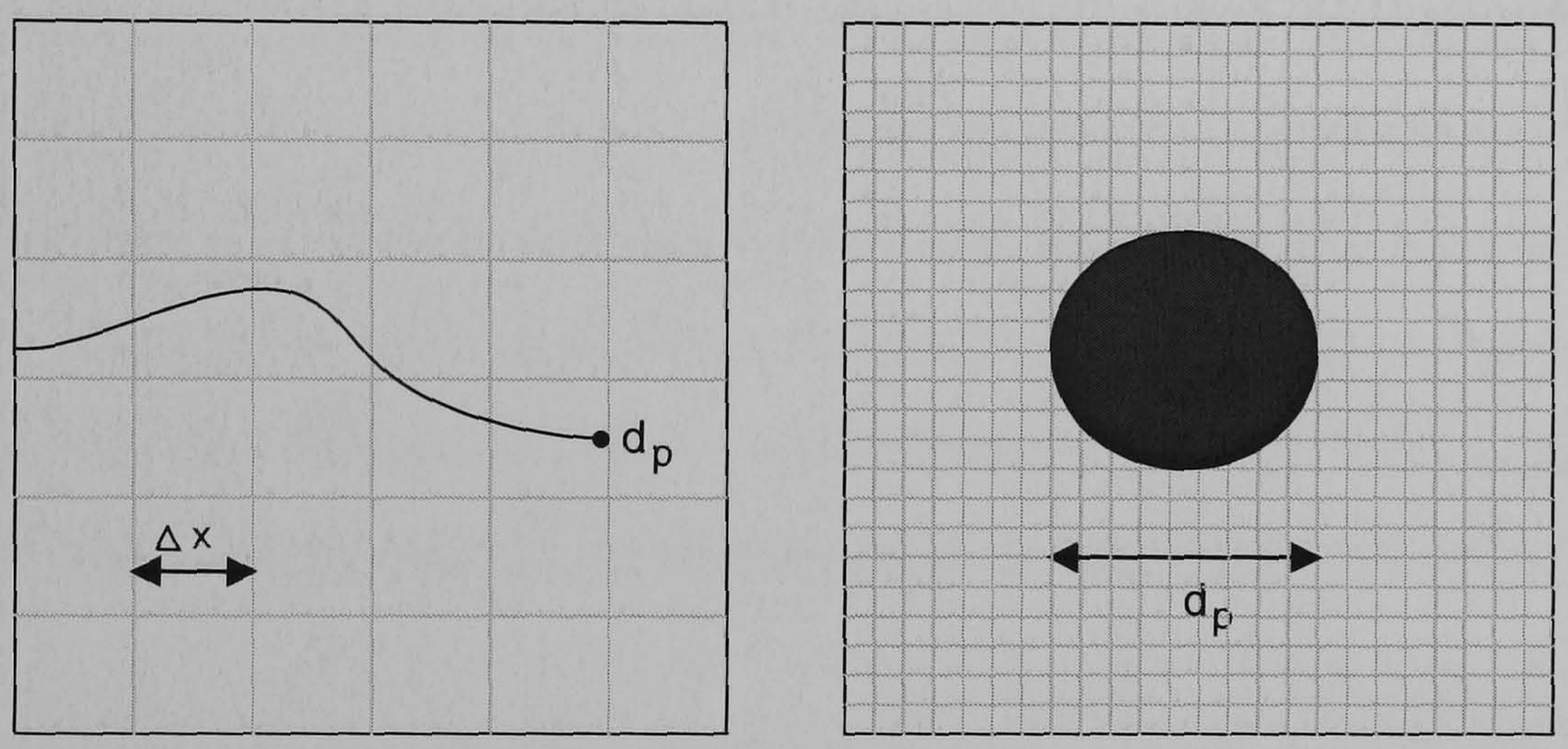

(a) point-volume particles ($d_p \ll \Delta x$) (b) resolved-volume particles ($d_p \gg \Delta x$)

Figure 3.1: point-volume versus resolved-volume particles [119]

3.1.3.3 Eulerian versus Lagrangian representation for modelling of inhaled drug delivery

In modelling aerosol transport and deposition for drug delivery applications, the separated-fluid Eulerian approach requires the effective diffusion coefficient, which can be obtained experimentally. Some empirical formulae have been suggested for this application [161], [47]. However, different profiles occur in different parts of lungs, therefore very little direct experimental evidence is available for determining the effective diffusion coefficient. In addition, the Eulerian model with more than one spatial dimension is difficult to use when obtaining an inertial impaction term, whereas the Lagrangian model more naturally deals with this by tracking individual particles [58]. Hence, the point-volume Lagrangian representation is a more popular technique than the

Eulerian representation for drug delivery applications in two or three spatial dimension. Transport equations of the dispersed phase are defined in a Lagrangian reference frame and the continuous phase transport equations are defined in an Eulerian reference frame, which contain additional source terms for the interaction of both the continuous and dispersed phases. The turbulence dispersion of the dispersed phase can be simulated using a stochastic model based on the interaction between two phases. This approach is relatively economical compared with other techniques (except for the mixed-fluid approach). The main disadvantage of the point-volume Lagrangian technique is the sensitivity to initial conditions (i.e., size, position, and velocity distribution). Thus good values of initial conditions are required. These values, however, are very difficult to obtain experimentally. The governing equations for point-volume Lagrangian models are given in more detail in section 3.3.

3.2 Fluid governing equation

The governing equations of fluid flow represent mathematical statements of the conservation laws of physics:

- The mass of fluid is conserved.
- The rate of change of momentum equals the sum of forces on fluid particle (Newton's second law).
- The rate of change of energy is equal to the sum of the rate of heat addition and the rate of work done on fluid particle (The first law of thermodynamics).

The fluid flow can be described by either a Lagrangian or a Eulerian frame. However, the Eulerian description is often applied based on these conservation laws.

3.2.1 Mass conservation

The mass conservation equation is given by:

$$\frac{\partial \rho_c}{\partial t} + \nabla \cdot (\rho_c \mathbf{u}) = 0 \tag{3.3}$$

where $\mathbf{u}(x, y, z, t)$ is the velocity vector, and ρ_c is the density of fluid.

For an incompressible fluid (i.e., a liquid), the density ρ_c is a constant and the equation becomes

$$\nabla \cdot \mathbf{u} = 0 \tag{3.4}$$

3.2.2 Momentum conservation

The momentum equations along x-,y-,and z-directions with the body forces on fluid particle can be written as:

$$(x - momentum) \quad \frac{\partial(\rho_c u)}{\partial t} + \nabla \cdot (\rho_c u \mathbf{u}) = -\frac{\partial p}{\partial x} + \nabla \cdot (\mu \nabla u) + S_{Mx} \tag{3.5}$$

$$(y - momentum) \quad \frac{\partial(\rho_c v)}{\partial t} + \nabla \cdot (\rho_c v \mathbf{u}) = -\frac{\partial p}{\partial y} + \nabla \cdot (\mu \nabla v) + S_{My} \tag{3.6}$$

$$(z - momentum) \quad \frac{\partial(\rho_c w)}{\partial t} + \nabla \cdot (\rho_c w \mathbf{u}) = -\frac{\partial p}{\partial z} + \nabla \cdot (\mu \nabla w) + S_{Mz} \tag{3.7}$$

where p is a pressure, μ is a fluid viscosity, S_{Mx}, S_{My}, S_{Mz} are the body forces.

3.2.3 Energy conservation

The energy conservation is derived from the first law of thermodynamics. The energy of a fluid is often defined as the sum of internal (thermal) energy i. Thus energy conservation can be written as:

$$\frac{\partial(\rho_c i)}{\partial t} + \nabla \cdot (\rho_c i \mathbf{u}) = -p \nabla \cdot \mathbf{u} + \nabla \cdot (k \nabla T) + \Phi_d + S_i \tag{3.8}$$

where k is the thermal conductivity, S_i is the energy source term,Φ_d is the dissipation function defined by equation 3.9.

$$\Phi_d = 2\mu\left[\left(\frac{\partial u}{\partial x}\right)^2 + \left(\frac{\partial v}{\partial y}\right)^2 + \left(\frac{\partial w}{\partial z}\right)^2\right] + \mu\left(\frac{\partial u}{\partial y} + \frac{\partial v}{\partial x}\right)^2 + \mu\left(\frac{\partial u}{\partial z} + \frac{\partial w}{\partial x}\right)^2 + \mu\lambda(\nabla \cdot u)^2 \tag{3.9}$$

where λ is the second viscosity to describe stresses of volumetric deformation.

Fluid motion can be described by a system of five partial differential equations. Among the unknowns are included four thermodynamic variables: ρ_c, p, i, and T. At thermodynamic equilibrium, the state of a substance can be described by two state variable. If ρ_c and T are selected as state variables, the state equation for p and i can be expressed as

$$p = p(\rho_c, T) \quad and \quad i = i(\rho_c, T) \tag{3.10}$$

$$e.g.\ perfect\ gas \quad p = \rho_c RT \quad and \quad i = C_v T \tag{3.11}$$

where R is a gas constant value, and C_v is a specific heat capacity at the constant volume.

3.2.4 Numerical discretisation techniques

The motion of fluid in three dimensions as discussed in the previous section can be modelled by the system of five or more partial differential equations. The numerical techniques to discretise these equations often rely on three different methods, namely; Finite Difference, Finite Element, and Finite Volume methods. These numerical techniques are briefly introduced in this section. More details of these computational methods can be found in [53], and [27].

3.2.4.1 Finite difference method (FD)

The finite difference method is a combination of two components including a differential equation of the system and replacement of the differential operators with discrete difference approximations. The grid of points where the discrete difference approximation is calculated is termed a finite-difference grid. The

regular spacing of points is used practically in the finite difference method because this condition provides the optimal convergence rate for the solution.

The discrete difference approximation is primarily based on the Taylor series to approximate equations. The difference equations replacing partial operators requires an adequate small step to reduce an error in the approximation equation. The finite difference method is relatively simple to be implemented in the software. There are many existing finite-difference programs that can be applied to a wide range of problems. However, there are many disadvantages to this method. The primary disadvantage is that many engineering problems do not fit neatly into the restrictive nature of finite difference modelling due to material dissimilarities, complex geometry, and unusual boundary conditions. In addition, there are other disadvantages concerning important issues in verification of solution results and the implementation of boundary equations.

3.2.4.2 Finite element method (FEM)

The finite element method represents the partial differential equation of the computational domain, which is split into a number of sub-domains known as elements. The discretisation process of the finite element method is more complicated than that of finite difference method. Each finite element represents a discrete form of the dependent variables using a shape function and nodal values given by

$$\Phi(\mathbf{x}) = \sum_{i=1}^{n} N_i(\mathbf{x})\phi_i \tag{3.12}$$

where n is the number of nodes on element, N_i is a value of shape function to node i and ϕ_i is a nodal value of node i. The differential operator can be expressed through a shape function. Then a combination of all elements can be assembled by the algebraic equations of N unknowns.

3.2.4.3 Finite volume method (FVM)

The finite volume method was originally developed as a special finite difference formulation. The discretisation equations are derived by integrating the gov-

erning differential equation over a small region called the finite volume. Each control volume is associated with the discrete points. This technique is widely implemented for many commercial CFD packages. The governing equations of fluid transport are described by the transport equations of mass, momentum and energy.

The discretisation equation in the finite volume method represents the transport equation (convection-diffusion equation) by the integration over control volume and defines flux and source terms. These flux and source terms can be expressed as a function of dependent variables. All control-volume equations in the computational domain form a set of simultaneous linear equation.

3.2.4.4 Comparison of discretisation techniques

There are several differences between the three numerical discretisation method summarised as follows [169]:

1. The finite difference method and finite volume method create numerical equations at a given point based on the values at the neighbouring points, whereas the finite element method produces an equation for each element independently of all others.

2. The finite difference method and finite volume method are easily applied to the fixed-boundary conditions by inserting the values of variables into the solution, whereas in the finite element method it is easier to apply the derivative boundary condition when the element equations are formed.

3. The finite difference method generally requires regular topology of grid points to calculate the solution with fast speed and high efficiency. However an irregular topology can be converted to regular topology using grid transformation, but there are some limits in implementation depending on the complexity of the structure. The finite element and the finite volume methods are flexible in order to be used with irregular grids, but they pay a computational penalty for this geometrical flexibility.

The discretisation technique used by the FLUENT software is the finite volume method. However, the exported numerical results are represented as nodal data similar to the representation in the finite element method. The interpolation of nodal data in the developed software also uses the same interpolation techniques as the finite element method. The finite difference method is not used for the computation of airflow in this study, but it is used for solving the space charge field, and further discussed in chapter 4.

3.2.4.5 Numerical solvers for a set of algebraic equations

The set of algebraic equations constituted from any numerical discretisation technique with given boundary conditions can be solved by many numerical solver methods. They can be classified into two groups: direct and iterative methods. Simple examples of direct methods are Cramer's rule matrix inversion and Gaussian elimination. The number of operations to the solution of a system of N equations with N unknowns is of an order N^3. These techniques are not practical because of their large requirement of memory resource.

Iterative methods are the techniques based on the repeated calculations until solutions are convergent under the defined criterion. Well-known examples are the Jacobi and Gauss-Seidel point-by-point iterative methods. The total number of operations cannot be predicted in advance because it depends on the number of convergence cycles. However these techniques are practical to use because only non-zero coefficients of equations need to be stored in the memory. There are many algorithms based on the iterative concepts such as Tri-Diagonal Matrix Algorithm (TDMA), Algebraic Multigrid algorithm(AMG) and Conjugate Gradient algorithm(CG). The details of these algorithms are discussed in [171].

3.3 Dispersed phase governing equations

The dispersed phase governing equations in this study are represented by the point-volume particles based on a Lagrangian representation. The particle-fluid interaction refers to the exchange of properties between phases. The phenomena responsible for mass, momentum and energy transfer between phases are presented. Mass coupling can occur through a variety of mechanisms such as evaporation, condensation or chemical reaction. The momentum coupling transfers between phases arises through mass transfer and interphase forces such as drag and lift. Finally, the energy coupling can be affected by three mechanisms: radiation, convection and internal heating.

In a pharmaceutical aerosol, the particle cloud can be modelled as a dilute dispersed phase flow with one-way coupling between phases, neglecting the effect of evaporation, condensation and heat transfer [58]. Then only the momentum transfer between phase will be presented.

3.3.1 Momentum transfer

The general formulation is based on the momentum equation for a small rigid sphere in an unsteady, non-uniform flow. The momentum equation relates the acceleration of the particle mass and its added mass to the sum of the various forces acting on the particle given by [119]

$$\rho_p V_p \left(1 + \frac{C_M}{\Psi}\right) \frac{d\mathbf{u}_p}{dt} = \Sigma \mathbf{F}_k \tag{3.13}$$

where V_p is the particle volume, k is a summation index for all force components, C_M is the added mass coefficient, and Ψ is the ratio of particle density to continuous-fluid density.

The summation of forces are typically combined with the effects of drag ($\mathbf{F}_D$), gravity ($\mathbf{F}_g$), lift ($\mathbf{F}_L$), fluid stress gradients arising from the continuous-phase acceleration ($\mathbf{F}_S$), Basset history term ($\mathbf{F}_H$), wall interaction ($\mathbf{F}_W$), and

the other body forces ($\mathbf{F}_B$), which are expressed as

$$\Sigma \mathbf{F}_k = \mathbf{F}_D + \mathbf{F}_g + \mathbf{F}_L + \mathbf{F}_S + \mathbf{F}_H + \mathbf{F}_W + \mathbf{F}_B \tag{3.14}$$

However, the particle motion of aerosols for inhaled drug delivery mainly consider only drag, gravity, diffusion and body forces. Therefore these primary forces (drag, gravity, and diffusion) are only discussed here. The electrostatic forces are considered as the body forces, which are discussed in detail in the next chapter. The details of other force terms can be found in [119] and [36].

The particle size is one of the most important attributes of aerosol mechanisms. Inhaled drug aerosols can be modelled as either monodisperse or polydisperse aerosols. The monodisperse aerosol contains particles of single size which may have irregularly shaped particles. The particle can be approximated to a spherical shape that has the aerodynamic properties equivalent to those of the irregular shapes. Using the same settling velocity with different shape and density, the aerodynamic diameter (d_a) can be calculated with the standard particle density ($\rho_0 = 1000\ kg/m^3$) by using the following equation:

$$d_a = d_e \left(\frac{\rho_p}{\rho_0 \chi} \right)^{1/2} \tag{3.15}$$

where d_e is the equivalent volume diameter, ρ_p is the particle density, and χ is the dynamic shape factor.

Practically most of the pharmaceutical aerosols are polydisperse aerosols. Particle sizes can be described by the particle size distribution, usually as the log-normal distribution. These aerosols are often described in term of mass median diameter (MMD) instead of the count median diamter (CMD). One often encoounters the terms CMAD and MMAD, which refer to the count and mass medians of the distributions of count and mass with respect to aerodynamic diameter. The calculation details of these terms are given in [83], [58].

3.3.1.1 Drag force

Drag force is a force generated by the interaction and contact of a body with a fluid in the direction of flow. It is a function of the difference in velocity between the object and the fluid. For the spherical solid particle, the drag force can be given as

$$\mathbf{F}_D = \frac{1}{8}\pi {d_p}^2 \rho_c C_D |\mathbf{u} - \mathbf{u}_p|(\mathbf{u} - \mathbf{u}_p) \tag{3.16}$$

where the drag coefficient C_D is primarily dependent on the particle's Reynolds number. The variation of the drag coefficient by Reynolds number for a non-rotating sphere is shown in Figure 3.2. At low Reynolds numbers, the drag coefficient varies inversely with Reynolds numbers, and is also known as the Stokes regime. For $750 < Re_p < 3.5 \times 10^5$, the drag coefficient varies by only 13 % from $C_D = 0.45$, called the "inertial range". With increasing Reynolds number the drag coefficient suddenly decreases at the critical Reynolds number.

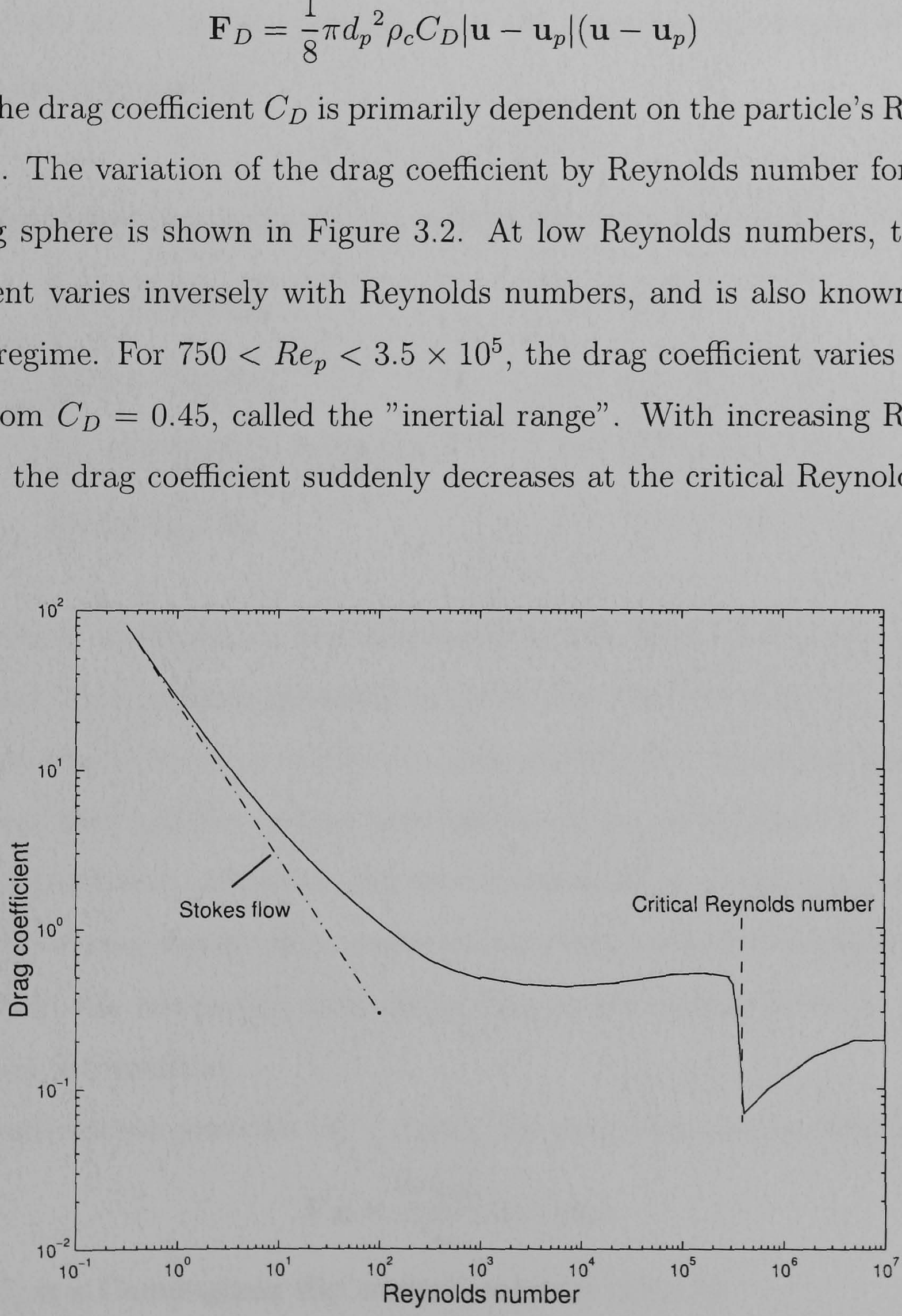

Figure 3.2: Drag coefficient of spherical solid particle as a function of Reynolds number [119]

In the Stokes flow regime, the drag coefficient can be expressed as

$$C_D = \frac{24}{Re_p} \qquad for \;\; Re_p \ll 1. \tag{3.17}$$

where Re_p is the particle Reynolds number defined as

$$Re_p = \frac{\rho_c d_p |\mathbf{u}_p - \mathbf{u}|}{\mu} \tag{3.18}$$

The drag force coefficient at higher Reynolds number can be adjusted with a correction factor derived primary from the experimental results of Clift et al. [29] and expressed as

$$C_D = f_{Re} \cdot \left(\frac{24}{Re_p}\right) \tag{3.19}$$

where f_{Re} is the drag factor for C_D at high Reynolds number(f_{Re}) given by

$$f_{Re} = \begin{cases} 1 + (3/16)Re_p & ; for \;\; Re_p < 1 \\ 1 + 0.1935{Re_p}^{0.6305} & ; for \;\; 1 < Re_p < 285 \\ 1 + 0.015Re_p + 0.2283{Re_p}^{0.427} & ; for \;\; 285 < Re_p < 2000 \\ 0.44(Re_p/24) & ; for \;\; 2000 < Re_p < 3.5 \times 10^5 \end{cases} \tag{3.20}$$

The drag coefficient is also influenced by the effect of the non-spherical shape and Mach number discussed in [119]. For droplets, there are two complications which can serve to alter the drag coefficient including internal circulation and deformability, where both effects can be complicated by the influence of a surfactant. However, the case of liquid drops in gas has been found not to affect drag significantly, such that the drag coefficient expressions for a solid sphere are reasonably accurate as long as the droplet does not undergo significant deformation.

For sub-micron particles ($d_p \leq 1\mu m$), the drag force can be simplified into

$$\mathbf{F}_D = \frac{3\pi\mu d_p}{C_c}(\mathbf{u} - \mathbf{u}_p) \tag{3.21}$$

where C_c is a Cunningham slip correction factor given by

$$C_c = 1 + \frac{2\lambda}{d_p}\left[1.257 + 0.4exp(-1.1(d_p/2\lambda))\right] \tag{3.22}$$

Note that λ is the mean free path of molecule in the fluid.

3.3.1.2 Gravitational force

The relationship between the gravitational force and Buoyancy effect can be expressed based simply on the density difference as

$$\mathbf{F}_g = \frac{(\rho_p - \rho_c)}{\rho_p} m_p \mathbf{g} \tag{3.23}$$

where $\mathbf{g}$ is the gravitational acceleration.

3.3.1.3 Brownian force

The effects of Brownian motion can be included in the additional force term for sub-micron particle. The components of the Brownian force are modelled as a Gaussian white noise process with spectral intensity S_{ij}^n given by [115]

$$S_{ij}^n = S_0 \delta_{ij} \tag{3.24}$$

where δ_{ij} is the Kronecker delta function, and

$$S_0 = \frac{216\nu\sigma T}{\pi^2 \rho_c {d_p}^5 \left(\frac{\rho_p}{\rho_c}\right)^2 C_c} \tag{3.25}$$

T is the absolute temperature of the fluid, ν is the kinematic viscosity, and σ is the Boltzmann constant.

The amplitude of the Brownian force components can be given by

$$\mathbf{F}_{Bn} = (\rho_p V_p)\zeta_{ijk}\sqrt{\frac{\pi S_0}{\Delta t}} \tag{3.26}$$

where ζ_{ijk} are zero-mean, unit-variance independent Gaussian random numbers for three dimensions. The amplitude of the Brownian force is computed at each time step. This formula is intended only for the non-turbulence models.

3.4 Airflow analysis in human airways

The study of inhaled aerosol transport and deposition requires an understanding of the fluid motion in the respiratory tract. This section gives an overview

of airflow analysis primarily based on a non-dimensional equation within the morphological airway model.

The momentum conservation equation in any generation number can be rewritten in a non-dimensional term, using a characteristic of an average airflow velocity U, tube diameter D, and time scale τ as [58]:

$$\frac{1}{St}\frac{\partial \mathbf{u}^{'}}{\partial t^{'}} + \mathbf{u}^{'} \cdot \nabla \mathbf{u}^{'} = -\nabla \mathbf{p}^{'} + \frac{1}{Re}\nabla^2 \mathbf{u}^{'} \tag{3.27}$$

where

$$\begin{aligned} \mathbf{u}^{'} &= \mathbf{u}/U \\ \mathbf{p}^{'} &= \mathbf{p}/(pU^2) \\ \mathbf{x}^{'} &= \mathbf{x}/D \\ t^{'} &= t/\tau \\ St &= \tau U/D \\ Re &= \rho U D/\mu \end{aligned} \tag{3.28}$$

The importance of the unsteady term $\left(\frac{1}{St}\frac{\partial \mathbf{u}^{'}}{\partial t^{'}}\right)$, the viscous term $\left(\frac{1}{Re}\nabla^2 \mathbf{u}^{'}\right)$, and the convective term $\left(\mathbf{u}^{'} \cdot \nabla \mathbf{u}^{'}\right)$ can be determined using the dimensionless parameter Strouhal number (St) and Reynolds number (Re). The Strouhal number indicates how important the unsteady term is relative to the convective term, and the Reynolds number indicates the how important the viscous term is relative to the convective term. For example, if airflows have a high Re, the viscous term maybe neglected, while the convective term can be neglected at low Re. Similarly, if a flow has a high St, it is possible to neglect the unsteady term.

3.4.1 Laminar vs Turbulent flow in human airways

In the non-dimensional momentum equation 3.27, the Reynolds number gives the relative importance of the convection term relative to the viscous term and can be used to consider the flow type as either laminar or turbulent.

In practice for a smooth cylindrical pipe, the flow transition to turbulence take place between Reynolds number of 2000 and 10^5. Using the Weibel's morphological models of airways, the average flow rate and Reynolds number in each generation corresponding to various breathing patterns (e.g., sedimentary and light exercise) can be estimated as shown in Table 3.1. The results show that the flow can be treated as laminar flow in branching airways. However, the Reynolds number in the upper branches may reach a turbulence condition depending on the breathing pattern.

Table 3.1: Average flow rate and Reynolds number corresponding to sedentary and light exercise breathing patterns.

			Sedentary		Light exercise	
Generation	Diameter (cm)	Length (cm)	$\bar{u}$ (cm/s)	Re	$\bar{u}$ (cm/s)	Re
Trachea	1.8	12	109.2	1330	312.4	3806
1	1.22	4.76	118.9	982	310.0	2808
2	0.83	1.9	128.4	722	367.3	2063
3	0.60	2.4	122.9	499	351.5	1427
4	0.45	1.27	109.2	333	312.4	951
5	0.35	1.07	90.3	214	258.2	612
10	0.13	0.46	20.4	18	58.5	51
15	0.066	0.20	2.47	1.1	7.09	3.2
20	0.045	0.083	0.16	0.05	0.47	0.15

In the case of mouth breathing, the airflow enters the trachea via the larynx,which has a vertical tubular structure, and then passes vocal cords acting as flow restrictions. The cross section of the laryngeal tube is affected by pressure. As it passes through the restriction of the larynx shown in Figure 3.3, the flow takes the format of a turbulent jet flow into the trachea. The study by Owen [143] reports that a tracheal Reynolds number of 3000 is required for the core to be turbulent and that the turbulence would decay when it passes through subsequent generations of airways. The intensity of turbulence

in the trachea ($Re = 3100$) would have to decrease to a quarter of its value by generation 3 ($Re = 1230$). The experiment also indicates the presence of turbulence in the extrathoracic region and trachea, but the turbulence decays rapidly as airflow moves deeper into the lungs. Thus it is reasonable to expect that turbulence is present in the extrathoracic airways and may be extend into the first few generations of upper bronchial airways.

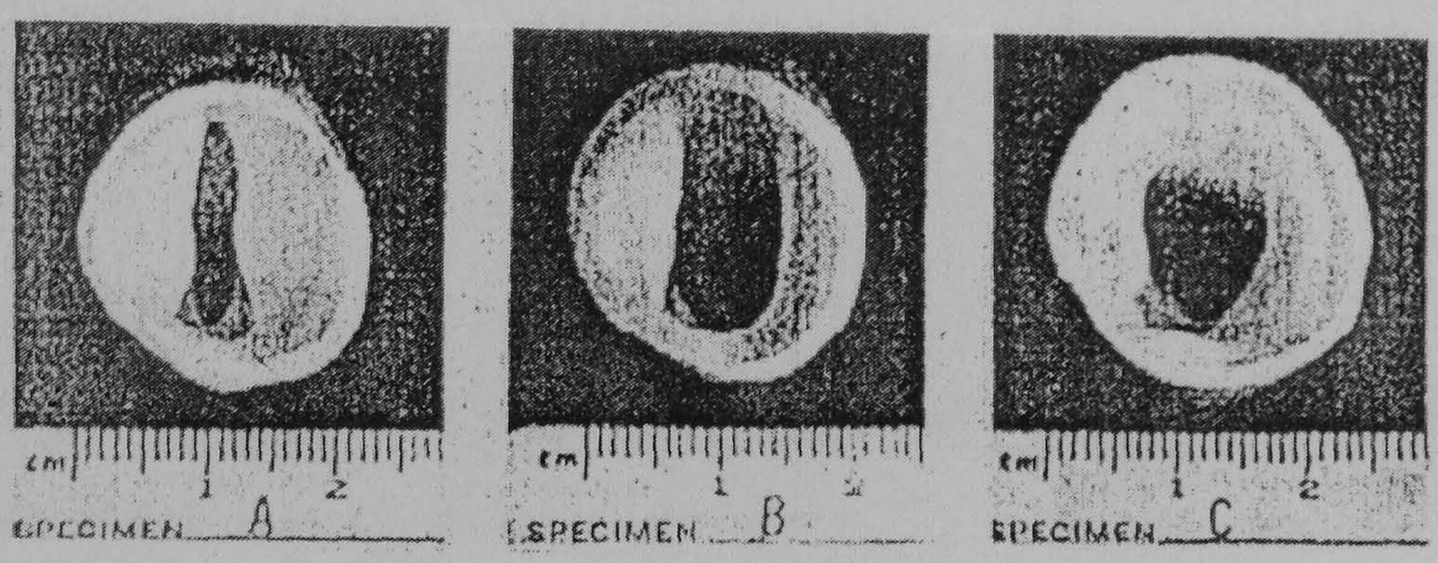

Figure 3.3: The glottal apertures correspond to Replica cast of human larynx at an inhalation rate of: A) 15, B) 30, C) 60 litres/min [99].

In the terminal airways, the Reynolds number is very small (see in Table 3.1). Thus, the convection term is unlikely to be important, pressure drop will be proportional to the flow rate [145]. The theoretical study by Davidson and Fitz-Gerad [40] describes how the gas entering an expanding region will achieve a closer proximity to the walls near the entrance than those which are far away.

3.4.2 Unsteady flow in human airways

The oscillatory characteristic of breathing results in a change in direction of flow twice every cycle. This unsteady flow effect can be analyzed using the Strouhal number (St) and Reynolds number (Re). Based on the laminar flow, Womersley [196] defined a new dimensionless parameter that is directly proportional to $\sqrt{\frac{\omega}{\nu}}$ for giving the importance of the unsteady term compared to

the viscous term, called the Womersley number as:

$$\alpha_w = \sqrt{\frac{Re}{St}} = \frac{D}{2}\sqrt{\frac{\omega}{\nu}} \tag{3.29}$$

where ω is the angular frequency. The ratio is proportional to the thickness of the Stokes boundary layer formed on the rigid wall in oscillatory flow. The unsteady term is an important term when α_w is greater than 1.

Therefore, since the airways are not a long straight tubes, the steady inspiratory flow can be dominated by a boundary layer on the flow divider. The maximum thickness of the boundary layer at any given generation is proportional to $\sqrt{(\nu L/\bar{u})}$, where L is the tube length,and $\bar{u}$ is the mean velocity. The oscillatory flow can be considered as quasi-steady even if the Stokes layer is thicker than the steady boundary layer [145] ($\varepsilon_s \leq 1$), which is defined as:

$$\varepsilon_s = \frac{L\omega}{\bar{u}} \tag{3.30}$$

The parameter α_w and ε_s can be estimated based on the morphometric model incorporating the breathing pattern given in Table 3.2. It shows that the unsteady term is important in the tracheobronchial region for both breathing patterns and less important in the alveolar regions.

3.5 Deposition of pharmaceutical aerosols in human airways

Inhaled pharmaceutical aerosols may deposit in various regions of the human respiratory tract by a complex interaction of basic mechanisms. This section is focused on these basic mechanisms of uncharged particles within the morphological lung model. Neglecting the added mass term in equation 3.13, the motion equation with terms of drag force, gravity, and other external force in Stoke's region can be rewritten as

$$\frac{d\mathbf{u}_p}{dt} = -\frac{1}{\tau_v}(\mathbf{u}_p - \mathbf{u}) + \mathbf{g} + \frac{\mathbf{F}_{ext}}{\rho_p V_p} \tag{3.31}$$

Table 3.2: Values of Womersley number and ε corresponding to sedentary and light exercise breathing patterns

	Sedentary		Light exercise	
Generation	α_w	ε_s	α_w	ε_s
Trachea	2.60	0.14	3.36	0.08
1	1.77	0.05	2.28	0.03
2	1.20	0.02	1.55	0.01
3	0.86	0.01	1.12	0.01
4	0.65	0.01	0.84	0.01
5	0.50	0.01	0.65	0.01
10	0.19	0.03	0.24	0.02
15	0.10	0.10	0.12	0.06
20	0.07	0.65	0.08	0.37

where τ_v is the momentum response time given by

$$\tau_v = \frac{\rho_p d_p^2 C_c}{18\mu} \tag{3.32}$$

Rewriting the dimensionless particle motion equation using an average velocity (U) and airway diameter (D) may be given as ([58])

$$Stk\frac{\mathbf{u}_p^{'}}{dt^{'}} = -\mathbf{u}_{p_{rel}}^{'} + \left(\frac{\tau_v g}{U}\right)\left(\mathbf{g}^{'} + \mathbf{F}_{ext}^{'}\right) \tag{3.33}$$

where

$$\begin{aligned}
\mathbf{u}_p^{'} &= \mathbf{u}_p/U \\
\mathbf{u}_{p_{rel}}^{'} &= (\mathbf{u}_p^{'} - \mathbf{u}/U) \\
t^{'} &= t/(D/U) \\
\mathbf{g}^{'} &= \mathbf{g}/g \\
Stk &= \tau_v U/D \\
\mathbf{F}_{ext}^{'} &= \frac{\mathbf{F}_{ext}}{\rho_p V_p g}
\end{aligned} \tag{3.34}$$

The Stk, called Stokes number, appears as the coefficient in front of the inertial term and is equivalent to a time constant of the first order difference

equation. The high values of Stk leads to the particles having more response time to reach a steady state. With a small value of Stk, the inertial term can be neglected so that the particles follow fluid streamlines (neglecting other forces). The non-dimensional motion of particles can be used to explain the particle deposition in terms of the displacement relative to the basic mechanisms such as inertial impaction, sedimentation, and diffusion.

3.5.1 Deposition by inertial impaction

During inhalation, the incoming air flow undergoes a series of direction changes as it flows from the nose or mouth down through the branching airway system. Each time the airflow changes direction, the suspended particles continue a short distance in their original direction due to their inertia. If the air-stream rapidly changes direction, some particles get trapped on the airways. The inertial impaction mechanism can be explained in terms of the particle stopping distance at the airway velocity, which can be written as

$$x_{stop} = \tau_v U = Stk \cdot D \tag{3.35}$$

Table 3.3 gives the ratio of particle stopping distances to airway dimension at an inlet velocity corresponding to 1.0 l/sec. At higher ratios, it results in higher deposition by inertial impaction. The ratio of stopping distance to airway diameter shows that a larger particle size leads to more deposition by inertial impaction. This mechanism is important for a large particle size ($\geq 1\mu m$), especially in the extrathoracic and upper bronchial regions. In the alveolar region the impaction mechanism is not so important because the air-flow velocity is slow. Based on the dimensionless particle motion equation, the ratio of stopping distance and airways diameter can be described by the Stokes number of the particles. However, the geometric parameter (i.e., branching angle, parent/daughter ratio) and the actual geometrical shape of airway will also influence the impaction mechanism.

There have been many experimental and numerical studies to measure

Table 3.3: Relative importance of inertial impaction mechanisms for deposition of standard density particles (1000 kg/m^3) in selected regions of the human lungs for a steady flow of 1.0 litres per second (adapted from [83]).

	Stopping distance (%)		
	Airway diameter		
Airway	0.1 μm	1.0 μm	10 μm
Trachea	0	0.08	6.8
Main bronchus	0	0.13	10.9
Segmental bronchus	0	0.31	27.2
Terminal bronchus	0	0.17	14.9
Terminal bronchiole	0	0.03	2.8
Alveolar duct	0	0	0.23
Alveolar sac	0	0	0.07

deposition of particles in airway replicas and castings. They have found that the inertial impaction in airways can be approximated as being a function of the Stokes number only. The various formulae for inertial impaction efficiency (P_i) by many authors are given in table 3.4 and figure 3.4. Various equations of inertial impaction efficiency give quite a wide range of efficiencies, because these equations are based on experiments or theory using only a single airway geometry, without the consideration of upstream generations.

3.5.2 Deposition by sedimentation

While impaction is a primary aerosol mechanism of deposition in large airways, sedimentation is the most important mechanism in the smaller airways and alveolar region, where airflow velocities are low and airways dimension are small. The sedimentation mechanism depends on the particle mass and the orientation of airways. It has a maximum efficiency in a horizontal direction. The sedimentation can be relatively easily explained using the settling distance

Table 3.4: Various formulae of deposition efficiency by inertial impaction (adapted from [58])

Formula	Source
$P_i = 0$ if $Stk < 0.02$, otherwise $= -0.0394 + 3.7417(2Stk\ D_r^3)^{1.16}$ for $D_r = 0.8 - 1.0$ $= -0.1299 + 1.5714(2Stk\ D_r^3)^{0.62}$ for $D_r = 0.64$ where $D_r = D_d/D_p$, in that D_d is a diameter of daughter branch D_p is a diameter of parent branch	Kim et al. [103]
$P_i = b\ Stk/(1 + bStk)$ where $b = 4{D_r}^3 sin\beta$, β is branching angle	Landahl [110]
$P_i = 6.4Stk^{1.43}$ for generations 1-3 $= 1.78Stk^{1.25}$ for generations 4-5	ICRP [140]
$P_i = 1.606\ Stk + 0.0023$	Chan and Lippmann [23]
$P_i = 1.3(Stk - 0.001)$	Taulbee and Yu [181]
$P_i = 0$ if $Stk < 0.1$, otherwise $= 4(Stk - 0.1)/(Stk + 1)$	Ferron et al. [52]

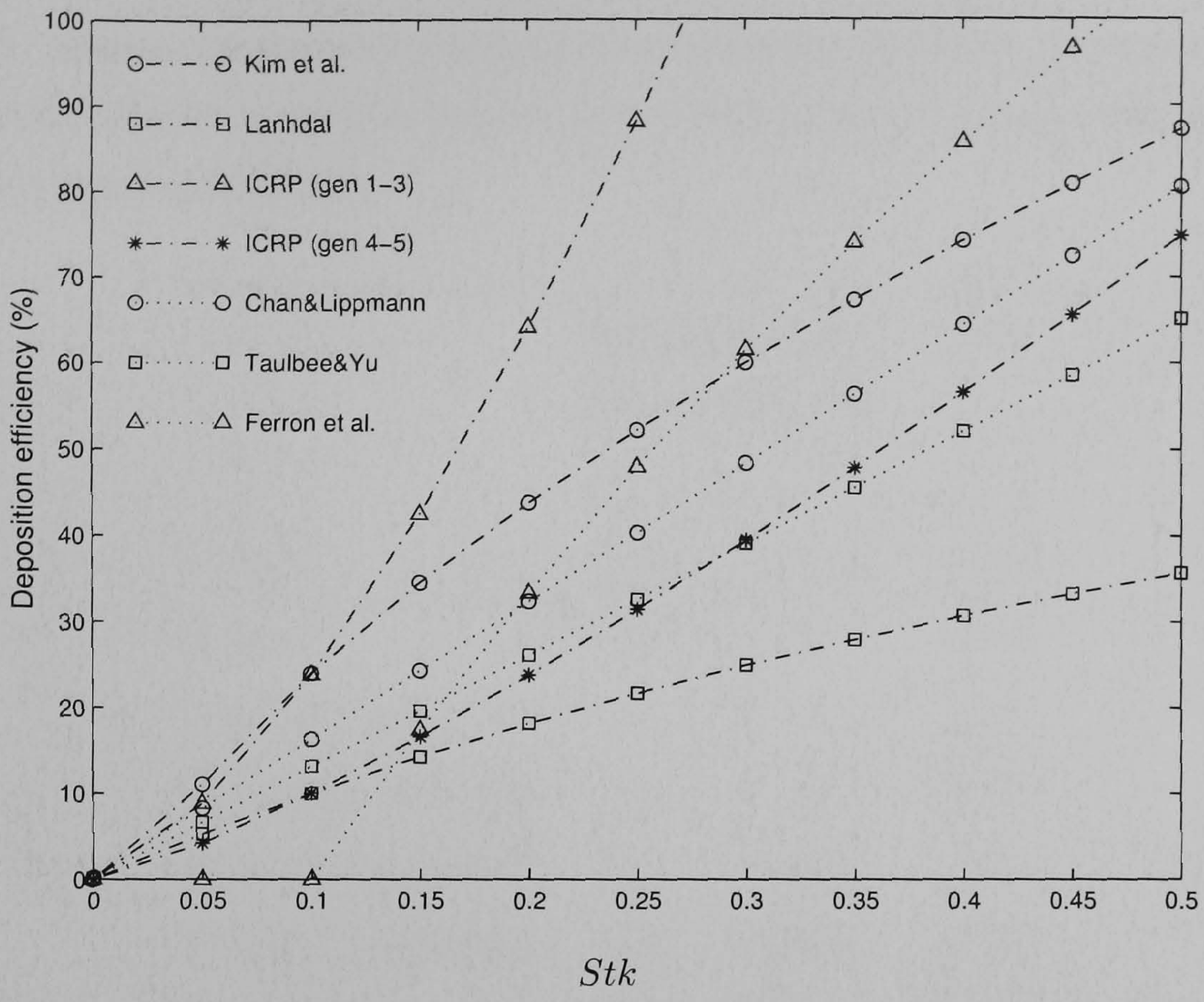

Figure 3.4: Deposition efficiency of impaction P_i as a function of Stokes number by various formulae given in Table 3.4 ($\beta = 35°$, $D_r = 0.7853$).

given by

$$x_{settling} = \tau_v t \tag{3.36}$$

where t is the residence time. The ratio of settling distance to airway diameter at a steady flow rate of 1.0 l/s is given in table 3.5. Sedimentation becomes an important mechanism for the particles in the size range of 0.1-1 μm, in the small airways and alveolar region.

The deposition efficiency due to gravitational sedimentation (P_s) can be examined in a cylindrical tube in which there is a laminar airflow. The velocity profiles can be defined for both parabolic and plug flow by neglecting the impaction term. The comparison of formulae for the velocity profiles are given in Table 3.6 and Figure 3.5. Calculation of the deposition efficiencies by sedimentation require the orientation angle θ_g. However, the different airways in the lung are oriented in many different directions. Koblinger and Hofmann [86] determined the sedimentation deposition using Monte-Carlo approach to give the orientation of each tube. This technique requires the probability of

Table 3.5: Relative importance of settling mechanisms for deposition of standard density particles (1000 kg/m^3) in selected regions of the human lungs for a steady flow of 1.0 litres per second (adapted from [83]).

	Settling distance (%)		
	Airway diameter		
Airway	0.1 μm	1.0 μm	10 μm
Trachea	0	0	0.52
Main bronchus	0	0	0.41
Segmental bronchus	0	0	0.22
Terminal bronchus	0	0.02	2.1
Terminal bronchiole	0	0.18	15.6
Alveolar duct	0.04	1.7	150
Alveolar sac	0.12	4.7	410

finding a tube at an angle θ. Yeh and Schum [198] presented their morphological lung airways with extended parameters of average branching and gravity angle for any airway generation numbers as shown in Table 3.7 .

3.5.3 Deposition by diffusion

Brownian motion is the irregular motion of a particle in air caused by random variations in the rentless bombardment of gas molecules against the particle. The diffusion due to Brownian motion is the primary transport mechanism for particle diameters less than 1.0 μm, in situations where the transport distances are small, such as in the alveolar region.

The diffusion coefficient of an aerosol particle is a function of absolute temperature (T) and particle mobility (B) given by

$$\Gamma = \sigma T B \tag{3.37}$$

where σ is Boltzman's constant. This equation is also known as the Stokes-

Table 3.6: Various formulae of deposition efficiency by sedimentation

formula	source
$P_s = \frac{2}{\pi}\left[2\kappa\sqrt{1-\kappa^{2/3}} - \kappa^{1/3}\sqrt{1-\kappa^{2/3}} + asin(\kappa^{1/3})\right]$ (for Poiseuille flow)	Pich [152]
$P_s = 1 - \frac{2}{\pi}\left[acos\left(\frac{4}{3}\kappa\right) - \frac{4}{3}\kappa\sqrt{1-\left(\frac{4}{3}\kappa\right)^2}\right]$ (for plug flow)	Heyder [82]
$P_s = 1 - exp\left(-\frac{16}{3\pi}\kappa\right)$ (for well-mixed plug flow)	Fuchs [66]

where : $\kappa = \frac{3}{4}\frac{\tau_v g}{U}\frac{L}{D}cos(\theta_g)$, θ_g is the gravity angle

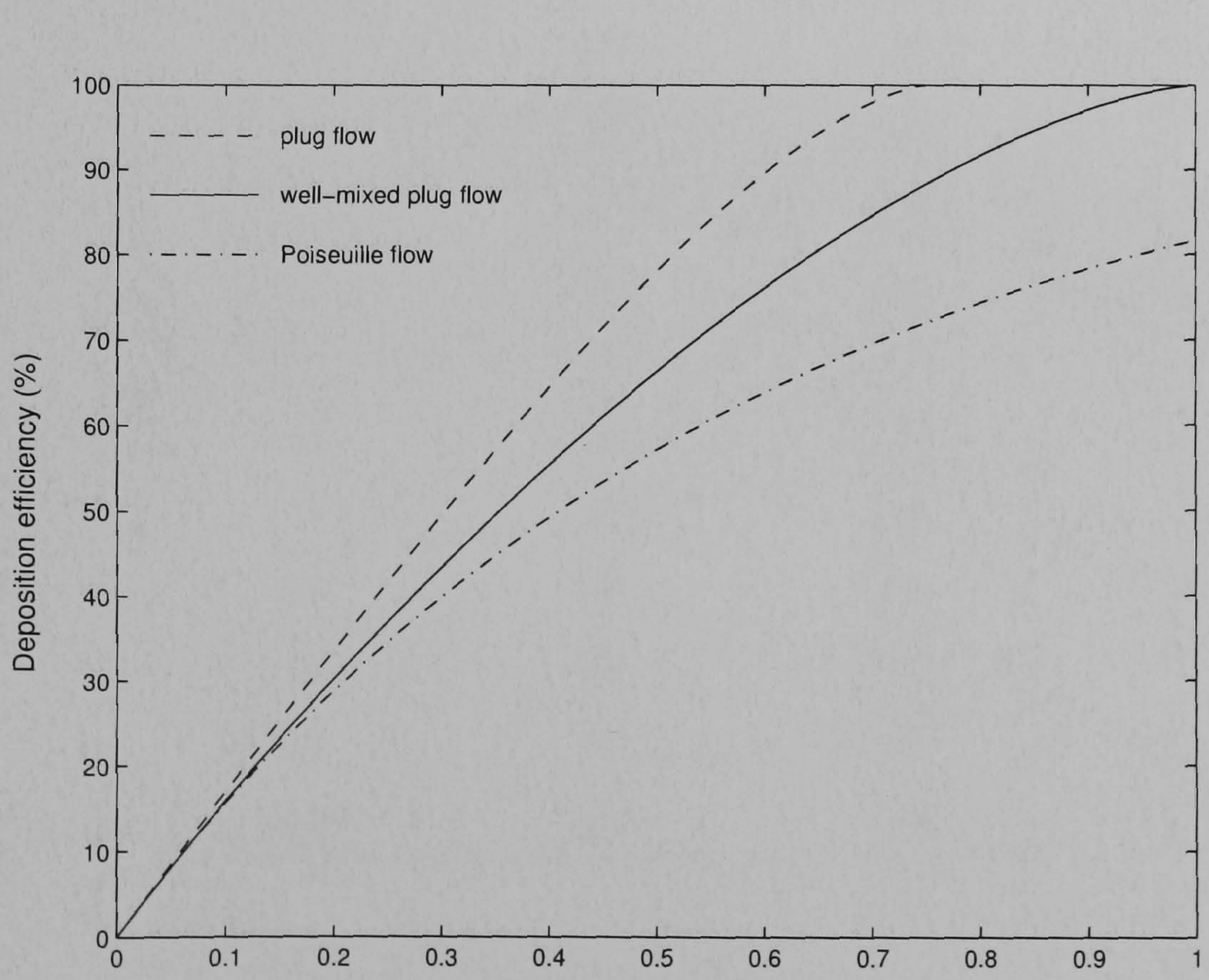

Figure 3.5: Deposition efficiency of sedimentation P_s for the different velocity profiles as a function of parameter κ by formulae given in Table 3.6.

Table 3.7: Average values of branching and gravity angles based on Yeh and Schum [198]

Generation Number	Branching angle (°)	Gravity angle (°)
0	0	0
1	33	20
2	34	31
3	22	43
4	20	39
5	18	39
6	19	40
7	22	36
8	28	39
9	22	45
10	33	43
11	34	45
12	37	45
13	39	60
14	39	60
15	51	60
16-23	45	60

Einstein equation. The smallest scale motion of an aerosol particle undergoing Brownian motion can be considered as the net displacement of the particles. Therefore the net displacement is a random variable and can be represented in terms of the root-mean-square (rms) net displacement expressed by

$$x_{rms} = \sqrt{2\Gamma t} \tag{3.38}$$

where t is a residence time of the particle. The ratio of the root-mean-square displacement during residence in selected airways to the airway diameter determines the relative likelihood of deposition by diffusion, as shown in Table 3.8. The data shows that diffusion becomes the important mechanism for sub-micron particles ($\leq 1.0\ \mu m$) in small airways.

Table 3.8: Relative importance of diffusion mechanisms for deposition of standard density particles (1000 kg/m^3) in selected regions of the human lungs for a steady flow of 1.0 litres per second (adapted from [83]).

	Rms displacement / Airway diameter (%)		
Airway	0.1 μm	1.0 μm	10 μm
Trachea	0.04	0.01	0
Main bronchus	0.03	0.01	0
Segmental bronchus	0.05	0.01	0
Terminal bronchus	0.29	0.06	0.02
Terminal bronchiole	1.1	0.22	0.06
Alveolar duct	3.9	0.79	0.23
Alveolar sac	6.7	1.3	0.40

To estimate the diffusion efficiency in the respiratory tract (P_d), the transport equations of motion for a particle moving in the air with Brownian motion can be represented by the convection-diffusion equation. However it is difficult to solve this equation with the complex geometry of human lung. Using the

assumption of Poiseuille and plug flow velocity profile, the expression for average deposition efficiency in a cylindrical tube can be summarised as shown in Table 3.9 and Figure 3.6.

Table 3.9: Various formulae of deposition efficiency by diffusion

formula		source
$P_d = 1 - 0.819e^{-14.63\Delta} - 0.0967e^{-89.22\Delta} - 0.0325e^{-228\Delta}$ $-0.0509e^{-125.9\Delta^{2/3}}$	(for Poiseuille flow)	Ingham [92]
$P_d = 1 - 4\sum_{m=1}^{\infty} \frac{1}{\lambda_m^2} e^{-4\lambda_m^2 \Delta}$	(for plug flow)	Fuchs [66]

where

$$\Delta = \Gamma \frac{L}{U} \frac{1}{4R^2}$$

$$\lambda_m = \beta + \frac{1}{8\beta} - \frac{124}{(8\beta)^3} + \frac{120928}{15(8\beta)^5} - \frac{401743168}{105(8\beta)^7}$$

$$\beta = \left(m - \frac{1}{4}\right)$$

Diffusion is generally a dominant mechanism of deposition especially in the distal parts of the human lung for inhaled pharmaceutical aerosols, which contains fine particles (less than 1.0 μm).

3.5.4 Regional and total deposition

The total deposition of inhaled aerosols is the combined deposition of particles in all regions of the respiratory tract including extrathoracic, tracheobronchial and alveolar regions. The total deposition is usually determined experimentally by measuring the concentration of inhaled and exhaled monodisperse test aerosols under controlled conditions of breathing frequency, volume of air and pause length between inhalation and exhalation. Figure 3.7 shows the total deposition of a wide range of particle sizes at three levels of exercise based on ICRP deposition model of average data for males and females.

Although many experimental studies have focused on the total deposition, regional deposition within lungs is also important for determining the drug

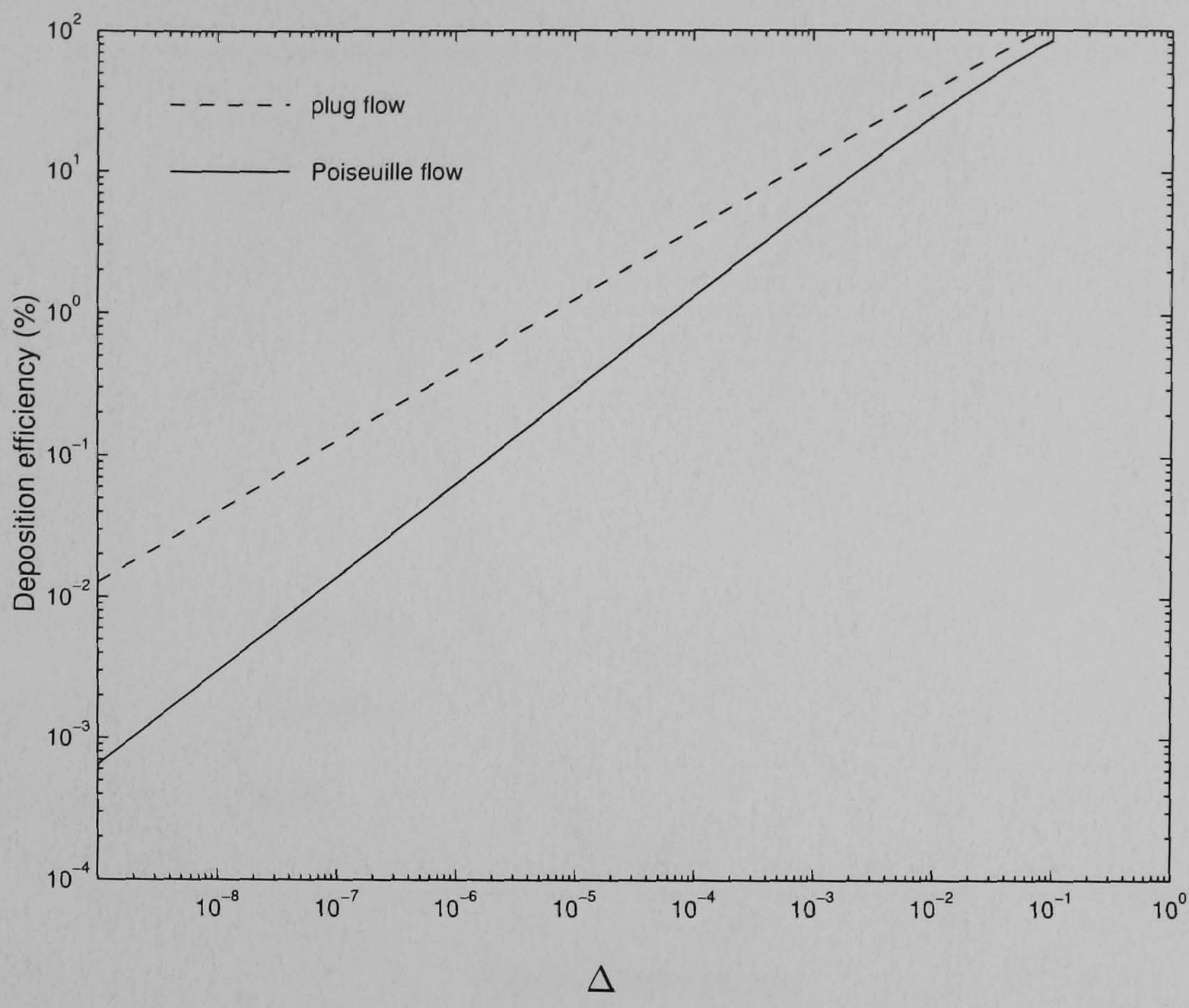

Figure 3.6: Deposition efficiency of diffusion P_d for the different velocity profiles as a function of parameter Δ by formulae given in Table 3.9.

delivery efficiency. The predicted regional deposition for light activity and nose breathing based on the ICRP deposition model is shown in Figure 3.8. Particles larger than 5 μm tend to be mainly deposited in the extrathoracic region due to the inertial impaction. In addition, ultra-fine particles less than 0.001 μm also have significant deposition in the extrathoracic region because of the high diffusion coefficient. Deposition in the tracheobronchial region for particles larger than 0.1 μm is quite small when compared to other regions. However, deposition in the tracheobronchial region tends to increase when the particles are smaller than 0.1 μm. In the alveolar region, particles in the range from 0.01-0.1 μm are mainly deposited by gravity and diffusion mechanisms. The deposition efficiency in this region is reduced whenever extrathoracic and tracheobronchial deposition is high.

The predicted deposition of particles in the extrathoracic region is highly variable and depends on several factors including whether the subject is mouth or nose breathing, flow rate, and particle size. For both mouth and nose

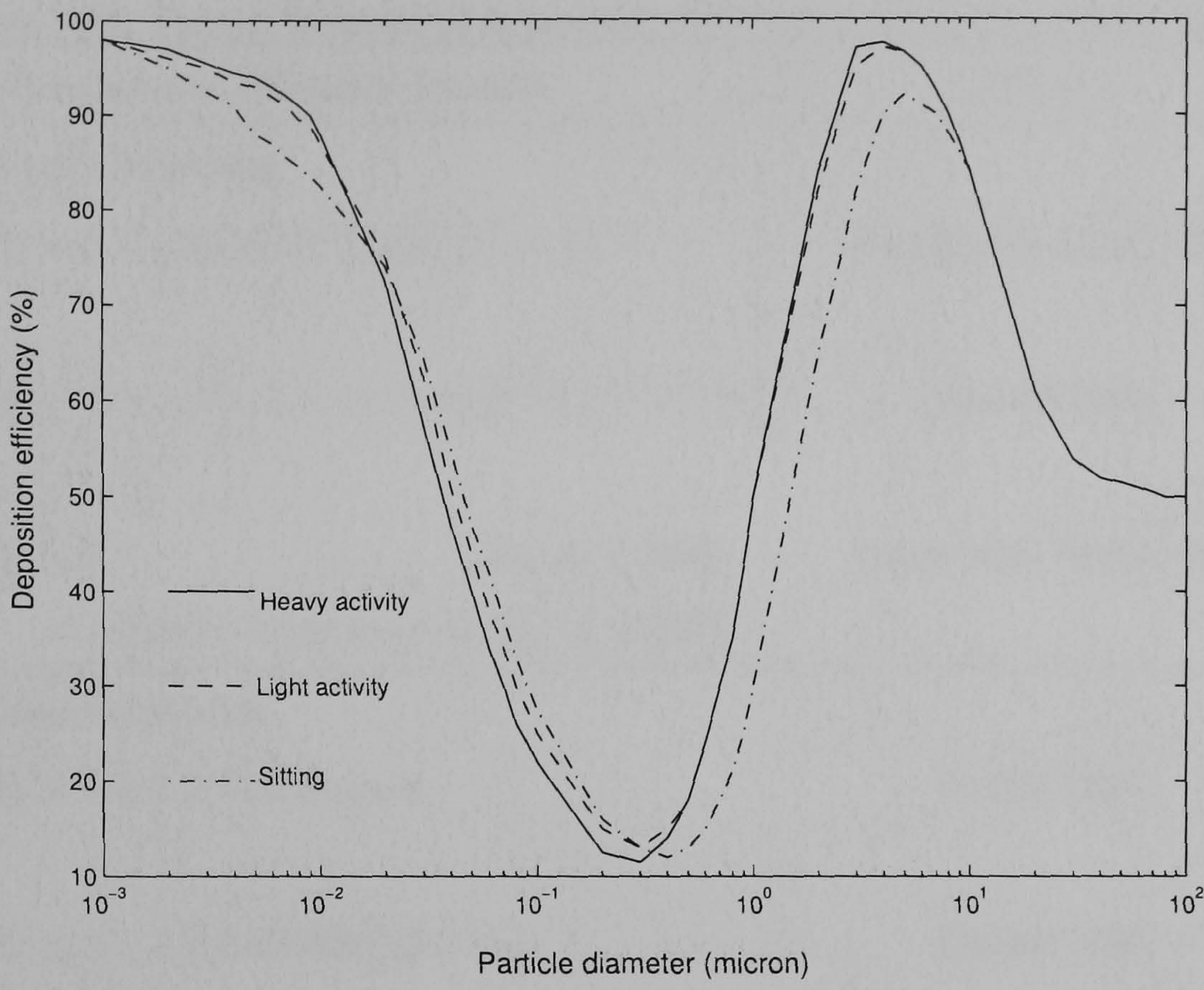

Figure 3.7: Predicted total deposition efficiencies at three breathing conditions based on ICRP deposition model (adapted from [83]).

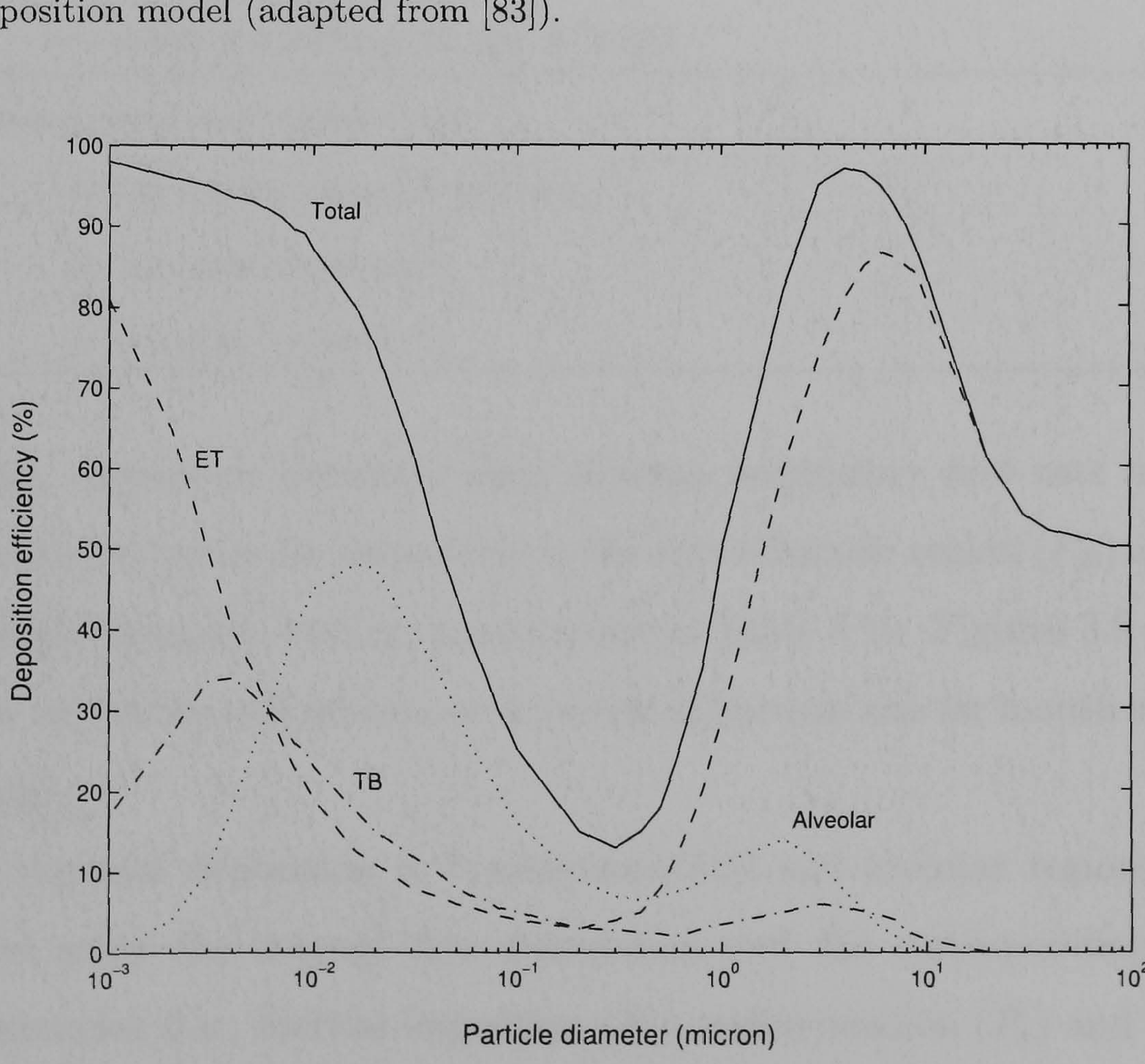

Figure 3.8: Predicted total and regional deposition efficiencies for light exercise conditions based on ICRP deposition model (adapted from [83]).

Table 3.10: Various formulae of deposition efficiency in the extrathoracic region

Extrathoracic efficiency formula	Sources
Mouth breathing	
$P_E = 1 - (3.5 \times 10^{-8}(d_p^2 Q)^{1.7} + 1)^{-1}$	Stahlhofen et al. [177]
$P_E = (1 - 1/(1.1 \times 10^{-4}(d_p^2 Q^{0.6} V_T^{-0.2})^{1.4} + 1)$	Rudolf [160]
$P_E = 0$, for $A < 3000$	Egan and Nixon [48]
$= -2.062 + 0.593log(A)$, for $A \geqslant 3000$	
Nasal breathing	
$P_E = -1.2 + 0.475log(A)$	Pattle [147]
$P_E = 1 - 1/(0.00033 d_p^2 Q + 1)$	Rudolf [159]
$P_E = -0.014 + 0.023log(A)$, for $A < 337$	Egan and Nixon [48]
$= -0.959 + 0.397log(A)$, for $A \geqslant 337$	

where d_p is a particle diameter (μm)

Q is an inhalation flow rate (cm^3/sec)

V_T is an tidal volume (cm^3)

$A = \rho_p d_p^2 Q \quad (g \cdot \mu m^2 s^{-1})$

breathing, deposition increases when average inspiratory flow rate increases. Most predicted values for deposition in the extrathoracic region (P_E) are based on empirical formulae, and are summarised in Table 3.10. Figures 3.9 and 3.10 show the deposition efficiencies as functions of particle size for mouth and nasal breathing.

The regional deposition in tracheobronchial and alveolar regions can be predicted using the average flow calculation and the corresponding deposition efficiencies (i.e., inertial impaction (P_i), sedimentation (P_s) and diffusion (P_d)) within the morphological lung model. The combination of deposition efficiencies by various aerosol mechanisms in any generation number can be

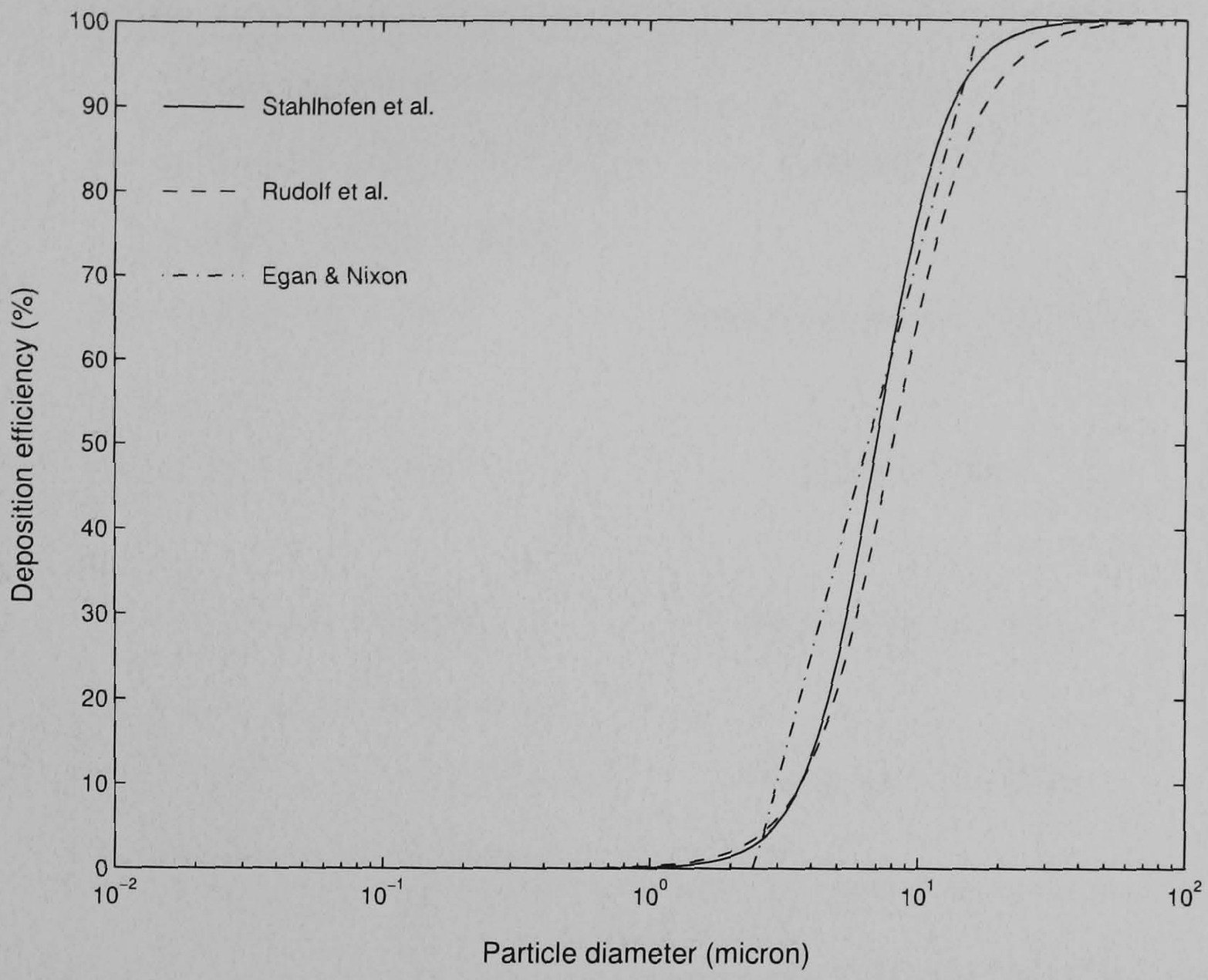

Figure 3.9: Deposition efficiency of impaction P_E as a function of particle size for mouth breathing by various formulae given in Table 3.10 ($Q = 500\ cm^3/s$).

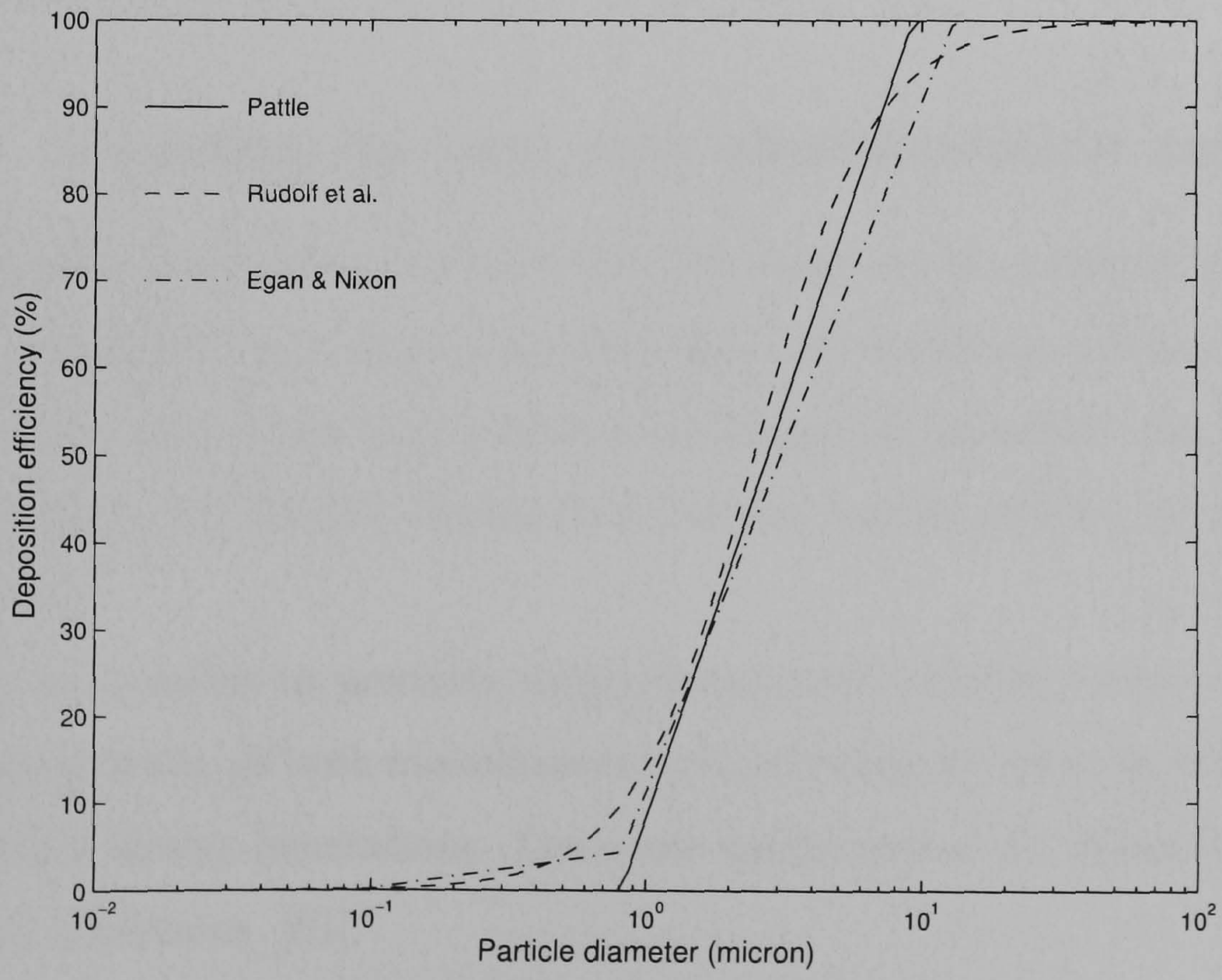

Figure 3.10: Deposition efficiency of impaction P_E as a function of particle size for nasal breathing by various formulae given in Table 3.10. ($Q = 500\ cm^3/s$)

Table 3.11: Various formulae of the total deposition efficiency

Total deposition formula	Source
$P_T = P_i + P_s + P_d + P_i P_s P_d$ $-P_i P_s - P_i P_d - P_s P_d$	Landahl [110]
$P_T = (P_i + P_d + P_s)^{\frac{1}{3}}$	Asgharian and Anjilvel [7]
$P_T = (P_i + P_d + P_s)^{\frac{1}{2}}$	ICRP [140]
$P_T = P_d + P_s - \frac{P_s P_d}{P_s + P_d}$ (for absence of inertial impaction)	Heyder et al. [79]
$P_T = \left({P_d}^2 + {P_s}^2 - (P_s P_d)^2\right)^{\frac{1}{2}}$ (for absence of inertial impaction)	Chen and Yu [25]

formulated in various ways as shown in Table 3.11. However, it is difficult at first to choose the most appropriate formulae for the computation, because these formulae are suitable for different situations depending on the respiratory region and particle size.

3.5.5 Targeting the lung with pharmaceutical aerosols

Targeting the therapeutic aerosol within the lungs can be achieved by manipulating the particle size, inspiratory flow rate, and inhalation volume. Each of these factors interacting with several mechanisms of deposition can be summarised using the particle displacement in the human airways as shown in Table 3.12.

It is not possible to precisely target therapeutic aerosols within a specific airway generation, as both monodisperse and polydisperse aerosols will deposit over several airway generations. Optimum targeting can be obtained for the following conditions [81]:

- Targeting of the extrathoracic region can be achieved by inspiring at a high flow rate and with a particle size much larger than 1 μm in

Table 3.12: Dependence of the inertial impaction, gravitational and diffusional displacement on particle size, particle density, breathing cycle period and flow rate [81].

Displacement by	Particle size	Particle density	Breathing cycle	Flow rate
Inertial impaction	increases with size	increase with density	independent of time	increase with flow rate
Gravitational sedimentaion	increase with size	increase with density	increase with time	independent of flow rate
Diffusion	decrease with size	independent of density	increase with time	independent of flow rate

aerodynamic diameter and suspended in tidal air of small inhaled volume.

- Targeting of lower bronchial regions can be achieved by inspiring at extremely low flow rate and with a particle size larger than 1 μm in aerodynamic diameter and suspended in tidal air of large volume.

- Targeting of distal lung can be achieved by inspiring at an extremely low flow rate and with a particle size in the range of about 1 μm in aerodynamic diameter and suspended in a large volume of tidal air.

Moreover, in addition to those discussed above, other factors may contribute to targeting the lung deposition such as pulmonary disease and age. In diseased lungs, the airways are often more constricted relative to healthy lungs, so one might expect significant differences in deposition patterns in the human airways [176]. The effects of constricted airways on aerosol deposition has been studied based on both modelling and experimental studies (i.e., [102],[162], and [112]), and can be concluded as follows:

- Increases the deposition efficiency in central airways.

- Reduces penetration of aerosol to the smaller, peripheral airways and alveoli.

- Deposition is non-uniform with regions of both high and low aerosol concentration.

The effect of age also influences the deposition efficiency. In healthy lung of adults more than 18 years old, it is likely that the total deposition within the lungs doesn't change significantly with age [17]. However, many models and experimental data indicate that total deposition will be significantly reduced in babies and young children compared to older children and adults (e.g., [87], [179]). Futher details of these factors affecting the targeting of lungs have been reviewed by Zenen and Laube [204].

3.6 Summary

The transport and deposition of inhaled pharmaceutical aerosols can be defined as a dispersed phase flow problem in which airflow is assumed to be dilute dispersed phase flow with one-way coupling. The airflow is simulated is using the Eulerian model. The equations governing fluid flow are represented by mathematical statements of conservation laws of mass, momentum and energy. The analysis of dispersed phase flow description for inhaled drug delivery in a human airway model often uses both Eulerian and Lagrangian representation. The Eulerian approach requires an effective diffusion coefficient, which can be obtained by experimentation. Different profiles of airflow occur in the different parts of the lungs. However, there is hardly any direct experimental evidence available for the determination of the effective diffusion coefficient. The point-volume Lagrangian approach is used for numerical studies of inhaled drug delivery because the motions of particles are more naturally dealt with by individual particle tracking.

The airflow in the human airways can be considered as either laminar or turbulent using the Reynolds number, which gives the relative importance between the convection and viscous term. The airflow in the extrathoracic airways and first few generations of larger airways can be considered as tur-

bulent corresponding to the normal breathing pattern. After that the inhaled air convects deeply into the lungs, and hence the velocity decreases rapidly. The airflow in lower bronchial and alveolar regions can be modelled as laminar flow. The deposition of inhaled pharmaceutical aerosol in human airways is governed by the basic aerosol mechanisms of impaction, sedimentation and diffusion. The initial impaction can be described by the Stokes number that is related to the particle sizes and airflow velocity. With larger particle size, the impaction becomes the more dominant mechanism. This mechanism is important for large airways and large particle sizes. The deposition by gravitational sedimentation is important for smaller airways and the alveolar region, where airflow velocities are low and airway dimensions are small. This mechanism depends on the particle mass and the orientation of airways. Finally, the deposition by diffusion is important for sub-micron particles ($\leq 1.0\ \mu m$) where the transport distances are small.

The aerosol deposition in the human respiratory system can be considered in terms of both total and regional deposition. The total deposition is the combined deposition in all regions, but the regional deposition focuses on individual regions including extrathoracic, tracheobronchial, and alveolar regions. Targeting inhaled pharmaceutical aerosols within the lung can be achieved by manipulation of particle size, inspiratory flow rate, and inhalation volume. Consideration should also be given to other factors such as pulmonary disease, age and clinical effects.

Chapter 4

Electrostatic Force Computation

Extending the theoretical background discussed in the previous chapter, this chapter focuses on the theory of aerosol transport and deposition with particular reference to the effect of electrostatic forces. Software implementations for computing the electrostatic forces on charged particles are also discussed.

The effect of electrostatic forces on particle trajectory can be considered as body forces in the particle motion of the Lagrangain reference frame as discussed in section 3.3. When particles carry charges on their surfaces, two electrostatic forces arise to lead these charged particles to deposit on wall surfaces: one due to the image charge on wall surface and the other due to the Coulombic repulsion among the particles, also known as space charge force. The image charge force occurs when a charged particle in the lung sets up an electrical field around it, which causes the molecules in the lung tissues to orient themselves (called the dielectric effect). The force of the molecules in the lung tissue appears like that from an "induced charge", where the magnitude of the force on the particle is equal to the force of attraction between two point charges in free space.

The electrostatic charges found in inhaled drug delivery devices are given in section 4.1. The effects of electrostatic forces on the deposition efficiency within human lungs is then discussed in section 4.2 using a mathematical analysis within the Weibel's morphometrical lung model. Section 4.3 gives

the results of a predicted deposition model developed by Brunel University with various mechanisms including the electrostatic forces. Owing to a large number of particles in the numerical simulation and the limitation of computational resources, the routines of the electrostatic force computations need to reduce complexity. More details of computation techniques for both space and image charge forces are presented in sections 4.4 and 4.5, respectively. The computational techniques and computer software have been specifically developed in this project. Finally, section 4.6 describes the effect of humidity on charged aerosol particles.

4.1 Electrostatic charges in inhaled drug delivery devices

4.1.1 Particle charging mechanisms

The three major particle charging mechanisms which are encountered in pharmaceutical aerosol applications consist of triboeletric, diffusion and field charging. Triboelectric charging results in bipolar charges, but diffusion and field charging results in unipolar charges. Other charge mechanisms such as frame charging, electric double layer charging and photo electric charging are not significant in pharmaceutical aerosols. More details of these charging mechanism can be found in [35].

4.1.1.1 Triboelectric charging

The triboelectric charging (also sometimes known as contact charging) arises during the separation of dry, non-metallic particle from the surface of device. When a particle contacts the surface, a transfer of charge between particle and surface occurs. The polarity and amount of charge on the particle depend on the nature of the material involved. Many authors suggests that triboelectric charging of pharmaceutical aerosols often results in bipolar charges ([142], and

[126]).

4.1.1.2 Diffusion charging

Diffusion charging appears when an ion randomly collides with a particle, then the particle acquires charges from ions. The collision process results from Brownian motion of the ions and particles. Once the particle accumulates charges, it produces a field that tends to repel additional ions. Consequently, the charging rate reduces because few ions have sufficient velocity to overcome the repulsive force arising from charges on the particle. For a particle less than 1 μm, diffusion charging is the main charging mechanism. The approximate number of charges acquired by a particle of diameter (d_p) during a time t can be estimated by [83]

$$n(t) = \frac{d_p \sigma T}{2K_E e^2} ln\left(1 + \frac{\pi K_E d_p \bar{c}_i e^2 N_i t}{2\sigma T}\right) \tag{4.1}$$

where $\bar{c}_i$ is mean thermal speed of ions ($\bar{c}_i = 240\ m/s$ at standard condition), σ is Boltzmann's constant, T is temperature, K_E is a constant value of $9.0 \times 10^9\ N \cdot m^2/C^2$ and N_i is the concentration of ions.

4.1.1.3 Field charging

In the presence of a strong electrical field, field charging is developed by unipolar ions. Ions rapidly impact on the particles at the initial stage because the electrical field lines guide the ions towards the particle. Then charges transfer from ions to the particle. As the collisions continue, the charge accumulated on the particle increases the strength of the electrical field around its surface. When the electrical field near the surface of particle is stronger, it bends the alignment of any external electrical field away from the particle. Consequently, the charge on the particle reaches a saturated charge level. Field charging is more significant for particles larger than 1 μm and the charge magnitude increases with the square of the particle diameter. The number of charges due to the field charging mechanism can be approximated by [83]

$$n(t) = \left(\frac{3\varepsilon}{\varepsilon + 2}\right)\left(\frac{E{d_p}^2}{4K_E e}\right)\left(\frac{\pi K_E e Z_i N_i t}{1 + \pi K_E e Z_i N_i t}\right) \tag{4.2}$$

where ε is the relative permittivity of the particle, E is an electrical field (Vm^{-1}) and Z_i is the mobility of ions (approximately 0.00015 $m^2/V \cdot s$).

Field charging is often generated by corona discharge that creates an electrical field when a high voltage potential exists between ground and the potential electrode. The details of theoretical and experimental analysis of corona discharge can be found in [35].

4.1.2 Charge limit

The charge limit imposed by the inherent efficiency of the charging methods is also limited in many fundamental ways. The limits are due to the structural integrity of the particle or droplet as well as its ability to hold the electrical charge on its surface. Perhaps, the most restrictive limit of charges on a particle is the Gaussian limit, which specifies the maximum charges by the breakdown strength of air. When the electrical field in the air reaches a value of approximately $3 \times 10^6\ V/m^2$, the air ionises and surface charge is dissipated. The Gaussian's charge limit on a particle can be expressed as

$$n_L|_{Gauss} = \pi \frac{d_p^2 E_b}{e} \tag{4.3}$$

where E_b is the breakdown electrical field (approximately $3 \times 10^6\ Vm^{-1}$).

A different type of charge limit, called the Rayleigh limit, exists for liquid droplets. This limit defines the maximum charge that can exist on the droplet before the Maxwell stress on the surface overcomes the cohesive force of surface tension, causing disintegration of the droplet. The Rayleigh limit of charge can be defined as

$$n_L|_{Rayleigh} = \left(\frac{2\pi\varrho d_p^3}{K_E e^2}\right)^{1/2} \tag{4.4}$$

where ϱ is the surface tension of droplet liquid.

According to Pauthenier's theorem, the charge on a particle will increase until the field from that charge is equal to the external field in which the particle is situated. The limit of charge on a powder particle suggested by Pauthenier can be determined as a function of dielectric constant (ε_r) and Electrical field (E) given as

$$n_L|_{Pauthenier} = \pi\varepsilon_0 d_p^2 E\left(1+2\left(\frac{\varepsilon_r-1}{\varepsilon_r+2}\right)\right) \tag{4.5}$$

where ε_0 is a a permittivity of vacuum.

A comparison of the charge limits defined by the Guassian, Rayleigh, and Pauthenier definitions as a function of particle size is shown in Figure 4.1. The other charge limit definitions such as positive ion limit and electron limit are not discussed here. More details of these charge limits can be found in [83].

4.1.3 Electrostatic charges on particles generated by inhaled drug delivery devices

Several experimental studies of charges on particles produced by drug delivery devices have been made. The charging mechanism within these devices are complex phenomena with a probabilistic nature of different mechanisms acting simultaneously.

The electrostatic charge in a DPI (Dry Powder Inhaler) device is generated by the processes of pharmaceutical processing, formulation, and aerosolisation because these processes create the ideal conditions for the triboelectric charging mechanism. Electrostatic forces can affect the performance of DPI devices in two major ways. Firstly, the Coulombic forces between the particles influence the drug dispersion characteristic. Secondly, the electrostatic forces contribute to the adhesion of particles, the formulation of drug particles and drug-carrier agglomerates [142]. The experimental study of the electrostatic properties of pharmaceutical powder by Yurteri et.al. [199] shows that most of the powder was bipolarly charged with a relative high charge-to-mass ratio and that the

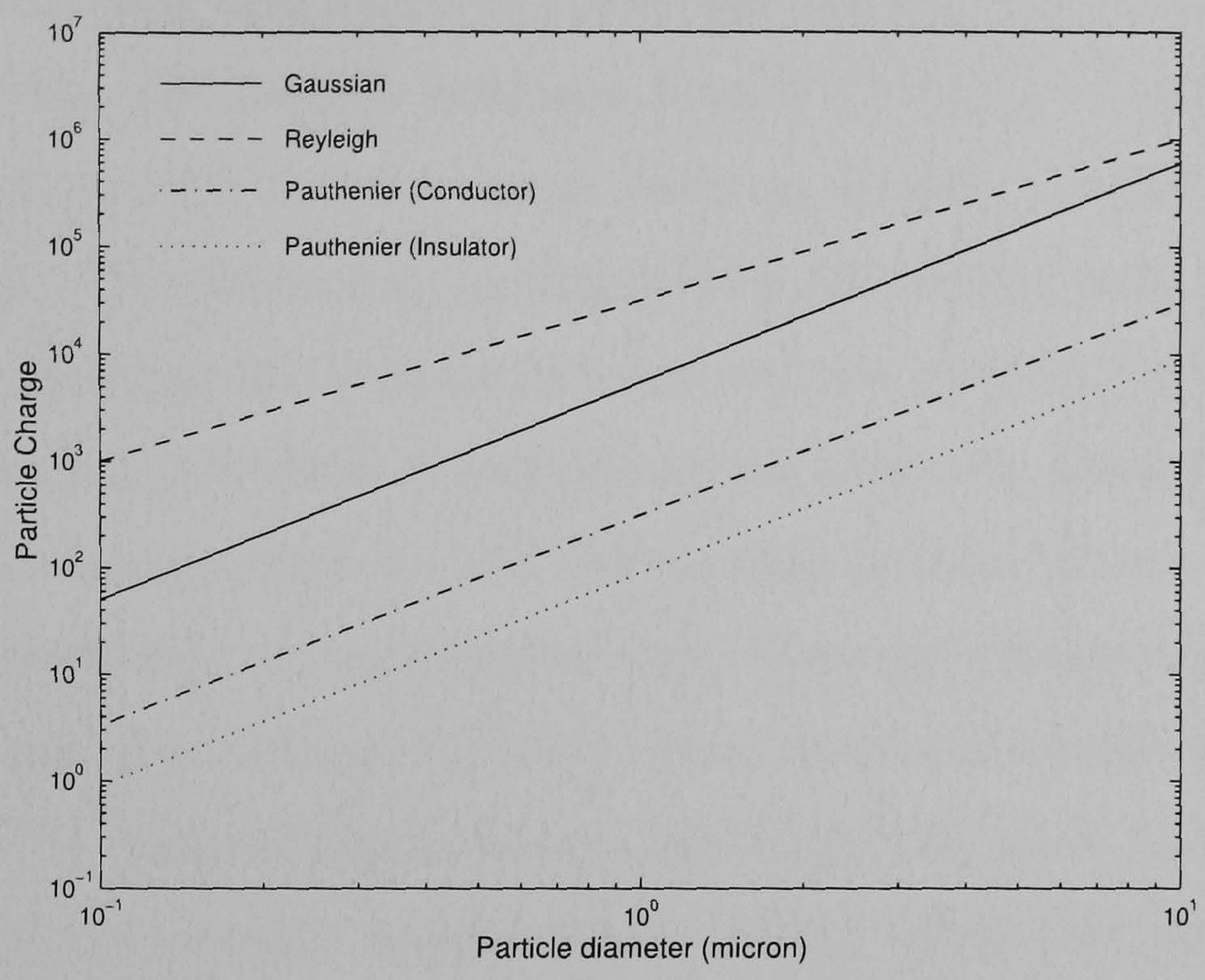

(a)

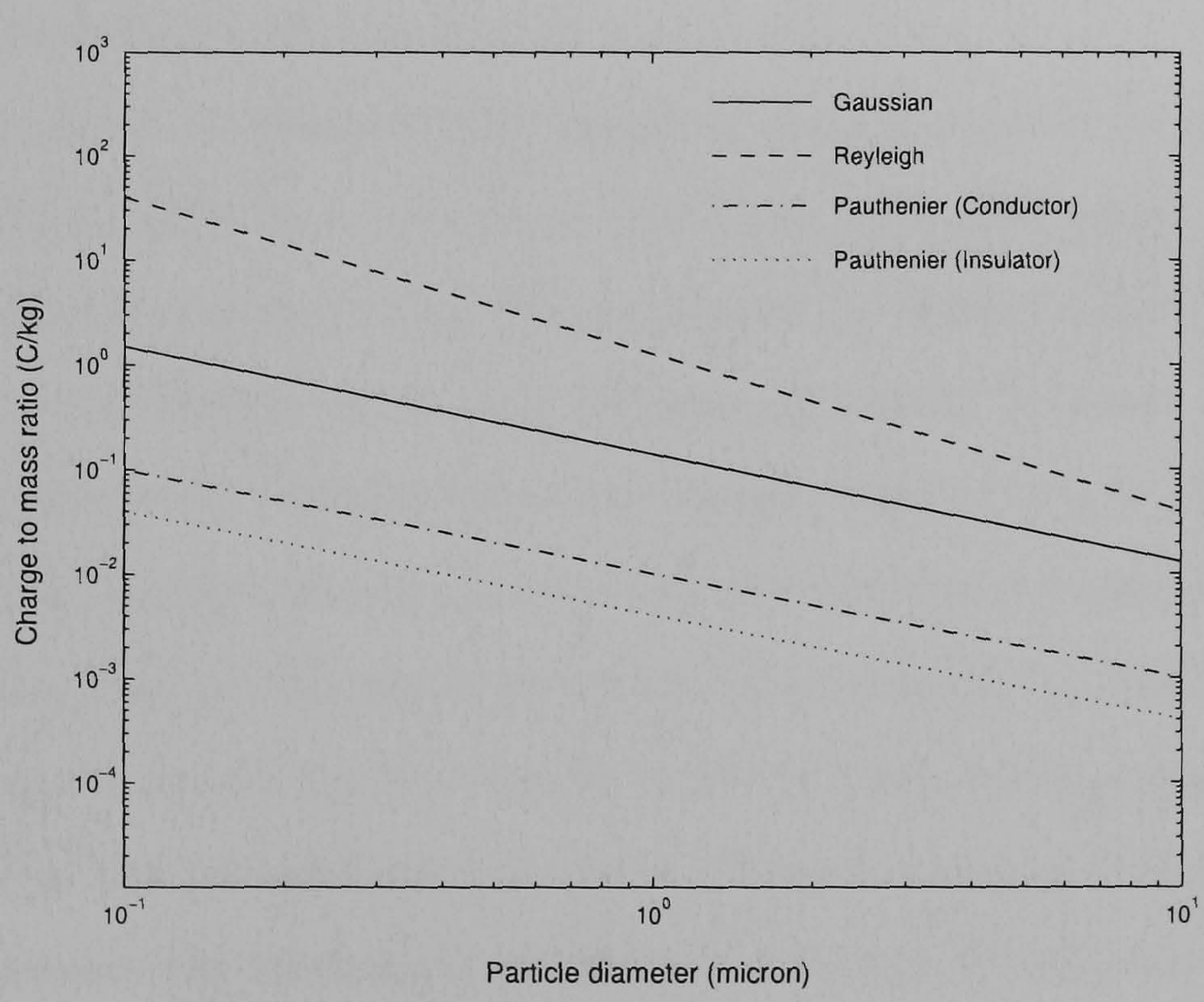

(b)

Figure 4.1: Comparison of the charge limit on particle based on Gaussian, Rayleigh, and Pauthenier charge limits ($\varrho = 0.0343\ N/m$, $E = 5 \times 10^5\ V/m$, and $E_b = 3 \times 10^6\ V/m$) [109]

surface structure particularly influences the tribocharging of powders.

An experimental study to measure charge levels in the droplets produced by a nebulizer has been undertaken by Chow and Mercer [26]. They measured the charge levels on droplets produced from 0.1% and 1 % NaCl aqueous solutions and reported that the charge levels on droplets increase with NaCl concentration. The charge may be obtained by the interaction of the electric double layer charging at the liquid interface and the triboelectric charging.

Only a little information is available in the literature about the level of charge on aerosols produced by MDI (Meter Dose Inhaler) devices. Peart and Byron [149] performed an experimental study to measure the net charge of fine particles generated by commercial MDIs. They found that the fine particles are highly negative charged (approximately 160 pC per 57 μg of particle mass). However, the experimental measurements did not reveal the bipolar charge nature of the aerosol plume. Therefore the values reported for charge per sample significantly underestimate the real charge level.

The comparison of electrostatic charge of pharmaceutical aerosols generated by pMDIs, DPIs and nebulizers has been measured using the bipolar charge measurement system (BCMS) developed by Brunel University [109]. The experimental results show that charges generated by these devices are bipolar in nature with different levels of bipolar charge fraction. The mechanism of charging in these inhaler devices has been neither well characterised nor well understood due to the complexity of the fluid dynamics and lack of systematic experimental studies for the rapidly evolving flash boiling aerosols. Additionally, due to the probabilistic nature of different charging mechanisms acting simultaneously the theoretical prediction of charge distribution on aerosols from these devices is very difficult.

4.2 Analysis of electrostatic force effects on aerosol transport and deposition

The non-dimensional analysis of electrostatic force effect on the deposition efficiency in human airways is provided in this section for the purpose of explaining the important roles of both the space and image charge forces relative to the drag and gravity forces. Inspection of the space and image charge forces by consideration of two neighbouring particles reveals that the magnitude of Coulombic repulsion force $|\mathbf{F}_{spc}|$ and image force $|\mathbf{F}_{img}|$ with charge value q_i and q_j is given by

$$|\mathbf{F}_{spc}(\mathbf{x}_{p_i}, \mathbf{x}_{p_j})| = \frac{q_i q_j}{4\pi\varepsilon_0 |\mathbf{x}_{p_i} - \mathbf{x}_{p_j}|^2} \tag{4.6}$$

$$|\mathbf{F}_{img}(\mathbf{x}_{p_i}, \mathbf{x}_{p_w})| = \frac{q_i^2}{16\pi\varepsilon_0 |\mathbf{x}_{p_i} - \mathbf{x}_{p_w}|^2} \tag{4.7}$$

where $\mathbf{x}_{p_i}$ and $\mathbf{x}_{p_j}$ are positions of particle index i,j, $\mathbf{x}_{p_w}$ is the position of nearest point on the airway wall, and ε_0 is the permitivity of vacuum.

The space charge force is an interactive forces of all particles. To simplify this complexity for the non-dimensional analysis, the spacing between particles Δx can be estimated by assuming uniform charged particle distribution and using the number of particles per unit volume N, as

$$\Delta x \approx N^{1/3} \tag{4.8}$$

The non-dimensional analysis of particle motion accounting for both space and image charge forces in the motion equation is given by ([58])

$$Stk \frac{d\mathbf{u}'_p}{dt'} = -\mathbf{u}'_{p_{rel}} + \frac{v_{settle}}{U}\mathbf{g}' + Spc\ \mathbf{x}'_s + Img\ \mathbf{x}'_w \tag{4.9}$$

where

$v_{settling} = \tau_v g$,

$\mathbf{x}'_w$ is a unit vector pointing from the particle to the nearest point on the wall, and $\mathbf{x}'_s$ is a unit vector pointing away from the particle.

The coefficient of the space charge term (Spc)and image charge force term (Img) are defined as

$$Spc = \frac{C_c}{3\pi\mu U d}\frac{e^2}{4\pi\varepsilon_0}n'^2 N^{2/3} \tag{4.10}$$

$$Img = \frac{C_c}{3\pi\mu U d}\frac{e^2}{16\pi\varepsilon_0 D^2}\frac{n'^2}{{x'_w}^2} \tag{4.11}$$

where

n' is an integer number of elementary electronic charges on the particle,
$x'_w = x_w/D$ is the non-dimensional distance of the particle from the wall,
and $e = 1.6 \times 10^{-19}C$ is the magnitude of the charge on an electron.

The effect of the space charge force can be compared relative to the impaction and gravity sedimentation mechanisms based on the dimensionless transport equation of particle in equation 4.9. The relative term of these comparisons can be written as

$$\frac{Spc}{Stk} = \frac{3e^2}{2\pi^2 d_p^3 \rho_p \varepsilon_0}\left(\frac{D}{U^2}\right)\left(n'N^{\frac{1}{3}}\right)^2 \tag{4.12}$$

$$\frac{Spc \times U}{v_{settling}} = \frac{3e^2}{2\pi^2 d_p^3 \rho_p \varepsilon_0}\left(\frac{1}{g}\right)\left(n'N^{\frac{1}{3}}\right)^2 \tag{4.13}$$

The space charge force cannot be ignored, if the ratios $\frac{Spc}{Stk}$ and $\frac{Spc\times U}{v_{settling}}$ have values greater than 0.1. The ratio $\frac{Spc}{Stk}$ is used for investigation in the conducting airways because the inertial impaction is dominant and related to Stk. Figure 4.2 shows the values of $n'N^{\frac{1}{3}}$ satisfying the conditions of $\frac{Spc}{Stk} = 0.1$ during the sedentary breathing pattern for the particle sizes of 0.1, 0.5, and 1.0 μm in diameter, respectively. When the particle size increases, the space charge force is less significant. The space charge force depends significantly on the concentration of particles and arises only when there is a high concentration of particles with sufficient charge. For example, particles carrying $100e$ in the airway generation number 5 require concentrations of $1.48 \times 10^{10}\ particle/m^3$

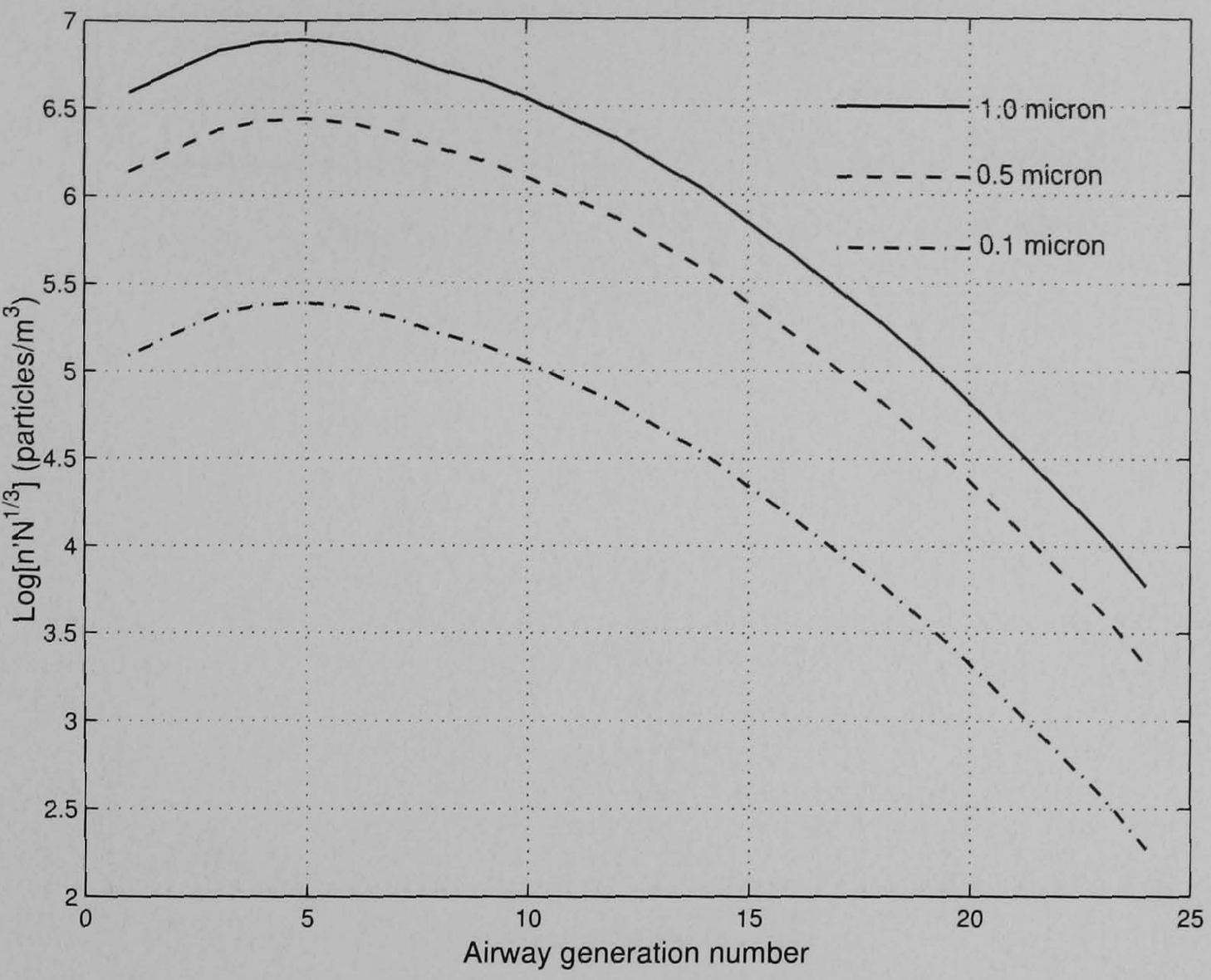

Figure 4.2: Values of $n'N^{\frac{1}{3}}$ satisfying the condition of $\frac{Spc}{Stk} = 0.1$ under sedentary breathing condition with the particle sizes of 0.1, 0.5 and 1.0 μm in diameter

for $d_p = 0.1\mu m$, 2.07×10^{13} $particle/m^3$ for $d_p = 0.5\mu m$, and 4.69×10^{14} $particle/m^3$ for $d_p = 1.0\mu m$) to satisfy $\frac{Spc}{Stk} = 0.1$.

Similarly, the ratio $\frac{Spc \times U}{v_{settling}}$ giving the relative magnitude of the space charge force to gravity sedimentation is important for the small airways and alveolar regions. The ratio $\frac{Spc \times U}{v_{settling}}$ is not a function of the airway dimension or airflow. As a result, the values of $n'N^{\frac{1}{3}}$ in Figure 4.3 are constant. The concentration of particles carrying $100e$ satisfying $\frac{Spc \times U}{v_{settling}} \geq 0.1$ for the particle sizes of 0.1, 0.5 and 1.0 μm under sedentary breathing condition are 1.05×10^8, 1.47×10^{11} and 3.33×10^{12} $particle/m^3$, respectively. These requisite concentrations are quite high in the alveolar region, because the concentration reduces rapidly after convecting into the lungs. Thus, the space charge force does not play an important role in the small airways and alveolar regions.

Considering the image charge force, the effect of this can be represented by the relative term of $\frac{Img}{Stk}$ and $\frac{Img \times U}{v_{settling}}$ such that [58]

$$\frac{Img}{Stk} = \frac{3e^2}{8\pi^2 U^2 {d_p}^3 \rho_p \varepsilon_0 D} \frac{{n'}^2}{{x'_w}^2} \tag{4.14}$$

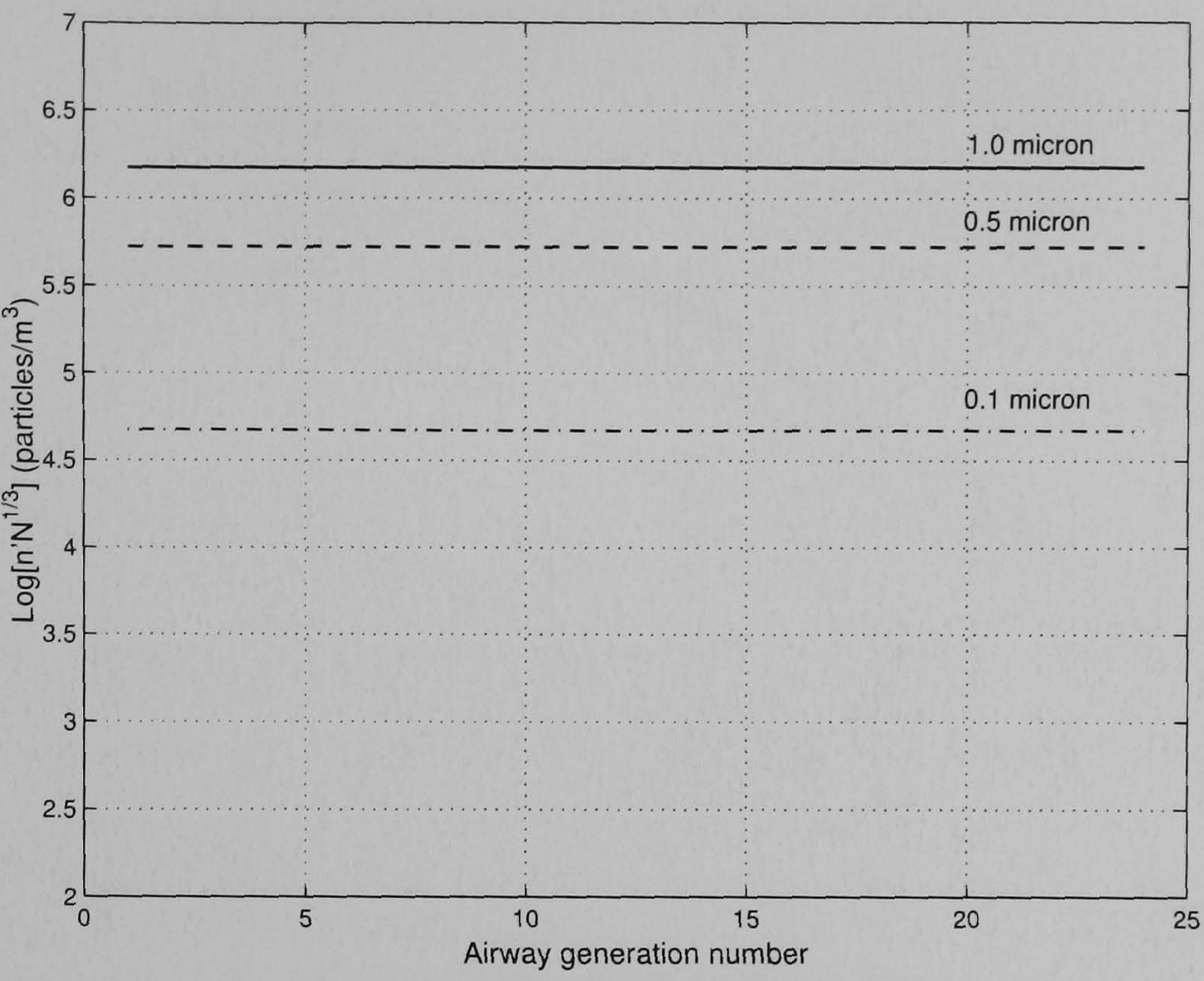

Figure 4.3: Values of $n'N^{\frac{1}{3}}$ satisfying the condition of $\frac{Spc \times U}{v_{settling}} = 0.1$ under sedentary breathing condition with the particle sizes of 0.1, 0.5 and 1.0 μm in diameter

$$\frac{Img \times U}{v_{settling}} = \frac{3e^2}{8\pi^2 g {d_p}^3 \rho_p \varepsilon_0 D^2} \frac{{n'}^2}{{x_w}'^2} \tag{4.15}$$

The ratio of $\frac{Img}{Stk}$ indicates the importance of the image charge force compared to inertial impaction. Similarly, the ratio of $\frac{Img \times U}{v_{settling}}$ gives the importance of image charge force compared with gravity. In a cylindrical tube, 10% of the cross-sectional area is contained within a distance of $0.0025D$ from the outer wall, so a reasonable value of x'_w to use is $x'_w = 0.025$. The effect of the image charge force can be the predominant term when this ratio is greater than 0.1. The charge values for sedentary breathing to satisfy the conditions of $\frac{Img}{Stk}$ and $\frac{Img \times U}{v_{settling}}$ equal to 0.1 for each generation number is shown in Figure 4.4 and 4.5, respectively . In the large airways, the ratio of $\frac{Img}{Stk}$ becomes important because the inertial impaction is the primary aerosol mechanism, due to the higher airflow velocities. After the particles reach deep into small airways, the gravity mechanism is the dominant term, and then the ratio of $\frac{Img \times U}{v_{settling}}$ is used. For example, in the case of a particle carrying a charge value of $100e$, this charge value has little affect on the deposition in large airways for the 0.5

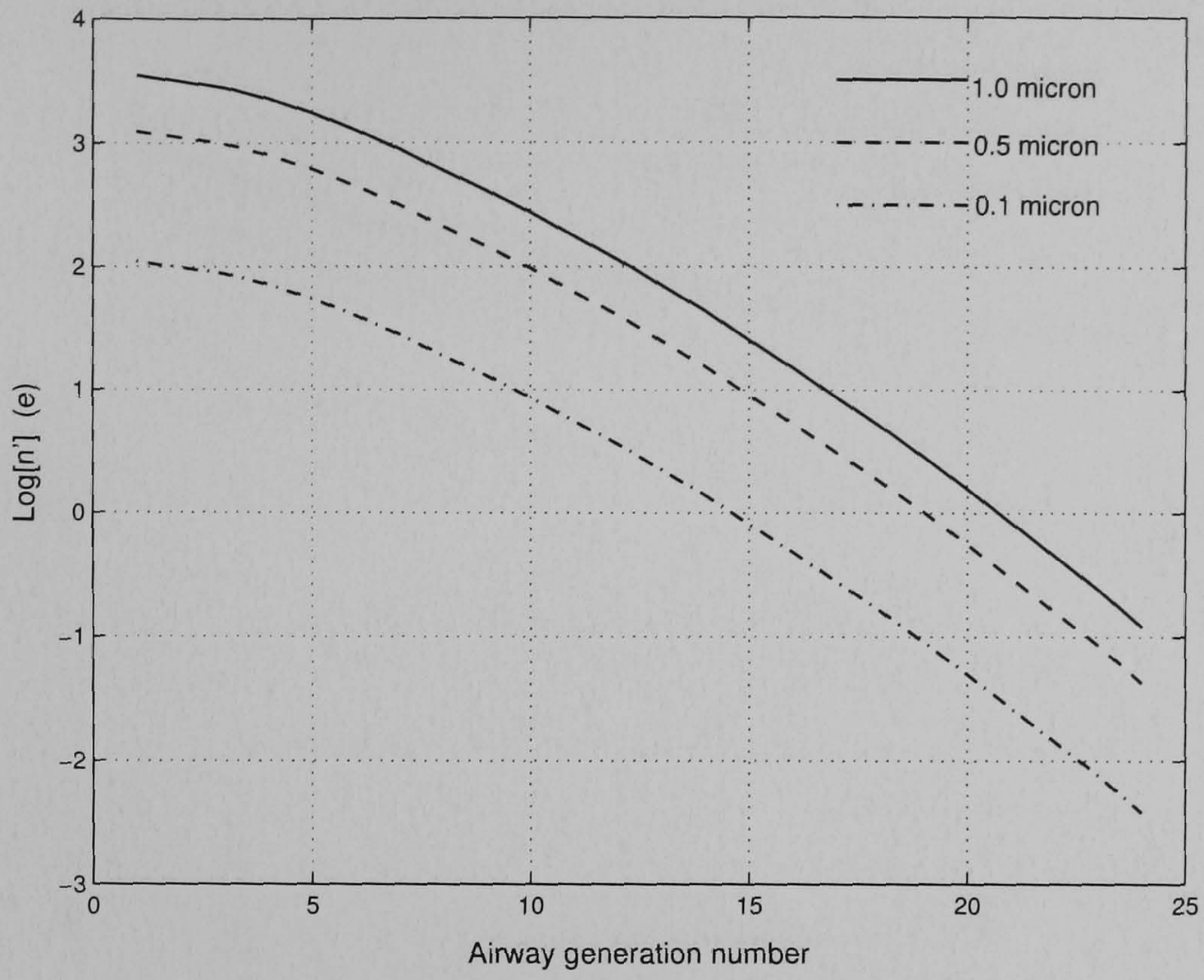

Figure 4.4: Values of n' satisfying the condition of $\frac{Img}{Stk} = 0.1$ under sedentary breathing condition with the particle sizes of 0.1, 0.5 and 1.0 μm in diameter

and 1.0 μm particles, but it becomes an important mechanism for the 0.1 μm particle. Whereas, a charge value of $100e$ affects deposition in small airways for all particle sizes. In addition, a 0.1 μm particle has an image charge effect larger than the 0.5 and 1.0μm particles. Thus, the image charge force is the important mechanism for the transport of charged aerosol in small airways and alveolar regions when the particles carry sufficient charge.

4.3 Deposition of charged aerosol in human airways using the one-dimensional predicted deposition model

The effect of electrostatic forces on the aerosol deposition discussed in the previous section shows the relative comparison of both space and image charge forces to impaction and gravity. This section provides more details of charged aerosol deposition efficiency arising from all basic mechanisms (i.e., impaction,

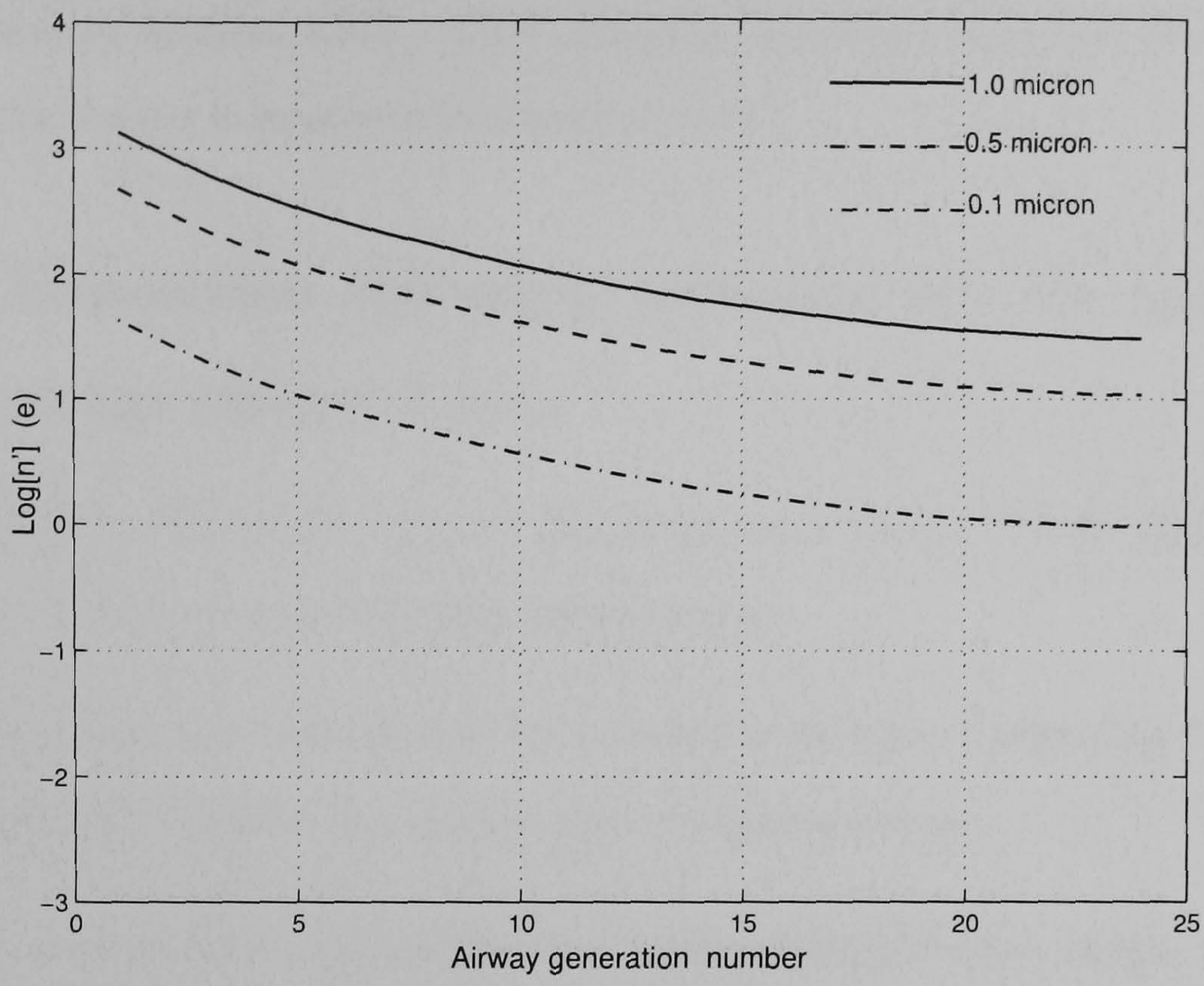

Figure 4.5: Values of n' satisfying the condition of $\frac{Img \times U}{v_{settling}} = 0.1$ under a sedentary breathing condition for the particle sizes of 0.1, 0.5 and 1.0 μm in diameter

gravity, diffusion, space charge and image charge) under defined conditions. The deposition model used in this section was developed at Brunel University based on the Weibel's morphological lung. The model calculates the deposition efficiency in any airway generation using a linear combination of all basic mechanisms and electrostatic forces. The details of the model can be found in [9] and [10]. The predicted deposition model assumes that particles are monodisperse and carry a uniform charge value within the Weibel's based lung model. The model was implemented only for the inhalation phase. Many previous theoretical studies have shown that the electrostatic forces have a significant effect on deposition efficiency for a sub-micron particle and less important effect for the larger particle size because impaction and sedimentation are dominant mechanisms. Particle sizes above 5 μm tend to be trapped in the extrathoracic and tracheobronchial regions [8]. The deposition efficiency formulae for space and image charge forces are given in section 4.3.1. The predicted deposition of charged aerosols under various conditions such as the charge value, particle size, number concentration, and inhalation flow rate will

be discussed in section 4.3.2 - 4.3.4. Finally, the deposition increment due to electrostatic forces is presented in section 4.3.5.

4.3.1 Deposition efficiency formulae for the space and image charge forces

The deposition efficiencies due to the space and image charge forces can be formulated based on the following assumptions:

- The airways are represented by tubular structures neglecting the branching region between the parent and daughter tubes.
- The concentration of aerosol is a uniform distribution within an airway.
- The airflow in an airway is a plug flow.

The space charge force can be expressed in terms of charge value and dimensionless residence time as follows ([202])

$$P_{spc} = \frac{4\pi N_0 R^3 \tau_e}{1 + 4\pi N_0 R^3 \tau_e} \tag{4.16}$$

where N_0 is the concentration of particles at the entrance of the tube, R is the radius and τ_e is the dimensionless residence time defined by

$$\tau_e = \frac{Bq^2 L}{4\pi\varepsilon_0 R^3 U_0} \tag{4.17}$$

in which B is the particle mobility, q is the charge per particle, ε_0 is the air permitivity, L is the length of tube and U_0 is the average velocity. For $4\pi N R^3 \tau_e \ll 1$, simplified formula for space charge force can be obtained

$$P_{spc} = 4\pi N_0 R^3 \tau_e \tag{4.18}$$

The deposition efficiency due to the image charge force can be derived based on the assumption that the wall is electrical conducting. The efficiency can be expressed as

$$P_{img} = 1 - \left(\frac{r_c}{R}\right)^2 \tag{4.19}$$

where r_c is the critical radius vector outside of which all particles are deposited. It is related to τ_e by the expression

$$\tau_e = 4\left(\frac{R}{r_c} + 2ln\frac{r_c}{R} - \frac{r_c}{R}\right) \tag{4.20}$$

For $\tau_e \ll 1$, a simplified formula was obtained by Pich [153] to give

$$P_{img} = (6\tau_e)^{\frac{1}{3}} \tag{4.21}$$

To compare the relative terms of the space and image charge force, the ratio of P_{spc} to P_{img} using the simplified formulae of equation 4.18 and 4.21 can be obtained as

$$\alpha = \frac{P_{spc}}{P_{img}} = \left(\frac{32}{3}\right)^{\frac{1}{3}} \pi N R^3 {\tau_e}^{\frac{2}{3}} \tag{4.22}$$

The values of α in an aerosol of 1 μm particle diameter and a charge value of $100e$ which is breathed into a Weibel's lung model at 1000 cm^3 tidal volume and 15 $cycles/min$ are given in Table 4.3.1. A number concentration $N = 10^{11}$ and $N = 10^{13}$ $particles/m^3$ are considered. It shows that for $N = 10^{11}$ $particles/m^3$, the values of α are less than unity in all airway generations, and these values exceed unity when $N = 10^{13}$ $particles/m^3$. The data indicates that space charge plays an important role in particle deposition when a high concentration of aerosol is generated.

4.3.2 Effects of charged values and particle sizes

Electrostatic forces play an important role in the deposition efficiency in the lower bronchial and alveolar parts particularly when the particle size is small. Figures 4.6 and 4.7 show the comparisons of deposition efficiencies at various charge values for 0.5 and 2.0 μm particles, respectively. The predicted model was set up for an inhalation flow rate of 0.5 l/s, an inlet number concentration of 10^{11} $particles/m^3$, and a particle density of 1000 kg/m^3. They show that higher charge values increase deposition efficiency, especially in the alveolar region. At this concentration, the image charge is a dominant mechanism at higher charge values. The electrostatic forces on 0.5 μm particles give a higher

Table 4.1: Ratios of P_{spc} to P_{img} at different airway generations for 1 μm particle with 100e breathed into Weibel's lung at 1000 cm^3 tidal volume and 15 cycles/min (Adapted from Yu [203])

Generation Number	τ_e	$R\ (cm)$	α $(N = 10^{11}\ m^{-3})$	α $(N = 10^{13}\ m^{-3})$
0	0.992×10^{-9}	0.90	0.502	50.2
1	1.168×10^{-9}	0.61	0.174	17.4
2	1.368×10^{-9}	0.44	0.0727	7.24
3	1.616×10^{-9}	0.28	0.0209	2.09
4	6.760×10^{-9}	0.225	0.0282	2.82
5	1.456×10^{-9}	0.175	0.0221	2.21
10	5.392×10^{-7}	0.065	0.0126	1.26
15	1.480×10^{-5}	0.033	0.0150	1.50
20	2.912×10^{-4}	0.0225	0.0346	3.46

relative deposition than those on 2.0 μm particles because of different particle mobilities. Figure 4.8 gives a comparison of deposition efficiency for various particle sizes carrying a charge of 100 e. Electrostatic forces can enhance deposition efficiency for the smaller particle sizes. For large particle sizes, impaction and gravity tend to dominate.

4.3.3 Effects of particle concentrations

The particle concentration is an important parameter for the space charge force. A higher concentration leads to more space charge force due to the smaller distances between particles. The particle concentration depends on the inhaler devices and the drug. The predicted deposition model was set up at various concentrations for a particle size of 0.5 μm. Figure 4.9 shows that a higher concentration of particles leads to a greater deposition efficiency due to the space charge force.

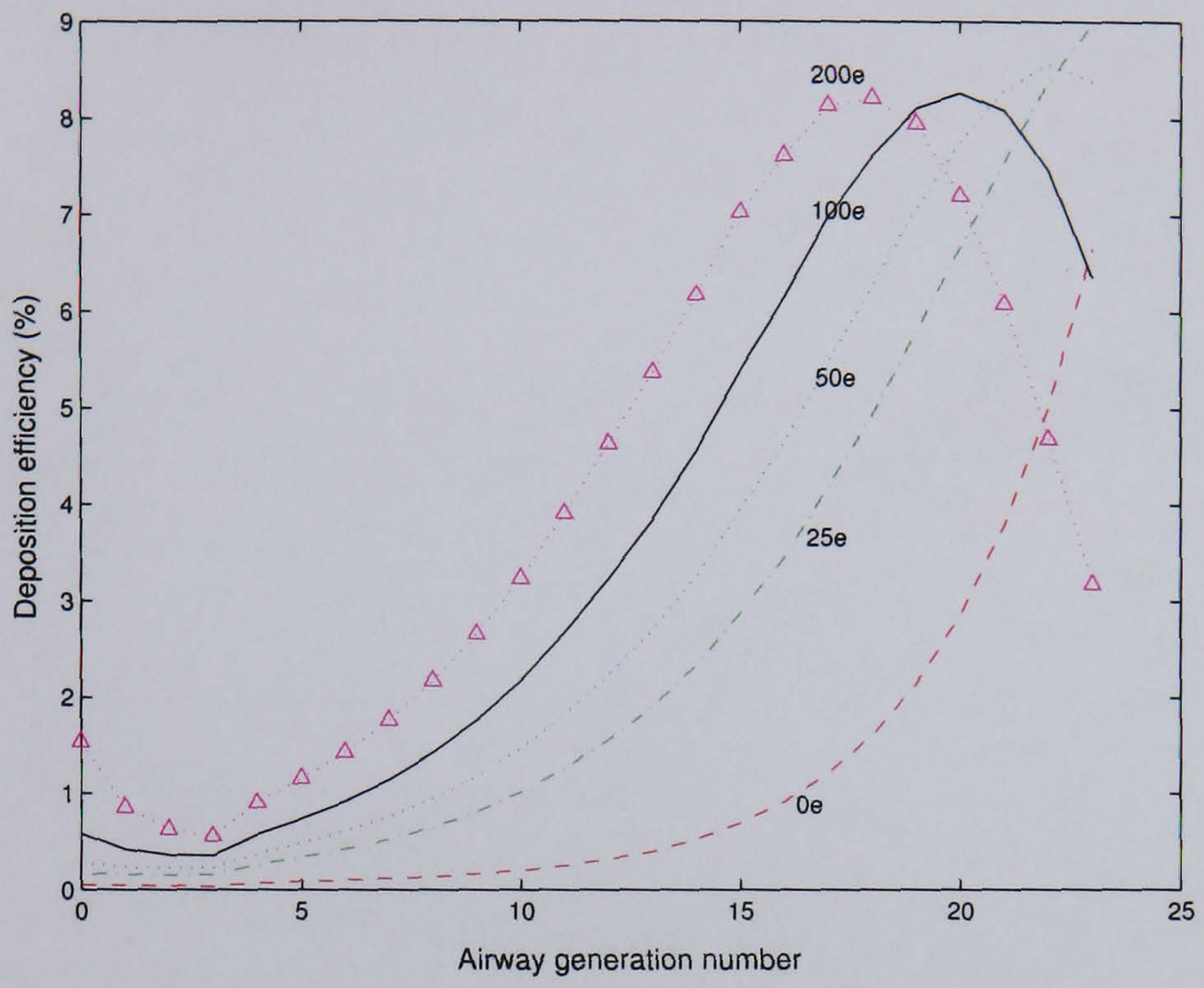

(a) Deposition efficiency vs airway generation

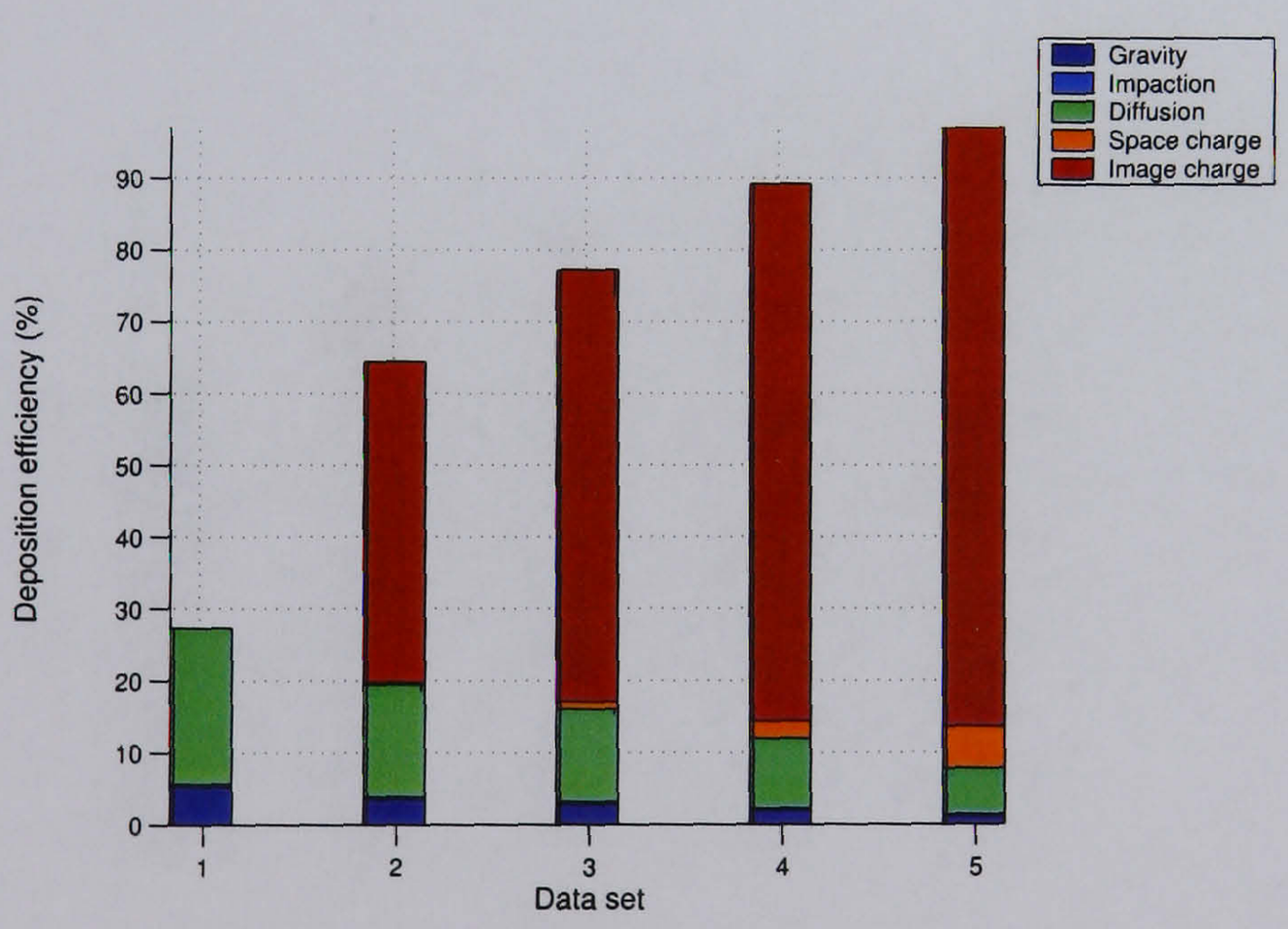

(b) Stacked bars of deposition efficiency of various mechanisms

Figure 4.6: Comparison of deposition efficiencies of 0.5 μm particles carrying various charge values with an inhalation flow rate 0.5 l/s, $C_0 = 10^{11}$ $particles/m^3$, and $\rho_p = 1000$ kg/m^3. (data set: (1) 0 e, (2) 25 e, (3) 25 e, (4) 100 e, and (5) 200 e)

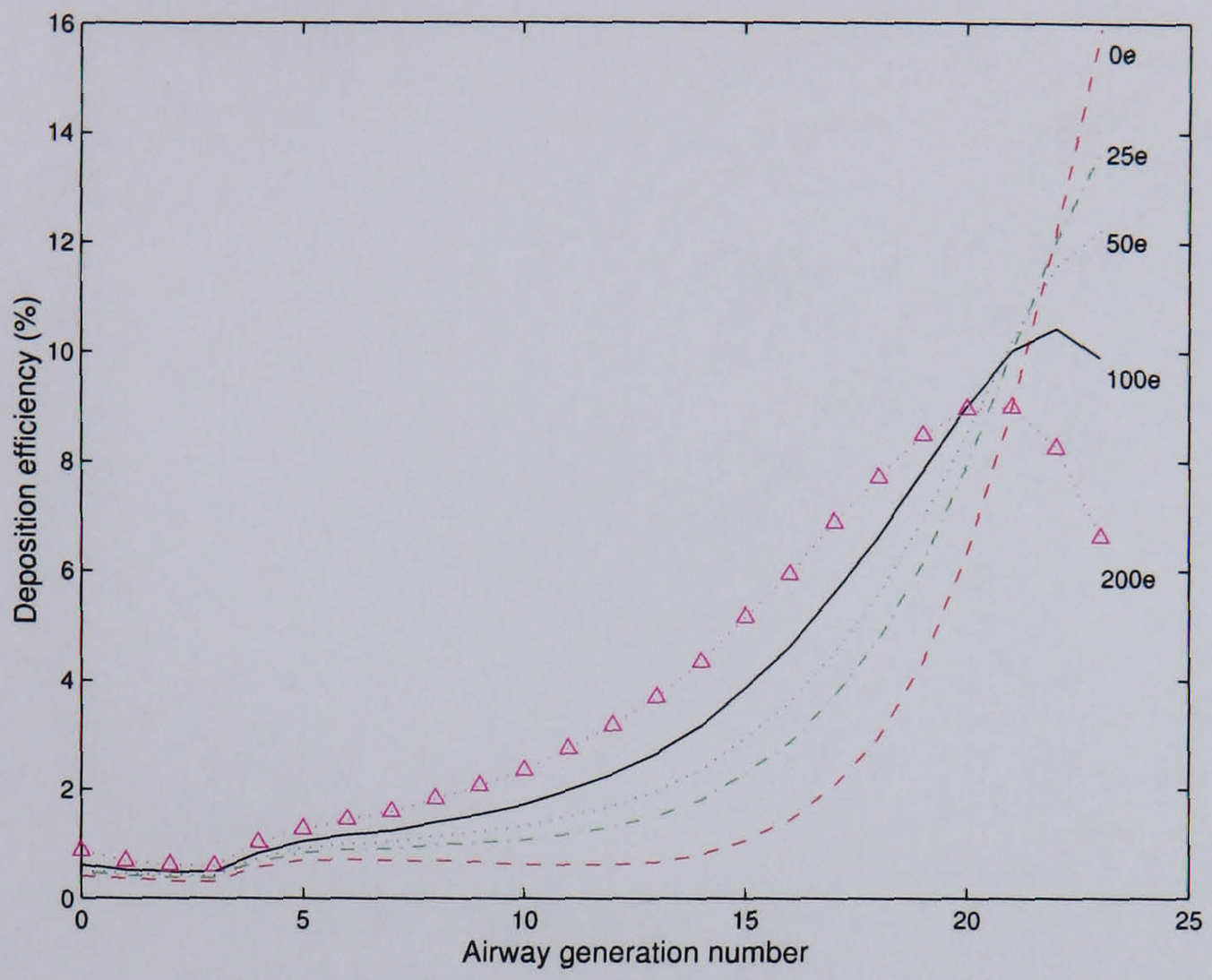

(a) Deposition efficiency vs airway generation

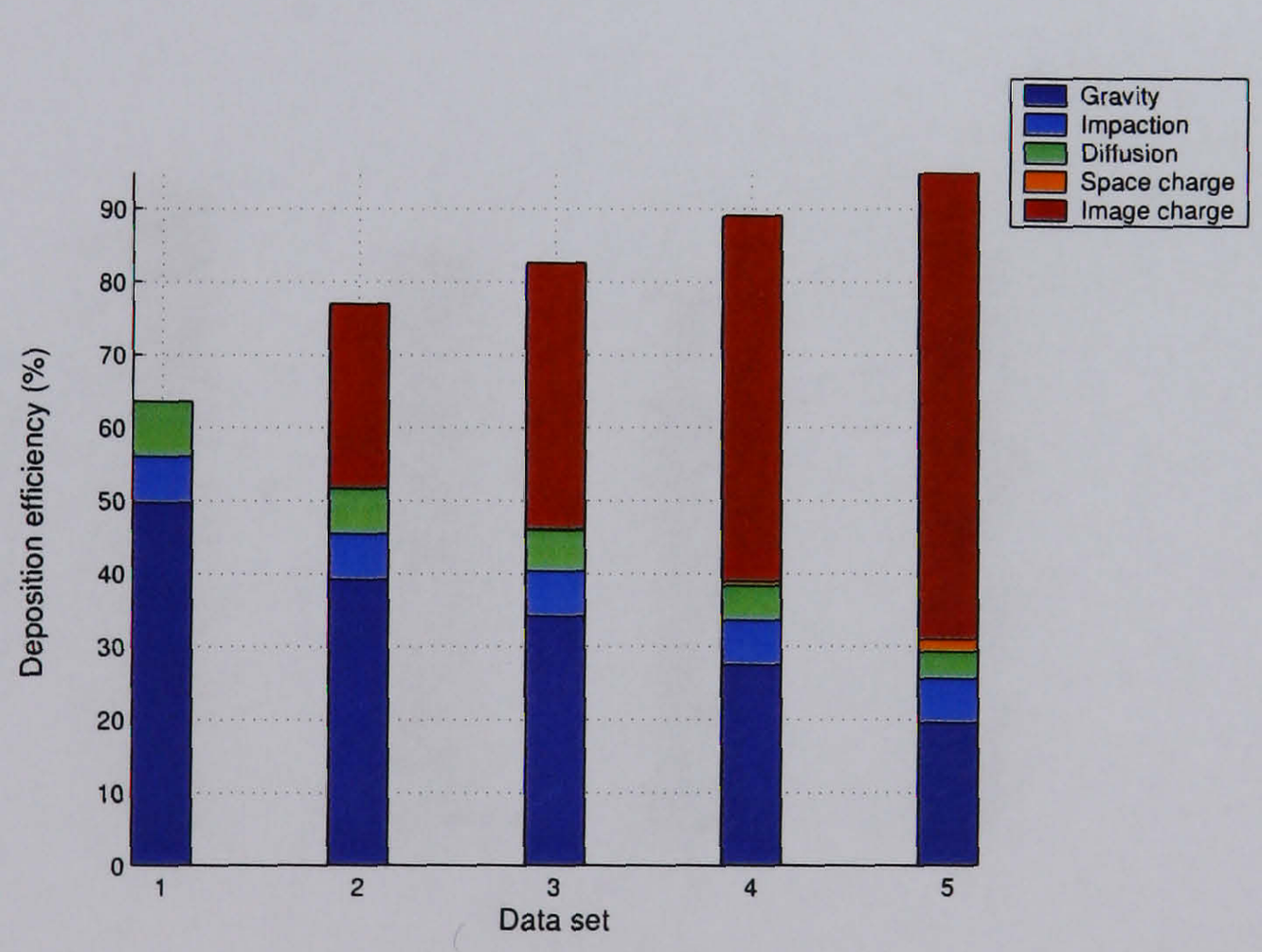

(b) Stacked bars of deposition efficiency of various mechanisms

Figure 4.7: Comparison of deposition efficiencies of 2.0 μm particles carrying various charge values with an inhalation flow rate 0.5 l/s, $C_0 = 10^{11}$ $particles/m^3$, and $\rho_p = 1000$ kg/cm^3. (data set: (1) 0 e, (2) 25 e, (3) 25 e, (4) 100 e, and (5) 200 e)

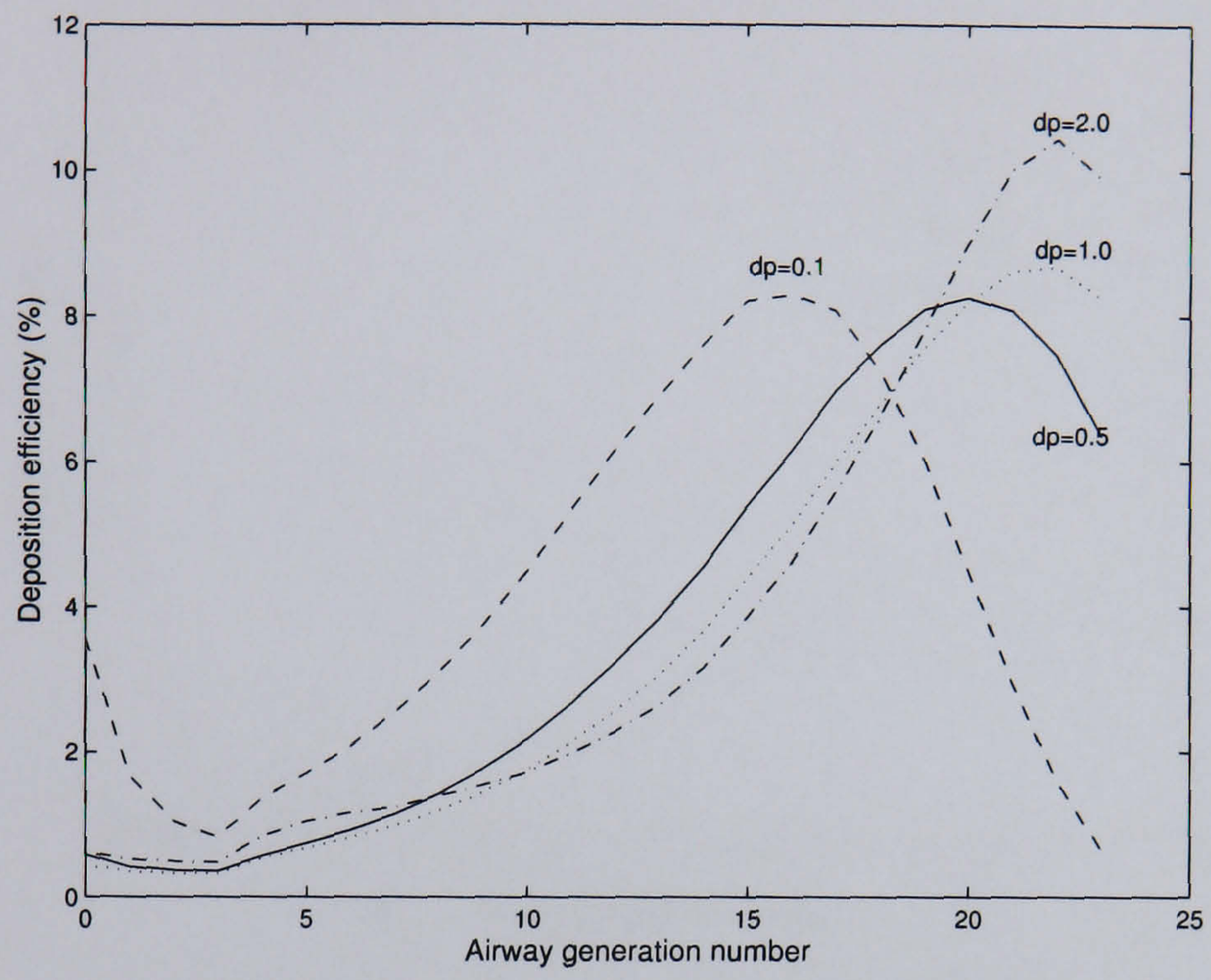

(a) Deposition efficiency vs airway generation

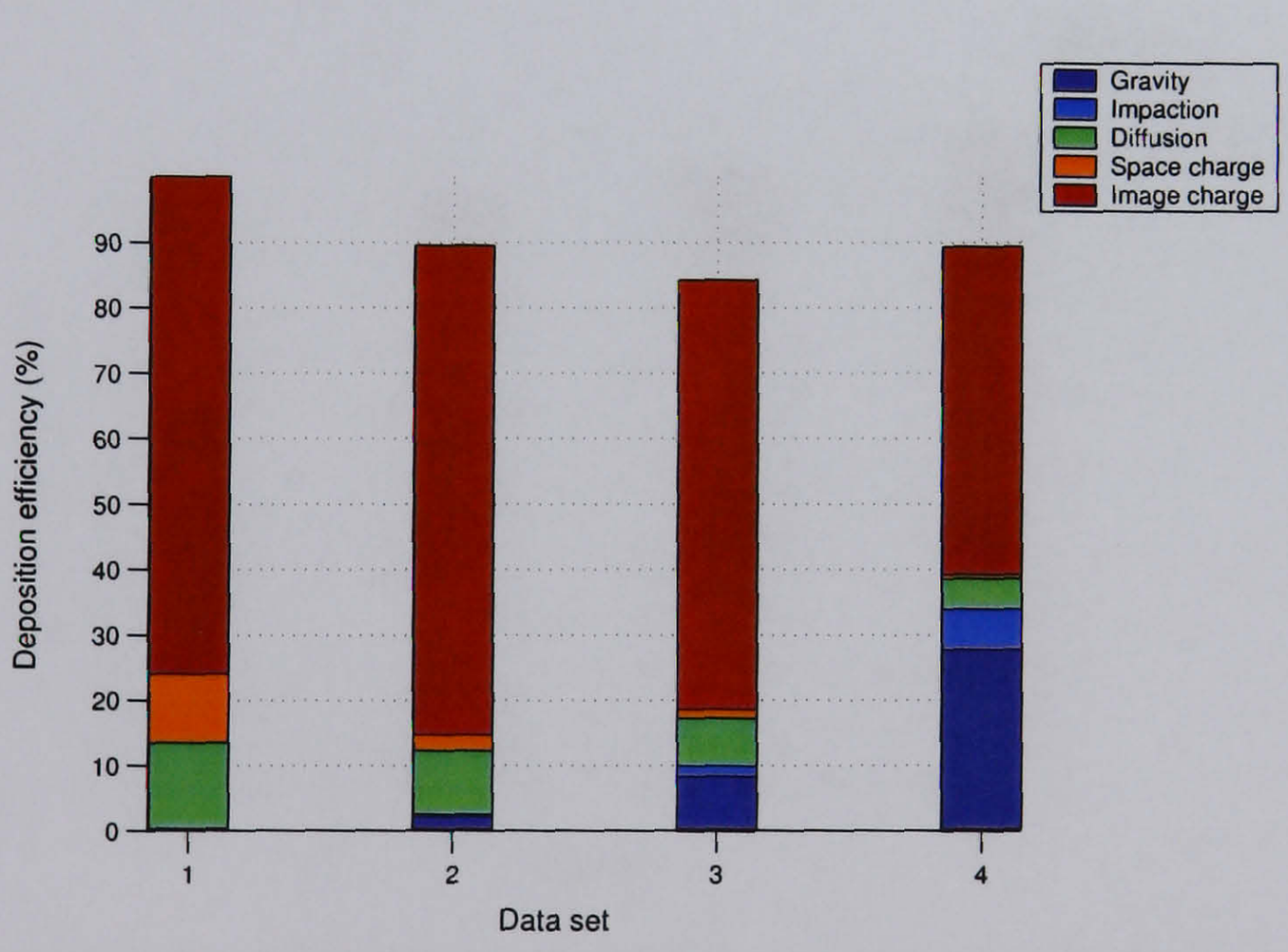

(b) Stacked bars of deposition efficiency of various mechanisms

Figure 4.8: Comparison of deposition efficiencies of various particle sizes with an inhalation flow rate 0.5 l/s, $q_p = 100\ e$, $C_0 = 10^{11}\ particles/m^3$, and $\rho_p = 1000\ kg/m^3$ (data set: (1) 0.1 μm, (2) 0.5 μm, (3) 1.0 μm, and (4) 2.0 μm)

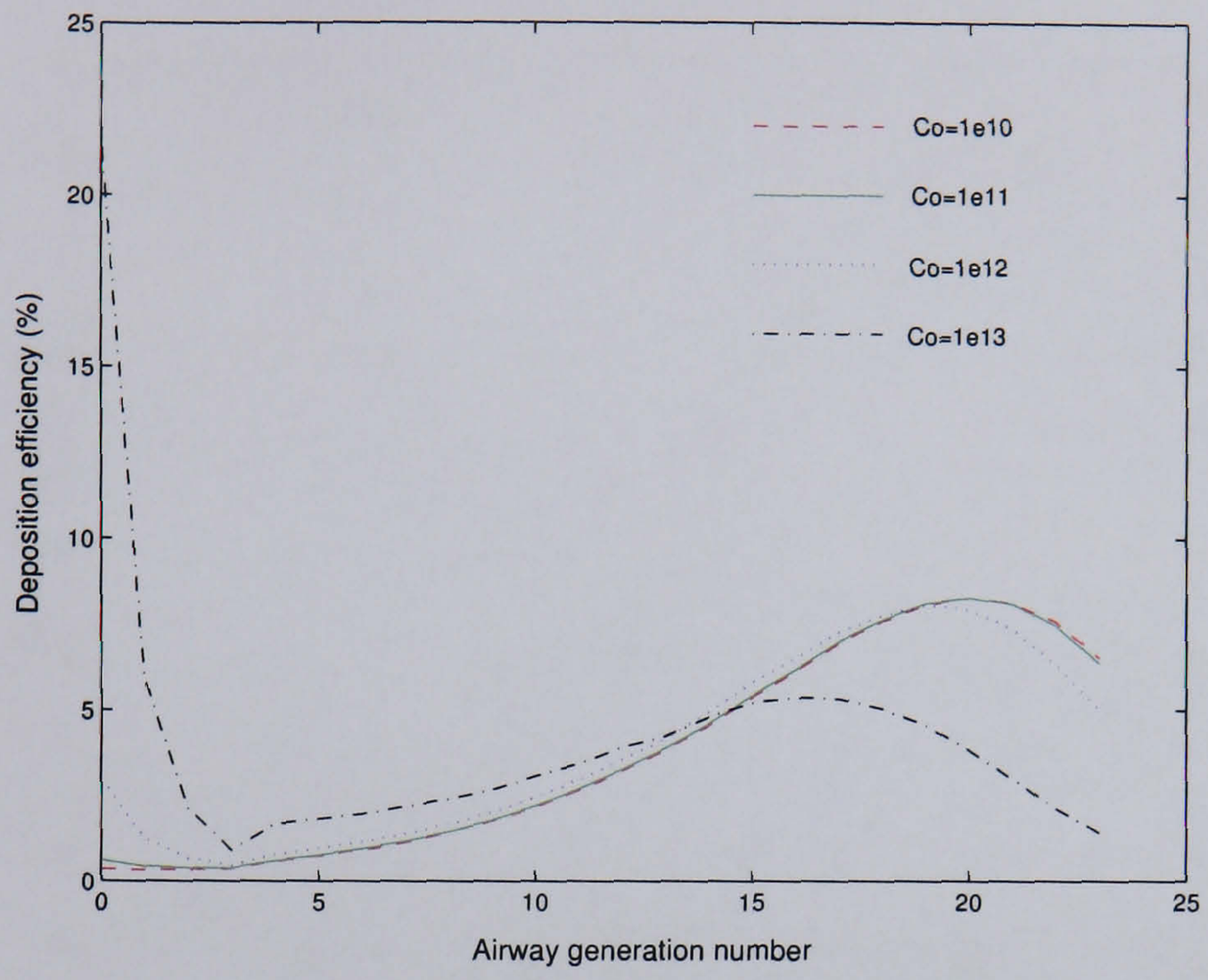

(a) Deposition efficiency vs airway generation

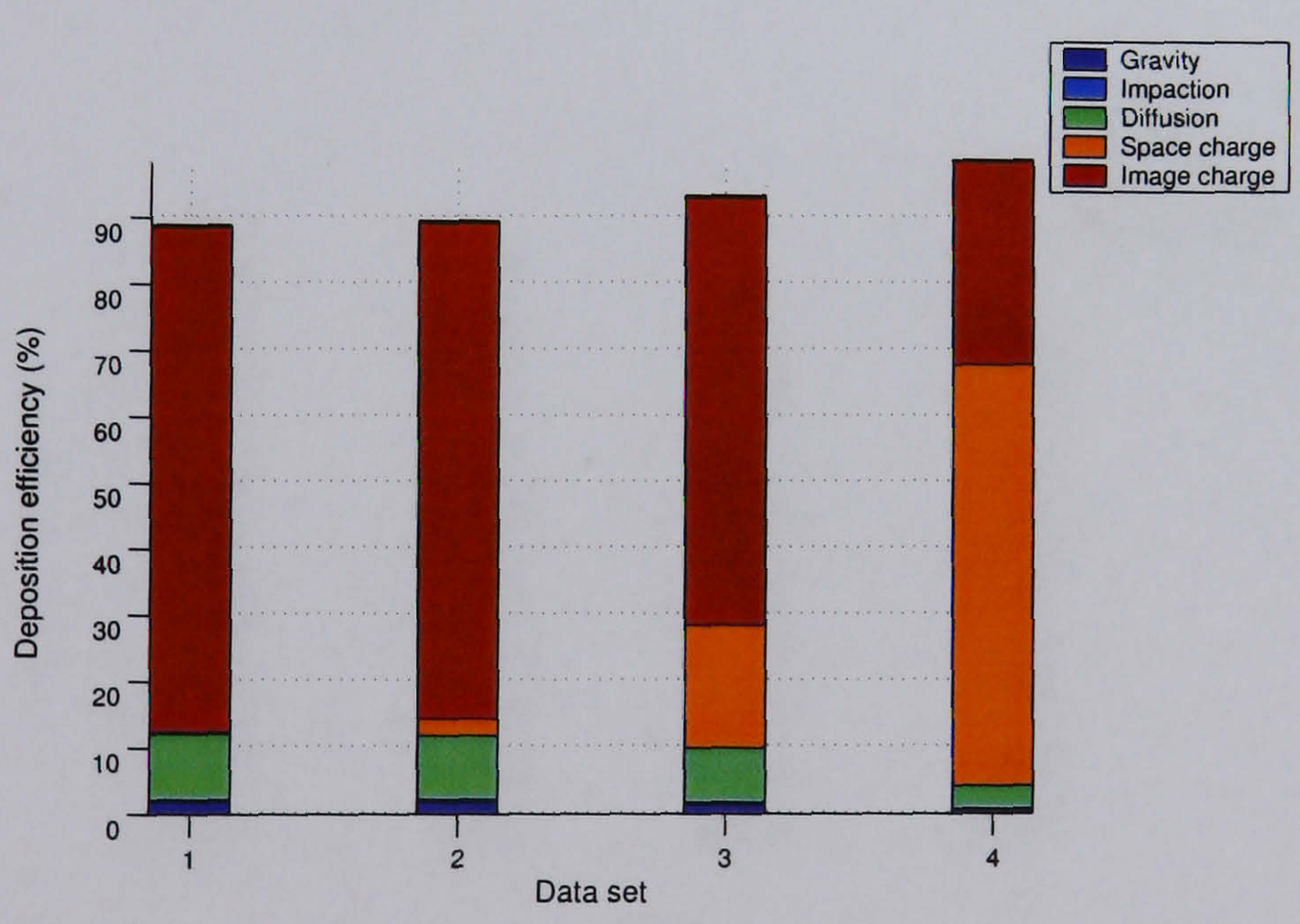

(b) Stacked bars of deposition efficiency of various mechanisms

Figure 4.9: Comparison of deposition efficiencies of various inlet concentration of 0.5 μm particles with an inhalation flow rate 0.5 l/s, $q_p = 100\ e$, $C_0 = 10^{11}\ particles/m^3$, and $\rho_p = 1000\ kg/m^3$ (data set: (1) $1.0 \times 10^{10}\ particles/m^3$, (2) $1.0 \times 10^{11}\ particles/m^3$, (3) $1.0 \times 10^{12}\ particles/m^3$, and (4) $1.0 \times 10^{13}\ particles/m^3$)

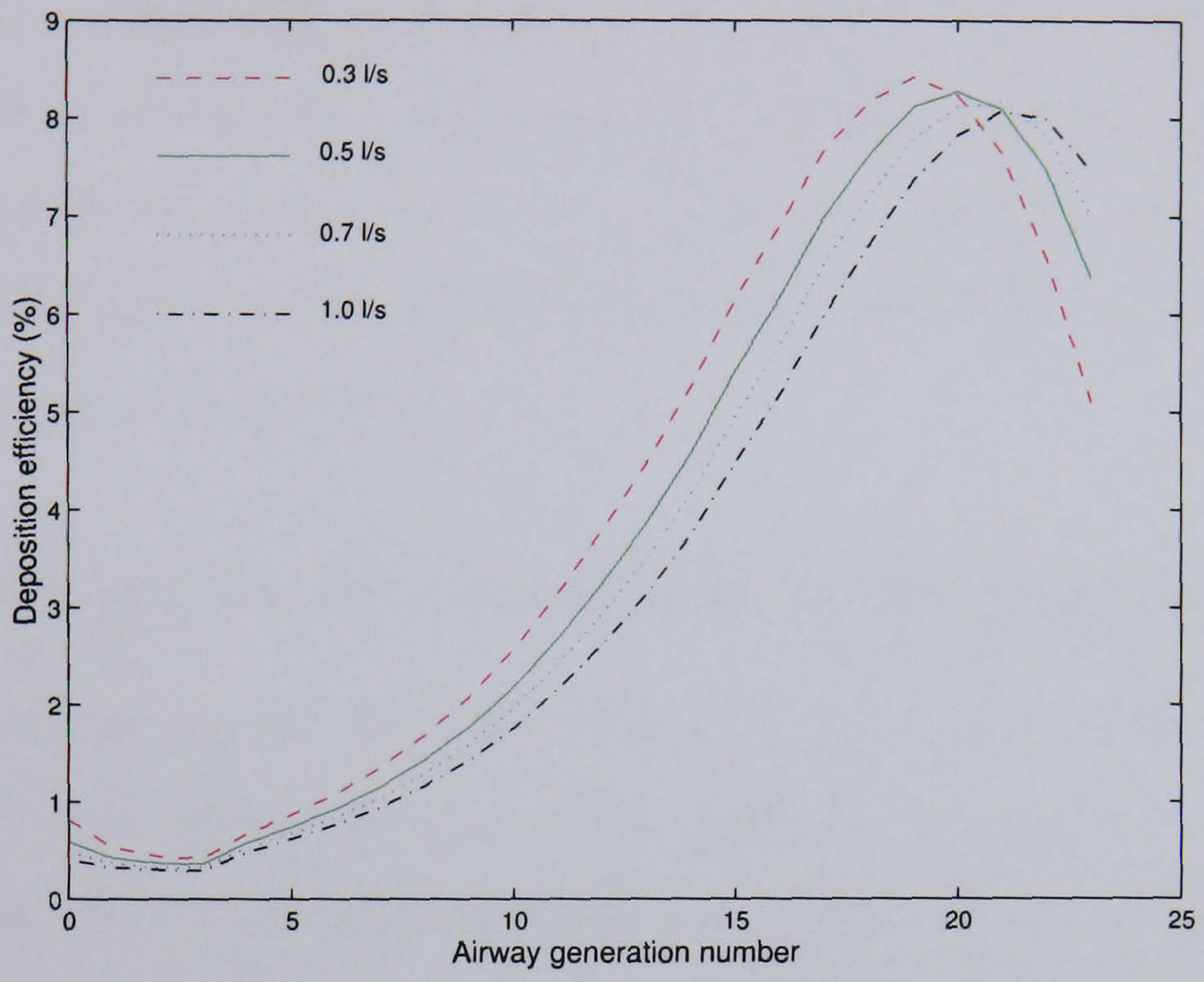

(a) Deposition efficiency vs airway generation

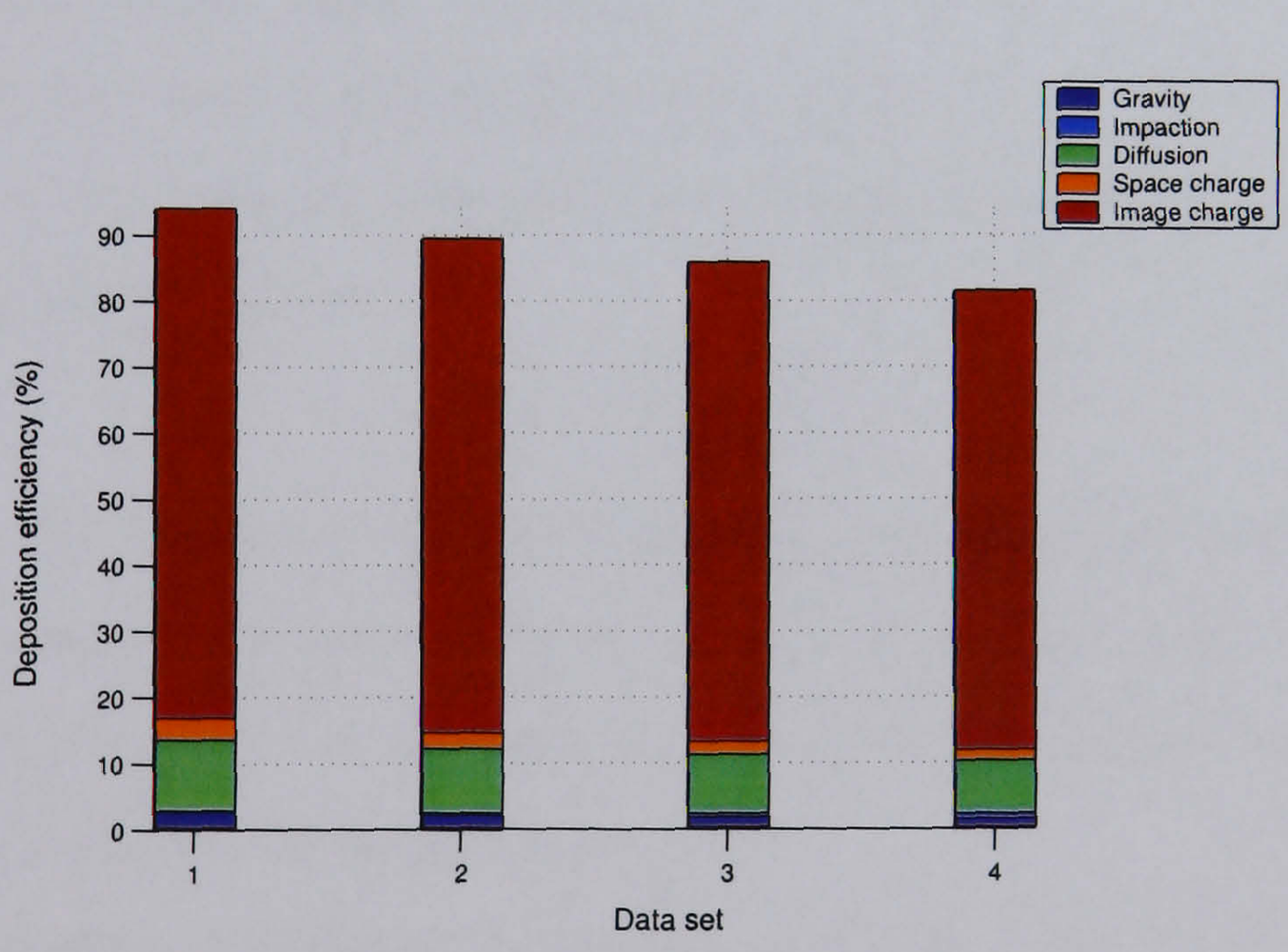

(b) Stacked bars of deposition efficiency of various mechanisms

Figure 4.10: Comparison of deposition efficiencies of various inhalation flow rates of 0.5 μm particles with $q_p = 100\ e$, and $\rho_p = 1000\ kg/m^3$ (data set: (1) 0.3 l/s, (2) 0.5 l/s, (3) 0.7 l/s, and (4) 1.0 l/s)

4.3.4 Effects of inhalation flow rates

The inhalation flow rate can be varied depending on breathing condition and airway calibre which may be influenced by disease. In the analysis of electrostatic forces on deposition efficiency, the airflow affects the residence time of particle. Fast inhalation flow rate reduces the residence time of particles. Slow inhalation flow rate has a greater deposition efficiency due to electrostatic forces, as shown in Figure 4.10.

4.3.5 Deposition increment due to electrostatic forces

The results given by the predicted deposition model show that the electrostatic forces can improve the deposition efficiency in the human respiratory tract. For an aerosol system with a relatively low number concentration (i.e., environmental aerosol), the image charge acting on charged particles is the predominant electrostatic force. The deposition efficiencies for a fine particle size (less than 1 μm) can be simplified by accounting only for gravity and image charge forces. The relative efficiency can be defined in term of the deposition increment given by ([203])

$$\Delta P = \frac{P_{is} - P_s}{1 - P_s} \tag{4.23}$$

where P_{is} is the deposition efficiency resulting from the combined mechanisms of the image charge and gravity forces, and P_s is the deposition efficiency due only to gravity force. The incremental deposition can be approximated by a straight line with an intersection point q_c.

The calculated deposition increments in the lung for both the tracheobronchial and alveolar region versus $|q/e|$ for unit density particles of diameter 0.3, 0.6, and 1.0 μm are shown in Figure 4.11. The 1 μm particles require a higher charge value to reach the same deposition increment as 0.3 and 0.6 μm particles. The electrostatic forces tend to enhance deposition in alveolar region rather than in the tracheobronchial region. The comparison between the predicted deposition increment and some experimental data by Tarroni et

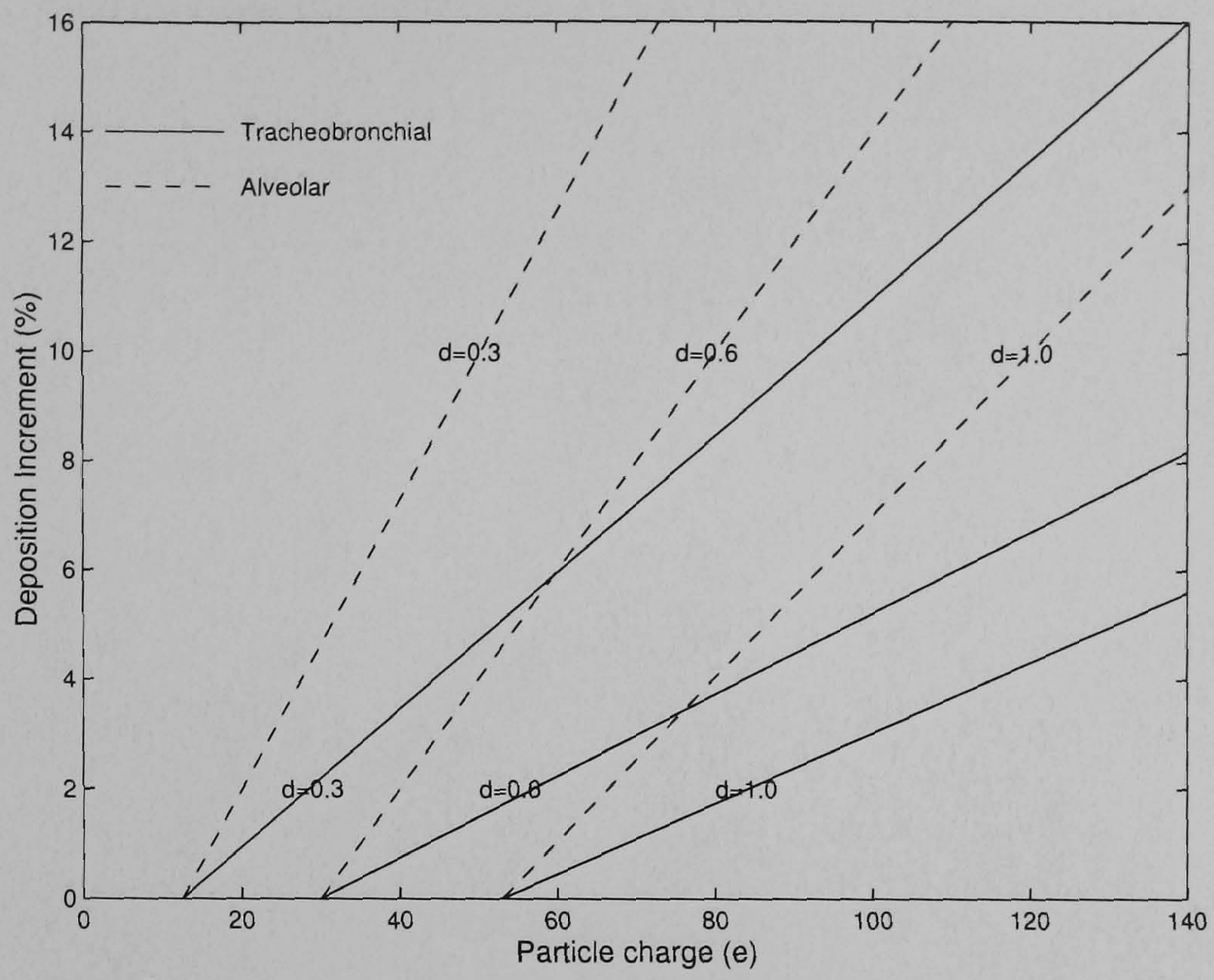

Figure 4.11: Deposition increment of various charge values for three particle sizes of 0.3,0.6, and 1.0 μm in tracheobronchial and alveolar regions [203]

al.[180] and Melandri et al. [129] has a good agreement as shown in Figure 4.12.

4.4 Space charge computation

The space charge force on a particle cloud can be considered as the N-body problem. A direct method for calculating the interacting forces among particles due to space charge field is the Particle-Particle (PP) technique, which is the simplest way of implementation. The PP technique accumulates forces acting on all particles by finding the force $\mathbf{F}(\mathbf{x}_{p_i}, \mathbf{x}_{p_j})$ of particle j on particle i for all particles. Although the PP technique is a flexible method, it has a high computational cost of $O(N_p^2)$ operations required to evaluate the forces on all N_p particles. Many techniques can be implemented to reduce complexity to compared to the PP method, i.e., Particle-Mesh method (PM), Tree-code Particle Mesh method (TPM), Nested Grid Particle Mesh (NGPM) and Fast Multipole Method (FMM). Some techniques also have a high efficiency when

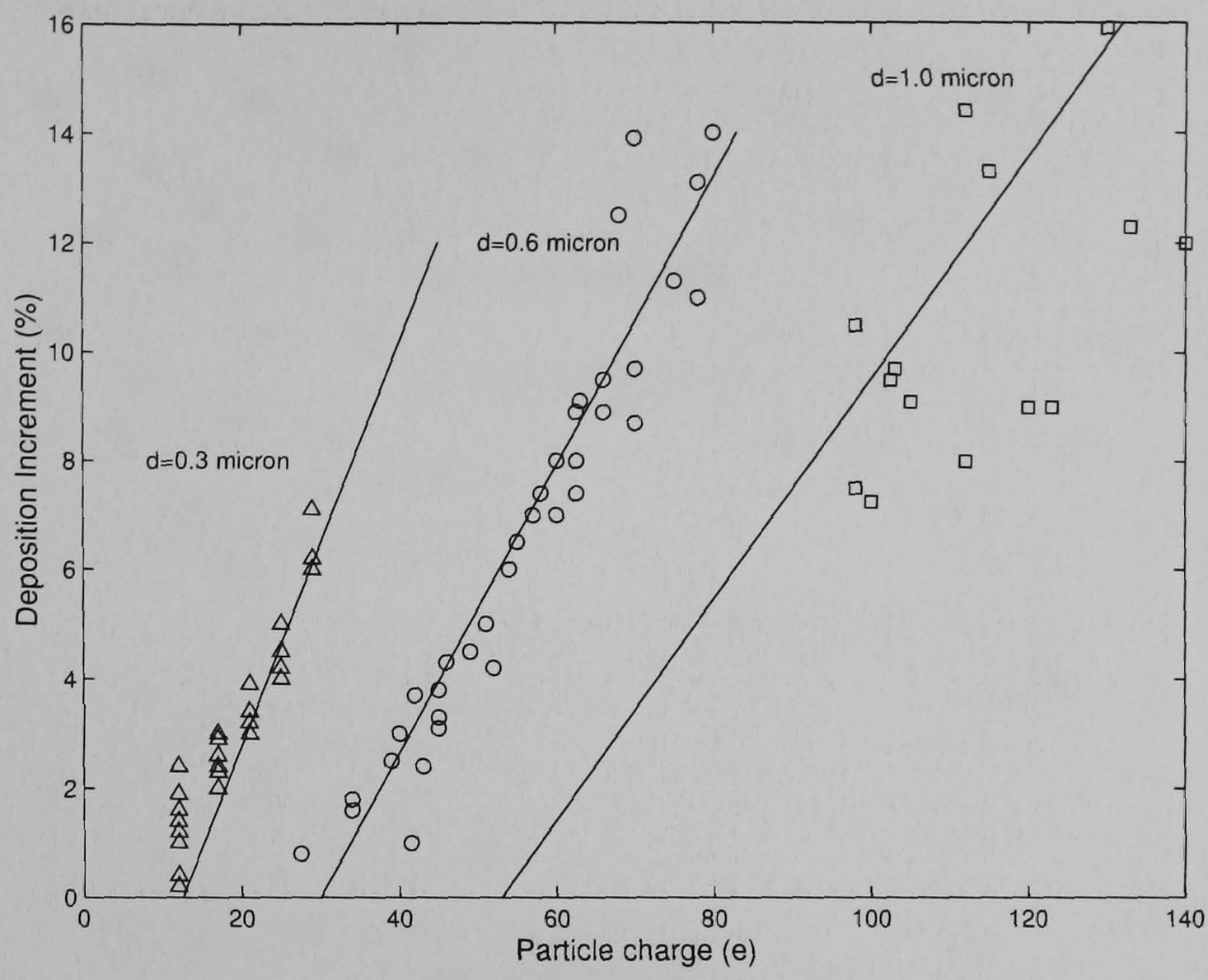

Figure 4.12: Comparison of deposition increment of various charge values based on Yu's formulae for three particle sizes of 0.3, 0.6, and 1.0 μm (displayed by solid line), and the experimental data obtained by Tarroni et al.[180] and Melandri et al.[129] (indicated by Δ, $\odot$, $\boxdot$, for 0.3, 0.6, 1.0 μm particles, respectively) [203].

they are applied using parallel computation. The details of these alternative methods can be found in [84],[175],[71], and [197].

In this study, the Particle-Mesh (PM) technique is selected to solve the space-charge force, sometimes known as the Particle-In-Cell (PIC). Particle-mesh codes can be divided into two basic categories as pure particle-mesh, and a combination of particle-mesh and particle-particle known as P3M. The P3M technique presented by Hockney ([84]) improves the accuracy of the PM technique by mixing the PP and PM methods with some modifications. However, the P3M method is more complex to implement than the PM method. P3M technique is suitable in cases where the aerosol cloud has a high concentration of particles. The pure particle mesh was used in this study because it is optimal between speed and accuracy. The main advantage of the PM method is speed with a computational complexity of order $O(N_p + N_g log N_g)$, where N_g is the number of grid points. The slowest step of PM computation is the potential

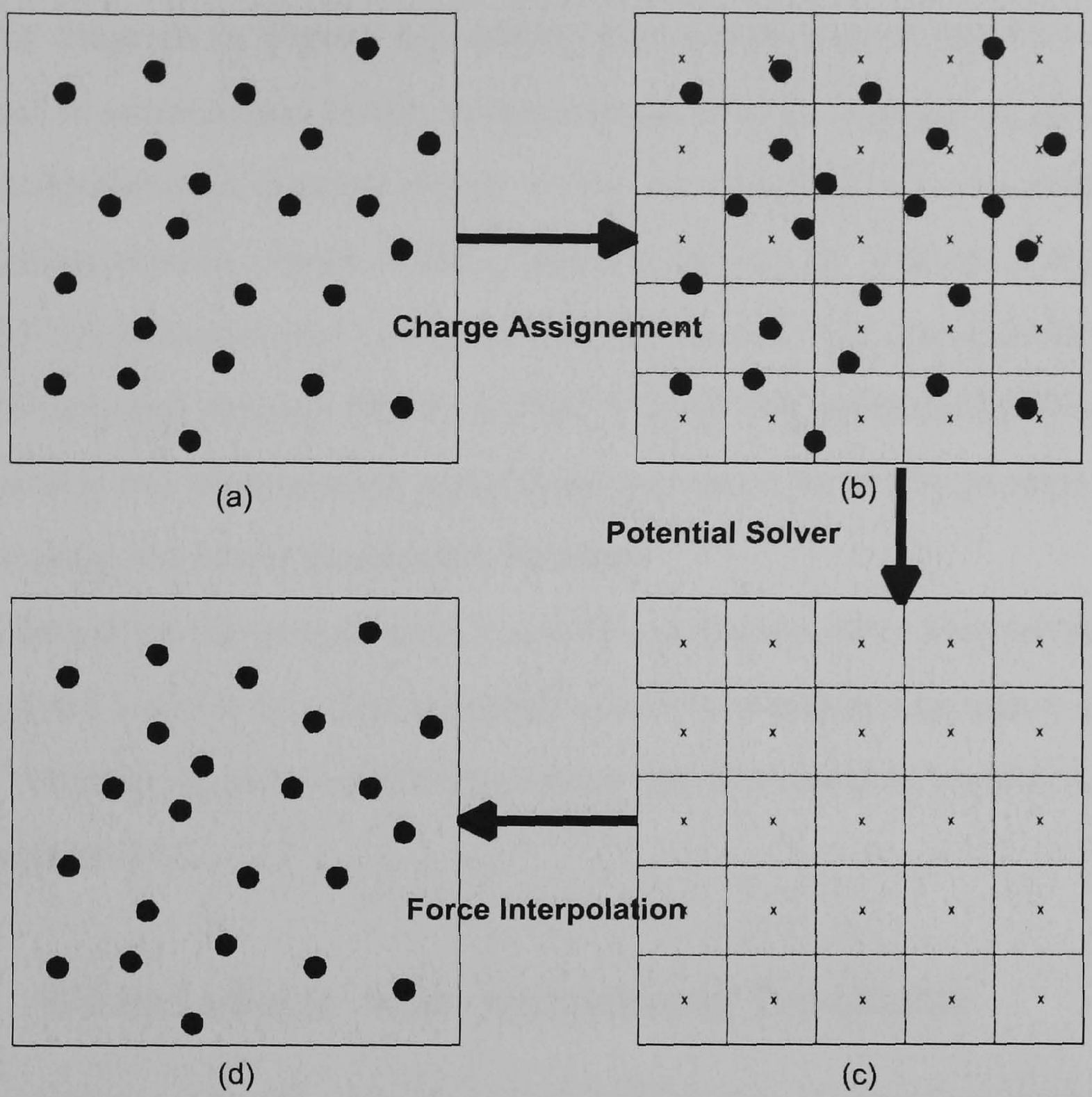

Figure 4.13: 2D schematic of particle mesh technique. (a) particles are located in the computational domain, (b) all charges on particles are assigned into the mesh, (c) electrical potential is calculated using a charge density on the mesh, (d) space charge forces acting on particles are obtained by the force interpolation

equation solver, which often relies on a Fast Fourier Transform (FFT). The computational speed can be improved significantly by using a hardware-based FFT solver.

In the continuous domain, the electrical potential $\Phi_E(\mathbf{x})$ can be represented by Poisson's equation, which is a function of the continuous charge density $\rho_q(\mathbf{x})$ given by

$$\nabla^2 \Phi_E(\mathbf{x}) = \frac{\rho_q(\mathbf{x})}{-\varepsilon_0}. \tag{4.24}$$

The concept of PM method is to solve electrical potential in Poisson's equation using mesh representing the continuous domain. The electrical field can be evaluated from the first derivative of the electrical potential. A 2D

schematic diagram in Figure 4.13 shows the overall step of the PM method, which can be summarised briefly in three steps. Firstly, charges on all particles in the computational domain (figure 4.13a) are assigned into the present and neighbouring meshes (figure 4.13b), which is known as "charge assignment". Secondly, the potential and electrical field are solved. The variables are represented in the mesh domain (figure 4.13b). Finally the electrical force acting on every particle can be evaluated using mesh interpolation at the present particle position using the same assignment function.

The details of charge assignment and charge density functions are presented in section 4.4.1 and 4.4.2. The potential solver for Poisson's equation governed by FFT techniques and force interpolation are discussed in section 4.4.3 and 4.4.4, respectively.

4.4.1 Cloud shape and assignment functions

The cloud shape function describes the distribution of charge in each particle with a finite width. The shape function with the distribution of overlapping finite-sized particles leads to a smoothly varying continuous charge density. The common cloud shape function consists of Nearest Grid Point (NGP), Cloud-in-cell (CIC) and Triangular Shaped Clouds (TSC). The one dimensional cloud shape interpretation of charge assignment is shown in Figure 4.14 and the assignment function is summarised in Table 4.2 . The NGP scheme is the simplest scheme with least expense in computation. All particles in NGP schemes are assigned to their nearest grid points. This may lead to inter-particle force changing discontinuously. The CIC scheme is the most popular scheme, because it has better numerical properties than the NGP scheme and is a compromise with computational time. Every particle is represented by a cube of uniform density. Finally, the TSC scheme defines every particle as a cube of tri-linearly rising density. Most particles will intersect 3^d cells with the size of 2 grid cells, where d is the dimension of the system. However, this is rarely used for a PM method because it is more expensive to implement than

Table 4.2: One-dimensional cloud and assignment functions [84]

Scheme	Cloud shape function $S(x)$
NGP	$\delta(x)$
CIC	$\frac{1}{H}\Pi\left(\frac{x}{H}\right)$
TSC	$\frac{1}{H}\Lambda\left(\frac{x}{H}\right)$

Scheme	Assignment function $W(x)$
NGP	$\Pi\left(\frac{x}{H}\right)$
CIC	$\Lambda\left(\frac{x}{H}\right)$
TSC	$\frac{1}{H}\Pi\left(\frac{x}{H}\right) * \Lambda\left(\frac{x}{H}\right)$

the CIC scheme.

For the cloud shape function $S(x)$ of a unit charged particle, the fraction of the charge assignment from the particle of shape $S(x)$ to mesh cell p is given by the overlap of the cloud with cell p. The area of overlap of the cloud is defined in terms of the assignment function $W(x)$, which can be expressed using the top-hat function as

$$\begin{aligned} W(x) &= \int \Pi\left(\frac{x'}{H}\right) S(x'-x)dx' \\ &= \Pi\left(\frac{x}{H}\right) * S(x) \end{aligned} \tag{4.25}$$

where H is a cell width.

The multidimensional version of the schemes listed in Table 4.3 gives the cloud shapes function $S(x)$ and the assignment function $W(x)$, which are given by the products of the corresponding one-dimensional functions of each component.

In this study, the three-dimensional CIC assignment function is selected for both charge density assignment and mesh interpolation because of the optimal point between speed and accuracy. The CIC assignment function can

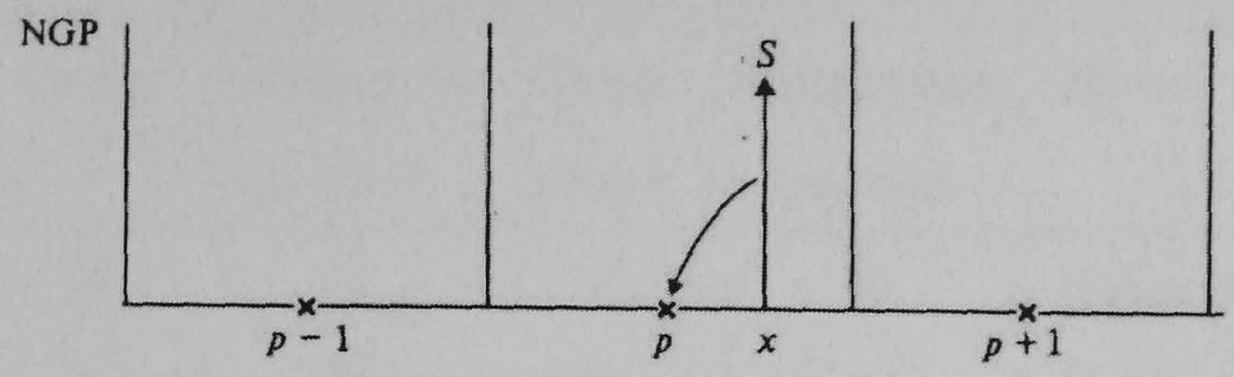

Figure 4.14: 1D cloud and assignment function shape interpretations of charge assignment [84]

Table 4.3: Hierarchy of assignment schemes of the production form [84]

Scheme	Order	Number of points*	Cloud shape	Assignment function	Force
NGP	0	1^d	δ	Π	Stepwise
CIC	1	2^d	Π	Λ	Continuous piecewise linear
TSC	2	3^d	Λ	$\Lambda * \Pi$	Continuous values and first derivative

* d is a dimension of system

be expressed as

$$W(\mathbf{x}) = \begin{cases} \left(1 - \frac{|x|}{H_x}\right)\left(1 - \frac{|y|}{H_y}\right)\left(1 - \frac{|z|}{H_z}\right) & ; -\mathbf{H} < \mathbf{x} < \mathbf{H} \\ 0 & ; \mathbf{x} \geq \mathbf{H} \end{cases} \tag{4.26}$$

where H_x, H_y, H_z are cell widths in x, y, and z directions, respectively.

4.4.2 Charge density assignment

The discrete charge density assigned to the discrete mesh position $\mathbf{x}_{ijk}$ (where i, j, and k are mesh indexes) is given by the summation of all charged particles assigned at (i, j, k) cell divided by the mesh volume such that

$$\rho_{q,ijk} = \sum_{m=1}^{N_p} \frac{q_m}{H_x H_y H_z} W(\mathbf{x}_{p_m} - \mathbf{x}_{ijk}). \tag{4.27}$$

where m is the particle index, $\mathbf{x}_p$ is a position vector of particle.

The continuous charge density by analogy can be represented by

$$\rho_q(\mathbf{x}) = \frac{1}{H_x H_y H_z} \int\int\int W(\mathbf{x}' - \mathbf{x}) n(\mathbf{x}') dz' dy' dx'. \tag{4.28}$$

Note that

$$\rho_{q,ijk} \equiv \rho_q(\mathbf{x}_{ijk})$$

$$n(\mathbf{x}) = \sum_{m=1}^{N_p} q_m \delta^3(\mathbf{x} - \mathbf{x}_{p_m}) \tag{4.29}$$

It means that a set of $\rho_{q,ijk}$ values can be obtained by sampling from the continuous $\rho_q(\mathbf{x}_{ijk})$. This continuous form will be used for representing the charge density in Poisson's equation, which will be discussed in more detail in the next section.

4.4.3 The potential solver

The step to solve the potential equation is the slowest step of computation. It often relies on a Fast Fourier Transform (FFT) as giving a good computational speed with the order of complexity of $O(N_g log N_g)$. The method limits the direct solution of second-order PDE without variable coefficients and/or arbitrary shaped boundaries. Other numerical methods may be also used to solve Poisson's equation, such as a wavelet transform, a finite element method or a finite volume method.

Recall the Poisson's equation,

$$\nabla^2 \Phi_E(\mathbf{x}) = -\frac{\rho_q(\mathbf{x})}{\varepsilon_0}$$

the solution of the second-order PDE can be evaluated by the convolution between the Green function $G(\mathbf{x})$and the charge density function $\rho_q(\mathbf{x})$.

$$\begin{aligned} \Phi_E(\mathbf{x}) &= -\int G(\mathbf{x}, \mathbf{x}') \frac{\rho_q(\mathbf{x}')}{\varepsilon_0} d\mathbf{x}' \\ &= -G(\mathbf{x}) * \frac{\rho_q(\mathbf{x})}{\varepsilon_0} \end{aligned} \tag{4.30}$$

where $G(\mathbf{x})$ is the Green function of Poisson's equation (see in Appendix D), which is given by

$$G(\mathbf{x}, \mathbf{x}') = -\frac{1}{4\pi \left|\mathbf{x} - \mathbf{x}'\right|}$$

In this work, the solution of Poisson's equation is solved in the Fourier domain, where the Fourier transform of the convolution between $G(\mathbf{x})$ and $\rho_q(\mathbf{x})$ can be written in terms of the product of $\hat{G}(\mathbf{x})$ and $\hat{\rho}_q(\mathbf{x})$. The Fourier transform of $G(\mathbf{x})$ and $\rho_q(\mathbf{x})$ is obtained using the Fast Fourier Transform (FFT), then the solution of potential is solved by taking the Inverse Fast Fourier Transform (IFFT) to $\hat{\Phi_E}(\kappa)$, κ is a fourier variable of $\mathbf{x}$.

$$\hat{\Phi_E}(\kappa) = -\frac{1}{\varepsilon_0}\,\mathfrak{F}\{G(\mathbf{x}) * \rho_q(\mathbf{x})\} \tag{4.31}$$
$$= -\frac{1}{\varepsilon_0}\,\hat{G}(\kappa)\hat{\rho}_q(\kappa)$$

$$\Phi_E(\mathbf{x}) = \mathfrak{F}^{-1}\{\hat{\Phi_E}(\kappa)\} \tag{4.32}$$

where $\mathfrak{F}\{\cdot\}$ and $\mathfrak{F}^{-1}\{\cdot\}$ are Fourier and inverse Fourier operators, respectively.

4.4.3.1 Fourier space representation

The concept of Fourier space is used to represent a function using sinusoids of different frequency and the summation of these sinusoids is equal to the original function. The transformation into Fourier space is called Fourier transform. On the other hand, the transformation of Fourier space into the original function is known as inverse Fourier transform. In the Fourier domain, the mathematical operations of functions have greater simplicity i.e., convolution and correlation. The details of Fourier transform can be found in many signal processing books, i.e., [141] and [111].

Using the Fourier transform, the continuous representation of discrete charge density can be written as

$$\hat{\rho}_{q_c}(\kappa) = \sum_{n=-\infty}^{\infty} \hat{\rho}_{q_d}(\kappa' + 2n\kappa_{N_y}) \tag{4.33}$$

where $\hat{\rho}_{q_d}$ represents the $\hat{\rho}_{q_c}$ on a discrete mesh, and is periodic in κ with the period $2n\kappa_{N_y}$. The bandwidth of the continuous function is limited by a range of the $-\kappa_{N_y} < \kappa \leq \kappa_{N_x}$, called a "principal zone", whereas those outside these limits are called "aliases". The extra contributions from aliases in the principal zone, called aliasing, can be reduced by narrowing the Fourier band of the assignment function $\hat{W}(\kappa)$. In Figure 4.15 the wider assignment function leads to narrowing of the Fourier band $\hat{W}(\kappa)$ in the principal zone.

In this study, the Fast Fourier Transform (FFT) is selected for solving the Fourier transform and inverse Fourier transform. This technique is a DFT

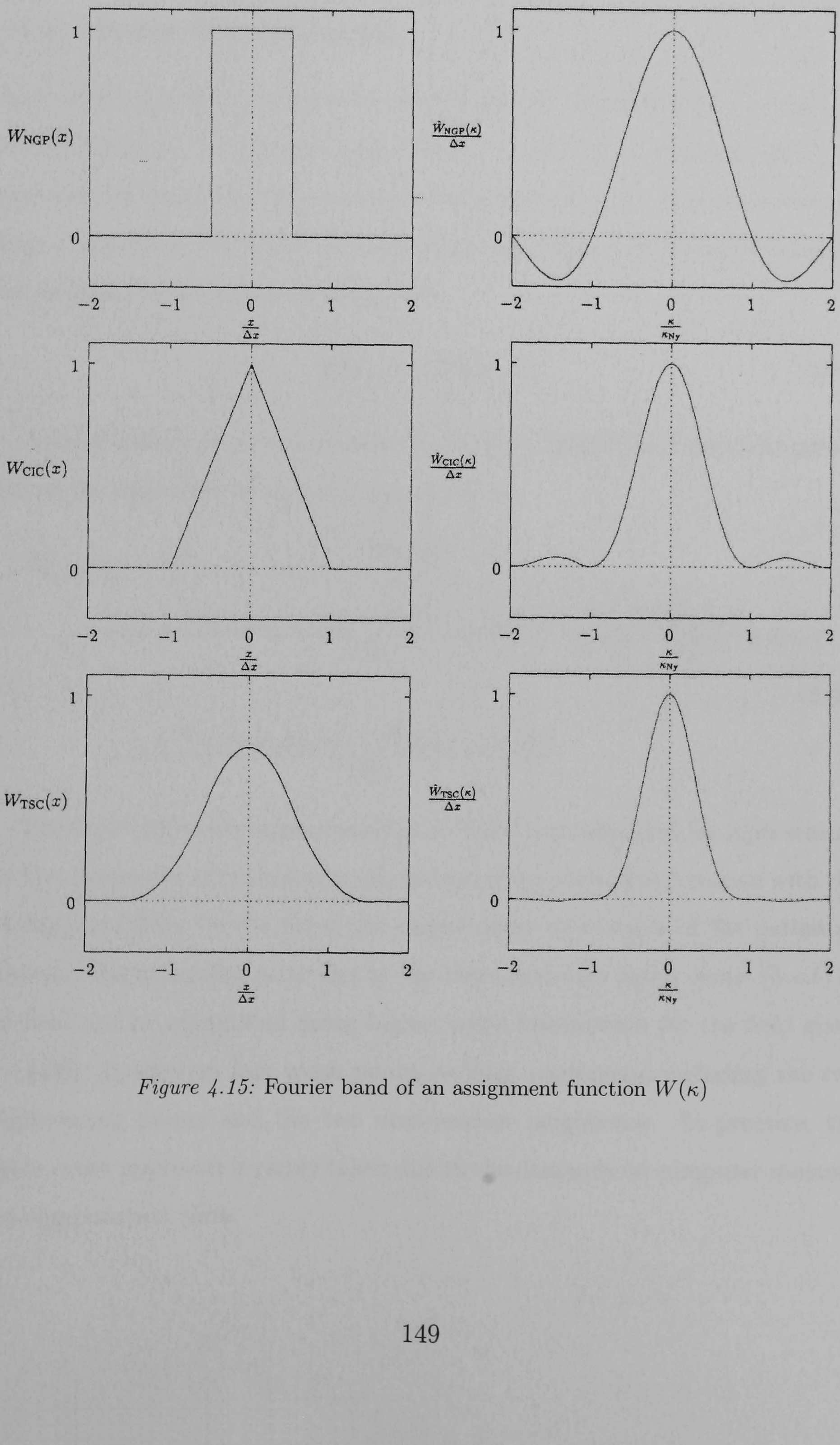

Figure 4.15: Fourier band of an assignment function $W(\kappa)$

algorithm developed by Cooley and Tukey [34] which reduces the complexity order $O(N^2)$ to $O(NlogN)$. The details of the numerical algorithm being introduced in [155].

4.4.4 Force Interpolation

The space charge force on particles is a product of their charge values and the electrical field at the present mesh point. The electrical field for any mesh point can be evaluated from the first derivative of their electrical potential given in equation 4.34 which is obtained by the solution of Poisson's equation and assigned to the centre of those cells.

$$\mathbf{E}(\mathbf{x}) = -\nabla\Phi_E\,(\mathbf{x}) \tag{4.34}$$

A finite-difference approximation for the first derivative of electrical potential can be expressed by a Taylor expansion as

$$\begin{aligned} E_{x_{i,j,k}}(\mathbf{x}) = E_x(x_i, y_j, z_k) &= -\frac{\partial\Phi_E(\mathbf{x})}{\partial x}_x \\ &= -\frac{\Phi_E(x_{i+1}, y_j, z_k) - \Phi_E(x_{i-1}, y_j, z_k)}{2H_x} + \frac{{H_x}^2}{6}\frac{\partial^3\Phi_E(\mathbf{x})}{\partial x^3} + h.o.t \\ &\simeq -\frac{\Phi_E(x_{i+1}, y_j, z_k) - \Phi_E(x_{i-1}, y_j, z_k)}{2H_x} \end{aligned} \tag{4.35}$$

The finite-difference approximation in (4.35) typically used for representing the first derivative of potential, is the second order derivative accurate with the leading error term by the third and higher order derivatives of the potential. However, the truncated error due to the third and high order terms ($h.o.t$) in the field can be eliminated using higher order formulation for the field given by (4.36). It involves four mesh points on each component including the two neighbouring points and the two next-nearest neighbours. In practice, the higher order approach is rarely taken due to the demands on computer memory and computation time.

$$E_{x_{i,j,k}}(\mathbf{x}) \simeq -\alpha \frac{\Phi_E(x_{i+1}, y_j, z_k) - \Phi_E(x_{i-1}, y_j, z_k)}{2H_x} - (1-\alpha)\frac{\Phi_E(x_{i+2}, y_j, z_k) - \Phi_E(x_{i-2}, y_j, z_k)}{4H_x} \tag{4.36}$$

The electrical field $E_y(\mathbf{x})$ and $E_z(\mathbf{x})$ can be approximately expressed using the same concept as the x-direction given by (4.37) and (4.38),respectively.

$$E_{y_{i,j,k}}(\mathbf{x}) \simeq -\frac{\Phi_E(x_i, y_{j+1}, z_k) - \Phi_E(x_i, y_{j-1}, z_k)}{2H_y} \tag{4.37}$$

$$E_{z_{i,j,k}}(\mathbf{x}) \simeq -\frac{\Phi_E(x_i, y_j, z_{k+1}) - \Phi_E(x_i, y_j, z_{k-1})}{2H_z} \tag{4.38}$$

Finally, the space charge force on an individual particle is treated in a similar way to charge density assignment with the same assignment function. The force interpolation function of particle at $\mathbf{x_p}$ is given by

$$\mathbf{F_{spc}}(\mathbf{x}_p) = q_p \sum_{i,j,k=1}^{N_g} W(\mathbf{x}_p - \mathbf{x})\mathbf{E}_{ijk}(\mathbf{x}) \tag{4.39}$$

4.5 Image charge computation

The image charge force computation requires the nearest wall distance for each particle at every step of the trajectory calculation. In the complex surface structure of the geometrical model, the wall boundary is normally represented by a set of triangular faces. To speed up the tracking of the nearest wall distance of any particle, nearest wall indexes corresponding to any node are initialised and stored as nodal data, called the nearest wall index. Then, the nearest wall distance of the particle can be calculated based on nearest wall indices of the current cell. The algorithm discussed in this section has been developed specifically for this research.

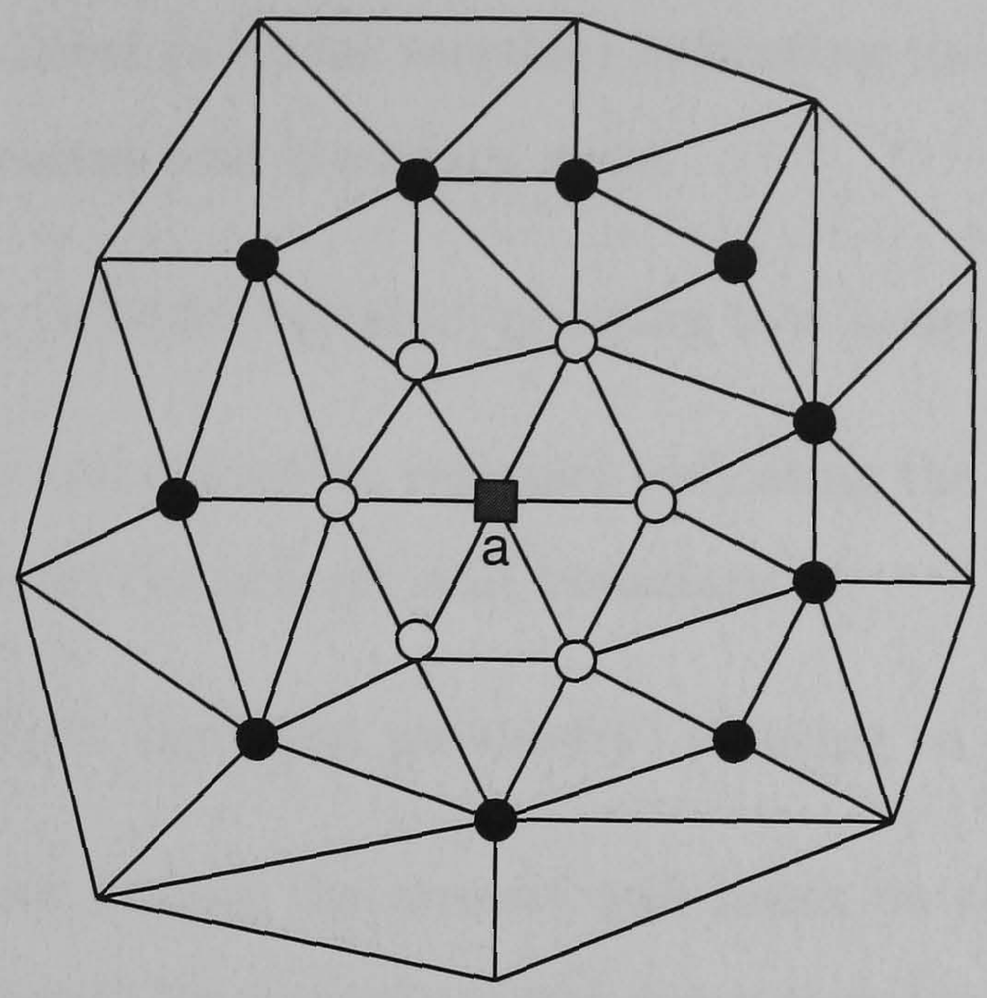

Figure 4.16: 2D mesh representing the neighbouring nodes within depth level 2 of node a

4.5.1 An algorithm for finding nearest wall index on the mesh

The nearest wall index is defined as nodal data pointing to the nearest face on wall boundaries corresponding to the considered node. An algorithm searches the nearest wall index using the information of node, face, cell and boundary configurations within the mesh. Before giving a description of the algorithm, the specific meaning of a neighbouring node in terms of *a neighbouring node within the depth level i* is defined in the definition 4.1.

> *Definition 4.1: A neighbouring node within depth level i of node j* is defined as a node that has the number of edges in the shortest path to node j equal or less than i.

For example, neighbouring nodes with depth level 1 of node **a** shown in Figure 4.16 are indicated by the white circles. Similarly, the neighbouring nodes within depth level 2 of node **a** are indicated by both white and black circle marks.

The main variables discussed in the algorithm consists of:

1. A *nearest_wall_index* (a nodal variable) pointing to the nearest face.

2. A *wall_depth_level* (a nodal variable) indicating the number of shortest paths from nearest wall boundary node.

3. A *node_index* (a nodal variable) pointing to a node in the mesh.

4. A *depth_index* (an algorithm variable) indicating the numbers of shortest paths of edges to the nearest wall boundary.

5. A *tracking_depth* (an input parameter) pointing to node in the mesh.

The algorithm for finding the nearest wall index on the mesh can be explained step by step with an example of two dimensional mesh shown in Figure 4.17, where the wall boundary is represented by a thick line AB.

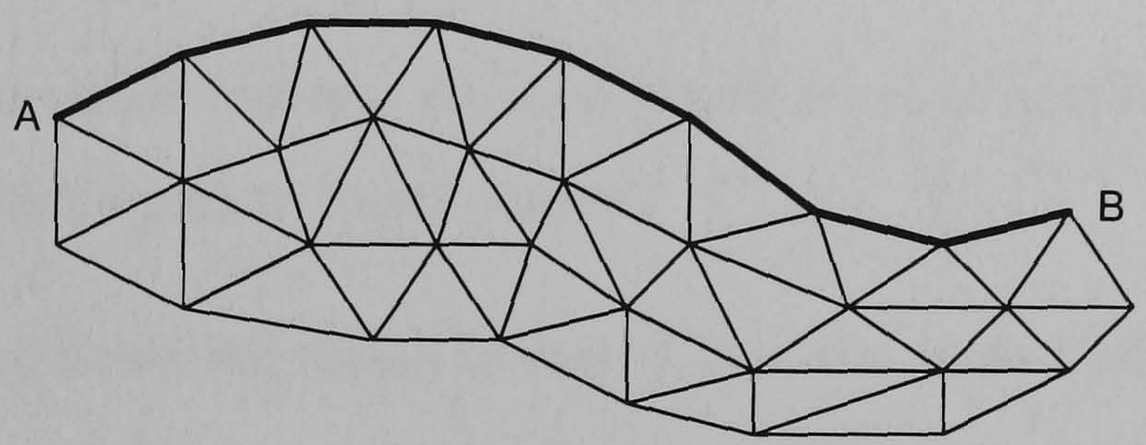

Figure 4.17: 2D mesh with the wall boundary AB

Step 1 Initial *nearest_wall_index* of all nodes within a mesh is assigned as $NULL$ and set *wall_depth_level* of all nodes equal to -1. Then, the *depth_index* is set equal to 0.

Step 2 Set *nearest_wall_index* of all nodes on wall boundaries to zero indicating wall boundary nodes. All *wall_depth_level* of wall boundary nodes are also set equal to *depth_index*. Then, *node_index* corresponding to all nodes on wall boundary are added into the node buffer. For example, nodes on wall boundary of mesh in Figure 4.17 are indicated by black circle marks shown in Figure 4.18.

Step 3 Set $depth\_index = depth\_index + 1$.

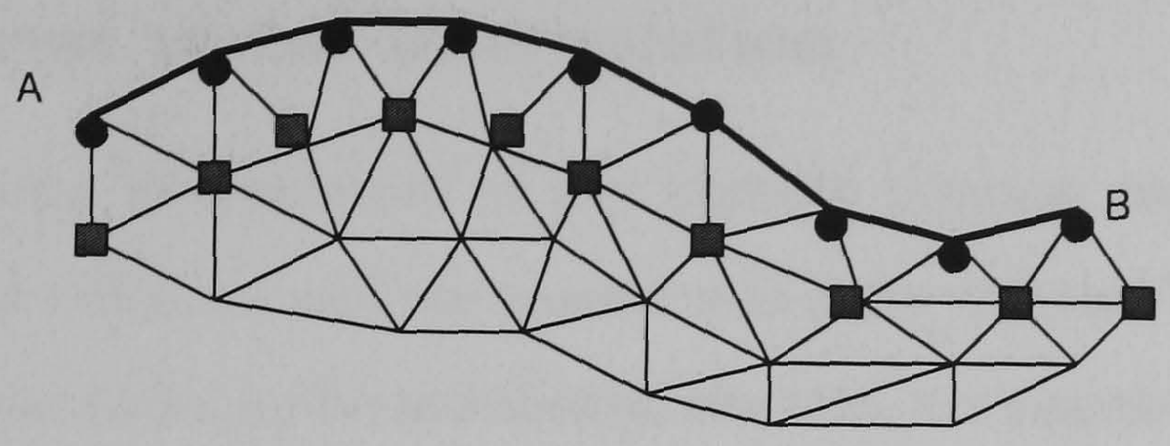

Figure 4.18: Wall nodes and neighbouring nodes of 2D mesh with the wall boundary AB

Step 4 Find neighbouring nodes within depth level 1 of all nodes stored in the node buffer satisfied by the condition that the *wall_depth_level* of the node is equal to -1. The neighbouring nodes within depth level 1 of wall nodes in Figure 4.17 are indicated by black rectangular marks shown in Figure 4.18.

Step 5 Clear all the node buffers. All *wall_depth_level* of neighbouring nodes in step 4 are set equal to *depth_index*.

Step 6 Add all neighbouring nodes in step 4 into the node buffer.

Step 7 Run the subroutine to search the nearest wall index using *nearest_wall_index* of neighbouring nodes within the depth level of the *tracking_depth* of all nodes stored in the node buffer. For example, the node **a** in Figure 4.19 represented by the rectangular mark, search for the nearest wall index using *nearest_wall_index* of neighbouring nodes within depth level 2 represented by white circle marks. This subroutine results in the *nearest_wall_index* pointed by the arrow line.

Step 8 If *nearest_wall_index* of all nodes is not complete, go back to step 3.

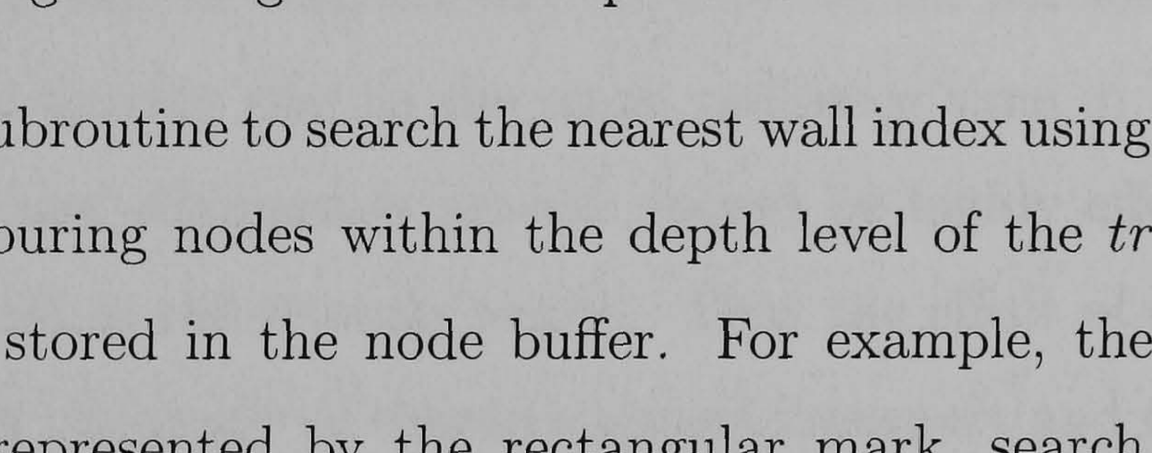

Figure 4.19: Neighbouring nodes of node a in the 2D mesh with the wall boundary AB

4.5.2 Nearest vector interpolation

The nearest vector interpolation of any particle position can be calculated using the present cell index and the nearest wall index discussed in the previous section. With four nodes in the tetrahedral element, the nearest wall index may have four different values. The minimum distance between the particle position and these nearest wall faces will be used for the image charge computation.

4.6 Effect of humidity on charged aerosols

The air inside the human lung has a high humidity (typically 99.5 % relative humidity). Nguyen and Nieh [20] have suggested that under these conditions particle charges are effectively eliminated. Furthermore their experimental studies showed that the charges are practically neutralised at a level of 78 % relative humidity. However this process has a decay time to complete the charge neutralisation. In drug delivery application, the particles reach the alveolar region very quickly due to the small residence time in tracheobronchial region. The charge elimination process should be highly effective when particles are suspend in the alveolar region. Thus the effect of humidity will be accounted for in the study of charged aerosol transport and deposition in the alveolar model, which is further discussed in chapter 6.

4.7 Summary

The effect of electrostatic forces on the particle trajectory can be considered as body forces in the particle motion of a Lagrangian reference frame. When the particles carry charges on their surfaces, there are two electrostatic forces causing these charged particles to deposit on wall surfaces: one due to the image charge on the wall surface and another one due to the repulsion between the particles, called the space charge force. Both space and image charge forces are influenced by the charge values on particles. At higher levels of charge, the

electrostatic force becomes an important mechanism.

The deposition efficiency due to electrostatic forces depends on many variables such as the inlet airflow, particle concentration, particle size, particle density, and charge value. Based on a non-dimensional analysis, the space charge force is highly effective in deposition in the upper bronchial region, when the aerosol concentration is high with adequate charge values. The image charge force plays an important role in the lower bronchial and the alveolar region due to a long residence time. The results from a predicted deposition model show that the electrostatic forces improve the deposition efficiency when the particle size is small (approximately less than 2 μm).

The space charge force among particles is the N-body problem. The direct method to calculate the interacting forces has a high computational cost. The PM technique is chosen for calculating space charge force that treats the force as a field quantity by approximating it on a mesh. The PM method consists of three steps: (1) assign charge to mesh, (2) Solve Poisson's equation on the mesh and calculate electric field from the mesh-defined potential, and (3) interpolate force from the mesh-defined potential at the particle position. However, the effect of space charge force plays a significant role if the particle number density is raised to a sufficiently high level with the adequate level of charge, i.e., a concentration of $1.0 \times 10^{12} - 1.0 \times 10^{13}$ $particles/m^3$ for 0.5 μm particles carrying $q = 100e$. The space charge effect does not play a key role in the lower bronchial and alveolar regions, because of low particle number concentration in these regions.

The image charge force computation requires calculation of the nearest wall distance for each particle. The program starts to initiate the nearest wall index corresponding to any node and stores this as nodal data called the nearest wall index. Then, the nearest wall distance of the particle can be calculated based on nearest wall indexes of the present cell.

Chapter 5

Implementations and Numerical results of Airflow

This chapter provides the implementations and numerical results of airflow in the geometrical airway models. The numerical results discussed in this chapter were obtained by use of the FLUENT, a Computational Fluid Dynamic software package.

The complex flow field in the bronchial airways network mainly dominates the behaviour of inhaled aerosol transport and deposition. Thus velocity vectors of airflow should be as accurate as possible for modelling aerosol transport and deposition. The airflow field is mainly determined by physical states of breathing including the sedentary, and light activity. The entry condition and the geometry of the bronchial airway model strongly influences the precision of the velocity field distribution. This chapter aims to give the details of numerical results of airflow within the geometrical airway models previously described in chapter 2.

The local velocity field in the geometrical model calculated using the FLUENT package is introduced in section 5.1. The details of the fluid model and its boundary conditions are then presented in section 5.2. This section also gives information regarding numerical schemes for solving the governing equations of the flow system. Then the results of airflow fields in the 3D bifurcation, 2D

alveolar, and 3D reconstructed airway models are given in section 5.3, 5.4 and 5.5 respectively.

5.1 Computational Fluid Dynamics

A Computational Fluid Dynamic (CFD) package was used as a computational tool for solving the fluid governing equations and providing velocity vectors for calculating the fluid forces acting on particles. Various technologies including mathematic, computer science, engineering and physics are integrated to model the fluid flow. However, there is no universal fluid model for all flow situations, so the appropriate flow model needs reasonable boundary conditions and initialisations. An overview of the CFD package and a general procedure for using the solver based in FLUENT software will be discussed in this section.

The available commercial CFD packages generally consist of 3 main sets of software: pre-processer, solver, and post-processer. The FLUENT software package was selected for this study, which had been developed by Fluent Inc., based on the Finite Volume Method. The basic program structures of the FLUENT package are shown in Figure 5.1. The details discussed in this section are confined to FLUENT software.

Pre-processing programs carry out two main tasks of the mesh generation and flow specification. Firstly, the mesh generation is the most difficult task in pre-processing and it commonly interfaces with the CAD file. FLUENT provides the pre-processing modules including GAMBIT and TGRID softwares to create the geometry model and mesh generation, respectively. Secondly, the flow specification is required to provide a specific model of the fluid system (i.e., incompressible or compressible, laminar or turbulent flow) and boundary conditions to specify the flow and thermal variables on boundaries of physical model (i.e., inlet, outlet, internal cell, and wall).

The solver computes the numerical equations of the physical model. Two main numerical methods in FLUENT (segregated solver and couple methods)

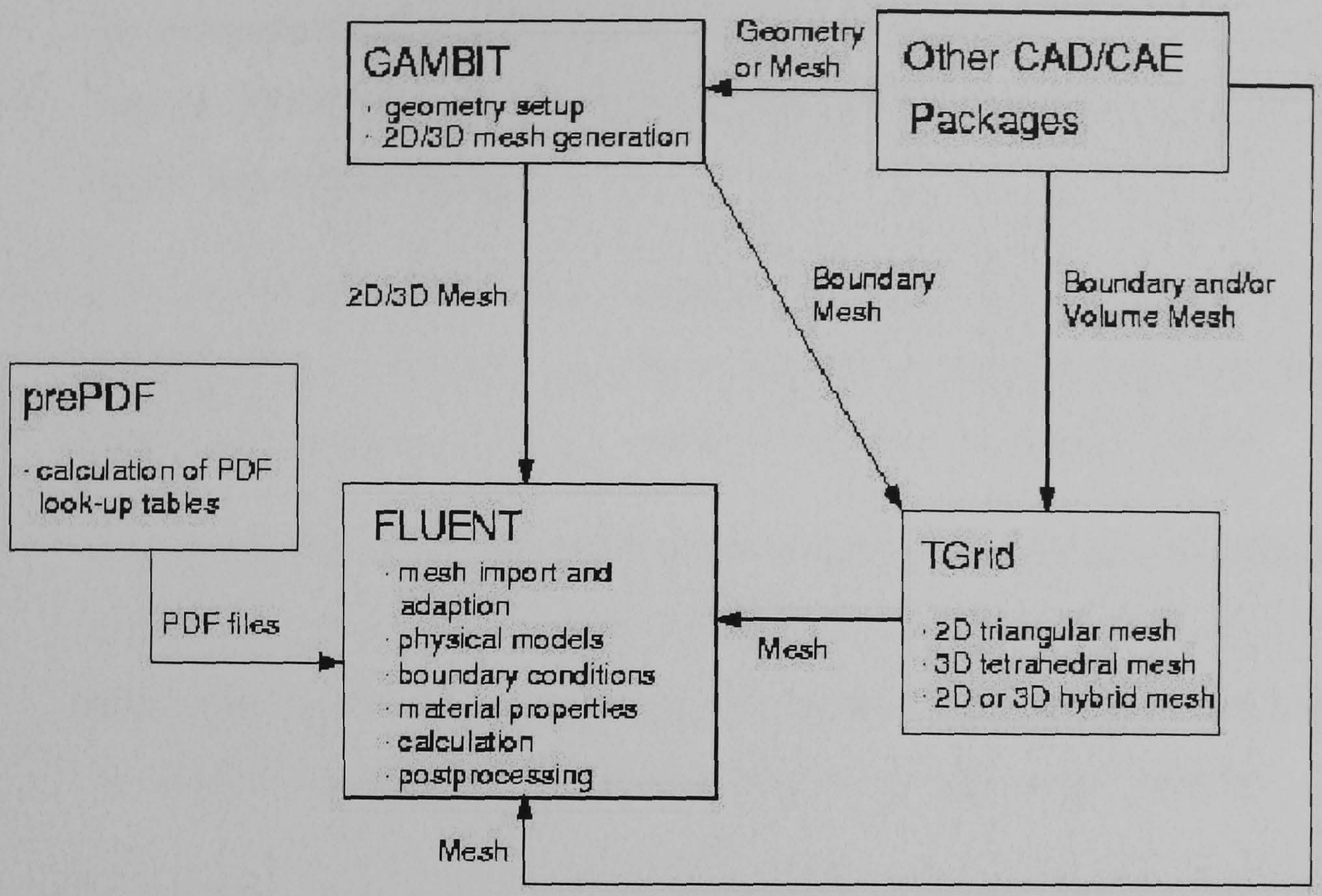

Figure 5.1: Basic program structure of FLUENT package [60]

are used for solving the governing integral equation of the conservation of mass, momentum, energy and other scalar variables. The segregated method solves the governing equation sequentially starting by solving the momentum equation, then solving the pressure-correction (continuity) equation, and finally solving energy and other scalar equations. Because the governing equations are non-linear, many iterations of the solution loop must be preformed until a convergence criterion is satisfied. Using a different concept, the coupled method solves the continuity, momentum, energy and species equations simultaneously, and then solves turbulence and other scalar equations until a convergence solution is obtained. Both segregated and coupled methods employ a similar discretisation method, but the approach used to linearise and solve the discretised equation is different.

In both methods the control-volume-based technique is employed and the fundamental concepts consist of the following features[60]:

1. The computational domain is divided into discrete control volumes using

the computational grid (discretisation). Some discretisation techniques used in FLUENT consists of first-order upwind, second-order upwind, power law and QUICK.

2. The governing equations are integrated in respect of the individual control volumes to construct algebraic equations for discrete dependent variables, i.e., velocities, pressure, temperature, and conserved scalars.

3. The discretised equations are linearised to produce a system of equations and the resultant linear system of linear equations are then solved to yield updated flow-field solutions. The linearisation technique may take an implicit or explicit form with respect to the dependent variable.

The FLUENT solver for a system of equations obtained from both segregated solver and couple methods can be performed using the Multigrid method. There are two forms of multigrid: Algebraic Multigrid method (AMG) and full-approximation storage method (FAS). The AMG is an essential solver for both the segregated and coupled implicit solvers, while the FAS is an important solver for coupled explicit solver. Although the solver is the core of any CFD software system, the user can see little of its operation.

The steps that outline a general procedure for using the solver can be summarised as following [60]:

1. Choose the discretization scheme and the pressure interpolation scheme (only for the segregated solver).

2. Select the pressure-velocity coupling method (only for the segregated solver).

3. Set the under-relaxation factors which are used by the solver.

4. Turn on the FAS multigrid (only for the coupled explicit solver).

5. Make any additional modifications to the solver setting (optional).

6. Initialize the solution.

7. Enable the appropriate solution and convergence criterion.

8. Start calculating.

9. If there is no convergence, modify the flow specification or mesh quality of the model.

Finally, post-processing programs are proposed to visualise a large number of points within the flow domain using computer graphics. The visualised picture may contain a section of mesh together with vector or contour plots of velocity and scalar variables. In addition, the post-processing program may create a movie file to animate the transient of variables. These features enable global trends in the data to be seen.

5.2 Fluid model and Boundary conditions

The airflow in the geometrical airway model is calculated based on the following basic assumptions:

- The airflow is modelled as an incompressible laminar flow.
- The airflow neglects the energy transfer with the airway wall.
- The wall boundary condition is modelled as a rigid wall with non-slip condition.

All airflow governing equations in this study were carried out using the implicit segregated solver. The discretisation schemes for any variables based on the guideline in the previous numerical studies by Comer [33] are summarised in Table 5.1. The solutions of these variables were continuously solved until mass residual of all variables were less than 0.001.

Table 5.1: Details of set-up discretisation schemes in numerical studies

Discretization	Schemes
pressure	Standard
momentum	Second-order Upwind
pressure-velocity coupling	SIMPLEC

Under relaxation factor	Value
Pressure	0.3
Momentum	0.7

5.3 Airflow in Bifurcation airways model

Bifurcation airway models are often used to study the transport and deposition of aerosols in the tracheobronchial region, where the Reynolds number of airflow is slightly high. The aerodynamic force strongly influences the trajectory of particles. This section aims to investigate the airflow field in the bifurcation airway model under the physical state of sedentary and light activity breathing conditions. The Reynolds numbers corresponding to both physical states given in Table 5.2 are less than 2000, thus it can be assumed that the airflow is laminar.

Table 5.2: Respiratory rate data [122]

Physical state	Sedentary	Light activity
Respiratory rate	7.0 $l(min)^{-1}$	20.0 $l(min)^{-1}$
Time ratio of inspiratory phase (t_{insp}/t_{total})	0.42	0.42
Mean flow rate during inspiration	16.71 $l(min)^{-1}$	47.71 $l(min)^{-1}$
Mean inspiratory Re at an inlet of bifurcation airway model	475	1360

5.3.1 Numerical technique

The numerical model of the airflow equations was set up as an incompressible steady-laminar flow. The inlet velocity profile was defined as a parabolic profile corresponding to both Reynolds numbers given in Table 5.2. A uniform pressure condition was employed at all outlets. The wall boundary condition was defined as the non-slip rigid wall. The discretisations of all equations were also set up as given in table 5.1.

Mesh elements in the bifurcation airway model were tetrahedral elements generated by GAMBIT software. The number of mesh elements was determined by refining the mesh until the field solution was independent of the number of grids, details of which are given in Table 5.3.

Table 5.3: Mesh details of the 3D bifurcation airway model

Mesh details	value
Minimum volume (m^3)	3.419801×10^{-13}
Maximum volume (m^3)	2.309927×10^{-11}
Total volume (m^3)	2.961232×10^{-6}
No. of cells	640578
No. of faces	1310294
No. of nodes	121878
Total memory ($Mbytes$)	387

5.3.2 Results and discussion

An airflow simulation with a parabolic inlet profile and average velocity corresponding to the Reynolds number of 2000 was set up to compare the results with that of Comer et al. [33]. The comparison of profiles between Comer's reported result and the simulation results obtained in this study in plane $z = 0$ is shown in Figure 5.2. The numerical results obtained for the profile agrees with Comer's study.

The results of velocity vectors and profiles carried out for the Reynolds

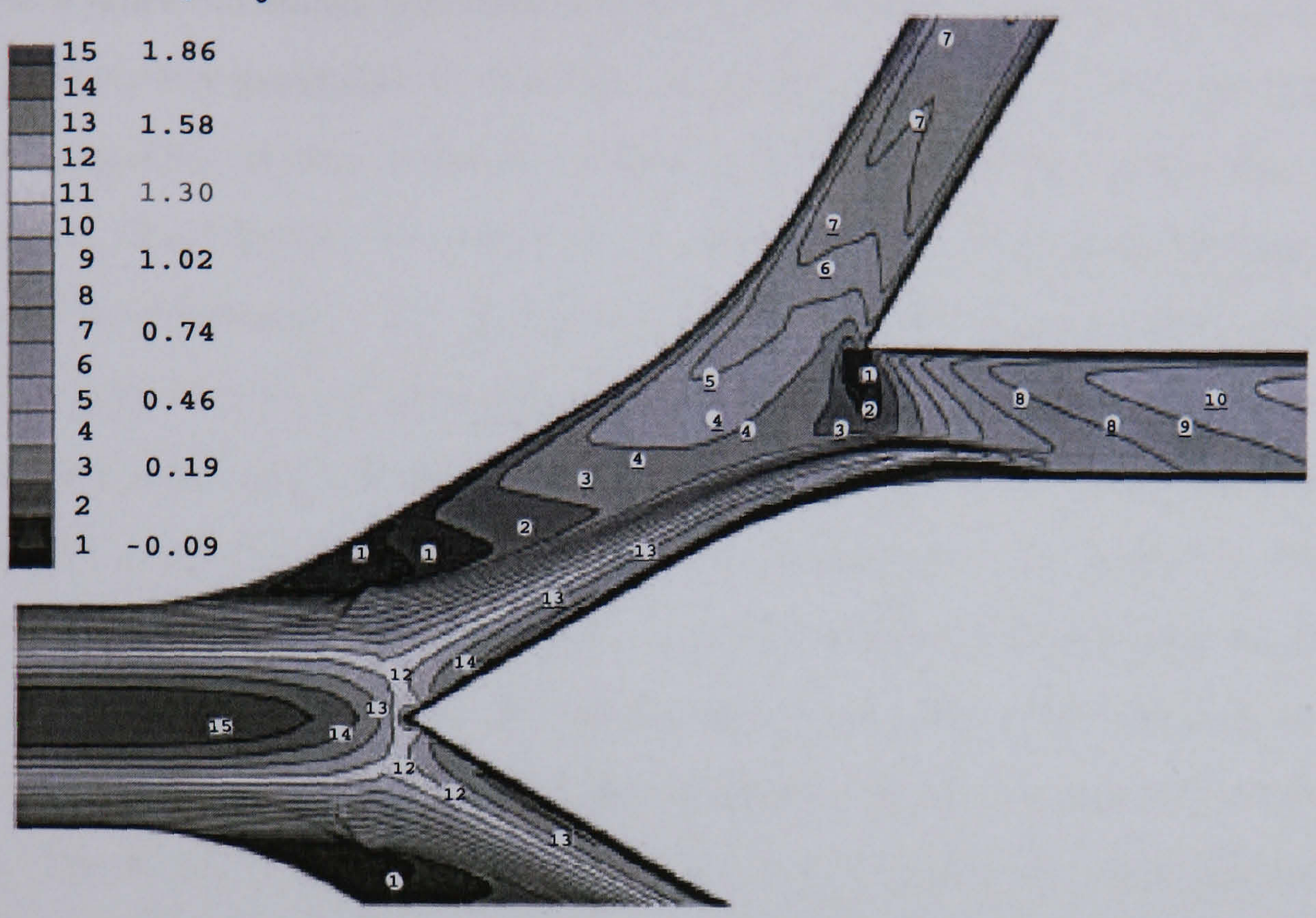

(a)

(a) Velocity profile of Comer's results for Re = 2000

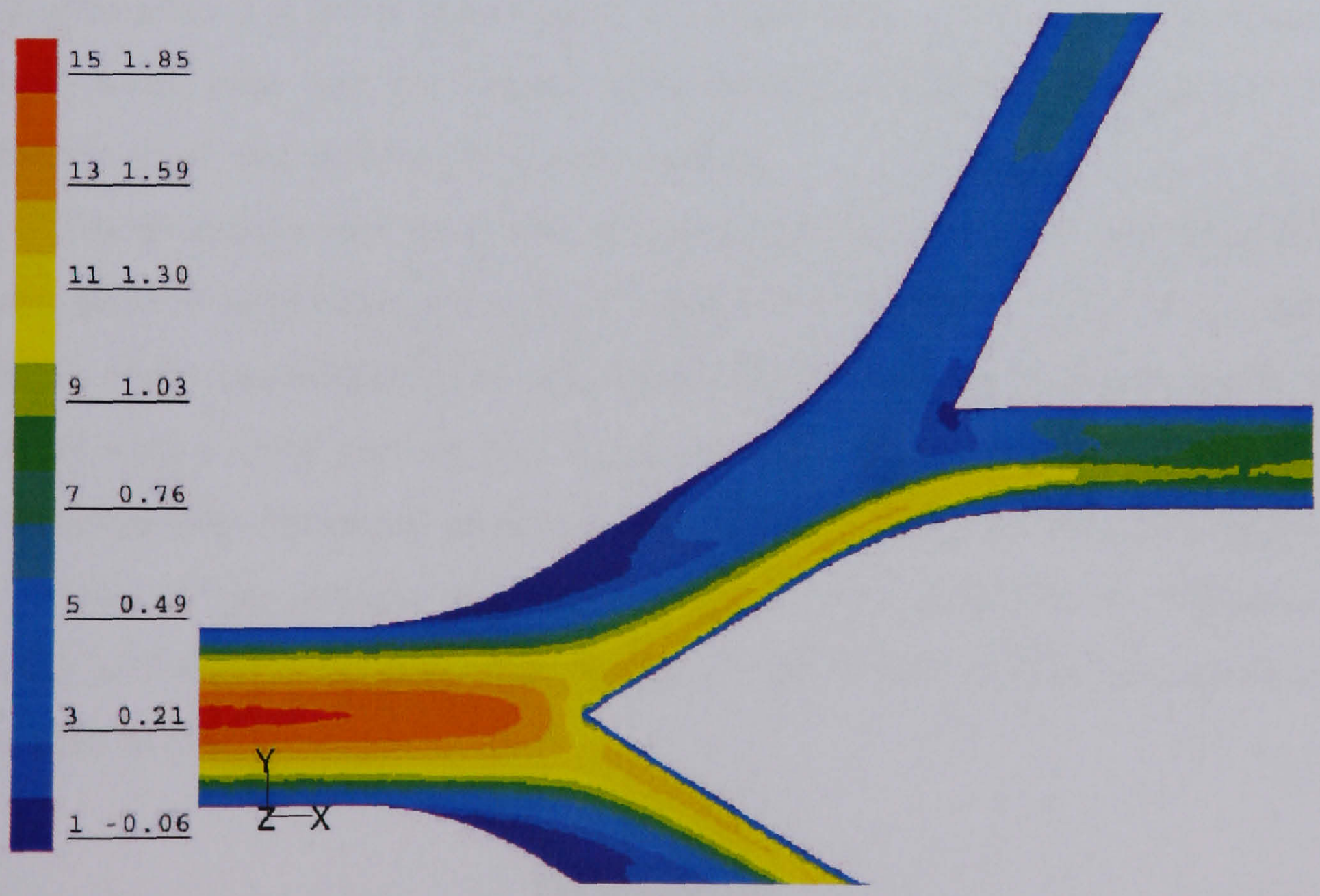

(b) Velocity profile of simulation results for Re = 2000

Figure 5.2: Comparison of velocity magnitudes of Comer's reported result and simulation results for $Re = 2000$ at plane z=0

numbers corresponding to sedentary and light activity conditions will be discussed. Figure 5.3 shows the line contour of the velocity magnitudes on plane $z = 0$. At airway generation 3, the flow profile from the main inlet to the inlet of the branching section remains as parabolic flow. The flow then starts to divide into the daughter branches with a distinct shear layer along the inside wall and a recirculation zone at the outer wall after passing the first carina. Figure 5.4 shows the colour contour of velocity magnitudes at the first bifurcation with four axial planes indicated by A, B, C, and D. The line contours of velocity magnitudes on these axial planes are also given in Figure 5.5. The faster velocities corresponding to both Reynolds numbers move closer to the inside wall near the carina. In the second bifurcation, the colour contour and line contour of the velocity magnitudes are given in Figure 5.6 and 5.7, respectively. The distinct shear layer in the second bifurcations bends away from the second carinae to the inner tubes of airway generation 5 (aligned in the same direction as the airway generation 3). The airflow velocity in the inner tubes of generation 5 is faster than that of the outer tubes of the same generation. It is clearly seen that the distinct shear layer at higher Reynolds number is thinner than that at lower Reynolds number.

The secondary flow generated by centrifugal forces in the bend of model also plays an important role in flow through the bifurcation tube. When flow turns, these centrifugal forces are balanced mainly by the pressure gradient forces with a given velocity and turning radius. The airflow profile then becomes the fully developed after passing the developing length in which airflow continues in the straight tube. The secondary flow effect can be explained using a dimensionless parameter known as the Dean number (De) which is defined as [73]

$$De = \sqrt{\frac{d}{2R}} Re \tag{5.1}$$

where d is a diameter of the airway cross-section, and R is the radius of curvature. The Dean number can be used to consider the length in which the profile

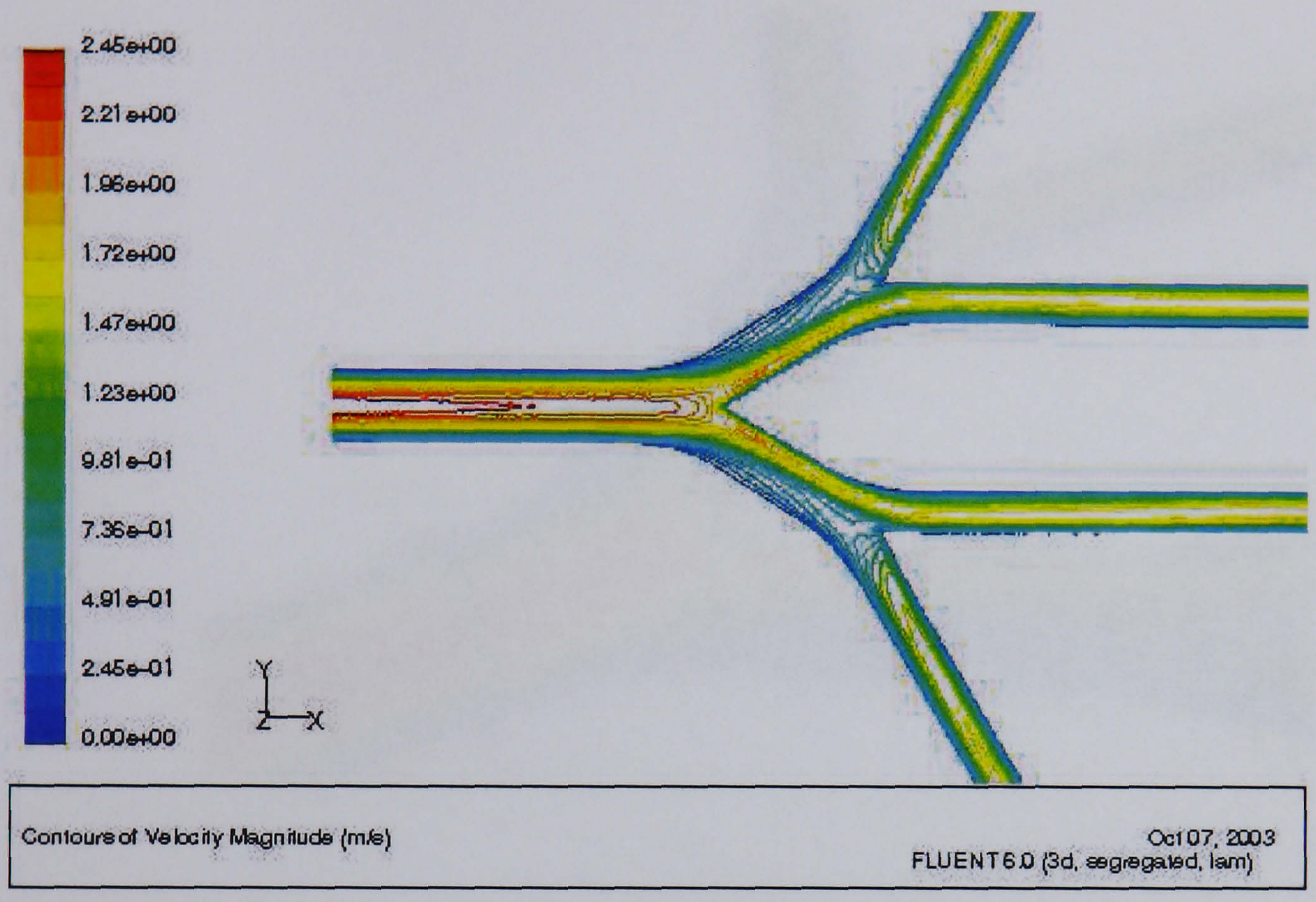

(a) Sedentary activity

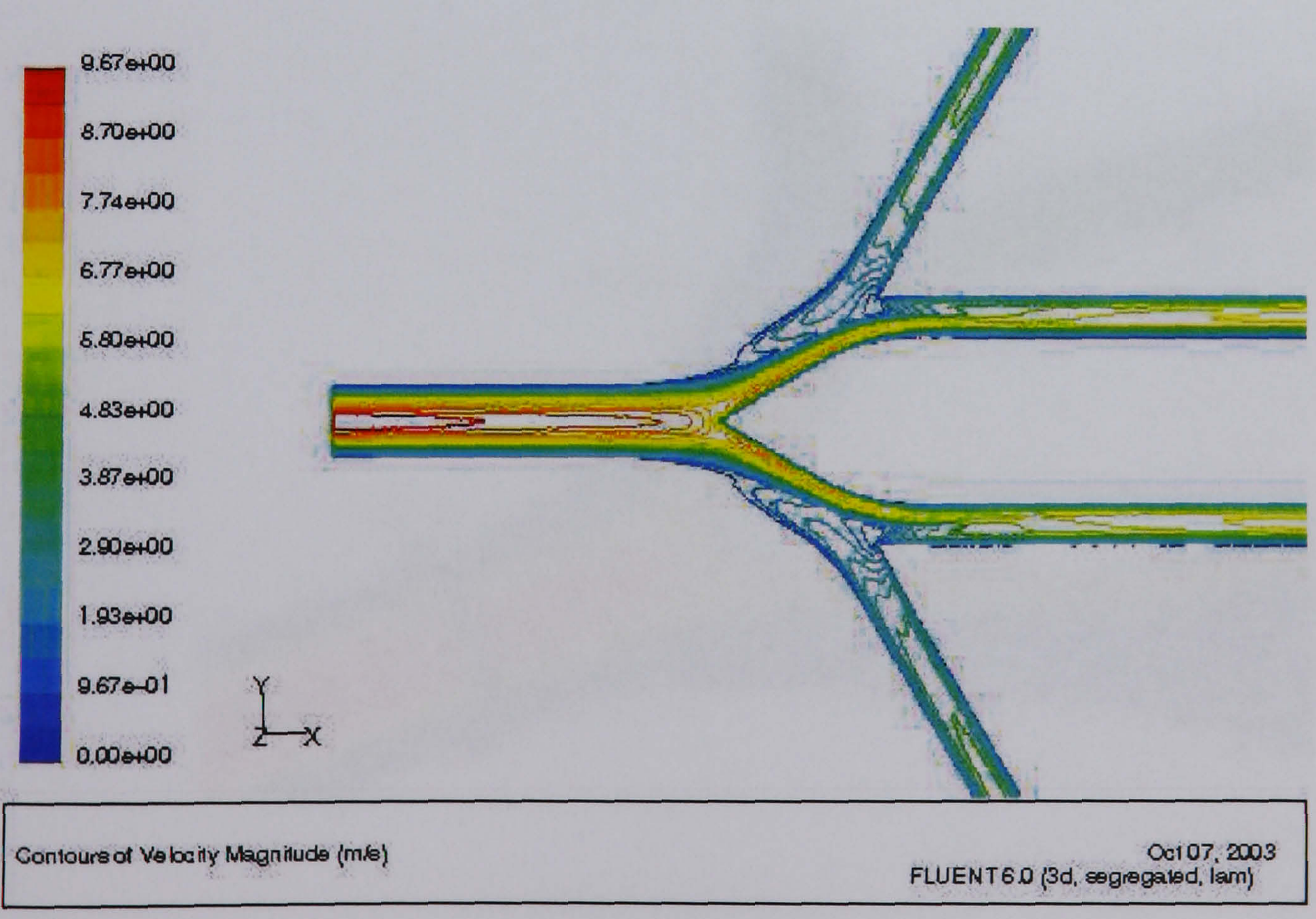

(b) Light activity

Figure 5.3: Velocity magnitudes of sedentary and light activity conditions at plane z=0

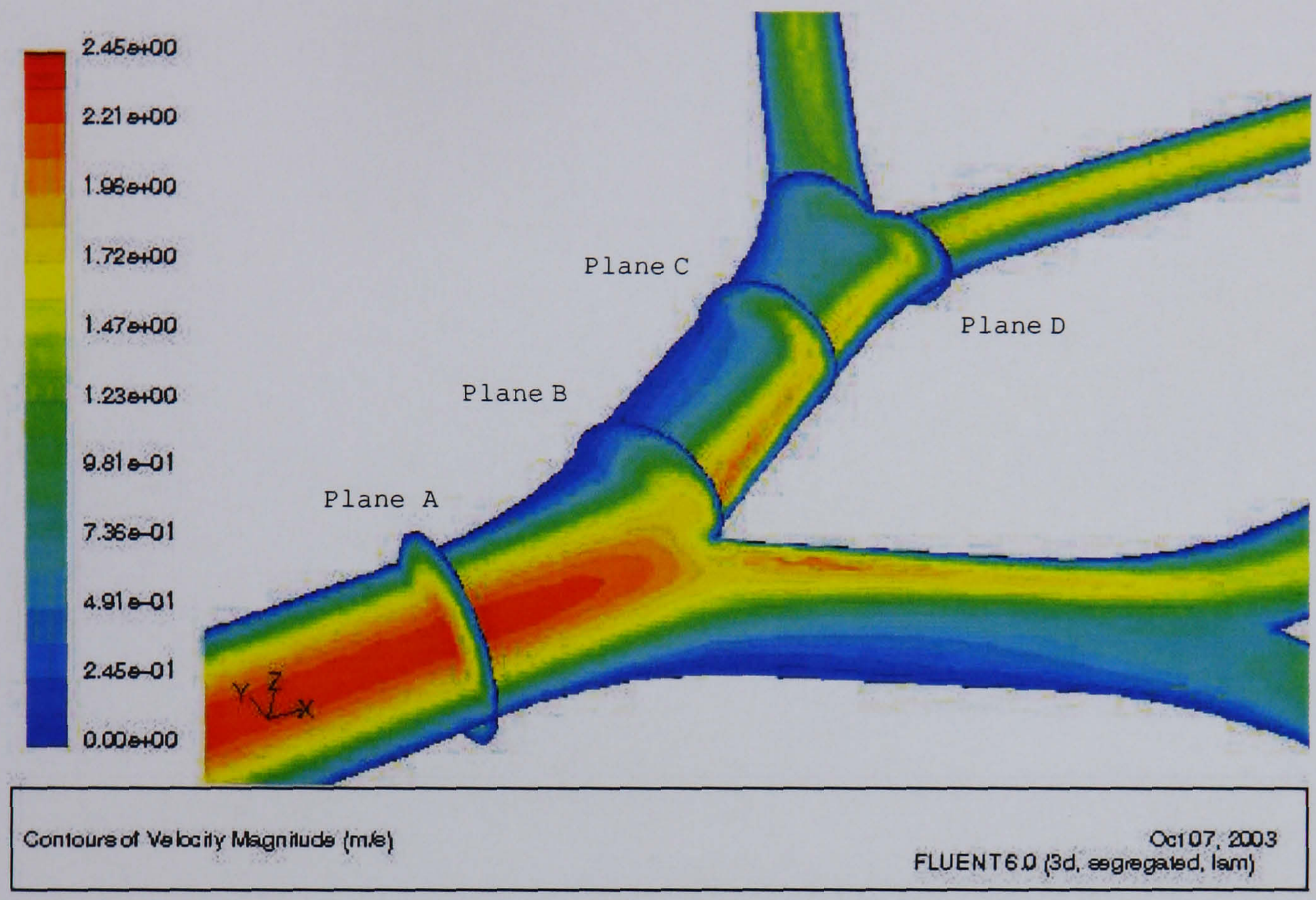

(a) Sedentary activity

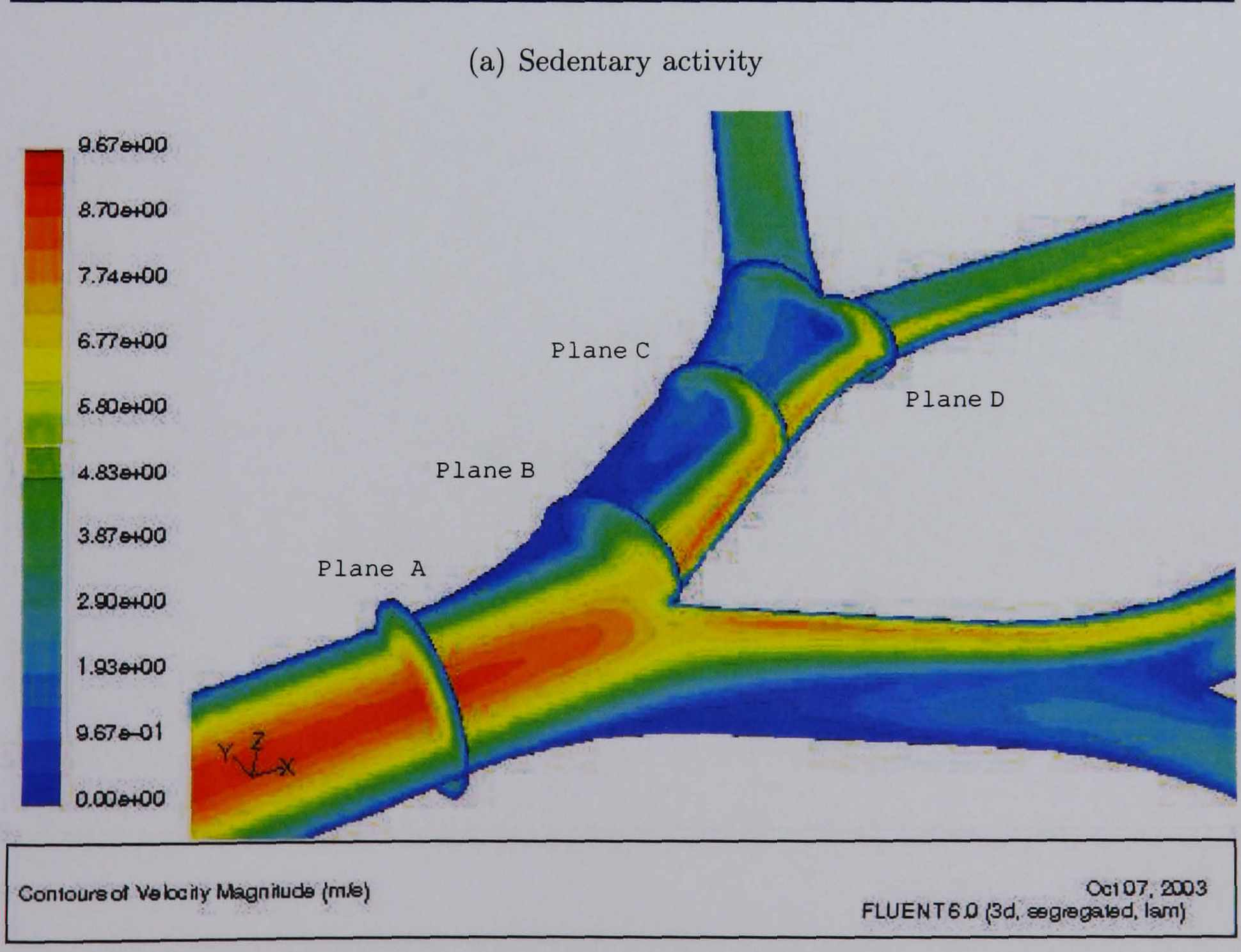

(b) Light activity

Figure 5.4: Colour contours of the velocity magnitudes at the first bifurcation

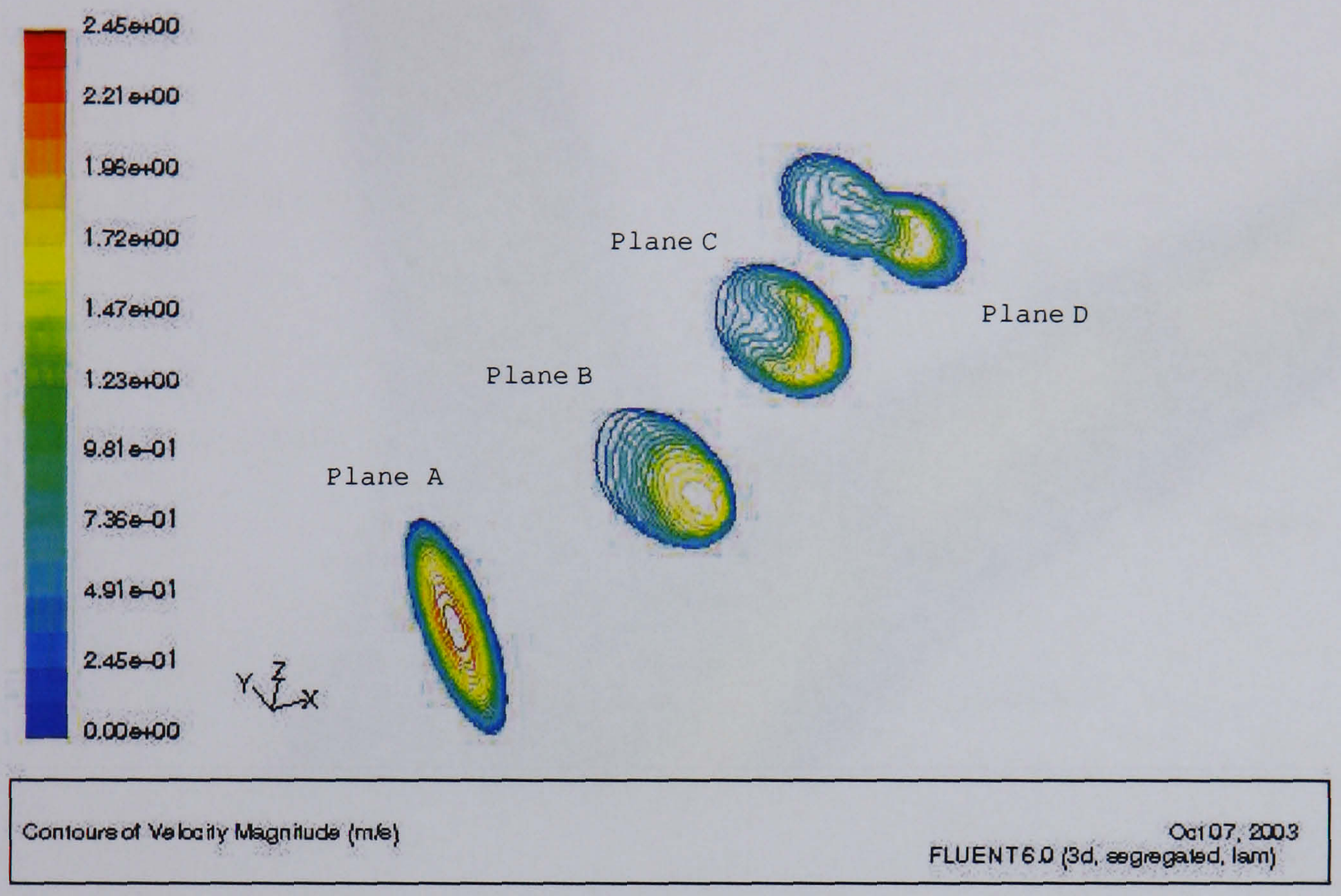

(a) Sedentary activity

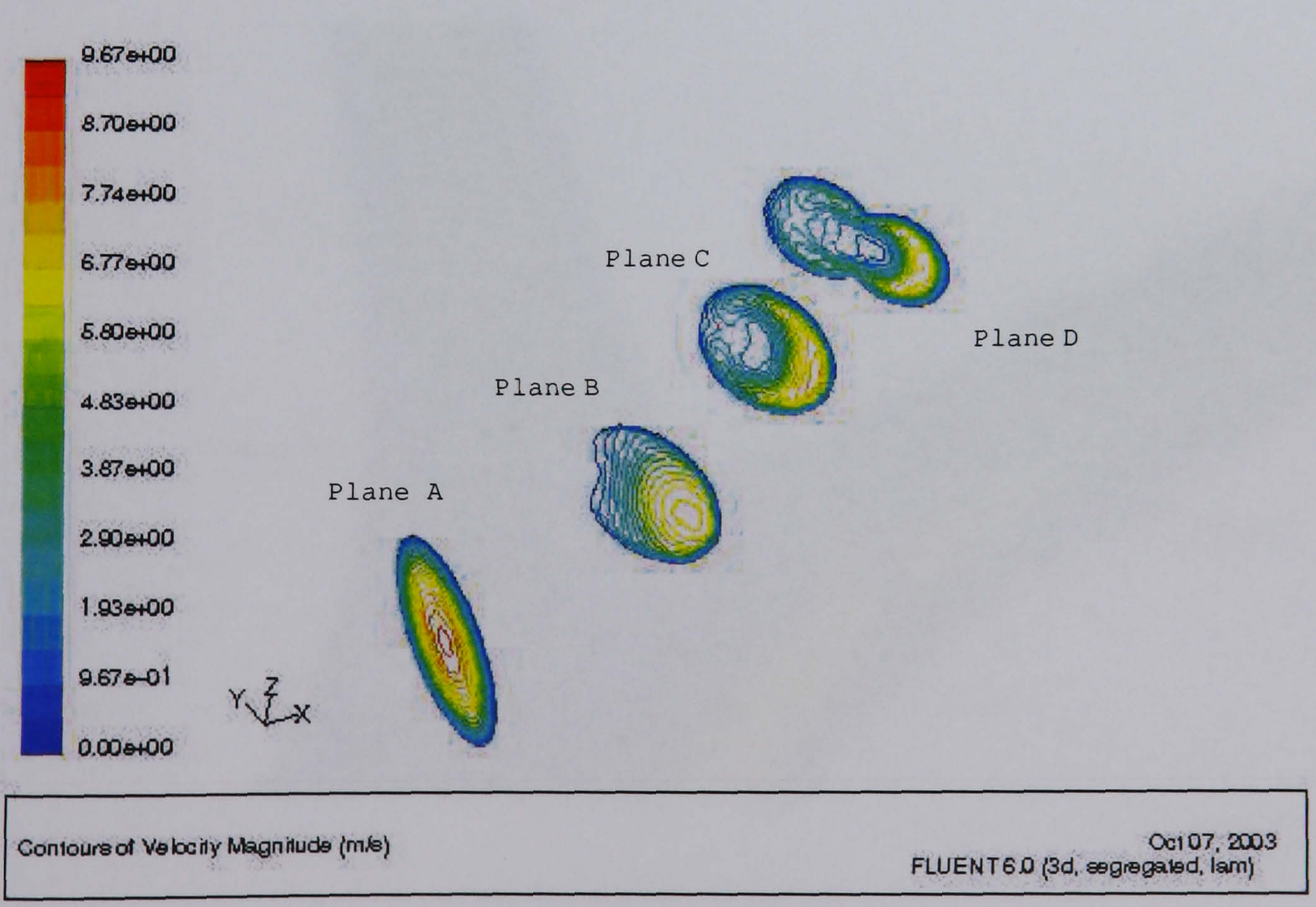

(b) Light activity

Figure 5.5: Line contours of the velocity magnitudes at the first bifurcation

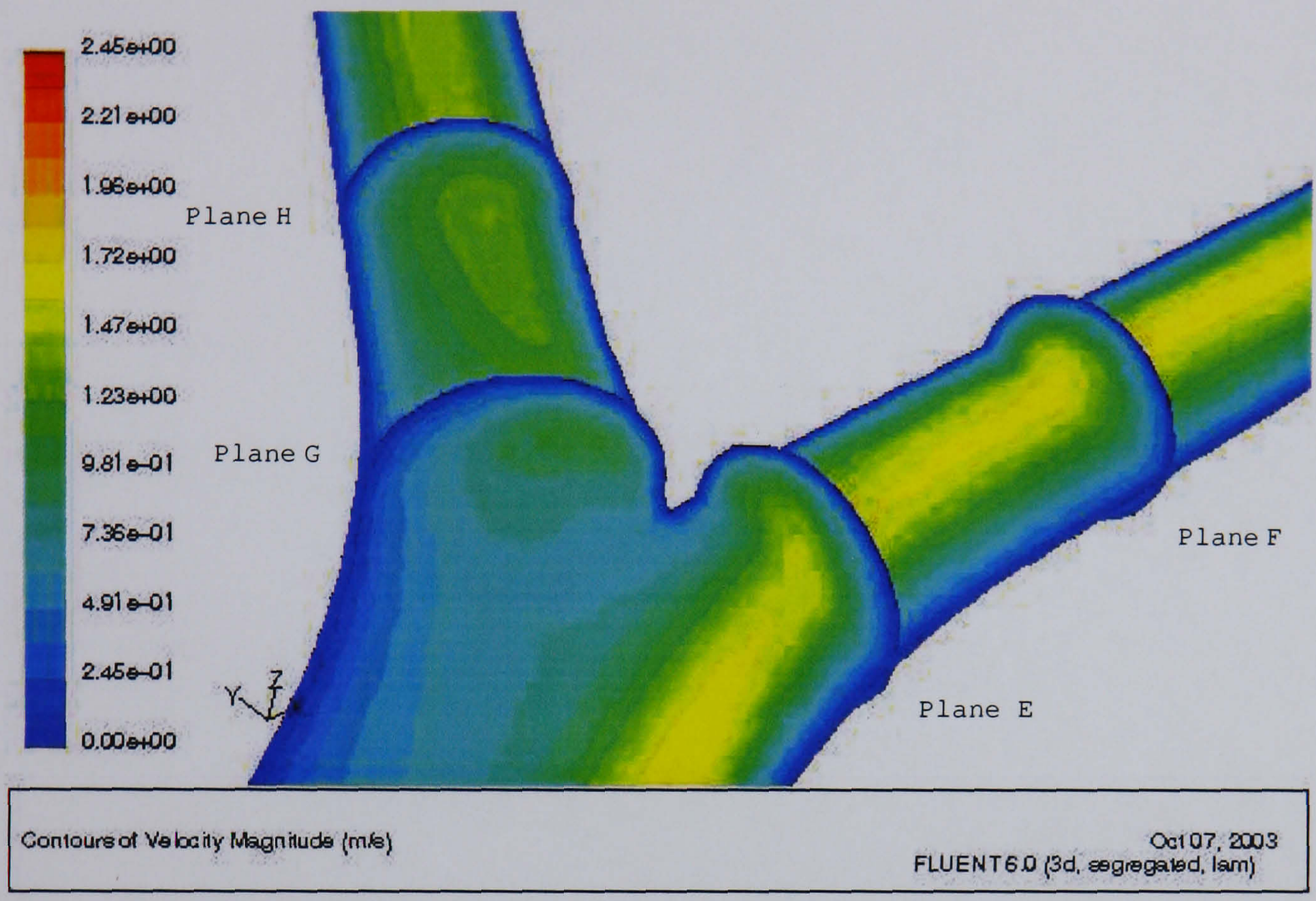

(a) Sedentary activity

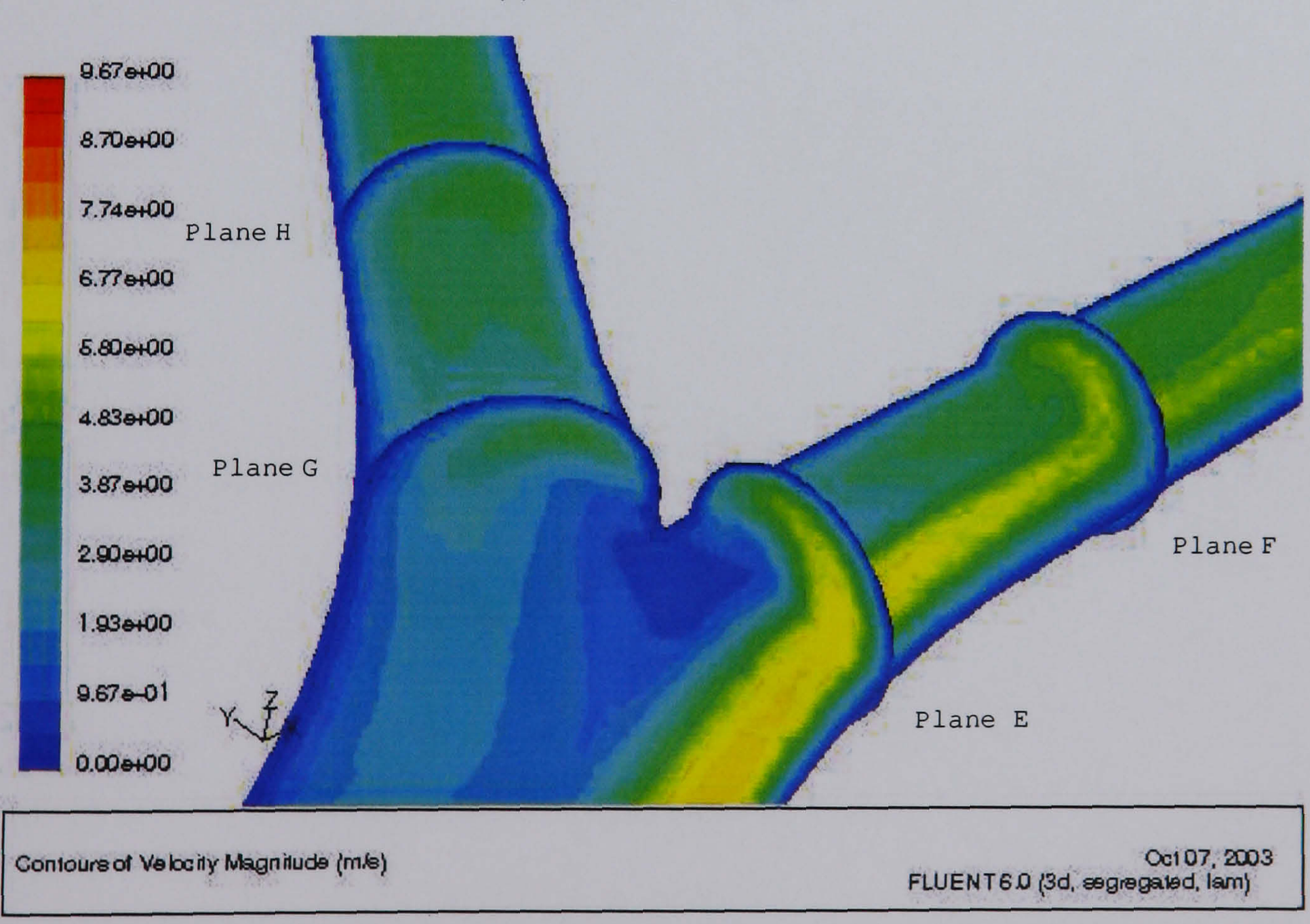

(b) Light activity

Figure 5.6: Colour contours of the velocity magnitudes at the second bifurcation

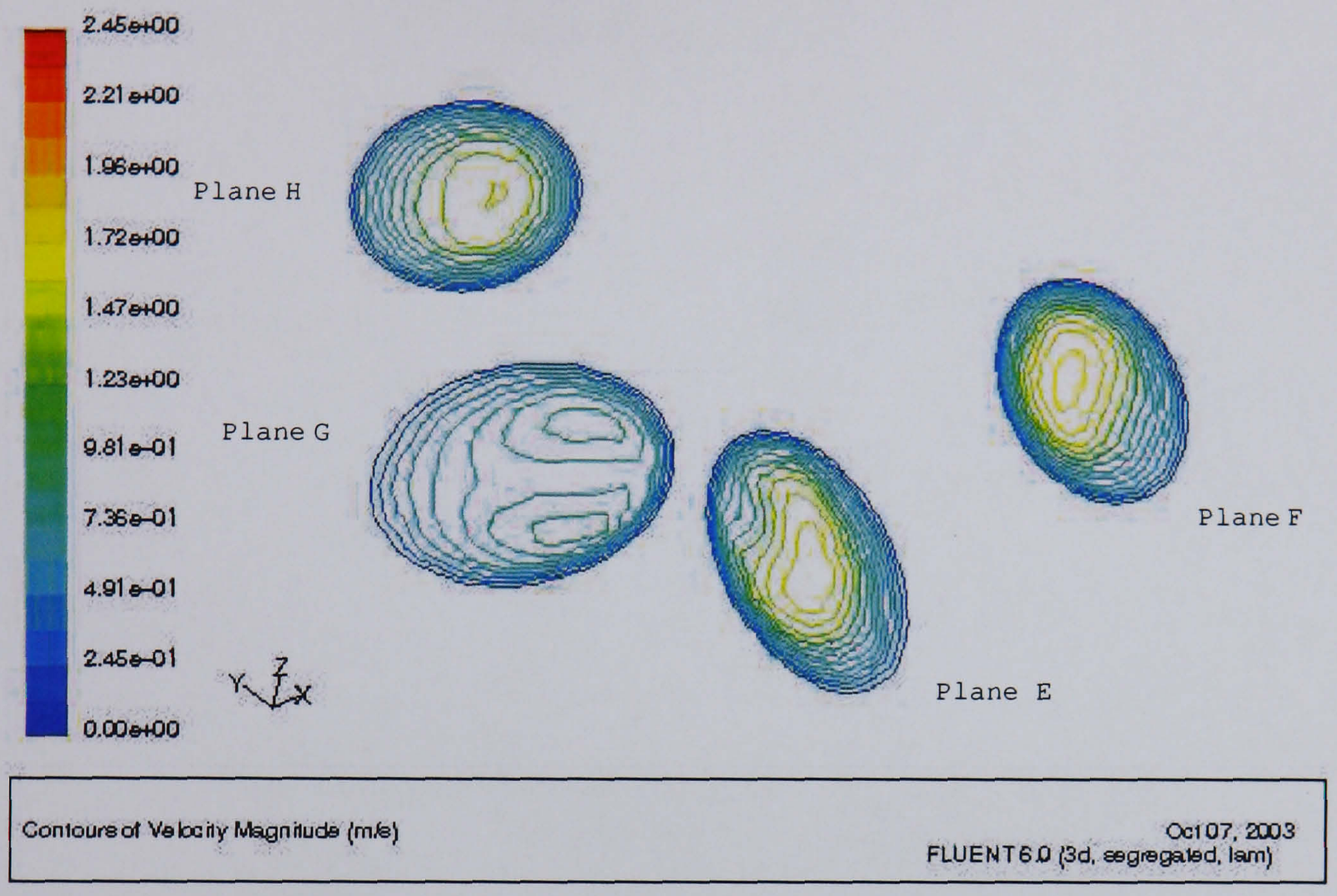

(a) Sedentary activity

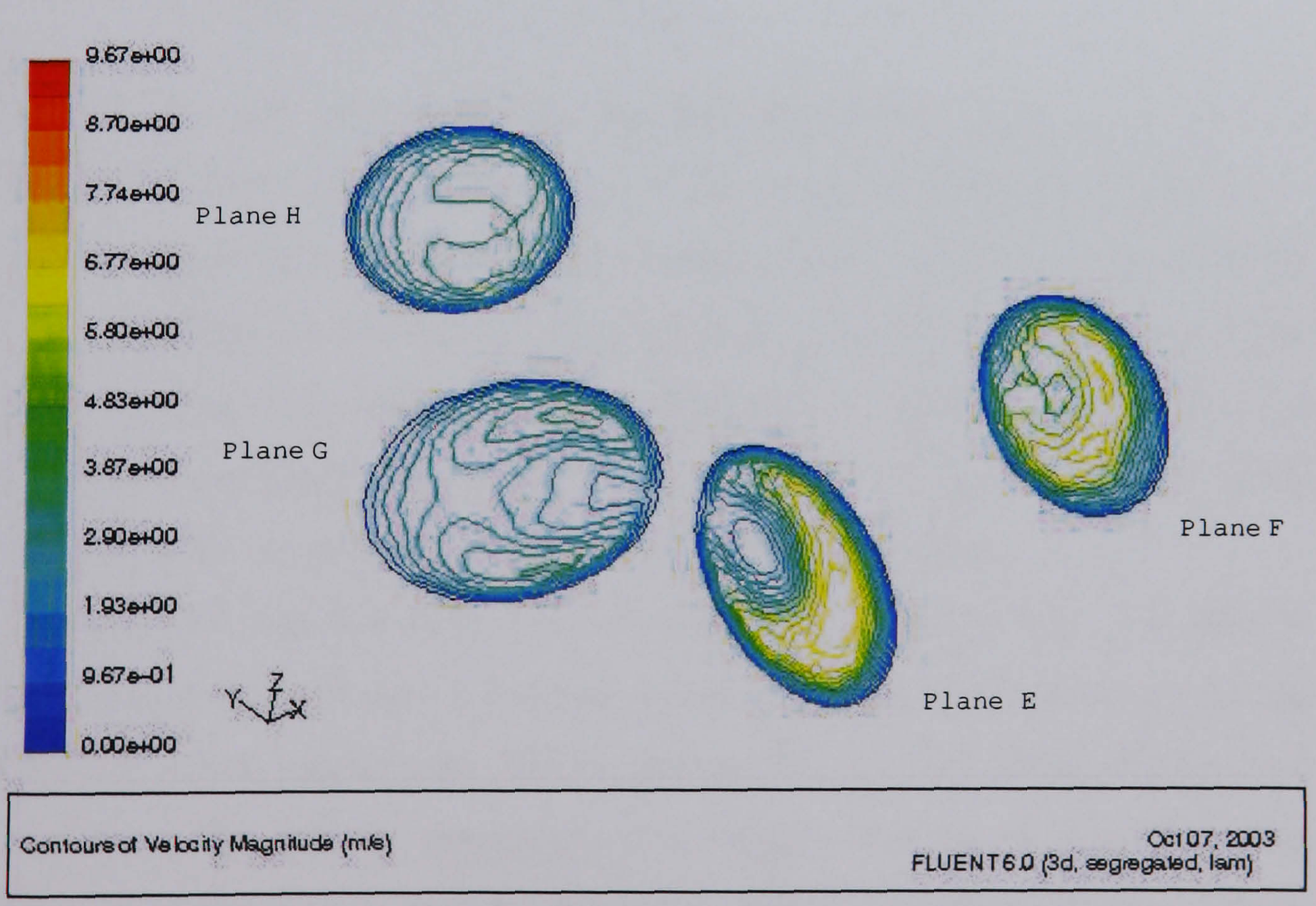

(b) Light activity

Figure 5.7: Line contours of the velocity magnitudes at the second bifurcation

Table 5.4: Developing lengths of fluid motion in curved tube [73]

Dean number	L_c/d
10	3.5
50	7.3
100	26.1
125	48.0
150	62.9
175	64.8
200	71.6
225	74.4
250	76.8

Table 5.5: Values of Dean number in the double bifurcation model

Activity	first bifurcation	second bifurcation
Sedentary	286	216.8
Light activity	827.7	627.3

becomes the fully developed. The developing length L_c expressed in term of L_c/d for different Dean numbers can be summarised as shown in Table 5.4.

For higher Dean numbers, the centrifugal forces are as important as viscosity and inertia. The values of the Dean number of this bifurcation model corresponding to breathing activities are given in Table 5.5 and show that the centrifugal forces are important for both activities in this model. Fully developed flow is not achieved for either breathing activity.

Figure 5.8 and 5.9 show the comparison of secondary flow for different activities at plane B and E located at the beginning of the first and second daughter tubes, respectively. The secondary flow patterns are similar for both activities. The velocity magnitude of secondary flow for the high Reynolds numbers is faster than that for low ones. Due to the non-uniform axial velocity, the fluid particles with higher Reynolds numbers tend to turn with a larger radius, and those with lower velocity with a smaller radius. For example

in Figure 5.8, the axial velocity magnitudes at the right-hand side (near the branching point) are greater than those of the left-hand side, so the secondary flow at the right-hand side is also faster moving causing a reduction of momentum in the axial flow. In addition, two vortices arise around both the top and bottom of the tube toward the outside of the bifurcation.

In Figure 5.9, the maximum velocity at the low Reynolds number shifts towards the centre of the daughter tube. Secondary flow moves toward the inside of the second bifurcation with two vortices circulating around both the top and bottom of the tube. At higher Reynolds numbers, the profile of maximum velocity is wrapped around the top and bottom of daughter airways with two vortices moving near the centre. These results show that secondary flow profiles vary with Reynolds number and also the internal curved geometry of the model.

As a consequence of these centrifugal forces, the particle residence time tends to increase which may result in higher particle deposition on the wall. The secondary flow is expected to diminish when centrifugal force is no longer present, i.e., at a position far from the carina.

5.4 Airflow in the alveolar airways

Airflow in alveolar regions can be modelled as laminar flow due to the very low Reynolds number in this region. The 2D alveolar airway model presented by Darquenne [38] is used in this study, since the model is made more realistic than a tubular model by inclusion of alveoli surrounding alveolar ducts. This section aims to investigate the effect of airflow in the alveolar model.

5.4.1 Numerical technique

Triangular mesh elements were used in the 2D alveolar model. The number of mesh elements was determined by refining parameters until the grid was independent of the results, summarised in Table 5.6. A laminar flow model

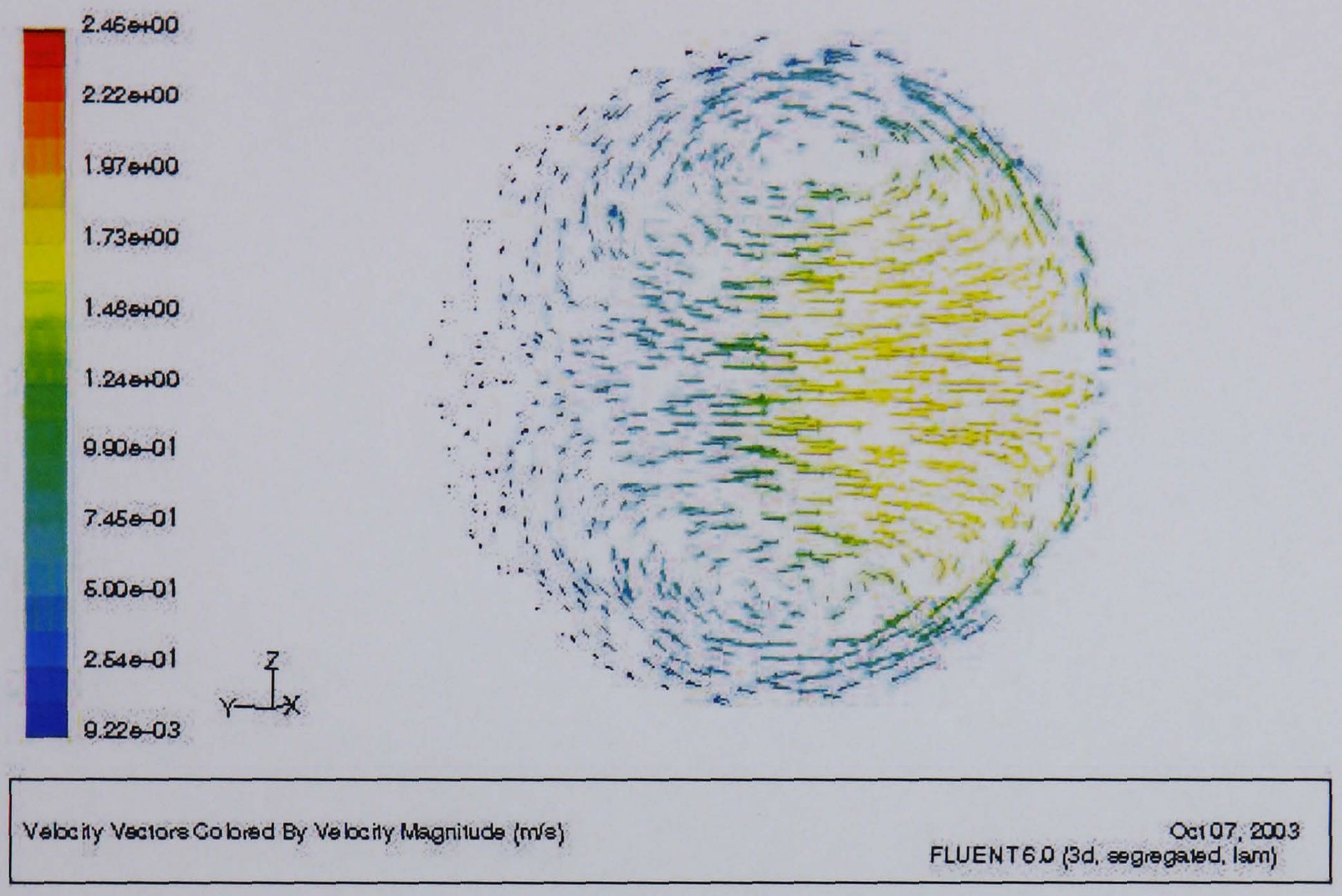

(a) Sedentary activity

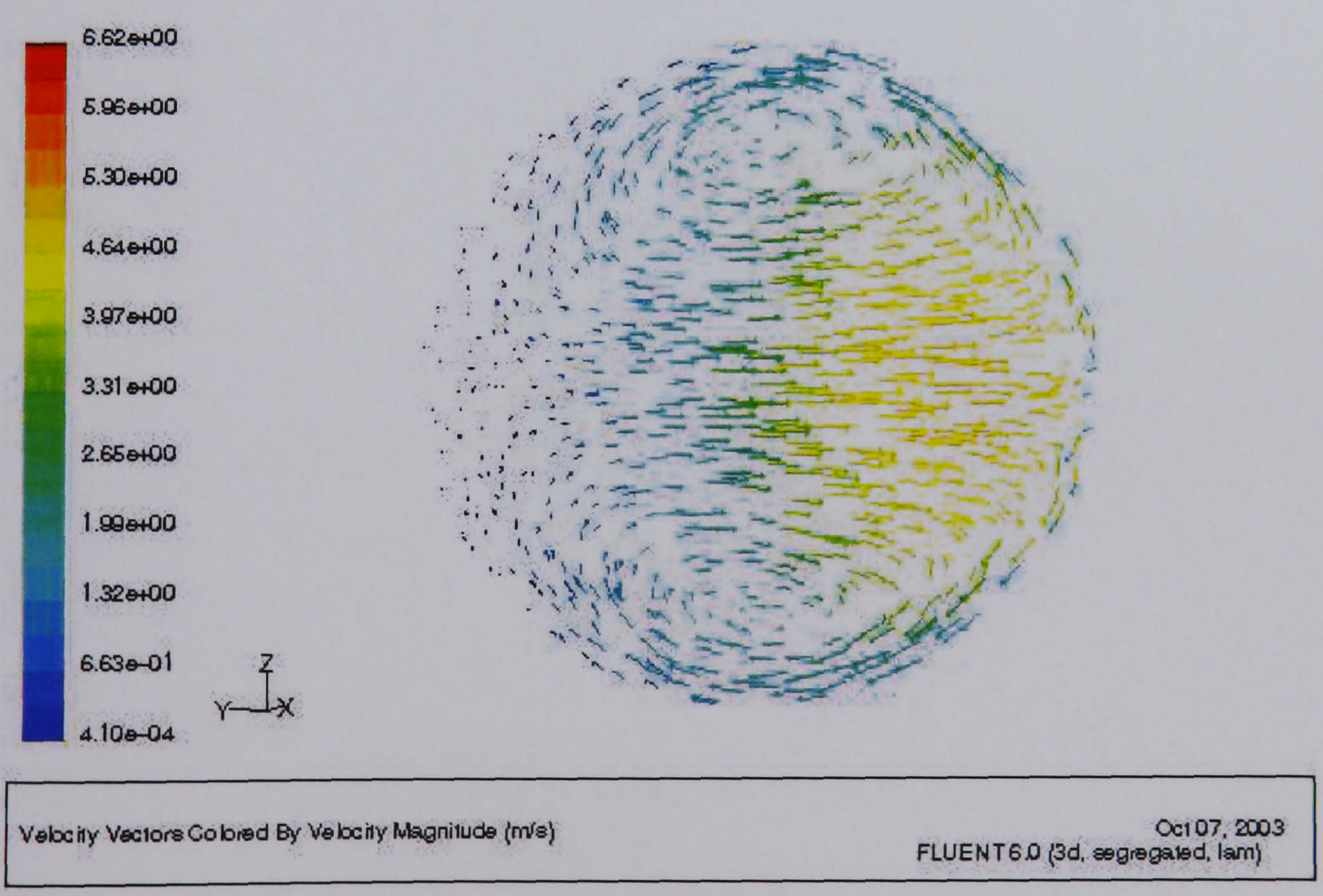

(b) Light activity

Figure 5.8: Vector plots of the secondary velocity magnitudes in the first bifurcation at plane B (see in Figure 5.4)

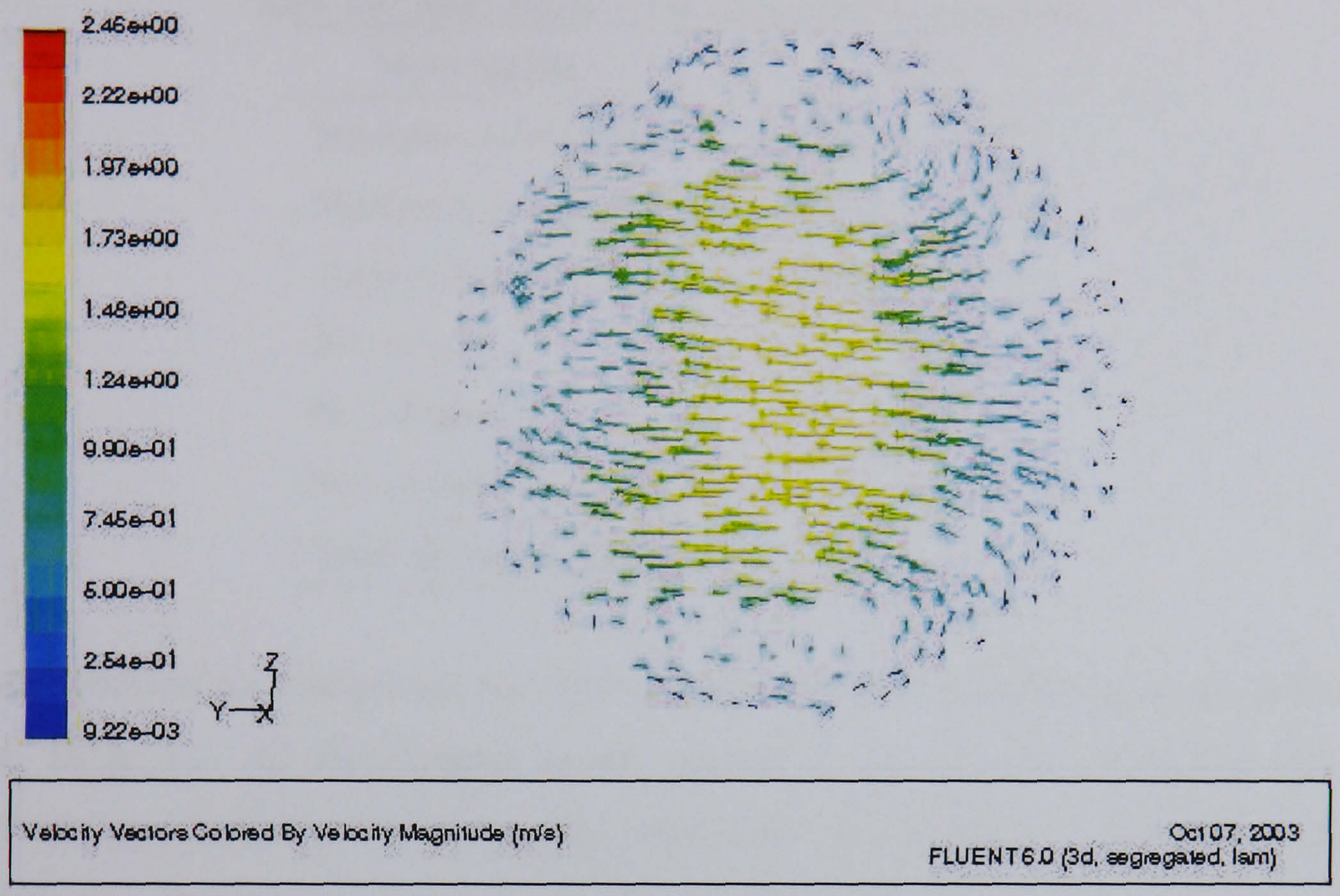

(a) Sedentary activity

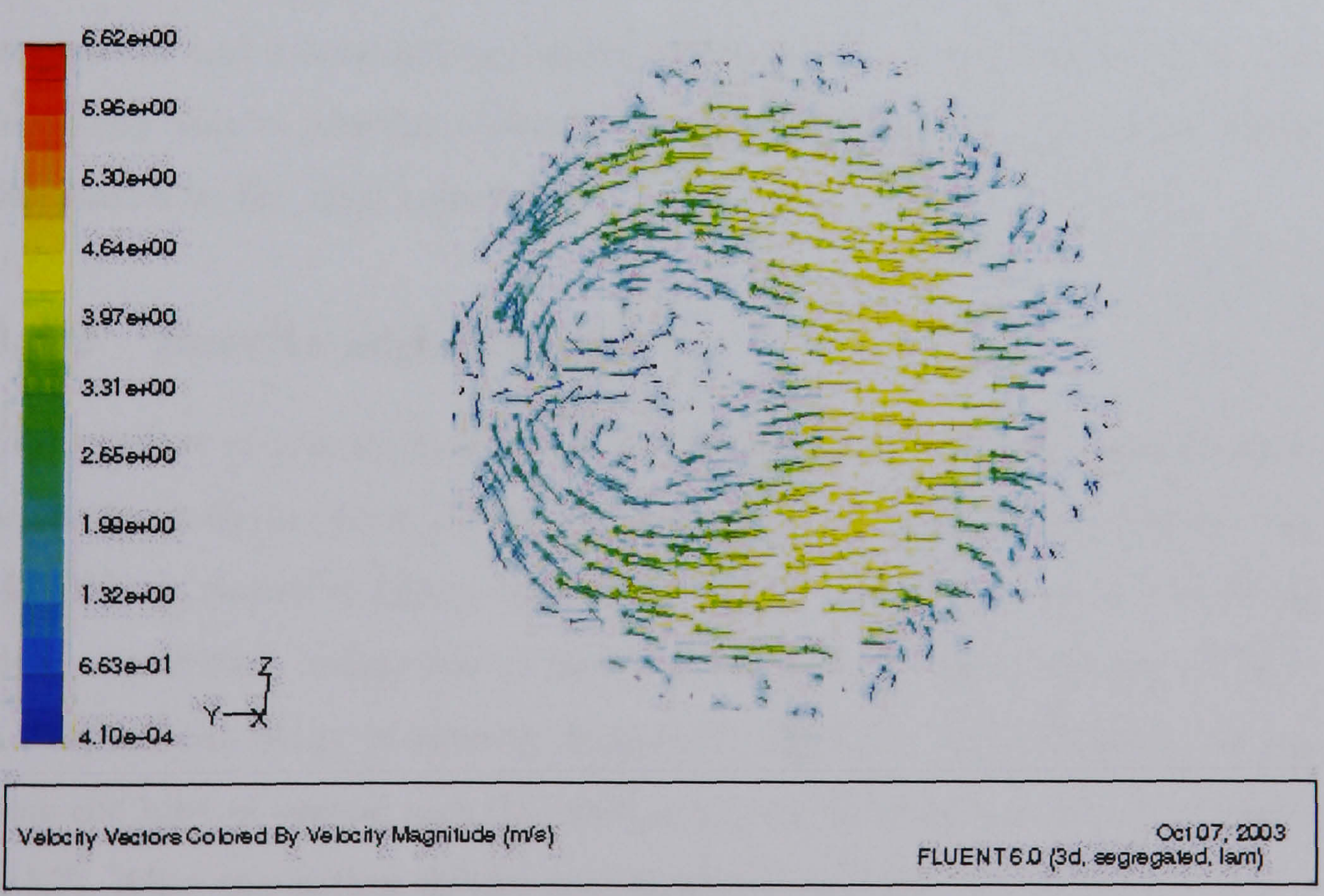

(b) Light activity

Figure 5.9: Vector plots of the secondary velocity magnitudes in the second bifurcation at plane E (see in Figure 5.6)

Table 5.6: Mesh details of the 2D alveolar airway model

Mesh details	value
Minimum volume (m^2)	2.009589×10^{-11}
Maximum volume (m^2)	1.556003×10^{-10}
Total volume (m^2)	2.261891×10^{-5}
No. of cells	326434
No. of faces	501417
No. of nodes	174880
Total memory (*Mbytes*)	86

was selected for computing the airflow using the discretisation schemes given in Table 5.1. In the alveolar airway model, it was assumed that the wall boundary condition was a non-slip rigid-wall. The inlet flow condition was defined corresponding to a mouth flow rate of 500 mls^{-1} with a parabolic profile. The transient of airflow for one breathing cycle consists of a 2-second inspiration and a 2-second expiration. Because of a small Dean number, the secondary flow in alveolar region is not significant and the airflow is mainly dominated by the axial velocity.

5.4.2 Results and discussion

The contours of velocity magnitude of airflow in the 2D alveolar model with a parabolic profile at the central unit corresponding to the inlet Reynolds number of 0.068 are shown in Figure 5.10. The velocity magnitudes rapidly decrease along the central lumen due to flow dividing into daughter airways. Figure 5.11 shows the decay of velocity magnitude along the central lumen starting from the inlet of central unit (labelled as L1) to the end of section C (labelled as L7). After the airflow divides into daughter sections, the magnitude at the central lumen reduces rapidly and reaches a constant peak velocity.

Because of the small Reynolds and Dean numbers, the developing length required (L_c) is short. The fully developed velocity profile is then regained

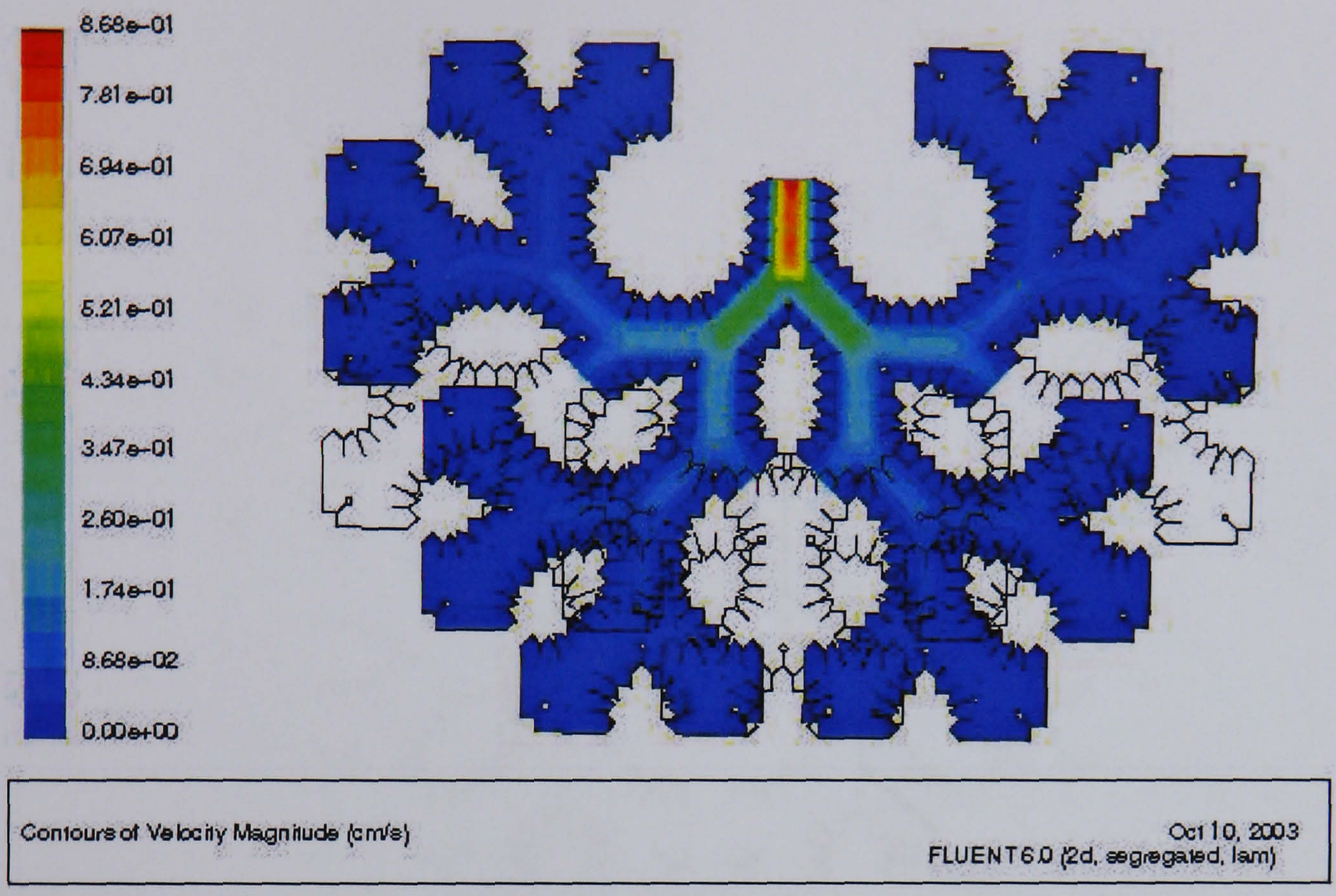

Figure 5.10: Velocity magnitudes of inhaled steady state airflow in the 2D alveolar model airway model ($Re = 0.068$)

shortly after passing the branching point. The peak magnitude of flow in a daughter branch reduces approximately to one half of the original value. At the last section, the outlet velocity magnitude is very small, approximately 0.015625 times of that of inlet section. The velocity vector near the inlet of the alveolar model given in Figure 5.12 shows that the axial flow is concentrated at the central lumen with a slow recirculated flow in the alveolar cavities. Figure 5.13 gives a clear vector profile of recirculated flow inside the alveoli with a pattern similar to that of the previous study by Darquenne [38].

These visualisations of velocity profiles represent inspiratory flow. The expiratory flow is assumed to have the same magnitude as those of inspiratory flow but the velocity vectors are in opposite directions. Transient flows of inspiration and expiration are based on steady-state flow. The direction of airflow changes abruptly after the end of each inspiratory and expiratory cycle.

The airflow in the 2D alveolar model highlights the difference of the local velocity vectors compared with the tubular structure without the alveolar sacs.

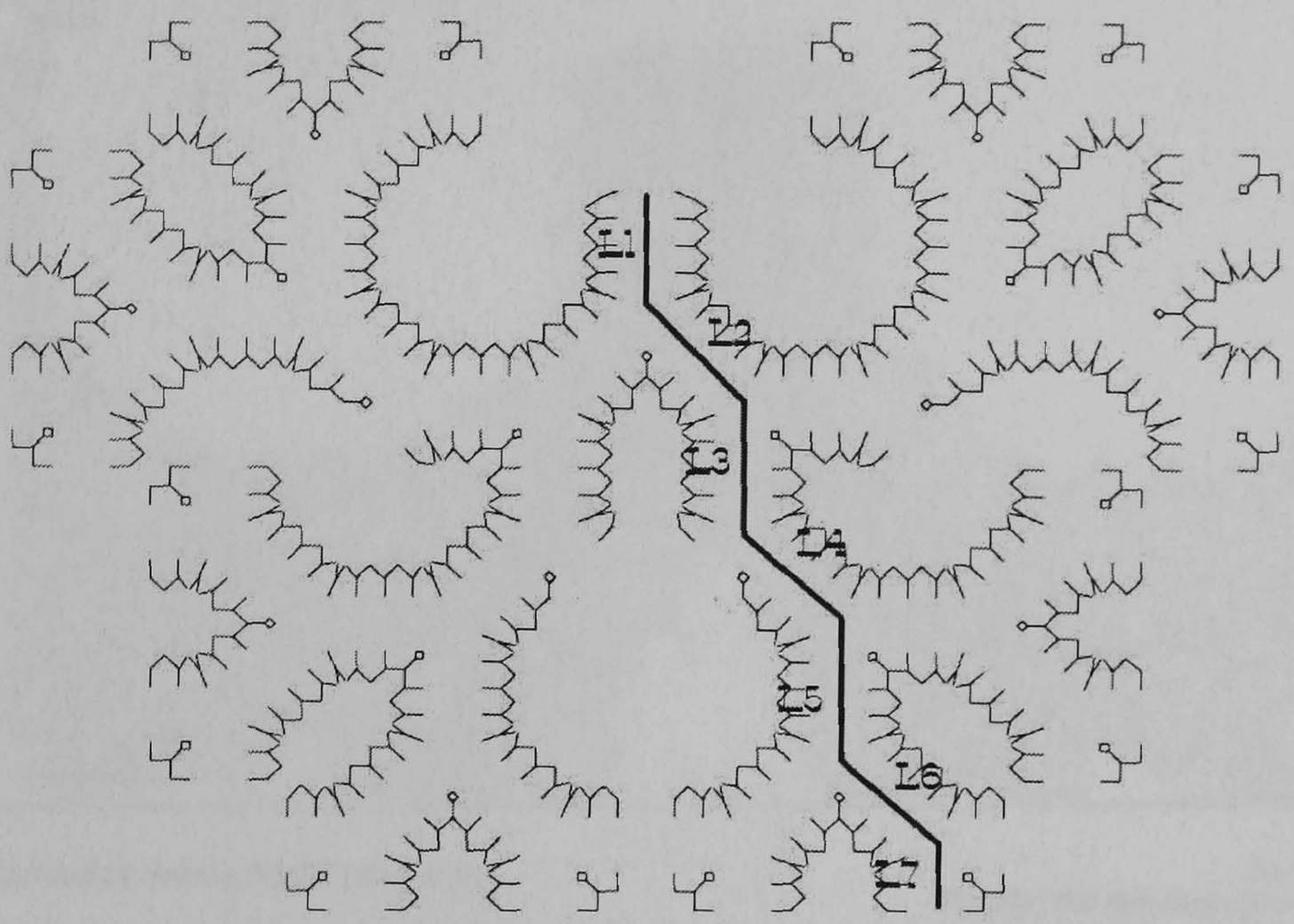

(a) a path of central lumen

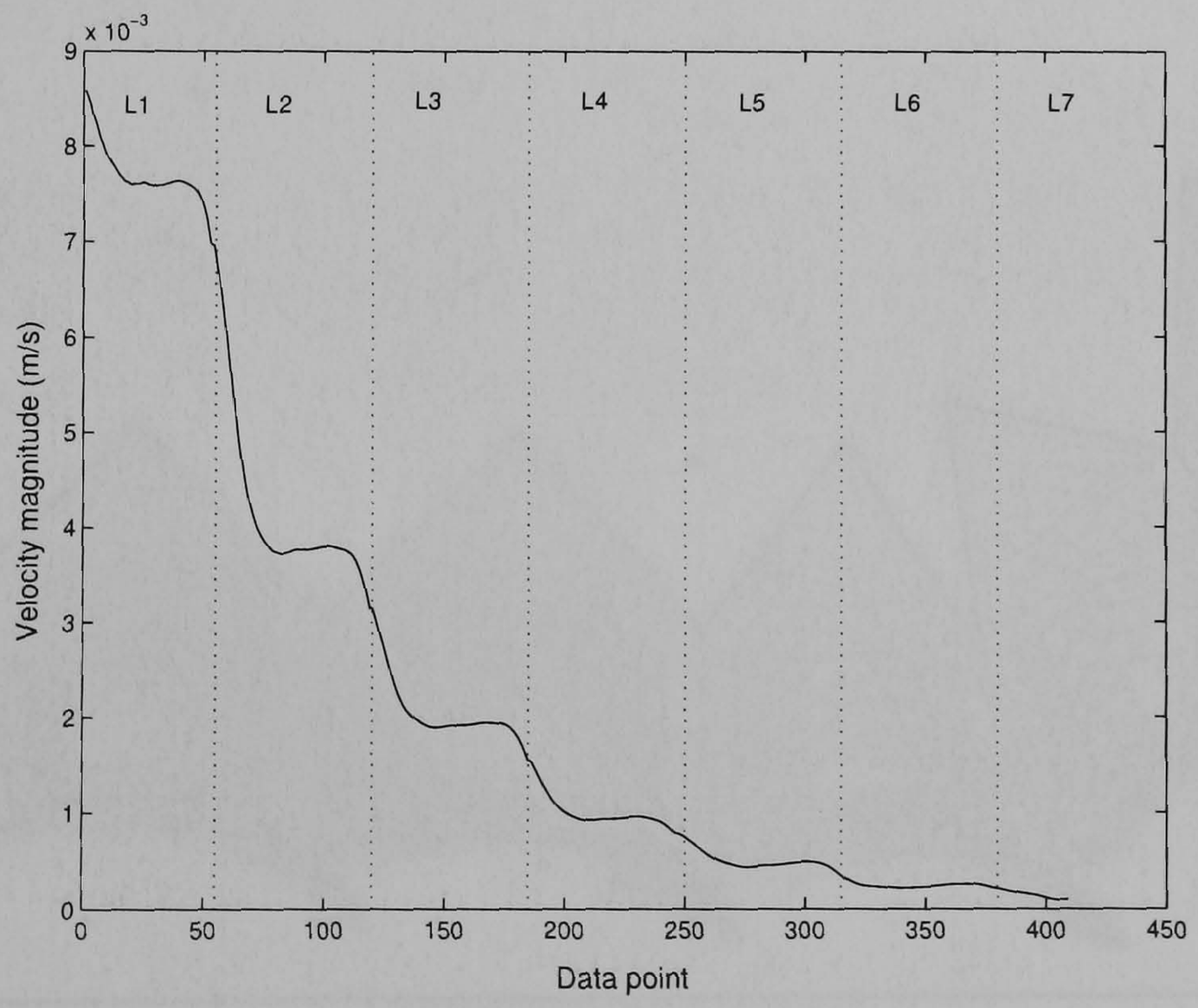

(b) a velocity magnitude

Figure 5.11: Velocity magnitudes along the central lumen of the 2D alveolar airway model (displayed sections: main, A, C, F, and H).

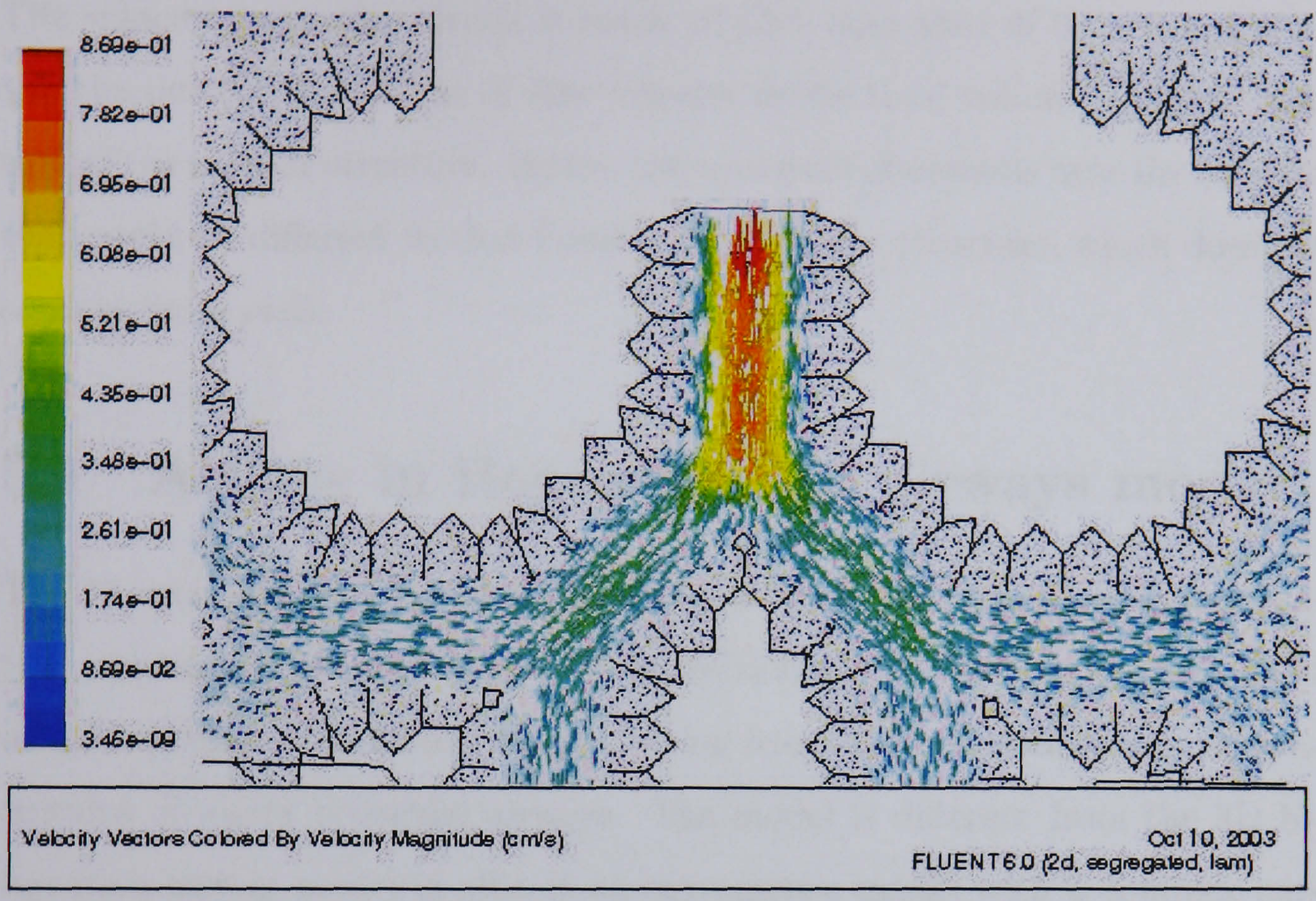

Figure 5.12: Velocity vectors of inhaled steady airflow near the inlet of 2D alveolar airway model with the inlet Reynolds number of 0.068

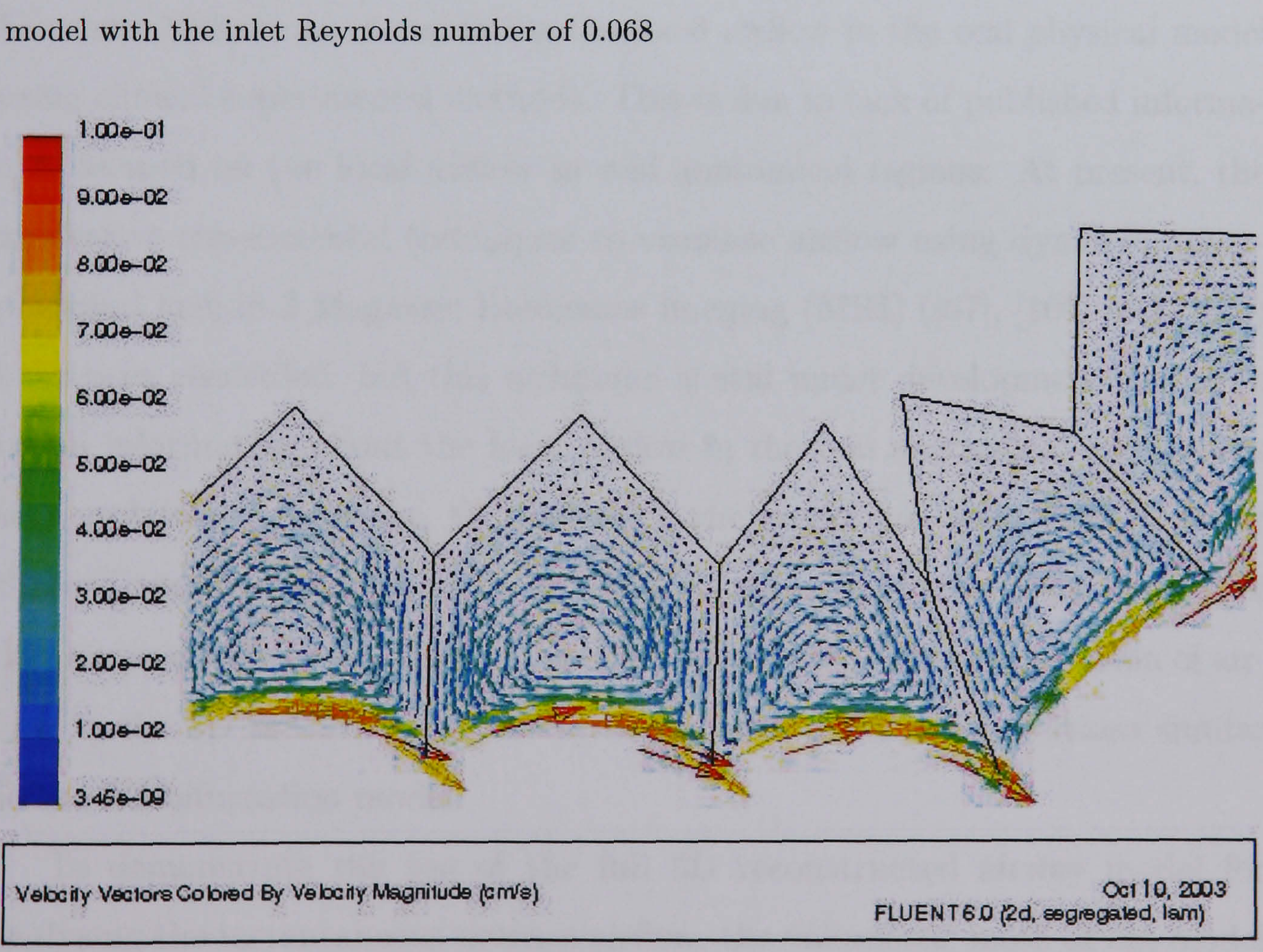

Figure 5.13: Velocity vectors of inhaled steady airflow inside alveoli near the inlet of 2D alveolar airway model with the inlet Reynolds number of 0.068

The velocity inside the alveoli is much smaller than that of the central axis, and the ratio of the volume of slow velocity to the total volume is higher than that of the tubular structure. Hence, the transport of aerosols near the alveolar wall would be different to that found in the tubular structure, which does not contain the alveoli.

5.5 Airflow in Reconstructed airways model

The 3D reconstructed airway model was generated from the image reconstruction techniques discussed previously in section 2.3. The whole reconstructed model represents the human lungs starting from trachea down to several generations of upper bronchial airways. The model is different from the 3D bifurcation airway model in that is an asymmetric model with a complex curvature of the surface. The study of airflow in the reconstructed airway model has some limitations in validating the local airflow in the real physical model using clinical experimental methods. This is due to lack of published information focused on the local airflow in real anatomical regions. At present, the innovative experimental techniques to visualise airflow using dynamic hyperpolarised helium-3 Magnetic Resonance imaging (MRI) ([67], [100] and [185]) have been recoreded, but this technique is still under development and little useful information about the local airflow in the real anatomical regions has been published. However, the airflow in the model has been used to study charged aerosol transport and deposition in terms of relative improvement of deposition efficiency compared to uncharged particles. The computation of airflow in the 3D reconstructed airway model uses boundary conditions similar to the 3D bifurcation model.

To demonstrate the use of the full 3D reconstructed airway model for analysing the instantaneous average airflow, the volumetric mesh of the model was created and is summarised in Table 5.7. The airflow in the trachea is normally turbulent as a consequence of flow passing through the glottal aper-

Table 5.7: Mesh details of the full 3D reconstructed airway model

Mesh details	value
Minimum volume (m^3)	5.30728×10^{-13}
Maximum volume (m^3)	9.99965×10^{-10}
Total volume (m^3)	8.767125×10^{-5}
No. of cells	2,650,481
No. of faces	5,967,270
No. of nodes	796,050
Total memory (*Mbytes*)	770

ture. The calculation of the average flow field within the model was set up using an unsteady $k - \varepsilon$ turbulence model. The inlet velocity of the model was set up as a sinusoid function of time with a period of 4 seconds (2-second inspiration, 2-second expiration) corresponding to the average flow of 0.5 litres per second. The wall boundary conditions assumed a rigid wall. The numerical study neglects the effect of non-uniform outlet pressure in the asymmetric reconstructed airways by assuming a uniform pressure condition at all outlets.

Figure 5.14 gives the results of unsteady average airflow during a complete breathing cycle in the reconstructed airway model. The results show the vector of velocity for a cycle of breathing starting from the peak of inhalation (t=0 s) to the next peak of inhalation (t=4 s). At the end of inhalation and exhalation phases, the airflow velocity is slow. The high velocity of airflow in the inspiration phase moves from the trachea into the the first branch of airways and then divides into the left and right lungs. The magnitudes of airflow velocities reduce rapidly when passing into the deeper airway generations. In the expiration phase, the distribution of velocity in the whole model is generally similar to that of inspiration phase, but the direction of airflow is reversed.

Although the number of mesh elements used for calculating airflow in the reconstructed airway model can give an instantaneous average airflow within the model, it is not adequate for the computation of particle trajectory. In addition, there was the limitation of computational resources, hence this re-

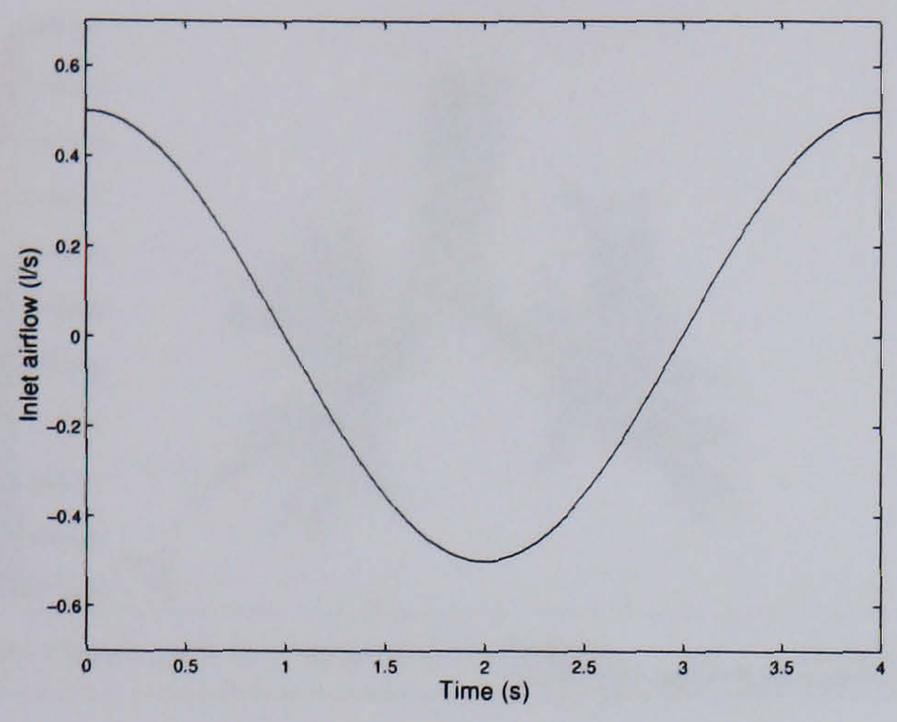

(a) Inlet airflow profile

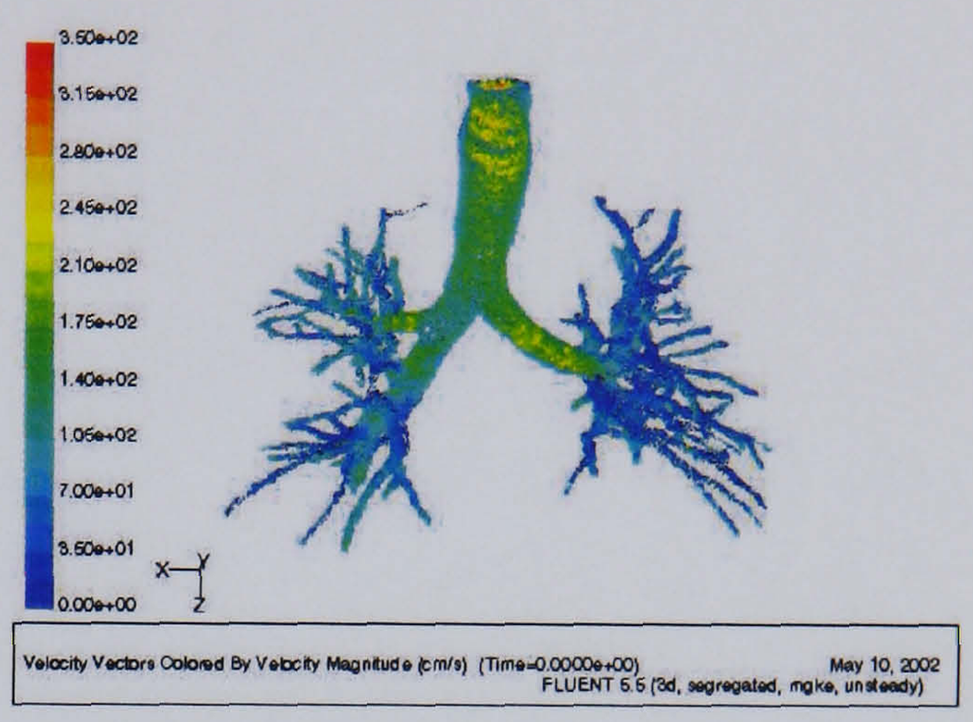

(b) t = 0 s

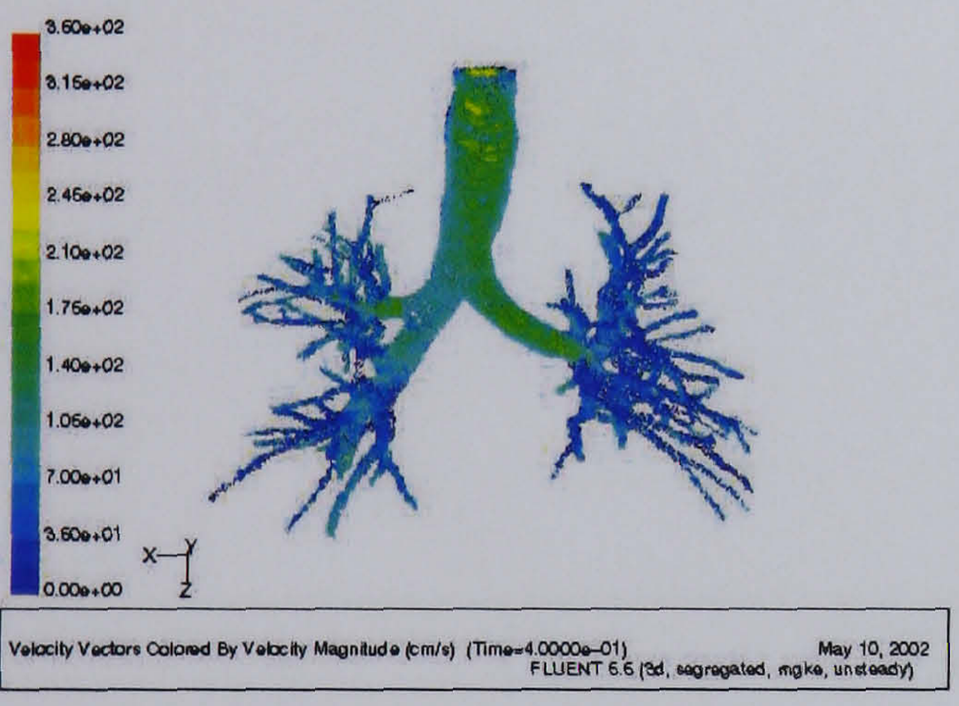

(c) t = 0.4 s

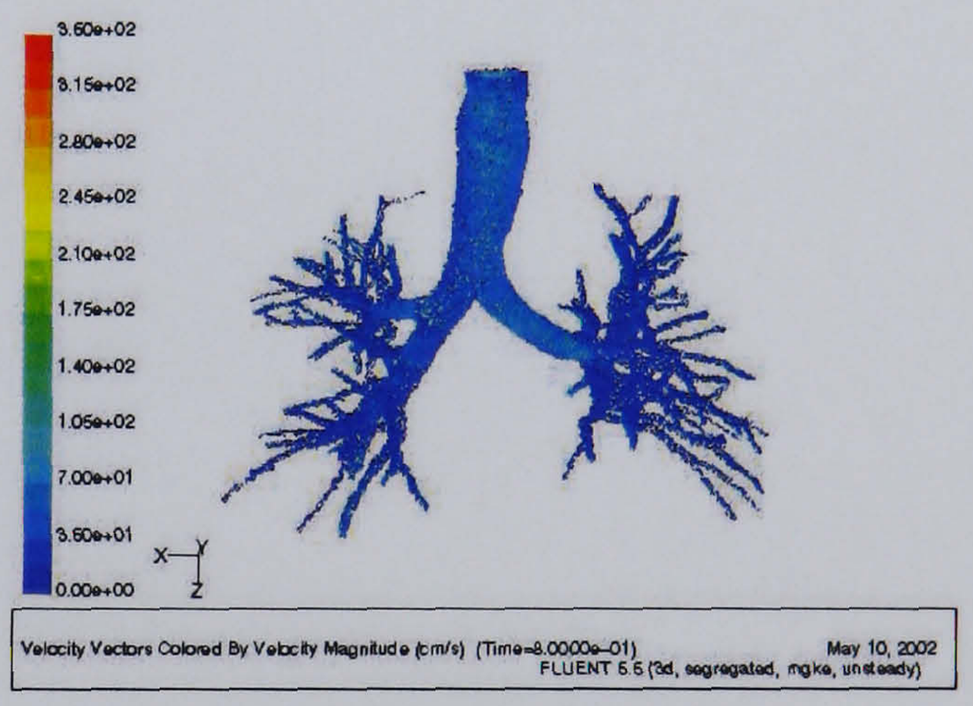

(d) t = 0.8 s

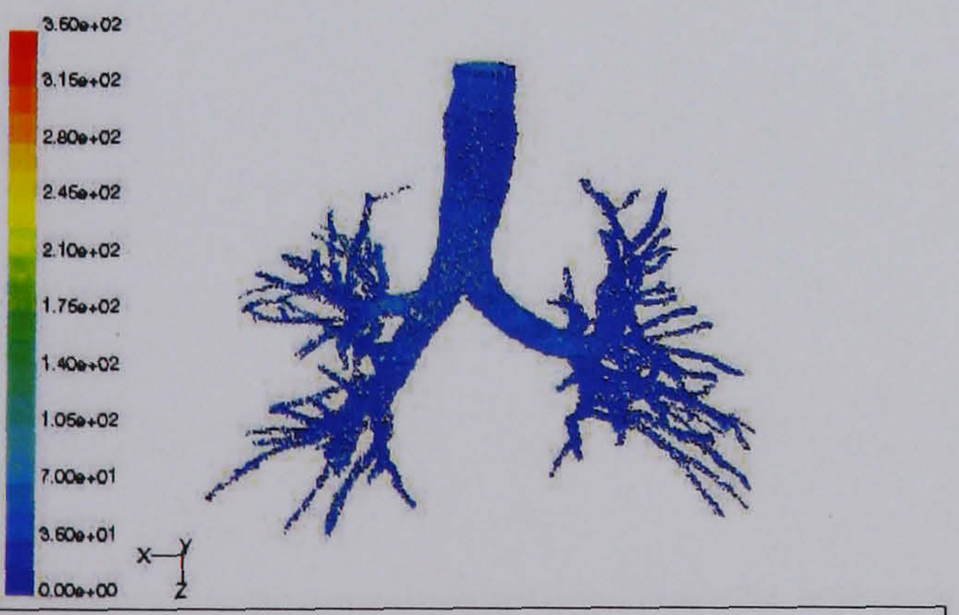

(e) t = 1.2 s

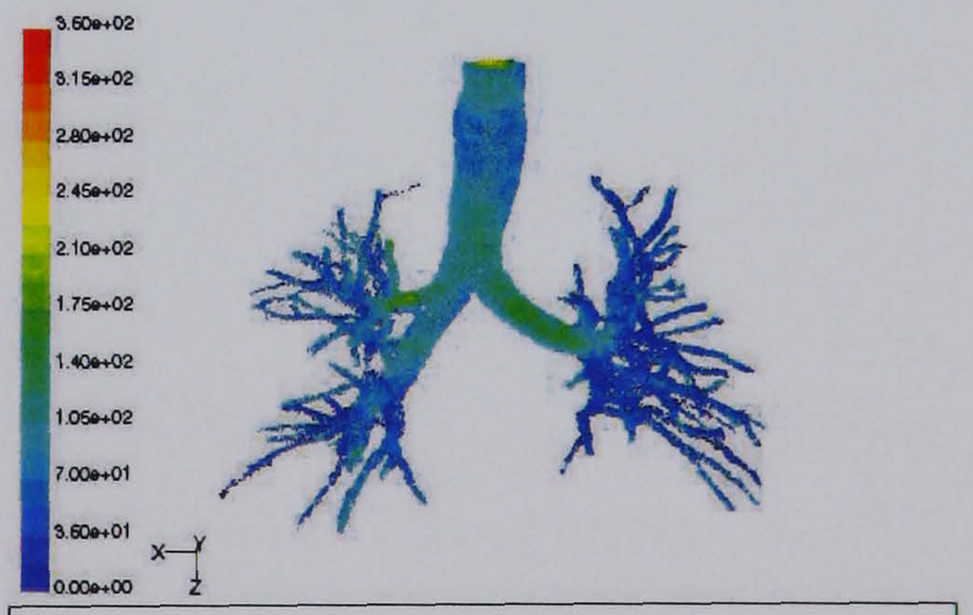

(f) t = 1.6 s

Figure 5.14: Velocity vectors of the transient of airflow in the full 3D reconstructed airway model

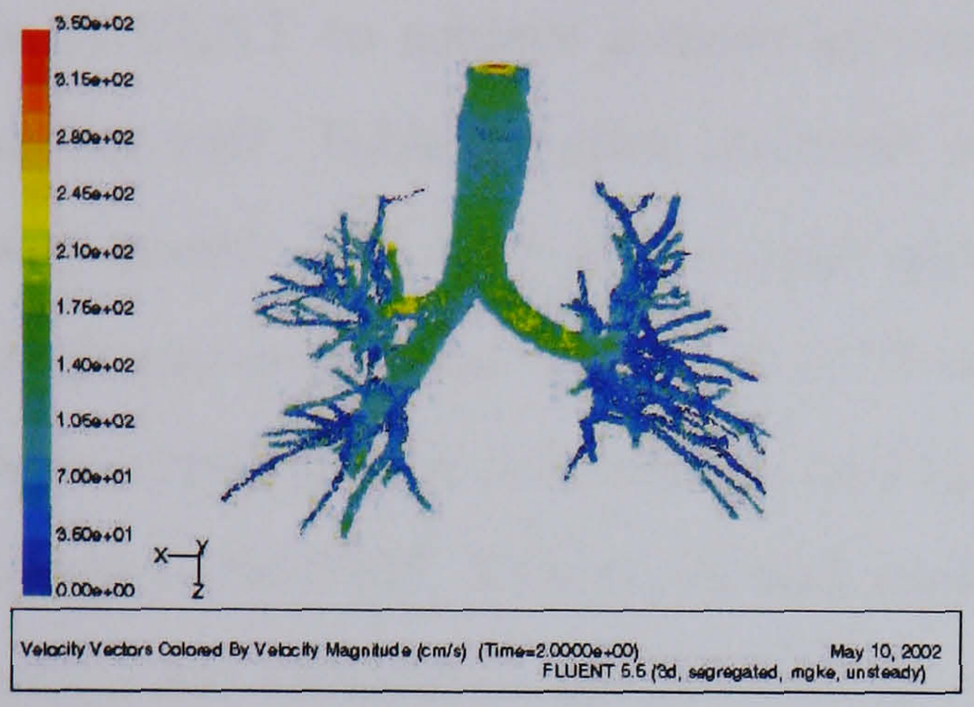

(g) t = 2.0 s

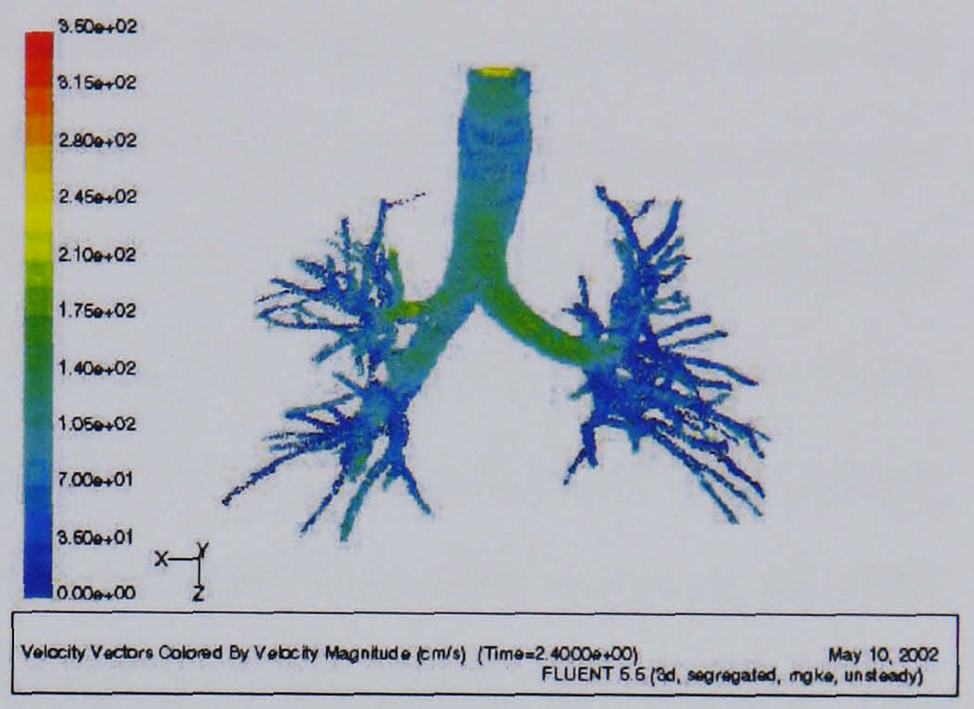

(h) t = 2.4 s

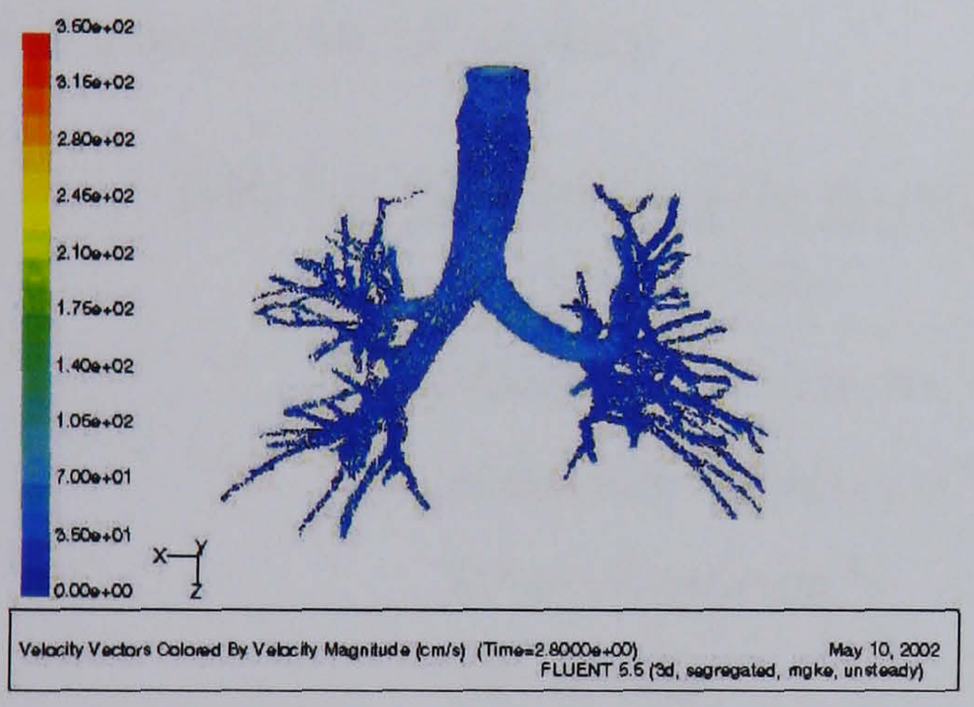

(i) t = 2.8 s

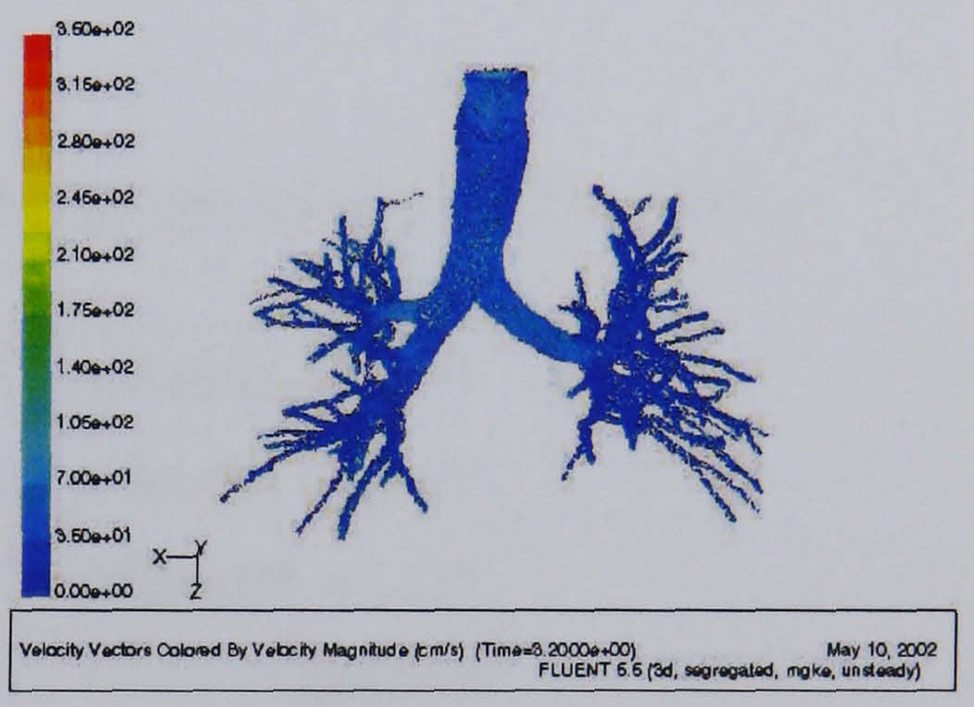

(j) t = 3.2 s

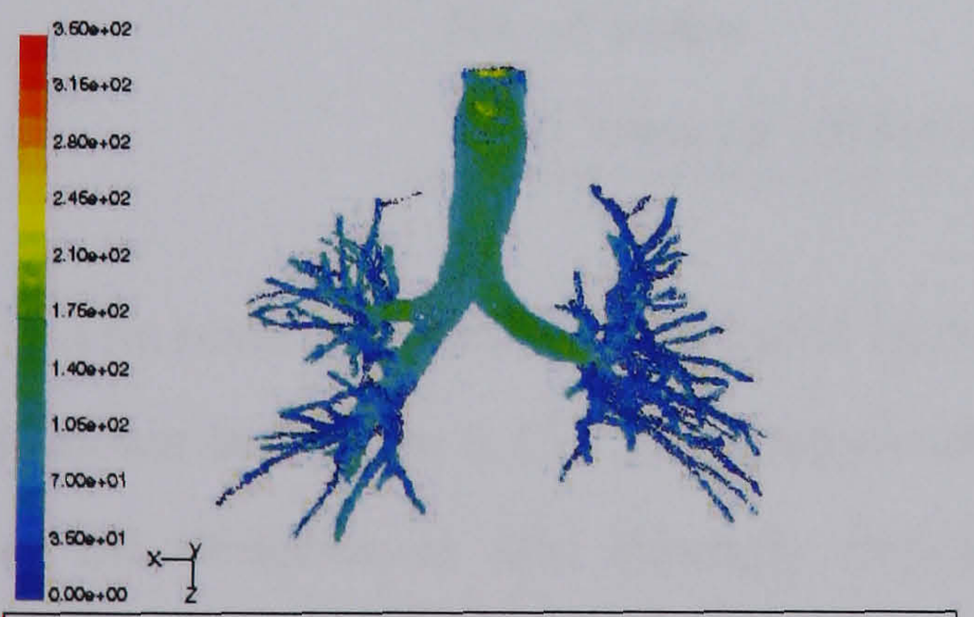

(k) t = 3.6 s

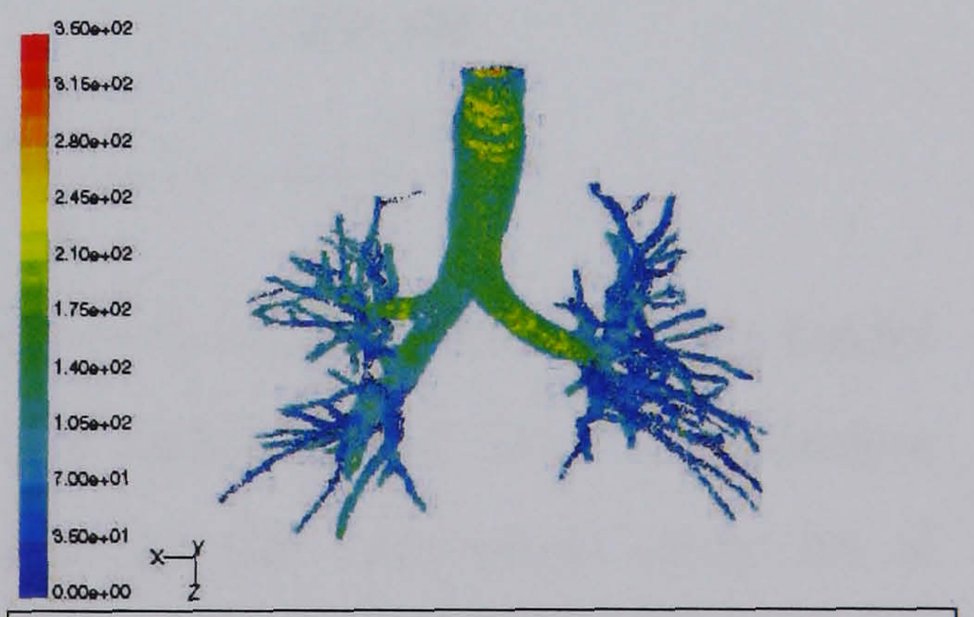

(l) t = 4.0 s

Figure 5.14: Velocity vectors of the transient of airflow in the full 3D reconstructed airway model (Cont.)

search focuses only on the right-upper lung model. The right-upper lung model was meshed into 1,404,767 tetrahedral meshes using the grid adaption feature in FLUENT to achieve a more accurate local flow field, especially near the airway wall. Table 5.8 gives the mesh details of right-upper reconstructed airway model. The inlet of the right-upper reconstructed airways is equivalent to airway generation number 2 of Weibel's model. The inlet Reynolds numbers corresponding to sedentary and light activity breathing conditions range between 700-2100. This study had selected the inlet Reynolds number of 1750 with a flat velocity profile to avoid the transition region near $Re = 2000$. The non-slip conditions are defined at wall boundaries, and zero gauge pressure was selected for all outlets.

Table 5.8: Mesh details of the 3D right-upper reconstructed airway model

Mesh details	value
Minimum volume (m^3)	3.756045×10^{-14}
Maximum volume (m^3)	3.890804×10^{-11}
Total volume (m^3)	6.258237×10^{-6}
No. of cells	1,404,767
No. of faces	2,892,019
No. of nodes	296,496
Total memory (*Mbytes*)	495

The results of airflow (displayed by vectors of inhaled velocity) in the model is shown in Figure 5.15. The magnitudes of airflow in the daughter branches are inhomogeneous and strongly dependent on the anatomical structure of airway model. The secondary flow in this region is also important for aerosol transport due to the high Reynolds number. The visualisation of velocity magnitudes in the daughter branches of the model is complex because of the irregular structure of the model. Figure 5.16 shows the velocity magnitudes at some selected planes in the x-direction.

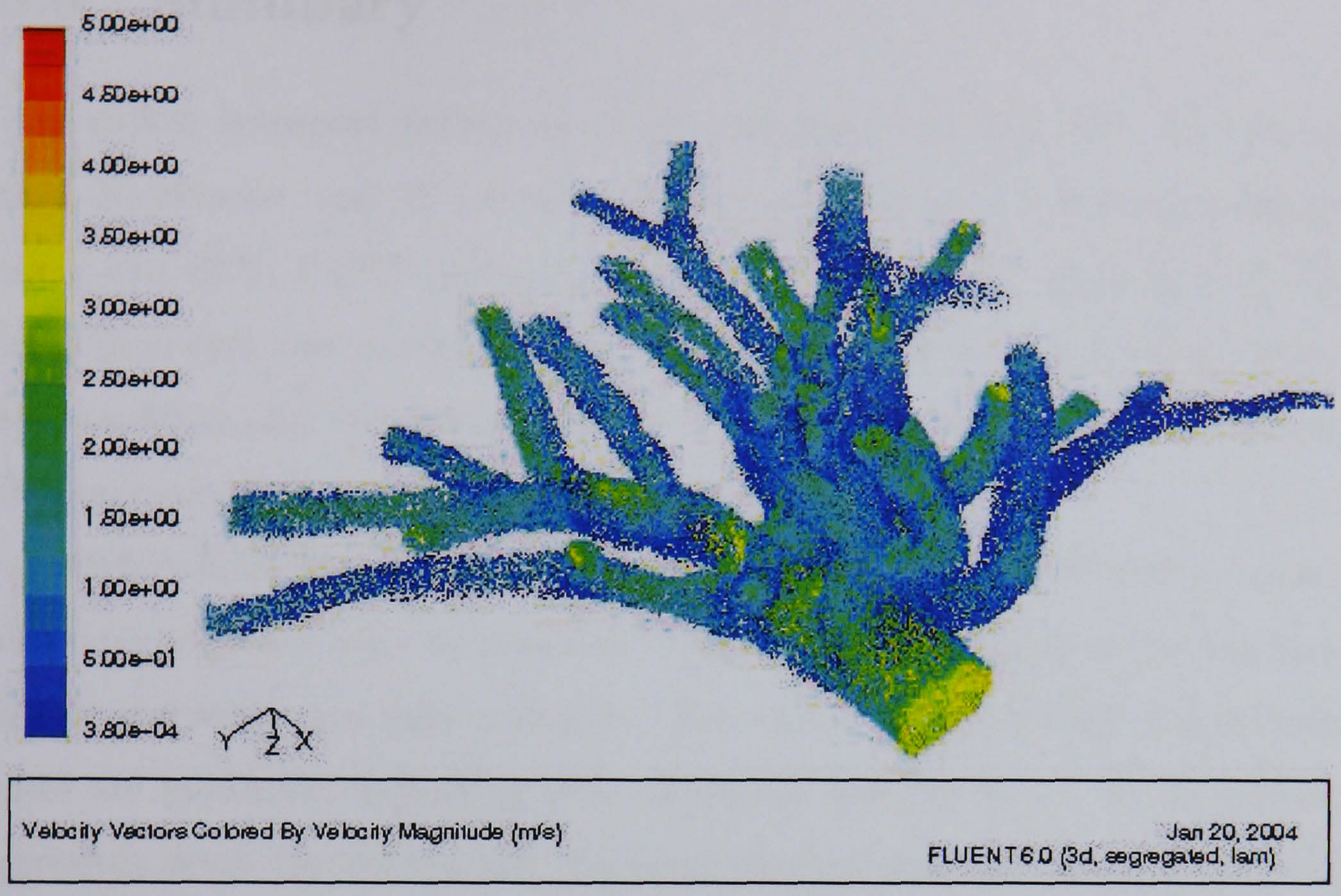

Figure 5.15: Velocity vectors of inhaled steady airflow in the 3D right-upper airway model with an inlet Reynolds number of 1750

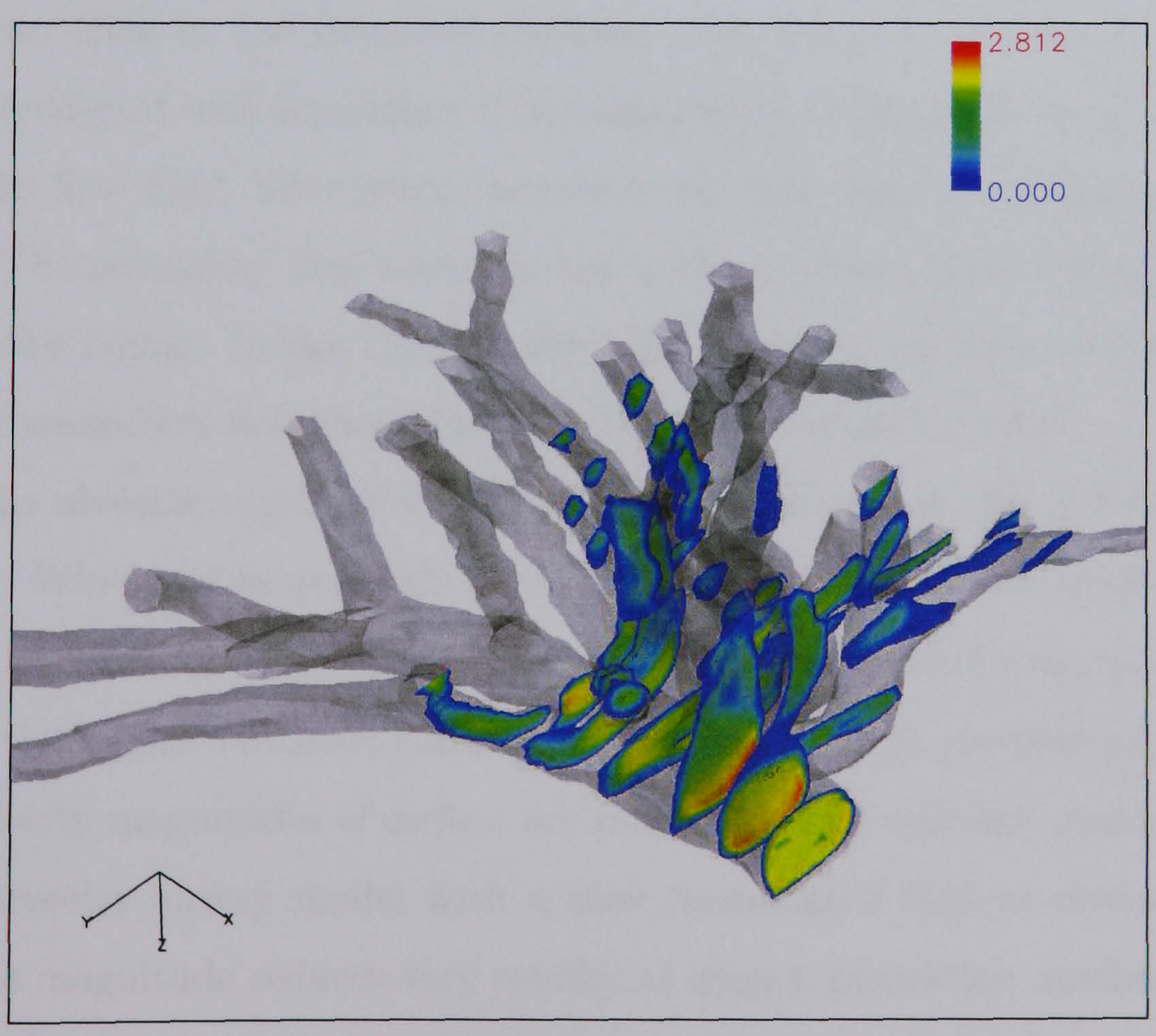

Figure 5.16: Velocity magnitudes of inhaled steady airflow in the 3D right-upper airway model with an inlet Reynolds number of 1750 (unit:m/s)

5.6 Summary

The airflow transport within the three geometrical models (i.e., 3D bifurcation, 2D alveolar, and 3D reconstructed airway models) has been investigated using FLUENT, a CFD package. Airflow fields are mainly determined by the inhalation rate and position within the respiratory cycle. In addition the entry condition and the geometry of the bronchial airway models are a strong determinant of the precise airflow field distribution.

Airflow fields in the bifurcation model, representing Weibel's airway generation numbers 3-5, were investigated in the steady state condition corresponding to sedentary and light activities. The axial velocity profiles at upstream sites are parabolic, indicating fully developed laminar flow. As the airflow proceeds down the bifurcation, the axial velocity profiles steadily change. A distinct shear layer occurs along the inside wall with a recirculation zone at the outer wall. At higher Reynolds numbers, this distinct shear layer tends to be thinner than at low Reynolds numbers. Secondary flow is also important for the transport and deposition of aerosols due to multiple interactions of the upstream flow field, bifurcation curvature and the effect of the carinal ridge shape. The secondary flow normally has a strong vortex near the highest axial velocity region. In this respect, the high Reynolds number case has much stronger secondary flow than that with the low Reynolds number.

In the alveolar region, the airflow field is laminar due to a low Reynolds number. When airflow proceeds down to daughter branches, the axial velocity rapidly regains a fully developed profile. The secondary flow is not so important in this region (without considering the expansion of alveolar sacs). The high velocity magnitudes of airflow are mainly located near the central lumen of the alveolar airway model with a slow recirculated flow at alveolar cavities. The magnitude reduces very rapidly at deeper generation numbers. As a result, suspended particles have a long residence time in these regions.

The study of airflow field in the 3D reconstructed airway model has focused

only on the right-upper zone in order to be able to compare the deposition efficiency between charged and uncharged particles. The computation of airflow is based on experience gained using the 3D bifurcation model. The magnitudes of airflow in the daughter branches are inhomogeneous and significantly depend on the structure of the airway model. The secondary airflow in this region is also important for the aerosol transport due to the high Reynolds number ($800 < Re < 2000$).

Chapter 6

Implementations and Numerical results of Charged Aerosol Transport and Deposition

This chapter provides extensive details of software implementations for calculating the trajectories of charged aerosols incorporating the effect of space and image charge forces. Numerical results of deposition efficiencies in the geometrical airway models are also investigated as a function of charge values under various breathing conditions.

The aerosol cloud in this study is assumed to be a dilute dispersed phase flow and modelled by the Lagrangian dynamic model. The particle size normally plays an important role in aerosol transport and deposition. The motion of particles is mainly dominated by the convection of the airflow. In chapter 4 it has been stated that the electrostatic forces are also the dominant aerosol mechanism in the aerosol transport of sub-micron particles. Numerical studies in this chapter focus on extending the understanding of the role of space and image charge forces affecting the transport and deposition of aerosols in the human airways.

Numerical results were computed using my developed software, which had been designed specifically for these studies. All fluid flow data provided by

the CFD software were imported into the software, and then the particle trajectories in response to various forces acting on particles were calculated. The details of subroutines for calculating trajectories of particles are presented in section 6.1. The transport and deposition of aerosols in the 3D tubular airway model are then described in section 6.2. This section also gives the comparison between the 1D predicted model and the numerical results. With more complex geometrical airway structures, the aerosol transport and deposition in the 3D bifurcation, 2D alveolar and 3D reconstructed airway models are then discussed in sections 6.3, 6.4, and 6.5, respectively.

6.1 Software design

New software is needed to be designed for the following reasons:

- The computation of hydrodynamics and electrostatics is a coupled system. Current commercial CFD packages lack a module for computing the electrostatic forces of charged particles.

- The space charge force calculation requires a large number of particles to represent a dense particle cloud, but the number of particles in the particle tracking module in CFD packages is often limited. Also, the manipulation of transient data of particle trajectories in the CFD packages is not flexible.

- The image charge requires information about the nearest wall distance to individual particles. This is possible to implement by the algebraic equation using the user-defined function for a simple geometrical model, but it is too complicated for the geometrical models used in this thesis due to the complex surfaces.

The software design aims to calculate the particle trajectories including the effects of space and image charge forces. The flowchart of this software is

summarised in Figure 6.1. Firstly the mesh and data (velocity components) obtained by the FLUENT software [60] were imported into designed software (section 6.1.1). Secondly, the variables and parameters for computational routines (such as the mesh size, and time step) were initialised. Thirdly, the particle file was imported into the designed software for initialising size, position, and velocity of particles. Fourthly, electrostatic forces (space and image charge forces) and particle trajectories were calculated. The computational details of space and image charge forces have been previously presented in sections 4.4, and 4.5, respectively. These computations had the longest computational times for updating particle trajectories (section 6.1.2) and tracking the new cell position (section 6.1.3). Finally, the report and post-processing files were created for visualisation and analysis (section 6.1.4). In this chapter, the discussions of computational techniques are based on the 3D geometrical model. For the 2D geometrical model, the general concepts are still similar to the 3D case.

Two types of mesh elements were employed in the designed software: the tetrahedral and hexahedral meshes. The geometrical model and fluid computational domain were represented by the tetrahedral mesh, whereas the hexahedral mesh was used as an auxiliary mesh in the Particle Mesh method for solving the space charge field. The hexahedral mesh was generated by my novel software, which had a symmetric grid and was independent from the tetrahedral mesh. For the 2D geometrical model, two types of mesh elements were represented by triangular and rectangular meshes.

The software code was developed based on the object-oriented programming using the Microsoft Visual C++. This object-oriented programming enables programmers to create modules that do not need to be changed when a new type object is added, and it is easy to modify the program code.

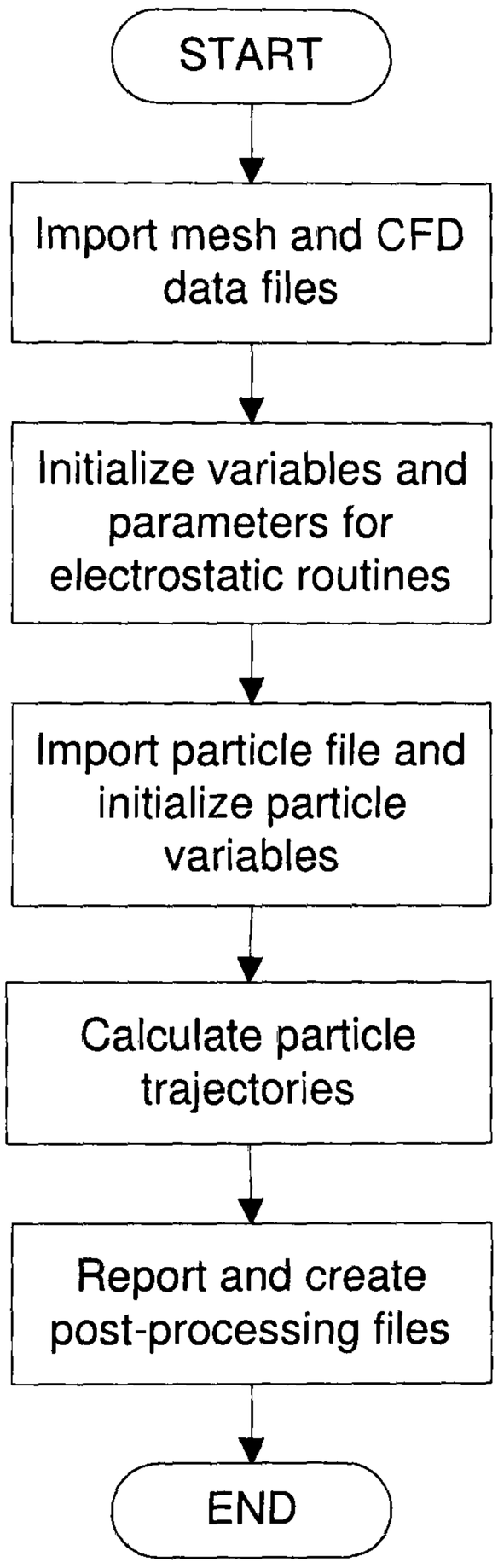

Figure 6.1: Flowchart of designed software

6.1.1 Mesh and CFD data files

The mesh and data files were imported to define the computational domain of airways and local velocity vectors of airflow. The verification of mesh and the data which are used was performed using the following statistical data; the numbers of nodes, the numbers of cells, the minimum and maximum position in any directions, the minimum and maximum of cell volumes, the minimum and maximum velocity magnitudes. The velocity vectors of fluid were represented as the nodal data, and the local velocity within the computational domain could be interpolated by a linear or a higher-order interpolation function. The higher-order interpolation can improve the accuracy of interpolation, but it requires higher numbers of nodes in the element with more complexity of interpolation. Consequently, the linear interpolation was selected for this study. Only four nodal data at vertices of tetrahedral elements were required for the linear interpolation.

In the x-direction of the cartesian coordinate, the linear function of the velocity component u can be written in terms of coordinate positions x, y and z as

$$u = a_1 + a_2 x + a_3 y + a_4 z \tag{6.1}$$

or

$$u = \left\{ \begin{array}{cccc} 1 & x & y & z \end{array} \right\} \left\{ \begin{array}{c} a_1 \\ a_2 \\ a_3 \\ a_4 \end{array} \right\} = \{X\}^T \{A\} \tag{6.2}$$

where a_i is the constant to be determined. The interpolation could be written in terms of the nodal variables at four nodes. Therefore, substituting x,y and z values at each node gives

$$\begin{Bmatrix} u_1 \\ u_2 \\ u_3 \\ u_4 \end{Bmatrix} = \begin{bmatrix} 1 & x_1 & y_1 & z_1 \\ 1 & x_2 & y_2 & z_2 \\ 1 & x_3 & y_3 & z_3 \\ 1 & x_4 & y_4 & z_4 \end{bmatrix} \begin{Bmatrix} a_1 \\ a_2 \\ a_3 \\ a_4 \end{Bmatrix} \tag{6.3}$$

or

$$\{u\} = [X]\{A\} \tag{6.4}$$

in which

$$\{u\} = \{ \; u_1 \quad u_2 \quad u_3 \quad u_4 \; \}^T \tag{6.5}$$

Equation 6.2 can be rewritten as

$$u = \{X\}^T[X]^{-1}\{u\} = \{H\}^T\{u\} \tag{6.6}$$

where

$$\{H\}^T = \{ \; H_1 \quad H_2 \quad H_3 \quad H_4 \; \} = \{X\}^T[X]^{-1} \tag{6.7}$$

are the shape functions of a tetrahedral element with four nodes. The values of shape function vary with the position of the considered node, and the summation of all components in $\{H\}$ is equal to one.

For the two-dimension model, the triangular mesh was selected to represent the velocity component. The linear interpolation used was similar to the tetrahedral mesh. The interpolation can be given as:

$$u = \{X\}^T[X]^{-1}\{u\} = \{H\}^T\{u\} \tag{6.8}$$

where

$$\{u\} = \{ \; u_1 \quad u_2 \quad u_3 \; \}^T \tag{6.9}$$

$$\{X\} = \{ \; 1 \quad x \quad y \; \}^T \tag{6.10}$$

$$\{H\}^T = \{ \; H_1 \quad H_2 \quad H_3 \; \} = \{X\}^T[X]^{-1} \tag{6.11}$$

6.1.2 Trajectory computation

The particle trajectory equation in the Lagrangian reference frame is derived from the conservation of momentum discussed in section 3.3. The dominant forces acting on the charged particle, namely drag, gravity, diffusion, space charge and image charge forces, can be written as

$$\begin{aligned} \frac{d\mathbf{u}_p}{dt} &= \frac{1}{m_p}\mathbf{F}_p \\ \frac{d\mathbf{x}_p}{dt} &= \mathbf{u}_p \end{aligned} \tag{6.12}$$

where $\mathbf{F}_p$ is a total force acting on the particles

A "leapfrog" integration scheme was selected to solve the trajectory equation in this developed software. Given $\mathbf{u_p}^{n-1/2}$ and $\mathbf{x_p}^{n}$ as initial data, the updated velocity and position for a constant time step Δt can be given by

$$\mathbf{x}_p^{n+1} = \mathbf{x}_p^n + \mathbf{u}_p^{n+1/2}\Delta t \tag{6.13}$$

$$\mathbf{u}_p^{n+1/2} = \mathbf{u}_p^{n-1/2} + \frac{1}{m_p}\mathbf{F}_p^n\Delta t \tag{6.14}$$

The characteristics of the leapfrog integration scheme are discussed in terms of consistency, accuracy, stability and efficiency.

6.1.2.1 Consistency

Consistency is a requirement for any algebraic approximation to a differential equation that should tend toward the differential equation in the limit of an infinitesimal timestep. The leapfrog integration scheme in equation 6.13 is consistent with the differential equation as follows

$$\frac{d\mathbf{x}_p}{dt} = \mathbf{u}_p \tag{6.15}$$

since

$$\mathbf{x}_p^{n+1} - \mathbf{x}_p^n = \mathbf{x}_p(t^n + \Delta T) - \mathbf{x}_p(t^n) \tag{6.16}$$

$$= \left[\mathbf{x}_p(t^n) + \left.\frac{d\mathbf{x}_p}{dt}\right|_{t=t^n} \Delta t + ...\right] - \mathbf{x}_p(t^n) \tag{6.17}$$

gives

$$\lim_{\Delta t \to 0} \left[\frac{\mathbf{x}_p(t^n + \Delta t) - \mathbf{x}_p(t^n)}{\Delta t}\right] = \frac{d\mathbf{x}_p}{dt} \tag{6.18}$$

6.1.2.2 Accuracy

The accuracy means the truncation error associated with approximating derivatives with differences. Combining the difference equations for the leapfrog integration with a constant timestep Δt gives

$$\frac{\mathbf{x}_p^{n+1} - 2\mathbf{x}_p^n + \mathbf{x}_p^{n-1}}{(\Delta 2)^2} = \frac{\mathbf{F}_p^n}{m_p} \tag{6.19}$$

The exact equation for the trajectory equation is

$$\frac{d^2\mathbf{x}_p}{dt^2} = \frac{\mathbf{F}_p}{m_p} \tag{6.20}$$

Using Taylor series expansion, $\mathbf{x}_p^{n+1}$ and $\mathbf{x}_p^{n-1}$ can be written in terms of $\mathbf{x}_p$ as

$$\mathbf{x}_p^{n+1} = \mathbf{x}_p^n + \left.\frac{d\mathbf{x}_p}{dt}\right|_n \Delta t + \frac{1}{2!}\left.\frac{d^2\mathbf{x}_p}{dt^2}\right|_n (\Delta t)^2 + \frac{1}{3!}\left.\frac{d^3\mathbf{x}_p}{dt^3}\right|_n (\Delta t)^3 + \frac{1}{4!}\left.\frac{d^4\mathbf{x}_p}{dt^4}\right|_n (\Delta t)^4 + ... \tag{6.21}$$

$$\mathbf{x}_p^{n-1} = \mathbf{x}_p^n - \left.\frac{d\mathbf{x}_p}{dt}\right|_n \Delta t + \frac{1}{2!}\left.\frac{d^2\mathbf{x}_p}{dt^2}\right|_n (\Delta t)^2 - \frac{1}{3!}\left.\frac{d^3\mathbf{x}_p}{dt^3}\right|_n (\Delta t)^3 + \frac{1}{4!}\left.\frac{d^4\mathbf{x}_p}{dt^4}\right|_n (\Delta t)^4 + ... \tag{6.22}$$

Combining these expansion terms into equation 6.19 gives

$$\frac{\mathbf{x}_p^{n+1} - 2\mathbf{x}_p^n + \mathbf{x}_p^{n-1}}{(\Delta t)^2} = \left.\frac{d^2\mathbf{x}_p}{dt^2}\right|_n - \frac{1}{12}\left.\frac{d^4\mathbf{x}_p}{dt^2}\right|_n (\Delta t)^2 + h.o.t \tag{6.23}$$

It can be seen that the leapfrog approximation for a second order derivative term has an error as a second order of the time step.

6.1.2.3 Stability

A numerical method is considered to be stable if a small error at any stage does not lead to a larger cumulative error [84]. To get a quantitative measurement of stability, the evaluation of errors must be described and then investigated.

Let $\mathbf{X}_p^n$ represent the exact solution to the difference equation 6.19. The term of $\mathbf{e}^n = \mathbf{x}_p^n - \mathbf{X}_p^n$ is defined for the numerical error at time t^n, then the cumulative error term can be written as

$$\mathbf{e}^{n+1} - 2\mathbf{e}^n + \mathbf{e}^{n-1} \approx \frac{(\Delta t)^2}{m_p} (\mathbf{e} \cdot \nabla) \mathbf{F}_p^n|\mathbf{x}_p^n \tag{6.24}$$

The right hand side of this equation can be written as $M_{ij} \cdot \mathbf{e}$, where M is the matrix. The component in M is obtained by

$$M_{ij} = \frac{(\Delta t)^2}{m_p} \frac{\partial F_j}{\partial X_i} \tag{6.25}$$

In general, the error will grow fastest if $\mathbf{e}$ is an eigenvector of M corresponding to its largest eigenvalue in absolute value. Looking at bounded oscillatory solutions, the error $\mathbf{e}^n$ can be written as

$$\mathbf{e}^n = \hat{\mathbf{e}} \left(e^{iw\Delta t}\right)^n \equiv \hat{\mathbf{e}}\lambda^n \tag{6.26}$$

Substituting this into equation 6.24, we get

$$\lambda^2 - 2\lambda + 1 = -(\Omega\Delta t)^2 \lambda \tag{6.27}$$

where $-\Omega^2$ is the largest eigenvalue of $\frac{M}{(\Delta t)^2}$.

This scheme is numerically stable if the characteristic solution of λ lies in the unit circle.

6.1.2.4 Efficiency

The efficiency of the integration scheme can be considered by two factors including the cost of computation (i.e., intermediated memory, and floating point operations) and time consumption. The efficiency is particularly important in

Particle-Mesh simulation because of the large number of particles used. With a higher order leapfrog scheme, it leads to longer computational time. Conventionally, the simple second order leapfrog algorithm achieves the best balance between accuracy, stability and efficiency.

6.1.3 Tracking cell position

When particles are moving in the computational domain, the cell positions of particles in both the tetrahedral and hexahedral mesh must be tracked for the variable interpolation (i.e., velocity vectors). The tracking position in hexahedral meshes is simple to implement using the step-size because of the regularly structured mesh, whereas the tracking mesh position for tetrahedral ones is more complicated due to the irregular mesh structure. The general concept for the tracking position in tetrahedral mesh is performed using the conception of neighbouring cells sharing the same nodes with the previous cell position. The algorithm for checking particles in the mesh is evaluated using the shape function property $\{H\}$ in which if the particle lies in the considered cell, all values of shape function assigned for any node must be positive values.

In the designed software, the configuration of neighbouring cells were initialised using the configuration of the mesh, which was defined by definition 6.1. For example, neighbouring cells within depth level 2 of the node indicated by the solid square in Figure 6.2 are displayed by gray colour.

> *Definition 6.1:* A neighbouring cell within depth level i of node j is defined as a cell that is formed by neighbouring nodes within depth level i of node j

The important variable for the tracking cell algorithm is the *tracking_depth*, which defines the the depth level for neighbouring cells. The higher values of *tracking_depth* reduces the fault detection for setting trap status, but requires more computational time. The *tracking_depth* should be selected for optimal value, which is a compromise between the computational speed and accuracy. Additionally, the algorithm requires a memory buffer for storing the cell index,

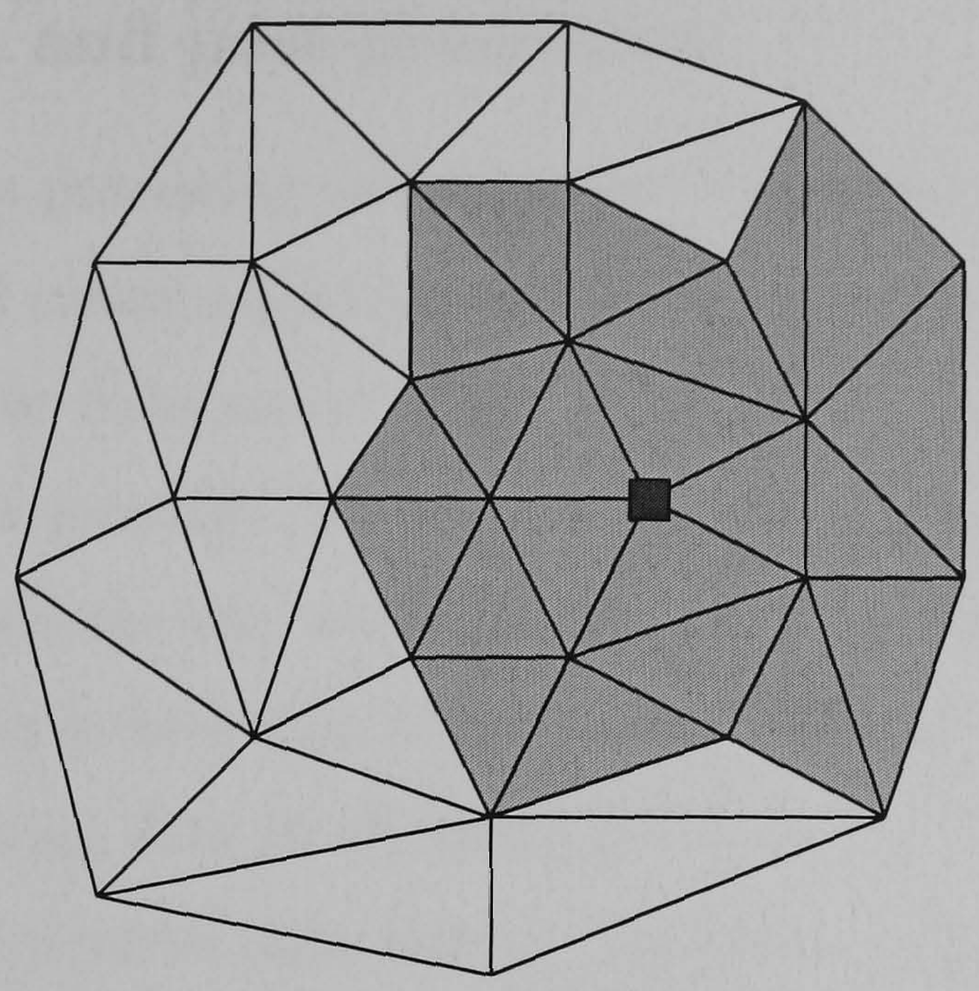

Figure 6.2: 2D mesh representation for neighbouring cells within depth level 2 of a node indicated by solid square

called the cell buffer. The details of the routine for tracking cell position are listed step by step as follows.

Step 1 Check the new cell position of the particle with the previous cell position. If the particle still lies in the same cell position, then exit the routine for tracking cell position

Step 2 Find the node of cells that has the nearest distance to the particle.

Step 3 Clear all data in the cell buffer.

Step 4 Find all neighbouring cells within depth level *tracking_depth* of the node that is obtained from Step 2 and store the cell indexes in the cell buffer.

Step 5 Search the new cell position of the particle from the cell indexes stored in the cell buffer. If the new cell position is found, then the new cell position will be updated. If the new cell position is not found, then the particle status will be set to the trapped status.

6.1.4 Report and post-processing

The report and post-processing was proposed to summarise the results of particle deposition and create a post-processing file to visualise the space charge field and the particle trajectories. The FIELDVIEW software, developed by the Intelligent Light company [94], was selected for visualisation.

Since the space charge field was represented by an independent hexahedral mesh, the space charge field data within the geometrical model could be obtained by interpolating data at all nodes of the model. These data are then written in the unstructured data format. Because of a large number of particles in the computation, sampling data of these particles was required. The format of the output file for visualisation was specified for the FIELDVIEW software, as given in [94].

6.1.5 Software Validation

The validation of the Particle-Mesh (PM) and particle trajectory calculations was set up to compute the deposition efficiencies of the unipolarly charged particles in a cylindrical tube using the same assumptions as those in Yu's study [202]. The analysis of deposition efficiency in a cylindrical tube by Yu assumes a slug flow profile and a uniform distribution of particles along the tube. In the computation of space charge force, the particle mesh-size also affects the accuracy of the results. Thus, an adequate mesh size for the PM calculation must be selected. The 3D tubular model used for the validation represents the airway generation number 9 of Weibel's model. Particles of 0.5 μm carrying $500e$ were used in this simulation at various particle concentrations. The inlet airflow was set up as a slug flow profile corresponding to the sedentary breathing condition.

Considering only the space charge computation, Figure 6.3 shows the deposition results of different mesh sizes compared with results obtained using the analytical predicted model by Yu. The deposition results agree with the

analytical results for the appropriate mesh size. At higher concentrations, the results of deposition efficiencies are less than the analytical results because the short-range force terms have a more predominant effect. Comparing three mesh sizes, the results of mesh size of $64 \times 64 \times 64$ is less accurate than those of higher mesh sizes, because the spatial discretisation of $64 \times 64 \times 64$ mesh is coarser than the higher mesh sizes. On the other hand, the higher mesh sizes require more computing time and memory resources. Thus, the mesh size should be selected to optimise both accuracy and computational time.

For the image force computation, the results are a function of distance between the nearest wall and a particle. The wall distance was calculated using the algorithm presented in section 4.5. These results are validated within a tube of generation 3 ($0.003\ m.$ in diameter). With a given number of $227,700$ particles, the average error of the nearest wall distance is $1.7.7 \times 10^{-6}\ m$, with a standard deviation of $0.172 \times 10^{-6}\ m$. This error occurs due to the discretisation of the triangular surface of the lung wall.

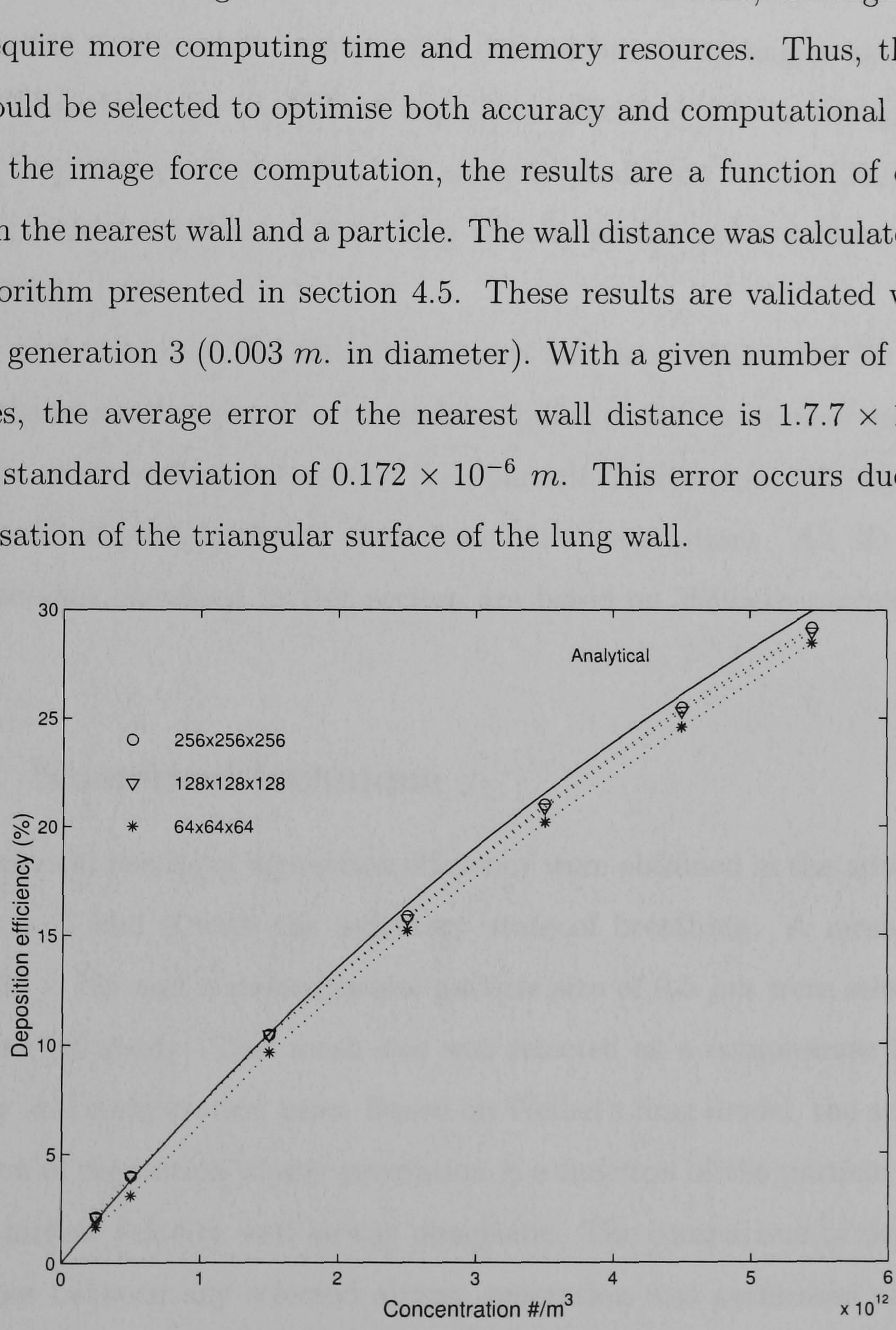

Figure 6.3: Deposition efficiencies of $0.5\ \mu m$ particles carrying $q = 500e$ due to space charge with various mesh sizes in the 3D tubular airway model

6.2 Aerosol transport and deposition in Simple tubular airway models

Morphologically based airway models are normally used for the theoretical and numerical studies of drug aerosol transport and deposition. These models are often represented by a series of cylindrical tubes starting from the trachea leading to the small airways with defined branching angles and gravity angles. Therefore, the analysis of deposition efficiency due to the space and image charge forces is complex, the analysis prediction by Yu [202] simplifies the particle conditions using a slug velocity profile and a uniform particle distribution.

The numerical model of aerosol transport and deposition in the 3D tubular airway model aims to give a better understanding of the variation of deposition efficiency under various parameters (i.e., particle distribution, velocity profile, and volume of particle cloud) apart from Yu's assumptions. All 3D tubular airway models discussed in this section are based on Weibel's morphological model.

6.2.1 Numerical technique

The numerical results of deposition efficiency were obtained in the airway generations 5, 7 and 9 with the sedentary state of breathing. A mesh size of $128 \times 128 \times 128$ and a monodisperse particle size of 0.5 μm were selected for the numerical study. This mesh size was selected as a compromise between accuracy and computation time. Based on Weibel's lung model, the analytical prediction of deposition in any generation is a function of the particle concentration, airflow velocity, and airway dimension. The comparison of deposition efficiencies between any selected airway generation was performed using the normalised concentration corresponding to 30% of predicted deposition efficiency by space charge force. The deposition efficiency of these selected airway generations was considered as only for a single tube in each airway generation.

Summary details of setup parameters in the airway generations 5, 7, and 9 are given in table 6.1.

Table 6.1: Setup parameters for various airway generation numbers

Variables	Generation 5	Generation 7	Generation 9
tube diameter (cm)	0.35	0.23	0.154
tube length (cm)	1.07	0.76	0.54
tube volume (cm^3)	0.10295	0.03158	0.01006
inlet flow (cm/s)	90.403	52.337	29.185
particle sizes (μm)	0.5	0.5	0.5
charge values (e)	500	500	500
No. of particles*	875040	217880	54818

*calculated using 30 % deposition efficiency by space charge force based on Yu [202]

6.2.2 Results and discussion

Considering only the space charge force, the effects of particle spatial distribution (uniform and parabolic distributions) on the deposition efficiency in the 3D tubular airway models were investigated. The parabolic distribution implied that distribution density function for radial coordinates in the parabolic regime is given by

$$\frac{C(r)}{C} = 2\left(1 - \left(\frac{r}{R}\right)^2\right) \tag{6.28}$$

where $C(r)$ and C are the local and average particle concentrations, respectively.

The numerical results of both uniform and parabolic distributions with slug airflow are shown in Figure 6.4 . The results are also compared with the predicted deposition efficiency based on a uniform particle distribution. It shows that the distribution of particle position has very large effect on particle deposition. The parabolic distribution has a lower deposition efficiency than

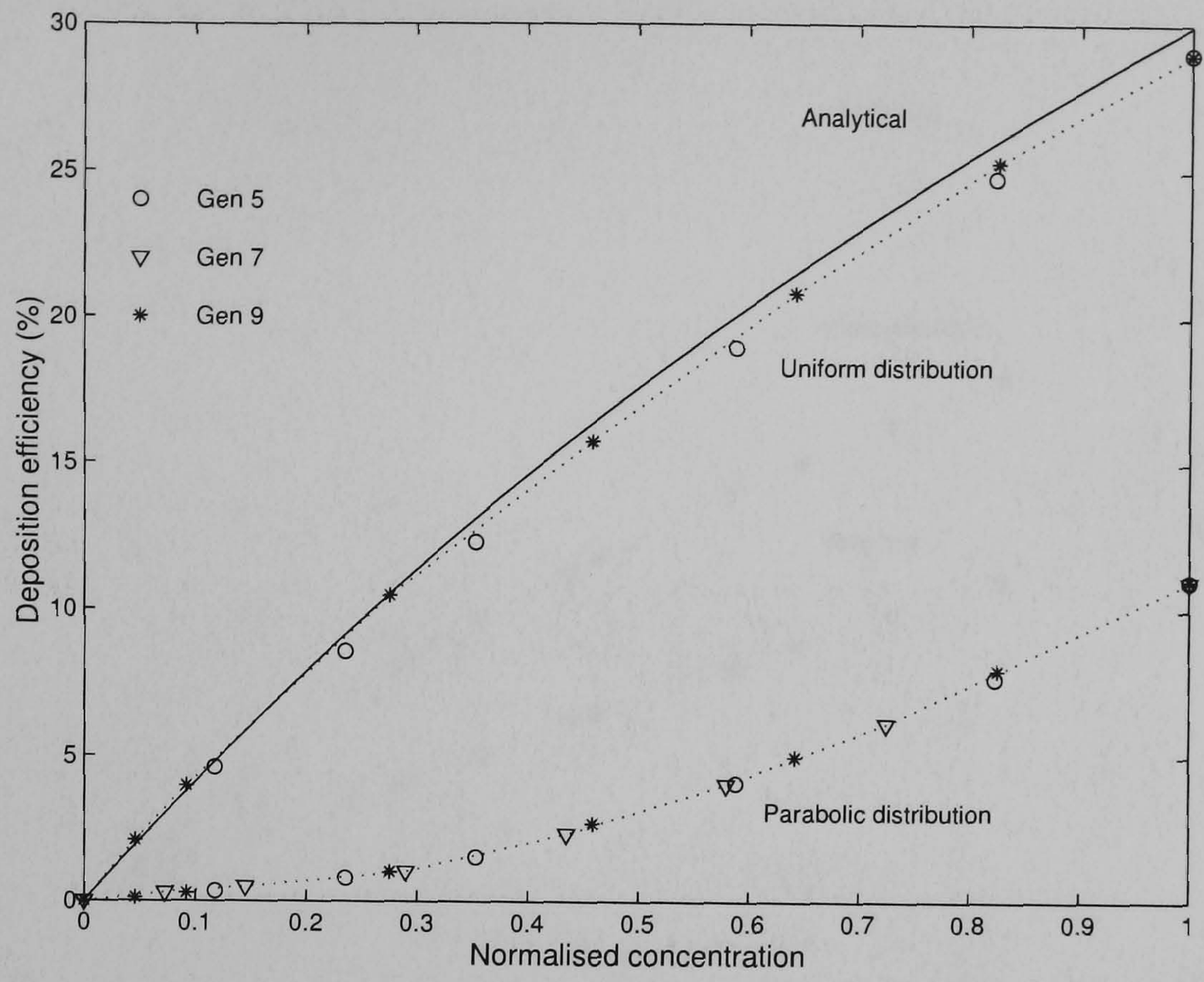

Figure 6.4: Deposition efficiencies of 0.5 μm particles carrying $q = 500e$ due to space charge with the uniform and parabolic distribution in the 3D tubular airway model

that of a uniform distribution, because many particles are located near the central axis of the tube.

This theoretical analysis assumes that the number of particles entering the system is equal to the number of particles leaving at the outlet under the given residence time. Investigating the effect of flow profile without adding particles to the system, the numerical results of the uniform particle distribution in both slug and parabolic flow profiles are shown in Figure 6.5. Deposition efficiencies of both slug flow and parabolic airflow with a uniform distribution of particle positions are less than the predicted deposition efficiencies. The numerical results for the parabolic profile has a deposition efficiency higher than the slug profile, since the residence times of particles near the airway wall with the a parabolic profile are longer than that for a slug profile. It therefore leads to greater deposition efficiency.

Provided the particle cloud concentrations are the same, the initialised volume of the particle cloud, represented in terms of the percentage of tube

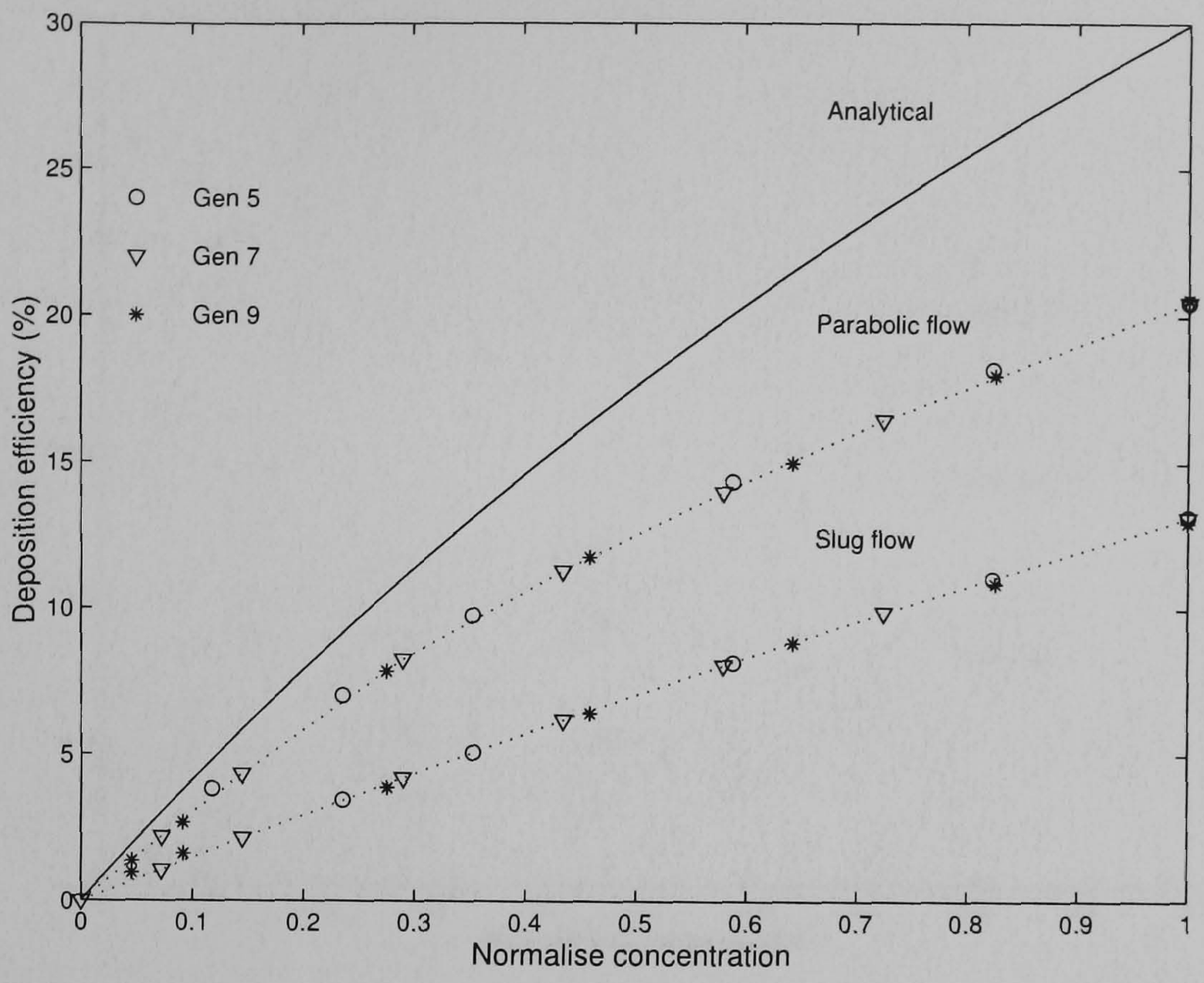

Figure 6.5: Deposition efficiencies of 0.5 μm particles carrying $q = 500e$ due to space charge with the slug and parabolic flow profiles in the 3D tubular airway model

volume, also has affects on the deposition efficiency as shown in Fig 6.6. The higher initialised volume has a greater deposition efficiency than the lower initialised volume, because of a stronger space charge field. The deposition efficiency also increases with the incremental particle concentration.

Many theoretical predictions approximate the deposition efficiency of space charge force and image charge force as a linear combination term (i.e., Yu [203], Balachandran et al. [10], and Bailey et al. [8]). Figure 6.7 shows the simulation results of both space and image charge forces in airway generation 9. The comparison of the deposition efficiency difference between analytical predictions and numerical results was discussed in the previous section. The error in the space charge at high concentrations occurs because the short-range force has more predominant effects. Considering the image charge force at low concentrations, numerical results show lower deposition than those derived from predicted by analytical expressions. The linear combinations of the space and image charge efficiencies (a summation of two solid lines) are compared

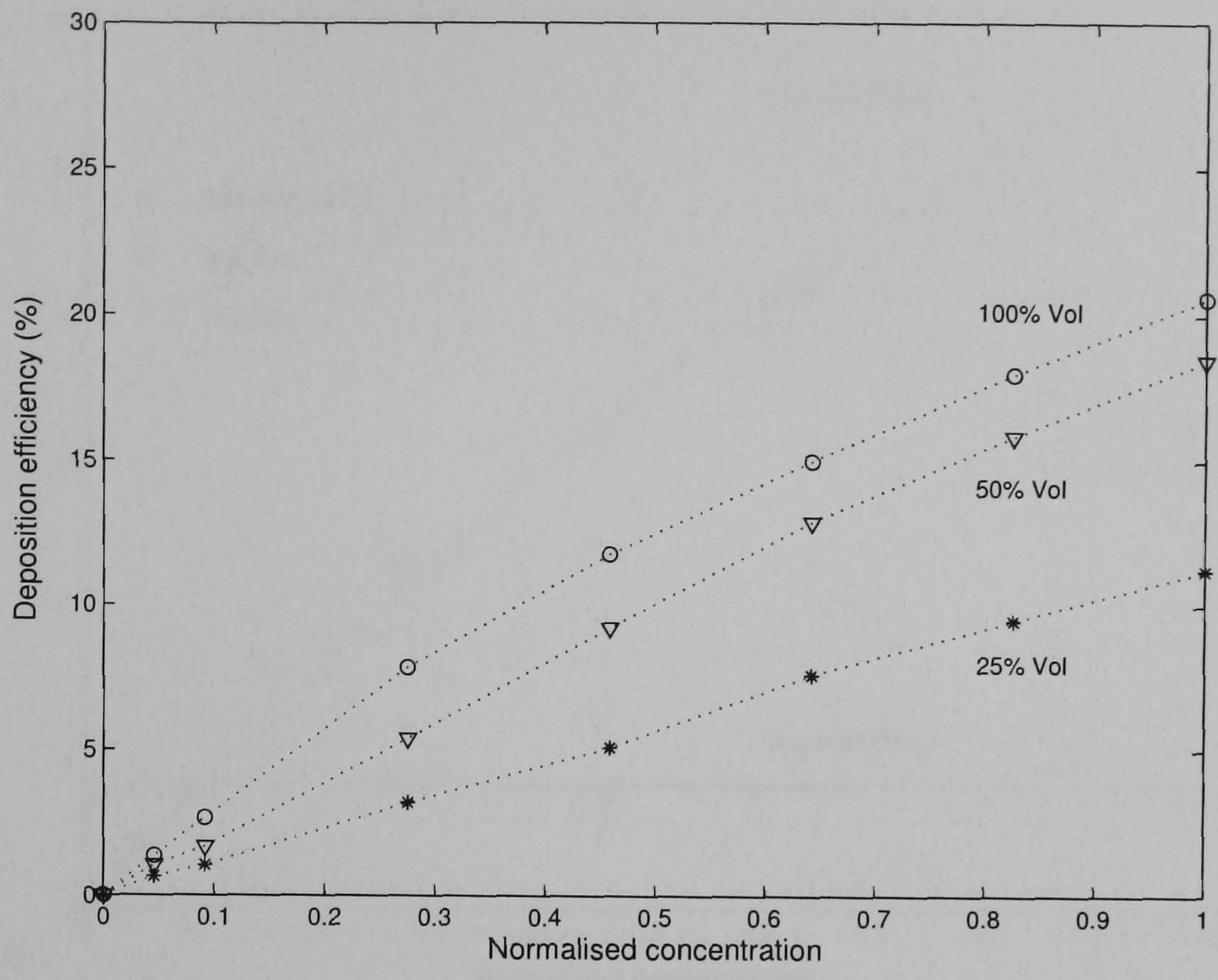

Figure 6.6: Deposition efficiencies of 0.5 μm particles carrying $q = 500e$ due to space charge with various initialised volume

with the numerical results including both space and image charge forces in the particle trajectory equation (indicated by circles). The linear combination of efficiencies overestimates the numerical results obtained directly from the combination of forces in the particle trajectory equation. At higher concentrations, where the space charge force is a dominant mechanism, the deposition efficiency for both space and image charge forces is similar to the deposition efficiency due to space charge force only. It implies that the linear combination of the space and image charge efficiencies give a good approximation of deposition efficiency for both space and image charge forces when the space charge efficiency is not higher than the image charge efficiency.

These results show that the particle distribution, the velocity profile and the volume of particles would influence the deposition of charged particles in airways. However, these results are based on the tubular model without considering the effect of flow near branching points. Charged aerosol transport and deposition in models which account for the branching point between airway

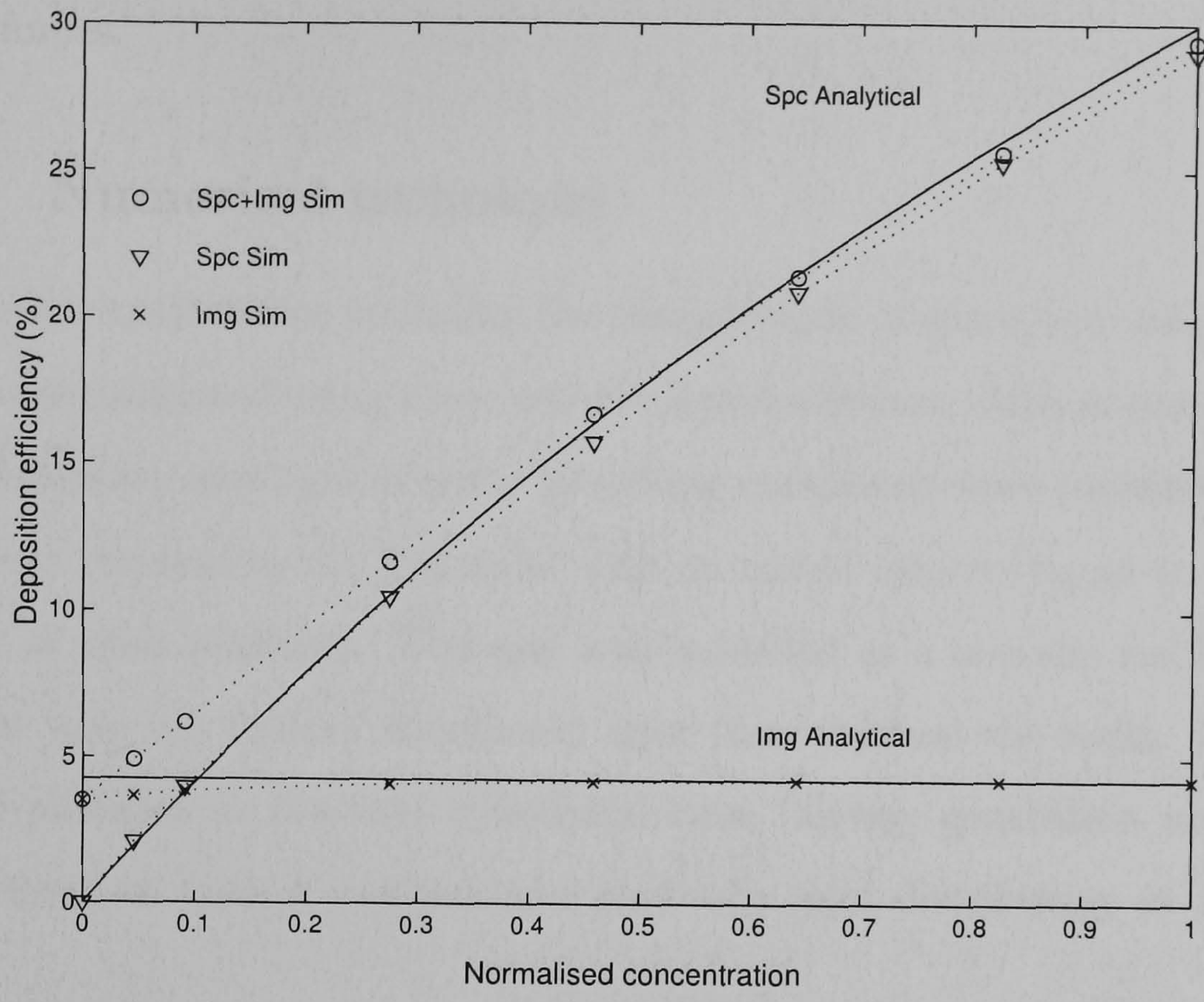

Figure 6.7: Deposition efficiencies of 0.5 μm particles carrying $q = 500e$ due to both space and image charge in the 3D tubular airway model

generation will be discussed in the next section.

6.3 Aerosol transport and deposition in Bifurcation airways model

Weibel's tubular structure does not account for the branching region of the model, and the analytical deposition can estimate only average deposition without giving the local deposition pattern. The distribution of particles also can be altered by the airflow, especially in the upper bronchial region (previously discussed in section 5.3). The study in the 3D bifurcation airways aims to investigate the electrostatic force effects on particle deposition patterns under various breathing conditions, especially near the branching tube. The study also provides the local deposition pattern of charged aerosols. The study of deposition efficiencies with the effect of electrostatic forces in this section is separated into 2 cases: 1) only image charge force, 2) both image and space

charge forces.

6.3.1 Numerical technique

The particle trajectories including the computation of space and image charge forces were computed using the novel developed software. Airflows corresponding to sedentary and light activity breathing conditions were considered. Particles were released in the first tube with an initial velocity equal to the fluid velocity at their positions. The wall was modelled as a non-slip rigid surface. Particles were not further considered after they touched the walls. Distributions of particles in the first cylindrical tube (airway generation number 3) were defined as both a uniform and parabolic inlet distribution in the axial plane.

In the first case, the study focuses only on the effects of image charge force that represents a low particle cloud concentration. A total number of particles was set up as 50,000 for this case. In the second case, the numerical study investigated the deposition efficiency with both space charge and image charge forces. The mesh size in the PM method was defined as 128×128×128. Two particle concentrations of 2.0×10^{11} and 2.0×10^{12} $particles/m^3$ were selected to define the number of initial particles in the first airway generation of the model.

The numerical model assumed no charge elimination as a result of the high humidity in the lung, because of the short residence time in tracheobronchial region (< 50 ms for the sedentary breathing condition using Weibel's model).

6.3.2 Model validation and preprocessing

The validation of the numerical model in the 3D bifurcation airway was set up to compute the deposition efficiencies of uncharged particles and then compare it with the experimental data provided by Kim and Fisher [104] in a range of Reynolds number 944-2831. The particle size and density were defined

corresponding to a Stokes number ranging between 0.02 - 0.10 and an inlet Reynolds number of 500 and 2000.

The comparisons between the numerical results and the experimental data are shown in Figure 6.8. They show that the numerical results agree with the experimental results. The Reynolds number also affects the results of deposition efficiency in which the results for a higher Reynolds number are greater than those for a low Reynolds number. The errors between numerical results and experimental results in the first bifurcation are approximately 3% for the Stokes number greater than 0.05. In the second bifurcations, the errors are approximately 1% for the numerical results of Reynolds number 2000, but they are greater values for the Reynolds number 500. Therefore, the maximum Stokes number of particles used in the simulation is less than 0.01, the deposition efficiency in the model is nearly zero.

In the preprocessing for the computation of image charge, the nearest wall distance was determined using the developed software. The magnitudes of the nearest wall distance vector from any position within the model are shown in Figure 6.9(a), which gives the contour at a plane z=0. Figure 6.9(b) also shows the contour on cutting planes at various x values. These vectors have directions corresponding to the nearest face on the wall boundary.

6.3.3 Results and discussion

6.3.3.1 Depositions of charged particles by the image charge force

This section focuses on the effect of the image charge force on deposition of charged aerosols. Numerical simulations of monodisperse aerosol under sedentary and light activity breathing conditions with particle sizes of 0.3, 0.5, 0.7, and 1.0 μm, respectively, are performed.

The airflow in the 3D bifurcation representing the large airways typically has a high Reynolds number ($450 < Re < 1450$) corresponding to the breathing conditions. A distinct shear layer occurs along the inside wall with the

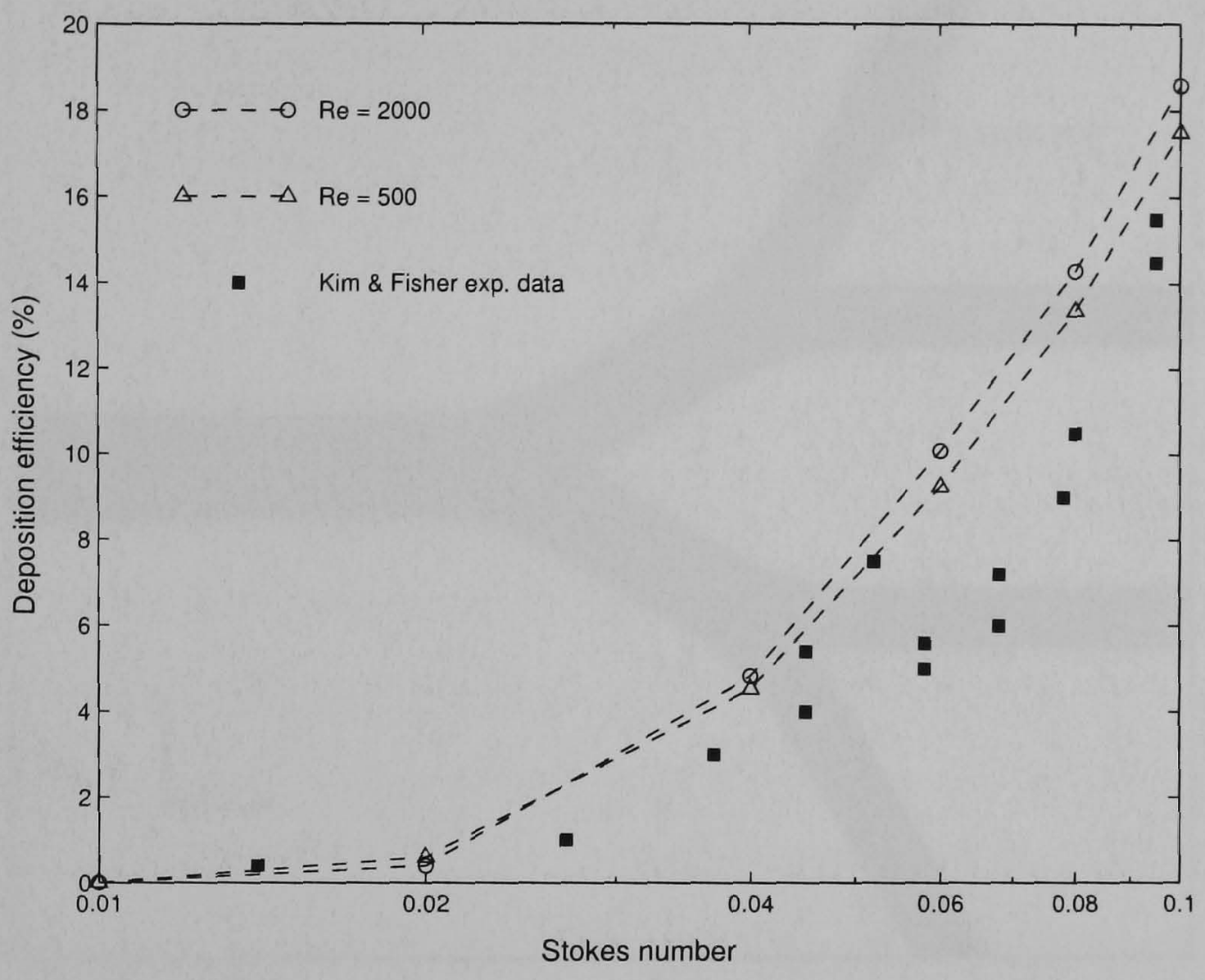

(a) first bifurcation

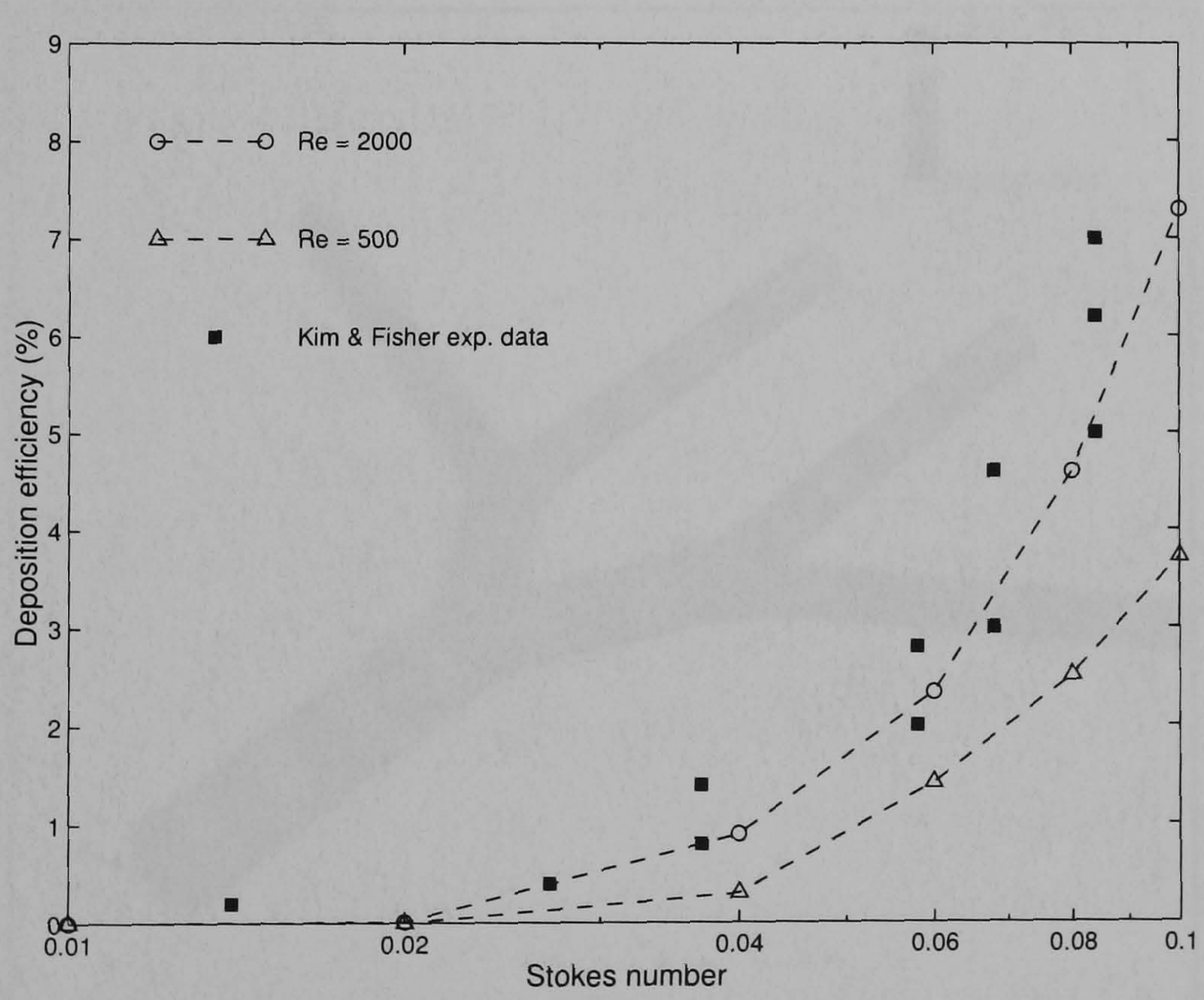

(b) second bifurcation

Figure 6.8: Comparison deposition efficiencies of numerical results and curve fitted experimental data by Kim and Fisher [104]

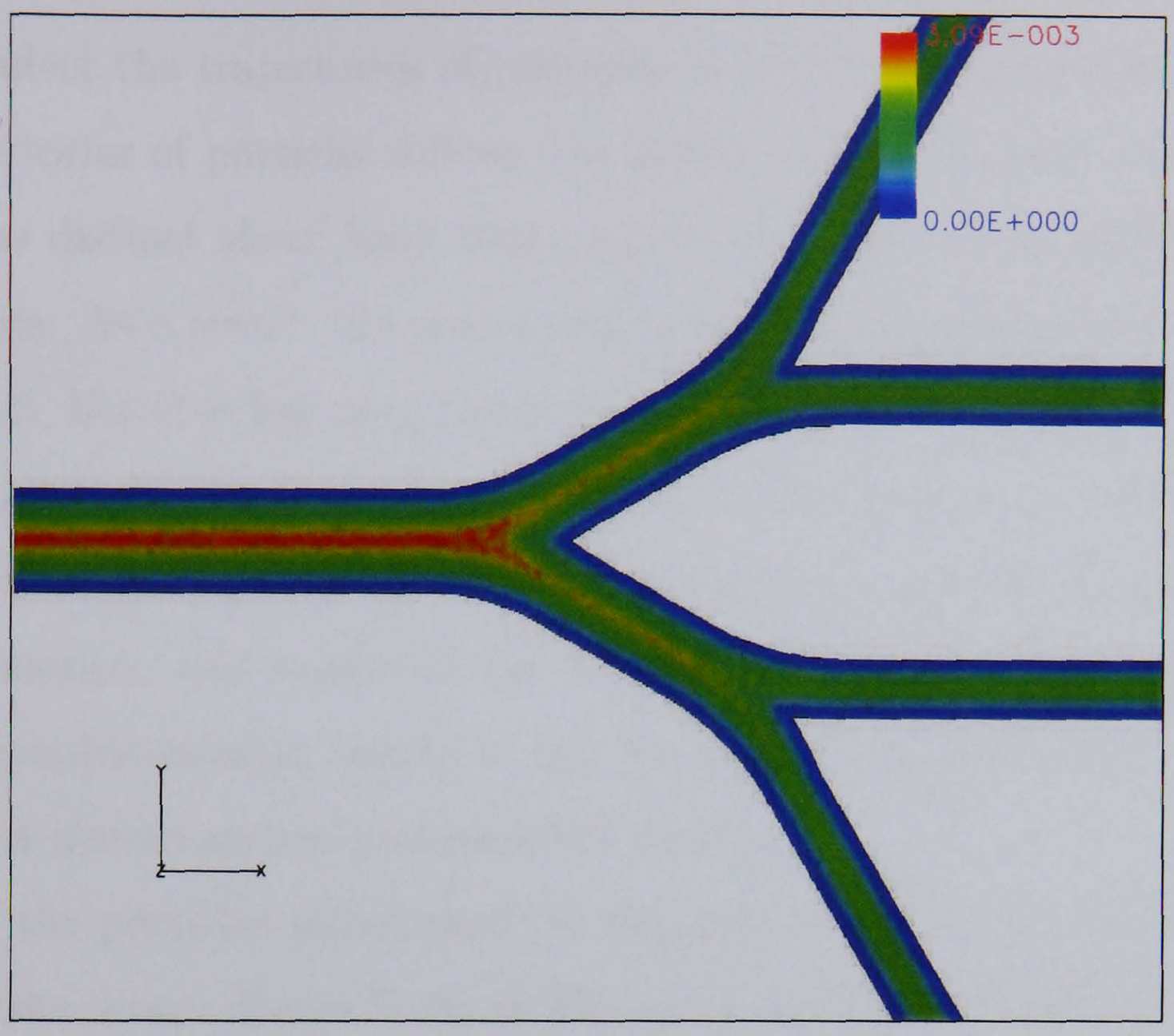

(a) at a cutting plane z = 0

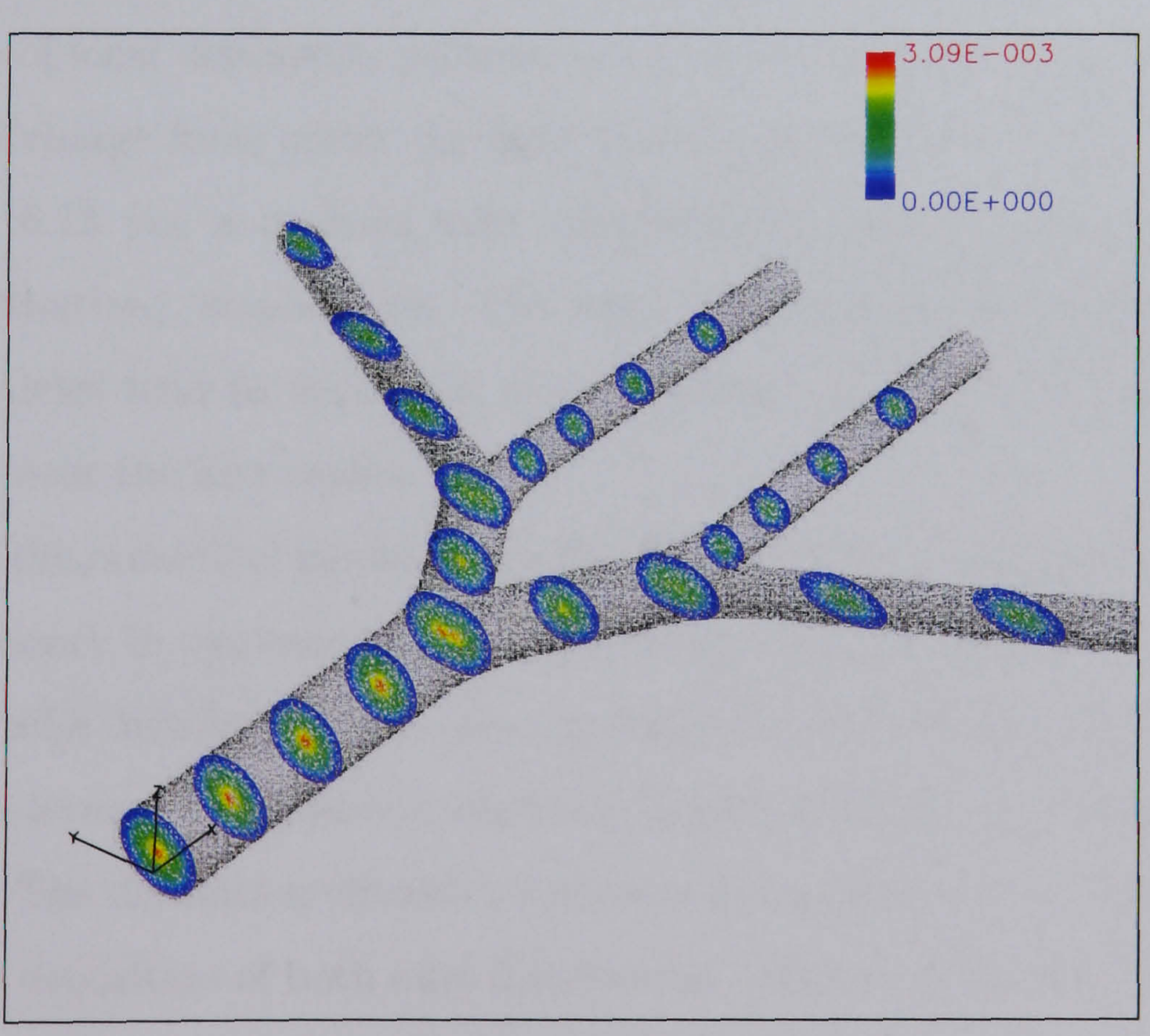

(b) at various cutting planes in x-axis

Figure 6.9: Magnitude of the nearest wall distance vector in the 3D bifurcation airway model (unit: m)

recirculation zone near carina as discussed in section 5.3. The fluid forces strongly affect the trajectories of particles as shown in Figure 6.10 and 6.11. The trajectories of particles follows the profile of high velocity (especially in that of the distinct shear layer near carina), and then move into the second bifurcations. As a result, the concentration of particles is high near the inner airway wall, but it is low near the outer airway wall as shown in Figure 6.10 (c)(d) and 6.11 (c)(d). Under both sedentary and light activity breathing conditions, the secondary flow also affects the trajectory of particles moving with a vortex motion, and results in the longer residence time of particles. The higher Reynolds number results in the stronger effect of secondary flow and reduces the instantaneous concentration rapidly.

When the particles move closer to the airway wall near the carinas, the effects of the image charge force on the aerosol transport increase. Particles may then deposit near these regions in response to the image charge force. Examples of local deposition patterns in the bifurcation model resulting from the image charge force under the light activity breathing condition are given in Figure 6.12 (for a uniform inlet distribution), and 6.13 (for a parabolic inlet distribution), respectively. The local deposition patterns indicate that many particles tend to deposit in the transition region between generations, especially near the first carina.

When the numerical model varies the charge values on aerosols, the deposition efficiency in response to the image charge force for both of uniform and parabolic inlet distributions are given in Figure 6.14 and 6.15, respectively. At low charge levels, the deposition efficiency increases rapidly as the charge value increases. The deposition efficiency increases less rapidly at the higher charge level. The deposition of both inlet distribution patterns in the first bifurcation has greater deposition efficiency than in the second bifurcation, therefore the airflow velocity decreases with the distinct shear layer bending away from the second carinas. At the same charge value, a small particle size is affected more by the image charge force than a larger particle size because the small particle

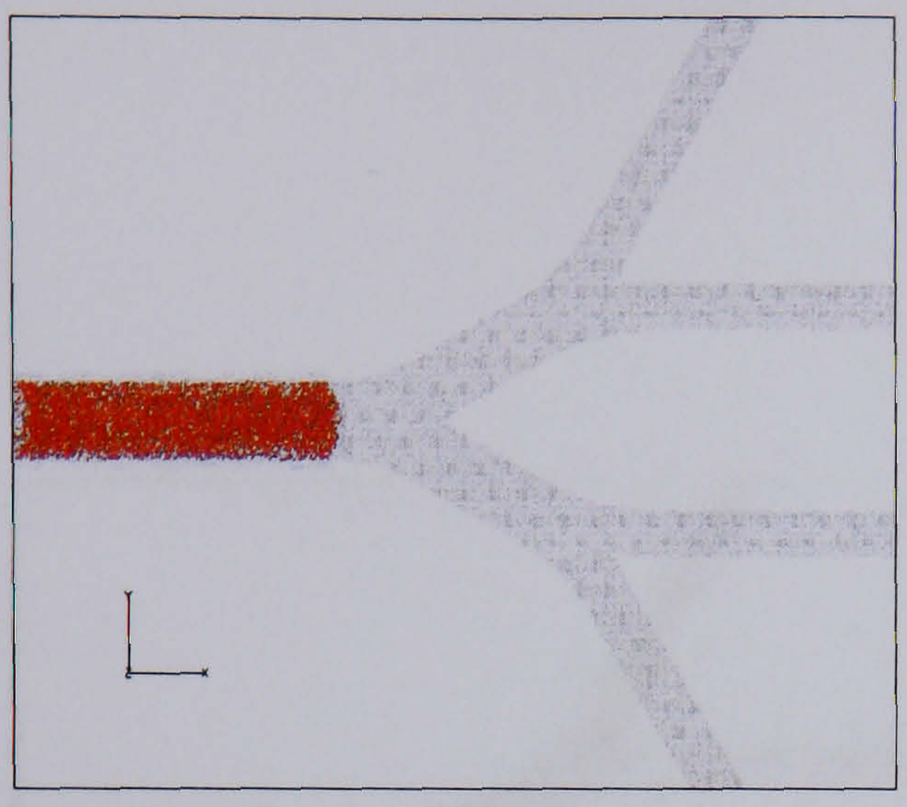

(a) $t = 0.2\ ms$

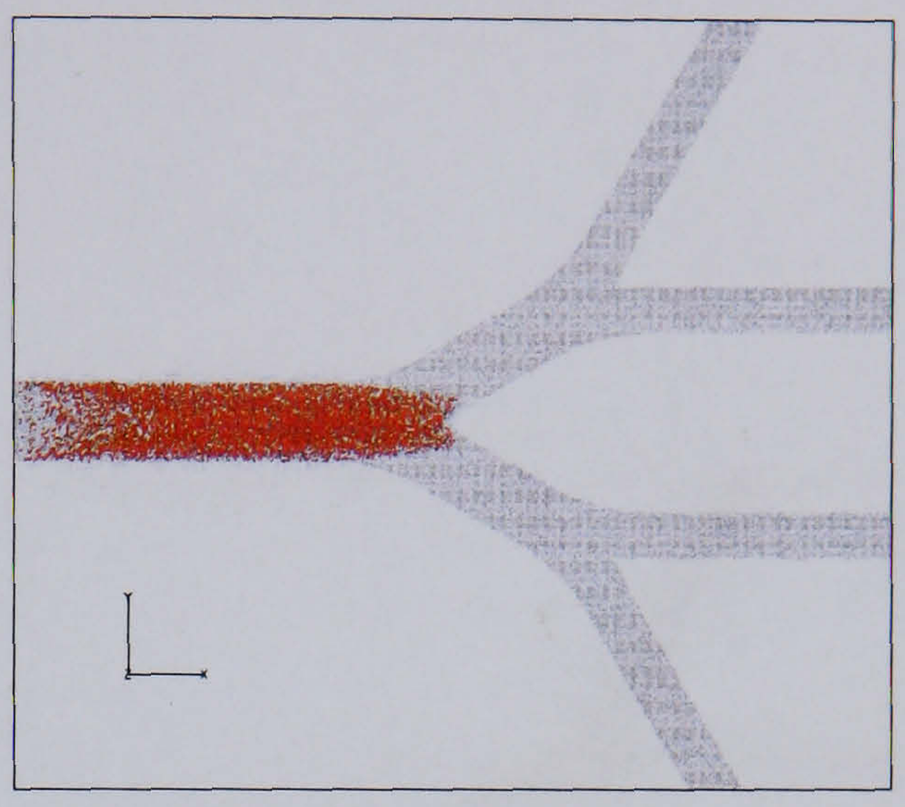

(b) $t = 2\ ms$

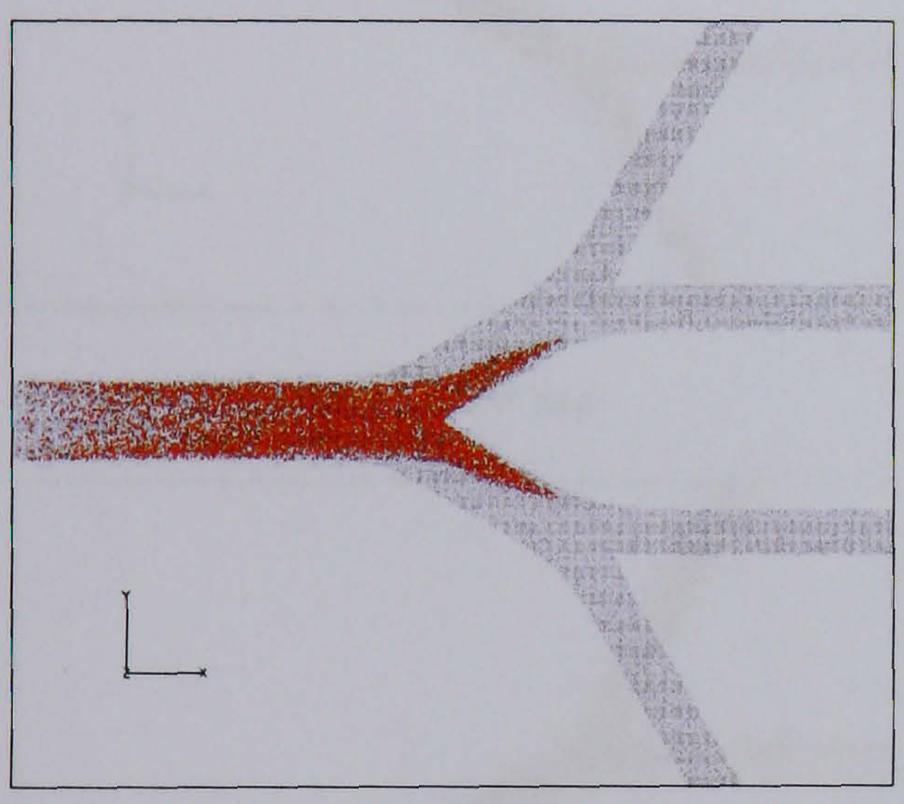

(c) $t = 4\ ms$

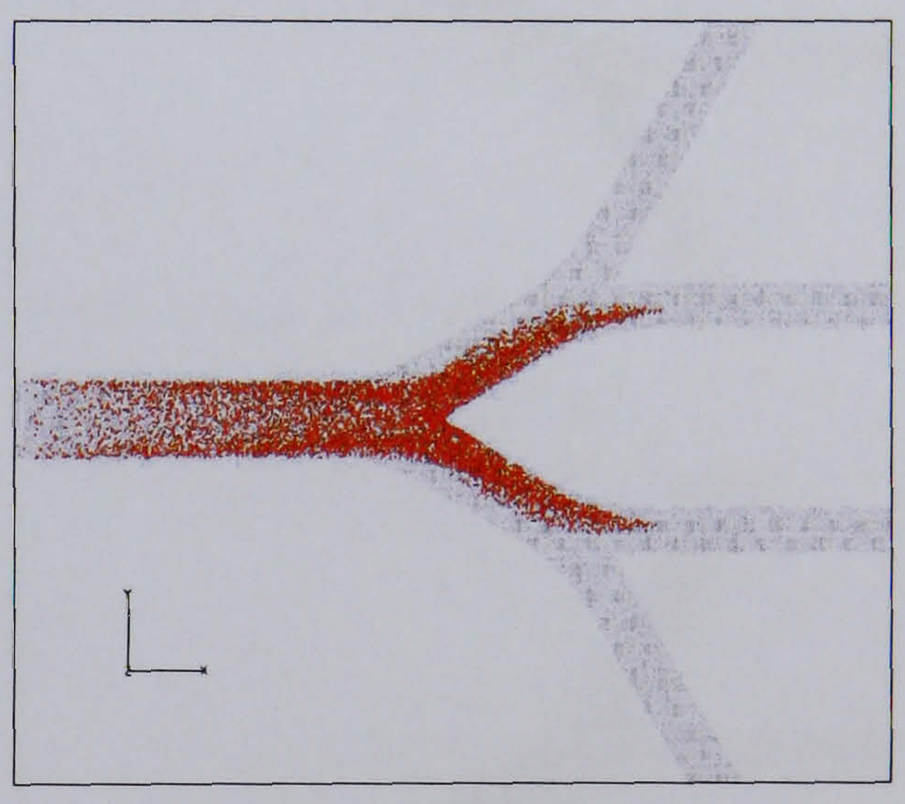

(d) $t = 6\ ms$

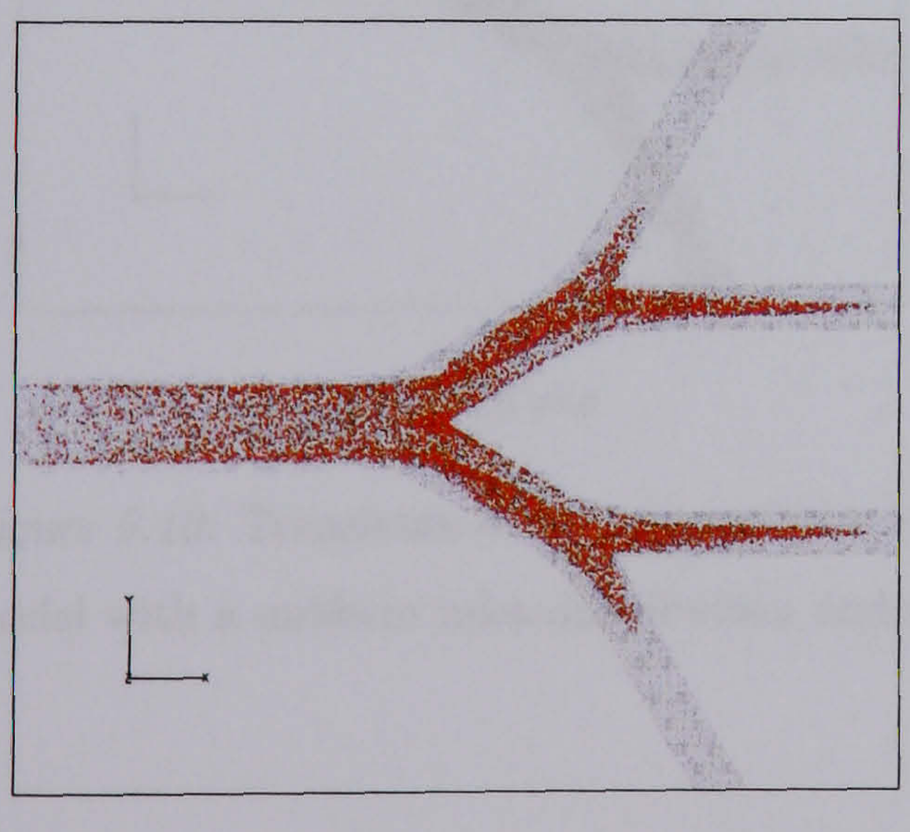

(e) $t = 10\ ms$

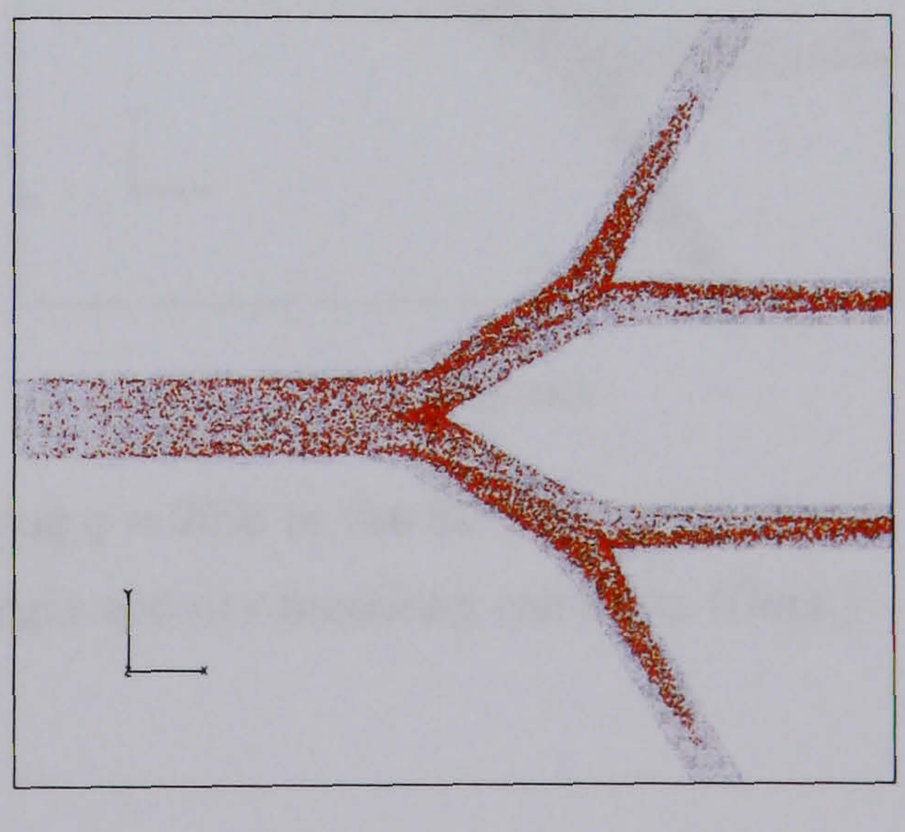

(f) $t = 14\ ms$

Figure 6.10: Transients of 0.5 μm particles carrying $q = 250e$ in the 3D bifurcation airway model with a uniform inlet distribution under a light activity breathing condition

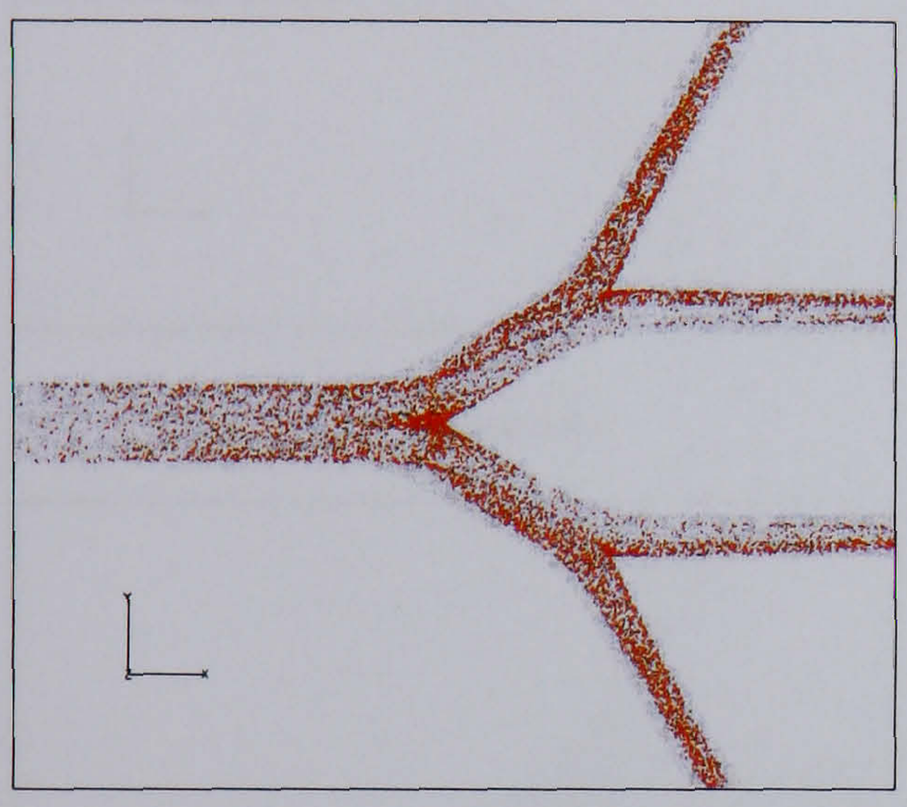

(g) $t = 18\ ms$

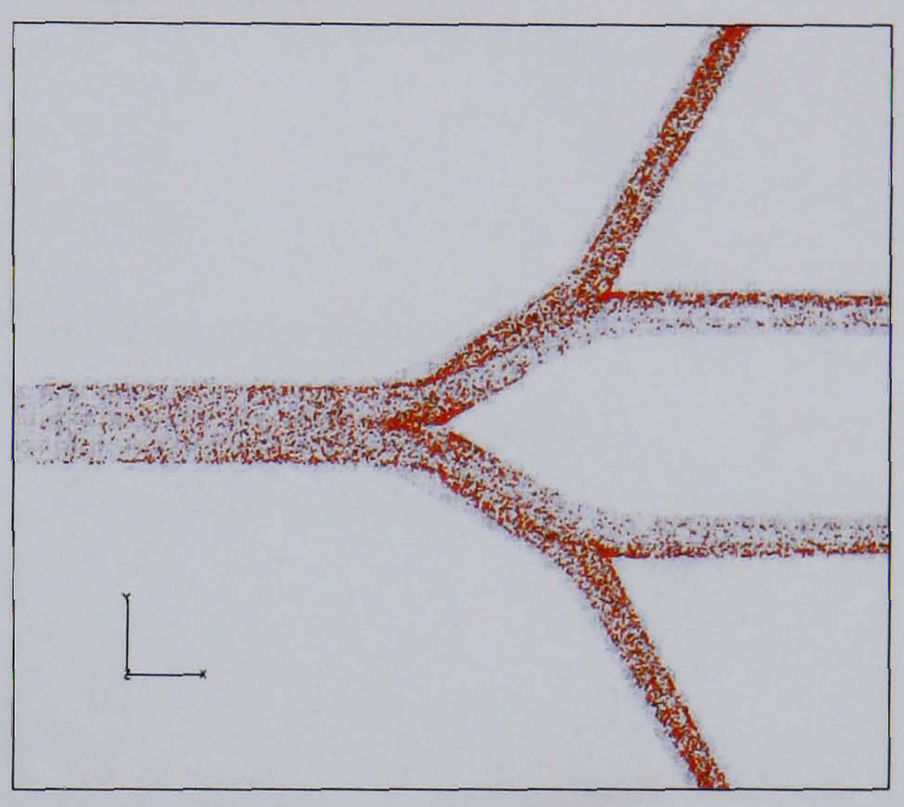

(h) $t = 22\ ms$

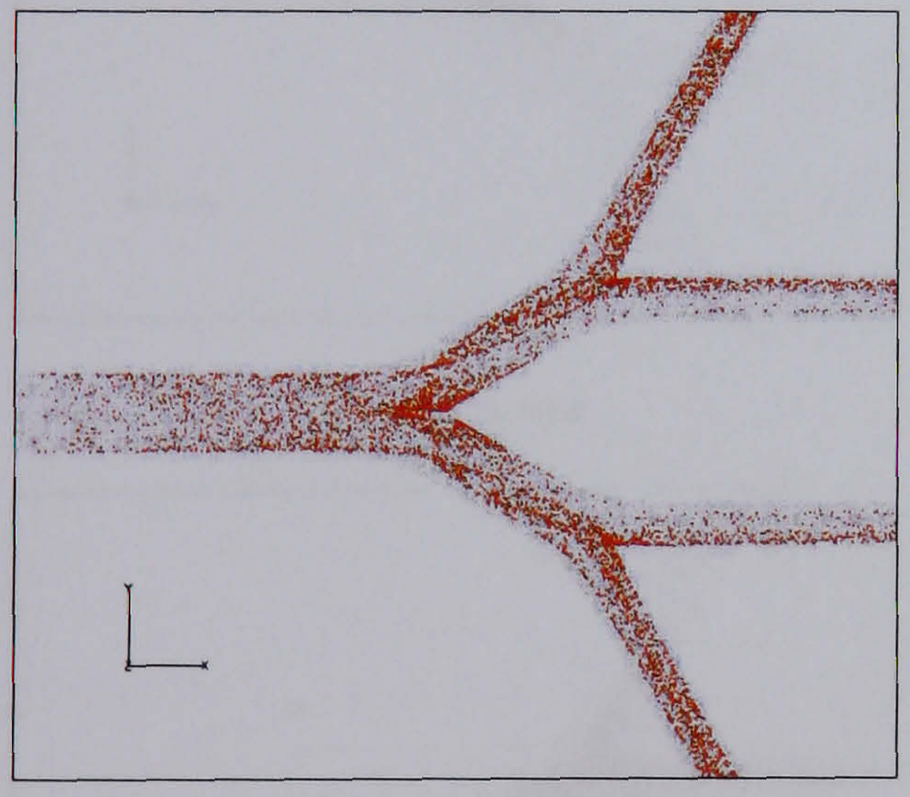

(i) $t = 26\ ms$

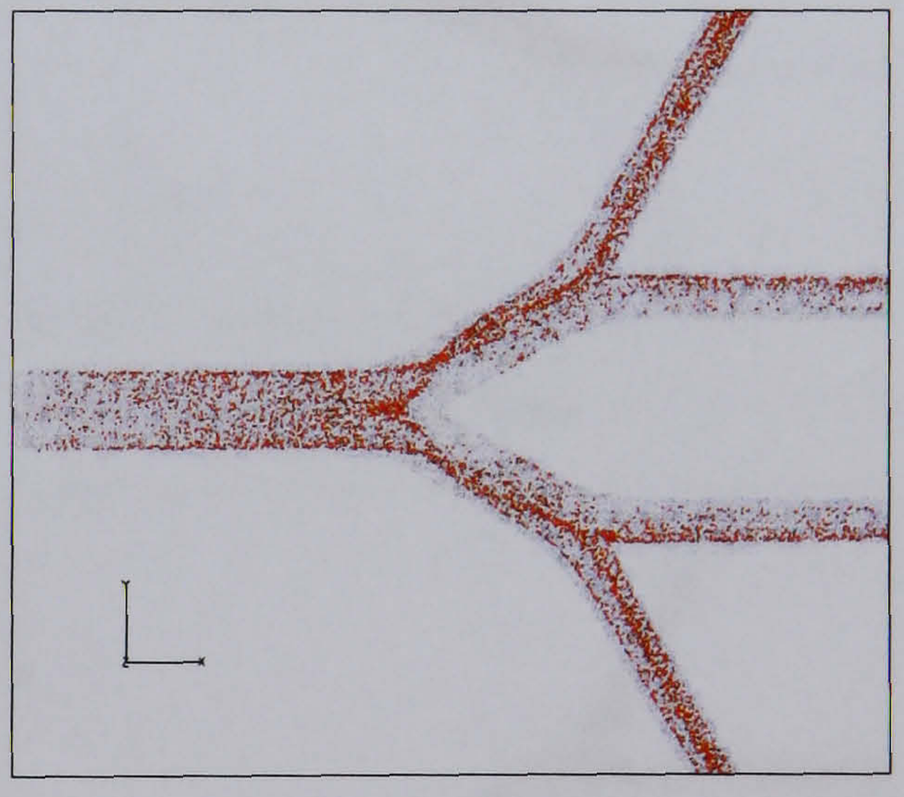

(j) $t = 30\ ms$

Figure 6.10: Transients of 0.5 μm particles carrying $q = 250e$ in the 3D bifurcation airway model with a uniform inlet distribution under a light activity breathing condition (Cont.)

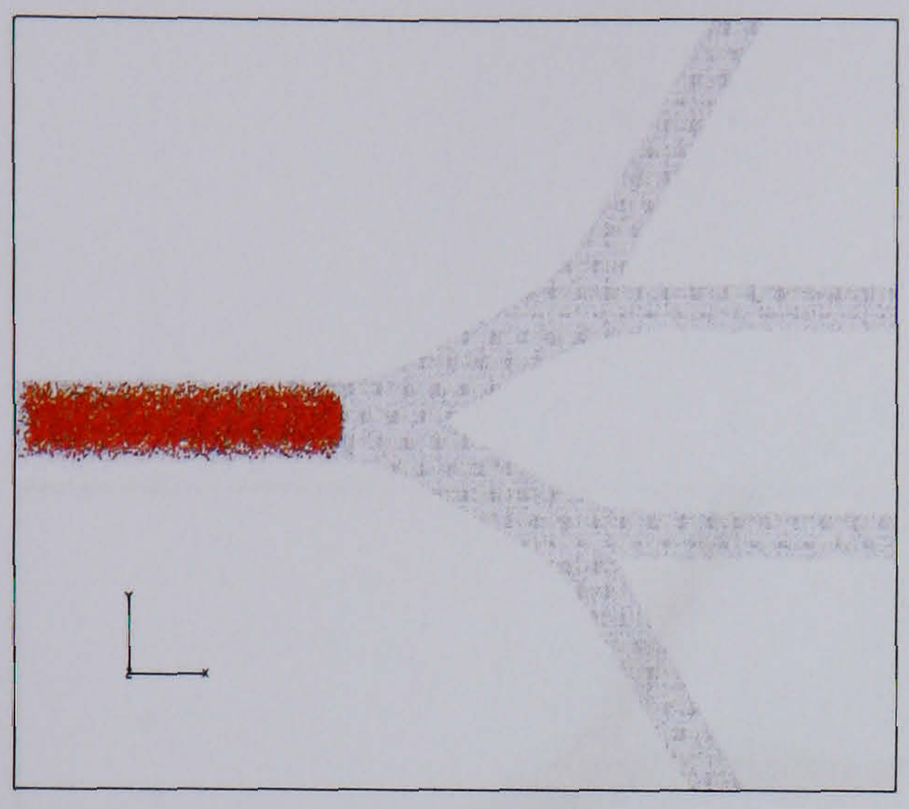

(a) $t = 0.2\ ms$

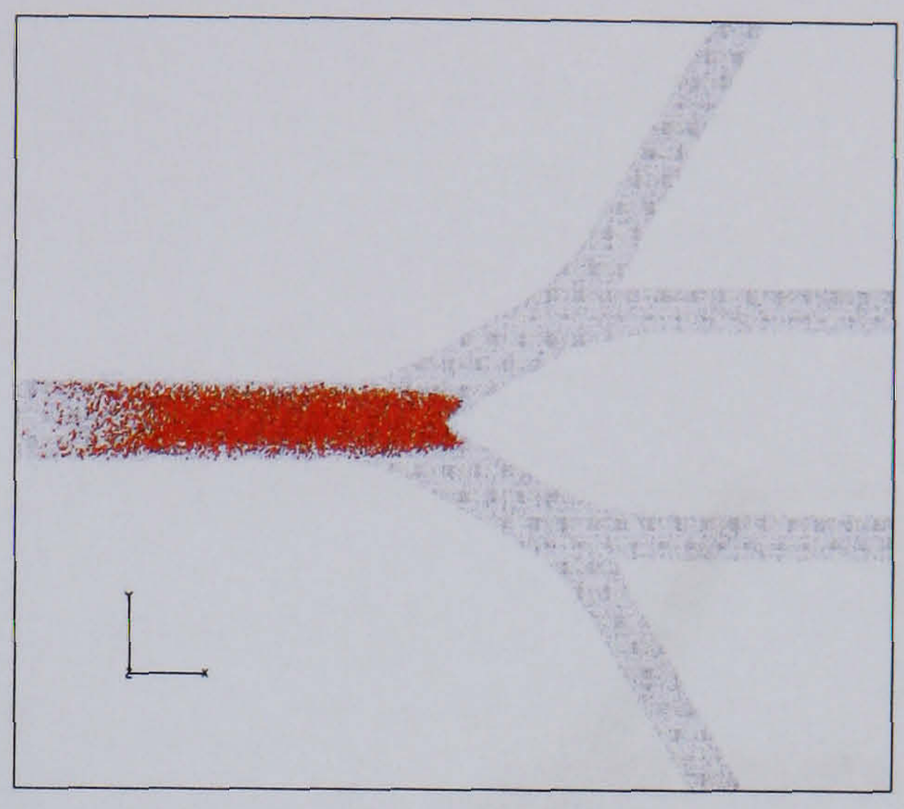

(b) $t = 2\ ms$

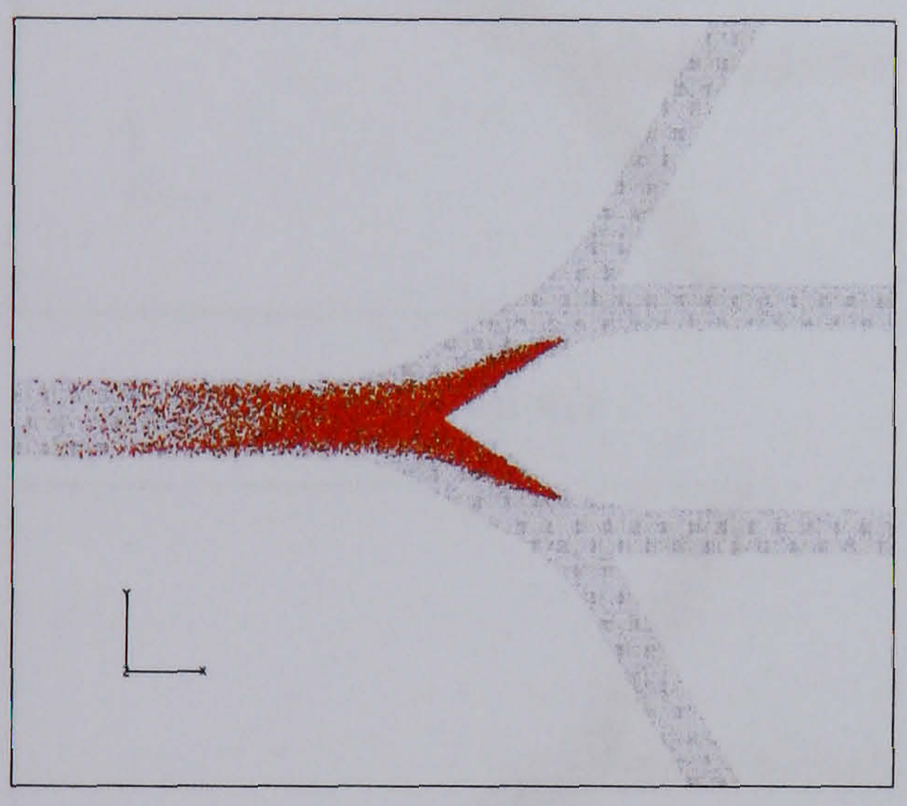

(c) $t = 4\ ms$

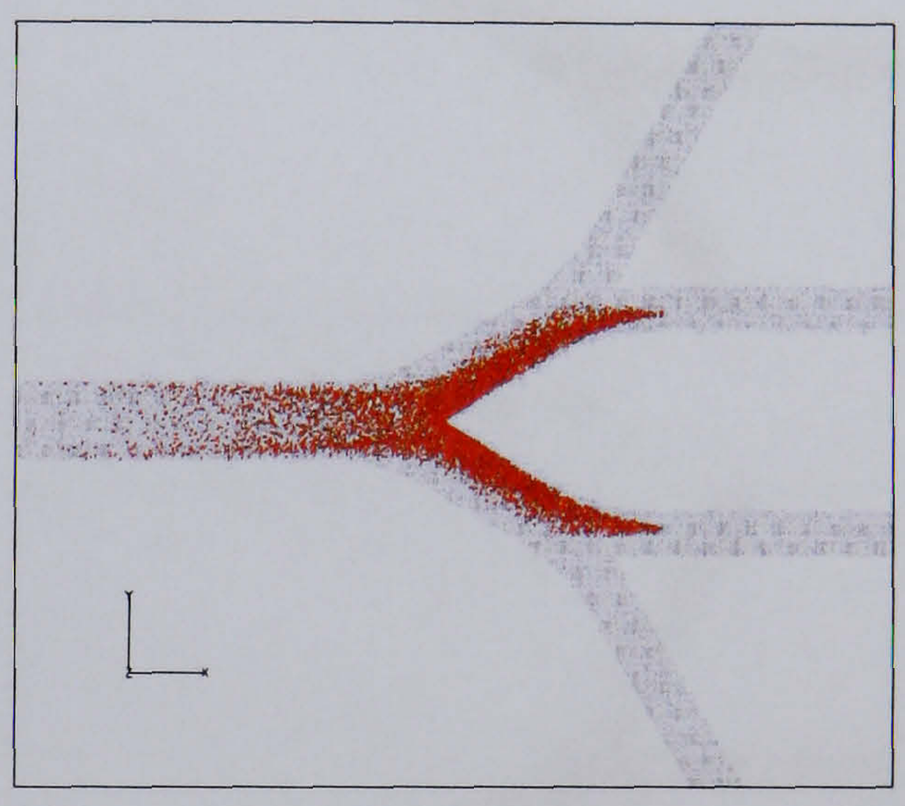

(d) $t = 6\ ms$

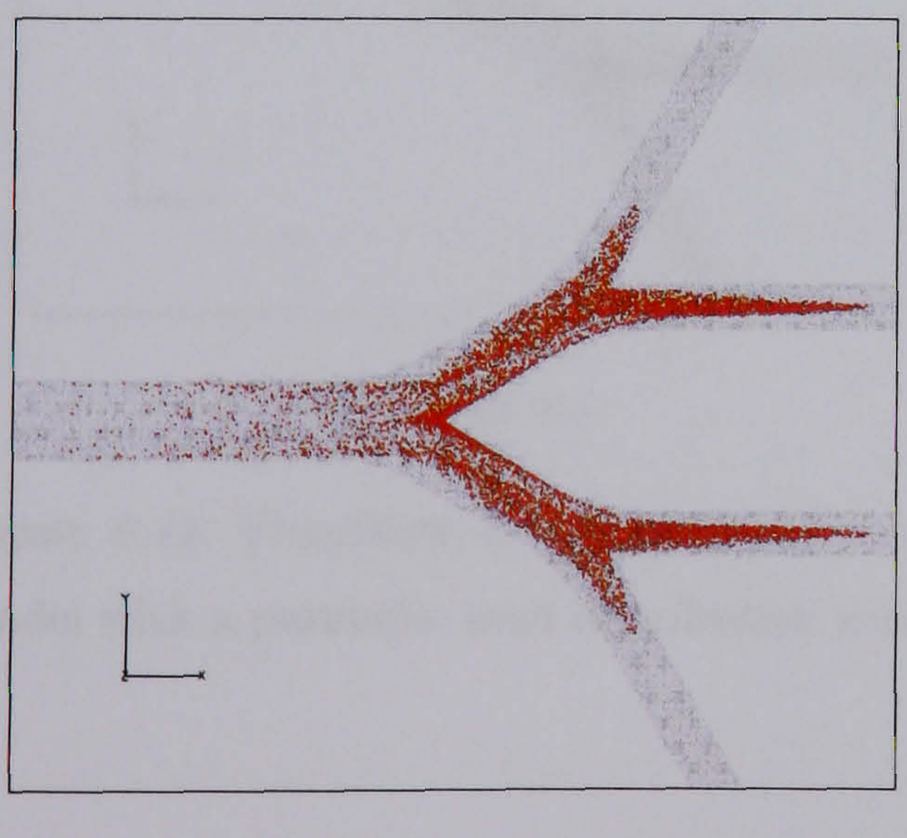

(e) $t = 10\ ms$

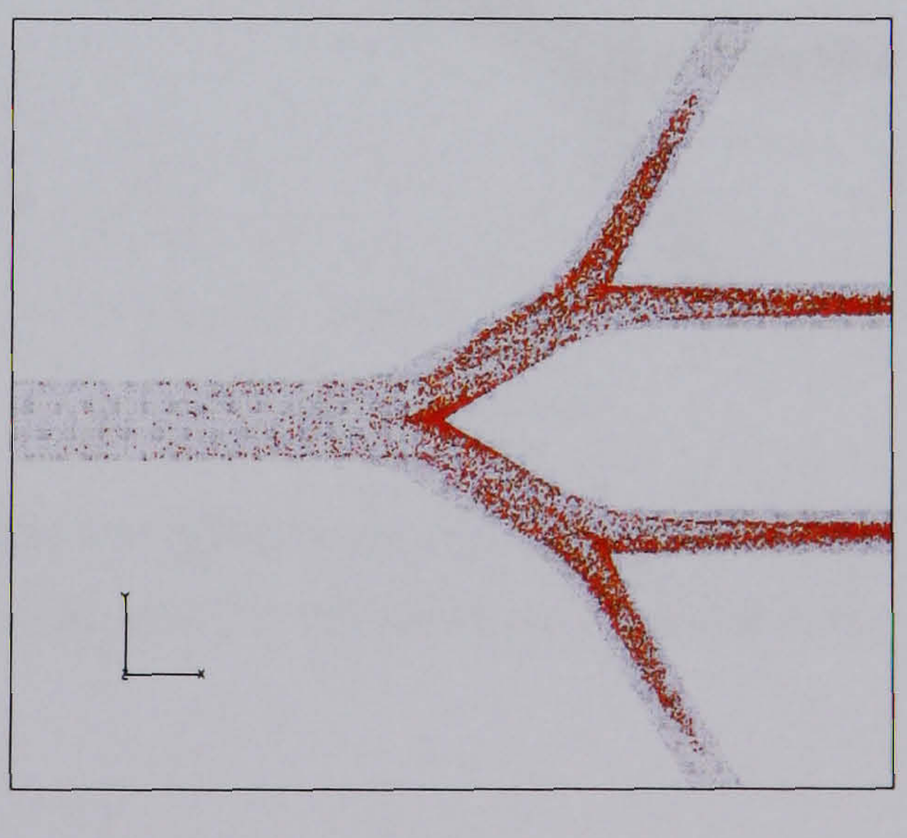

(f) $t = 14\ ms$

Figure 6.11: Transients of 0.5 μm particles carrying $q = 250e$ in the 3D bifurcation airway model with a parabolic inlet distribution under a light activity breathing condition

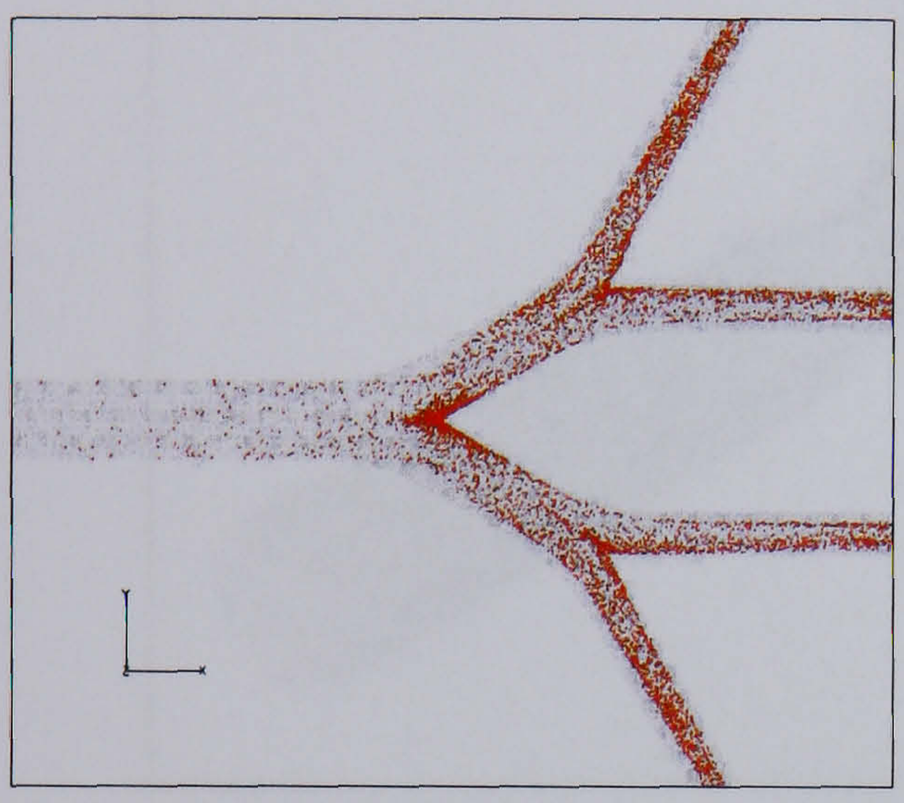

(g) $t = 18\ ms$

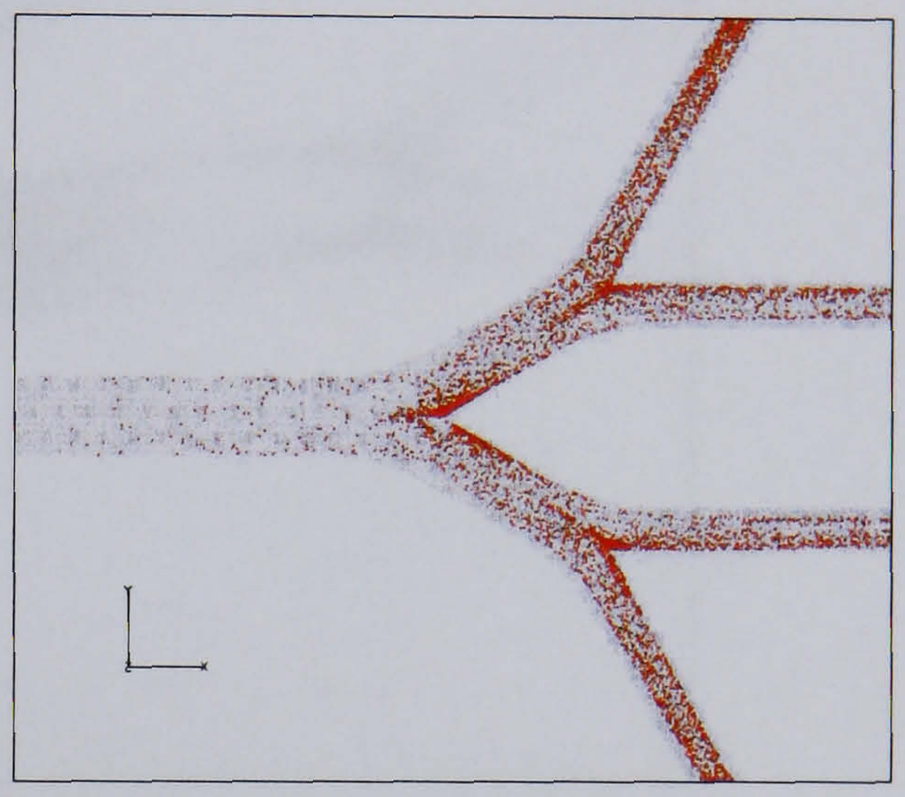

(h) $t = 22\ ms$

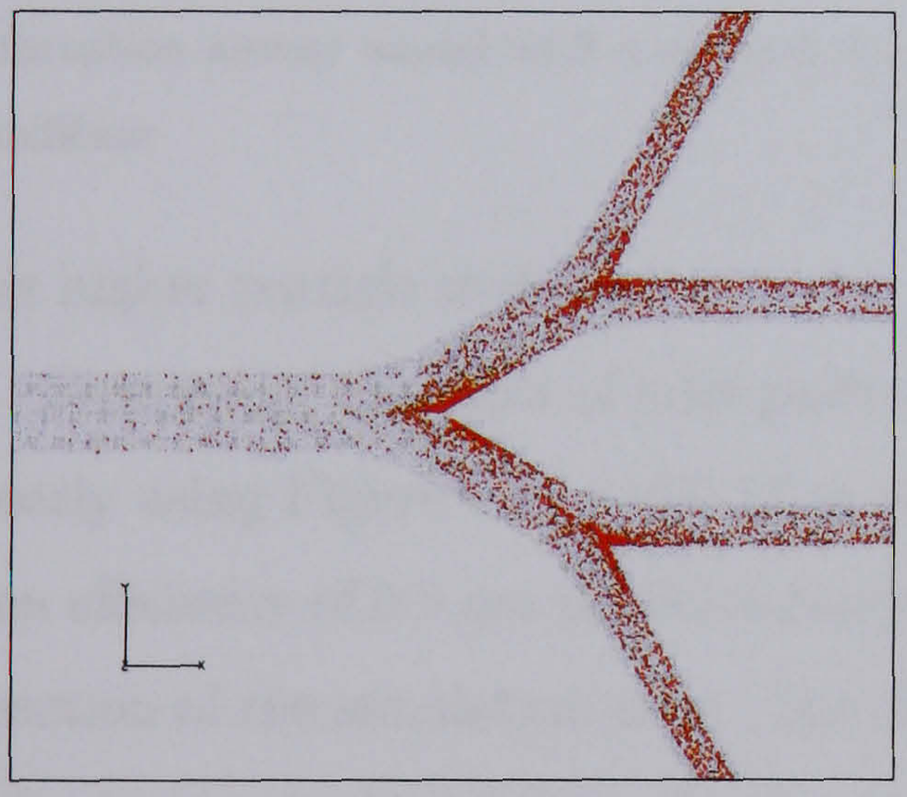

(i) $t = 26\ ms$

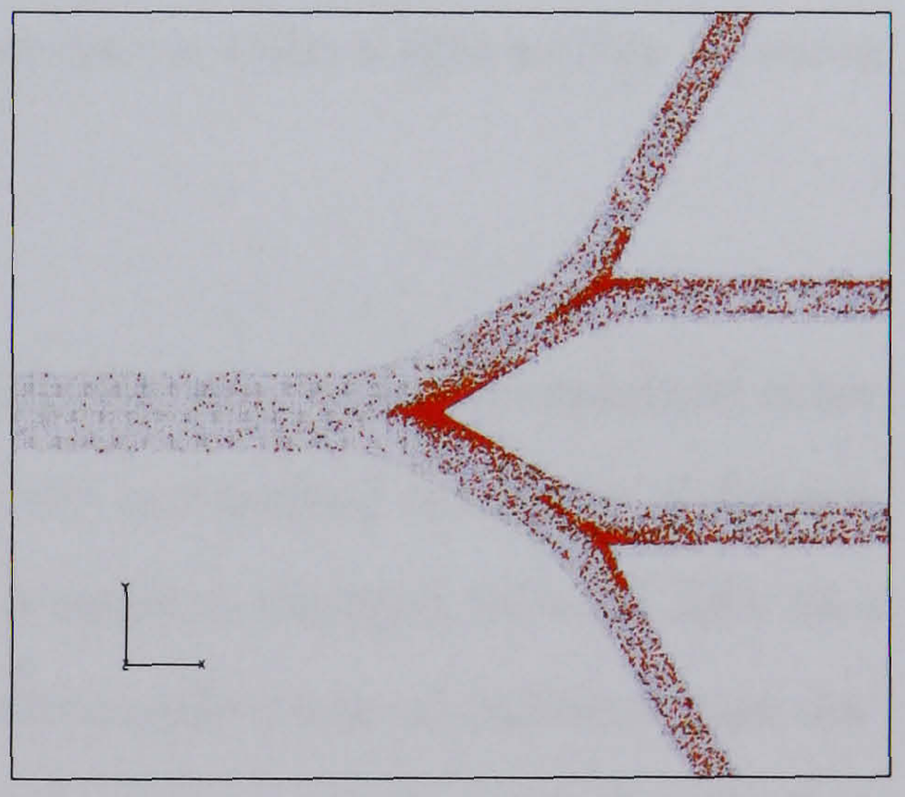

(j) $t = 30\ ms$

Figure 6.11: Transients of 0.5 μm particles carrying $q = 250e$ in the 3D bifurcation airway model with a parabolic inlet distribution under a light activity breathing condition (Cont.)

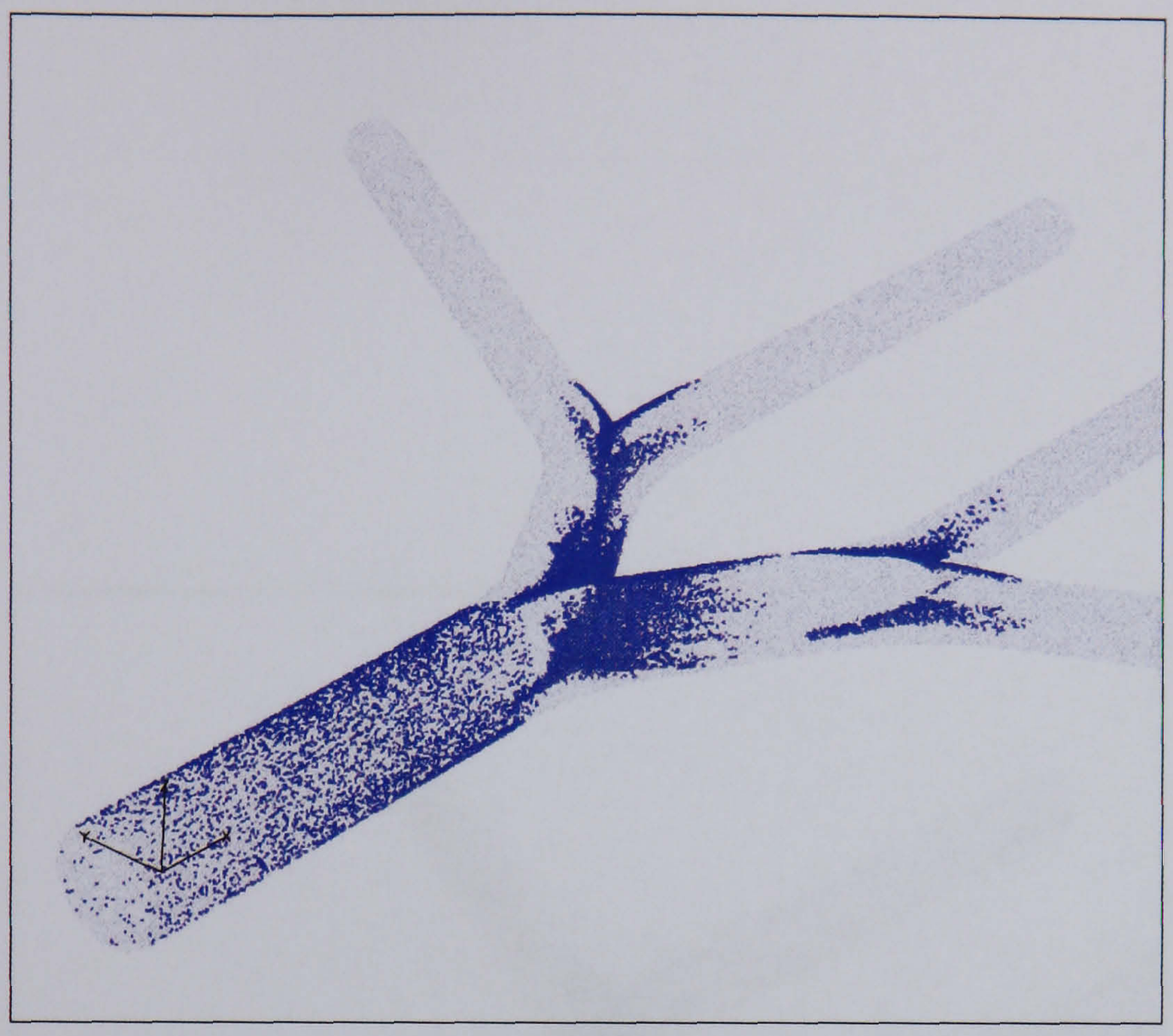

Figure 6.12: Local deposition pattern of 0.5 μm particles carrying $q = 250e$ in the 3D bifurcation airway model with a uniform inlet distribution under a light activity breathing condition

has higher particle mobility.

Comparing the effect of inlet particle distribution, it can be explained more clearly using Figure 6.16 and 6.17 to show the normalised functions of deposition efficiency of 0.5 μm particles carrying a uniform charged value of $250e$ as a function of the simulation time. The deposition efficiency of uniform inlet distribution in the first bifurcation is greater that of parabolic inlet distribution because many particles located near the airway wall of the first tube (generation number 3) are deposited rapidly after these particles are released from the first tube.

The deposition efficiency of uniform inlet distribution is less than that of parabolic distribution after these particles move near the wall of the transition region. Since many particles with parabolic inlet distribution are located near the central axis where the airflow velocity is high, there are more par-

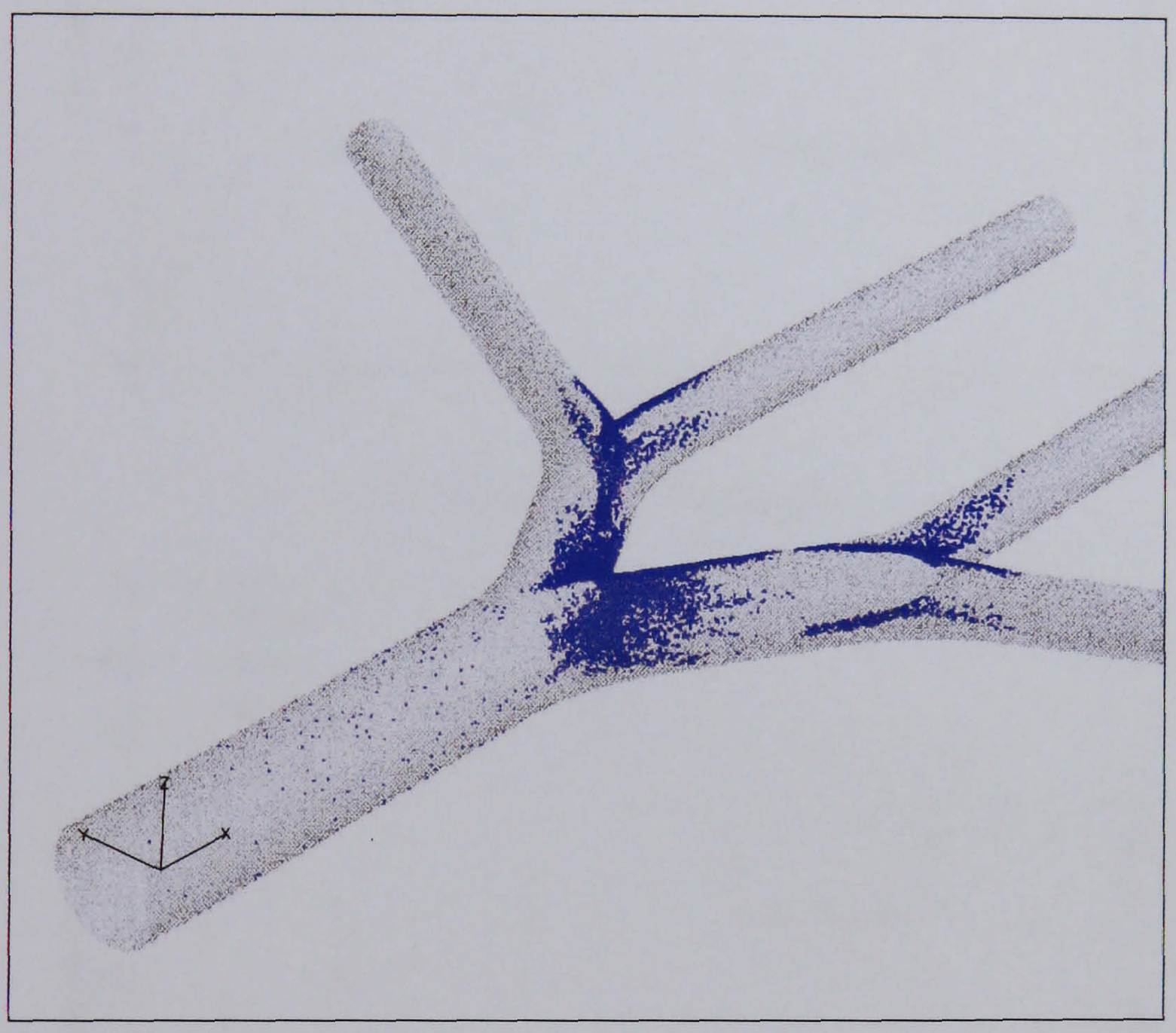

Figure 6.13: Local deposition pattern of 0.5 μm particles carrying $q = 250e$ in the 3D bifurcation airway model with a parabolic inlet distribution under a light activity breathing condition

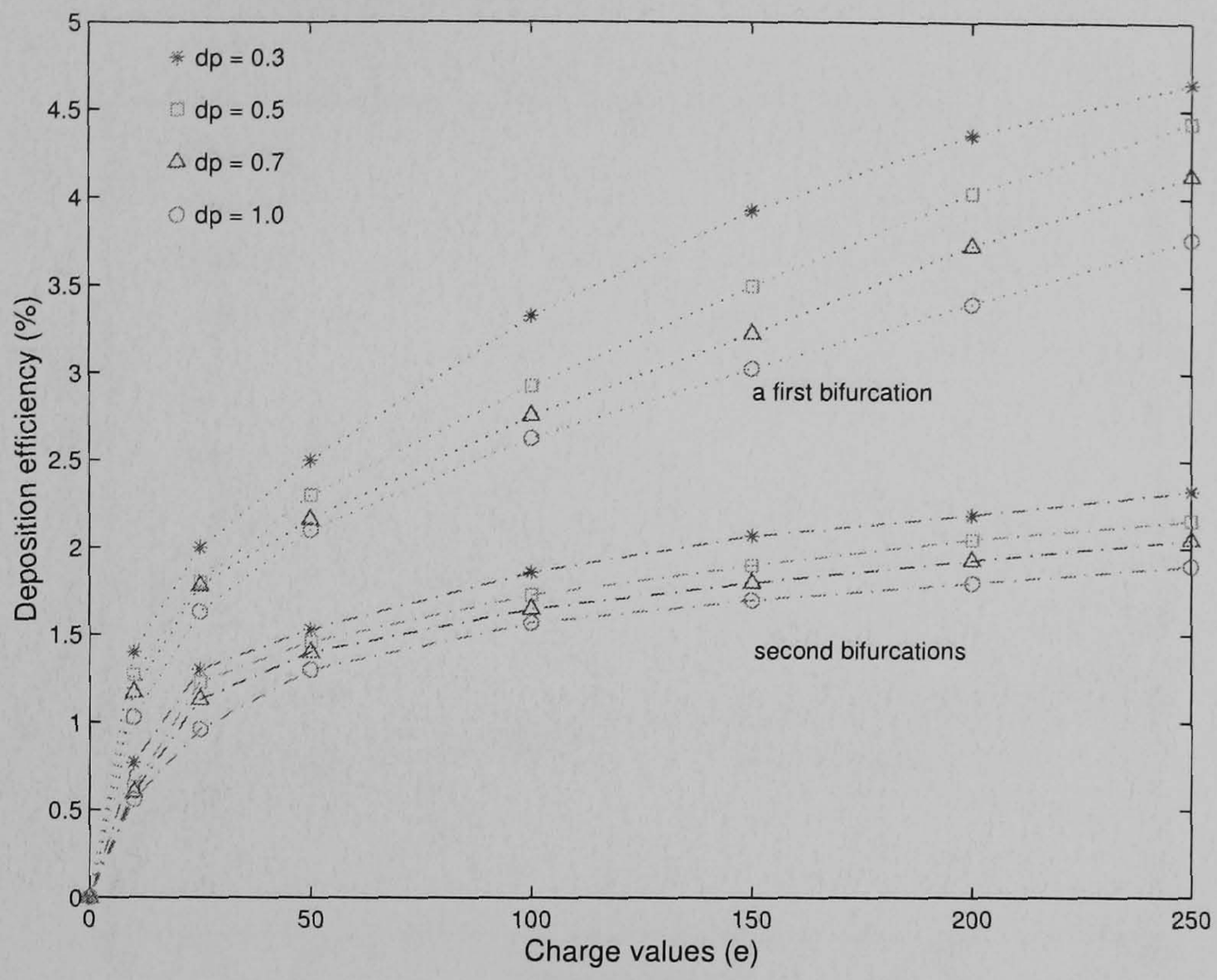

(a) uniform inlet distribution

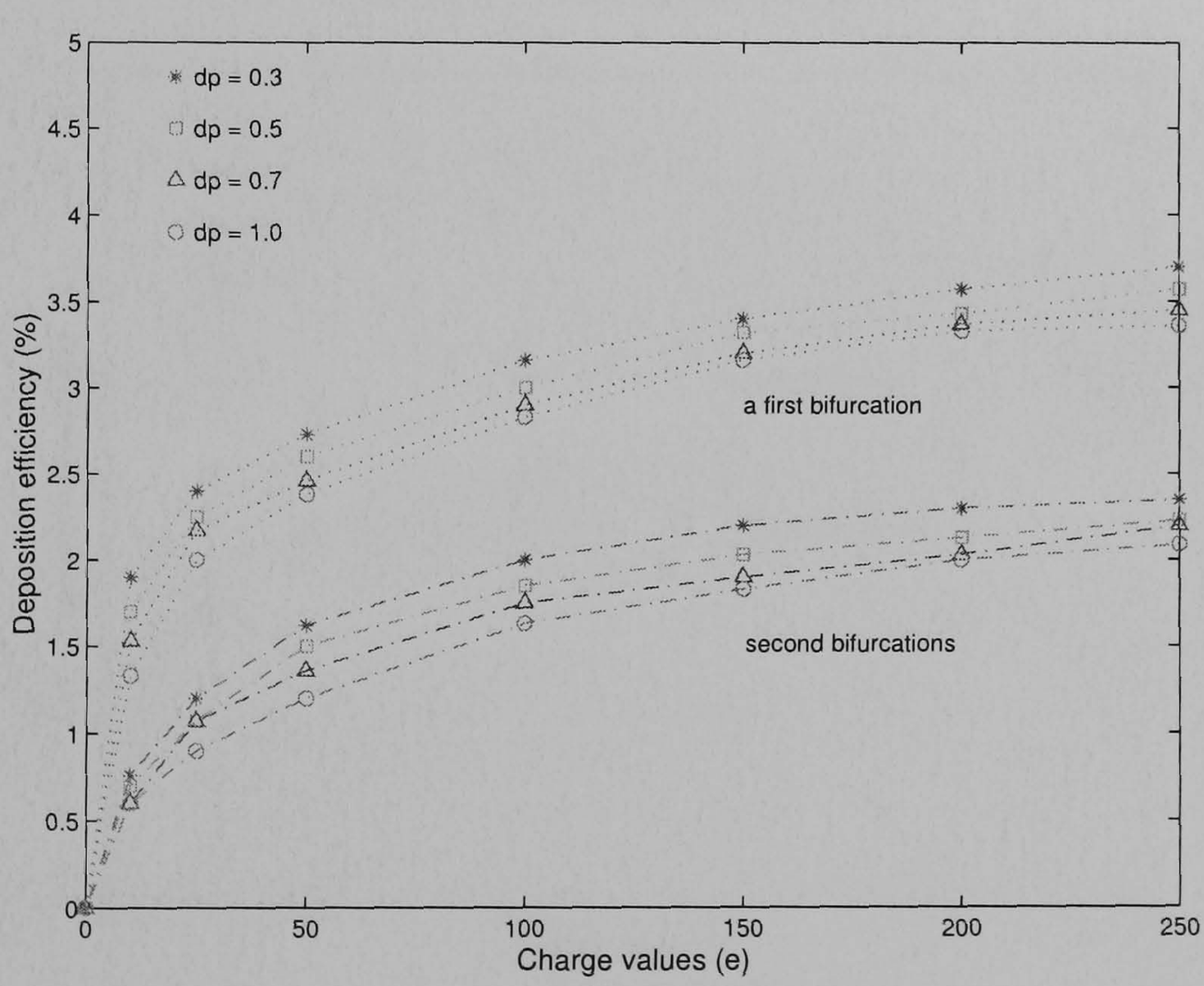

(b) parabolic inlet distribution

Figure 6.14: Deposition efficiencies of 0.5 μm particles carrying various charge values in the 3D bifurcation airway model due to the image charge force with a sedentary breathing condition

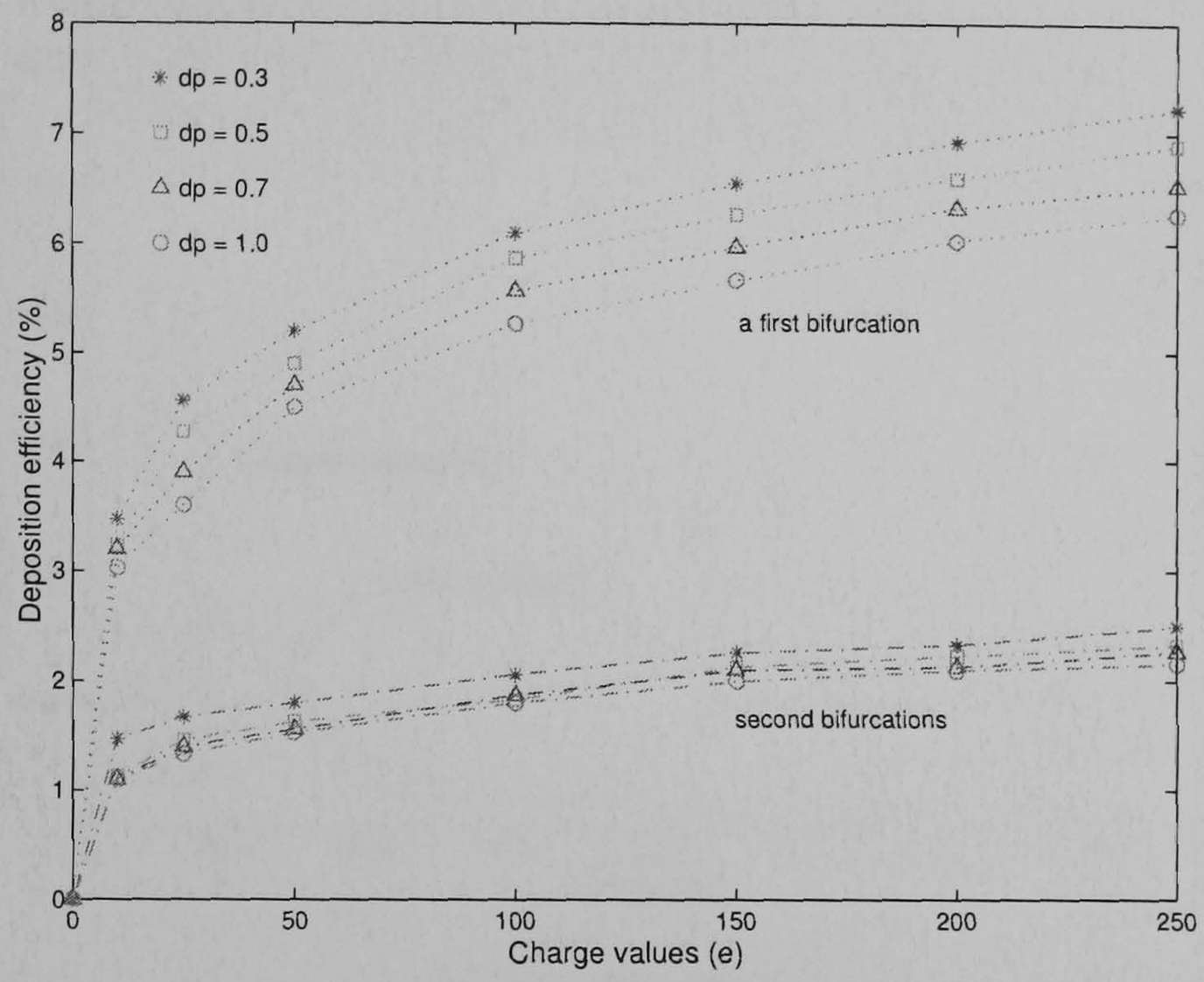

(a) uniform inlet distribution

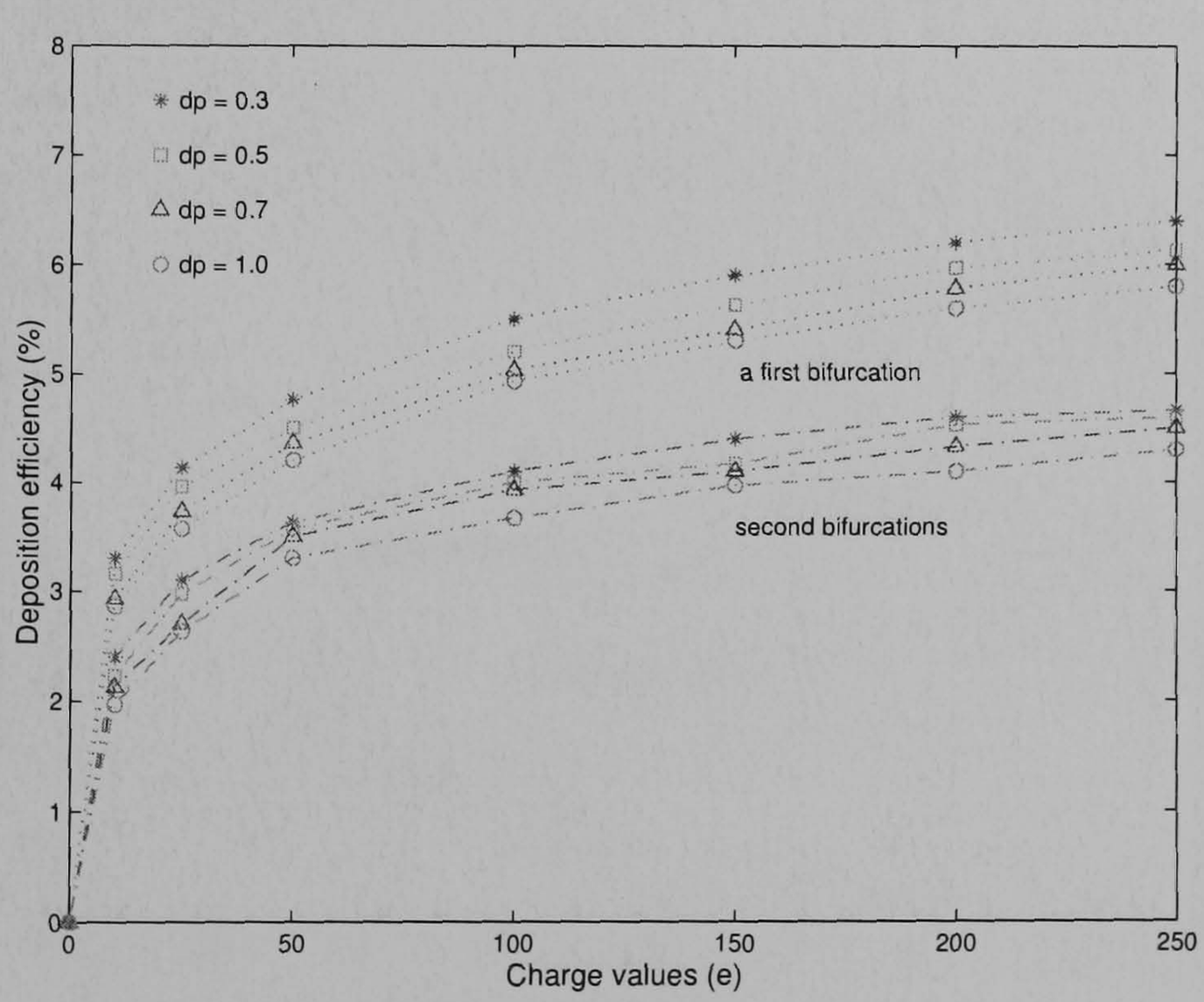

(b) parabolic inlet distribution

Figure 6.15: Deposition efficiencies of 0.5 μm particles carrying various charge values in the 3D bifurcation airway model due to the image charge force with a light activity condition

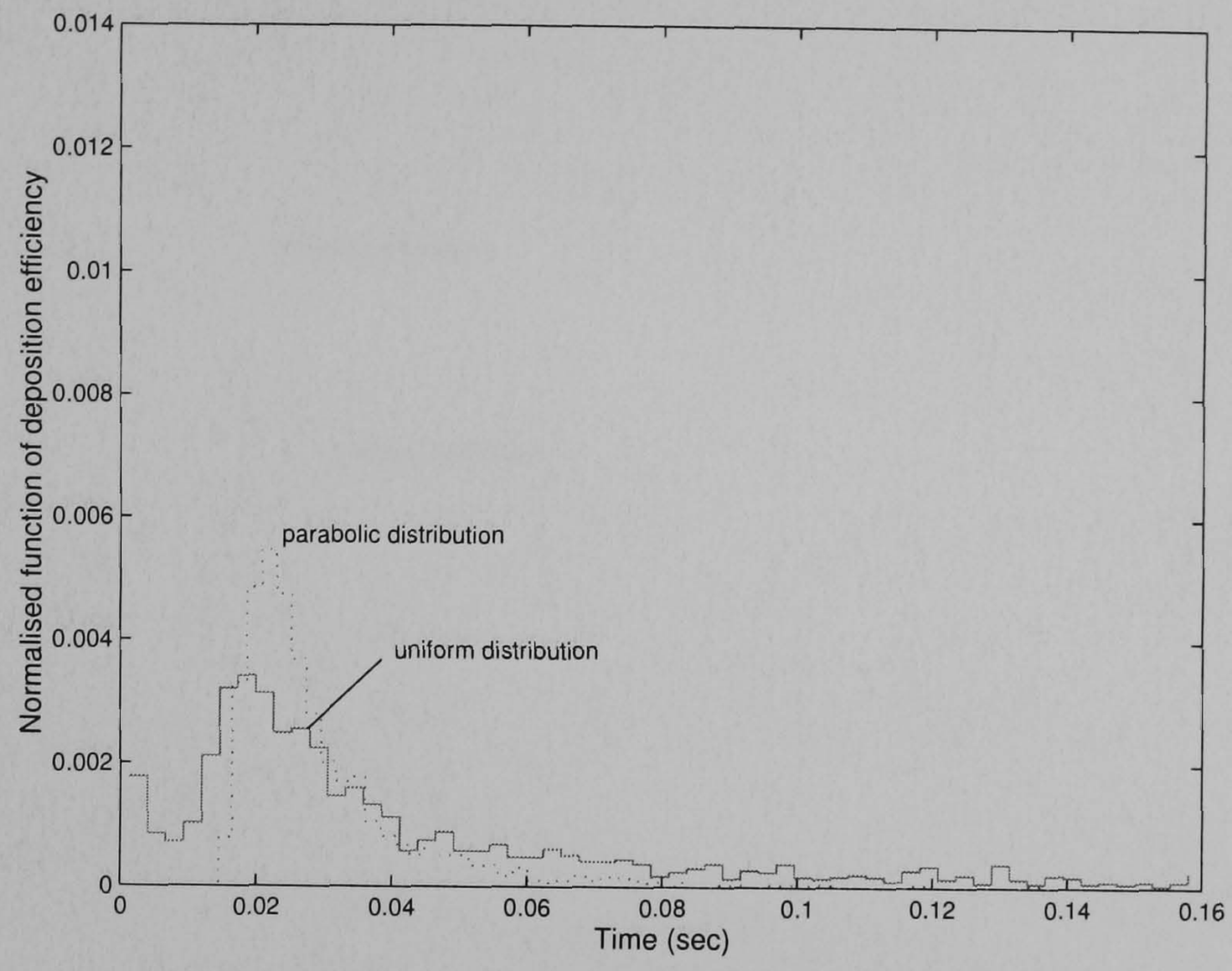

(a) first bifurcation

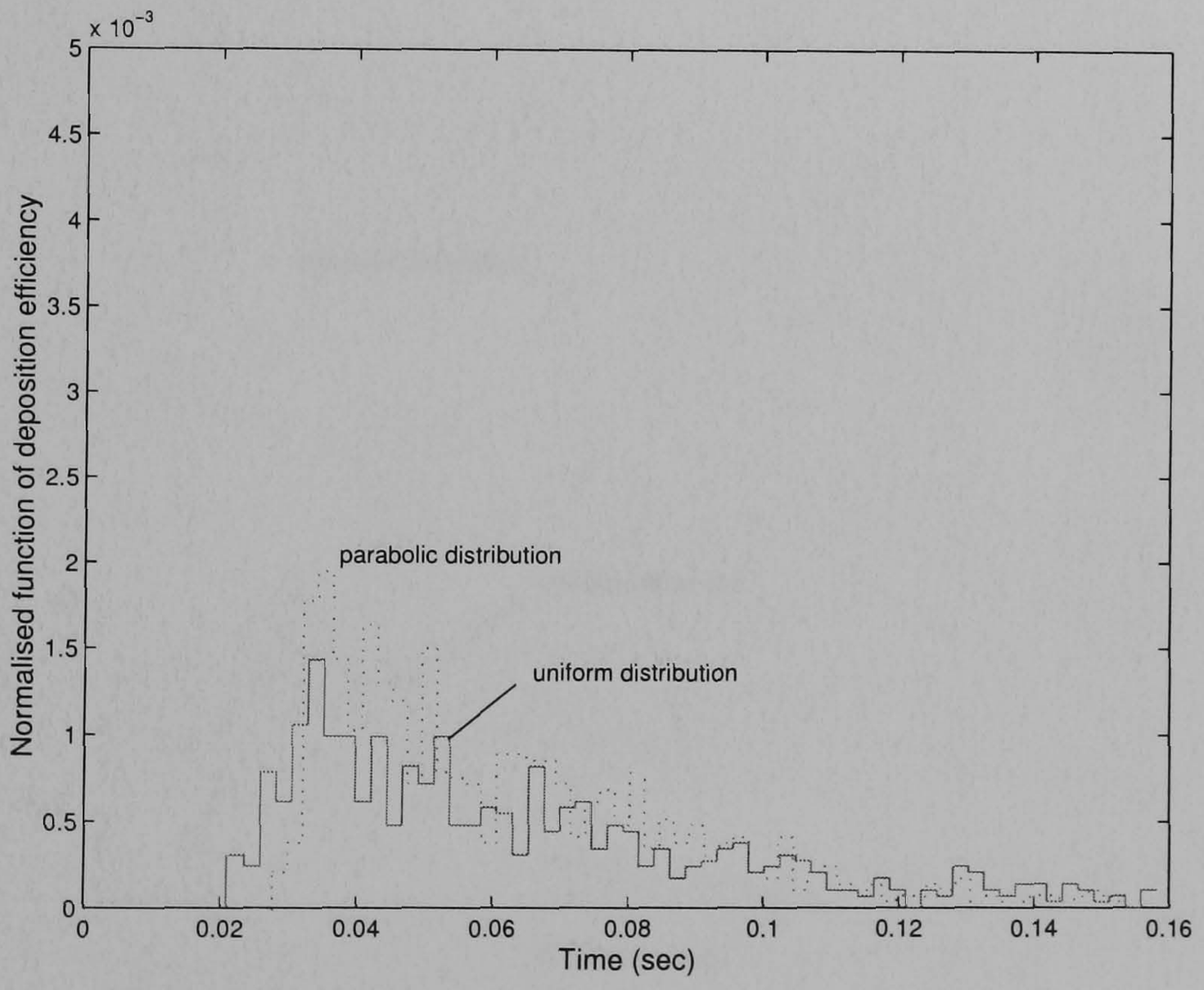

(b) second bifurcations

Figure 6.16: Normalised functions of deposition efficiencies of 0.5 μm particles carrying $q = 250e$ in the 3D bifurcation airway model due to the image charge force with a sedentary breathing condition

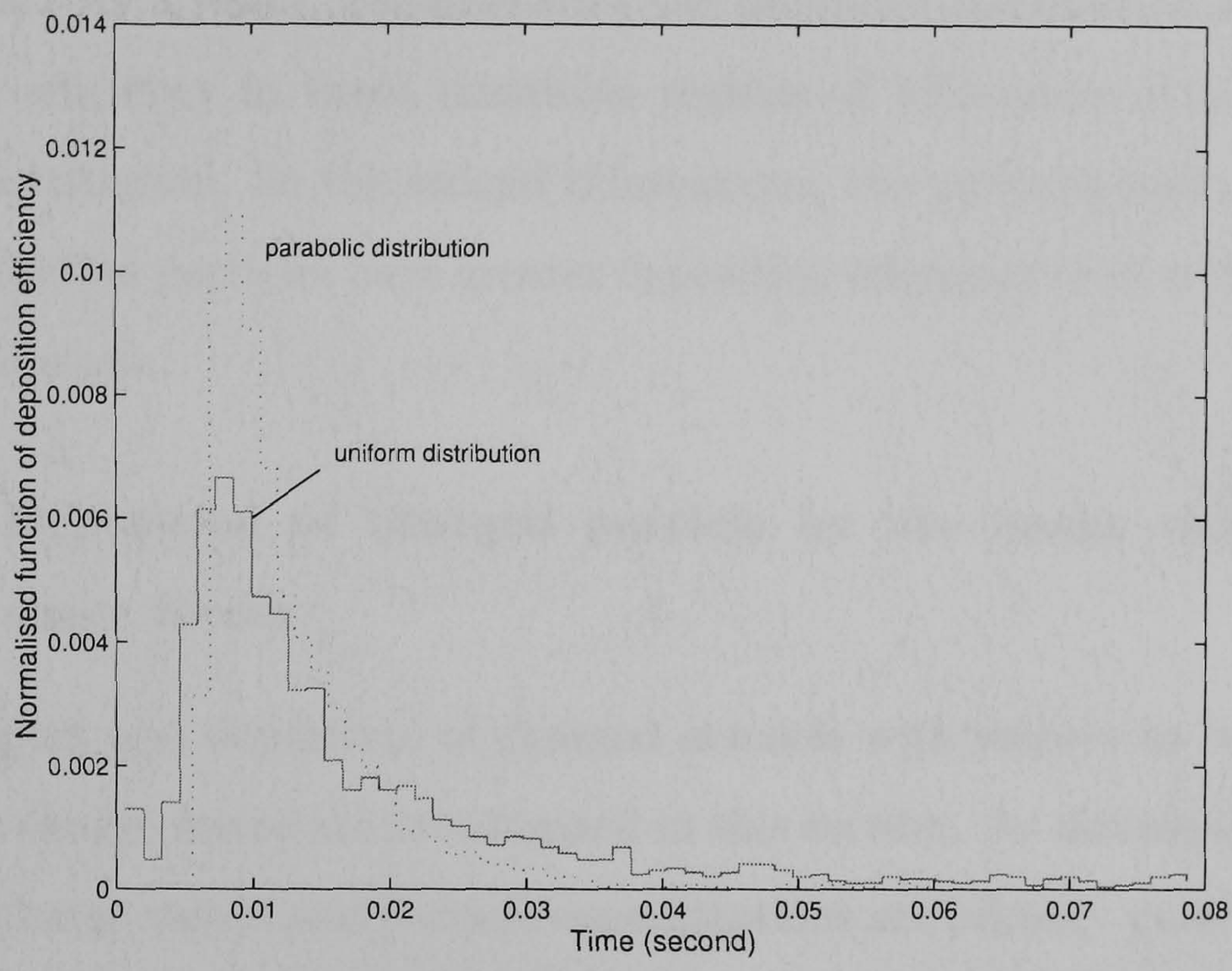

(a) first bifurcation

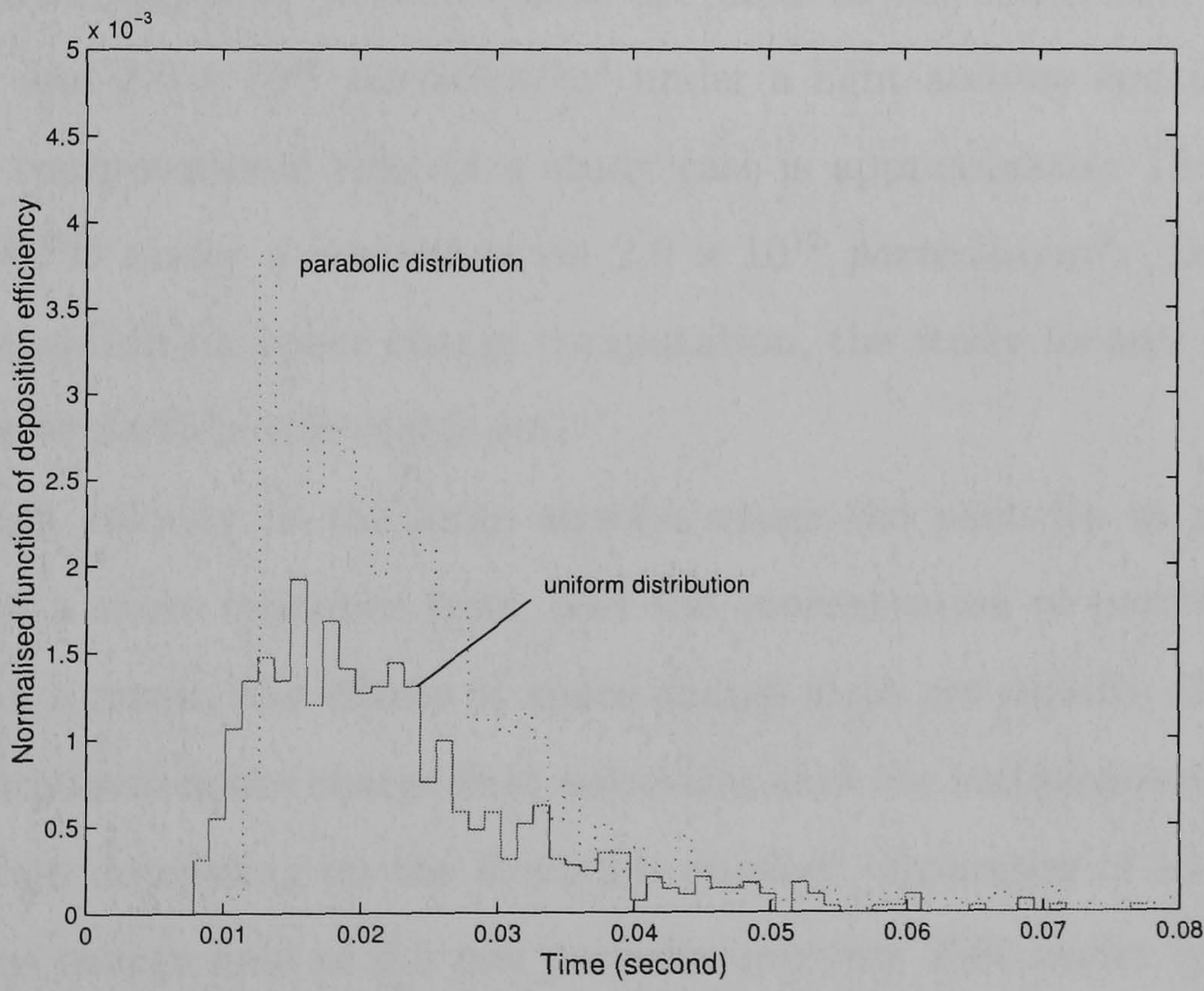

(b) second bifurcations

Figure 6.17: Normalised functions of deposition efficiencies of 0.5 μm particles carrying $q = 250e$ in the 3D bifurcation airway model due to the image charge force with a light activity breathing condition

ticles with higher inertia moving close to the wall than with uniform inlet distribution. As a result, particles with the parabolic distribution have more deposition efficiency in these transition regions of bifurcation than those of uniform distribution. In the second bifurcations, the particles with parabolic inlet distribution particles have greater deposition efficiency than with uniform inlet distribution.

6.3.3.2 Deposition of charged particle by the image charge and space forces

The transport and deposition of charged aerosols with respect to both space and image charge forces are investigated in this section. As discussed in chapter 4, the charge values and particle concentrations are primary parameters for the space charge force which play an important role in deposition in the large airways. Two values of concentrations are used in the simulations, namely, 2.0×10^{11} and 2.0×10^{12} $particles/m^3$ under a light activity breathing condition. A computational time of a study case is approximately 15 hours for a 5 GHz CPU under a concentration 2.0×10^{12} $particles/m^3$. Due to the time consumption for space charge computation, the study focuses only on a monodisperse particle size of 0.5 μm.

The high velocity in the large airways cause the particles to move into the lung in a short residence time, and the concentration of particles decay rapidly. As a result, the effects of space charge force are rapidly diminished. The instantaneous space charge field associates with the instantaneous particle concentration depending on the Reynolds number. Examples of an instantaneous space charge field of 0.5 μm particles carrying $250e$ under light activity breathing conditions for the uniform and parabolic inlet distributions are shown in Figure 6.18 and 6.19, respectively. After the particles are released, strong space charge fields occur. The particles located near the central axis of the parent tube move quickly into the daughter branches, and then the space charge field near the central axis decays rapidly. At a time period of $4-6$ ms,

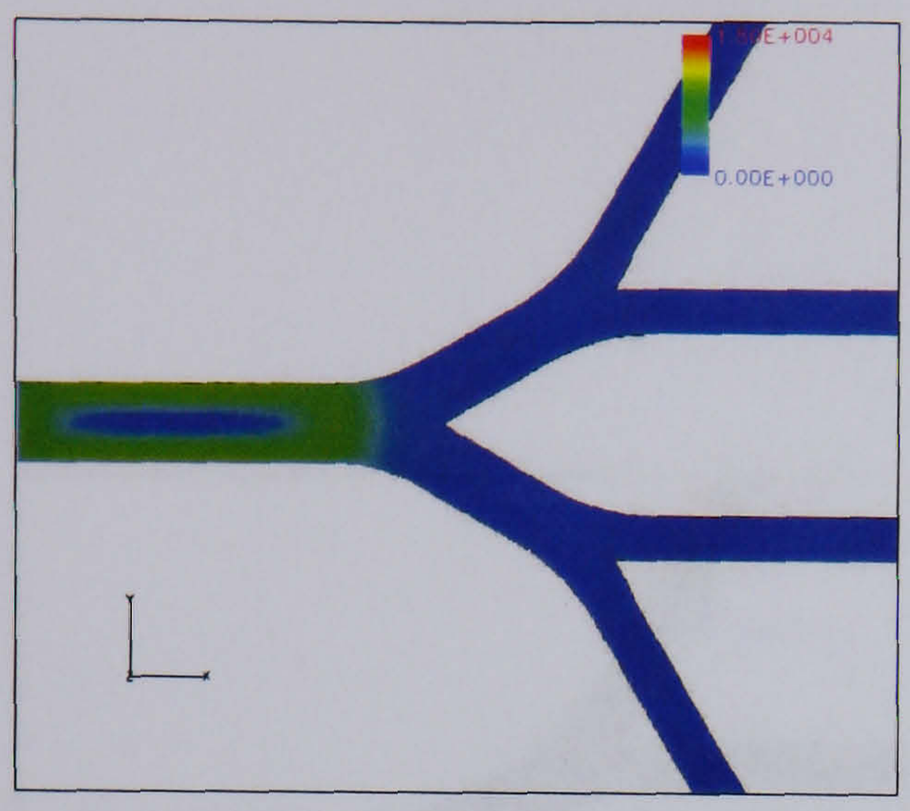

(a) $t = 0.2\ ms$

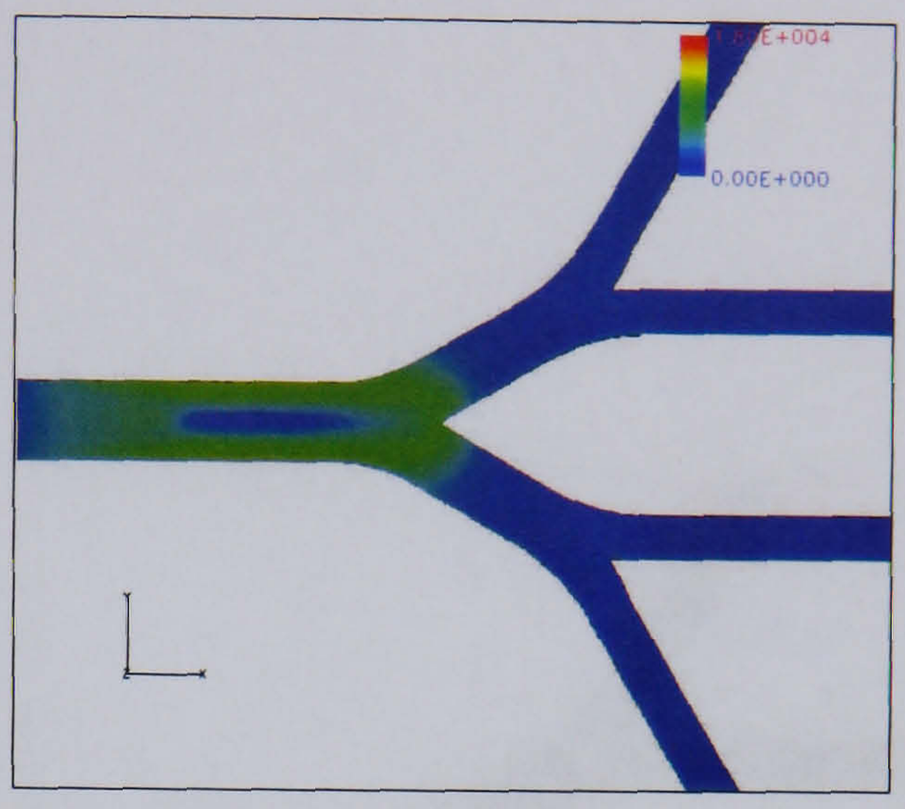

(b) $t = 2\ ms$

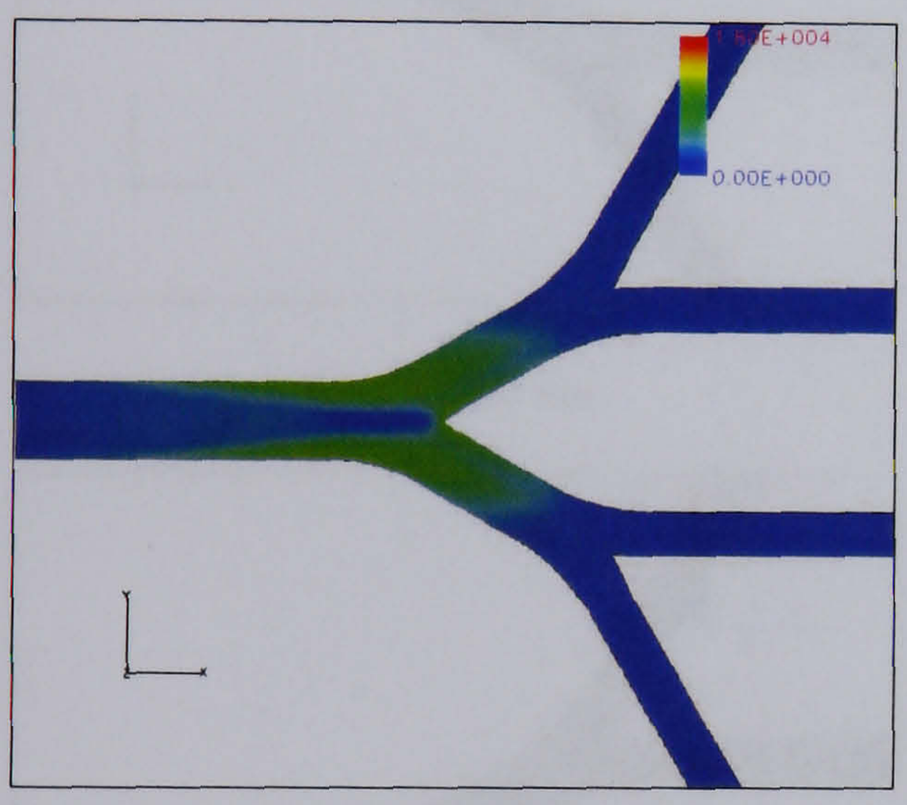

(c) $t = 4\ ms$

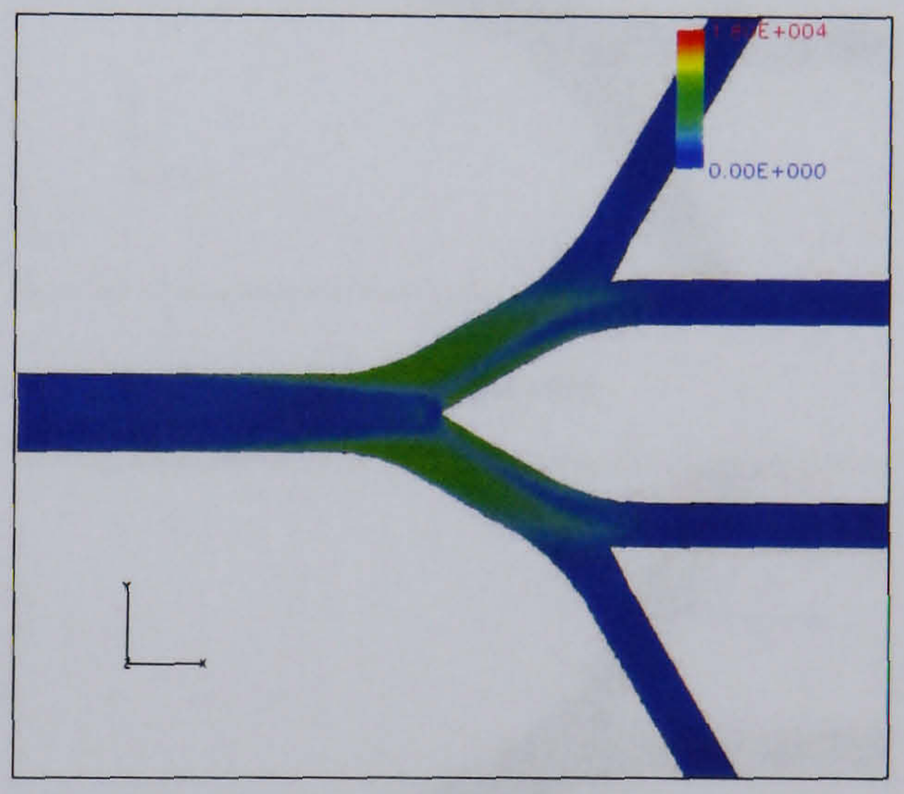

(d) $t = 6\ ms$

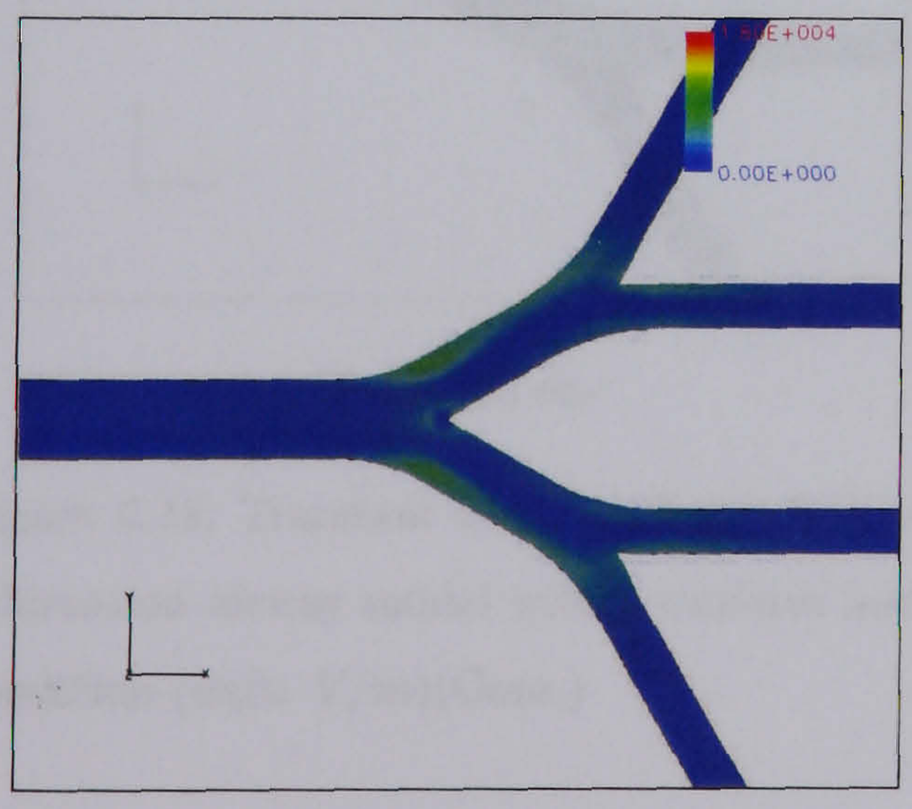

(e) $t = 10\ ms$

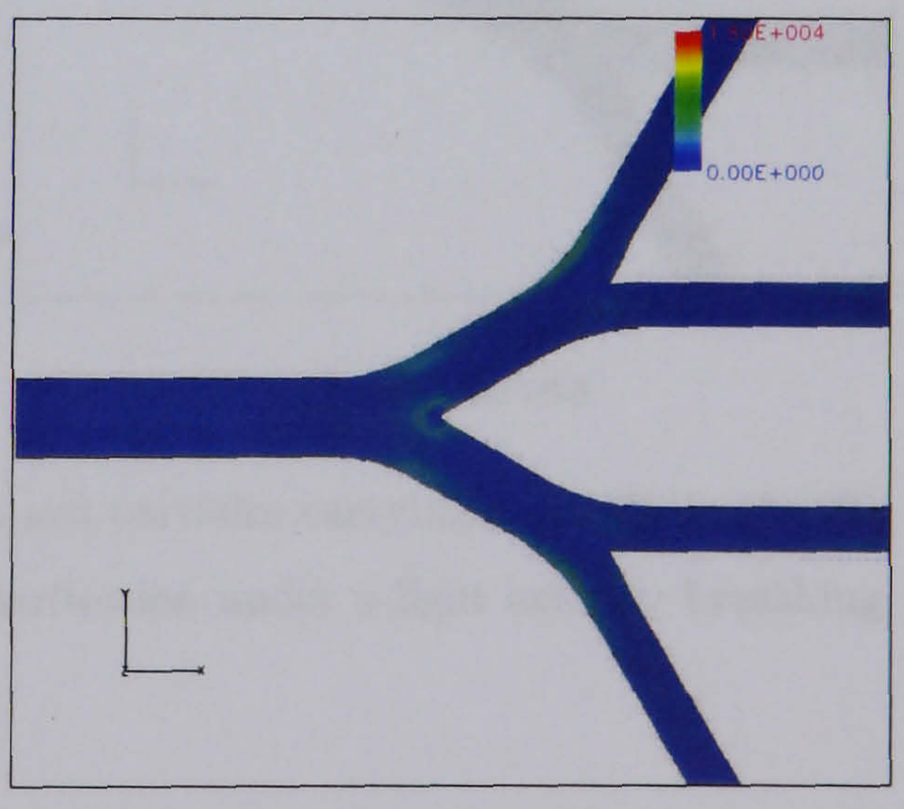

(f) $t = 14\ ms$

Figure 6.18: Transient of space charge field of 0.5 μm particles carrying $q = 250e$ in the 3D bifurcation airway model with a uniform inlet distribution under a light activity breathing condition (unit: V/m)

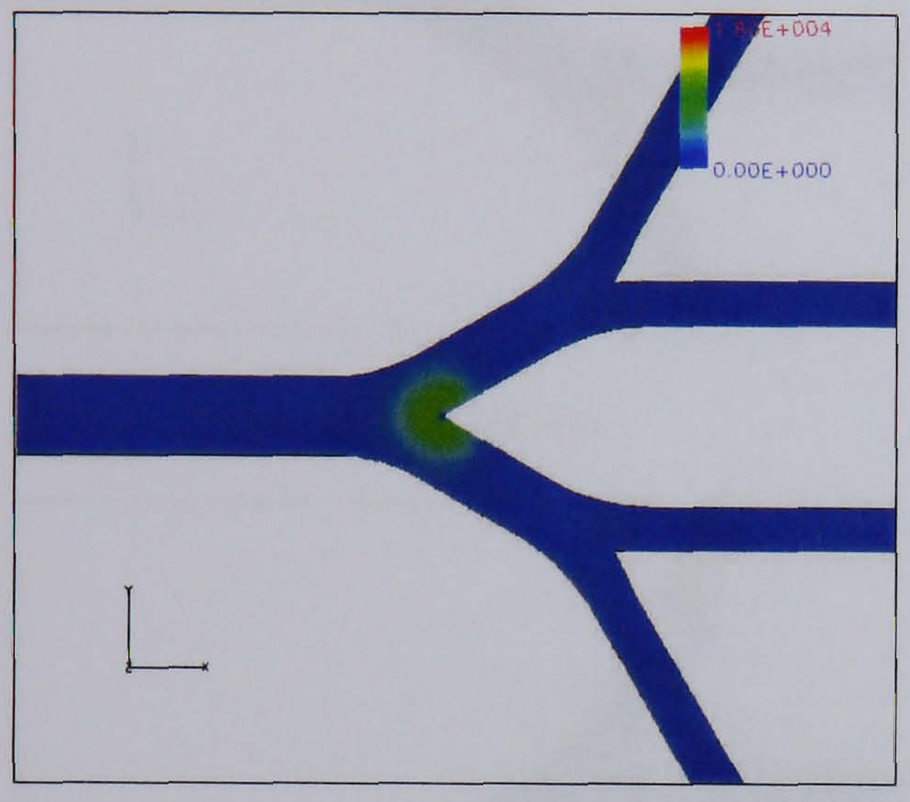

(g) $t = 18\ ms$

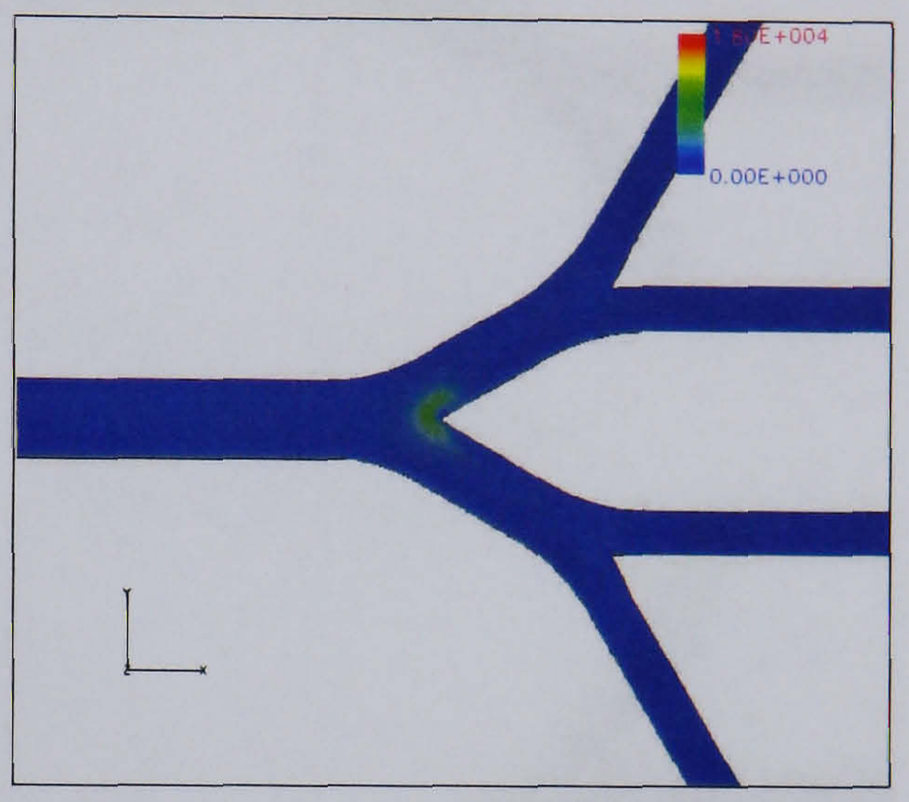

(h) $t = 22\ ms$

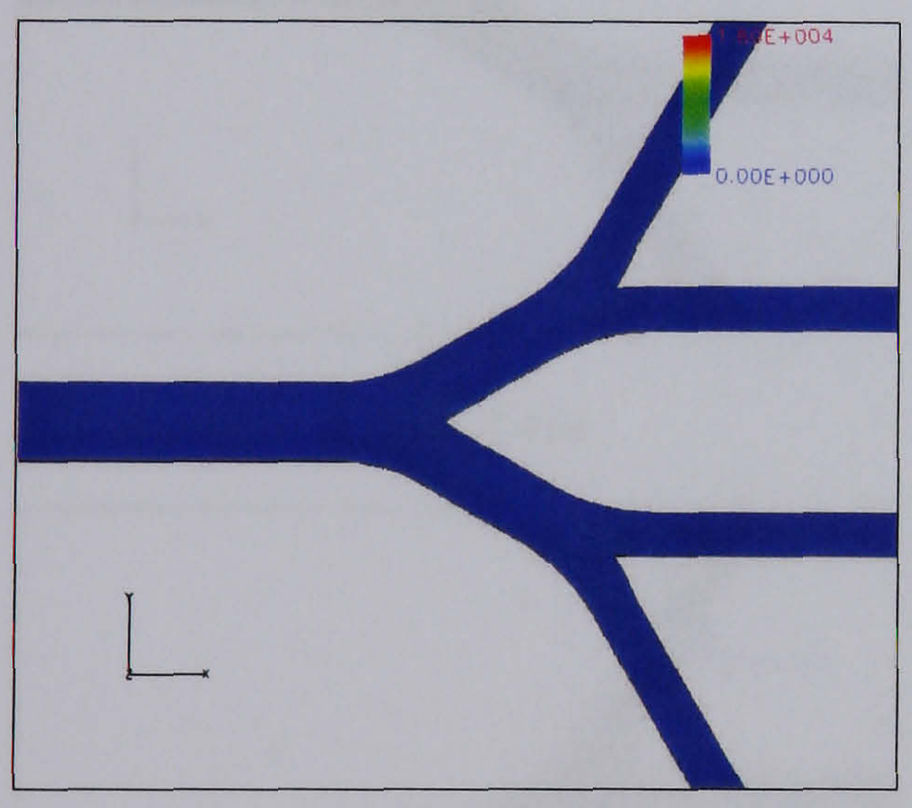

(i) $t = 26\ ms$

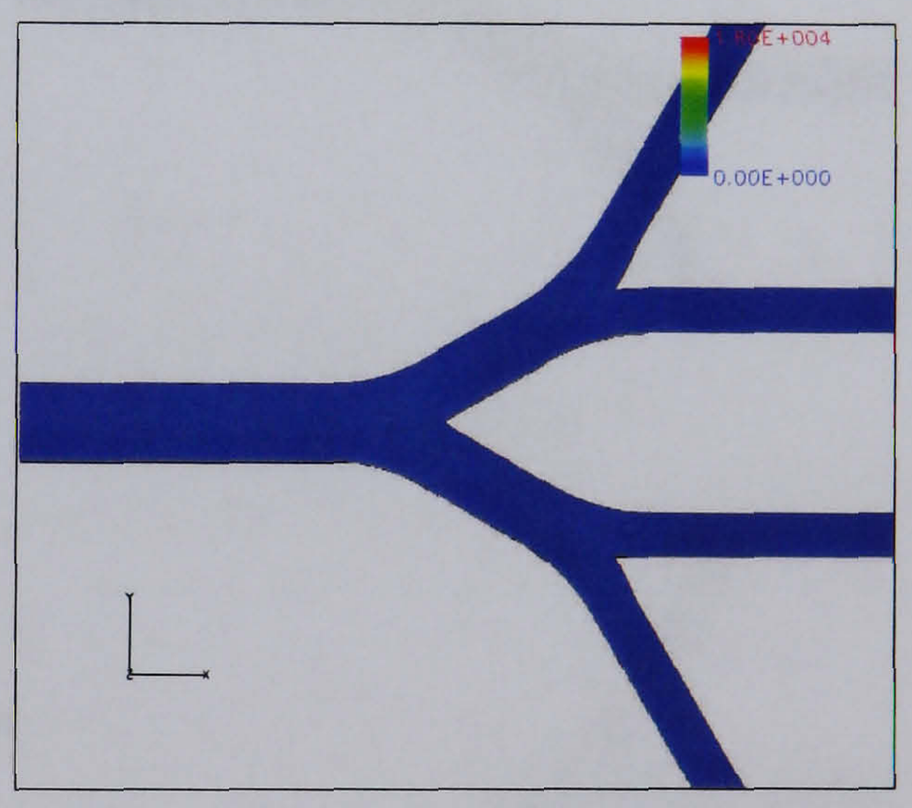

(j) $t = 30\ ms$

Figure 6.18: Transient of space charge field of 0.5 μm particles carrying $q = 250e$ in the 3D bifurcation airway model with a uniform inlet distribution under a light activity breathing condition (unit: V/m)(Cont.)

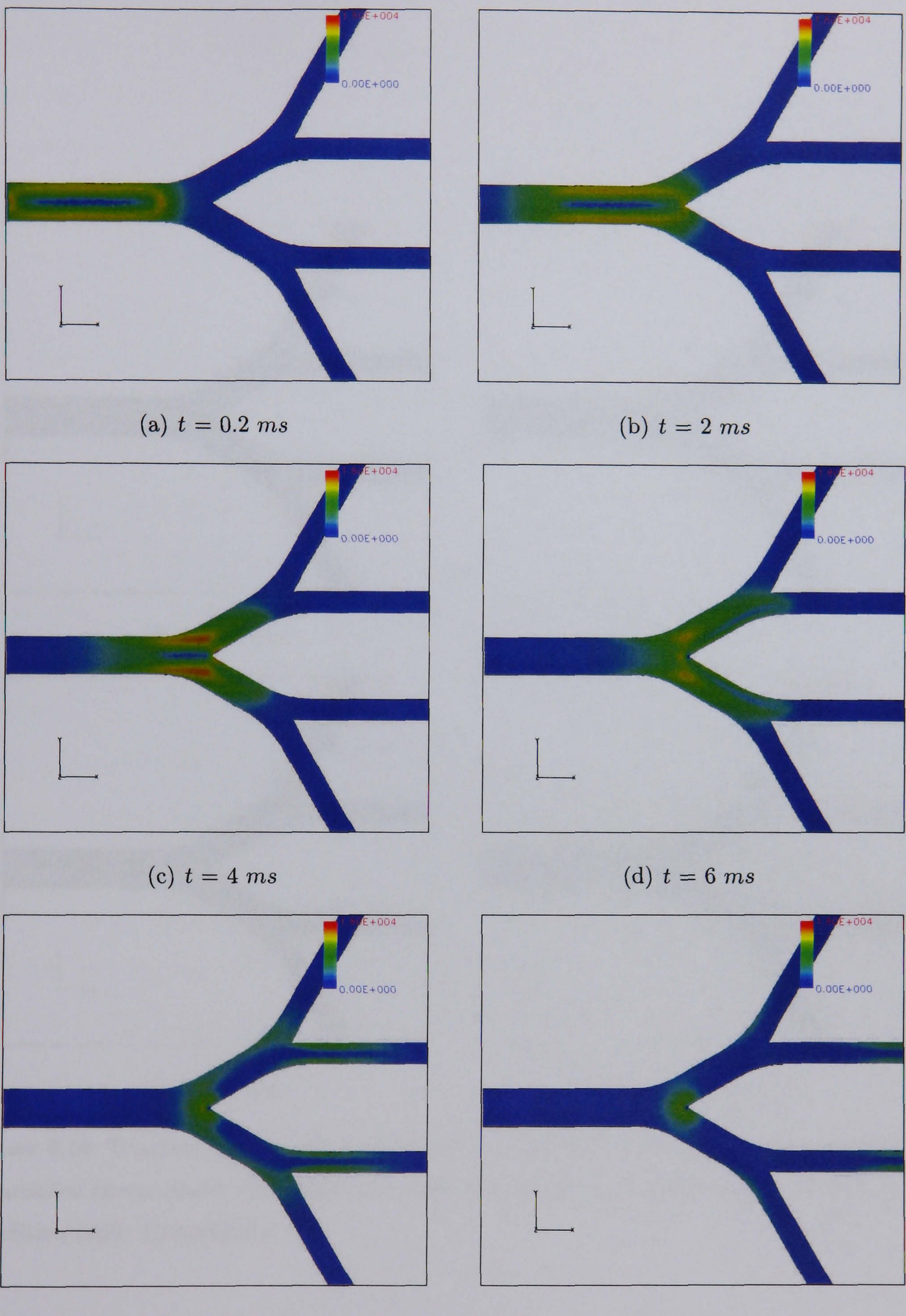

(a) $t = 0.2\ ms$ (b) $t = 2\ ms$

(c) $t = 4\ ms$ (d) $t = 6\ ms$

(e) $t = 10\ ms$ (f) $t = 14\ ms$

Figure 6.19: Transient of space charge field of 0.5 μm particles carrying $q = 250e$ in the 3D bifurcation airway model with a parabolic inlet distribution under a light activity breathing condition (unit: V/m)

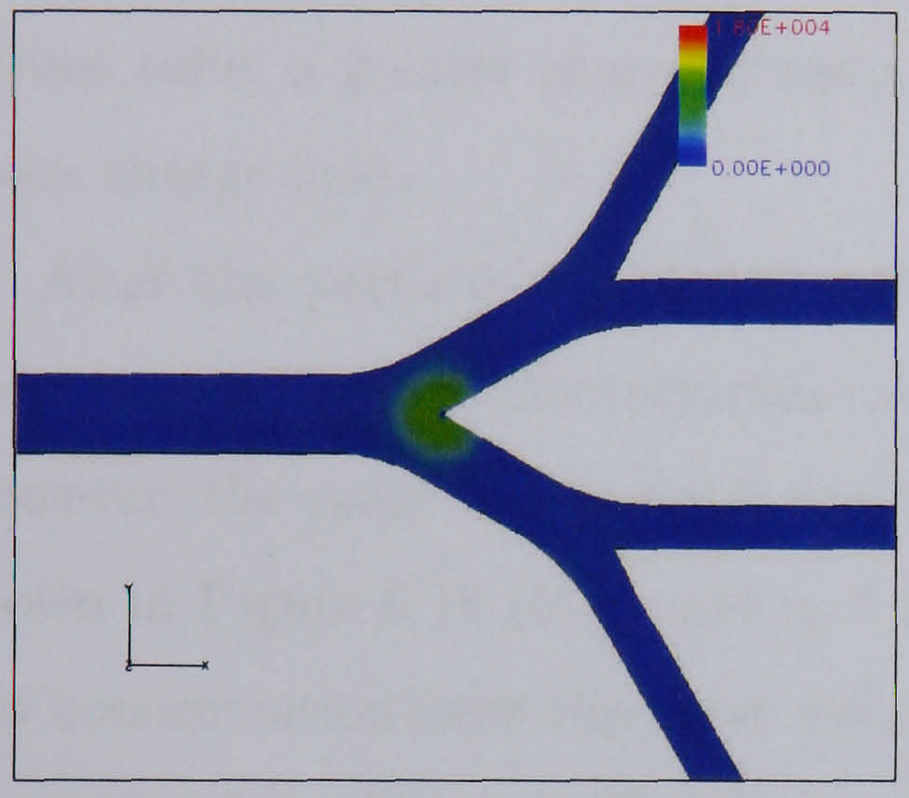

(g) $t = 18\ ms$

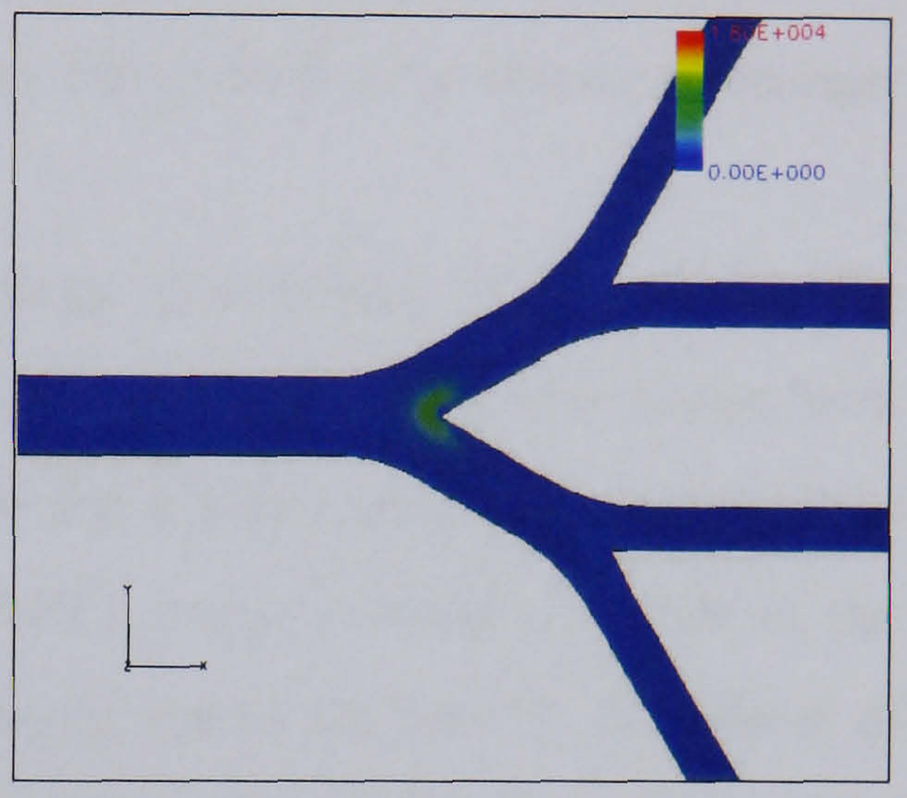

(h) $t = 22\ ms$

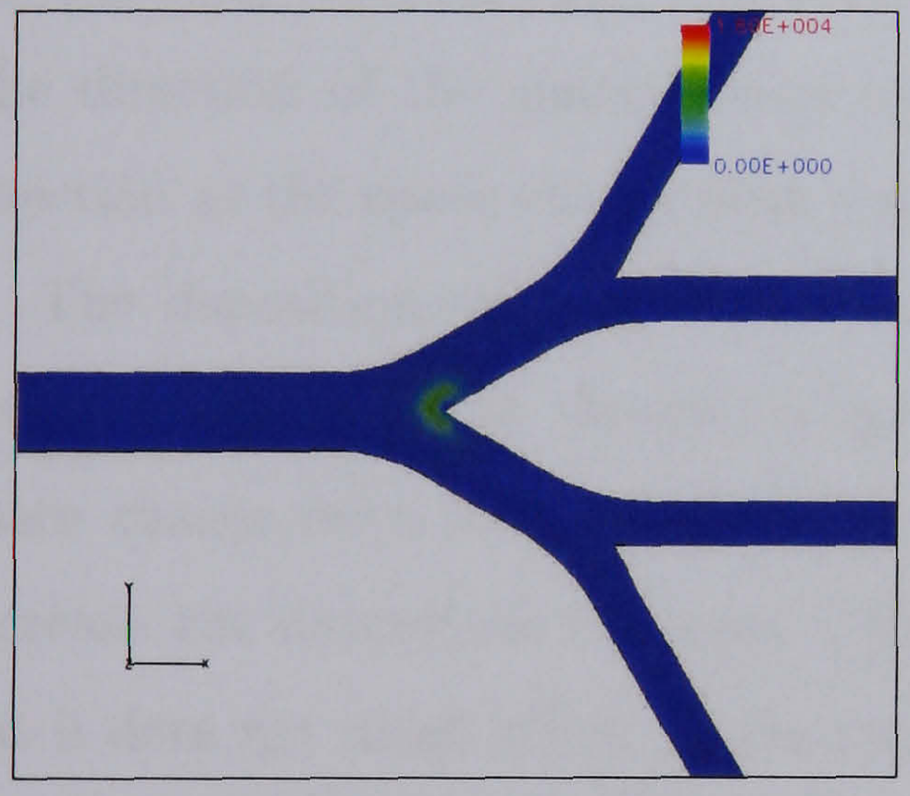

(i) $t = 26\ ms$

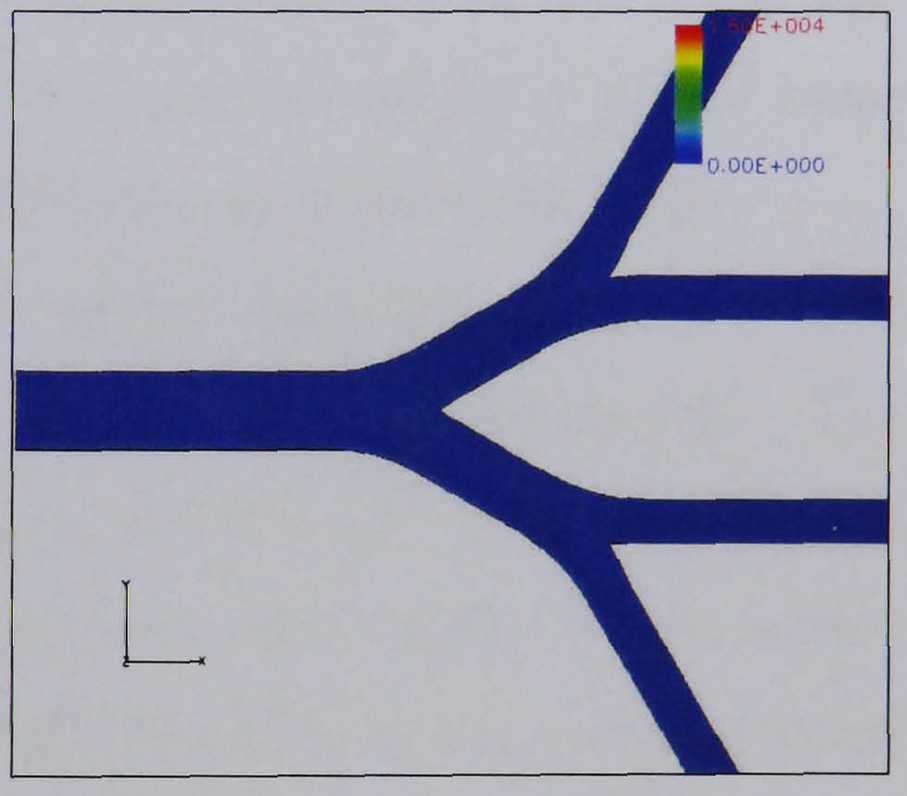

(j) $t = 30\ ms$

Figure 6.19: Transient of space charge field of 0.5 μm particles carrying $q = 250e$ in the 3D bifurcation airway model with a parabolic inlet distribution under a light activity breathing condition (unit: V/m)(Cont.)

a high concentration of particles located near the inner wall cause the space charge fields to be stronger near the carinas. The comparison between Figures 6.18 (c)(d) and 6.19 (c)(d) show that the space charge field of a parabolic inlet distribution is stronger than that of uniform distribution. Because more particles with parabolic inlet distribution are located near the central axis of the parent tube, a greater charge density near the central axis causes a stronger space charge field.

After the particles reach the final airway generations of the model, the reduction in particle concentration causes the decay of the space charge field. However, the space charge fields still exist for a while near the outer wall as shown in Figure 6.18 (e)(f) and in 6.19 (e)(f), because many particles in the low concentration near the outer wall move in vortex motion by the effects of secondary flow. Figure 6.20 shows an example of electrical field vectors of 0.5 μm particles carrying $250e$ with a parabolic inlet distribution at $t = 4\ ms$. The direction of the space charge force on a particle aligns it in the same direction as the space charge field, typically pointing towards the wall.

The deposition efficiencies of charged aerosol, including both space and image charge forces at various charge values, are given in Figure 6.21. The space charge force of an inlet concentration of $2.0 \times 10^{12}\ particles/m^3$ can increase the deposition efficiency when particles carry higher charge values, but it does not much affect the deposition efficiency for an inlet concentration of 2.0×10^{11}. However, these numerical results have been calculated using the assumption that no particles are added into the system after starting the simulation. Systems with constantly increasing particle numbers may have a greater aerosol deposition as a results of space charge force.

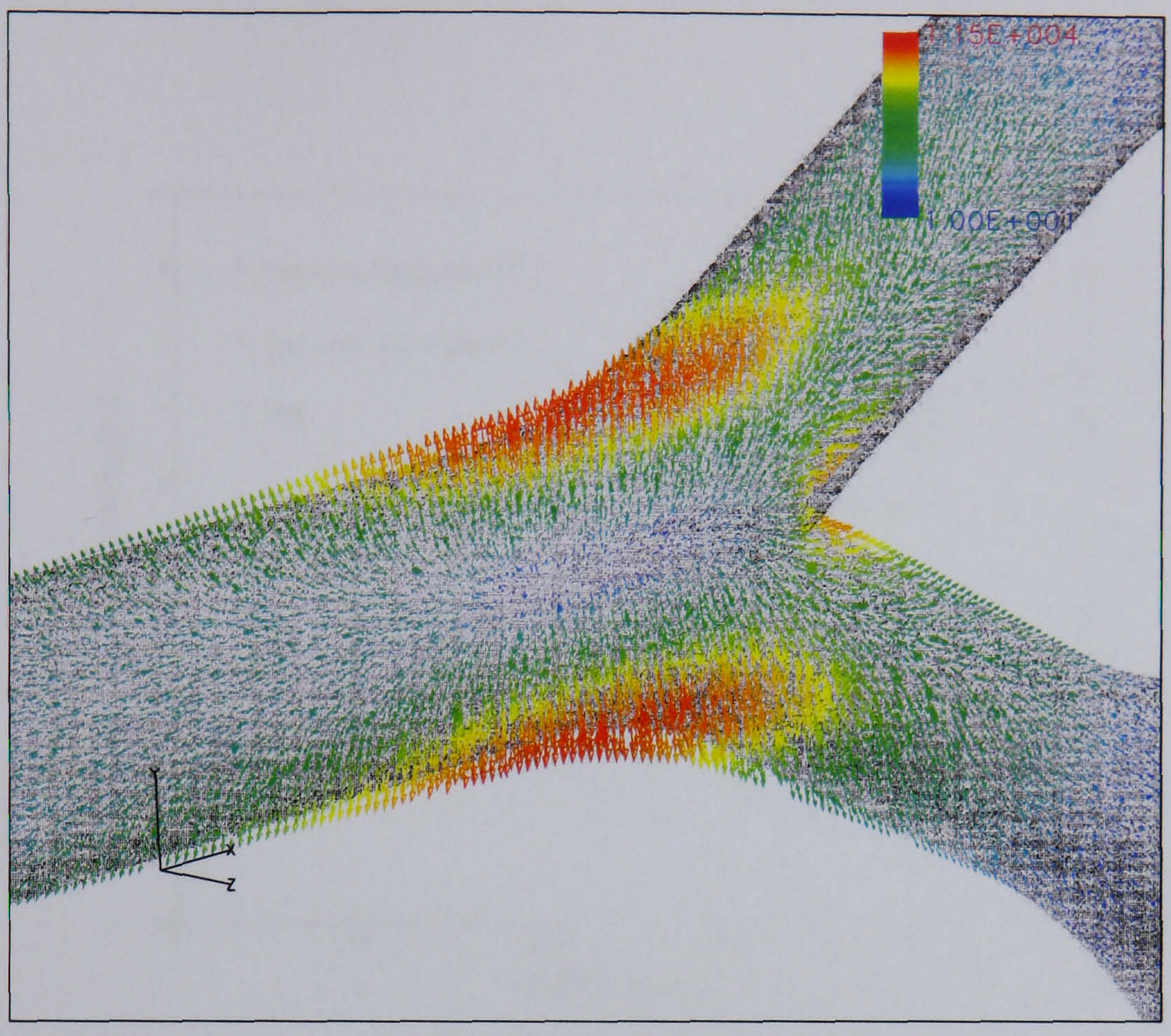

(a) at a cutting plane z=0

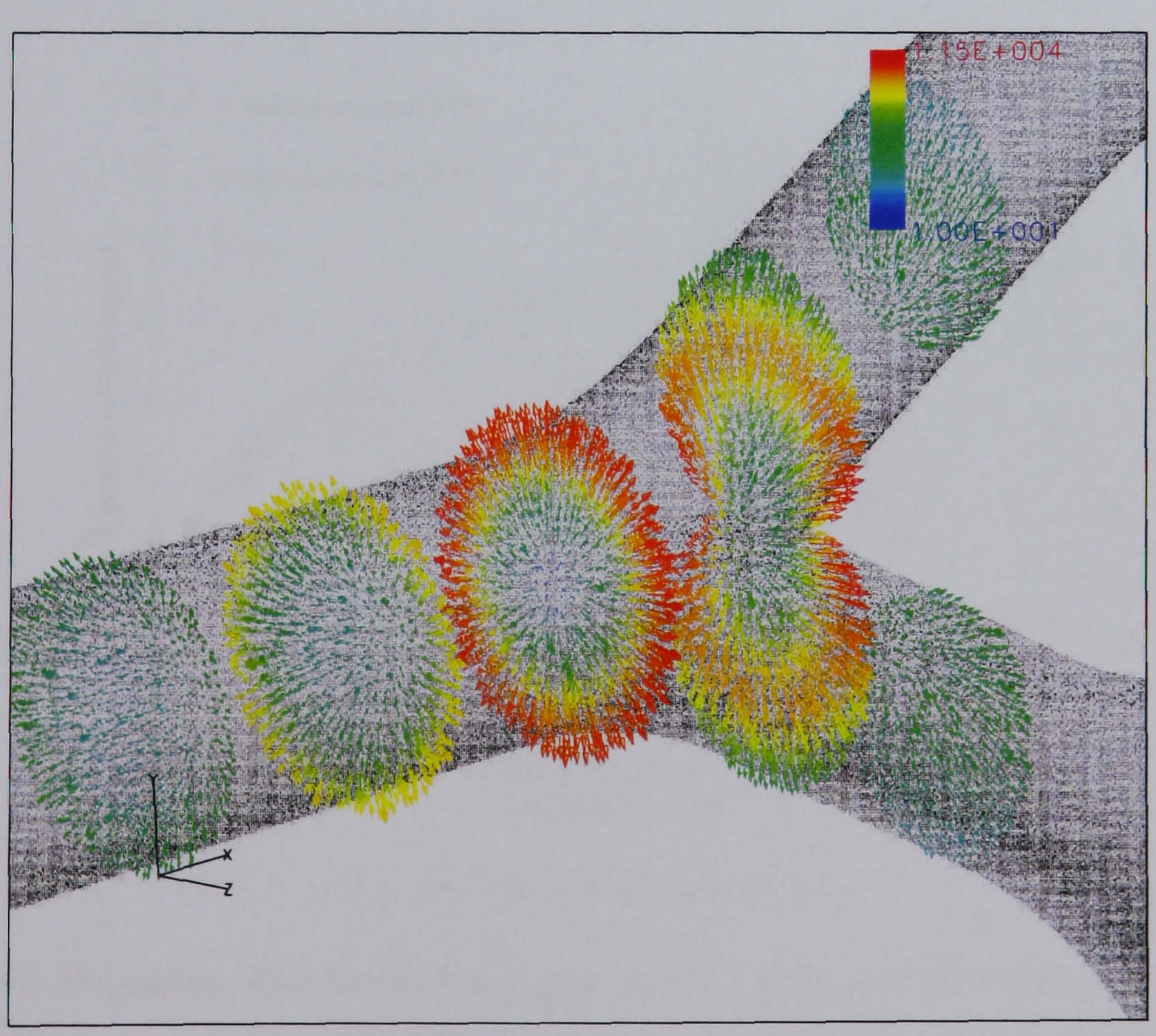

(b) at various cutting planes in x-axis

Figure 6.20: Vector display of space charge field of 0.5 μm particles carrying $q = 250e$ in the 3D bifurcation airway model at $t = 4\ ms$ with a parabolic inlet distribution under a light activity breathing condition (unit: V/m)

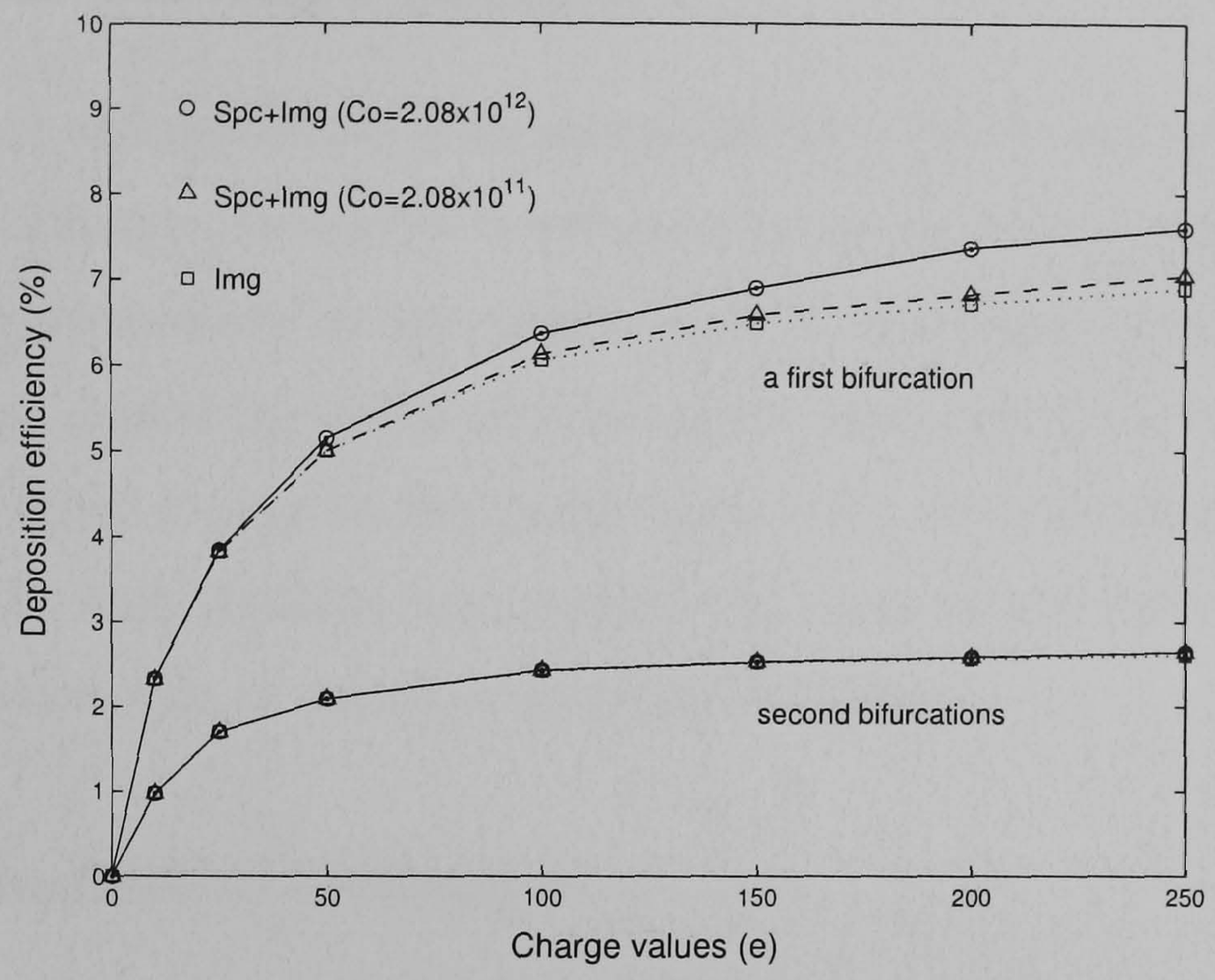

(a) uniform inlet distribution

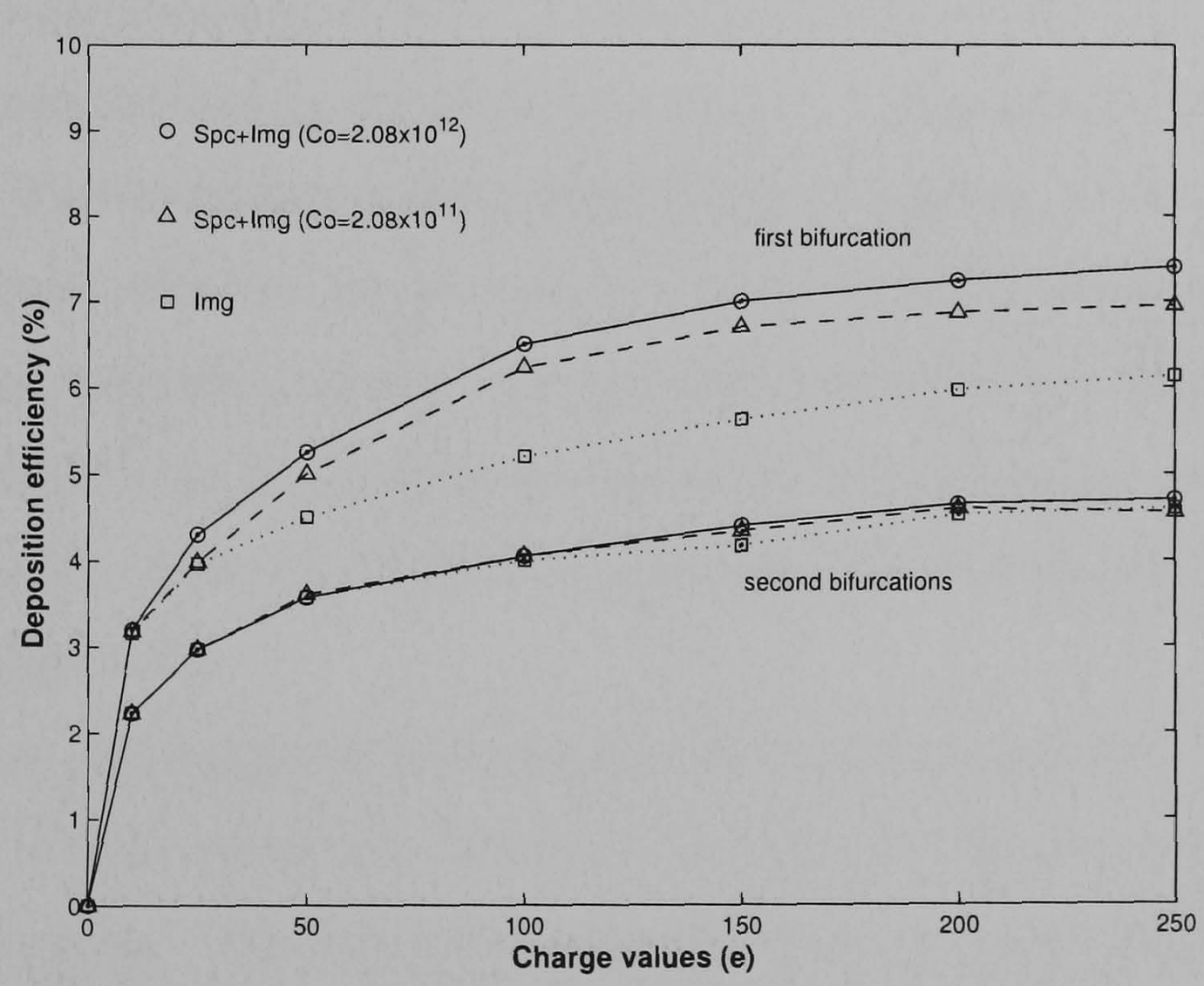

(b) parabolic inlet distribution

Figure 6.21: Deposition efficiencies of 0.5 μm particles carrying various charge values in the 3D bifurcation airway model with both space and image charge forces under a light activity breathing condition

6.4 Aerosol transport and deposition in Alveolar airways model

The transport and deposition of uncharged particles are mainly dominated by gravity and diffusion (mainly for sub-micron particles) as discussed in chapter 3. The numerical study in this section aims to investigate charged aerosol transport and deposition in the alveolar region using the 2D alveolar airway model. The study focuses on the image charge force with the effect of charge elimination by high humidity, and neglects the space charge force because of the low concentration of aerosol in the alveolar region.

6.4.1 Numerical technique

The set of monodisperse aerosols used for the numerical study consisted of 0.3, 0.5, and 1.0 μm particle sizes. A particle number of 20,000 particles was chosen to make the results of deposition efficiency independent of the number of particles. Particle positions were generated in a parabolic distribution along the inlet lumen, with the initial particle velocity equal to the local flow field at the current particle position. The particle transport was simulated with multi-breathing cycles at a respiratory frequency of 15 cycles per minute. Each breathing cycle consists of a 2-second inspiration and immediately followed by a 2-second expiration.

Darquenne [38] suggested that this alveolar model agreed with the ICRP66 model with a 95% confidence bound for deposition efficiency at the end of 5 breathing cycles. The simulation was therefore set up to terminate after 5 breathing cycles. The orientation of the 2D alveolar model was setup at $\theta_g = 60$, which was the average gravitational angle suggested by Yeh and Schum [198]. It was assumed that there was no charge elimination before entering the alveolar region due to the small residence time in the extrathoracic and tracheobronchial regions. This study did not consider the outcome of any hygroscopic effect. The charge decay function in the alveolar region was

Table 6.2: Effects of diffusion mechanism on uncharged aerosol deposition efficiency in the alveolar model

Particle size	0.3 μm	0.6 μm	1.0 μm
No diffusion	3.86	17.54	48.63
with diffusion	7.39	18.64	48.57

modelled as the first order decay function with a time constant (τ_d) ranging between 4-8 seconds, which can be written as:

$$q(t) = q_0 e^{-\frac{t}{\tau_d}} \tag{6.29}$$

where q_0 is an initial charge value on a particle.

The particle size in this study were no greater than 1 μm. The diffusion mechanism becomes one of the dominant mechanisms. Table 6.2 gives a comparison of numerical results between a diffusion mechanism and no such mechanism. It shows that the diffusion mechanism affects particle deposition when particle size is less than 1 μm. Thus the diffusion term is included in the numerical model in the 2D alveolar model.

6.4.2 Model validation and preprocessing

Validation of the 2D alveolar model was undertaken by computation of the deposition efficiencies of uncharged particles and then comparing them with the results from the empirical model ICRP66. A particle size range of 0.6 - 5.0 μm was selected for validation with a respiratory frequency of 15 cycles per minute.

Comparison between the numerical results and the deposition data predicted by the empirical model ICRP66 given in Figure 6.22 shows that the numerical results agree with the results of the ICRP66 model with 95% confidence bound as suggested by Darquenne [38]. Particles less than 2 μm still remains suspended in the alveolar model at the end of 5 breathing cycles. However, the summation of suspended and deposited particles is still in the

95% confidence bound.

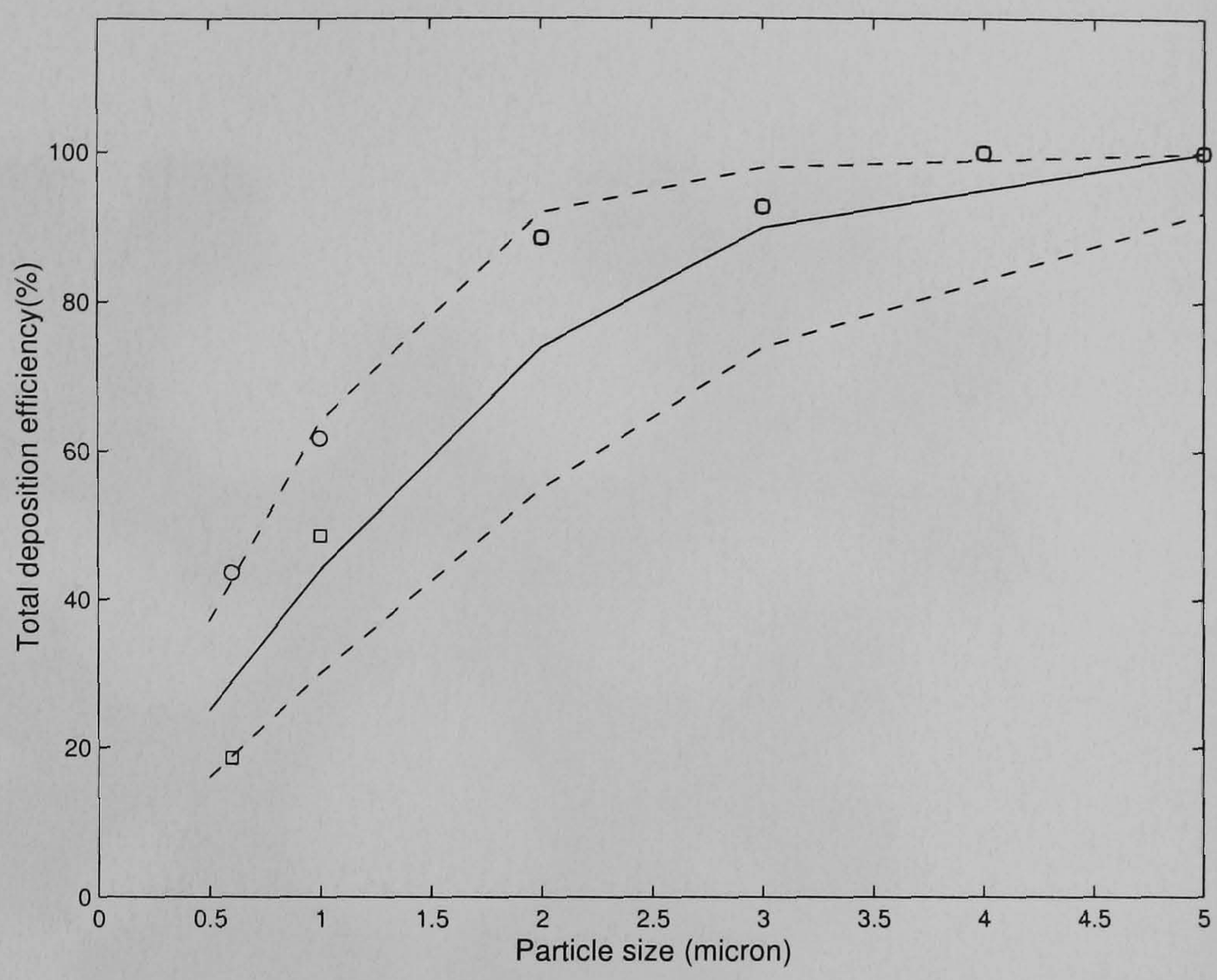

Figure 6.22: Comparison between deposition data from the 2D simulation and the predicted deposition data from the ICRP66 model. The solid and dashed lines represent the mean, and upper and lower 95 % confidence bounds of the predictions. The squares represent the deposited particles by simulation, and the circles represent the combination of deposition and suspended particles at the end of the fifth breath (ICRP66 data obtained from [39])

In the pre-processing step, the developed software searches for the nearest wall distance for the image charge force computation. Figure 6.23 shows the magnitude of the nearest wall vector. The longest distance align at the central lumen of structures. The directions of vectors are perpendicular to, and directed towards the nearest edge of structure.

6.4.3 Results and discussion

6.4.3.1 Transport and deposition of charged aerosols

Numerical results of deposition efficiencies of charged particle sizes of 0.3, 0.5, and 1.0 μm with a decay time constant of 4 seconds are shown in Figure 6.24 as a function of the airway generation number (numerical data can be found in Table C.7, C.8, and C.9). The deposition efficiencies increase when particles

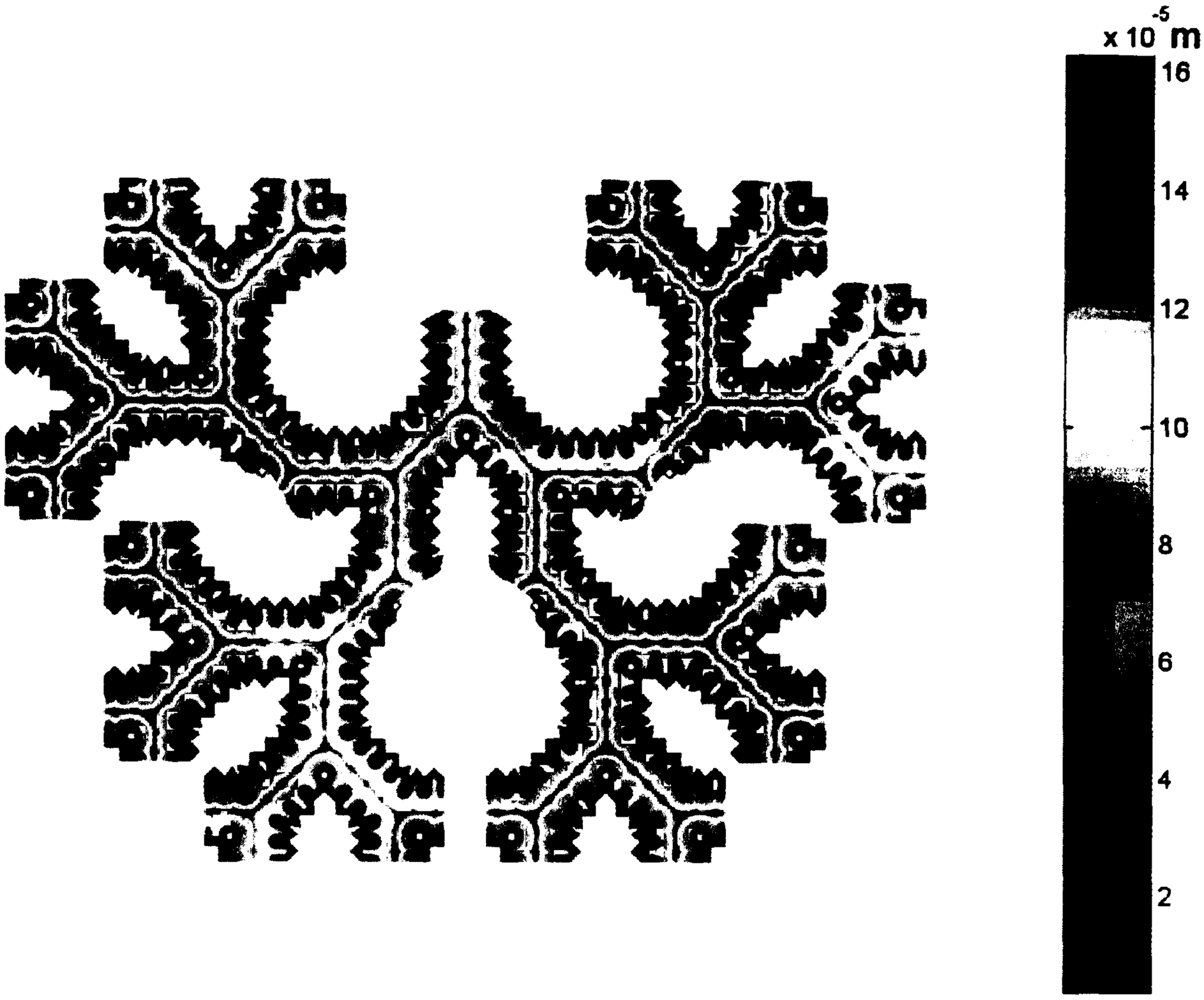

Figure 6.23: Magnitudes of the nearest wall distance vector in the 2D alveolar model (displayed sections: main, A, C, F, and H based on Figure 2.3)

carry high charge values, especially in the airway generation numbers 20 and 21. However, the increase in deposition efficiency also depends on the particle size. The deposition efficiency of 0.3 μm particles increases more than that of 0.6 and 1.0 μm particles at the same value of charge because the mobility of 0.3 μm particle is higher than that of 0.6 and 1.0 μm particles.

The residence time of particles in the alveolar region is longer than that in the tracheobronchial region due to the low Reynolds number ($Re < 2.0$) . Many particles may be suspended in the lungs after completing a breathing cycle. Examples of the aerosol transport of 0.3, 0.6, and 1.0 μm particles are shown in Figure 6.25, 6.26, and 6.27, respectively. In the first breathing cycle, the particles convect into the deeper airway generations and finally reach airway generation number 22 at the end of the inhalation phase. Then the

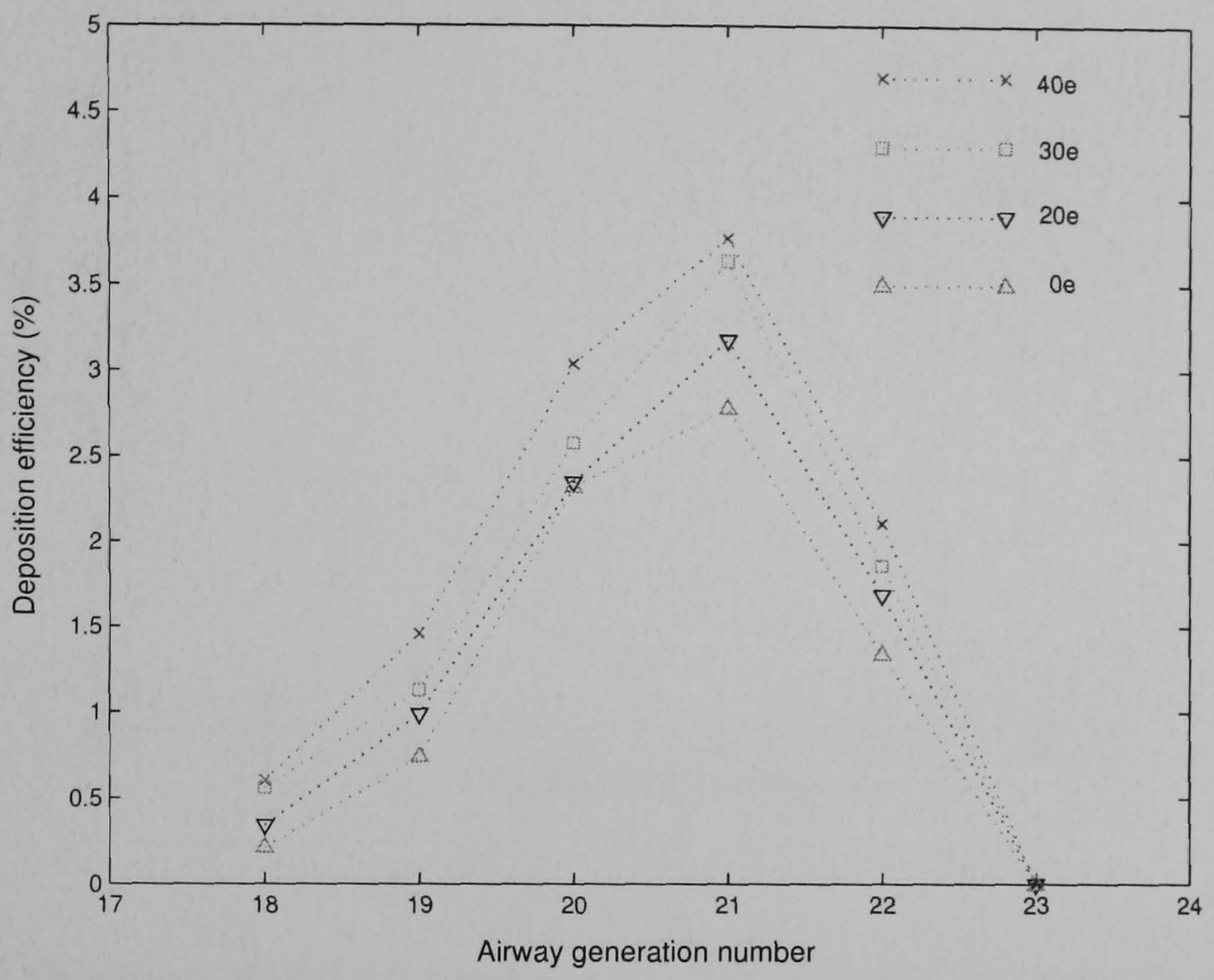

(a) $d_p = 0.3\ \mu m$

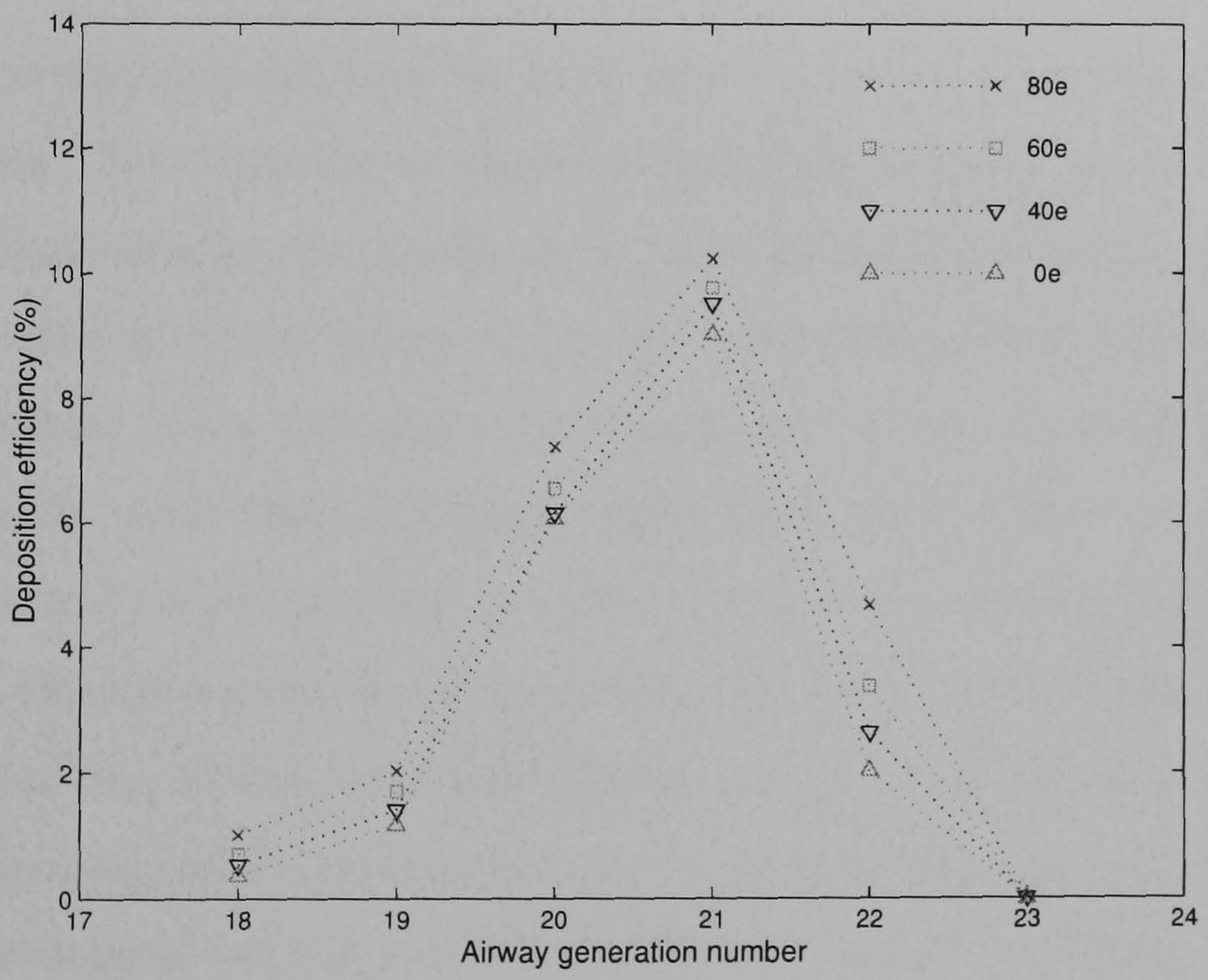

(b) $d_p = 0.6\ \mu m$

Figure 6.24: Deposition efficiencies of charged particles in the 2D alveolar model as a function of airway generation number with various charge values

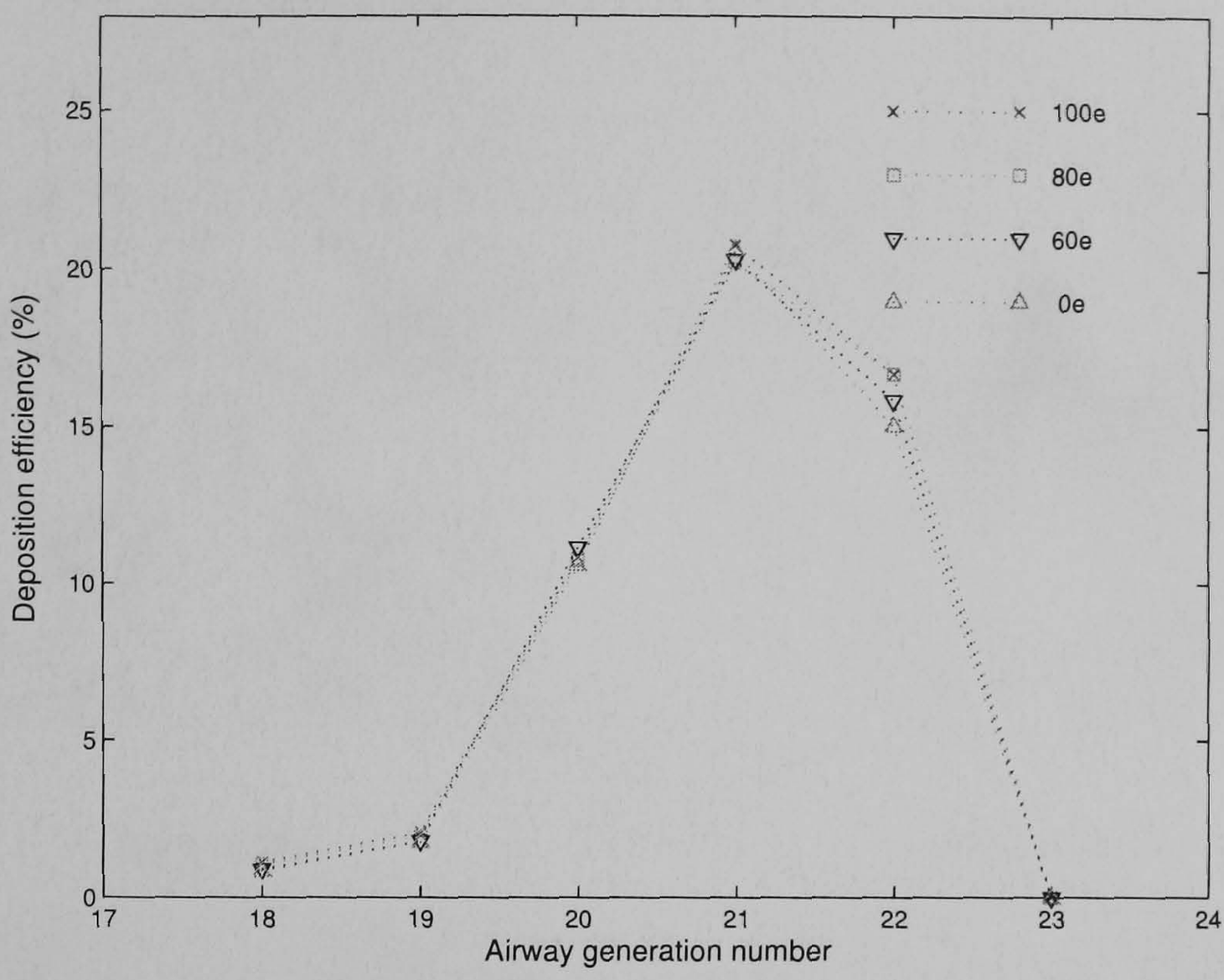

(c) $d_p = 1.0\ \mu m$

Figure 6.24: Deposition efficiencies of charged particles in the 2D alveolar model as a function of airway generation number with various charge values (Cont.)

particles reverse direction into the main alveolar section when the exhalation phase starts. The transient of suspended particles of these particles sizes is different depending on the gravity force. The transient of 0.3 μm particles is less dominated by gravity forces, hence the suspended particles are distributed in all directions. Many particles are still suspended at the end of the breathing cycles. On the other hand, the gravity effect has a greater effect on the transport of 0.6, and 1.0 μm particles, therefore, the number of suspended particles reduces in the subsequent breathing cycles. The trajectories of particles tend to move into the airway branches followed by the same direction of gravity vector. The comparison of local deposition patterns between uncharged and charged particles of 0.3, 0.6, and 1.0 μm after the end of 5 breathing cycles are given in Figure 6.28, 6.29, and 6.30, respectively. Many particles are deposited in the acinus by gravity and diffusion forces because of the long residence times. The local depositions of charged particles of 0.6 and 1.0 μm are slightly different from those of the uncharged particles, whereas that of 0.3 μm particles is

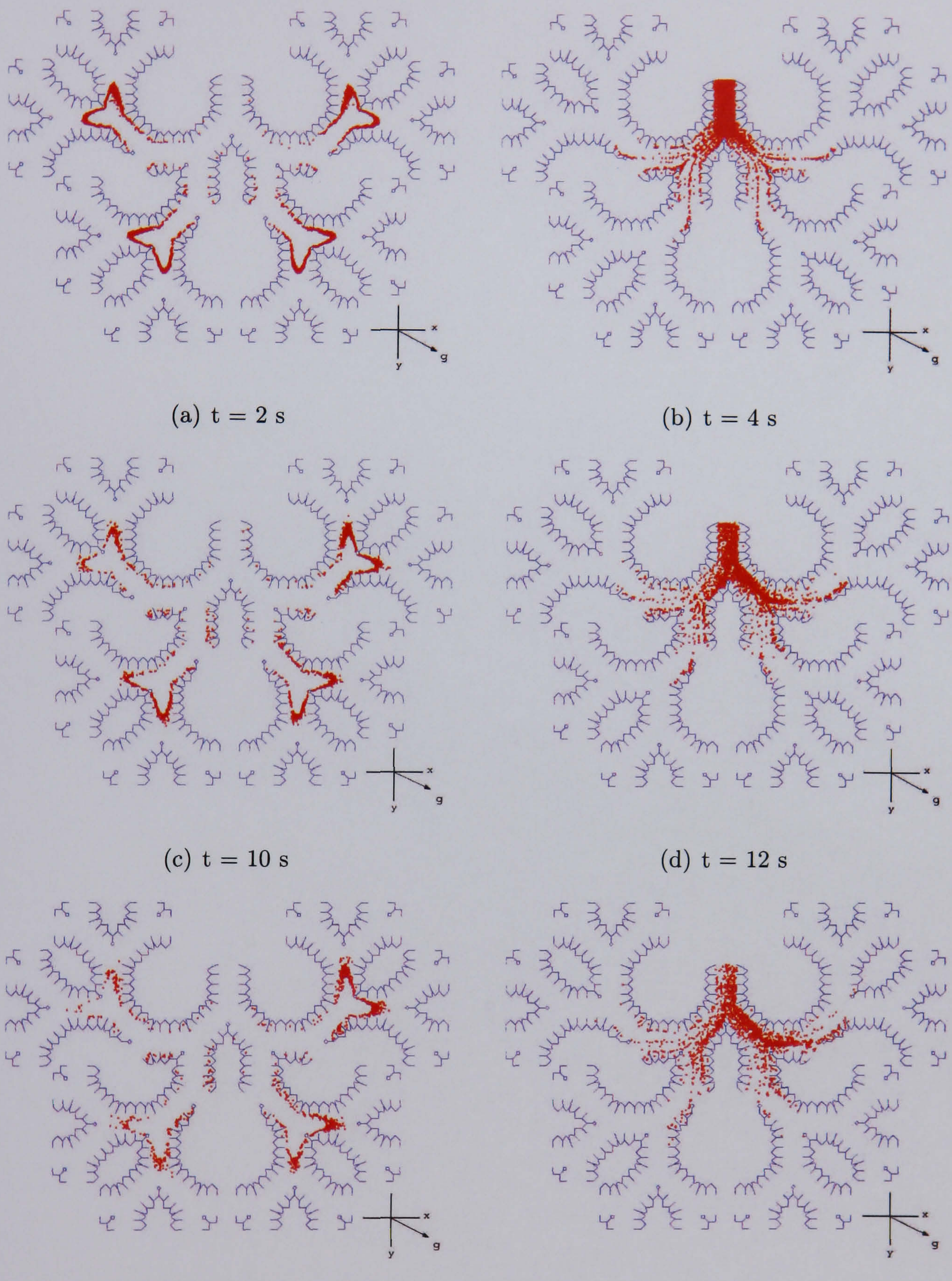

(a) t = 2 s

(b) t = 4 s

(c) t = 10 s

(d) t = 12 s

(e) t = 18 s

(f) t = 20 s

Figure 6.25: Transient of 0.3 μm suspended particles in the 2D alveolar model during 5 breathing cycles (displayed sections: main, A, C, F, and H based on Figure 2.3)

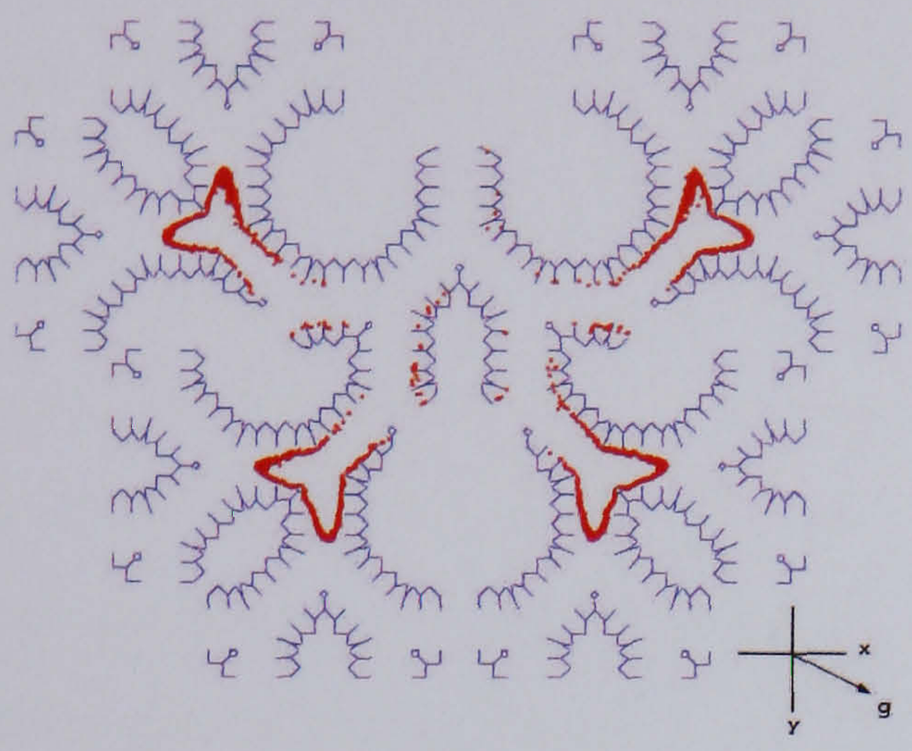

(a) t = 2 s

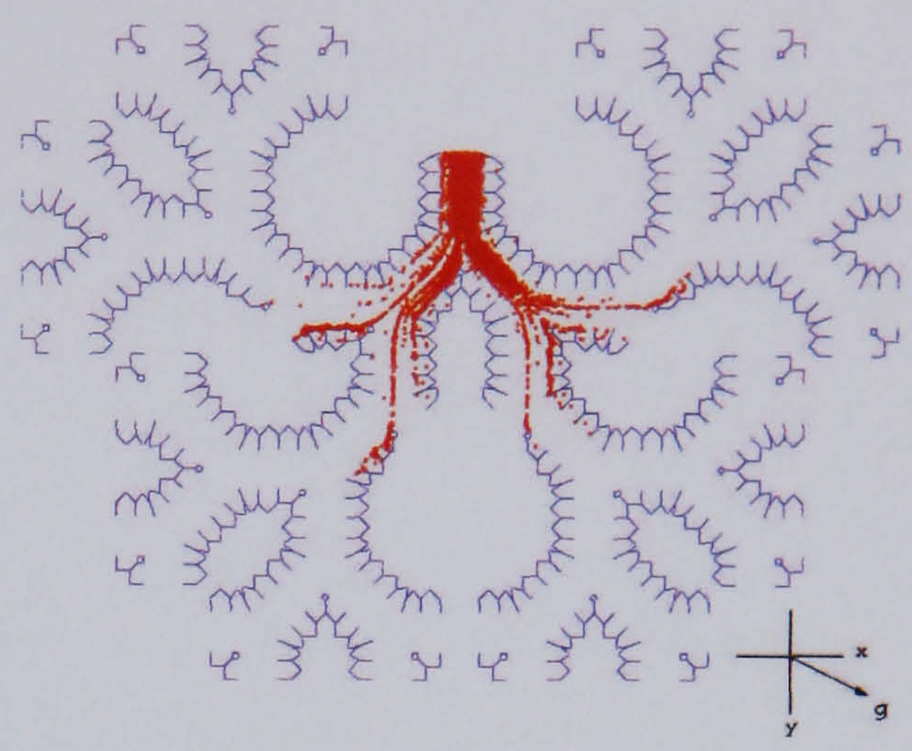

(b) t = 4 s

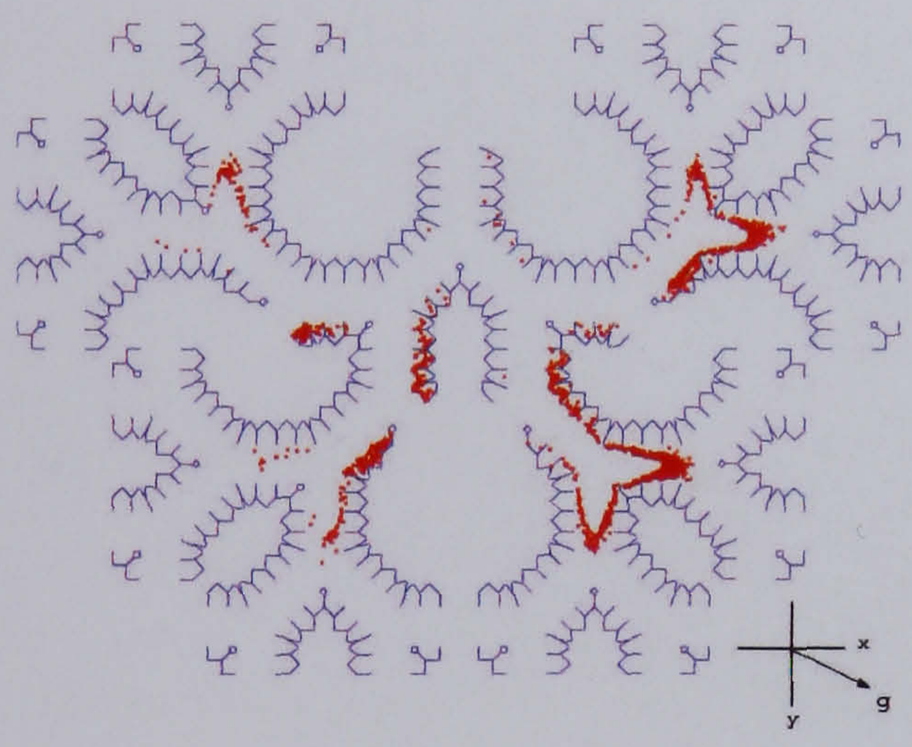

(c) t = 10 s

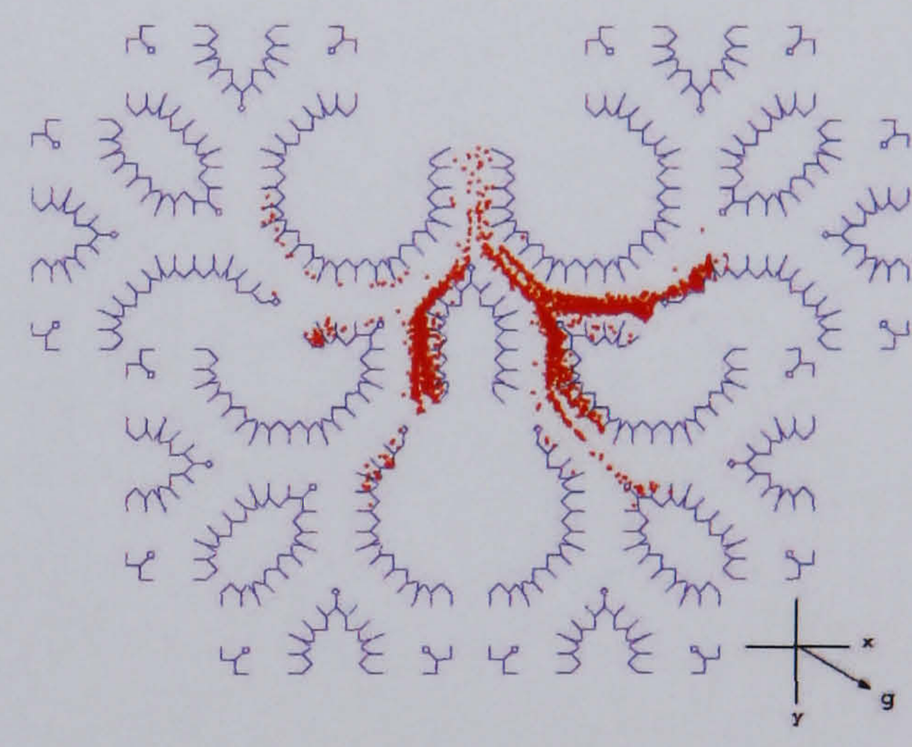

(d) t = 12 s

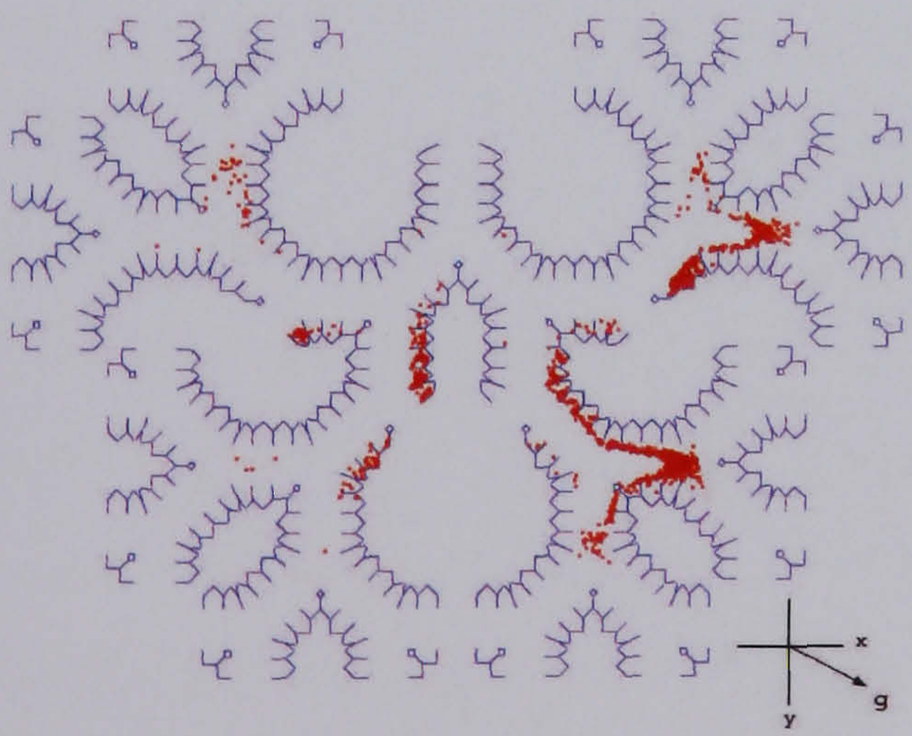

(e) t = 18 s

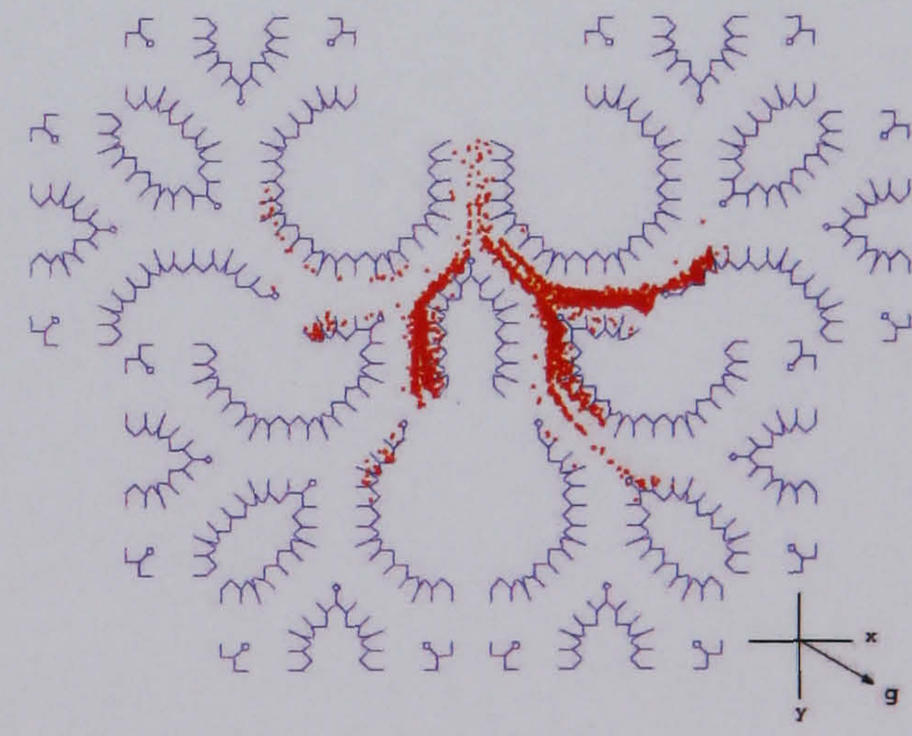

(f) t = 20 s

Figure 6.26: Transient of 0.6 μm suspended particles in the 2D alveolar model during 5 breathing cycles (displayed sections: main, A, C, F, and H based on Figure 2.3)

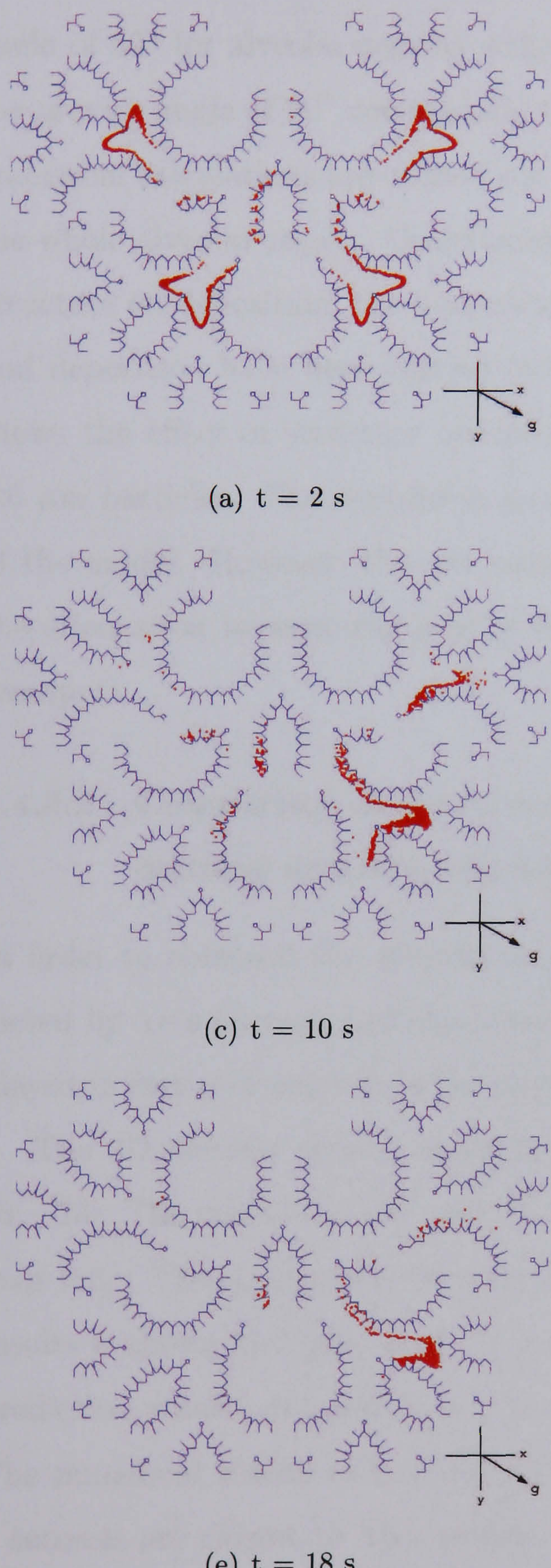

(a) t = 2 s

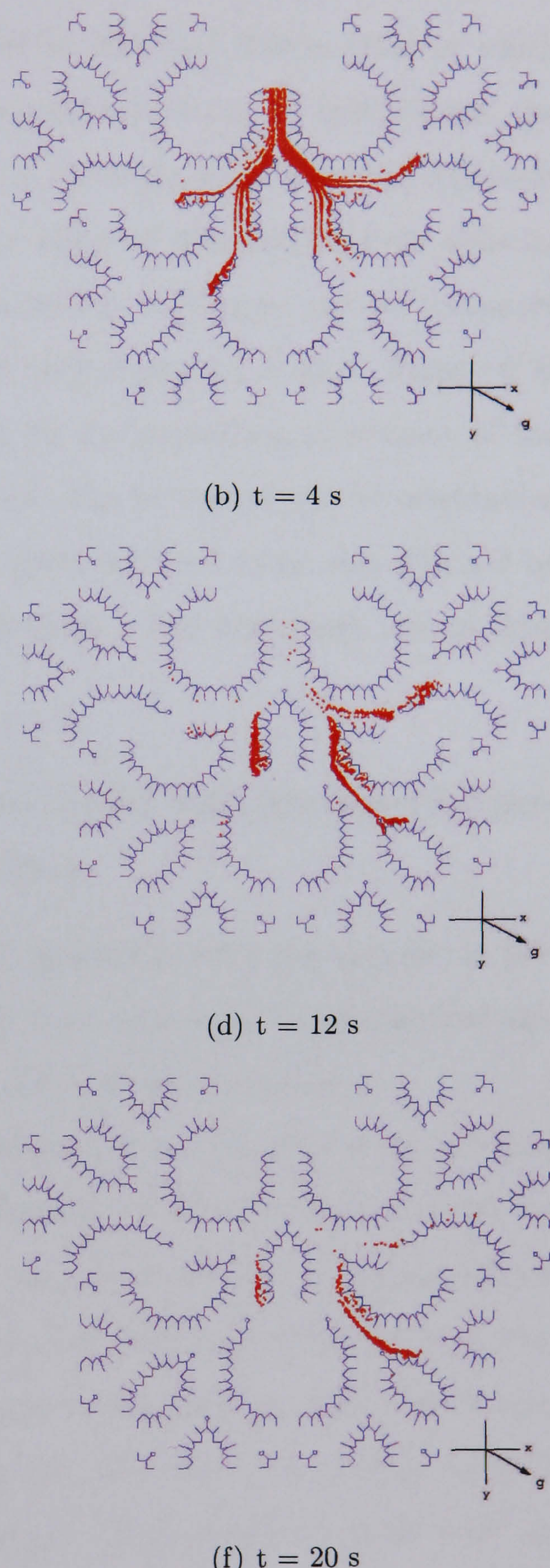

(b) t = 4 s

(c) t = 10 s

(d) t = 12 s

(e) t = 18 s

(f) t = 20 s

Figure 6.27: Transient of 1.0 μm suspended particles in the 2D alveolar model during 5 breathing cycles (displayed sections: main, A, C, F, and H based on Figure 2.3)

more obviously altered by the image charged force.

The numerical results discussed above are calculated based on a gravity angle of 60° for alveolar regions suggested by Yeh and Schum [198] in which the gravity angle of 90° corresponds to a horizontal tube. In this respect, the numerical calculations are carried out with a gravity angle of 60° to represent the whole alveolar region. Considering the effect of orientation of the alveolar structure on deposition, the numerical modelling of charged aerosol transport and deposition have been carried out at various gravity angles. Figure 6.31 shows the effect of structure orientation on the deposition increment of the 0.6 μm particles. The deposition increment can be varied by the orientation of the model. However, the sub-micron particles tend to be less affected by the orientation because the gravity force plays a less important role in their transport.

6.4.3.2 Comparison of the numerical results with the analytical predictions and experimental data

In order to compare the alveolar model deposition with the deposition predicted by Yu's formula and experimental data, numerical results are also displayed in terms of deposition increment ΔP defined in chapter 4.

The 2D alveolar airway model represents the airway generation numbers 18 - 23. The model can be used to represent the alveolar region of the human lung. The comparison between the numerical results and Yu's predicted results is shown in Figure 6.32. The numerical results are different from Yu's prediction results depending on the charge decay function and particle size. The numerical results of 0.3 and 0.6 μm particle sizes with a decay time of 8 seconds are closest to Yu's results, whereas the numerical results with the other decay functions are less than the Yu's results. The numerical results for 1.0 μm particles have a curve with a slope less than that of Yu. The deposition efficiencies are higher than Yu's results when a particle charge is less than $80e$, but they become less when the charge value is more than $110e$. However, Yu's

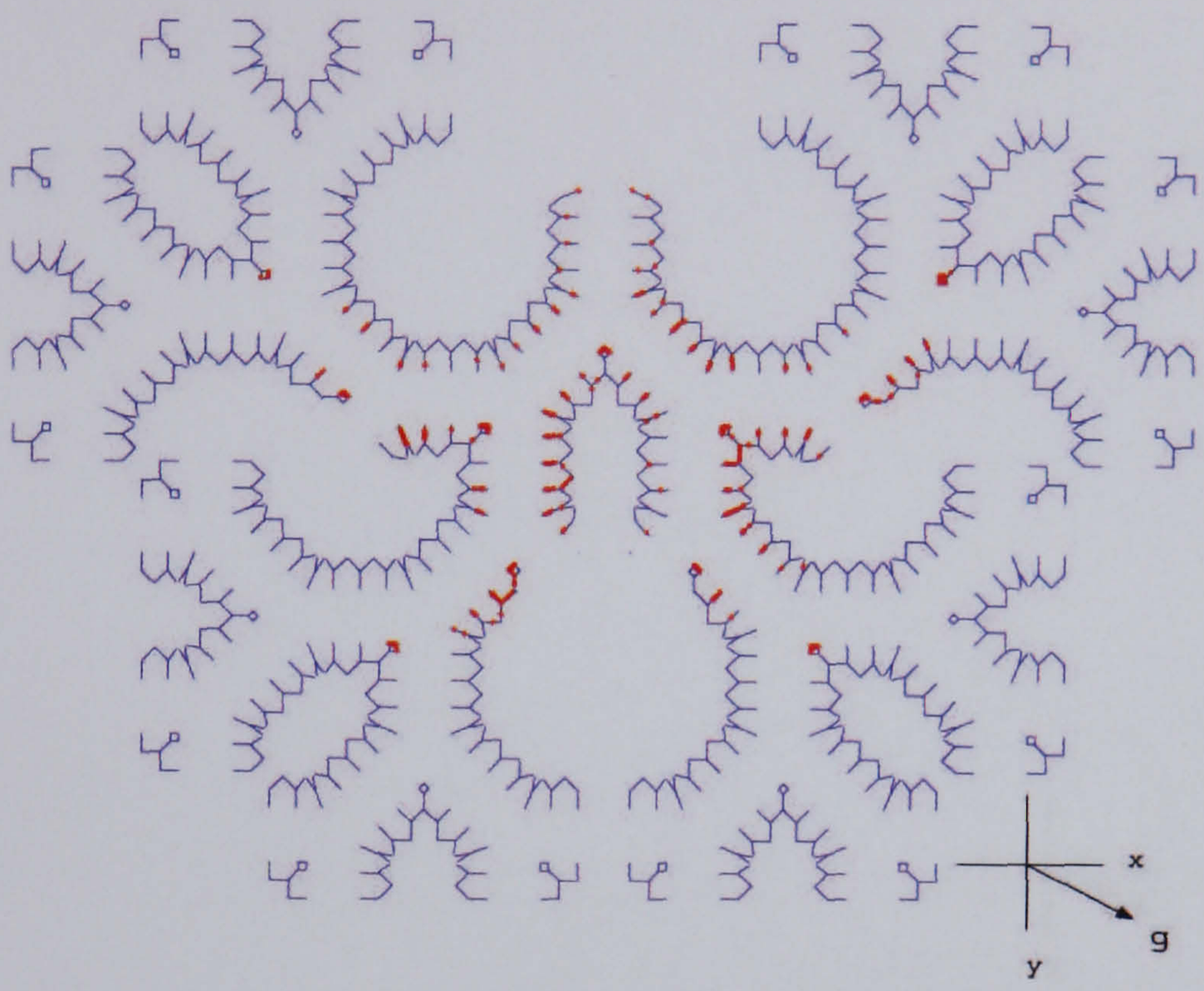

(a) $q = 0e$

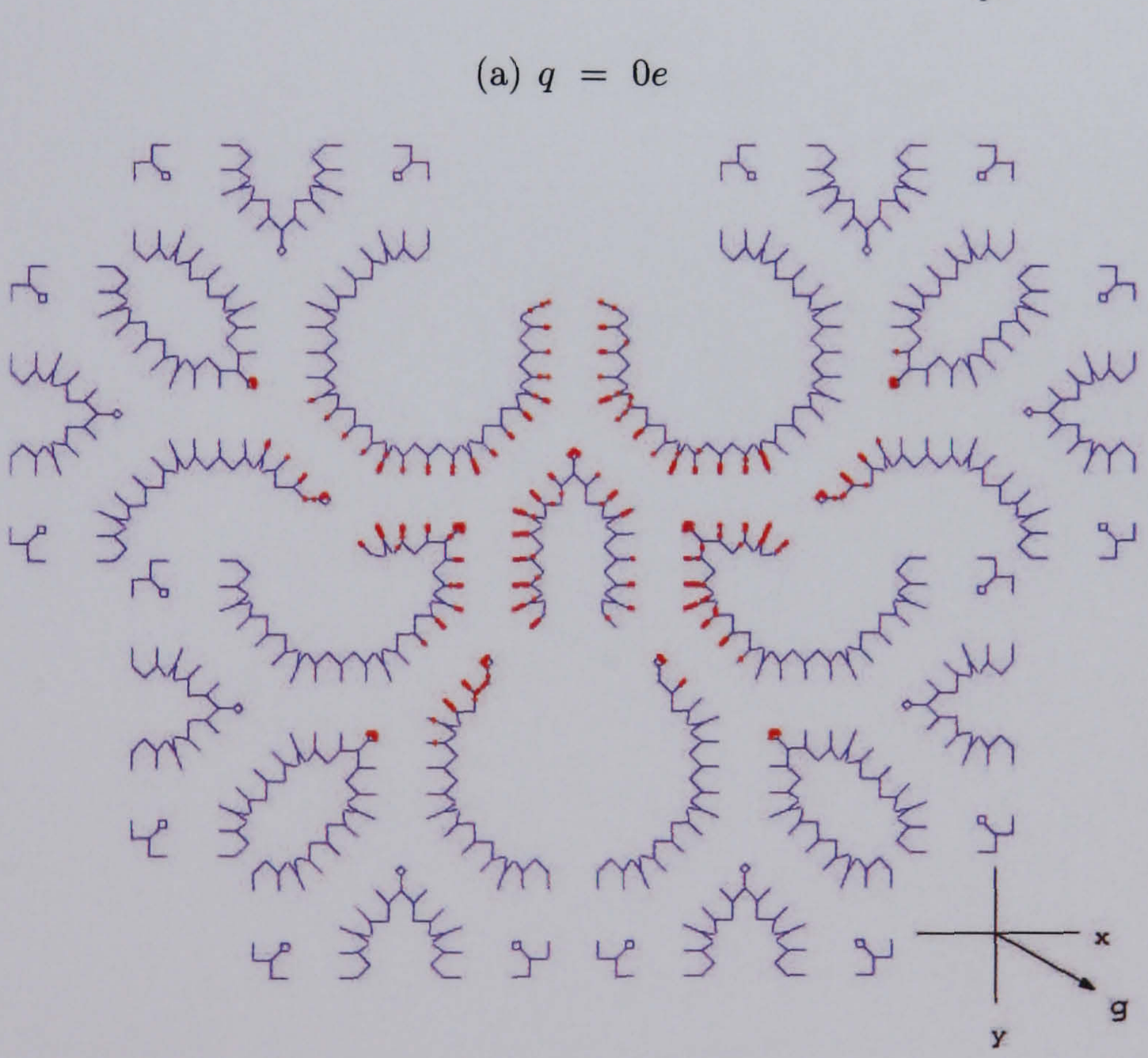

(b) $q = 50e$

Figure 6.28: Local deposition patterns of 0.3 μm particles in the 2D alveolar model after 5 breathing cycles (displayed sections: main, A, C, F, and H based on Figure 2.3)

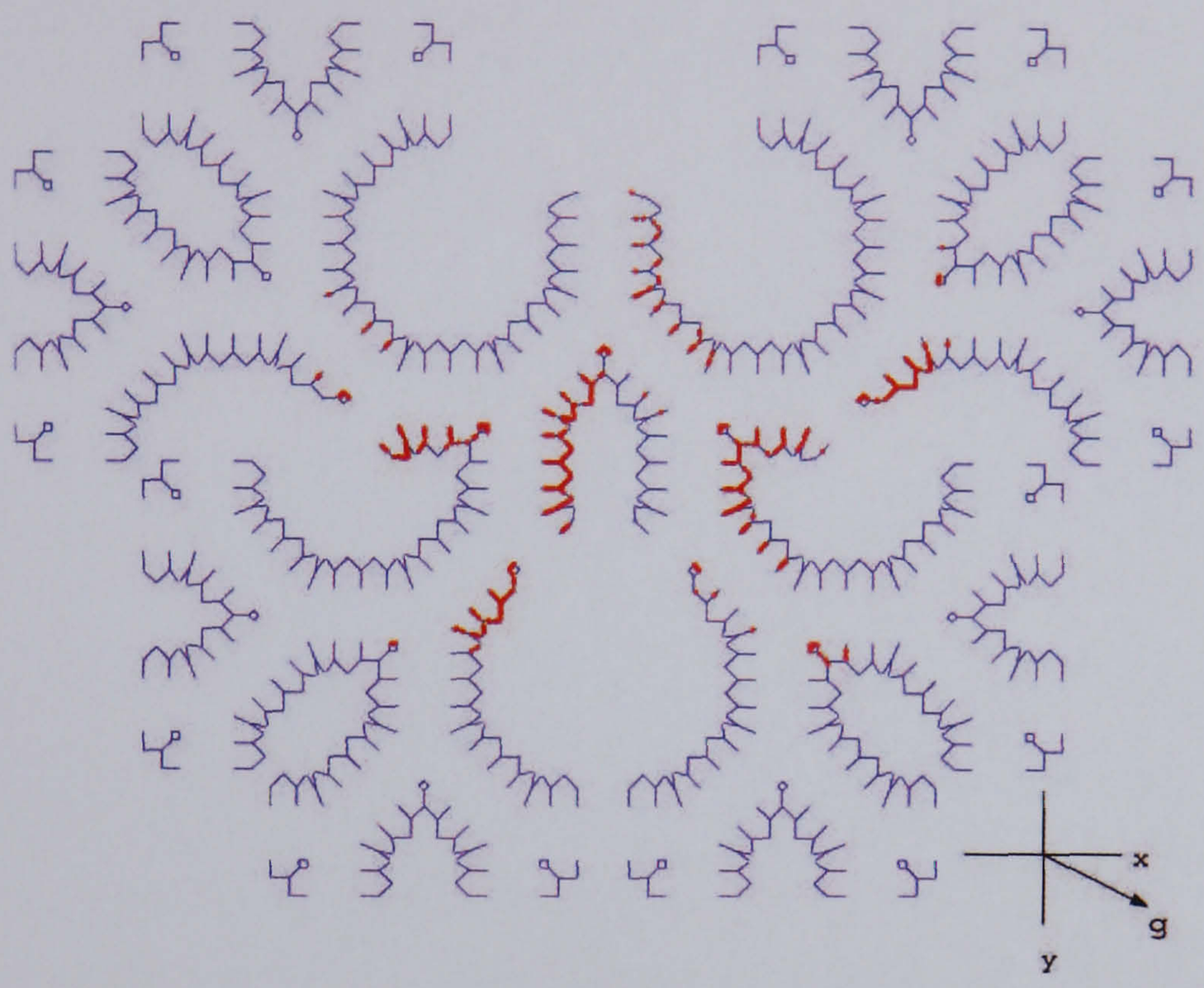

(a) $q = 0e$

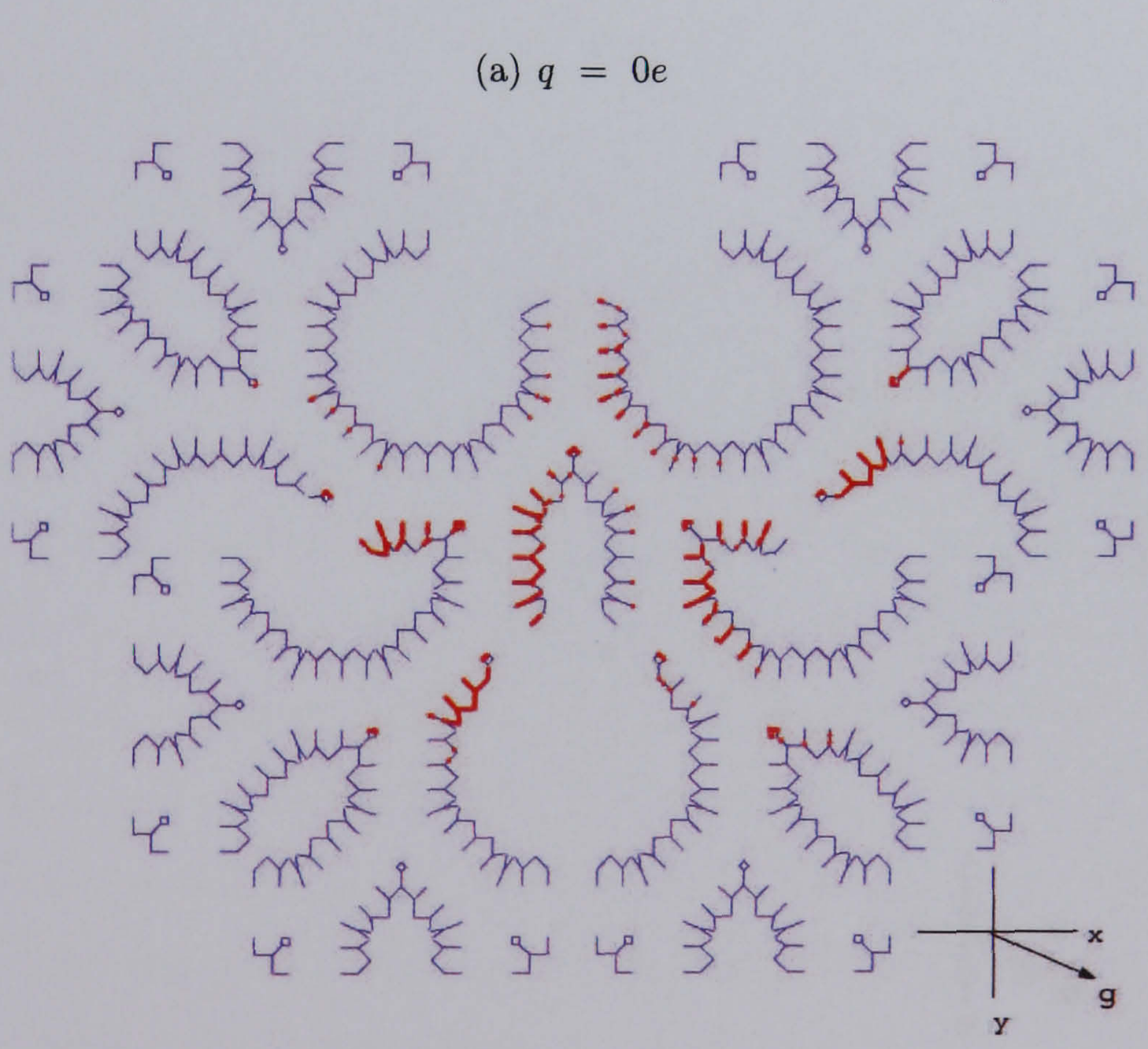

(b) $q = 80e$

Figure 6.29: Local deposition patterns of 0.6 μm particles in the 2D alveolar model after 5 breathing cycles (displayed sections: main, A, C, F, and H based on Figure 2.3)

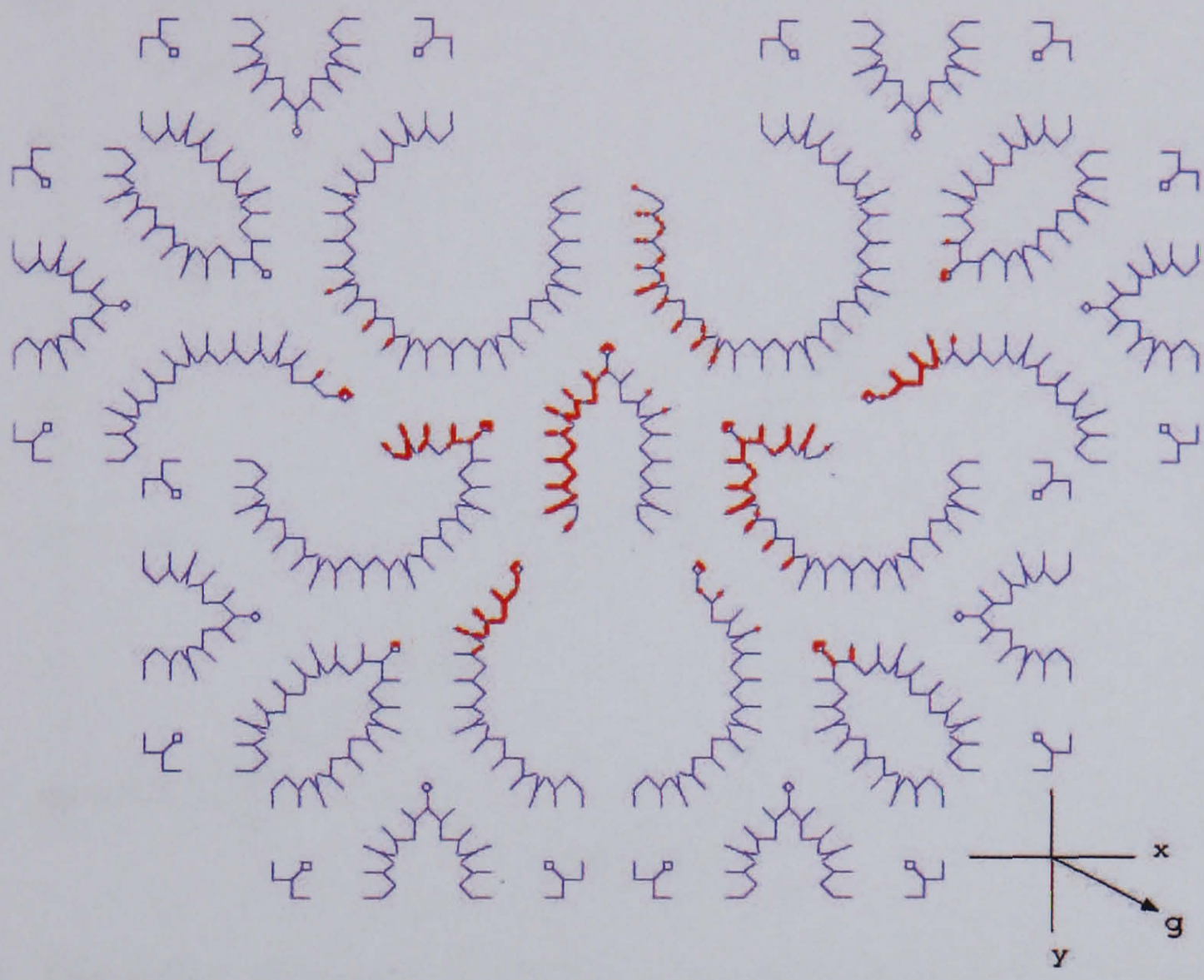

(a) $q = 0e$

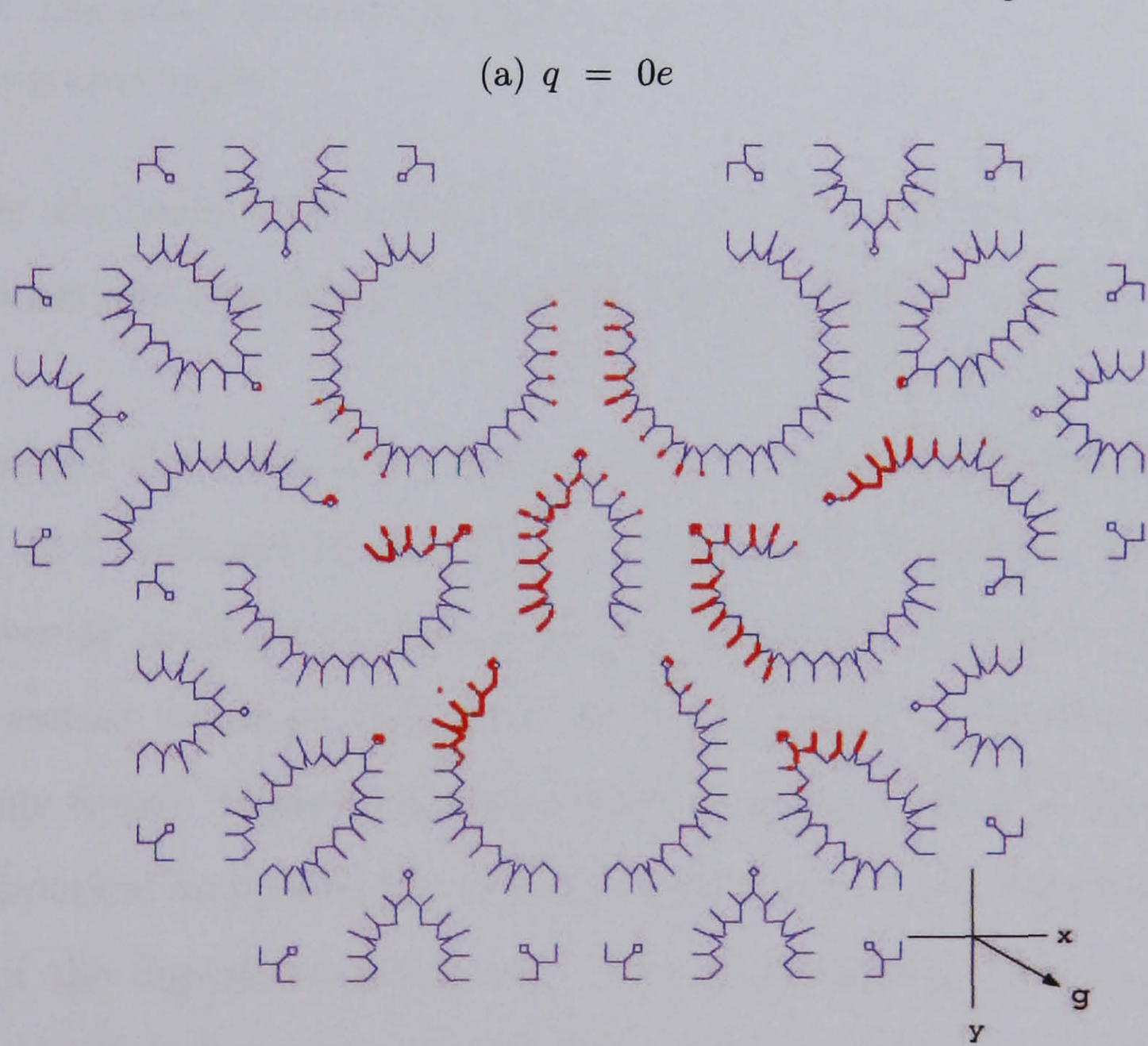

(b) $q = 120e$

Figure 6.30: Local deposition patterns of 1.0 μm particles in the 2D alveolar model after 5 breathing cycles(displayed sections: main, A, C, F, and H based on Figure 2.3)

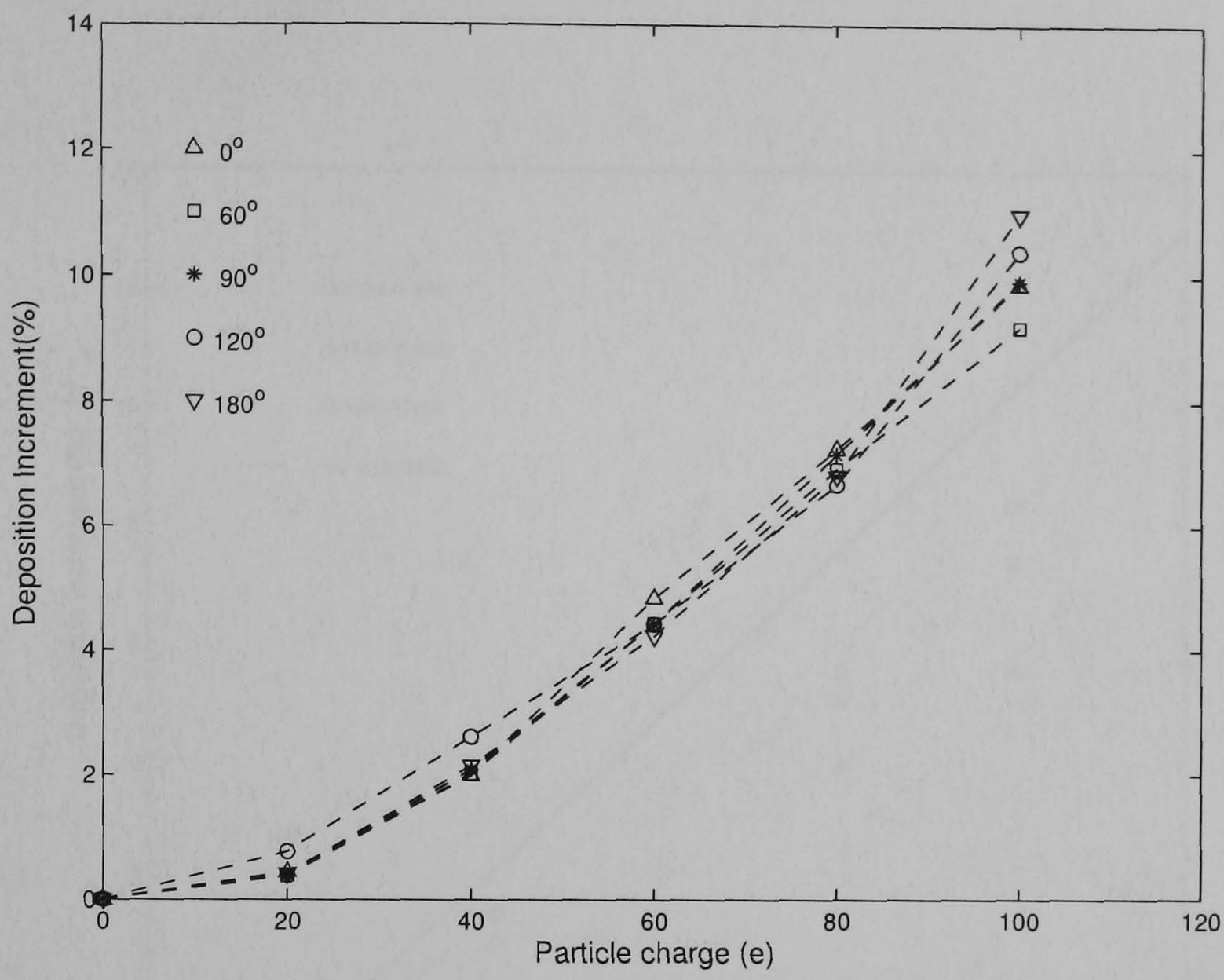

Figure 6.31: Deposition increment of 0.6 μm charged particles in the 2D alveolar model with various gravity angles

predictions are based on a smooth tubular structure without considering the diffusion force and the charge elimination due to the high humidity in human lung.

To compare the numerical results with the experimental data by Tarroni et al.[180] and Melandri et al. [129], the numerical deposition efficiencies in the 2D alveolar model are added with the predicted deposition efficiency in tracheobronchial region as calculated by Yu's formula (without the effect of space charge force). Figure 6.33 shows the comparison between the combined results (numerical and predicted deposition efficiencies) and experimental data in terms of the deposition increment. The experimental data has a greater variance at higher charge levels, especially for a particle size of 1.0 μm. The increase of deposition by image charge force strongly depends on the charge values and the particle sizes. The combined results of 0.6, and 1.0 μm particles with $\tau_d = 8\ s$ agree well compared to the experimental data, but those of 0.3 μm particles are an underestimate with an error about 1%. Since the

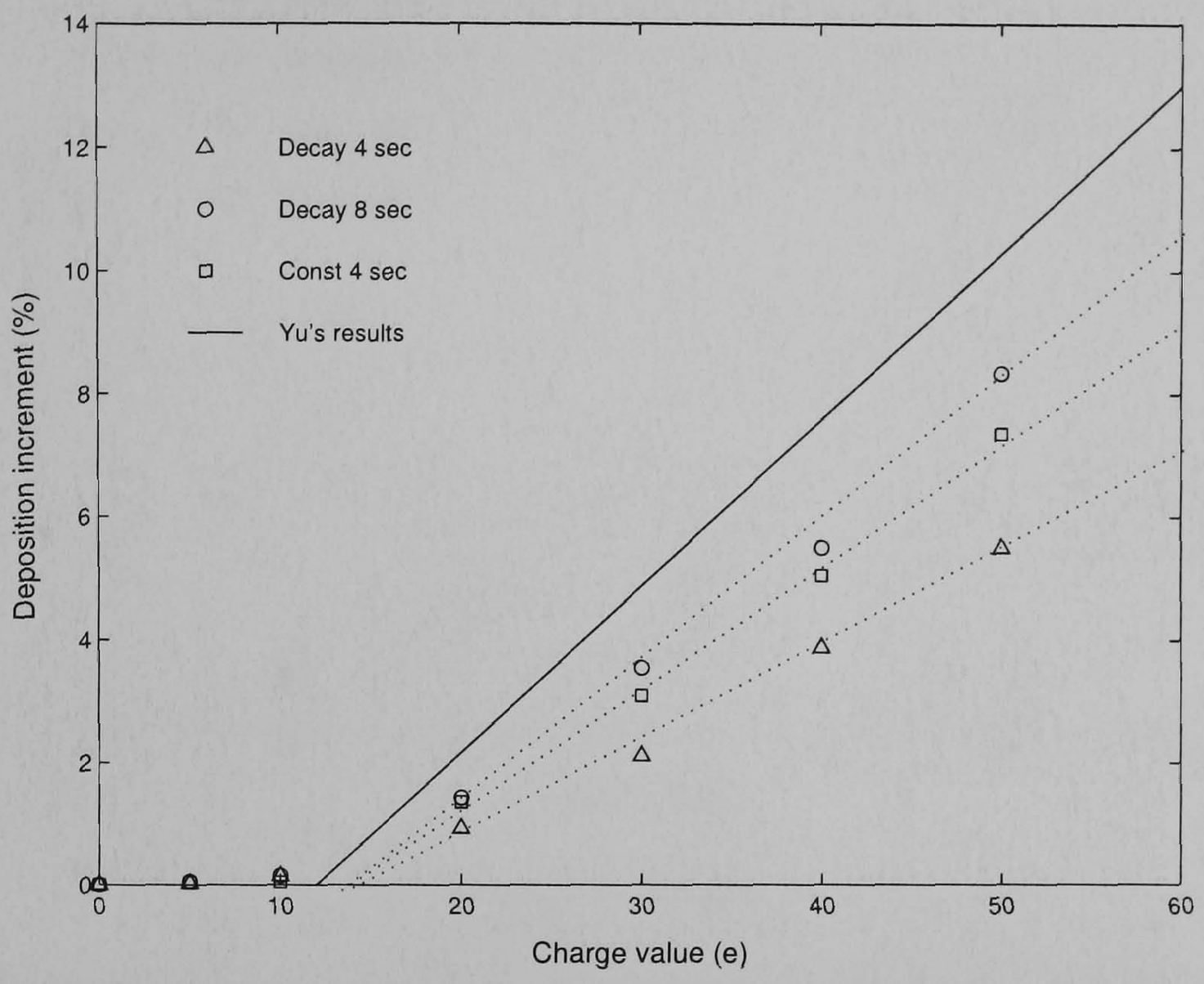

(a) $d_p = 0.3\ \mu m$

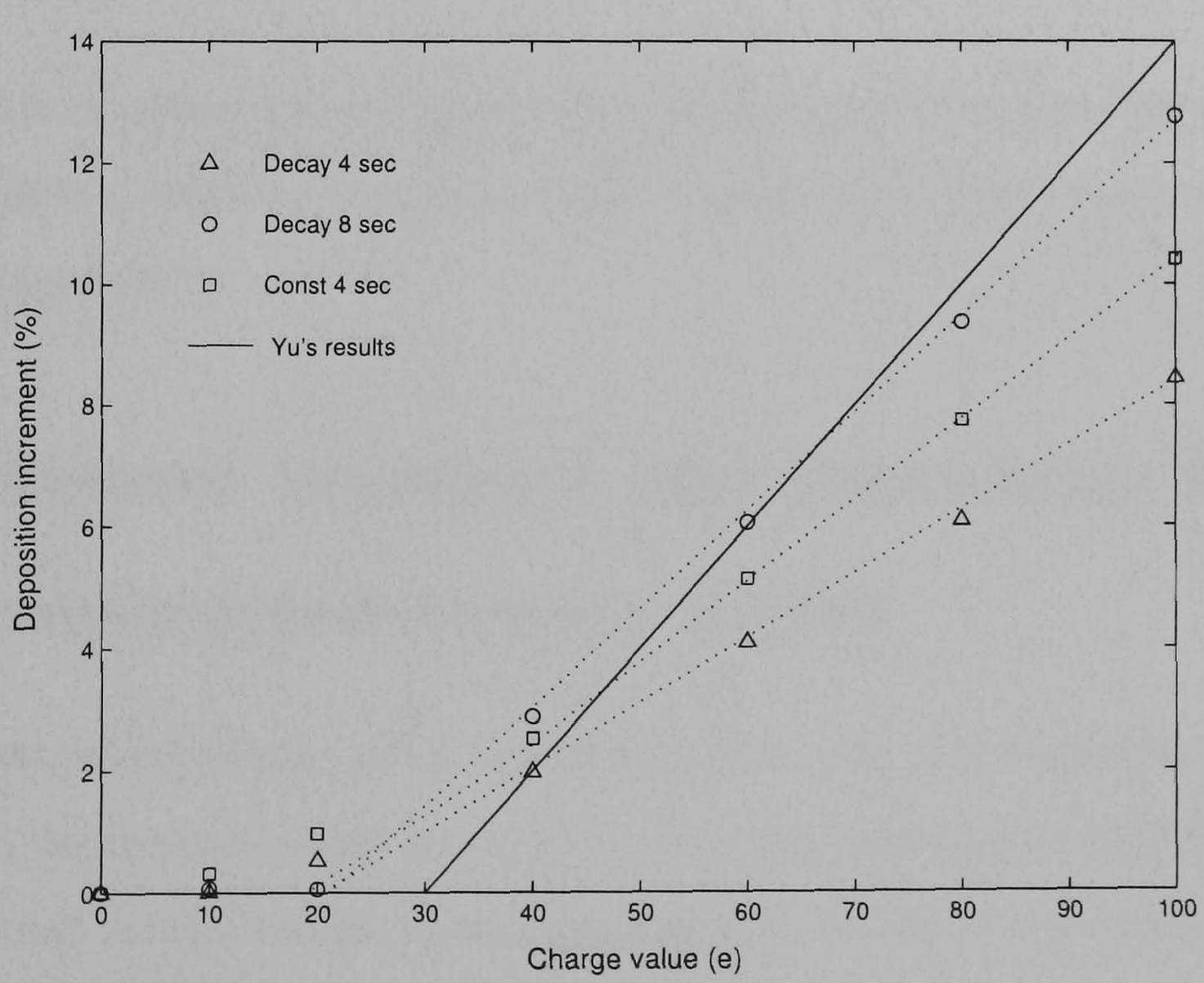

(b) $d_p = 0.6\ \mu m$

Figure 6.32: Comparison of deposition increments in alveolar model with Yu's prediction results

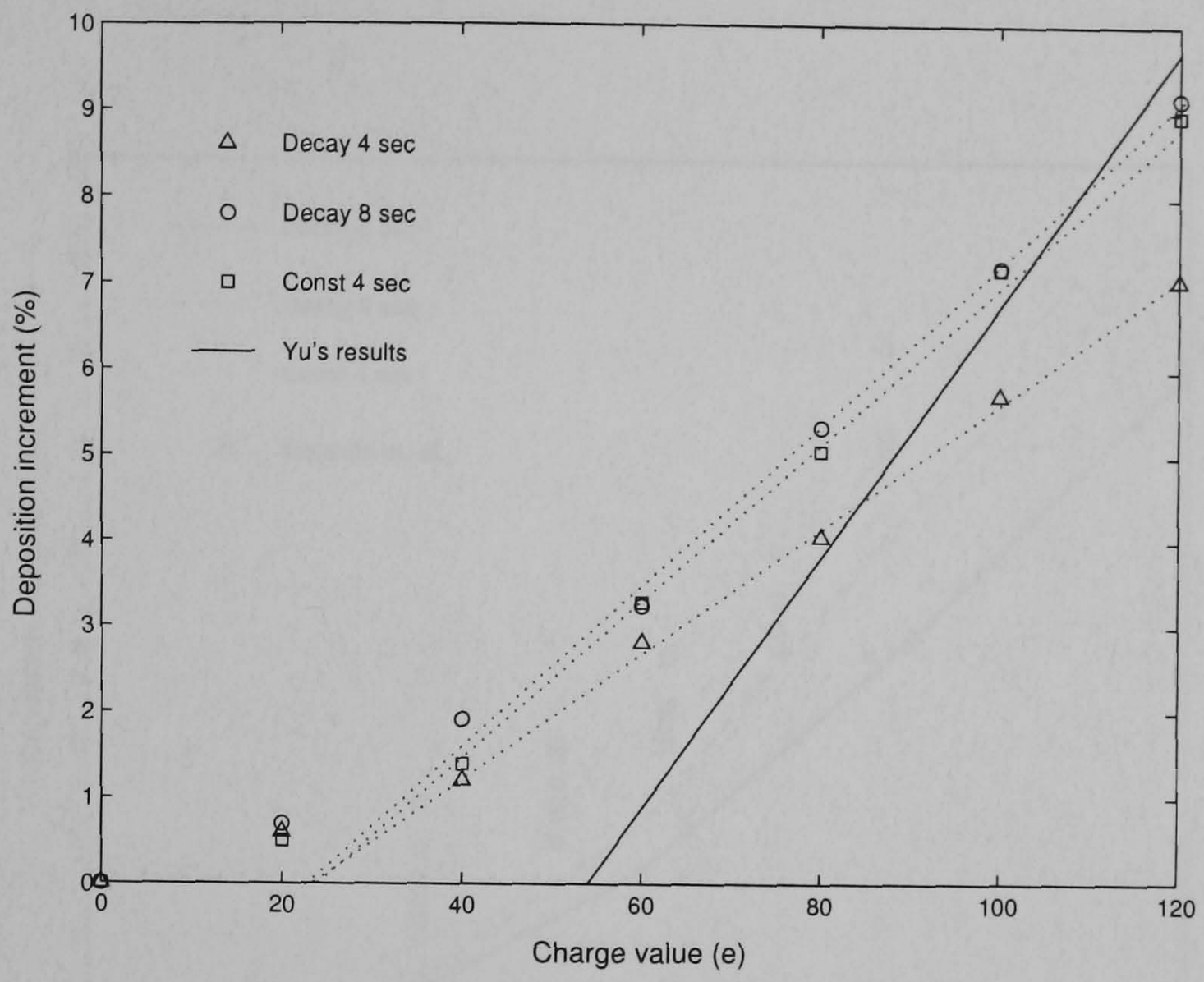

(c) $d_p = 1.0\ \mu m$

Figure 6.32: Comparison of deposition increments in alveolar model with Yu's prediction results (Cont.)

combination of numerical and predicted results neglects the space charge force, it can result in a greater error at the higher charge levels where the space charge has a stronger effect.

6.5 Aerosol transport and deposition in Reconstructed airways model

The reconstructed airway model is different from the morphometrically based model and depends on many factors, i.e., sex, age, and health conditions. The reconstructed airway model is an asymmetrical structure and more complex than the double bifurcation model. Because of the limitation of computational resources, the 3D reconstructed model is focused only on the right-upper part of reconstructed airways as presented in chapter 5. The numerical study in this section aims to investigate the aerosol transport and deposition in the 3D reconstructed airways using a similar numerical scheme to the double bifurca-

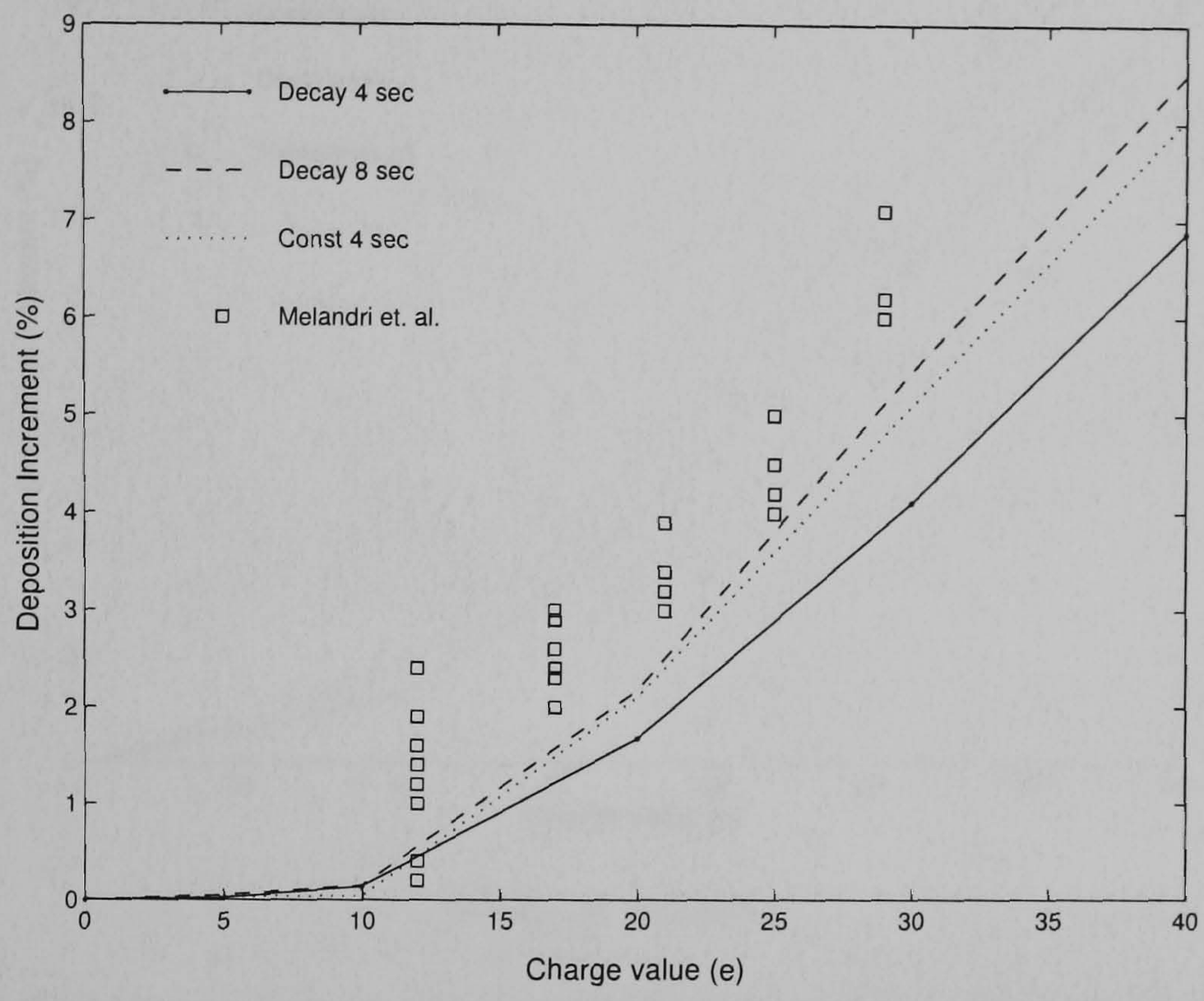

(a) $d_p = 0.3\ \mu m$

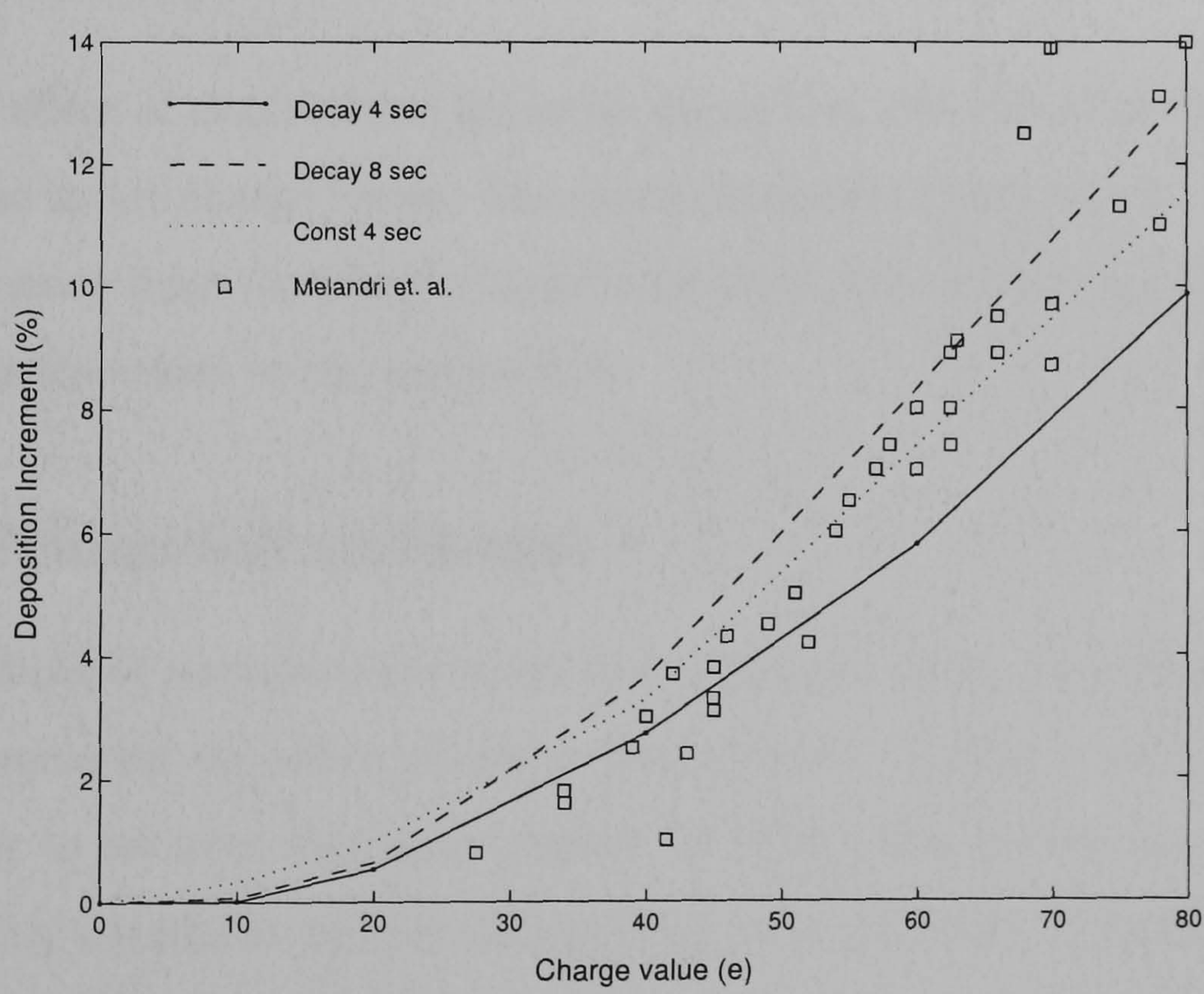

(b) $d_p = 0.6\ \mu m$

Figure 6.33: Comparison between the numerical results and the experimental data of Melandri et al. [129]

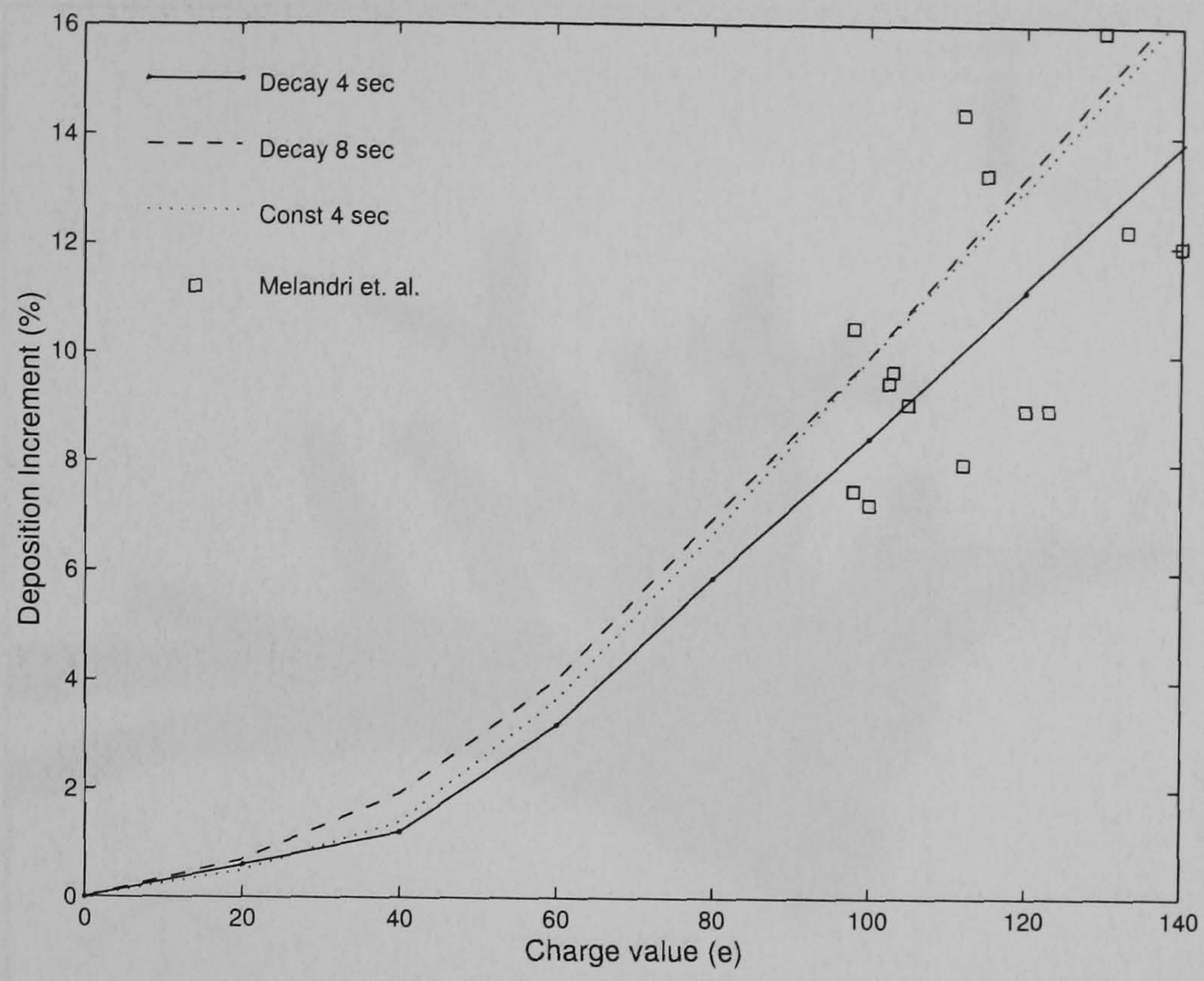

(c) $d_p = 1.0\ \mu m$

Figure 6.33: Comparison between the numerical results and the experimental data of Melandri et al. [129] (Cont.)

tion. The effect of electrostatic forces on deposition efficiencies are considered only for the image charge forces. The space charge force can improve the deposition efficiency from the image charge force when the concentration of aerosol is high, (as discussed in the section 6.3).

6.5.1 Numerical technique

The modelling of particle trajectories was computed using our developed software and included the effect of space charge forces. Airflow is calculated corresponding to an inlet Reynolds number of 1750. The initial particles were located with a uniform particle distribution near the inlet of model with an initial velocity equal to the fluid velocity at the same position. The wall is modelled as a non-slip rigid wall. The particles were not further considered after they touched the walls. A particle number of 100,000 was set up for the numerical calculation, with a constant time step of 1.0 μs.

As in the 3D bifurcation airway model, the numerical model assumes that

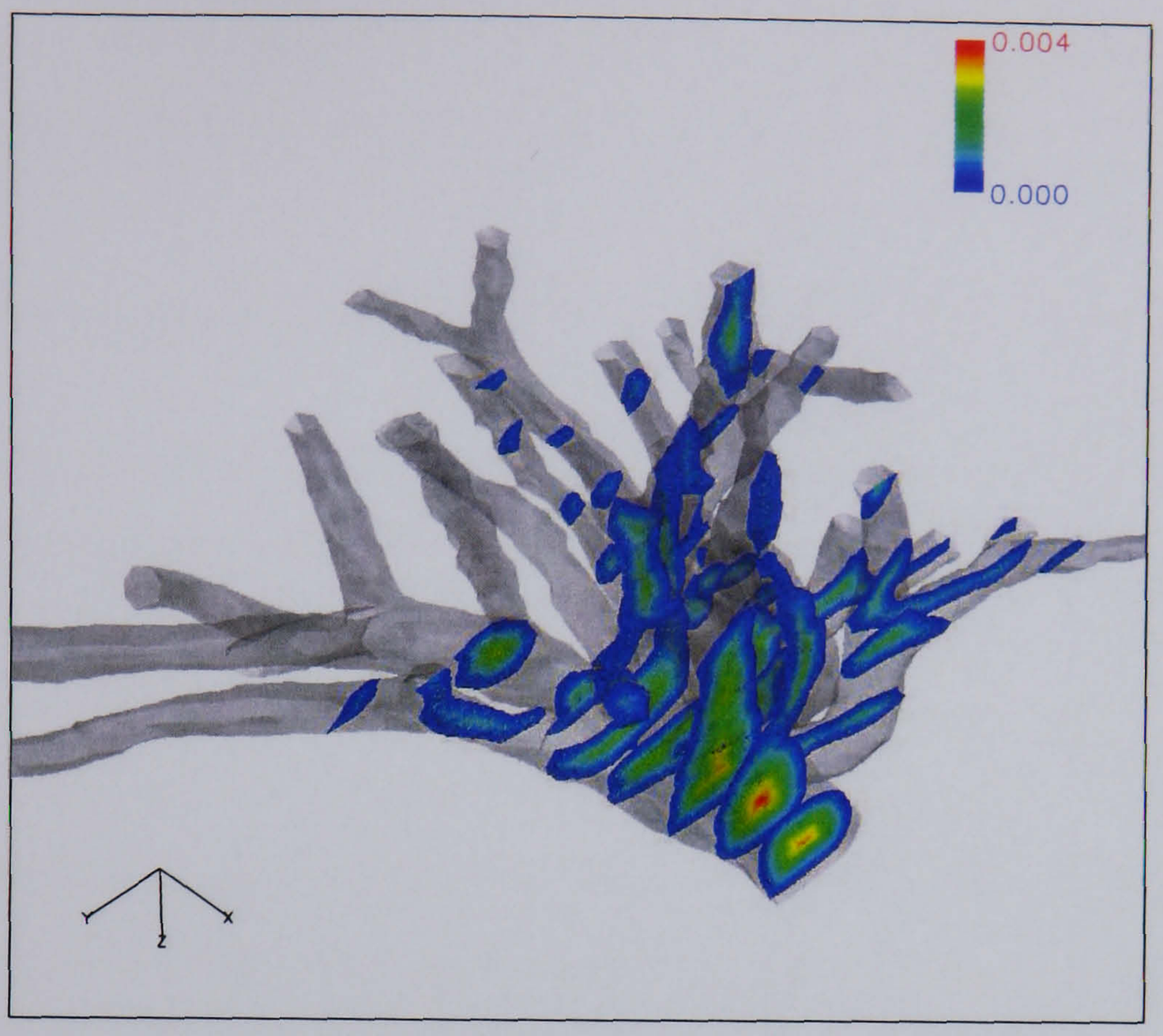

Figure 6.34: Magnitudes of the nearest wall distance vector in the 3D right-upper reconstructed airway model in x-plane (unit: m)

there is no effect of charge elimination due to high humidity in the lung because of the short residence time in the tracheobronchial region ($< 50\ ms$).

In the preprocessing stage, the magnitude of the nearest wall distance vector from any position within the model is shown Figure 6.34, which gives the contour at a plane z=0. Figure 6.35 shows the contour on planes at various x values as well. These vectors are directed to the nearest face on the wall boundary.

6.5.2 Results and discussion

The 3D reconstructed airway model is an asymmetrical structure with a complex curvature of the wall surface. The airflow in the model previously discussed in 5.5 shows that airflow in the daughter branches is not homogeneous. Therefore the airflow in the model representing the upper bronchial region still has a high Reynolds number, a distinct shear layer along the lung wall in the branching regions and the secondary flow effects arises. The transport

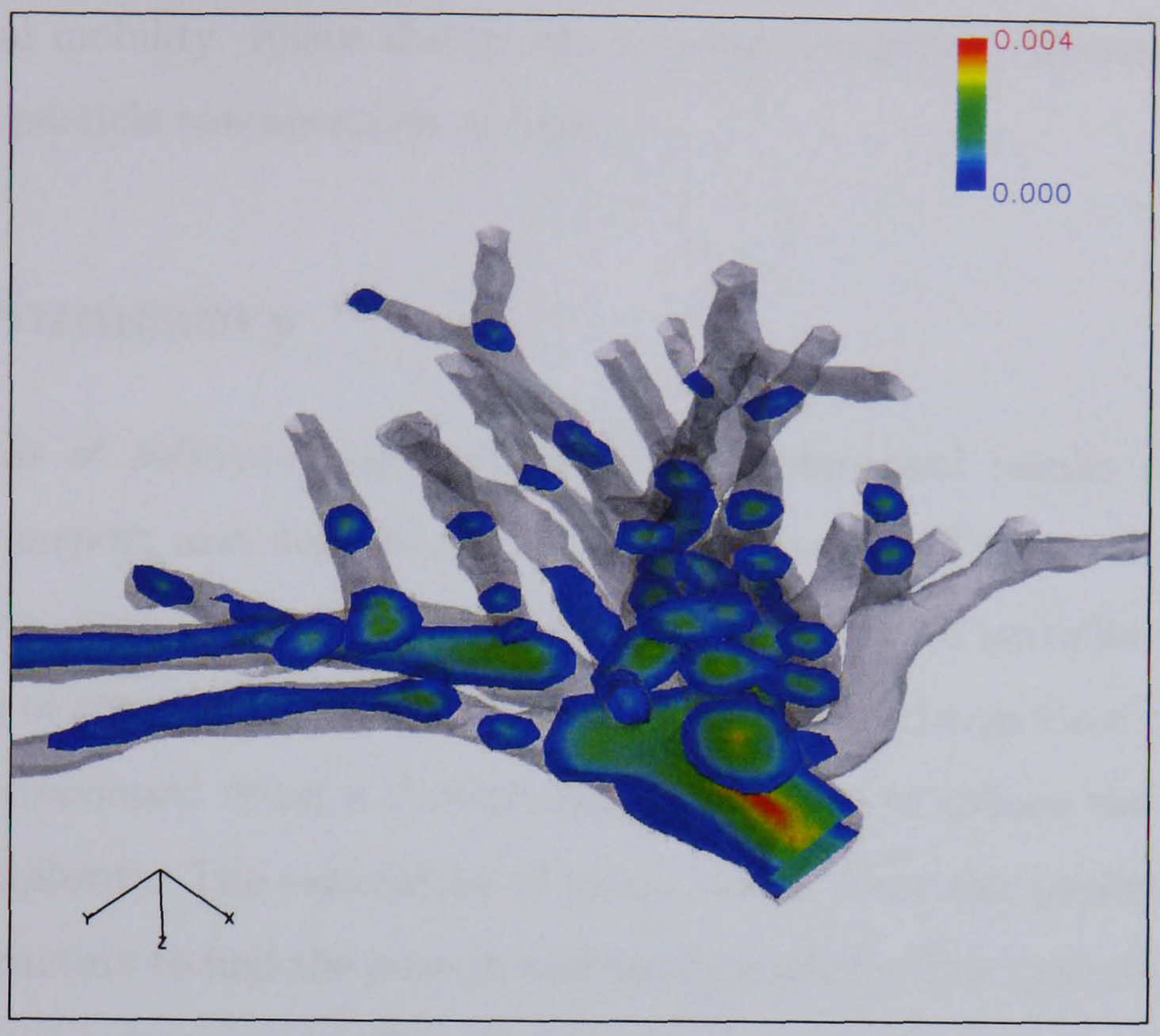

Figure 6.35: Magnitudes of the nearest wall distance vector in the 3D right-upper reconstructed airway model in z-plane (unit: m)

of sub-micron particles in the airways is mainly dominated by local airflow. Charged particles tend to deposit near the branching regions because many particles follow the distinct shear layer and move closer to the lung wall where the image charge force arises.

The examples of local deposition pattern of 0.5 μm particles carrying a charge of $50e$ and $200e$ are shown in Figure 6.36. Many charged particles are trapped in the branching regions. The local deposition patterns in the daughter branches differ depending on the local airflow pattern and charge values.

The comparison of deposition efficiencies of 0.3, 0.5, and 0.7 μm particles with the charge value are shown in Figure 6.37. The curves of deposition efficiencies in the 3D reconstructed airway model are similar to the 3D bifurcation model in which the deposition increases when the charge value increases, then they increase slightly more at the high charge value. The deposition of 0.3 μm particles is greater than that of 0.5 and 1.0 μm ones, due to their higher

mechanical mobility. Space charge can increase deposition efficiency in cases when the particle concentration is high.

6.6 Summary

The details of software implementations and numerical results of charged aerosol transport and deposition have been discussed. The novel developed software has been designed to calculate the trajectories of particles to include the effects of space and image charge forces. The space charge force calculation has been developed using a Particle-Mesh technique to reduce the computational complexity. The calculation of image charge force was performed using a mesh structure to find the nearest wall to the particle. The designed software also creates post-processing files for visualisation and data analysis.

The numerical results of the transport and deposition of charged aerosol in the 3D tubular, 3D bifurcation, 2D alveolar, and 3D reconstructed airways models have been investigated. The results in individual models can be summarised as follows.

In the 3D tubular airway model, the numerical study investigates the effects of parameters (i.e. particle distribution, velocity profile, and volume of particle cloud) on the deposition efficiency of charged particles. The numerical results are also compared with the predicted deposition results by Yu, which are analysed based on a uniform spatial distribution and slug flow profile. The numerical results also show that the variations of particle distributions, airflow profiles, and initialised volumes influence the deposition efficiency of charged particles. The results also indicate that the linear combination of the separate space and image charge deposition efficiencies gives a good approximation of both space and image charge forces if the deposition efficiency of the space charge force is less than that of the image charge force.

In the 3D bifurcation airway model, the numerical model gives an understanding of space and image charge force affecting the deposition efficiency,

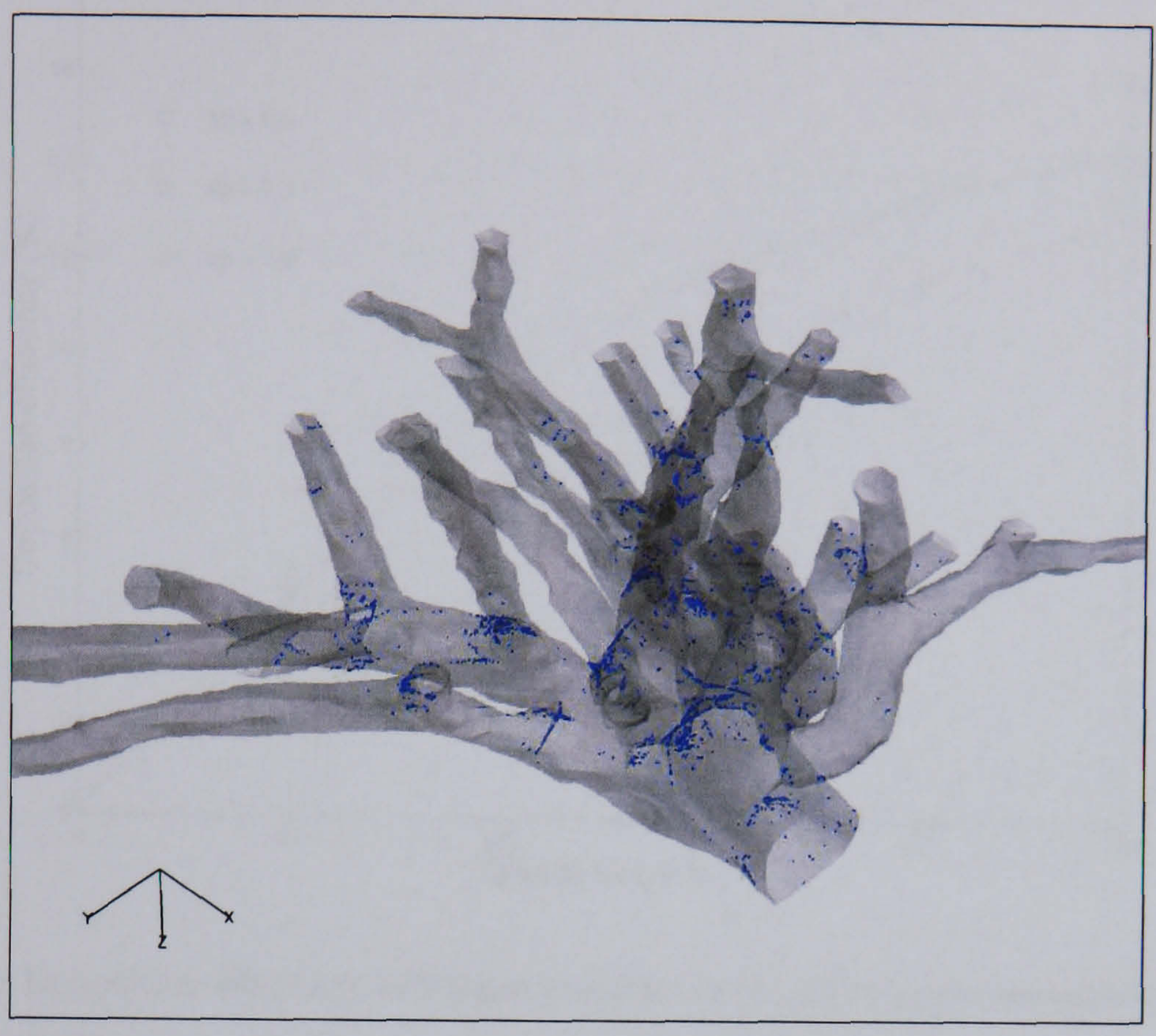

(a) $q = 50e$

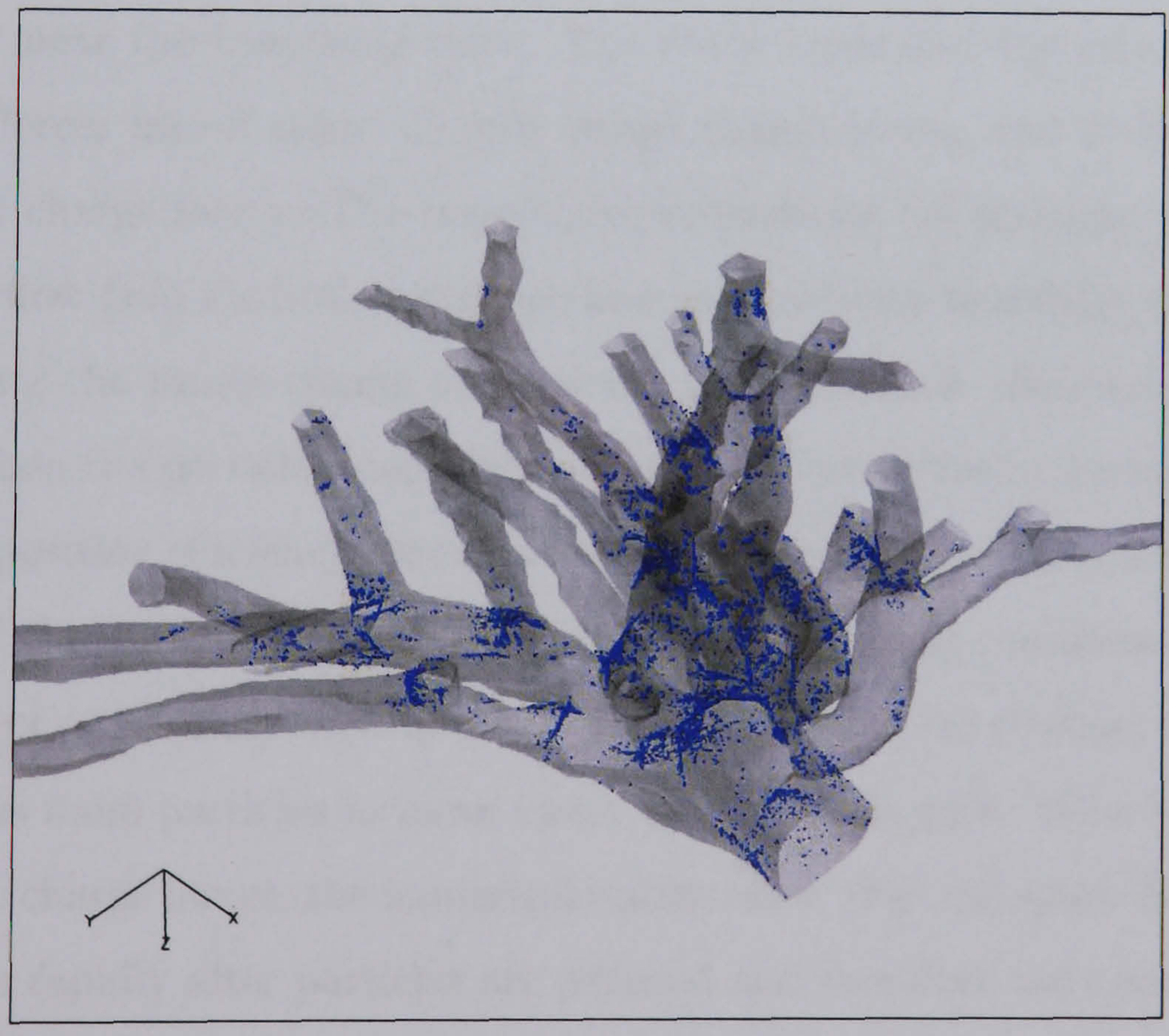

(b) $q = 200e$

Figure 6.36: Local deposition of 0.5 μm particles in the right-upper reconstructed airway model (Re=1750)

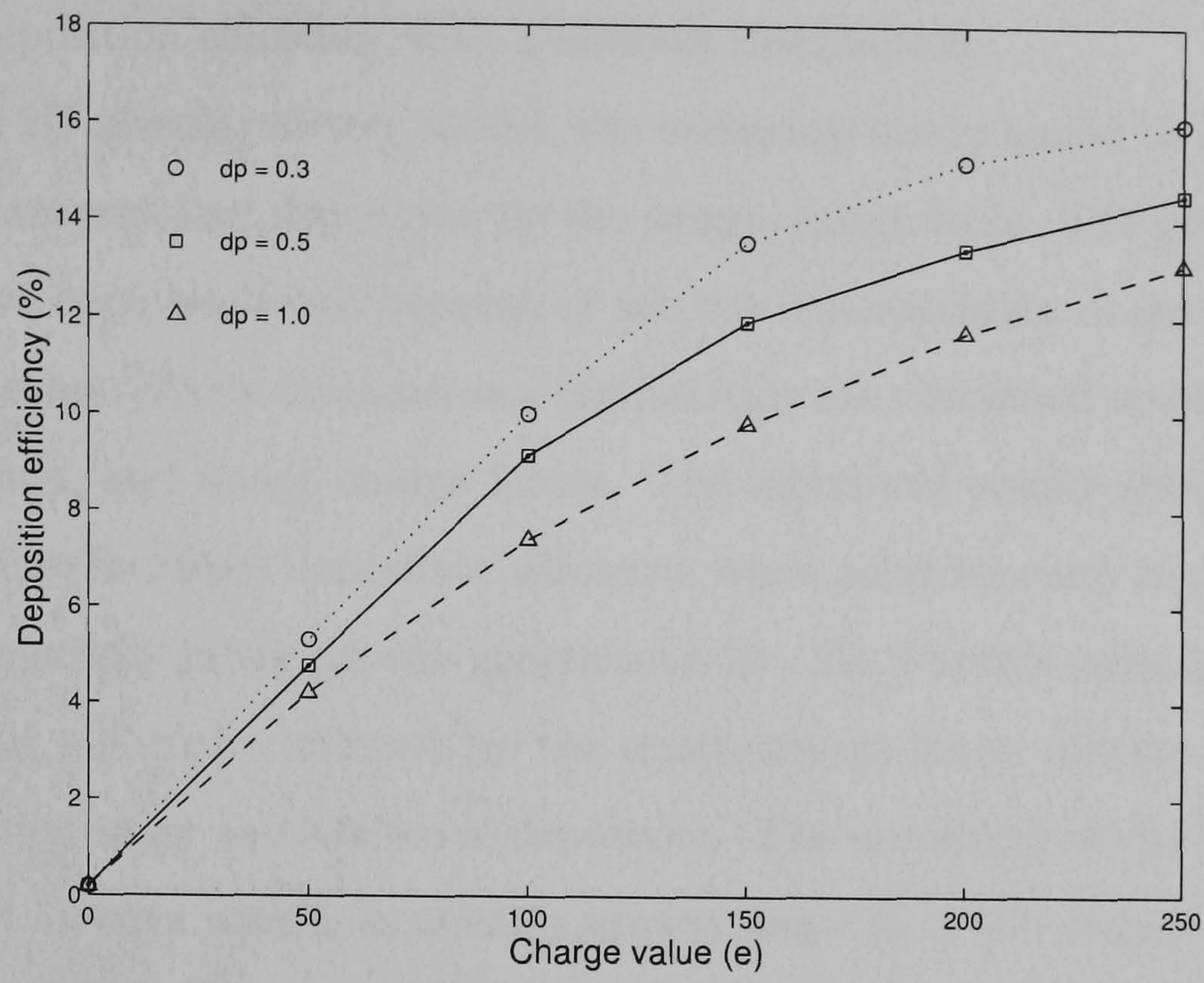

Figure 6.37: Deposition efficiency of 0.5 μm particles in the right-upper reconstructed airway model (Re=1750)

especially near the branching tube. The study separated the effects of electrostatic forces into 2 cases: 1) only image charge forces, and 2) both image and space charge forces. The trajectories of particles are strongly dominated by the airflow field for both sedentary and light activity breathing conditions. Considering the image charge force alone, the deposition efficiency increases rapidly when the particles gain higher charged values. Finally the incremental rate of deposition efficiency lessens for higher charge values. The deposition efficiency of charged particles under light activity breathing condition is greater than that of a sedentary breathing condition because of the stronger fluid force that causes more particles to move closer to the airway wall. With both space and image charge forces, the numerical results show that the space charge field diminishes rapidly after particles are released and therefore the concentration of particles decays very fast. The space charge force improves deposition efficiency when particles carry high charge values and are in sufficient concentration. The distribution of particle position also affects the deposition efficiency by the space charge force, in which a parabolic distribution tends to have a

greater deposition efficiency than a uniform distribution.

In the 2D alveolar airway model, the numerical study aimed to investigate aerosol transport and deposition by the image charge force. The space charge forces have been neglected because of the low concentration of aerosol in the alveolar region. Three main aerosol mechanisms are concerned involving gravity, diffusion, and image charge forces. The numerical results show that the image charge increases deposition efficiency when particles carry higher charge values, especially in the airway generations 20 - 22. Particle sizes larger than 1 μm tend not to be affected by the image charge force because gravity is the more dominant mechanism of deposition. The numerical model mainly investigated airways within an average gravity angle $\theta_g = 60°$ suggested by Yeh and Schum [198], and the results obtained correlate well with the experimental data by Melandri et.al. [129].

In the 3D reconstructed airways, the numerical investigation of charged aerosol focused on the image charge force alone with a slug inlet profile corresponding to a Reynolds number of 1750. The particles were assumed to enter the airways as a uniform particle distribution and carrying a constant charge value. The results indicates that the trend of deposition increment due to the image charge force is similar to the 3D bifurcation model. The higher charge value results in better deposition efficiency. However, local deposition is asymmetrical in the daughter branches and is strongly dependent on the local airflow velocity.

Chapter 7

Conclusion

7.1 Discussion and Conclusion

One of the most successful methods of treating respiratory diseases is to deliver an aerosolised drug to the human respiratory tract. Targeting of pharmaceutical drugs to specific sites in the lung is important to reduce systemic side effects. Some control over aerosol properties and breathing patterns is possible if the drug is formulated for the desired purpose. A tool that permits parametric exploration of drug deposition is useful in order to optimise these parameters and guide pre-clinical development. In this thesis the development of numerical models to study the transport and deposition of electroaerosols in the geometrical airway models has been reported.

The in-vivo assessment of inhaled drug delivery to the lung, a clinical experiment, allows parametric exploration in the real anatomical lungs (i.e., Planar gamma scintigraphy, SPECT, and PET). However, these imaging technologies are complex and expensive. The use of radiolabelled dose may cause side effects in subjects. The alternative method is to use numerical deposition models for simulation of deposition of aerosolised drug in the lung. These deposition models are becoming increasingly common in respiratory drug delivery.

At the present time, the 1D predicted (analytical) deposition models are also often used to estimate the deposition efficiency in the human respiratory

tract, but a major limitation is that they can not provide information at the local regions of interest for both airflow and aerosol transport. Thus the numerical deposition models in the 2D/3D realistic geometrical airway model have been introduced. The comparisons between 1D predicted and 2D/3D numerical deposition models of aerosols can be listed as follows:

- The 1D predicted deposition models often calculate the deposition efficiency based on 1D geometrical model (such as tube length, tube diameter, branching angle) and simplified airflow structure. The deposition efficiencies of individual mechanisms are used in the predicted deposition model: inertial impaction, sedimentation, diffusion, image charge, and space charge forces. However, the calculations of these deposition efficiencies are based on strict conditions of airflow profile, particle inlet distribution, and size distribution. The numerical deposition model in the 2D/3D airway models can give a better realistic airflow field and enables us to see the transient of aerosol transport inside the model in any specific regions of interest.

- The results of 1D predicted deposition models can give the total and regional deposition efficiencies in the whole lung (often based on the airway generation numbers), but they can not provide the local deposition pattern relative to the anatomical human respiratory tract. The numerical deposition model can provide the local deposition patterns when a good description of aerosol characteristics are defined. However, these numerical deposition models in the 2D/3D geometrical models often represent the partial lung due to a limitation of computational resources.

- The computational requirement for implementation of 1D predicted deposition models is not demanding compared to that of numerical deposition models in the 2D/3D airway models, because the calculation of accurate airflow field and aerosol transport requires extensive computational resources and long computational time.

Geometrical airway models used in this thesis were described in two regions of human airway models (upper bronchial and the alveolar regions), because some published experimental and numerical studies could be used to validate the numerical models. In the upper bronchial region, there were two methods to create the geometrical models: the morphology based and the reconstructed approaches. The morphology based technique generates a model based on morphology and the statistical characteristics of airways. The 3D bifurcation airway model was created by the morphology-based technique to represent a symmetrical branching of generation numbers 3-5 of Weibel's morphological model using CAD software (see section 2.1). In an alternative approach, the reconstruction technique generated the geometrical airway model by extracting the surface directly from the voxel data of scanned image, obtained by CT, MRI and other scanners (see section 2.3). This technique was utilised to generate the 3D reconstructed airway model from the CT scanned image data of a male cadaver. The first contribution to knowledge is the reconstruction of an airway model based on existing techniques. Although it was a time consuming exercise, but it was essential to the research program. In the alveolar region, the model was created based on Darquenne's alveolar model consisting of 6 generations of alveolar ducts (see section 2.2). This was a 2D static model representing an infinitely long central channel surrounded by alveoli with a circular shape. The first generation was equivalent to the airway generation number 18 of Weibel's morphological model. These geometrical models have some limitations that the model of wall surfaces neglected the histology of airway, and a dynamic deformation of airways. The histology of airways is different depending on the airways regions. The airflow field with the real histology of airways has not been well understood and there is a lack of theoretical studies. The geometrical airway model with dynamic moving wall boundary is also complex due to a coupled problem between the elasticity of airway wall and dynamic airflow. These airway wall effects still remain as an underdeveloped topic in the modelling of airflow dynamics and aerosol transport in the

human respiratory tract.

Calculations of the aerosol transport in the human respiratory tract based upon the Lagrangain representation were selected for this study rather than the Eulerian representation, because the motion of particles is similar to the Lagrangian frame. The Lagrangain representation of aerosols is also easier to implement with the effects of particle reflection, particle deposition, polydisperse size of aerosol, and turbulence diffusion when compared to the Eulerian representation. In the thesis, the transport of aerosols was assumed as a dilute dispersed phase flow with one-way coupling between phases, neglecting the effects of evaporation, condensation, and heat transfer. The trajectories of particles were calculated based on the momentum equation relating the acceleration of the particle mass to the sum of various forces acting on the particle i.e., drag, gravity, diffusion and electrostatic forces. The targeting of the therapeutic aerosols within the lung could be achieved by manipulating the particle size, inspiring flow rate, and inhalation volume. For a case of charged aerosols, the electrostatic charge on aerosols also affects the targeting of aerosols within the lungs, especially for sub-micron particles (see section 4.3). With the effect of electrostatic forces, the space and image charge forces are added into the trajectory equations. The Particle-Mesh technique was selected to reduce the complexity of computation of the space charge force, which was the N-body problem. In the image charge force computation, the algorithm for finding the nearest distance from a particle to the wall was required. The development of computational techniques for calculating both space and image charge forces is the second contribution to knowledge. However, the time consumption for computing the space charge force using the Particle-Mesh technique is still relatively high, especially in the 3D FFT calculation. The computational speed can be improved using the hardware-based FFT computation.

An investigation of airflow velocities within the geometrical airway models depends on the physical state of breathing and the shape of the geometrical model. The local airflow field is needed for calculating the fluid forces acting on

particles in the trajectory equations. In the upper bronchial region (3D bifurcation and 3D reconstructed airway models), the secondary flow is important for aerosol transport due to multiple interactions of the upstream flow field, branching curvature and shape of the carinal ridge (see figure 5.3). Higher Reynolds numbers produce a stronger secondary flow field ($400 < Re < 1500$). In the reconstructed airway model, the airflow is asymmetrical in the daughter branches depending on the structure and curvature of wall surface (see figure 5.15). The limitation of airflow calculation is that it is only based on steady airflow condition during the inhalation phase. The instantaneous velocity of transient airflow in the bronchial region experienced by particles to be deposited is strongly dependent on the activation time of inhaler devices. In the alveolar region, the flow field is laminar because of the low Reynolds number ($Re < 0.1$). After the airflow proceeds down to the daughter branches, the axial velocity rapidly regains a fully-developed profile and reduces significantly at the deeper airway generation numbers (see figure 5.11). As a result, suspended particles in this region have a long residence time.

The software implementation for the numerical deposition model has been developed to incorporate electrostatic and hydrodynamic forces in the transport and deposition of charged aerosols, which is a major challenge in the development of the numerical deposition model. The implementation of this coupled electro-hydrodynamic model is the third and major contribution to knowledge. Other capabilities of the numerical model can be listed as follows.

- The deposition model is capable of loading the transient profile corresponding to a specific breathing condition.
- The deposition model is capable of varying a specific characteristic of aerosols (i.e., density, and size distribution). For any specific cases of inhaler devices, the characteristic of aerosol can be obtained from the in vitro measurement.
- The deposition model is capable of calculations of aerosol transport and

deposition for a specific distribution of charge on aerosols.

- The deposition model is capable of generating a file for visualising the motions of particles.

The numerical results of transport and deposition of charged aerosols in the geometrical models (including the 2D tubular, 3D bifurcation, 2D alveolar and 3D reconstructed models) discussed in sections 6.3-6.5 are the fourth contribution to knowledge. These results obtained using the numerical deposition model give a greater understanding of the role of electrostatic forces in the transport and deposition of charged aerosols in the human respiratory airways.

The numerical study in the 3D tubular airway model investigates the effects of parameters (i.e. particle distribution, velocity profile and volume of particle cloud) on the deposition efficiency of charged particles. The numerical results were validated against the predicted deposition results by Yu [202], which are analysed based on a uniform spatial distribution and slug flow profile. Focusing on the branching regions between the parent and daughter tubes, the study in the 3D bifurcation airway model with a more realistic local airflow shows that the air velocity highly influences the deposition in both axial and radial directions. The skewed axial air velocity near the carinae greatly enhances the image charge force, and consequently improves deposition of particles near the carinae (see figure 6.12 and 6.13). In addition, the space charge force increases deposition efficiency mainly in the upper bronchial region if the number concentration of particles is high. The study in the 3D reconstructed airway model shows a similar trend in the deposition patterns near the branching regions. However the deposition patterns in the daughter branches are inhomogeneous, and strongly depends on the structure and surface curvature of the lung wall. In the 2D alveolar model, the image charge plays an important role in deposition efficiency for sub-micron particles, when carrying a high charge value ($20e < q < 200e$). The results obtained for the 2D alveolar model agree well with the experimental results for a decay time constant ranging between 4-8

seconds. There are some limitations of these numerical deposition models, which are listed below:

- The numerical studies were focused based on healthy lung conditions in both geometrical airway models and breathing patterns. The subjects with pulmonary diseases might have different results from the healthy one.

- The airflow field in these geometrical models is strictly based on a rigid wall structure, which is significantly different from the real anatomical airways. The transient airflow field with a deformation of lung wall can be different from the static one, especially in alveolar regions.

The numerical deposition model provides a valuable tool for respiratory clinicians and the pharmaceutical industry to study the complex mechanisms of drug aerosol deposition in human airways. Although this model is adequate for the intended purpose, it can be further improved by extending this work to develop a complete 3D model of the entire human airway system incorporating the full breathing cycle. Such a model will require an extensive computing facility, nevertheless it would be of great benefit to clinicians and the pharmaceutical industry to provide a better treatment for respiratory patients. These numerical models can also be used for environmental applications to simulate the deposition of airborne particles in the human respiratory tract. The generated numerical model can also be utilised to study charged aerosol transport and deposition in many industrial applications (agriculture, chemical, process and automotive, etc.) provided one coupling between dispersed and continuous-phase is maintained.

7.2 Further work

The work carried out and presented in this thesis can be further researched and developed in various directions as follows.

The first direction is to improve the speed of computation of the space charge force, which is the slowest step for calculating particle trajectories. In the particle mesh method, the time that was taken to solve the Poisson's equation is slow and it depended on the size of mesh used. A simple technique to improve the speed of computation with an appreciable software modification is a FFT hardware based solver. This hardware solver significantly improves the speed of computation by increasing the memory resource of the system. In an alternative concept, the space charge computation can be calculated using parallel computation techniques to distribute the computational load and improve the computational speed.

The second direction is to extend the study of transport and deposition of charged aerosols in extrathoracic and lower bronchial regions to fulfil the understanding in all regions of human respiratory tract. Since airflow in extrathoracic region is turbulent, the transport of charged aerosols must include the turbulent dispersion with a high concentration of particles. In the lower bronchial region, the airflow is laminar with lower Reynolds number ($Re < 100$) than in the upper bronchial region ($200 < Re < 4000$). The distinct shear layer near the carinae is different from that of the upper bronchial region, and then result may in different deposition efficiencies.

The third direction is to numerically investigate transport and deposition of charged aerosols in the geometrical airway models of diseased lungs, which often has more constricted airways relative to healthy lungs. The airflow inside the diseased geometrical airway models may be significantly different, and influence the aerosol deposition pattern. The geometrical airway specific to any lung disease must be generated, which can be created using the reconstructed technique from the scanned image data.

The fourth direction is to develop interface techniques between submodels to represent all parts of human lungs including extrathoracic, upper bronchial, lower bronchial, and alveolar parts. Based on the framework of the COPHIT project, the extrathoracic and upper bronchial regions can be obtained by the

reconstruction techniques, then the lower bronchial region can be extended using the morphology based technique. The lower bronchial region also connects to the 1D alveolar model, which can be represented by balloons inflating and deflating by the airflow from each of the open ended bronchi. The reconstructed airways must be used to produce a skeletal model and morphological details of the reconstructed branches. These details can then be used to extend branches of the lower bronchial regions by morphology based techniques such as the technique developed by Tawhai [182] of filling the small tubes in a host shape without an overlapped structure. In addition, the interfacing surface must be adjusted to produce smooth connections between the new branches in the reconstructed model. In connecting the tracheobronchial and the 1D alveolar models, the technique to interface data to modify the boundary conditions of open ended bronchi must be developed.

The final direction is the development of the flexible alveolar model. However this is much more complicated than the static model. In addition, the analysis of fluid flow with flexible wall boundaries uses a set of fluid governing equations different from the system with static wall boundaries. The advantage of this development is that it can be used to develop more accurate 1D alveolar models under different inlet conditions and orientations.

Appendix A

List of publications

1. D. Koolpiruck, S. Prakoonwit, W. Balachandran, Numerical modelling of inhaled charged aerosol deposition in human airways, *IEEE Transactions on industry applications*, Vol 40, No. 5 , 2004, pp. 1239-1248.

2. D. Koolpiruck, S. Prakoonwit, W. Balachandran, Deposition of charged inhaled aerosols with steady and transient airflow in sequential lung airway model, *IEEE Transactions on industry applications*, (submitted) .

3. D. Koolpiruck, S. Prakoonwit, W. Balachandran, Numerical investigation of charged aerosol deposition in tracheobronchial and alveolar regions, *Proceedings of Lung Modelling: Numerical and Experimental* , 16 November 2004, Sheffield, UK.

4. D. Koolpiruck, S. Prakoonwit, W. Balachandran, Deposition of charged inhaled aerosols with transient airflow in sequential lung airway model, *Proceedings of 39th IAS Annual Meeting* , 3-7 October 2004, Seattle.

5. D. Koolpiruck, S. Prakoonwit, W. Balachandran, Charged aerosol transport and deposition in a two-dimensional model of human alveolar duct, *Proceedings of Drug Delivery to the Lungs XIV*, 11-12 December 2003, London, pp. 141-143 (Poster Prize award).

6. D. Koolpiruck, S. Prakoonwit, W. Balachandran, Numerical modelling

of inhaled charged aerosol deposition in human airways, *Proceedings of ESA/IEEE-IAS Joint Conference*, 24-27 June 2003, Arkansas, USA.

7. D. Koolpiruck, S. Prakoonwit, W. Balachandran, Deposition of charge aerosol in reconstructed human airways, *Proceedings of ICLASS 2003*, 13-18 July 2003, Sorrento, Italy.

8. D. Koolpiruck, S. Prakoonwit, W. Balachandran, A numerical study of charged aerosol transportation in human airways, *Proceedings of Drug Delivery to the Lungs XIII*, 12-13 December 2002, London, pp. 49-51.

9. J. Kulon, D. Koolpiruck, S. Prakoonwit, W. Balachandran, 3D Numerical and experimental study of the bipolar charge particle separator, *Proceedings of Electrostatics 2003 IOP Conference Edinburgh*, 23-27 March 2003, Scotland.

Appendix B

Dimensions of Geometrical models

B.1 3D Bifurcation airway model

The geometrical details of the double symmetrical bifurcation model are created based on a guidance by Comer et. al. [33]. The model shown in figure B.1 represents Weibel's airway generation numbers of 4, 5, and 6 with a rigid wall surface. The first bifurcation is defined as the region starting from the first tube to the section of second tubes indicated by the dashed lines, whereas the second bifurcations start from the dashed lines and go to the end of the third tubes.

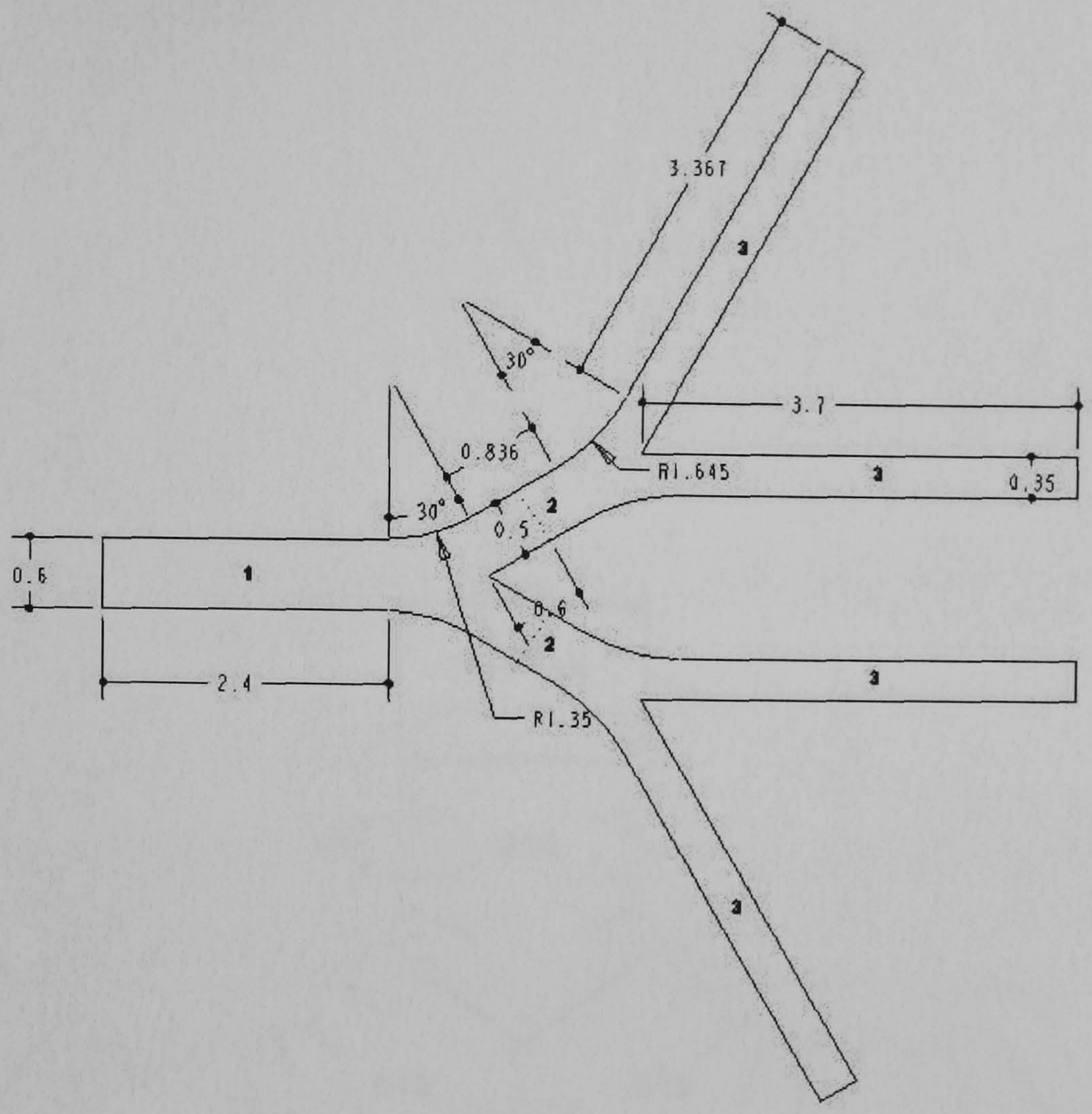

Figure B.1: Dimension details of the double bifurcation airway model (unit: *cm*)

B.2 2D Alveolar airway model

The 2D alveolar model, developed by Darquenne [38], consists of 6 consecutive generations of identical alveolated airways, equivalent to Weibel's airway generation number of 18 - 23. The model is formed by dichotomous branching with a branching angle of 45°. Figure B.2 shows the first three generations of the model. The dimensions are 265 μm for the lumen diameter, 575 μm for the outer diameter, 600 μm for the duct length, and 150 μm for the alveolar opening. These dimensions were derived morphological data based on a report of Haefeli-Bleuer and Weibel with a total lung volume of 3.5 litres [74].

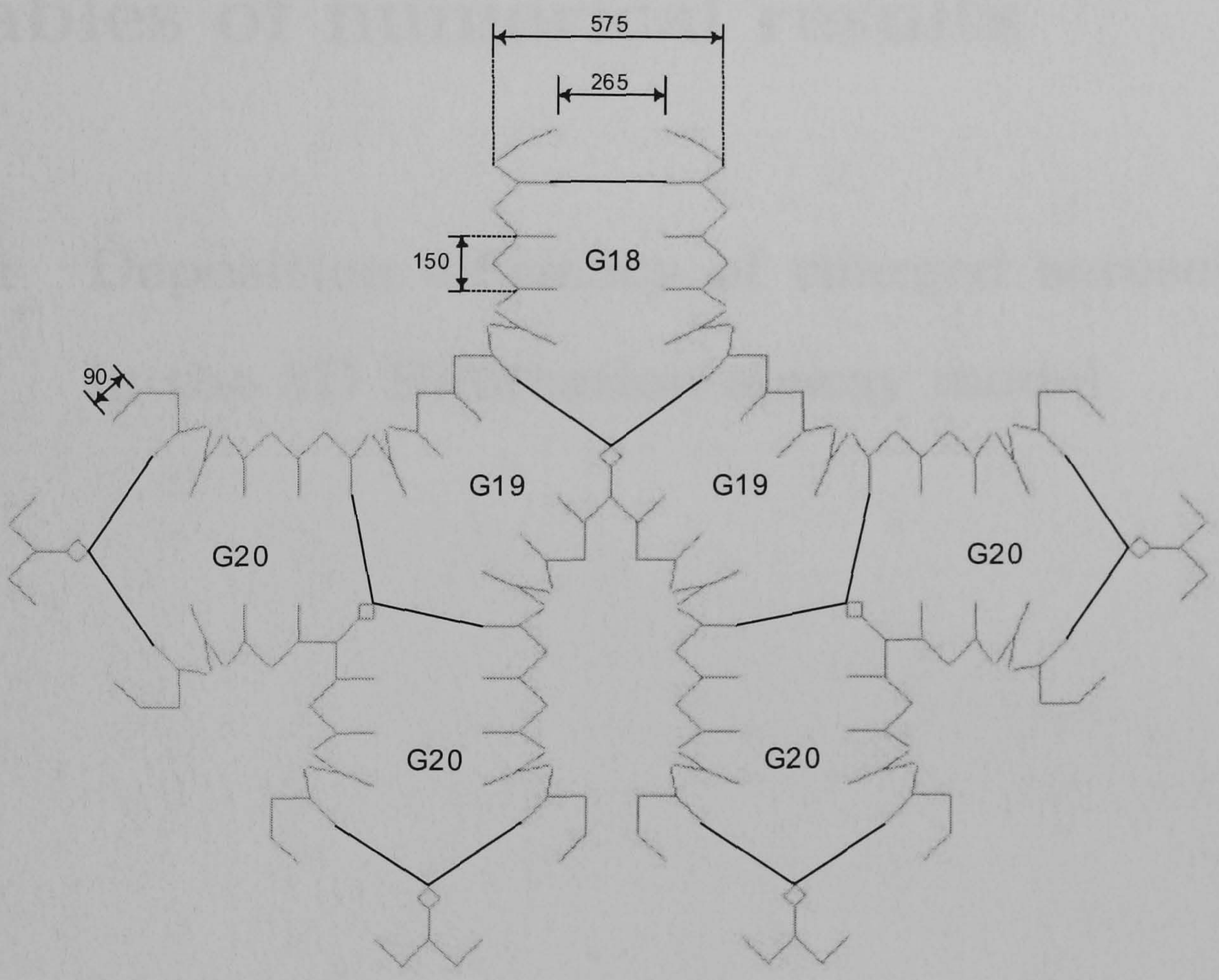

Figure B.2: Dimension details of the 2D alveolar airway model (unit: μm)

Appendix C

Tables of numerical results

C.1 Deposition efficiency of charged aerosols in the 3D Bifurcation airway model

Table C.1: Numerical results of charged aerosol deposition in the first bifurcation of the 3D bifurcation airway model for a sedentary breathing condition (no space charge force)

Charge value (e)	Deposition efficiency (%)							
	Uniform distribution				Parabolic distribution			
	0.3 μm	0.5 μm	0.7 μm	1.0 μm	0.3 μm	0.5 μm	0.7 μm	1.0 μm
0	0.00	0.00	0.00	0.00	0.00	0.00	0.00	0.00
10	1.40	1.27	1.17	1.03	1.90	1.70	1.33	1.33
25	2.00	1.80	1.80	1.63	2.20	2.17	2.17	2.00
50	2.50	2.30	2.16	2.10	2.73	2.60	2.46	2.23
100	3.33	2.93	2.76	2.53	3.16	3.00	2.90	2.83
150	3.93	3.40	3.23	3.03	3.36	3.37	3.20	3.16
200	4.36	4.03	3.73	3.30	3.57	3.43	3.37	3.33
250	4.60	4.43	4.13	3.77	3.90	3.57	3.50	3.36

Table C.2: Numerical results of charged aerosol deposition in second bifurcations of the 3D bifurcation airway model for a sedentary breathing condition (no space charge force)

Charge value (e)	Deposition efficiency (%)							
	Uniform distribution				Parabolic distribution			
	0.3 μm	0.5 μm	0.7 μm	1.0 μm	0.3 μm	0.5 μm	0.7 μm	1.0 μm
0	0.00	0.00	0.00	0.00	0.00	0.00	0.00	0.00
10	0.77	0.63	0.60	0.56	0.76	0.70	0.60	0.60
25	1.30	1.23	1.13	0.93	1.20	1.07	1.07	0.90
50	1.53	1.40	1.43	1.40	1.67	1.50	1.36	1.20
100	1.36	1.63	1.60	1.67	1.90	1.80	1.73	1.63
150	2.07	1.90	1.80	1.70	2.20	2.03	1.87	1.83
200	2.16	2.13	1.93	1.77	2.30	2.13	2.03	2.00
250	2.33	2.16	2.10	2.03	2.27	2.23	2.20	2.13

Table C.3: Numerical results of charged aerosol deposition in the first bifurcation of the 3D bifurcation airway model for a light activity breathing condition(no space charge force)

Charge value (e)	Deposition efficiency (%)							
	Uniform distribution				Parabolic distribution			
	0.3 μm	0.5 μm	0.7 μm	1.0 μm	0.3 μm	0.5 μm	0.7 μm	1.0 μm
0	0.00	0.00	0.00	0.00	0.00	0.00	0.00	0.00
10	3.47	3.23	3.20	3.03	3.30	3.16	2.93	2.86
25	4.56	4.27	3.90	3.60	4.13	3.96	3.73	3.57
50	5.20	4.80	4.70	4.70	4.76	4.50	4.36	4.20
100	6.10	5.67	5.57	5.27	5.50	5.20	5.03	4.93
150	6.43	6.27	5.97	5.67	6.00	5.63	5.40	5.30
200	6.93	6.50	6.33	6.23	6.20	5.97	5.77	5.60
250	7.23	6.90	6.53	6.37	6.40	6.13	6.00	5.80

Table C.4: Numerical results of charged aerosol deposition in second bifurcations of the 3D bifurcation airway model for a light activity breathing condition (no space charge force)

Charge value (e)	Deposition efficiency (%)							
	Uniform distribution				Parabolic distribution			
	0.3 μm	0.5 μm	0.7 μm	1.0 μm	0.3 μm	0.5 μm	0.7 μm	1.0 μm
0	0.00	0.00	0.00	0.00	0.00	0.00	0.00	0.00
10	1.67	1.13	1.10	1.10	2.40	2.23	2.13	1.97
25	1.47	1.46	1.40	1.33	3.10	2.97	2.70	2.63
50	1.80	1.63	1.56	1.53	3.63	3.63	3.50	3.30
100	2.06	1.83	1.87	1.80	4.10	4.00	3.93	3.67
150	2.26	2.13	2.10	2.00	4.50	4.17	4.10	3.97
200	2.33	2.23	2.13	2.16	4.60	4.53	4.33	4.10
250	2.50	2.33	2.27	2.16	4.66	4.60	4.60	4.40

Table C.5: Numerical results of charged aerosol deposition in the first bifurcation of the 3D bifurcation airway model for a light activity breathing condition

Charge value(e)	Deposition efficiency (%)			
	Uniform distribution		Parabolic distribution	
	$C_0 = 2.0 \times 10^{11}$ (m^{-3})	$C_0 = 2.0 \times 10^{12}$ (m^{-3})	$C_0 = 2.0 \times 10^{11}$ (m^{-3})	$C_0 = 2.0 \times 10^{12}$ (m^{-3})
0	0.00	0.00	0.00	0.00
25	3.82	3.84	3.98	4.10
50	5.00	5.15	5.00	5.25
150	6.59	6.90	6.70	7.00
250	7.05	7.60	6.95	7.40

Table C.6: Numerical results of charged aerosol deposition in the second bifurcations of the 3D bifurcation airway model for a light activity breathing condition

Charge value(e)	Deposition efficiency (%)			
	Uniform distribution		Parabolic distribution	
	$C_0 = 2.0 \times 10^{11}$ (m^{-3})	$C_0 = 2.0 \times 10^{12}$ (m^{-3})	$C_0 = 2.0 \times 10^{11}$ (m^{-3})	$C_0 = 2.0 \times 10^{12}$ (m^{-3})
0	0.00	0.00	0.00	0.00
25	1.72	1.70	2.97	2.99
50	2.11	2.09	3.61	3.57
150	2.40	2.43	4.34	4.40
250	2.62	2.65	4.55	4.70

C.2 Deposition efficiency of charged aerosols in the 2D Alveolar airway model

Table C.7: Numerical results of charged aerosol deposition in the 2D alveolar model for $d_p = 0.3\ \mu m$

Charge	Deposition efficiency			Deposition increment		
values(e)	$\tau = 4\ s$	$\tau = 8\ s$	*const* 4 *s*	$\tau = 4\ s$	$\tau = 8\ s$	*const* 4 *s*
0	7.39	7.39	7.39	0.00	0.00	0.00
10	7.52	7.53	7.51	0.14	0.15	0.13
20	8.25	8.71	8.65	0.93	1.43	1.36
30	9.34	10.68	10.26	2.11	3.55	3.10
40	10.98	12.48	12.07	3.88	5.50	5.05
50	12.48	15.11	14.20	5.50	8.34	7.35

Table C.8: Numerical results of charged aerosol deposition in the 2D alveolar model for $d_p = 0.6\ \mu m$

Charge	Deposition efficiency			Deposition increment		
values(e)	$\tau = 4\ s$	$\tau = 8\ s$	*const* 4 *s*	$\tau = 4\ s$	$\tau = 8\ s$	*const* 4 *s*
0	18.64	18.64	18.64	0.00	0.00	0.00
20	19.07	18.95	19.44	0.53	0.64	0.98
40	20.42	20.99	20.70	2.19	2.89	2.53
60	21.98	23.57	22.82	4.10	6.06	5.14
80	23.59	26.26	24.94	6.08	9.37	7.74
100	25.50	29.03	27.11	8.43	12.77	10.41

Table C.9: Numerical results of charged aerosol deposition in the 2D alveolar model for $d_p = 1.0\ \mu m$

Charge values(e)	Deposition efficiency			Deposition increment		
	$\tau = 4\ s$	$\tau = 8\ s$	*const* 4 *s*	$\tau = 4\ s$	$\tau = 8\ s$	*const* 4 *s*
0	48.57	48.57	48.57	0.00	0.00	0.00
40	49.19	49.56	49.01	1.21	1.92	0.84
60	50.02	50.24	50.26	2.82	3.25	3.29
80	50.66	51.32	51.18	4.06	5.53	5.07
100	51.51	52.28	52.27	5.72	7.21	7.19
120	51.84	53.28	54.05	7.06	9.16	8.96

Table C.10: Numerical results of charged aerosol deposition in the 2D alveolar model for $d_p = 0.6\ \mu m$

Charge values(e)	Deposition efficiency				
	$\theta_g = 0°$	$\theta_g = 60°$	$\theta_g = 90°$	$\theta_g = 120°$	$\theta_g = 180°$
0	18.72	18.64	19.76	20.76	18.98
20	19.19	19.07	20.08	21.42	19.44
40	20.71	20.42	20.81	22.57	21.18
60	22.87	21.52	22.34	24.74	23.36
80	24.60	23.59	24.80	26.15	25.48
100	25.75	25.50	27.01	28.49	27.89

C.3 Deposition efficiency of charged aerosols in the 3D Reconstructed airway model

Table C.11: Numerical results of charged aerosol deposition in the first bifurcation of 3D reconstructed airway model for an inlet Reynolds number of 1750 (no space charge force)

Charge value(e)	Deposition efficiency (%)		
	0.3 μm	0.5 μm	1.0 μm
0	0.20	0.28	0.53
50	5.30	4.76	4.20
100	10.03	9.14	7.40
150	13.54	11.91	9.80
200	15.20	13.42	11.70
250	16.20	14.54	13.10

Appendix D

Special function

D.1 Special function

D.1.1 The Top-Hat function $\Pi(x)$

$$\Pi(x) = \begin{cases} 0 & , |x| > 0.5 \\ 0.5 & , |x| = 0.5 \\ 1 & , |x| < 0.5 \end{cases} \tag{D.1}$$

$$\mathfrak{F}\left\{\Pi(x)\right\} = \frac{sin(\kappa/2)}{\kappa/2} \tag{D.2}$$

D.1.2 The Triangle function $\Lambda(x)$

$$\Lambda(x) = \begin{cases} 0 & , |x| > 1 \\ 1 - |x| & \|x| < 1 \end{cases} \tag{D.3}$$

$$\mathfrak{F}\left\{\Lambda(x)\right\} = sinc^2\left(\frac{\kappa}{2\pi}\right) \tag{D.4}$$

D.1.3 The Dirac Delta function $\delta(x)$

$$\delta(x) = \begin{cases} 1 & , x = 0 \\ 0 & , x \neq 0 \end{cases} \tag{D.5}$$

$$\mathfrak{F}\{\delta(x)\} = 1 \tag{D.6}$$

D.2 Green function of Poisson's equation

The Poisson's equation for electrostatic system is

$$\nabla^2 \Phi(\mathbf{x}) = -\frac{\rho(\mathbf{x})}{\varepsilon_0} \tag{D.7}$$

where $\Phi(\mathbf{x})$ is an electrical potential function and $\rho(\mathbf{x})$ is a charge density function. So the differential operator in this case is $L = \nabla^2$. As usual, we are looking for a Green's function $G(\mathbf{x_1}, \mathbf{x_2})$ such that

$$\nabla^2 G(\mathbf{x_1}, \mathbf{x_2}) = \delta^3(\mathbf{x_1} - \mathbf{x_2}) \tag{D.8}$$

From Laplacian,

$$\nabla^2 \left(\frac{1}{|\mathbf{x_1} - \mathbf{x_2}|} \right) = -4\pi\delta^3(\mathbf{x_1} - \mathbf{x_2}) \tag{D.9}$$

so

$$G(\mathbf{x_1}, \mathbf{x_2}) = \frac{1}{-4\pi\,|\mathbf{x_1} - \mathbf{x_2}|} \tag{D.10}$$

The solution of Poisson's equation in term of Green's function is

$$\Phi(\mathbf{x}) = \int G(\mathbf{x}, \mathbf{x}') \left[-\frac{\rho(\mathbf{x}')}{\varepsilon_0} \right] d^3\mathbf{x}' \tag{D.11}$$

$$= \int \frac{\rho(\mathbf{x}')}{4\pi\,|\mathbf{x} - \mathbf{x}'|}\, d^3\mathbf{x}' \tag{D.12}$$

Bibliography

[1] 3M Inc. 3M drug delivery systems. http://www.3m.com/us/healthcare/manufacturers/dds/jhtml/mdi_anatomy.jhtml.

[2] 3M Inc. Maxair Autohaler. http://www.3m.com/us/healthcare/pharma/maxair/index.jhtml.

[3] Aerogen Inc. AeroNeb nebulizer product. http://www.aerogen.com/theproducts.htm.

[4] The Allergy Site. Serevent Accuhaler. http://www.theallergysite.co.uk/drugsheets/sereventaccu.html.

[5] M.J. Andrews and P.J. O'Rourke. The multiphase particle-in-cell method for dense particle flows. *International Journal of Multiphase Flows*, 22:379–402, 1996.

[6] Aradigm Corporation. Technology Platform: AERx drug delivery devices. http://www.aradigm.com/tech/delivery.html.

[7] B. Asgharian and S. Anjilvel. A Monte Carlo calculation of deposition efficiency of inhaled particles in lower airways. *Journal of Aerosol Science*, 25:711–721, 1994.

[8] A.G. Bailey, A.H. Hashish, and T.J. Williams. Drug delivery by inhalation of charged particles. *Journal of Electrostatics*, 44:3–10, 1998.

[9] W. Balachandran, C.N. Ahmad, and S.A. Barton. Deposition of electrically charged aerosol in lungs. In *Proceedings of Electrostatic 1991 IOP Conference*, pages 57–62, 1991.

[10] W. Balachandran, W. Machowski, E. Gaura, and C. Hudson. Control of drug aerosol in human airways using electrostatic forces. *Journal of Electrostatics*, 40:579–584, 1997.

[11] I. Balashazy and W. Hofmann. Particle deposition in airway bifurcations: Part 1 Inspiratory flow. *Journal of Aerosol Science*, 24:745–772, 1993.

[12] I. Balashazy and W Hofmann. Particle deposition in airway bifurcations: Part 2 Expiratory flow. *Journal of Aerosol Science*, 24:773–786, 1993.

[13] I. N. Bankman. *Handbook of Medical Imaging: Processing and Analysis.* Academic Press., 2000.

[14] Q. Barequet, M. Dickeron, and D. Eppstien. On triangulating three-dimensional polygons. *Computing Understanding*, 63:251–72, 1996.

[15] J.M. Beeckmans. The deposition of aerosols in the respiratory tract: Part 1 Mathematical analysis and comparison with experimental data. *Canadian Journal of Physiology and Pharmacology*, 43:6157–172, 1965.

[16] K.A. Bell and S.K. Friedlander. Aerosol deposition in models of a human lung bifurcation. *Staub-Reinhalt. Luft*, 33:178–182, 1973.

[17] W.D. Bennett, K.L. Zeman, and C. Kim. Variability of fine particle deposition in healthy adults: Effects of age and gender. *American Journal of Respiratory and Critical Care Medicine*, 153:1641–1647, 1996.

[18] Boehringer Ingelheim GmbH. Respimat soft mist inhaler. http://www.respimat.com/com/homepage.jsp.

[19] L. Borgstrom, H. Bisgaard, C. O'Callaghan, and S. Pedersen. Dry-powder inhaler. *Lung Biology in Health and Disease: Drug Delivery to the Lung (Edited by Bisgaard, H.)*, 162:421–448, 2002.

[20] Stephen B.P. *Turbulent flows.* Cambridge University Press, 2000.

[21] J.U. Brackbill and H.M. Ruppel. A method for adaptively zoned, particle-in-cell calculations of fluid flows in two dimensions. *Journal of Computational Physics*, 65:314, 1986.

[22] K.R. Castleman. *Digital image processing.* Prentice-Hall, Upper Saddle River, 1996.

[23] T.L. Chan and M. Lippmann. Experimental measurement and empirical modeling of the regional deposition of inhaled particles in humans. *American Industrial Hygiene Associate Journal*, 41:399–409, 1980.

[24] Y.S. Cheng, Y. Zhou, and B.T. Chen. Particle deposition in a cast of human oral airways. *Aerosol science and Technology*, 31:286–300, 1999.

[25] Y.K. Chen and C.P. Yu. Particle deposition from duct flows by combined mechanisms. *Aerosol Science and Technology*, 19:389–395, 1993.

[26] H.Y. Chow and Mercer T.T. Charges on droplets produced by atomisation of solutions. *American Industrial Hygiene Association Journal*, pages 247–255, 1971.

[27] T.J. Chung. *Computational Fluid Dynamics.* Cambridge University Press, 2002.

[28] T. Clark. Nasal drug delivery grows in effectivemess (industrial overview). *BBI Newsletter*, November 1999.

[29] R. Clift, J.R. Grace, and M.E. Weber. *Bubbles, droplets and particles.* Academic Press, New York, 1978.

[30] H.E. Cline, W.E. Ludke, C.R. Crawford, and B.C. Teeter. Two algorithms for three-dimensional reconstruction of tomograms. *Medical Physics*, 15:320–327, 1988.

[31] J. Cohen, A. Varshney, D. Manocha, G. Turk, H Weber, P. Agarwal, F Brooks, and W Wright. Simplification envelopes. *ACM Computer Graphics*, SIGGRAPH:119–128, 1996.

[32] J.K. Comer, C. Kleinstreuer, C. Hyun, and Z. Zhang. Flow structures and particle deposition patterns in double-bifurcation airway models: Part 2. Aerosol transport and deposition. *Journal of Fluid Mechanics*, 435:55–80, 2001.

[33] J.K. Comer, C. Kleinstreuer, C. Hyun, and Z. Zhang. Flow structures and particle deposition patterns in double-bifurcation airway models: Part 1. Air flow fields. *Journal of Fluid Mechanics*, 435:25–54, 2001.

[34] J.W. Cooley and J.W. Tukey. An algorithm for machine calculation for complex fourier series. *Mathematics of Computation,*, 19:297–301, 1965.

[35] J.A. Cross. *Electrostatics: Principles, Problems and Applications.* Adam Hilger, Bristol, 1987.

[36] C. Crowe, M. Sommerfeld, and Y. Tsuji. *Multiphase flows with droplets and particles.* CRC Press, Florida, 1998.

[37] C. Darquenne and M. Paiva. Two- and three-dimensional simulations of aerosol transport and deposition in alveolar zone of human lung. *Journal of Applied Physiology*, 80:1401–1414, 1996.

[38] C. Darquenne. A realistic two-dimensional model of aerosol transport and deposition in the alveolar zone of the human lung. *Journal of Aerosol Science*, 32:1161–1174, 2001.

[39] C. Darquenne. Heterogeneity of aerosol deposition in two-dimensional model of human alveolated ducts. *Journal of Aerosol Science*, 33:1261–1278, 2002.

[40] M.R. Davidson and J.M. Fitz-Gerald. Flow patterns in models of small airway units of the lung. *Journal of Fluid Mechanics*, 52:161–177, 1972.

[41] J.H. Dennis and O. Nerbrink. Atomization and nebulizers. *Lung Biology in Health and Disease: Inhalation Aerosols (Edited by Hickey, A.)*, 94:273–312, 1996.

[42] J.H. Dennis and O. Nerbrink. New nebulizer technology. *Lung Biology in Health and Disease: Drug Delivery to the Lung (Edited by Bisgaard, H.)*, 162:303–336, 2002.

[43] S.G. Devadason, M.L. Everard, MacEarlan, C. Roller, Q.A. Summers, P. Swift, L. Borgstrom, and P.N. Le Souef. Lung deposition from Turbuhaler in children with cystic fibrosis. *European Respiratory Journal*, 10:2023–2028, 1997.

[44] R. Dhand. Nebulizers that use a vibrating mesh or plate with multiple apertures to generate aerosols. *Respiratory Care*, 47:1406–1416, 2002.

[45] M. Eck, T. DeRose, T. Duchamp, H. Hoppe, M. Lounsbery, and W. Stuetzle. Multiresolution analysis of arbitrary meshes. *Computer Graphics*, 29(Annual Conference Series):173–182, 1995.

[46] D.A. Edwards. A general theory of the macrotransport of nondepositing particles in the lung by convective dispersion. *Journal of Aerosol Science*, 25:533–565, 1994.

[47] D.A. Edwards. The macrotransport of aerosol particles in the lung: aerosol deposition phenomena. *Journal of Aerosol Science*, 26:293–317, 1995.

[48] M.J. Egan and W. Nixon. A model of aerosol deposition in the lung for use in inhalation dose assessments. *Radiation Protection Dosimetry*, 11:5–17, 1985.

[49] M. Everade and M.B. Dolovich. In vivo measurements of lung dose. *Lung Biology in Health and Disease: Drug Delivery to the Lung (Edited by Bisgaard, H.)*, 162:173–208, 2002.

[50] M. Farrashkhalvat and J.P. Miles. *Basic structure grid generation.* Butterworth-Heinemann, 2003.

[51] J. Ferin, Mercer T.T., and L.J. Leach. The effect of charge on the deposition and clearance of TiO_2 particles in rats. *Environmental Reseach*, 31:148–151, 1983.

[52] G.A. Ferron, W.G. Kreyling, and B. Haider. Inhalation of salt aerosol particles: Part 2 Growth and depostion in the human respiratory tract. *Journal of Aerosol Science*, 19:611–631, 1988.

[53] J.H. Ferziger and M. Perice. *Computational Methods in Fluid Dynamics.* Springer-Verlag Telos, 2001.

[54] C. Fetita and F. Prteux. Three-dimensional reconstruction of human bronchial tree in HRCT. In *Proceedings of SPIE Conference on Nonlinear Image Processing X, IS&T/SPIE's Electronic Imaging 99, San Jose, CA*, pages 281–295, January 1999.

[55] M. Filipiak. Mesh generation.
http://citeseer.nj.nec.com/heckbert97survey.html.

[56] J.B. Fink, P. Uster, D. Schmidt, and M Simon. In vitro characteristics of the AeroNeb portable nebulizer system. In *Proceeding of 13th International Congress on Aerosols in Medicine*, September 2001.

[57] W.H. Finlay, C.F. Lange, and M. Hoskinson. Validating deposition models in disease: What is needed? *Journal of Aerosol Medicine*, 13:381–385, 2000.

[58] W.H. Finlay. *The mechanics of inhaled pharmaceutical aerosols: An introduction.* Academic press, Bath UK., 2001.

[59] J.S. Fleming, A.H. Hashish, J.H. Conway, N.A. Nassim, S.T. Holgate, E. Moore, A.G. Bailey, and T.B. Martonen. Assessment of deposition of inhaled aerosol in respiratory tract of man using three dimensional multi-modality imaging and mathematical modeling. *Journal of Aerosol Medicine*, 9:317–327, 1996.

[60] FLUENT Dynamics International Inc. *FLUENT 5.2 User Guide.* 1998.

[61] FLUENT Dynamics International Inc. *GAMBIT 2.0 User Guide.* 2001.

[62] T.F. Fok, S. Monkman, M. Dolovich, S. Gray, G. Coates, B. Paes, F. Rashid, M. Newhouse, and Kirpalani H. Efficiency of aerosol medication delivery from a metered-dose inhaler versus jet nebulizer in infants with bronchopulmonary dysplasia. *Pediatric Pulmonary*, 21:301–309, 1996.

[63] D.A. Fraser. The deposition of unipolar charge particles in the lung of animals. *Archives of Environmental Health*, 13:152–157, 1966.

[64] B.W.J. Freund. The Respimat system (BINEB): A new approach to inhalation therapy. *Journal of Aerosol Medicine*, 10:246, 1997.

[65] H. Fuchs, Z.M. Keden, and S.P. Uselton. Optimal reconstruction from planar contours. *Comunications of ACM*, 20:693–702, 1977.

[66] N.A. Fuchs. *The Mechanics of Aerosols.* Dover,New York, 1964.

[67] K.K. Gast, M.U. Puderbach, I. Rodriguez, B. Eberle, K. Markstaller, Hanke A.T., J. Schiedeskamp, J. Weiler, N. amd Lill, W.G. Schreiber,

M. Thelen, and H.U. Kauczor. Dynamic ventilation 3He-MRI with lung motion correction: Gas flow distribution analysis. *Invest Radiology*, 37:126–134, 2002.

[68] GlaxoSmithKline. Product: Relenza (using Diskhaler). http://www.gsk.com/products/relenza_us.htm.

[69] R.C. Gonzalez and R.E. Woods. *Digital Image Processing*. Addison-Wesley Publishing company, Reading, MA, 1993.

[70] L. Gradon and Orlicki. Deposition of inhaled aerosol particles in a generation of the tracheobronchial tree. *Journal of Aerosol Science*, 21:3–19, 1990.

[71] L. Greengard and V. Rokhlin. A fast algorithm for particle simulations. *Journal of Computational Physics*, 73:187–207, 1987.

[72] B.J. Greenspan. Anatomy and physiology of respiratory tract. In *Inhalation drug delivery: Principles, techniques, and applications product development (AAPS Short course)*, November 1995.

[73] X. Guan and T.B. Martonen. Flow transition in bends and applications to airways. *Journal of Aerosol Science*, 31:833–847, 2000.

[74] B Haefeli-Bleuer and E.R. Weibel. Morphometry of the human pulmonary acinus. *The Anatomical Record*, 220:401–414, 1988.

[75] Harlow-1964. The particle-in-cell computing method in fluid dynamics. *Methods in Computational Physics*, 3:319, 1964.

[76] G.T. Herman and H.K. Liu. Three dimensional display of human organs from computed tomograms. *Computer Graphic and Image Processing*, 9:1–21, 1979.

[77] D.R. Hess. Nebulizers: Principles and performance. *Respiratory Care*, 45:609–622, 2000.

[78] J Heyder, J.D. Blanchard, H.A. Feldman, and J.D. Brain. Convective mixing in human respiratory tract: estimates with aerosol boli. *Journal of Applied Physiology*, 64:1273–1278, 1988.

[79] J. Heyder, J. Gebhart, and G. Scheuch. Interaction of diffusion and gravitational transport in aerosols. *Aerosol Science and Technology*, 4:315–326, 1985.

[80] J. Heyder and G. Rudolph. Mathematical models of particle deposition in the human respiratory tract. *Journal of Aerosol Science*, 15:697–707, 1984.

[81] J. Heyder and M.U. Svartengren. Basic principles of particle behavior in the human respiratory tract. *Lung Biology in Health and Disease: Drug Delivery to the Lung (Edited by Bisgaard, H.)*, 162:21–45, 2002.

[82] J. Heyder. Gravitational deposition of aerosol particles within a system of randomly oriented tubes. *Journal of Aerosol science*, 6:133–137, 1975.

[83] W.C. Hinds. *Aerosol Technology: Properties, Behavior, and Measurement of airborne particles.* John Wiley and Sons Inc, NY, 1998.

[84] R.W. Hockney and J. W. Eastwood. *Computer simulation using particles.* Adam Hilger, PA. USA., 1988.

[85] L. Hoffman and H. Smithline. Comparison of Circulaire to conventional small volume nebulizer for the treatment of bronchospasm in the emergency department. *Respiratory Care*, 42:1170–1174, 1997.

[86] W. Hofmann and L. Koblinger. Monte Carlo modeling of aerosol deposition in human lungs: Part 2 Deposition fraction and their sensitivity to parameter variation. *Journal of Aerosol Science*, 21:675–688, 1990.

[87] W. Hofmann, T.B. Martonen, and R.C. Graham. Predicted deposition of nonhygroscopic aerosols in the human lungs as a function of age. *Journal of Aerosol Medicine*, 2:49–68, 1989.

[88] D.G. Holmes and D.D. Snyder. The generation of unstructured triangular meshes using Delaunay triangulation. *Numerical Grid Generation in Computational Fluid Mechanics (Edited by Sengupta, et. al.)*, pages 643–652, 1988.

[89] H. Hoppe. Progressive meshes. *ACM Computer Graphics* , SIGGRAPH:99–108, 1996.

[90] K. Horsefield and G. Cumming. Morphology of the bronchial tree in man. *Journal of Applied Physiology*, 24:373–383, 1968.

[91] K. Horsefield, G. Dart, D.E. Olsen, G.F. Filley, and G. Cumming. Models of the human bronchial tree. *Journal of Applied Physiology*, 31:207–217, 1971.

[92] D.B. Ingham. Diffusion of aerosols from a stream flowing through a cylindrical tube. *Journal of Aerosol Science*, 6:125–132, 1975.

[93] Innovata Biomed (ML Laboratories Plc.). Products: Clickhaler. http://www.innovata-biomed.com/.

[94] Intelligent Light Inc. *FIELDVIEW 8.0 User's guide.* 2002.

[95] H. Itoh, Y. Ishii, H. Maeda, G. Toso, K. Torizuka, and Smalldone. Clinical observations of aerosol deposition in patients with airways obstruction. *Chest*, 80(suppl):837–840, 1981.

[96] A.K. Jain. *Fundamentals of digital image processing.* Prentice Hall, Englewood Cliffs, NJ, 1989.

[97] J.R. Johnston, K.D. Isles, and D.C.F. Muir. Inertial deposition of particles in human branching airways. *Inhaled Particles IV (Edited by Walton, W.H.)*, pages 61–73, 1977.

[98] I.M. Katz and T.B. Martonen. A numerical study of particle motion within the human larynx and trachea. *Journal of Aerosol Science*, 30:173–183, 1999.

[99] I.M. Katz. Computer modeling of fluid dynamics and particle motion in the larynx and trachea. *Medical Applications of Computer Modelling: The respiratory system (Edited by Martonen, T.B.)*, pages 47–63, 2001.

[100] H.U. Kauczor, A. Hanke, and Van B.ERJ. Assessment of lung ventilation by MR imaging: current status and future perspectives. *European Radiology*, 12:1962–1970, 2002.

[101] E. Keppel. Approximating complex surface by triangulation of contour lines. *IBM Journal of Research and Developement*, 19:2–11, 1975.

[102] C.S. Kim, L.K. Brown, G.C. Lewars, and M.A. Sackner. Deposition of aerosol particles and flow resistance in mathematical and experimental airway models. *Journal of Applied Physiology*, 55:154–163, 1983.

[103] C.S. Kim, D.M. Fisher, D.J. Lutz, and T.R. Gerrity. Particle deposition in bifurcating airway models with varying airway geometry. *Journal of Aerosol Science*, 25:567–581, 1994.

[104] C.S. Kim and D.M. Fisher. Deposition characteristics of aerosol particles in sequentially bifurcating airway models. *Aerosol Science and Technology*, 31:198–220, 1999.

[105] C.S. Kim and Iglesias. Deposition of inhaled particles in bifurcating airways model: Part 1 Inspiratory deposition. *Journal of Aerosol Medicine*, 2:1–14, 1989.

[106] H. Kitaoka, R. Takaki, and B Suki. A three-dimensional model of the human airway tree. *Journal of Applied Physiology*, 87:2207–2217, 1999.

[107] L. Koblinger and W. Hofmann. Analysis of human-lung morphometric data for stochastic aerosol deposition calculation. *Physics in Medicine and Biology*, 30:541–556, 1985.

[108] L. Koblinger and W. Hofmann. Monte Carlo modeling of aerosol deposition in human lungs: Part 1 Simulation of particle transport in a stochastic lung structure. *Journal of Aerosol Science*, 21:664–674, 1990.

[109] J. Kulon. *Real-time measurement of bipolar charge distribution on pharmaceutical aerosols and powders using phase doppler anemometry and a bipolar charge measurement system.* PhD Thesis, Dept. Systems Engineering, Brunel University, 2003.

[110] H.D. Landahl. On the removal of airborne droplets by the human respiratory tract. Part 1 the lung. *Bulletin of Mathematical Biology*, 12:43–56, 1950.

[111] B.P. Lathi. *Linear systems and signals.* Oxford University Press Inc., USA, 2001.

[112] B.L. Laube, J.M. Links, N.D. LaFrance, H.N. Wagner, and B.J. Rosenstein. Homogeneity of bronchopulmonary distribution of ^{99}mTc aerosol in normal subjects and cystic fibrosis patients. *Chest*, 95:822–830, 1989.

[113] C. Leach. Enhanced drug delivery through reformulating MDIs with HFA propellants-drug deposition and its effect on preclinical and clinical programs. In *Proceeding of Respiratory Drug Delivery V. (Buffalo Grove)*, pages 133–144, 1996.

[114] R. A. Lewis. *Factors influencing delivery of and response to nebulised solutions.* DM Thesis, Dept. of Medicine, Southampton General Hospital, 1985.

[115] A. Li and G. Ahmadi. Dispersion and deposition of spherical particles from point sources in a turbulent channel flow. *Aerosol Science and Technology*, 16:209–226, 1992.

[116] A. Li and G. Ahmadi. Computer simulation of particle deposition in the upper tracheobronchial tree. *Aerosol Science and Technology*, 23:201–223, 1995.

[117] W.I. Li, M. Perzl, G.A. Ferron, R. Batgeky, J. Heyder, and D.A. Edward. The macrotransport properties of aerosol particles in the human oral-pharyngeal region. *Journal of Aerosol Science*, 29:995–1010, 1998.

[118] W.E. Lorensen and H.E. Cline. Marching cubes: A high resolution 3D surface construction algorithm. *Computer Graphics*, 21:136–169, 1987.

[119] E. Loth. Numerical approaches for motion of dispersed particles, droplets and bubbles. *Progress in Energy and Combusion Science*, 26:161–223, 2000.

[120] Lunar company. Aradigm SmartMist. http://www.lunar.com/portfolio/client_archive/aradigm.html.

[121] J. Maintz and M. Viergever. A survey of medical image registration. *Medical Image Analysis*, 2(1):1–36, 1998.

[122] T.B. Martonen, Z. Zhang, and Z.Q. Xue. Effects of carinal ridge shapes on lung airstreams. *Aerosol science and Technology*, 21:119–136, 1994.

[123] T.B. Martonen, Z. Zhang, G. Yue, and C.J. Musante. 3D particle transport within the upper respiratory tract. *Journal of Aerosol Science*, 33:1095–1110, 2002.

[124] Materialise Inc. Mimics software. http://www.materialise.com/mimics/main_ENG.html.

[125] D.J. Mavriplis. Adaptive mesh generation for viscous flows using Delaunay triangulation. *Journal of Computational Physics*, 90:271–291, 1990.

[126] M.K. Mazumder, C.U. Yurteri, G. Ahuja, N. Grable, H.K. Chan, and N. Chew. Bipolar electrostatic charging of fine pharmaceutical powders by dispersion and transport processes and its implications to lung deposition of inhaled DPI aerosol. In *Proceeding of Respiratory Drug Delivery VIII*, pages 667–670, Tucson, Arizona 2002.

[127] K. McCormack, B.S. Brook, R. Hose, J.M. Wild, E.J.R. Van Beek, and T.W. Higenbottam. A complete mathematical model of pulmonary drug uptake. In *Proceedings of Drug Delivery to the lungs XIV*, page 66, December 2003.

[128] C. Melandri, V. Prodi, G. Tarroni, M. Formignani, Bompane F. DeZaiacomo, T., and Maestri G. On the deposition of unipolary charged particles in the human respiratory tract. *Inhalation Particles IV (edited by Walton WH)*, pages 193–201, 1977.

[129] C. Melandri, G. Tarroni, V. Prodi, T. De Zaiacomo, M. Formignani, and P. Bassi. Deposition of charged particles in the human airways. *Journal of Aerosol Science*, 14:657–669, 1983.

[130] W.C. Miller, J.W. Mason, and S. Small. Comparison of aerosol delivery via Circulaire system vs conventional small volume nebulizer. *Respiratory Care*, 39:1157–1161, 1994.

[131] J.D. Muller, P.L. Roe, and H. Deconinck. A frontal approach for node generation in Delaunay triangulations. *International Journal for Numerical Methods in Fluids*, 17:241–255, 1993.

[132] Netdoktor. Easyhaler. http://www.netdoktor.dk/sygdomme/fakta/astma_easyhaler.htm.

[133] S.P. Newman, J Brown, K.P. Steed, S.J. Reader, and H. Kladders. Lung deposition of Fenoterol and Flunisolide using a novel device for inhaled medication: comparison of Respimat with conventional metered-dose inhalers with and without spacer devices. *Chest*, 113:960–964, 1998.

[134] S.P. Newman and I.R. Wilding. Imaging technology techniques for assessing drug delivery in man. *Pharmaceutical Science Technology Today*, 2:181–189, 1999.

[135] S.P. Newman. Optimizing delivery of drugs to the lungs. *Clinical asthma reviews*, 2:123–128, 1998.

[136] Novartis Pharmaceuticals Corporation. Products: Foradil Aerolizer. http://www.pharma.us.novartis.com/products/name/foradil.jsp.

[137] C. O'Callaghan and P. Wright. The metered-dose inhaler. *Lung Biology in Health and Disease: Drug Delivery to the Lung (Edited by Bisgaard, H.)*, 162:337–370, 2002.

[138] U.S. National Library of Medicine. The visible human project. www.nlm.nih.gov/research/visible.

[139] OMRON Helathcare Inc. MicroAir electronic nebulizer. http://www.omronhealthcare.com/enTouchCMS/FileUplFolder/brochure.pdf.

[140] International Commission on Radiological Protection. *Human Respiratory Tract Model for Radiological Protection*, volume 66 of *Annals of ICRP*. Elsevier Science Inc., Tarrytown NY, 1994.

[141] S. Orfanidis. *Introduction to signal processing*. Prentice Hall, 1995.

[142] S. Ose. *The characterisation of bipolar electrostatic charging of powders*. PhD Thesis, Dept. Electrical engineering, University of Southampton, 2001.

[143] P.R. Owens. Turbulent flow and particle deposition in the trachea. *In circulation and respiratory mass transport (edited by G.E.W. Wolstenholme & J. Knight)*, pages 236–255, 1969.

[144] S. Owen. A survey of unstructured mesh generation technology. http://citeseer.nj.nec.com/owen98survey.html.

[145] T.J. Padley. Pulmonary fluid dynamics. *Annual Review of Fluid Mechanics*, 9:229–274, 1999.

[146] S.V. Patankar, K.C. Karki, and K.M. Kelkar. Finite volume method. *The Handbook of Fluid Dynamics (Edited by Johnson, R.W.)*, pages 27.1–27.26, 1998.

[147] R.E Pattle. The retention of gases and particles in the human nose, in: Inhaled particles and vapours. pages 302–309, 1961.

[148] PA Knowledge Limited. Technology and innovation - product and process development: Developments in inhaler technology. http://www.paconsulting.com/services/tech_innovation/pharma/magazine/entry_inhaler_technology.htm#nebulisers.

[149] J. Peart and P.R. Byron. Electrostatic properties of metered dose inhalers. In *Proceedings of the Institute of Physics conference*, pages 77–80, Oxford 1999.

[150] R.F. Phelan, R.G. Cuddihy, G.L. Fisher, O.R. Moss, R.B. Schlesinger, D.L. Swift, and H.C. Yeh. Main features of the proposed NCRP respiratory tract model. *Radiation Protection Dosimetry*, 38:179–184, 1991.

[151] P. Phipps, J. Gonda, D. Bailey, P. Borham, G. Bautovich, and S. Anderson. Comparison of planar and tomographic gamma scintigraphy to measure the penetration index of inhalation aerosols. *American Reviews of Respiratory Disease*, 139:1516–1523, 1989.

[152] J. Pich. Theory of gravitational deposition of particles from laminar flow in channels. *Journal of Aerosol Science*, 3:351–631, 1972.

[153] J. Pich. Comments on the paper: C.P. Yu's precipitaion of unipolarly charged particles in cylindrical and spherical vessels. *Jourmal of Aerosol Science*, 9:275–278, 1978.

[154] L. Piegl and W. Tiller. Geometry-based triangulation of trimmed NURBS surfaces. *Computer-Aided Design*, 30:11–18, 1998.

[155] W.H. Press, B.P. Flannery, S.A. Teukolsky, and W.T. Vetterling. *Numerical Recipes: The art of scientific computing: C.* Cambridge Univeristy Press, 1992.

[156] C.G. Rhodes and J.M.B. Hughes. Pulmonary studies using positron emission tomography. *European Respiratory Journal*, 8:1001–1017, 1995.

[157] Marsden R.J. An international multicentre randomised parallel study comparing the HaloLite AAD system with a conventional nebulizer system delivering aerosolised medication at home in cystic fibrosis. In *Proceeding of the European Cystic Fibrosis Conference, Hague, Netherlands*, June 1999.

[158] R.A. Robb. *Biomedical Imaging, Visualization, and Analysis.* John Wiley and Son Inc., 2000.

[159] G. Rudolf, J. Gebhart, C. Heyder, C.F. Schiller, and W. Stahlhofen. An empirical formula describing aerosol deposition in man for any particle size. *Journal of Aerosol Science*, 17:350–355, 1986.

[160] G. Rudolf, R. Kobrich, and W. Stahlhofen. Modelling and algebraic formulation of regional and aerosol deposition in man. *Journal of Aerosol Science*, 21(suppl. 1):S403–S406, 1990.

[161] P.W. Scherer, L.H. Shendalman, N.M. Greene, and A. Bouhuys. Measurement of axial diffusivities in a model of the bronchial airways. *Journal of Applied Physiology*, 38:719–723, 1975.

[162] C.F. Schiller-Scotland, J. Gebhart, D. Hochrainer, and R. Siekmeier. Depsoition of inspired aerosol particles within the respiratory tract of patients with obstructive lung disease. *Toxiology Letter*, 88:255–261, 1996.

[163] W. Schroeder, J. Zange, and W. Lorensen. Decimation of triangular meshes. *Computer Graphics*, 25:65–70, 1992.

[164] R.C. Schroter and M.F. Sudlow. Flow patterns in models of human bronchial airways. *Respiratory physiology*, 7:341–355, 1969.

[165] D.P. Schuster. Positron emission tomography: theory and its application to the study of lung disease. *American Reviews of Respiratory Disease*, 139:818–840, 1989.

[166] G. Schuster, S. Farr, D. Cipolla, T. Wilbanks, J. Rosell, P. Lloyd, and I. Gonda. Design and performance validation of a highly efficient and reproducible compact aerosol delivery system AERx. In *Respiratory Drug Delivery VI*, pages 83–90, 1998.

[167] G. Schuster, R. Rubsamem, and G. Lloyd. The AERx aerosol delivery system. *Pharmaceutical Research*, 14:354–357, 1997.

[168] S.F. Scott, J.A. Pryor, R.J. Marsden, T. Tat, and M.E Hodson. Non-responders to rhDNase may respond to therapy with and adaptive aerosol delivery (AAD) system. In *Proceeding of the European Cystic Fibrosis Conference*, June 2001.

[169] C.T. Shaw. *Using computational fluid dynamics*. Prentice Hall, 1992.

[170] P. Shirley and A. Tuckman. A polygonal approximation to direct scalar volume rendering. *Computer Graphics*, 24:63–70, 1990.

[171] W. Shyy and R. Mittal. Solution methods for the incompressible Navier-Stokes equations. *The Handbook of Fluid Dynamics (Edited by Johnson, R.W.)*, pages 31.1–31.33, 1998.

[172] M. Sommerfield. *Modellierung and numerische Berechnung von Partikelbeladenen turbulenten Stromung mit Hilfe des Euler/Lagrange Verfahrens.* PhD Thesis, Habilitationsschrift, University of Erlangen-Nuernburg, Shaker-Verlag, Aachen, 1994.

[173] R.M. Spencer, J.D. Schroeter, and T.B. Martonen. Computer simulations of lung airway structures using data-driven surface modeling techniques. *Computers in Biology and Medicine*, 31:499–511, 2001.

[174] C.G. Speziale and R.M. So. Turbulence modeling and simulation. *The Handbook of Fluid Dynamics (Edited by Johnson, R.W.)*, pages 14.1–14.111, 1998.

[175] R.J. Splinter. A nested grid particle mesh code for high resolutions of gravitational instability in cosmology. *Monthly Notices of the Royal Astronomical Society*, 281:281, 1996.

[176] W. Stahlhofen, J. Gebhart, and J. Heyder. Biological variability of regional deposition of aerosol particles in the human respiratory tract. *American Industrial Hygiene Association Journal*, 42:348–352, 1981.

[177] W. Stahlhofen, G. Rudolf, and A.C. James. Intercomparison of experimental regional aerosol deposition data. *Journal of Aerosol Medicine*, 2:285–308, 1989.

[178] H. Takano, M. Nakazawa, S. Torii, and M. Yoshida. Performances of a new clinical nebulizer for drug administration based on the mesh-type ultrasonic atomization by elastic surface waves. *Journal of Aerosol Medicine*, 12:98, 1999.

[179] A. Tal, H. Golan, N. Grauer, M. Aviram, D. Albin, and M.R. Quastrer. Deposition pattern of radiolabelled salbutamol inhaled from a metered-dose inhaler by means of a spacer with mask in young children with airway obstruction. *Journal of Pediatrics*, 128:479–484, 1996.

[180] G. Tarroni, C. Melandri, V. Prodi, T. De Zaiacomo, M Formignani, , and P. Bassi. Computer modeling of fluid dynamics and particle motion in the larynx and trachea. *American Industrial Hygiene Association Journal*, 41:826–831, 1980.

[181] D.B. Taulbee and C.P. Yu. A theory of aerosol deposition in the human respiratory tract. *Journal of Applied Physiology*, 131:309–320, 1975.

[182] M.H. Tawhai. *An anatomically based mathematical model of the human lungs, applied to gas mixing and water vapour and heat transport.* PhD Thesis, Department of Engineering Science, School of Engineering, The University of Auckland, 2001.

[183] S.H. Teng. Unstructed mesh generation: theory, practice, and perspectives. *International Journal of Computational Geometry and Applications*, 10:227–266, 2000.

[184] J.F. Thompson. *Numerical grid generation.* McGraw-Hill, 1985.

[185] A.C. Tooker, K.S. Hong, E.L. McKinstry, P. Costello, F.A. Jolesz, and M.S. Albert. Distal airways in humans: Dynamic hyperpolarized ^3He MR imaging - Feasibility. *Radiology*, 227:575–279, 2003.

[186] A. Tsuda, J.P. Butler, and J.J Fredberg. Effects of alveolated duct structure on aerosol kinetics: Part 1 Diffusional deposition in absence of gravity. *Journal of Applied Physiology*, 76:2497–2509, 1994.

[187] A. Tsuda, J.P. Butler, and J.J Fredberg. Effects of alveolated duct structure on aerosol kinetics: Part 2 Gravitational sedimentation and inertial impaction. *Journal of Applied Physiology*, 76:2510–2516. 1994.

[188] Y.P. Tsuo and D. Gidaspow. Computational of flow paterns in circulating fluidized beds. *AIChE Journal*, 36:885–896, 1990.

[189] G. Turk. Re-tiling polygonal surfaces. *Computer Graphics*, 26:55–64, 1992.

[190] VIATRIS GmbH and Co. Novolizer. http://www.viatris-med.de/de/patient/novolizer.

[191] J.H. Vincent, W. B. Johnston, Jones A.D., and Johnston A.M. Static electrification of airborne asbestos: a study of it causes, assessment and effects on deposition in th elungs of rat. *American Industrial Hygiene Association Journal*, 42:711–721, 1981.

[192] C.Y. Wang, J.B. Bassingthwaighte, and L.Y. Weissmann. Bifurcation distributive system using Monte Carlo method. *Mathematical and Computer Modeling*, 16:91–98, 1992.

[193] E.R. Weibel. *Morphometry of human lung.* Academic Press, 1963.

[194] WestMed Inc. Aerosol delivery. http://www.westmedinc.com/products1024.asp?HomePageID=3.

[195] J. Widdicombe and A. Davies. *Respiratory Physiology.* Edward Arnold, London, 1983.

[196] J.R. Womersley. Method for the calculation of velocity, rate of flow and viscous drag in arteries when the pressure gradient is known. *Journal of Physiology*, 127:553–563, 1955.

[197] G. Xu. A new parallel N-body gravity solver. http://arxiv.org/abs/astro-ph/9409021, September 1994.

[198] H.C. Yeh and G.M. Schum. Models of human lung airways and their application to inhaled particle deposition. *Bulletin of Mathematical Biophysics*, 42:461–480, 1980.

[199] C.U. Yurteri, M.K. Mazumder, N. Grable, G. Ahuja, S. Trigwell, A.S. Biris, R. Sharma, and R.A. Sims. Electrostatic effects on dispersion, transport and deposition of fine pharmaceutical powders: Developement of an experimental method for quantitative analysis. *Particulate Science and Technology*, 20:59–79, 2002.

[200] C.P. Yu and C.K. Diu. A comparative study of aerosol deposition in different lung models. *American Industrial Hygiene Association Journal*, 43:54–65, 1982.

[201] C.P. Yu and C.K. Diu. A probabilistic model for intersubject deposition variability of inhaled particles. *Aerosol Science and Technology*, 1:355–362, 1982.

[202] C.P Yu. Precipitation of unipolar charged particles in cylindrical and spherical vessels. *Journal of Aerosol Science*, 8:237–241, 1977.

[203] C.P Yu. Theories of electrostatic lung deposition of inhaled aerosols. *Annals of Occupational Hygiene*, 29:219–227, 1985.

[204] P. Zanen and B.L. Laube. Targeting the lungs with therapeutic aerosols. *Lung Biology in Health and Disease: Drug Delivery to the Lung (Edited by Bisgaard, H.)*, 162:211–268, 2002.

[205] Z. Zhang, C. Kleinstreuer, and C.S. Kim. Cyclic micron-size particle inhalation and deposition in a triple bifurcation lung airway model. *Journal of Aerosol Science*, 33:257–281, 2002.

[206] Z. Zhang, C. Kleinstreuer, and C.S. Kim. Micro-particle transport and deposition in a human oral airway model. *Journal of Aerosol Science*, 33:1635–1652, 2002.

[207] Y. Zhao, C.T. Brunskill, and B.B. Lieber. Steady inspiratory flow in a model symmetric bifucation. *Journal of Biomechanical Engineering*, 116:488–496, 1994.